Transactions of the ASME®

Journal of Turbomachinery

Published Quarterly by The American Society of Mechanical Engineers

VOLUME 118 • NUMBER 1 • JANUARY 1996

Transactions of the ASME, Journal of Turbomachinery (ISSN 0889-504X) is published quarterly (Jan., Apr., July, Oct.) for $150.00 per year by The American Society of Mechanical Engineers, 345 East 47th Street, New York, NY 10017. Second class postage paid at New York, NY and additional mailing offices. POSTMASTER: Send address changes to Transactions of the ASME, Journal of Turbomachinery, c/o THE AMERICAN SOCIETY OF MECHANICAL ENGINEERS, 22 Law Drive, Box 2300, Fairfield, NJ 07007-2300.
CHANGES OF ADDRESS must be received at Society headquarters seven weeks before they are to be effective. Please send old label and new address.
PRICES: To members, $40.00, annually; to nonmembers, $150.00.
Add $24.00 for postage to countries outside the United States and Canada.

INDEXED by Applied Mechanics Reviews and Engineering Information, Inc.
Canadian Goods & Services Tax Registration #126148048

TECHNICAL PAPERS

ANNOUNCEMENTS

Controls and Diagnotics Committee Best 1994 Paper Award

Modeling for Control of Rotating Stall in High-Speed Multistage Axial Compressors

M. R. Feulner

G. J. Hendricks

United Technologies Research Center,
East Hartford, CT 06108

J. D. Paduano

Department of Aeronautics
and Astronautics,
Massachusetts Institute of Technology,
Cambridge, MA 02139

Using a two-dimensional compressible flow representation of axial compressor dynamics, a control-theoretic input–output model is derived, which is of general utility in rotating stall/surge active control studies. The derivation presented here begins with a review of the fluid dynamic model, which is a two-dimensional stage stacking technique that accounts for blade row pressure rise, loss, and deviation as well as blade row and interblade row compressible flow. This model is extended to include the effects of the upstream and downstream geometry and boundary conditions, and then manipulated into a transfer function form that dynamically relates actuator motion to sensor measurements. Key relationships in this input–output form are then approximated using rational polynomials. Further manipulation yields an approximate model in standard form for studying active control of rotating stall and surge. As an example of high current relevance, the transfer function from an array of jet actuators to an array of static pressure sensors is derived. Numerical examples are also presented, including a demonstration of the importance of proper choice of sensor and actuator locations, as well as a comparison between sensor types. Under a variety of conditions, it was found that sensor locations near the front of the compressor or in the downstream gap are consistently the best choices, based on a quadratic optimization criterion and a specific three-stage compressor model. The modeling and evaluation procedures presented here are a first step toward a rigorous approach to the design of active control systems for high-speed axial compressors.

1 Introduction

Considerable work has been done in recent years on modeling and controlling rotating stall and surge in axial compressors (see the review by Greitzer et al., 1992). In each of these studies, assumptions concerning the compressor operating characteristics are made, which are deemed consistent with the experimental apparatus of interest. As the technology of rotating stall and surge control becomes more advanced, and as the experiments conducted to verify the concepts become more sophisticated and realistic, the number of assumptions that can be maintained diminishes.

For example, early proof-of-concept studies in surge control (Ffowcs-Williams and Huang, 1989; Pinsley et al., 1991) assumed one-dimensional flow through the compression system. In axial compressors, however, the one-dimensional assumption is often not tenable; rotating stall instabilities are fundamentally (at least) two dimensional. Thus rotating stall control studies (Epstein et al., 1989; Paduano et al., 1993; Haynes et al., 1994) required two-dimensional models to motivate control system configuration and controller design. Demonstrations of rotating stall stabilization were conducted on low-speed compressors that exhibited behavior that was well described by linear incompressible theory; thus the assumptions of linearity and incompressibility proved to be valid for the purpose of stabilization and range extension by active control.

In high-speed compressors, which are the focus of current research, both nonlinearity and compressibility must be addressed. Nonlinear modeling of rotating stall and surge has been studied by various authors (Greitzer, 1976; McCaughan, 1989a, b; Adomaitis and Abed, 1993; Badmus et al., 1993; Mansoux et al., 1994), and may prove important to the success of stabilization efforts. Compressible modeling of the two-dimensional process, on the other hand, has received much less attention. To our knowledge, the only work on this problem has been by Bonnaure (1991) and Hendricks et al. (1993), who describe a rigorous two-dimensional, linearized, compressible analysis, which we will take as our starting point. Note that in this analysis the linearity assumption is maintained, which allows the circumferential perturbation at any axial station to be represented as a sum of sinusoidal harmonics (Paduano et al., 1990). Each harmonic perturbation develops independently in the linearized analysis, which allows modeling to be done on each circumferential harmonic separately.

In this paper, the fluid dynamic model developed by Bonnaure (1991) and Hendricks et al. (1993) is reviewed, modified, and augmented in the context of active control. Two primary steps are necessary to convert the model to one useful for active control. First, the model must be augmented to include the effects of actuator motion. The result of this process is an input–output form in the frequency (Laplace transform) domain. This form is important for control law analysis as well as for a basic understanding of the behavior of an actuated compressor.

Second, and perhaps more challenging, is the necessity to convert the model to a form that is a rational polynomial in the Laplace transform variable s. This form is essential for control system analysis and design: Rational polynomial representations are equivalent to (and routinely converted to) state-space representations, which are used in virtually every modern computational procedure for control system analysis and synthesis.

The source of irrational, or transcendental, transfer functions in axial compressors is compressibility. To understand this, first

Contributed by the International Gas Turbine Institute and presented at the 39th International Gas Turbine and Aeroengine Congress and Exposition, The Hague, The Netherlands, June 13–16, 1994. Manuscript received by the International Gas Turbine Institute February 25, 1994. Paper No. 94-GT-200. Associate Technical Editor: E. M. Greitzer.

consider the incompressible case: It has been shown both theoretically (Moore and Greitzer, 1986; Longley, 1994) and experimentally (Paduano et al., 1993; Haynes et al., 1994) that, in low-speed compressors, a finite number of eigenvalues (typically 1 to 3) can be used to completely describe the dynamic evolution of *each circumferential harmonic* of the flow perturbation. This is true because, in incompressible flow, the axial dimension of the compressor can be "solved out" of the system dynamics. When modeling compressibility, however, one introduces such effects as acoustic and convection time delays in the axial direction. The resulting dynamics are infinite dimensional (i.e., distributed) for each harmonic of the perturbation, reflecting the fact that flow variables can vary dynamically with axial distance along the duct. Similar effects occur in acoustic ducts (Takahashi et al., 1972), whose transfer functions (often called "transmission matrices") are transcendental functions of s.

Fortunately, arbitrarily accurate rational polynomial approximations to irrational transfer functions can be made. For high-speed compressors, however, this is by no means a trivial exercise, and thus model conversion constitutes the primary contribution of this paper. Eigenvalue locations and open-loop Bode plots are used to verify the approximations, and to compare the rational polynomial model to the analytical model.

The paper is organized as follows: Section 2 presents the fluid dynamics, and Section 3 describes conversion to input–output, and then rational polynomial, form. In Section 4, the rational approximate model is verified against the exact model, and several example applications are given. These examples demonstrate the model developed is useful for control system design studies in high-speed multistage compressors.

2 Review of the Compressible Model

2.1 Basic Equations. The two-dimensional compressible model is composed of one-dimensional blade row models and two-dimensional interblade row gap models, which are "stacked up" axially through the compressor using boundary conditions at each interface and closed by end conditions at the inlet and exit of the compressor ducts (see Fig. 1). Each equation is decomposed using a complex Fourier series around the annulus, which results in independent solutions for each circumferential harmonic (for details of modeling compressor dynamics with Fourier harmonics, see Paduano et al., 1990).

The blade rows are assumed to be a set of parallel one-dimensional passages with no circumferential crossflow. The one-dimensional flow equations linearized about the operating point are a set of constant coefficient equations:

Mass Continuity Equation:

$$\frac{\partial \delta\rho}{\partial t} + W\frac{\partial \delta\rho}{\partial x'} = -\rho\,\frac{\partial \delta W}{\partial x'}$$

Momentum Equation:

$$\frac{\partial \delta W}{\partial t} + W\frac{\partial \delta W}{\partial x'} = -\frac{1}{\rho}\frac{\partial \delta P}{\partial x'}$$

Energy Equation (for a perfect gas):

$$\frac{\partial \delta P}{\partial t} + W\frac{\partial \delta P}{\partial x'} = a^2\left(\frac{\partial \delta\rho}{\partial t} + W\frac{\partial \delta\rho}{\partial x'}\right)$$

where $x' = x/\cos\xi$ (ξ is the blade stagger angle). These equations can be manipulated into a wave equation in static pressure for the fluid in the blade row reference frame:

$$\left(\frac{\partial}{\partial t} + W\frac{\partial}{\partial x'}\right)^2 \delta P = a^2\,\frac{\partial^2}{\partial x'^2}\,\delta P.$$

Since the equations are linear, they can be solved by Fourier superposition; thus solutions of the form $\delta P = \sum_n A(n, x, s)e^{j(\omega+n\Omega)t}e^{jn\theta}$ are sought, where $A(n, x, s)$ is to be solved by substitution, and Ω is the rotor angular rate (solutions are in

Nomenclature

a = sound speed
$j = \sqrt{-1}$
r = rotor radius
s = Laplace variable
t = time
x = axial coordinate
x' = blade row coordinate
M = Mach number
P = pressure
S = entropy
V = velocity
W = velocity in blade row
γ = specific heat ratio
ρ = density
θ = circumferential coordinate
ξ = blade stagger
τ = time constant
Ω = rotor angular frequency
$\delta\beta$ = deviation

Subscripts and Superscripts

k = blade row or gap number
ka = gap location of actuator
ks = gap location of sensor
n = Fourier harmonic number
K = total number of blade rows
SS = steady state
T = complex conjugate transpose

PDE Solution Matrices and Vectors

$\mathbf{b}^1$ = jet actuator matrix (Eq. (12))
$\mathbf{v}$ = vector of gap unknowns (Eq. (4))
$\tilde{\mathbf{v}}$ = vector of blade row unknowns (Eq. (2))
$\mathbf{A}$ = transmission matrix (Eqs. (9) and (10))
$\mathbf{B}$ = blade row solution matrix (Eq. (2))
$\mathbf{B}_L, \mathbf{B}_T^1$ = boundary conditions matrices (Eqs. (5) and (6))
$\mathbf{D}^1$ = deviation matrix (Eq. (6))
$\mathbf{J}^1$ = jet actuator matrix (Eq. (12))
$\mathbf{N}$ = inlet condition matrix (Eq. (7))
$\mathbf{P}^1$ = total pressure loss matrix (Eq. (5))
$\mathbf{S}^1$ = sensor matrix (Eq. (13))
$\mathbf{V}$ = gap solution matrix (Eq. (4))
$\mathbf{V}_L, \mathbf{V}_T^1$ = boundary conditions matrices (Eqs. (5) and (6))
$\mathbf{X}$ = exit condition matrix (Eq. (8))

LQG Matrices and Vectors

$\mathbf{x}$ = state vector (Eq. (19))
$\mathbf{A}$ = state weighting matrix (Eq. (20))
$\mathbf{B}$ = control weighting matrix (Eq. (20))
$\mathbf{C}$ = optimal regulator gain (Eq. (20))
$\mathbf{F}, \mathbf{G}, \mathbf{H}, \mathbf{D}$ = state space representation matrices (Eq. (19))
$\mathbf{P}$ = solution to estimation Riccati equation (Eq. (20))
$\mathbf{Q}$ = process noise covariance (Eq. (20))
$\mathbf{R}$ = measurement noise covariance
$\mathbf{S}$ = solution to control Riccati equation (Eq. (20))

Acronyms

LQG = Linear Quadratic Gaussian
IGV = Inlet Guide Vanes

[1] Indicates matrices whose entries are linearization constants.

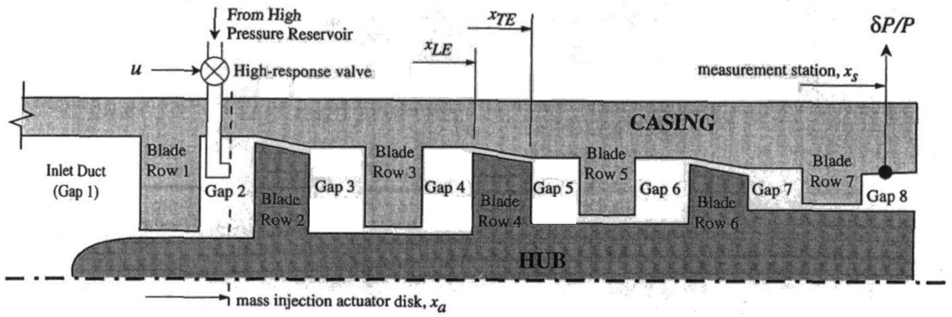

Fig. 1 Numbering of gap blade rows for stacking procedure, for a three-stage compressor with inlet guide vanes. In this example, $K = 7$, $ka = 2$, and $ks = 8$.

the stationary reference frame). Bonnaure (1991) carried out the substitution and found the following solutions:

$$\frac{\delta P}{P}(x,\theta,s) = \gamma \sum_{n=-\infty}^{\infty} [\tilde{B}_n(s)e^{\tilde{\alpha}_n(s)x} + \tilde{C}_n(s)e^{\tilde{\beta}_n(s)x}]e^{jn\theta}$$

$$\frac{\delta \rho}{\rho}(x,\theta,s) = \sum_{n=-\infty}^{\infty} [\tilde{B}_n(s)e^{\tilde{\alpha}_n(s)x} + \tilde{C}_n(s)e^{\tilde{\beta}_n(s)x} + \tilde{E}_n(s)e^{\tilde{\chi}_n(s)x}]\, e^{jn\theta}$$

$$\frac{\delta W}{a}(x,\theta,s) = \sum_{n=-\infty}^{\infty} [-\tilde{B}_n(s)e^{\tilde{\alpha}_n(s)x} + \tilde{C}_n(s)e^{\tilde{\beta}_n(s)x}]e^{jn\theta} \tag{1}$$

where the time part of the solutions has been Laplace transformed ($s = j\omega$) for use in later developments, and

$$\tilde{\alpha}_n(s) = \frac{1}{\cos\xi}\left(-\frac{jn}{r}\sin\xi + \frac{s + jn\Omega}{a - W}\right)$$

$$\tilde{\beta}_n(s) = \frac{1}{\cos\xi}\left(-\frac{jn}{r}\sin\xi - \frac{s + jn\Omega}{a + W}\right)$$

$$\tilde{\chi}_n(s) = \frac{1}{\cos\xi}\left(-\frac{jn}{r}\sin\xi - \frac{s + jn\Omega}{W}\right)$$

r is the rotor radius, ξ is the blade stagger angle, a is the local sound velocity, n is the circumferential harmonic number, and s is the Laplace transform variable. $\tilde{B}$ and $\tilde{C}$ represent upstream and downstream traveling static pressure perturbations, respectively, and $\tilde{E}$ represents entropy perturbations, which travel with the fluid velocity.

The solutions (1) are combinations of the functions $e^{\tilde{\alpha}_n(s)x}$, $e^{\tilde{\beta}_n(s)x}$, and $e^{\tilde{\chi}_n(s)x}$, which are the Laplace transforms of the various transport time delays across the blade row: $e^{\tilde{\alpha}_n(s)x}$ represents the transport time of upstream traveling pressure perturbations, $e^{\tilde{\beta}_n(s)x}$ represents the transport time of downstream traveling pressure perturbations, and $e^{\tilde{\chi}_n(s)x}$ represents the convection time of the downstream traveling entropy perturbation. The time (or s) dependence of the amplitude of each perturbation mode ($\tilde{B}$, $\tilde{C}$, and $\tilde{E}$ for the blade row) remains to be solved, as an eigenvalue problem in s, once all blade rows and gaps are interconnected.

A more compact way to write these equations is using a vector-matrix form:

$$\begin{bmatrix} \dfrac{\delta P}{P} \\ \dfrac{\delta \rho}{\rho} \\ \dfrac{\delta W}{a} \end{bmatrix}(x,\theta,s) = \sum_n e^{jn\theta}\mathbf{B}_n(x,s)\begin{bmatrix} \tilde{B}_n \\ \tilde{C}_n \\ \tilde{E}_n \end{bmatrix}(s) = \sum_n e^{jn\theta}\mathbf{B}_n(x,s)\tilde{\mathbf{v}}_n(s). \tag{2}$$

where $\mathbf{B}_n(x, s)$ is a matrix containing all of the ''known'' parts of the solution, and $\tilde{\mathbf{v}}_n(s)$ is a vector of perturbation magnitudes that are as yet unknown. The matrix form facilitates stage stacking, as well as manipulation of the equations into transfer function form; both procedures will be discussed below.

The interblade row gap and duct equations are similarly linearized and solved through the Laplace transform in time and a complex Fourier series in circumferential position. The two-dimensional solutions are (Bonnaure, 1991):

$$\frac{\delta P}{P}(x,\theta,s) = \sum_{n=-\infty}^{\infty} \gamma\left[\left(r\alpha_n(s)\mathrm{M}_x + \left(\frac{sr}{a} + jn\mathrm{M}_\theta\right)\right)B_n(s)e^{\alpha_n(s)x} + \left(r\beta_n(s)\mathrm{M}_x + \left(\frac{sr}{a} + jn\mathrm{M}_\theta\right)\right)C_n(s)e^{\beta_n(s)x}\right]e^{jn\theta}$$

$$\frac{\delta \rho}{\rho}(x,\theta,s) = \sum_{n=-\infty}^{\infty}\left[\left(r\alpha_n(s)\mathrm{M}_x + \left(\frac{sr}{a} + jn\mathrm{M}_\theta\right)\right)B_n(s)e^{\alpha_n(s)x} + \left(r\beta_n(s)\mathrm{M}_x + \left(\frac{sr}{a} + jn\mathrm{M}_\theta\right)\right)C_n(s)e^{\beta_n(s)x} + E_n(s)e^{\chi_n(s)x}\right]e^{jn\theta}$$

$$\frac{\delta V_x}{a}(x,\theta,s) = \sum_{n=-\infty}^{\infty}[-r\alpha_n(s)B_n(s)e^{\alpha_n(s)x} - r\beta_n(s)C_n(s)e^{\beta_n(s)x} + jn\mathrm{M}_x D_n(s)e^{\chi_n(s)x}]e^{jn\theta}$$

$$\frac{\delta V_\theta}{a}(x,\theta,s) = \sum_{n=-\infty}^{\infty}\left[-jnB_n(s)e^{\alpha_n(s)x} - jnC_n(s)e^{\beta_n(s)x} + \left(\frac{sr}{a} + jn\mathrm{M}_\theta\right)D_n(s)e^{\chi_n(s)x}\right]e^{jn\theta} \tag{3}$$

or, more compactly,

$$\begin{bmatrix} \dfrac{\delta P}{P} \\ \dfrac{\delta \rho}{\rho} \\ \dfrac{\delta V_x}{a} \\ \dfrac{\delta V_\theta}{a} \end{bmatrix}(x, \theta, s) = \sum_n e^{jn\theta} \mathbf{V}_n(x, s) \begin{bmatrix} B_n \\ C_n \\ D_n \\ E_n \end{bmatrix}(s)$$

$$= \sum_n e^{jn\theta} \mathbf{V}_n(x, s) \mathbf{V}_n(s) \tag{4}$$

where

$\alpha_n(s), \beta_n(s)$

$$= \frac{\mathrm{M}_x\left(\dfrac{sr}{a} + jn\mathrm{M}_\theta\right) \pm \sqrt{n^2(1 - \mathrm{M}_x^2) + \left(\dfrac{sr}{a} + jn\mathrm{M}_\theta\right)^2}}{r(1 - \mathrm{M}_x^2)}$$

$$\chi_n(s) = -\frac{\dfrac{sr}{a} + jn\mathrm{M}_\theta}{r\mathrm{M}_x}$$

M_x and M_θ are the axial and circumferential Mach numbers, B and C represent static pressure perturbations, and D and E represent vorticity and entropy perturbations, respectively.

Note that in our representation, each circumferential Fourier harmonic $e^{jn\theta}$ is an independent entity. Thus a complete model of the compressor dynamics consists of a set of independent models, each of which describes the dynamic evolution of one such harmonic. Experimental and theoretical results indicate that the first three such harmonics ($n = 1$, 2, and 3) are the most unstable and thus the most important for stability and control studies.

Although the *circumferential* space dimension is heretofore ''solved out'' of the dynamic equations by the decoupling of the harmonics, *axial* variations in the flow variables are not as easily represented. In fact, the form of Eqs. (1) and (3) yields an infinity of eigenvalues, which represent the axial continuum of flow variations. The simplification of this axial representation of the dynamics will be presented in Section 3.2.

All dependencies on the circumferential harmonic number, n, will be dropped throughout the rest of the paper for notational convenience.

2.2 Boundary Conditions. At each leading and trailing edge of a blade row, boundary conditions must be used to connect the solutions of the blade row to that of the gap or duct. The leading edge boundary conditions are continuity, relative total temperature conservation, and a relative total pressure loss characterized by a loss coefficient and a time lag. The trailing edge boundary conditions are continuity, relative total temperature conservation, relative total pressure conservation, and a deviation characterized by a deviation coefficient and a time lag. In terms of Eqs. (2) and (4) these conditions (Bonnaure, 1991) can also be written in vector-matrix form:

Leading Edge:

$$\mathbf{B}_{Lk}\mathbf{B}_k(x_{LEk}, s)\tilde{\mathbf{v}}_k(s)$$
$$= \left(\mathbf{V}_{Lk} + \frac{1}{1 + s\tau}\mathbf{P}_k\right)\mathbf{V}_k(x_{LEk}, s)\mathbf{v}_k(s) \tag{5}$$

Trailing Edge:

$$\mathbf{V}_{Tk+1}\mathbf{V}_{k+1}(x_{TEk}, s)\mathbf{v}_{k+1}(s)$$
$$= \mathbf{B}_{Tk}\mathbf{B}_k(x_{TEk}, s)\tilde{\mathbf{v}}_k(s) - \frac{1}{1 + s\tau}\mathbf{D}_k\mathbf{V}_k(x_{LEk}, s)\mathbf{v}_k(s) \tag{6}$$

where each equation is a matrix representation of the respective boundary equations (note that $\tilde{\mathbf{v}}_k(s)$ and $\mathbf{v}_k(s)$ appear in each), and the subscript k denotes the blade row or gap number. The numbering scheme for blades, gaps, and ducts is shown in Fig. 1 and used throughout. Equations (2) and (4) serve to define $\mathbf{B}_k(x, s)$, $\mathbf{V}_k(x, s)$, $\tilde{\mathbf{v}}_k$, and $\mathbf{v}_k$ for the kth blade or gap; $\mathbf{B}_{Lk}$, $\mathbf{V}_{Lk}$, $\mathbf{P}_k$, $\mathbf{B}_{Tk}$, $\mathbf{V}_{Tk}$, and $\mathbf{D}_k$ contain the (*s-independent*) coefficients, which result when the boundary conditions are linearized about the mean flow. The latter matrices allow one to incorporate the following characteristics for each blade row: the pressure rise coefficient (i.e., the slope of the pressure rise-mass flow characteristic), and the loss and deviation coefficients. We omit both the boundary condition equations and the detailed expansions of the coefficient matrices here for brevity; details appear in Feulner (1994).

End conditions are also required at the upstream end of the upstream duct and at the downstream end of the downstream duct (these ducts are represented using the gap Eqs. (3)). The end conditions depend on the compressor installation to be modeled. At the entrance to the inlet duct, we assume that total pressure is constant, and entropy and vorticity are zero. This corresponds to clean inlet conditions during an open-circuit compressor test. At the exit of the downstream duct, we assume that static pressure is constant, which models the case where the flow dumps into a plenum. These conditions can be written in vector-matrix form as well:

Upstream:

$$\begin{bmatrix} \delta(\text{total pressure}) \\ \delta(\text{entropy}) \\ \delta(\text{vorticity}) \end{bmatrix} = \begin{bmatrix} 0 \\ 0 \\ 0 \end{bmatrix} \Rightarrow \mathbf{N}(s)\mathbf{v}_1(s) = \begin{bmatrix} 0 \\ 0 \\ 0 \end{bmatrix} \tag{7}$$

Downstream:

$$\frac{\delta P}{P} = 0 \Rightarrow \mathbf{X}(s)\mathbf{v}_{K+1}(s) = 0 \tag{8}$$

where $\mathbf{X}(s)$ and $\mathbf{N}(s)$ are matrices containing the linearized end conditions combined with Eq. (4). These boundary conditions are modifications to those used by Bonnaure (1991), and are considered to be more realistic.

2.3 Solution. The overall solution can be obtained by ''stacking'' the solutions across each blade row and applying the end conditions. Figure 2 shows the way that the boundary conditions and end conditions interrelate to form the overall dynamic system. Across each blade row, the transformation is expressed as:

$$\mathbf{v}_{k+1}(s) = \mathbf{A}_k(s)\mathbf{v}_k(s) \tag{9}$$

where $\mathbf{A}_k(s)$ is obtained by eliminating $\tilde{\mathbf{v}}_k(s)$ from Eqs. (5) and (6), and solving for $\mathbf{v}_{k+1}(s)$ in terms of $\mathbf{v}_k(s)$. Note that Eqs. (5) and (6) use the transformations $\mathbf{B}_k(x, s)$ and $\mathbf{V}_k(x, s)$, which represent the dynamics of the blades and gaps, respectively. Thus $\mathbf{A}_k(s)$ represents all of the dynamics from the leading edge of blade row k to the leading edge of blade row $k + 1$. Stacking each of these transformations as in Fig. 2 results in an expression relating the inlet and exit duct solutions:

$$\mathbf{v}_{K+1}(s) = \mathbf{A}_K(s) \ldots \mathbf{A}_1(s)\mathbf{v}_1(s) = \mathbf{A}(s)\mathbf{v}_1(s) \tag{10}$$

Applying the end conditions, Eqs. (7) and (8), we get the following eigenvalue problem:

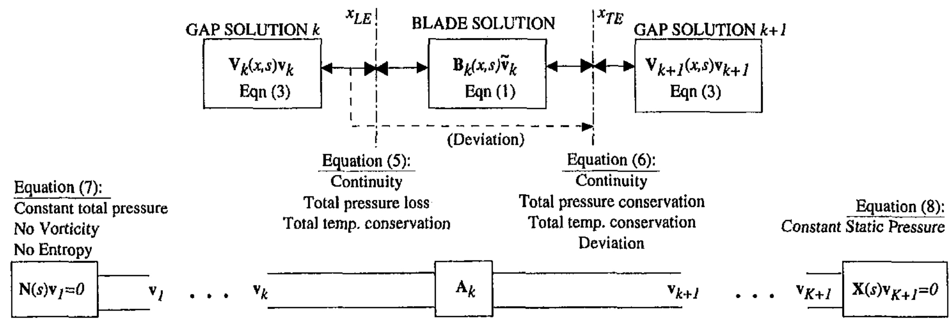

Fig. 2 Schematic of interconnections used to build system matrices. Each blade row + gap is represented by a transmission matrix $A_k(s)$. Combining A_k's and closing with boundary conditions gives homogeneous dynamics.

$$\begin{bmatrix} \mathbf{X}(s)\mathbf{A}(s) \\ \mathbf{N}(s) \end{bmatrix} \mathbf{v}_1(s) = \begin{bmatrix} 0 \\ 0 \\ 0 \\ 0 \end{bmatrix} \Rightarrow \begin{vmatrix} \mathbf{X}(s)\mathbf{A}(s) \\ \mathbf{N}(s) \end{vmatrix} = 0 \quad (11)$$

This relationship can be used to determine the stability of the system using a Nyquist contour around the entire right half plane (Bonnaure, 1991) or using a numeric search to solve for the eigenvalue locations (Hendricks et al., 1993). This numeric search requires starting with different initial guesses to converge to different eigenvalues. This can be a tedious procedure to make sure no important eigenvalues are missed. However, with an approximation to the system, utilizing rational polynomial functions instead of transcendental functions of the Laplace variable s, all of the dominant eigenvalues are determined by the eigenvalues of a single constant-coefficient matrix. A rational-polynomial approximation is useful for many other reasons, as described below.

2.4 Discussion. The model presented thus far is a modified version of that presented by Bonnaure (1991). The primary application of this form of model is stability calculations, which can be used to understand the importance of various design parameters on compressor operating range and stall inception behavior (Hendricks et al., 1993). For control law configuration and design, however, additional modifications are necessary.

Foremost is the necessity to transform the model from a homogeneous model to an input–output model. An input–output model describes *both* the homogeneous behavior (when the input is zero), and the effect of actuator motion. Such a model is necessary to incorporate the effects of feedback on the system stability. The addition of sensing and actuation to the model is presented below, and results in open-loop transfer functions for each Fourier harmonic of a given compressor.

Once an input–output form is found, one can evaluate the effects of feedback in a systematic way. For control law *design,* however, an additional modification is highly desirable. Modern control design procedures utilize state space descriptions, or equivalently, rational-polynomial based transfer functions. In Section 3 we will see that the input–output model that results from direct application of the fluid relations above contains transcendental (rather than polynomial) functions of the frequency parameter s, and thus cannot be represented using a finite number of states. To alleviate this difficulty, we will derive an approximation of the fluid-dynamic transfer function (or "truth model"). In Section 4 we will show that the approximate model is both an accurate representation of the flow physics of the truth model, and a useful form for control theoretic studies. The relative simplicity of the approximate model also makes it useful for system identification studies, which have proven to be important in rotating stall control research (Paduano et al., 1993; Haynes et al., 1994).

3 Control Theoretical Modifications

This section presents the modifications motivated by the preceding discussion. In Section 3.1, an input–output model is developed, for a specific choice of sensor and actuator type. This model is infinite dimensional, and completely captures the dynamics represented by the fluid dynamic Eqs. (1) and (3) with boundary conditions (5) and (6) and end conditions (7) and (8). This is our truth model for comparison with approximate models, and for ultimate evaluation of control system designs. In Section 3.2 the approximations are discussed. Section 4 verifies and applies the resulting approximate model.

3.1 Input–Output Model. To obtain an input–output (transfer function) model, one must choose the type and location of the actuation (inputs) and the sensors (outputs). For actuation we have chosen injection of high-momentum air, because it is predicted to be effective in controlling rotating stall (Hendricks and Gysling, 1992), and it is being implemented in current active control research compressors (see Fig. 1 for a schematic; a high-speed valve modulates the mass flow injected from a high-pressure source). For sensing (outputs), we have chosen static pressure, which is currently the most commonly sensed unsteady variable in high-speed compressors. The (injected mass)-to-(static pressure) transfer function is derived below, where actuator and sensor positions will be restricted to the interblade row gaps and the up- and downstream ducts.

The effect of a jet actuator at axial location x_a in gap number ka can be described by:

$$\mathbf{J}_{ka}\mathbf{V}_{ka}(x_a, s)\mathbf{v}_{ka,\text{downstream}}(s) = \mathbf{J}_{ka}\mathbf{V}_{ka}(x_a, s)\mathbf{v}_{ka,\text{upstream}}(s) + \mathbf{b}_{ka}u(s) \quad (12)$$

where the matrices $\mathbf{J}_{ka}$ and $\mathbf{b}_{ka}$ are the result of linearizing continuity, total temperature, and axial and circumferential momentum across an actuator disk at the air jet injection point. u is the control variable, in this case the ratio of injected mass flow to mean mass flow (Feulner, 1994). A static pressure sensor at axial location x_s in gap number ks can be described by:

$$\frac{\delta P}{P}(s) = \mathbf{S}_{ks}\mathbf{V}_{ks}(x_s, s)\mathbf{v}_{ks}(s) \quad (13)$$

where $\mathbf{S}_{ks}$ in this case is a row vector, which simply selects the first element of $\mathbf{V}_{ks}(x_s, s)\mathbf{v}_{ks}(s)$, the static pressure solution from Eq. (4). Combining the actuator in the stacking process and solving for the sensor outputs, we arrive at the following relation:

$$\frac{\delta P}{P} = (\mathbf{S}_{ks}\mathbf{V}_{ks}(x_s, s)) \times \left(\mathbf{A}_s(s) \begin{bmatrix} \mathbf{X}(s)\mathbf{A}(s) \\ \mathbf{N}(s) \end{bmatrix}^{-1} \begin{bmatrix} -\mathbf{X}(s)\mathbf{A}_a(s) \\ 0 \end{bmatrix} + \mathbf{A}_{as}(s) \right) \times (\mathbf{J}_{ka}\mathbf{V}_{ka}(x_a, s))^{-1}\mathbf{b}_{ka}u_{ka}(s) \quad (14)$$

where $\mathbf{A}_s(s) = \mathbf{A}_{ks-1}(s) \ldots \mathbf{A}_1(s)$ is the stacked solution from the inlet to the sensor, $\mathbf{A}_a(s) = \mathbf{A}_K(s) \ldots \mathbf{A}_{ka}(s)$ is the stacked solution from the actuator to the exit, and $\mathbf{A}_{as}(s) = \mathbf{A}_{ks-1}(s) \ldots \mathbf{A}_{ka}(s)$ is the stacked solution from the actuator to the sensor, or zero if the sensor is upstream of the actuator. Note that the matrix inverse is singular only at the eigenvalues of the system (Eq. (11)), which now appear as poles in our transfer function, Eq. (14), which is our truth model.

3.2 Rational Approximation of Compressible Input–Output ("Truth") Model. In this section, several of the important relationships used by the model are approximated by finite-order polynomial transfer functions. This allows the overall system to be converted to a rational approximation, or equivalently, a state-space representation, for use in control law analysis and design.

The transcendental functions to be approximated in the blade row solutions, Eq. (1), are the functions $e^{\tilde{\alpha}_n(s)x}$, $e^{\tilde{\beta}_n(s)x}$, and $e^{\tilde{\chi}_n(s)x}$. At the blade row boundaries, x is known, so the only unknown is the Laplace variable s (equivalently, the time part of the solution). For instance, $e^{\tilde{\alpha}_n(s)x}$ can be written as:

$$\exp\left[\frac{x}{\cos\xi}\left(-\frac{jn}{r}\sin\xi + \frac{jn\Omega}{a - W}\right)\right] \times \exp\left(\frac{x}{(a - W)\cos\xi}\cdot s\right).$$

Once all of the known values are evaluated, this expression is simply a complex constant times $e^{-\tau s}$, the Laplace transform of a time delay τ, which can be approximated to an arbitrary degree of accuracy using a polynomial transfer function, usually a Padé approximation (Truxal, 1958):

$$e^{-\tau s} \approx \frac{1 - a_1(\tau s) + a_2(\tau s)^2 - \ldots \pm a_q(\tau s)^q}{1 + a_1(\tau s) + a_2(\tau s)^2 + \ldots + a_q(\tau s)^q}. \quad (15)$$

Accuracy increases as the number of poles and zeros, q, increases, at the expense of increased model order and complexity. For the frequency range that is of interest for control law design of the first and second spatial harmonic, $q = 2$ yields acceptable accuracy (see Section 4.1 for details). The characteristic frequency for mode number n is Ωn, so higher order Padé approximations might be necessary to approximate higher harmonics.

The total pressure and deviation lags are already in rational polynomial form, so the next step in the approximation is to eliminate interblade row gaps. Eliminating gaps simplifies the system equations dramatically, and is valid in compressors with gaps that are short compared to the blade rows. To minimize the error introduced by this approximation, the blade rows are extended to account for the missing gap lengths. The boundary conditions for the model without gaps must of course be modified, and are as follows:

$$\mathbf{B}_k(x_{LEk}, s)\tilde{\mathbf{v}}_k(s) = \mathbf{B}_{Lk}^{-1}\left(\mathbf{V}_{Lk} + \frac{1}{1 + s\tau}\mathbf{P}_k\right)\mathbf{V}_{Tk}^{-1} \times \begin{pmatrix} \mathbf{B}_{Tk-1}\mathbf{B}_{k-1}(x_{TEk-1}, s)\tilde{\mathbf{v}}_{k-1}(s) - \\ \dfrac{1}{1 + s\tau}\mathbf{D}_{k-1}\mathbf{V}_{k-1}(x_{LEk-1}, s)\mathbf{v}_{k-1}(s) \end{pmatrix} \quad (16)$$

Notice that the relationship between $\mathbf{B}_{k-1}(x_{TEk-1}, s)\tilde{\mathbf{v}}_{k-1}$ and $\mathbf{B}_k(x_{LEk}, s)\tilde{\mathbf{v}}_k$ is a rational polynomial. The term involving the gap $k - 1$ solution, $\mathbf{V}_{k-1}(x_{LEk-1}, s)\mathbf{v}_{k-1}$, is due to the recursive nature of Eq. (6). It can be solved in terms of all the preceding blade row solutions and the inlet duct solutions, which will be approximated presently.

By assuming infinitesimal gaps, the interconnection diagram in Fig. 2 is simplified by replacing the frequency dependence of the gap solution with a constant transformation. In other words, the static pressure, density, and axial and circumferential velocities are now constant across the gap.

The final step in the approximation process is to combine the end conditions (7) and (8) with their respective boundary conditions (5) and (6), write the resulting transfer functions as ratios of analytic functions, and approximate these functions as polynomials using Taylor series expansions. For example, the exit condition, Eq. (8), combined with the trailing edge boundary condition for the last blade row, Eq. (6), can be written as:

$$\mathbf{X}(s)\mathbf{v}_{K+1}(s) = \mathbf{X}(s)(\mathbf{V}_{TK+1}\mathbf{V}_{K+1}(x_{TEK}, s))^{-1} \times \begin{pmatrix} \mathbf{B}_{TK}\mathbf{B}_K(x_{TEK}, s)\tilde{\mathbf{v}}_K(s) - \\ \dfrac{1}{1 + s\tau}\mathbf{D}_K\mathbf{V}_K(x_{LEK}, s)\mathbf{v}_K(s) \end{pmatrix} = 0 \quad (17)$$

Solving Eq. (17) for $\tilde{B}_K$, the magnitude of the upstream traveling pressure perturbation in the last blade row, in terms of the other variables, leads to the transfer functions $\tilde{B}_K/\tilde{C}_K$, $\tilde{B}_K/\tilde{E}_K$, $\tilde{B}_K/\delta\beta_K$. Each of these must be approximated by a polynomial transfer function. For example, $\tilde{B}_K/\tilde{C}_K$ is:

$$\frac{\tilde{B}_K(s)}{\tilde{C}_K(s)} = \frac{d_c\cosh(a\sqrt{y(s)}) + g_c(s)\dfrac{\sinh(a\sqrt{y(s)})}{\sqrt{y(s)}}}{d_b\cosh(a\sqrt{y(s)}) + g_b(s)\dfrac{\sinh(a\sqrt{y(s)})}{\sqrt{y(s)}}} \quad (18)$$

where d_b, d_c, and a are constants, g_b and g_c are polynomials in s, and

$$a = \frac{1}{1 - \mathrm{M}_x^2}\frac{\Delta x}{r}$$

$$y(s) = n^2(1 - \mathrm{M}_x^2) + \left(\frac{sr}{a} + jn\mathrm{M}_\theta\right)^2$$

Using Taylor series in the numerator and the denominator, one can derive a rational polynomial approximation for this equation:

$$\frac{\hat{B}_K(s)}{\tilde{C}_K(s)} \approx \frac{b_0 + b_1 s + b_2 s^2 + \ldots}{c_0 + c_1 s + c_2 s^2 + \ldots}$$

Approximating all of the relevant transfer functions in this way leads to a standard control form for the input–output dynamics.

4 Application of Control Model

In this section, we apply our control modeling and approximation techniques to a three-stage high-speed axial compressor geometry. The inputs to the procedure are the blade chords and staggers, the inlet and exit duct geometry, the mean flow conditions, and the individual blade row characteristics (pressure rise, loss, and deviation coefficients). All of these parameters were chosen to match, as closely as possible, an industrial high-speed three-stage compressor test facility.

After verifying that the control model characteristics are close approximations to the "truth" model characteristics (Section 4.1), we will turn our attention to the important question of sensor and actuator placement for feedback stabilization (Section 4.2). The primary purpose here is to demonstrate the capability provided by the control theoretical model, but we also intend to demonstrate the importance of careful choice of actuator location, sensor location, and sensor type. A method for making such choices is also developed below.

4.1 Accuracy of the Approximate Model. As a first check on the accuracy of our approximation, we can test whether its homogeneous response characteristics match those of the truth model. Similarity of the homogeneous response can be

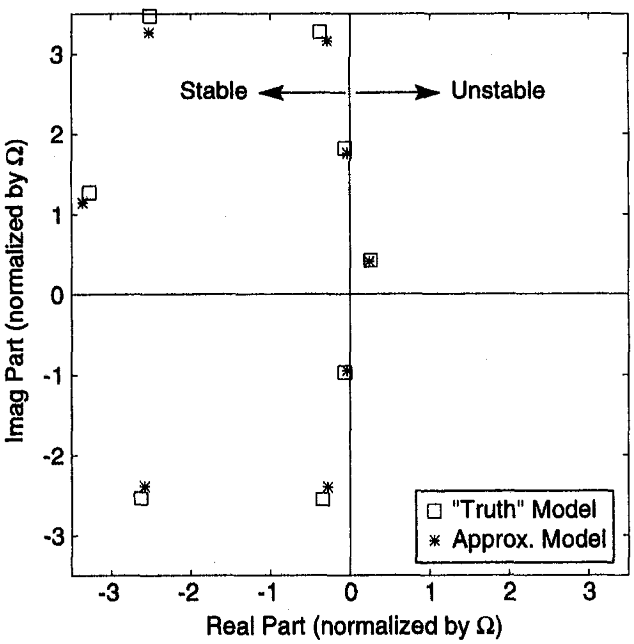

Fig. 3 Eigenvalue comparison between "truth" and approximate models

insured up to some maximum frequency by comparing the eigenvalues of the two systems up to that frequency.[2] If all of the eigenvalues are the same or similar, then the low-frequency homogeneous response characteristics will be comparable. Figure 3 shows this eigenvalue comparison, which confirms that the eigenvalue locations are nearly identical for low frequencies. At higher frequencies ($>2\Omega$) the approximate eigenvalues begin to lose accuracy, but as we will see, the difference exhibited does not have a severe adverse effect on the input–output response characteristics until well beyond 3Ω.

A more complete test of the accuracy of the approximation is to look at the forced response characteristic, or Bode plot, as a function of frequency. Such a plot incorporates both the homogeneous effects and the effects of forcing. From standard control theory (Saucedo and Shiring, 1968), we know that a control law design will remain stable if the actual model to which it is applied is not too much different from the model used for design. Typical designs exhibit more than 6 dB in gain margin and 40 deg in phase margin; this fact provides us with a rough rule of thumb for comparing the approximate model to the truth model: If the approximate model does not differ from the truth model by more than 3 dB in magnitude, and 20 deg in phase, then the model is useful for the purpose of robust controller design (especially if the truth model is used for final design validation).

Figure 4 shows a Bode plot (containing both positive and negative frequency responses) comparison of the truth model and the rational-approximate model with the actuator in gap 2 (after the first blade row) and the sensor in gap 1 (the inlet duct). Figure 4 shows a maximum difference of less than 1 dB in gain and 5 deg in phase for frequencies $<\Omega$ (rotating stall typically occurs at about one-half Ω). Therefore, the error in modeling is small compared to the desired robustness bounds in this region, and does not exceed our 3 dB/20 deg criterion until well above 3Ω.

4.2 Sensor-Actuator Placement. In this section, we briefly explore the important question of sensor and actuator placement, using the rational approximate model derived above. We will show that, in this compressor, some sensor and actuator locations are much more desirable than others. We will also see that the model is useful for sorting through the large number of options that exist, and for verifying that the best locations obtained are "robust" to variations in the input parameters, the operating conditions, and the modes to be stabilized.

In order to sort through the many combinations of actuator and sensor positions available, a performance metric must be adopted. Typically, one chooses a measure of optimality that reflects both the size of the perturbations that occur in the controlled system, and the amount of control activity required to achieve stabilization (one might also choose range extension as a performance measure, but this typically leads to nonlinear considerations, which are outside the scope of this study). A tradeoff exists between control activity reduction and perturbation magnitude reduction, so one must weight the importance of each. Also, some measure of the level of excitation and measurement noise inherent in the physical system must be provided.

Once a good set of sensor and actuator locations has been identified, it is necessary to determine the sensitivity of the result to the assumptions made. For example, the set chosen must be nearly optimal for different operating conditions, and its relative performance must not be too sensitive to the input parameters (such as the blade pressure rise, loss, and deviation characteristics). Since we expect to stabilize the second and perhaps the third circumferential harmonic as well as the first, we also want to choose actuator and sensor locations that are effective for these harmonics. The sensor and actuator location choice is "robust" if it remains desirable under all of these variations—stage characteristic variations, operating condition changes, and harmonics stabilized.

4.2.1 Procedure. Linear Quadratic-Gaussian (LQG) optimal control techniques will be used to measure optimality of sensor and actuator locations. LQG optimal control minimizes the mean square of a combination of control and state activity. LQG optimal controllers are known to have poor robustness to plant parameter uncertainty, so we do not expect the control law designs to be especially attractive for implementation. Solving the LQG problem does, however, allow one to determine the "best possible performance" (without regard for parameter robustness) that a given sensor/actuator pair can achieve, in the form of the LQG performance index. As such the so-called "LQG cost" is a rigorous, mean-square type measure for com-

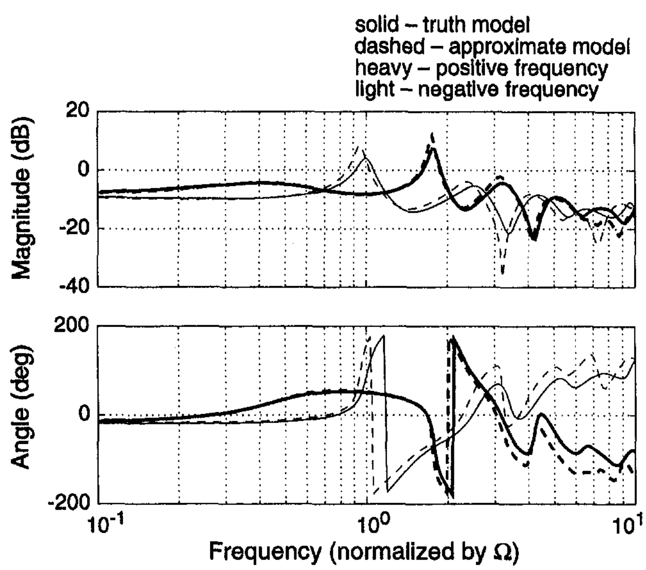

Fig. 4 Frequency response comparison between truth model and approximate model for positive and negative frequencies

[2] The desired accurate frequency range will be determined by many factors, including the bandwidth of the controller, the level of instability and frequency of the unstable eigenvalues, and the actuator dynamics.

Table 1 LQG cost, J^{SS}_{min}, nominal case

		Sensor Location (Figure 1 gap numbering scheme)							
		1	2	3	4	5	6	7	8
	1	2.05	3.67	4.12	5.56	5.53	10.06	9.22	2.37
	2	0.93	1.66	1.87	2.52	2.50	4.55	4.17	1.07
Actuator	3	1.20	2.14	2.41	3.24	3.23	5.87	5.38	1.38
Location	4	2.61	4.68	5.25	7.08	7.04	12.81	11.74	3.01
(cf. Fig 1)	5	3.12	5.60	6.28	8.48	8.43	15.34	14.06	3.61
	6	15.32	27.45	30.80	41.54	41.33	75.19	68.91	17.69
	7	9.19	16.46	18.46	24.90	24.78	45.08	41.31	10.60
	8	119.28	213.71	239.75	323.39	321.77	585.52	536.62	137.69

paring sensor/actuator location pairs. Once a good combination has been identified, robustness issues can be taken into account in a second control law design iteration by using, for instance, a μ-synthesis design technique (Doyle, 1983).

The first step in the procedure is to write the input–output system for a particular harmonic as a vector-matrix differential equation:

$$\dot{\mathbf{x}} = \mathbf{F}\mathbf{x} + \mathbf{G}u + \xi$$

$$\frac{\delta P}{P} = \mathbf{H}\mathbf{x} + \mathbf{D}u + \zeta \qquad (19)$$

where $\mathbf{x}$ is a vector of internal states (including pressure and velocity modes, which are not measured), and $\mathbf{F}$, $\mathbf{G}$, $\mathbf{H}$, and $\mathbf{D}$ result from the frequency-domain to state-space conversion of the rational approximate model. Such conversion is easily accomplished for any rational-polynomial transfer function (Reid, 1983). ξ and ζ are disturbance excitations, which are considered to be white noise with covariance $\mathbf{Q}$ and $\mathbf{R}$, respectively.

Using this state-space description, we can formulate and solve the standard LQG optimal control problem (Bryson and Ho, 1975). A performance index J, over a time interval t_0 to t_f, can be written:

$$J = E\left\{\frac{1}{2}\int_{t_0}^{t_f} (\mathbf{x}^T\mathbf{A}\mathbf{x} + \mathbf{u}^T\mathbf{B}\mathbf{u})dt\right\} \qquad (20)$$

where E is the expected value, and $\mathbf{A}$ and $\mathbf{B}$ are weighting matrices chosen by the designer (usually diagonal). J measures the *weighted mean-square state deviation* ($\int \mathbf{x}^T\mathbf{A}\mathbf{x}$; this could, for instance, be chosen to measure static pressure deviations), plus *the weighted mean-square actuator activity* ($\int \mathbf{u}^T\mathbf{B}\mathbf{u}$), associated with stabilizing the system (19). The solution to this optimization problem is beyond the scope of this paper, but the resulting minimum can be calculated, for $t_f - t_0$ approaching infinity (steady-state solution, SS), as:

$$J^{SS}_{min} = Tr\{\mathbf{S}\mathbf{Q} + \mathbf{C}^T\mathbf{B}\mathbf{C}\mathbf{P}\} \qquad (21)$$

where Tr is the trace, $\mathbf{C}[\mathbf{B}, \mathbf{G}, \mathbf{S}]$ is the optimal regulator gain, $\mathbf{S}[\mathbf{A}, \mathbf{B}, \mathbf{F}, \mathbf{G}]$ is the solution to the control Riccati equation, and $\mathbf{P}[\mathbf{F}, \mathbf{H}, \mathbf{Q}, \mathbf{R}]$ is the solution to the estimation Riccati equation (Bryson and Ho, 1975). Equation (21) can be used to compare different sensor and actuator location pairs, multiple sensors and actuators, different sensor types, but not different actuator types directly since different actuators will require different weightings in Eq. (20).

The procedure described above is complicated by the necessity to select state and control weightings ($\mathbf{A}$ and $\mathbf{B}$) and noise covariance matrices ($\mathbf{Q}$ and $\mathbf{R}$). $\mathbf{A}$ and $\mathbf{B}$ weight the relative importance of actuator motion and, for instance, mean square pressure fluctuations (which are modeled by $E\{\int_{t_0}^{t_f} \mathbf{x}^T\mathbf{A}\mathbf{x}dt\}$). $\mathbf{Q}$ and $\mathbf{R}$ model the size, location, and type of disturbances entering the system. Since few engineering data exist on the relative sizes of these terms, we will attempt to "bracket" the possibilities by testing several cases involving relative extremes. For instance, it is desired to have small control action so as not to saturate the jet actuator and not to recirculate too much air. It is also desired to have small state perturbations, since large perturbations lead to nonlinear behavior. To see how this tradeoff affects the choice of sensor and actuator locations, we perform the optimization both with actuator motion heavily weighted with respect to state perturbations ($\mathbf{B} \gg \mathbf{A}$), and vice versa.

4.2.2 Results. Our nominal case is as follows: The control weighting matrix $\mathbf{B}$ is chosen to be much higher than the state weighting. Both weighting matrices $\mathbf{A}$ and $\mathbf{B}$ are in the form of a constant multiplied by an identity matrix ($\mathbf{A} = \alpha\mathbf{I_A}$ and $\mathbf{B} = \beta\mathbf{I_B}$), i.e., no cross-weighting terms. The state process noise ξ is applied to the total pressure loss equation for each blade row with equal independent variance. The sensor noise ζ is chosen to be much smaller than the process noise with zero cross correlation (i.e., $\mathbf{Q}$ and $\mathbf{R}$ diagonal, $\mathbf{Q} \gg \mathbf{R}$).

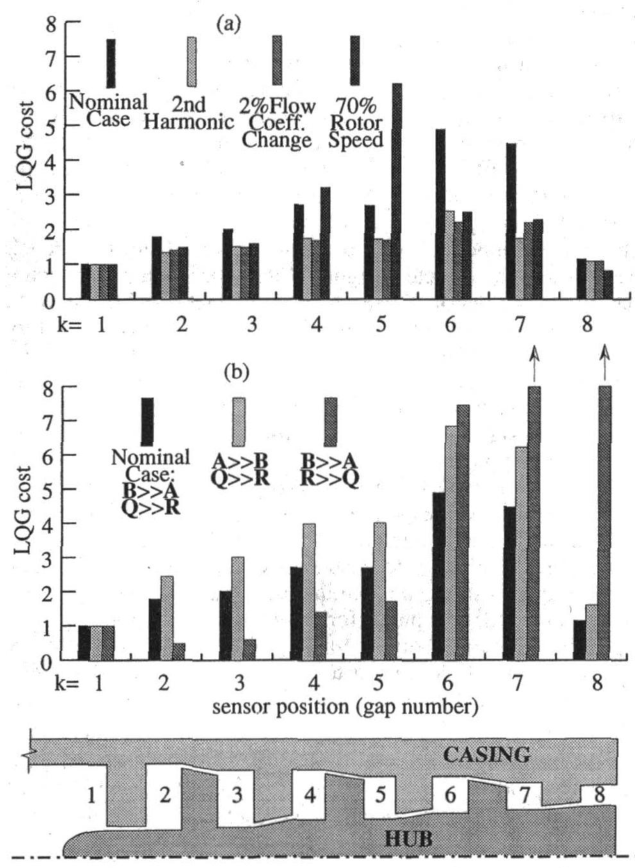

Fig. 5 Sensitivity of LQG cost to changes in test conditions. Results are normalized against station 1 costs. Actuator is at located in gap #2.

The nominal compressor operating conditions are for 100 percent design speed at a flow coefficient of 0.4506; this corresponds to the eigenvalue locations and frequency response plots in Figs. 3 and 4. Table 1 shows the costs for all of the sensor/actuator location pairs.

Table 1 clearly shows the necessity for careful choice of sensor and actuator location. For instance, placing the actuators upstream of the compressor (gap #1) yields good performance, but a factor of two improvement in the mean squared actuator motion required can be achieved by moving the actuators downstream of the inlet guide vanes (IGVs). Also note that collocation of actuators and sensors is not necessarily the best choice.

To check the sensitivity of our results to variations in the test conditions, we compare the variation of cost with sensor location for various cases. In each case, we use actuator location #2 because, based on tables such as Table 1, this appears to be the best location regardless of the test conditions. In Fig. 5(*a*), we compare the nominal case to various other cases: stabilization of the second harmonic instead of the first, stabilization at a different flow coefficient, and a stabilization at a different rotor speed. LQG costs are normalized to 1 at the front of the compressor (gap #1) to compare trends when using different assumptions. The absolute magnitudes are not important in this comparison. We conclude based on Fig. 5(*a*) that under all of the variations mentioned, sensor locations near the front of the compressor or in the downstream gap are consistently the best choices, and are therefore considered ''robust'' choices for the sensor location.

In Fig. 5(*b*) we demonstrate the insensitivity of the results to the choice of the weighting matrices **A** and **B**, as well as the noise covariance matrices **Q** and **R**. Again, the costs are normalized to 1 at gap #1. Based on Fig. 5(*b*) we conclude that, although a tradeoff exists between actuator activity and mean squared perturbation amplitudes, this tradeoff does not (in this case) strongly affect the choice of where to put the sensors. More detailed study of tables such as Table 1 indicates that the actuator location is similarly robust to the LQG cost weightings.

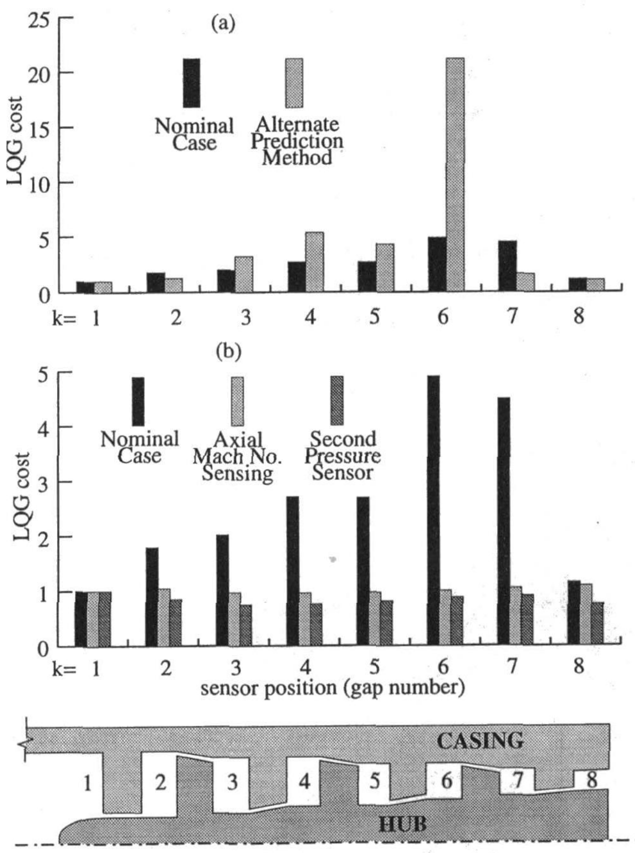

Fig. 6 Sensitivity of LQG cost to changes in test conditions. In (*a*), all costs are normalized against station 1 costs. In (*b*), costs are normalized against nominal station 1 cost. Actuator is at location 2 for all cases.

Figure 6(*a*) shows the effect on the cost of changing the mean-flow prediction method, again with costs normalized to 1 at gap #1. In the nominal case, stage characteristics supplied by the manufacturer were utilized, while in the second case, correlations (described by Hendricks et al., 1993) were utilized. Here strong variations in the costs are seen at some axial stations, demonstrating that the individual stage characteristics can have a strong effect on the behavior of the controlled system. Nevertheless, sensor locations near the front or the back of the compressor are still the most desirable, and studies not presented here indicate that actuator location choices are similarly robust.

Finally, it is of interest to look at various options for the sensor configuration. We have used static pressure sensing for our comparisons, because such sensing is relatively standard in modern high-speed compressor tests. If a different sensor type is determined to be much more attractive for active control, however, it may be desirable to develop new sensors specifically for active control. Further, we would like to know whether sensing at additional locations (i.e., at two rather than one axial station) has significant benefit. Figure 6(*b*) compares the nominal LQG costs to the costs if (1) axial velocity is sensed instead of static pressure, and (2) static pressure is measured at station 1, and an *additional sensor array* is placed at another axial station. Figure 6(*b*) is normalized by the nominal gap #1 results rather than the individual gap #1 results, since in this case all the assumptions are the same and the magnitude of the costs *between* cases is important.

The most notable difference seen in Fig. 6(*b*) between pressure and axial Mach number sensing is that axial Mach number sensing is much less sensitive to axial location than pressure sensing. This may be an important advantage during the experimental stages of stall control testing, and agrees with the general conclusion by Hendricks et al. that perturbation mass flow amplitudes are nearly uniform along the compressor, even in the case of compressible flow. Note also in Fig. 6(*b*) that a second static pressure sensor can lower the best cost by an additional 25 percent.

It is not known whether the results in Figs. 5 and 6 have more general implications for the behavior of actively controlled high-speed compressors. It is clear, however, that efforts in active control should rely on as much knowledge of the compressor dynamics as possible, because the effects on the overall performance of the controller can be highly dependent on these dynamics. The modeling and evaluation procedures presented here are a first step toward a rigorous approach to the design of active control systems for high-speed axial compressors.

5 Summary and Conclusions

A two-dimensional, compressible model of axial compressor dynamics has been extended to include the effects of the inlet and exit conditions of finite length ducts resulting in a new eigenvalue problem. This analytical model has been manipulated into an input–output form suitable for control analysis and design. By applying transcendental-to-rational transfer function approximation procedures, and by approximating the interblade row gaps as extensions of their adjacent blade rows, an approximate, finite dimensional, control-theoretical model has been derived. The resulting model is accurate in the region of the instability in the Laplace domain, which allows one to use the approximation model to deduce behavior of the analytical model.

The state-space form of the approximate model was used with the LQG performance index to identify LQG optimal axial locations for the sensors and actuators. The resulting optimal locations were found to be good for different harmonics, and were also insensitive to changes in operating conditions. The addition of a second static pressure sensor resulted in a lower (better) performance index. Finally, a comparison between axial velocity sensing and a static pressure sensing showed that axial velocity sensing yields slightly better performance and is less sensitive to axial placement.

Future modeling work will include modeling the interblade row gap equations in the rational approximate model. Approximating the gap equations directly will yield a state-space model that is even more accurate. Future control design work will include a μ-synthesis design procedure (Doyle, 1983) to increase stability robustness while still incorporating performance criteria.

6 Acknowledgments

This work was supported by the US Air Force Office of Scientific Research, James A. Fein, technical monitor. M. Feulner is supported by the Draper Laboratory Fellowship program. This support is gratefully acknowledged.

References

Adomaitis, R. A., and Abed, E. H., 1993, "Local Nonlinear Control of Stall Inception in Axial Flow Compressors," AIAA Paper #93-2230.

Badmus, O. O., Chowdhury, S., Eveker, K. M., Nett, C. N., and Rivera, C. J., 1993, "A Simplified Approach for Control of Rotating Stall, Parts I and II," AIAA Papers No. 93-2229 and 93-2234.

Bonnaure, L. P., 1991, "Modelling High Speed Multistage Compressor Stability," Masters Thesis, Massachusetts Institute of Technology, Cambridge, MA.

Bryson, A. E., and Ho, Y.-C., 1975, *Applied Optimal Control*, Hemisphere Publishing Corp., New York.

Doyle, J. C., 1983, "Synthesis of Robust Controllers and Filters," *Proc. IEEE Conf. on Decision and Control*, San Antonio, TX, pp. 109–114.

Epstein, A. H., Ffowcs-Williams, J. E., and Greitzer, E. M., 1989, "Active Suppression of Aerodynamic Instabilities in Turbomachines," *Journal of Propulsion*, Vol. 5, No. 2, pp. 204–211.

Feulner, M. T., 1994, "Modeling and Control of Rotating Stall in High Speed Multi-stage Axial Compressors," Ph.D. Thesis, Massachusetts Institute of Technology, Cambridge, MA.

Ffowcs Williams, F. E., and Huang, X., 1989, "Active Stabilization of Compressor Surge," *Journal of Fluid Mechanics*, Vol. 204, pp. 245–262.

Greitzer, E. M., 1976, "Surge and Rotating Stall in Axial Flow Compressors, Part I: Theoretical Compression System Model; Part II: Experimental Results and Comparison With Theory," ASME *Journal of Engineering for Power*, Vol. 98, pp. 190–216.

Greitzer, E. M., Epstein, A. H., Guenette, G. R., Gysling, D. L., Haynes, J., Hendricks, G. J., Paduano, J. D., Simon, J. S., and Valavani, L., 1992, "Dynamic Control of Aerodynamic Instabilities in Gas Turbine Engines," AGARD Lecture Series 183, *Steady and Transient Performance Prediction of Gas Turbine Engines*, AGARD-LS-183.

Haynes, J. M., Hendricks, G. J., and Epstein, A. H., 1994, "Active Stabilization of Rotating Stall in a Three-Stage Axial Compressor," ASME JOURNAL OF TURBOMACHINERY, Vol. 116, pp. 226–239.

Hendricks, G. J., and Gysling, D. L., 1992, "A Theoretical Study of Sensor-Actuator Schemes for Rotating Stall Control," presented at the AIAA/SAE/ASME/ASEE 28th Joint Propulsion Conference and Exhibit, Nashville, TN.

Hendricks, G. J., Bonnaure, L. P., Longley, J. P., Greitzer, E. M., and Epstein, A. H., 1993, "Analysis of Rotating Stall Onset in High-Speed Axial Flow Compressors," AIAA Paper No. 93-2233.

Longley, J. P., 1994, "A Review of Nonsteady Flow Models for Compressor Stability," ASME JOURNAL OF TURBOMACHINERY, Vol. 116, pp. 202–215.

Mansoux, C., Gysling, D. L., and Paduano, J. D., 1994, "Distributed Nonlinear Modeling and Stability Analysis of Axial Compressor Stall and Surge," *Proceedings of the 1994 American Control Conference*, Baltimore, MD, June 29.

McCaughan, F. E., 1989a, "Application of Bifurcation Theory to Axial Flow Compressor Stability," ASME JOURNAL OF TURBOMACHINERY, Vol. 111, pp. 426–433.

McCaughan, F. E., 1989b, "An Analytical and Numerical Study of Axial Flow Compressor Instability," ASME JOURNAL OF TURBOMACHINERY, Vol. 111, pp. 434–441.

Moore, F. K., and Greitzer, E. M., 1986, "A Theory of Post-Stall Transients in Axial Compression Systems: Part I—Development of Equations; Part II—Application," ASME *Journal of Engineering for Gas Turbines and Power*, Vol. 108, pp. 68–97.

Paduano, J. D., Valavani, L., Epstein, A. H., and Greitzer, E. M., 1990, "Modeling for Control of Rotating Stall," presented at the IEEE 29th Conference on Decision and Control, Dec.; *Automatica*, Vol. 30, No. 9, 1994.

Paduano, J. D., Epstein, A. H., Valavani, L., Longley, J. P., Greitzer, E. M., and Guenette, G. R., 1993a, "Active Control of Rotating Stall in a Low-Speed Axial Compressor," ASME JOURNAL OF TURBOMACHINERY, Vol. 115, pp. 48–56.

Paduano, J. D., Valavani, L., and Epstein, A. H., 1993b, "Parameter Identification of Compressor Dynamics During Closed-Loop Operation," ASME *Journal of Dynamic Systems, Measurement, and Control*, Vol. 115.

Pinsley, J. E., Guenette, G. R., Epstein, A. H., and Greitzer, E. M., 1991, "Active Stabilization of Centrifugal Compressor Surge," ASME JOURNAL OF TURBOMACHINERY, Vol. 113, pp. 723–732.

Reid, J. G., 1983, *Linear System Fundamentals*, McGraw-Hill, New York.

Saucedo, R., and Shiring, E. E., 1968, *Introduction to Continuous and Digital Control Systems*, Macmillan, New York.

Takahashi, Y., Rabins, M. J., and Auslander, D. M., 1972, *Control of Dynamic Systems*, Addison-Wesley.

Truxal, X. X., 1958, *Control Engineers Handbook*, McGraw-Hill, New York.

Heat Transfer Committee Best 1994 Paper Award

Experimental and Theoretical Investigations of Heat Transfer in Closed Gas-Filled Rotating Annuli II

D. Bohn

R. Emunds

V. Gorzelitz

U. Krüger

Institute of Steam and Gas Turbines,
Technical University of Aachen,
Aachen, Federal Republic of Germany

Increasing the thermal efficiency by higher turbine inlet temperatures is one of the most important aims in the area of gas turbine development. Because of the high temperatures, the turbine vanes and blades have to be cooled, and also knowledge of the mechanically and thermally stressed parts in the hottest zones of the rotor is of great interest. The prediction of the temperature distribution in a gas turbine rotor containing closed, gas-filled cavities, for example, in between two disks, has to account for the heat transfer conditions encountered in these cavities. In an entirely closed annulus, forced convection is not present, but a strong natural convection flow exists, induced by a nonuniform density distribution in the centrifugal force field. In Bohn et al. (1994), experimental and numerical investigations on rotating cavities with pure centripetal heat flux had been carried out. The present paper deals with investigations on a pure axially directed heat flux. An experimental setup was designed to realize a wide range of Ra numbers ($2 \cdot 10^8 < Ra < 5 \cdot 10^{10}$) usually encountered in cavities of gas turbine rotors. Parallel to the experiments, numerical calculations have been conducted. The numerical results are compared with the experimental data. The numerical scheme is also used to account for the influence of Re on heat transfer without changing Ra. This influence could not be pointed out by experiments, because a variation of the Re–Ra characteristic of the employed annuli was not possible. It was found that the numerical and experimental data are in quite good agreement, with exception of high Ra, where the numerical scheme predicts higher heat transfer than the experiments show. One reason may be that in the experiments the inner and outer cylindrical walls were not really adiabatic, an assumption used in the numerical procedure. Moreover, the assumption of a two-dimensional flow pattern may become invalid for high Ra. The influence of three-dimensional effects was studied with the three-dimensional version of the numerical code. In contrast to the radial directed heat transfer, it was found that Nu is much smaller and depends strongly on Re, whereas the radial heat transfer is only weakly influenced by Re.

Introduction

The development of gas turbines toward higher gas temperatures at the turbine inlet with a simultaneous increase of the compressor pressure ratio is a continuing trend to increase their thermal efficiency. In connection with this trend attention is being paid to the mechanically and thermally stressed parts of the gas turbine. To estimate these stresses, a proper evaluation of temperature distributions in units and components operating in the hottest zones is required. In such a zone temperature nonuniformities may lead to considerable supplementary stresses, the permissible value of which is also determined by the temperature level.

At present, only an approximate estimation of the temperature distribution in a gas turbine rotor containing gas-filled enclosures (Fig. 1) is possible. In those cavities a strong, free convective flow is induced. This convection is caused by the buoyancy force corresponding to centrifugal acceleration and temperature differences of the cavity walls. Such a flow increases the heat transfer throughout the cavities considerably.

In the past many theoretical and experimental investigations have been carried out to study the heat transfer in rotating enclosures with a throughflow of cooling fluid, e.g., Ong and Owen (1991), Farthing et al. (1992), Owen et al. (1985). For sealed cavities with a purely free convection flow, the known theoretical and experimental investigations pertain mainly to constant-temperature walls, and are limited to qualitative descriptions of the convective processes. These investigations differ with respect to the direction of the heat flux in the cavity (Fig. 2).

Most of the investigations have been performed for an axially directed heat flux applied to a cylindrical rotating enclosure, as shown in Fig. 2(I). Kapinos et al. (1981) performed experimental investigations on heat transfer in an enclosure as described above. They pointed out the influence of Coriolis forces on the fluid motion and compared their experimental results with numerical investigations given by Harada and Ozaki (1975). Abell and Hudson (1975) conducted experiments on an oil-filled rotating cylinder. They deduced a correlation between the Nusselt number and the temperature difference between the hot and cold wall of the cylindrical cavity and the rotational Reynolds number. Chew (1985) also did numerical

Contributed by the International Gas Turbine Institute and presented at the 39th International Gas Turbine and Aeroengine Congress and Exposition, The Hague, The Netherlands, June 13–16, 1994. Manuscript received by the International Gas Turbine Institute February 15, 1994. Paper No. 94-GT-175. Associate Technical Editor: E. M. Greitzer.

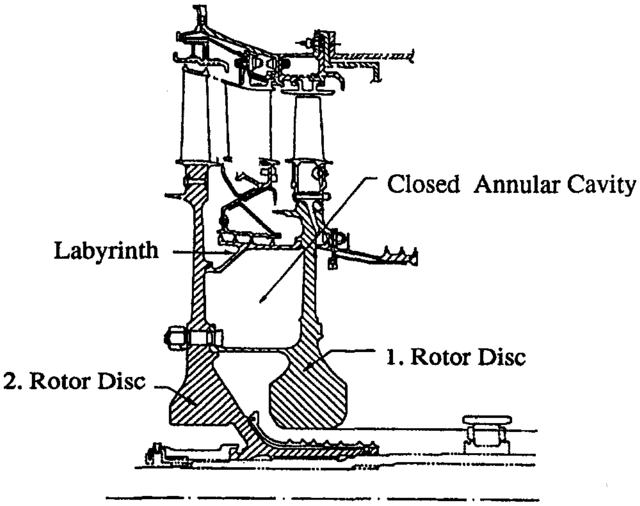

Fig. 1 Rotating enclosure in a turbine rotor

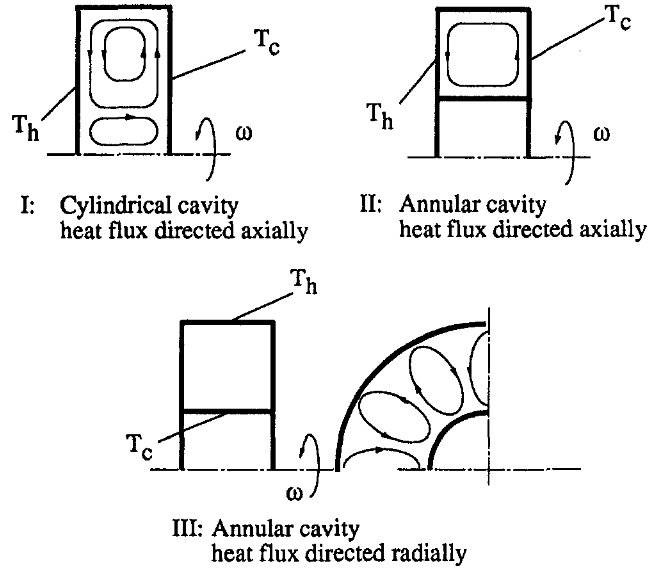

Fig. 2 Configurations of rotating enclosures

investigations on heat transfer in these enclosures, producing computations consistent with the experimental results achieved by Abell and Hudson (1975).

Investigations on rotating annular cavities, as in Fig. 2(II), were conducted by only a few authors. Most of these studies were not even performed under conditions as encountered in turbomachinery. Müller and Burch (1985) obtained measurements of the transient natural convection in an axially heated rotating annular enclosure simulating geophysical conditions. Similar experimental studies were made by Hignett et al. (1985). Bohn et al. (1994) made a first numerical study on the flow and the heat transfer in rotating cavities with a pure axial heat flux. It was pointed out that the employed numerical scheme seems to be well suited for the prediction of the physics occurring in such cavities.

Considering the heat transfer in a cavity as shown in Fig. 2(III), Lin and Preckshot (1979) calculated the temperature, velocity, and streamline distribution. Zysina-Molozhen and Salov (1977) analyzed experimentally the influence of rotational speed and various thermal boundary conditions on heat transfer in a rotating annular enclosure. The heat flux applied to the test rig was directed centripetally and photographs were taken, showing the flow pattern inside the enclosure. They note the absence of any regular fluid circulation contours in the cavity.

Experimental and theoretical investigations on the heat transfer in a closed rotating cavity with a centripetal directed heat flux were carried out in a previous paper by Bohn et al. (1995). There, the possibility of numerical prediction of the flow and the heat transfer was shown by comparison of the numerical results with the experimental data of Bohn and Gorzelitz (1992). It was found too, that the flow inside the cavity might be unstable. However, there is still a lack of knowledge on rotating sealed cavities, bounded by an outer and an inner cylindrical wall, operating under conditions valid for gas turbines.

At the Institute of Steam and Gas Turbines at the Technical University Aachen, experimental and theoretical investigations have been carried out studying the influence of heat flux direction and geometry on the convective heat transfer inside such enclosures. In this paper further experimental and numerical results of convective heat transfer in a rotating closed annulus with pure axial heat flux (Fig. 2(II)) are presented for conditions very close to turbomachinery operation.

Analyzing the basic conservation equations of mass, momentum, and energy (see below) it can be demonstrated that

$$\mathrm{Nu} = f(\mathrm{Ra}, \mathrm{Re}, \mathrm{Pr}, H/r_m, b/r_m) \qquad (1)$$

Nomenclature

a = thermal diffusivity
b = distance between lateral side walls
c_p = specific heat at constant pressure
H = distance between outer and inner cylindrical wall
L = distance between hot and cold wall ($L = H$ for heat flux directed radially, $L = b$ for heat flux directed axially)
p = pressure
$\dot{q}$ = heat flux from hot to cold wall
$\dot{q}_\lambda$ = heat transfer by conduction alone
r = radius
R = gas constant
T = temperature
ΔT = temperature difference between hot and cold walls
(x, r, φ) = axial, radial, circumferential coordinate
(u, v, w) = relative velocity components in (x, r, φ) direction
α = section angle
λ = thermal conductivity
μ = dynamic viscosity
ρ = density
ω = angular velocity of cavity
$\mathrm{Gr} = r_m \cdot \omega^2 \cdot \Delta T \cdot L^3 \cdot \rho^2 / T_m \cdot \mu^2$ = Grashof number
$\mathrm{Pr} = \mu \cdot c_p / \lambda = \mu / \rho \cdot a$ = Prandtl number
$\mathrm{Ra} = \mathrm{Gr} \cdot \mathrm{Pr}$ = Rayleigh number
$\mathrm{Re} = \rho \cdot \omega \cdot r_m \cdot L / \mu$ = Reynolds number
$\mathrm{Nu} = \dot{q} / \dot{q}_\lambda$ = Nusselt number
$\mathrm{Ec} = (\omega \cdot r_m)^2 / 2 \cdot c_p \cdot \Delta T$ = Eckert number

Subscripts

c = cold
h = hot
i = inner
m = arithmetical mean
max = maximum
min = minimum
o = outer
red = reduced
SB = solid body
w = water
0 = reference

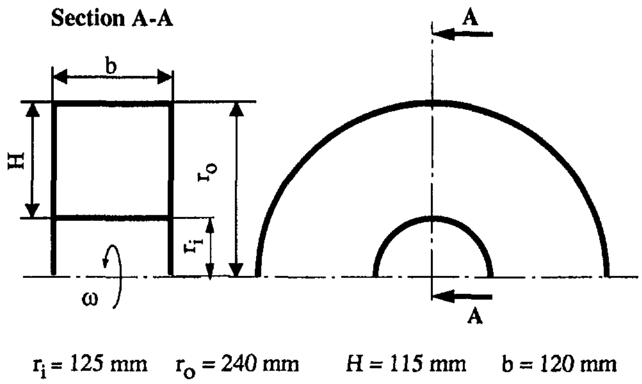

Fig. 3 Dimensions of the annular cavity

The Nusselt number (Nu) is defined as the ratio of the heat flux throughout the cavity to that flux that would occur in solid-body rotation without any motion relative to a corotating frame of reference; Thus, Nu is equal to unity for no convection and is greater than unity when convection takes place. The rotational Reynolds number (Re) has its origin in the Coriolis force terms in the momentum equations. The rotational Rayleigh number (Ra) is the product of the Grashof number and the Prandtl number and is related to the buoyancy term in the radial momentum equation. The Prandtl number (Pr) is a combination of fluid properties and does not change significantly due to temperature variations.

Experiments

Apparatus. The experimental investigations of heat transfer in a sealed rotating cavity with axially directed heat flux (case II in Fig. 2) were performed on one fixed geometric configuration. The dimensions of this enclosure are given in Fig. 3.

This geometry was used because it allowed comparison of the results with those from the radially directed heat flux investigations (Bohn et al., 1995). It has the same geometry as the cavity of configuration B in that paper. The test fluid contained in the enclosure was air. Figure 4 shows a cross section of the experimental apparatus.

The annulus is formed by two rotor disks with a cylindrical ring on the upper radius between them. The rotor shaft forms the inner cylindrical wall of the annulus. Heat input into the cavity is accomplished by an electrical heater placed at the left rotor disk. Power supply for the electrical heater is realized by a slip ring assembly. Heat is removed out of the cavity via the right rotor disc, which is cooled by water flow channels (Fig. 5).

To obtain well-defined conditions, the side walls have to be isothermal. Therefore, the electric resistance wire of the heater disk and the cooling channels of the cooling disk were designed ring-shaped (Fig. 6). Additionally, the heater disk is insulated against the rotor disk to minimize the influence of the rotor temperature distribution.

Another important condition is that the cylindrical walls should be adiabatic. So the radial cylindrical walls were also heat insulated. The cavity can be pressurized while running the rotor by using a labyrinth housing. The rotor shaft is driven by a DC motor using a belt drive. Measurements of the rotational speed are accomplished by mounting a perforated disk on the shaft and using a coil to produce a voltage spike when one of the perforations passes it. Double bearings are installed at the ends of the rotor shaft, enabling steady rotation.

The determination of the heat flux from the hot wall to the working fluid and from the fluid to the cold wall is realized by measuring the temperature differences across a thermal resistance (Fig. 5) and using the law of thermal conduction:

$$\dot{q} = -\lambda \left. \frac{dT}{dx} \right|_{x=b} \qquad (2)$$

This thermal resistance is constructed as a disk made of polymethacrylimid (PMI). Its conductivity and thickness are chosen in such a way that a sufficient temperature drop can be obtained due to the expected heat fluxes. Temperatures are measured using thin-film resistance thermometers of platinum. Seven thermoelements were radially distributed on each side of the thermal resistance, there were seven thermometers inside the heater disk and three on each side of the cylindrical walls. A telemetry unit, fixed on one end of the rotor shaft, registers the analogue signals of the resistance thermometers and converts them into digital. The digital data are transmitted out of the telemetry unit to an interface of a personal computer (RS 232 C) by a slip ring assembly.

Procedure. The procedure to get experimental results of the heat transfer in the closed rotating annulus with axial heat transfer is the same as described in the last paper Bohn et al. (1995) for heat flux directed radially. Only some technical data have been changed because of the constructional differences between the two test rigs. The maximum rotor speed was set up to 2500 rev/min. The maximum pressure was 3.5 bar and the temperature of the hot left side of the cavity was varied up to 62°C. The minimum temperature of the cooled side wall was 8°C. The temperature of the inner side of the thermal resistance depends on the absolute heat flux.

During the first experiments it was detected that the temperature on the hot side wall was not isothermal in spite of the ring-shaped electrical heater. The difference between the local and the average temperature was so large that the measurements could not be evaluated in the right way. Especially the Nusselt number, which is defined with the assumption of an isothermal wall, becomes wrong. The greatest difference occurs at the outer radius on the hot side wall (Fig. 7) because of heat losses to the rotor disk. To solve this problem, additional air heaters were applied on the outer surface of the rotor disk carrying the electrical heater.

Experimental Results. As shown above, the heat transfer can be expressed by Nu, which is given as a function of Ra, Re, Pr, H/r_m, and b/r_m. The geometry of the annulus was fixed—compare with Fig. 3—and also Pr was not varied in the present study. From Eq. (1) it can be obtained consequently that:

$$\mathrm{Nu} = f(\mathrm{Ra}, \mathrm{Re}) \qquad (2)$$

There is only a great influence of Re on Nu if the temperature ratio $\Delta T/T_m$ varies over a large range. As the temperature ratio has been varied only over a small range during the tests, Nu depends only on Ra. The influence of Re on the heat transfer, which is predicted by the numerical methods, is discussed later in this paper.

Values of Nu were obtained from the experiments by varying the temperature of the heated disk, the rotational speed, and the cavity pressure (Fig. 8).

From the experiments a heat transfer law was evaluated:

$$\mathrm{Nu} = 0.346\ \mathrm{Ra}^{0.124} \qquad (3)$$

The value of the exponent (0.124) shows that Nu depends only weakly on Ra.

Because of the very low convective heat flux—Nu has only values between four and eight—the heat transfer through the cylindrical radial walls has to be taken into account. It takes values up to 30 percent of the convective heat flux through the axial walls. The influence of the radiative heat transfer on the

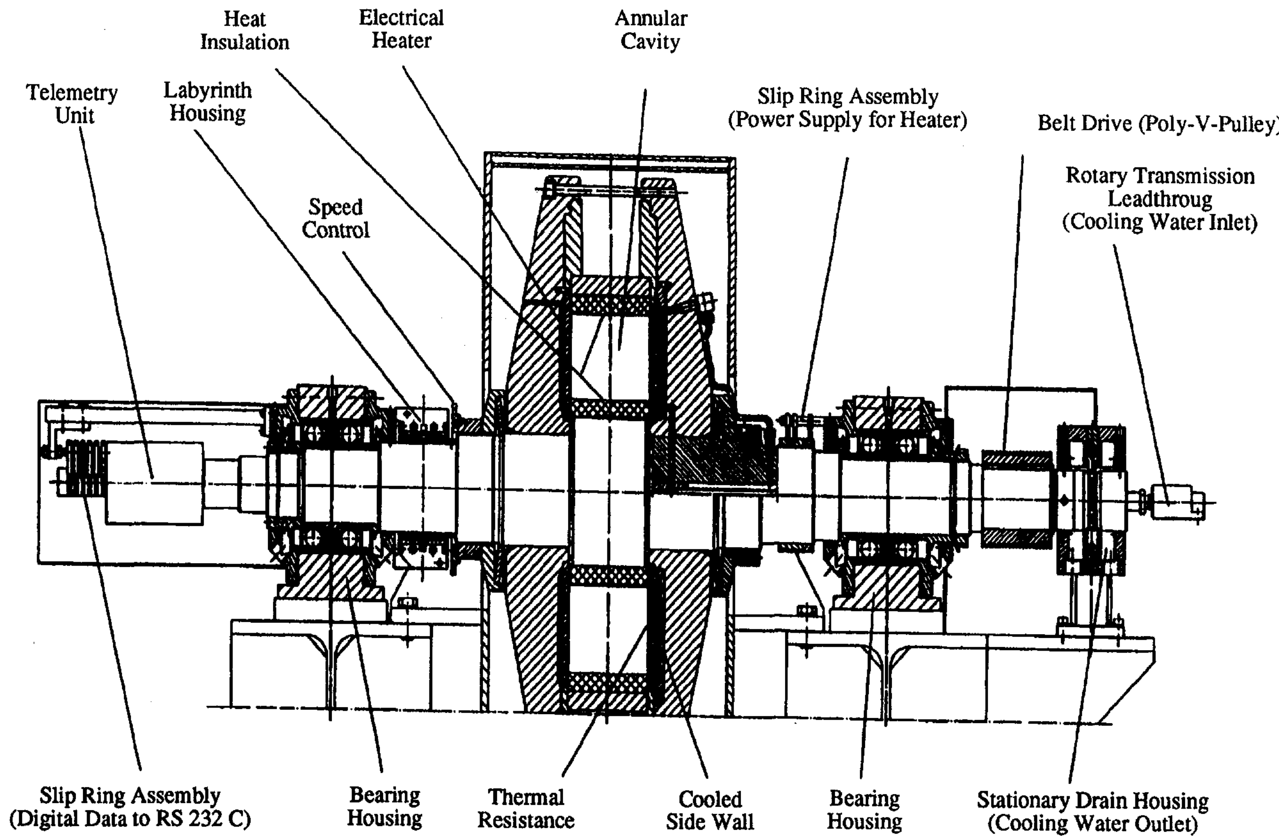

Fig. 4 Cross section of the experimental apparatus

heat flux was calculated. For Nu greater than five, this amounts less than 10 percent of the total heat flux.

In Fig. 9 the pure axial heat flux is compared to the radial one. There are only those measurements plotted that have the same ratio of $\Delta T/T_m$ and the same Re. It is clearly shown that over the whole range of Ra the heat transport in the case of pure radial heat flux is much greater than the one with pure axial heat flux. This dominance becomes stronger with increas-

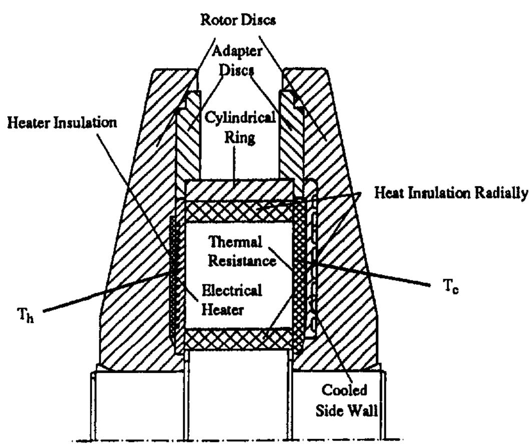

Fig. 5 Heating and cooling of the cavity

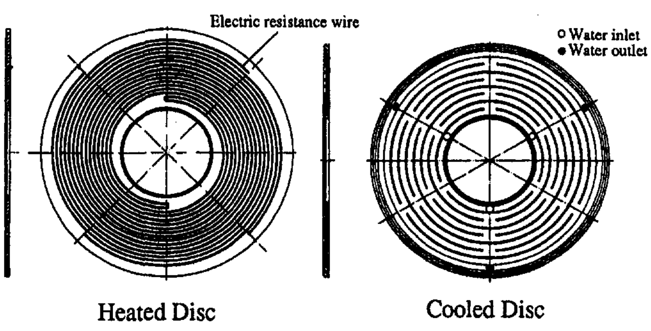

Fig. 6 Heated and cooled disk

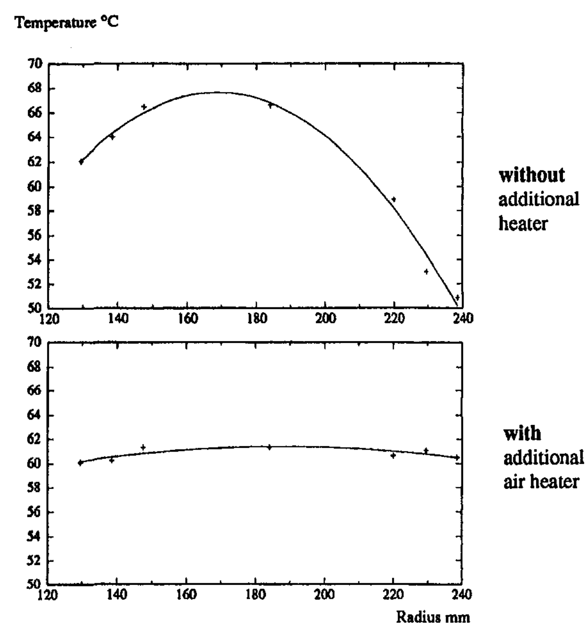

Fig. 7 Temperature distribution on the hot side wall

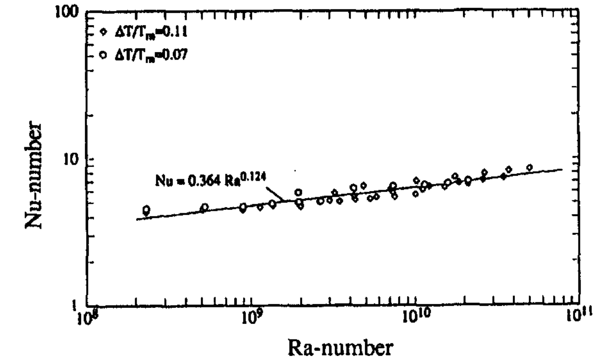

Fig. 8 Heat transfer law Nu = f(Ra) for a heat flux directed axially

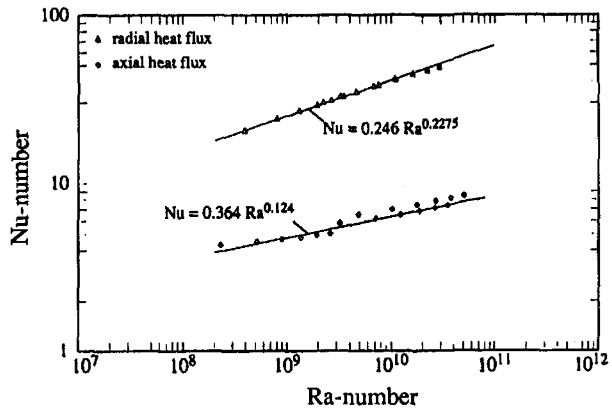

Fig. 9 Comparison between the heat directed axially and radially

ing values of the Ra. For Ra of about 2×10^8 the radial heat transfer is about a factor 2.5 larger than the axial heat transfer, for Ra $\approx 10^{11}$ this factor increases to 6. This comparison shows that the radial heat transfer is the important one for cavities with a mixture of axial and radial temperature distributions as occurring in gas-turbine rotors. Therefore, the heat loss over the radial walls has a great influence on the buoyancy-driven flow in a closed gas-filled cavity.

As explained before, only certain temperature ratios $\Delta T/T_m$ could be adjusted. The influence of the temperature ratio on the Ra–Re characteristic is shown in Fig. 10. The min/max values of $\Delta T/T_m$ are typical boundary conditions for gas turbine rotors.

To study the influence of Re on the heat transfer mechanism, the pure axial heat transfer and the radial heat transfer have

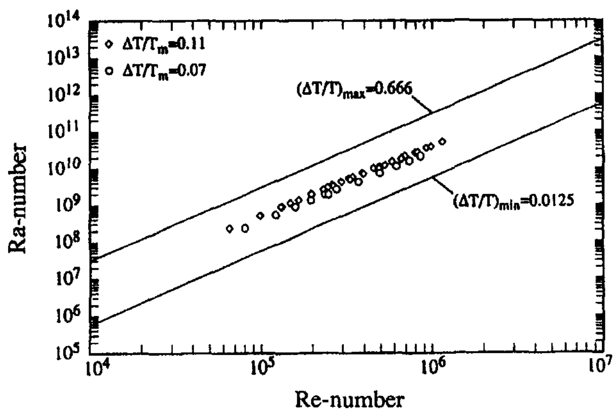

Fig. 10 Ra–Re characteristic for different $\Delta T/T_m$

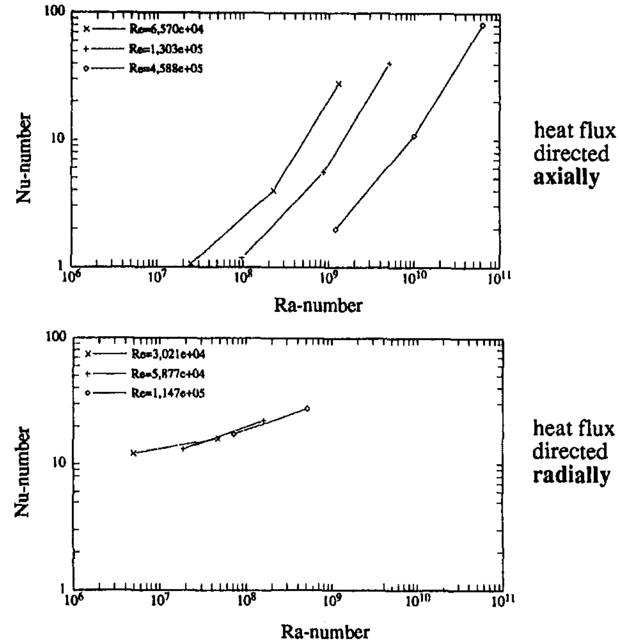

Fig. 11 Theoretical prediction of Nu numbers as a function of Ra for different Re numbers

been investigated with two-dimensional and three-dimensional numerical codes.

The results of these calculations are shown in Fig. 11, in which Nu is plotted as a function of Ra for different Re. During this analysis Re was varied over a wide range. It can be stated that the influence of Re is much lower in case of radial heat transfer than in case of axial heat transfer. The Re values differ in both cases, because they correspond to the $\Delta T/T_m$ ratios shown in Fig. 10.

Numerical Investigation

Although the geometry of the cavities under consideration is quite simple, the flow is characterized by a complex interaction of convection, viscous forces, pressure forces, buoyancy effects, and Coriolis forces. Bohn et al. (1994) analyzed flow structure and heat transfer for a test rig with a pure co-axial heat flux situation, and special attention was paid to the buoyancy and Coriolis forces, which were found to be the most important terms to determine the heat transfer. Bohn et al. (1995) carried out experimental and theoretical investigations for a pure centripetally directed heat flux situation for Ra values usually encountered in cavities of gas turbine rotors.

In the present case we started with experimental and theoretical examinations on the flow and the heat transfer for a pure co-axial heat flux situation for $2 \times 10^8 < \text{Ra} < 5 \times 10^{10}$, which is usually encountered in cavities of gas turbine rotors.

From our experiments, no information about the flow structure and only little information about the thermal conditions at the side walls can be obtained. Therefore, we restrict our numerical analysis to the idealized case of isothermal side walls and adiabatic cylindrical walls. Although this is not a common investigation of the flow pattern inside the cavity, it may highlight some basic features of this type of flow and can be considered as a basic case that is independent of special thermal conditions at the side walls.

Basic Modeling Assumptions. The co-axial heat flux was modeled assuming that the temperatures at the side walls were different but uniformly distributed, while all other walls were assumed to be adiabatic.

The computer code solves the conservation equations for mass, momentum, and energy. All computations were carried out for air, the density was calculated by the ideal gas law, and all other properties were treated as functions of temperature. Some common assumptions for natural convection flows are made: In the viscous terms of the momentum equations the compressibility is neglected because the velocities at this type of flow are very low. In the energy equation the influences of the dissipation and pressure changes are assumed to be negligible too, due to very small Ec ($Ec < 0.1$). The flow is assumed to be laminar in the range of Gr considered here. These assumptions for the axial heat flux mechanism in a rotating closed annulus with square cross section could be varified by theoretical studies (Bohn et al., 1994).

The Governing Equations. The steady-state governing equations are derived and discussed comprehensively by Bohn et al. (1994). The dimensionless form of the equations reads:

$$\frac{\partial \bar{\rho}}{\partial \bar{t}} + \frac{1}{\bar{r}}\cdot\left(\frac{\partial \bar{\rho}\bar{u}\bar{r}}{\partial \bar{x}} + \frac{\partial \bar{\rho}\bar{v}\bar{r}}{\partial \bar{r}} + \frac{\partial \bar{\rho}\bar{w}}{\partial \varphi}\right) = 0 \tag{4}$$

$$\begin{aligned}\frac{\partial \bar{\rho}\bar{u}}{\partial \bar{t}} &+ \frac{1}{\bar{r}}\left(\frac{\partial}{\partial \bar{x}}\overline{\rho r u u} + \frac{\partial}{\partial \bar{r}}\overline{\rho r v u} + \frac{\partial}{\partial \varphi}\overline{\rho w u}\right) \\ &- \frac{\mathrm{Pr}}{\bar{r}}\cdot\left(\frac{\partial}{\partial \bar{x}}\left(\bar{\mu}\bar{r}\frac{\partial \bar{u}}{\partial \bar{x}}\right) + \frac{\partial}{d\bar{r}}\left(\bar{\mu}\bar{r}\frac{\partial \bar{u}}{\partial \bar{r}}\right)\right. \\ &\left.+ \frac{\partial}{\partial \varphi}\left(\frac{\bar{\mu}}{\bar{r}}\frac{\partial \bar{u}}{\partial \varphi}\right)\right) = -\frac{\partial \bar{p}_{\mathrm{red}}}{\partial \bar{x}}\end{aligned} \tag{5}$$

$$\begin{aligned}\frac{\partial \bar{\rho}\bar{v}}{\partial \bar{t}} &+ \frac{1}{\bar{r}}\left(\frac{\partial}{\partial \bar{x}}\overline{\rho r u v} + \frac{\partial}{\partial \bar{r}}\overline{\rho r v v} + \frac{\partial}{\partial \varphi}\overline{\rho w v}\right) \\ &- \mathrm{Pr}\cdot\left(\frac{\partial}{\partial \bar{x}}\left(\bar{\mu}\bar{r}\frac{\partial \bar{v}}{\partial \bar{x}}\right) + \frac{\partial}{\partial \bar{r}}\left(\bar{\mu}\bar{r}\frac{\partial \bar{v}}{\partial \bar{r}}\right) + \frac{\partial}{\partial \varphi}\left(\frac{\bar{\mu}}{\bar{r}}\frac{\partial \bar{v}}{\partial \varphi}\right)\right) \\ &= -\frac{\partial \bar{p}_{\mathrm{red}}}{\partial \bar{r}} - \mathrm{Pr}\,\frac{\bar{\mu}}{\bar{r}^2}\left(\bar{v} + 2\frac{\partial \bar{w}}{\partial \varphi}\right) - \bar{\rho}\,\frac{\bar{w}^2}{\bar{r}} \\ &+ 2\bar{\rho}\bar{w}\,\frac{L}{r_m}\,\mathrm{Re}\cdot\mathrm{Pr} - \bar{\rho}_{SB}\bar{r}\,\frac{T_m}{T}\,\frac{L}{r_m}\,\mathrm{Ra}\cdot\mathrm{Pr}\cdot\bar{T}\end{aligned} \tag{6}$$

$$\begin{aligned}\frac{\partial \bar{\rho}\bar{w}}{\partial \bar{t}} &+ \frac{1}{\bar{r}}\left(\frac{\partial}{\partial \bar{x}}\overline{\rho r u w} + \frac{\partial}{\partial \bar{r}}\overline{\rho r v w} + \frac{\partial}{\partial \varphi}\overline{\rho w w}\right) \\ &- \mathrm{Pr}\left(\frac{\partial}{\partial \bar{x}}\left(\bar{\mu}\bar{r}\frac{\partial \bar{w}}{\partial \bar{x}}\right) + \frac{\partial}{\partial \varphi}\left(\frac{\bar{\mu}}{\bar{r}}\frac{\partial \bar{w}}{\partial \varphi}\right) + \frac{\partial}{\partial \bar{r}}\left(\bar{\mu}\bar{r}\frac{\partial \bar{w}}{\partial \bar{r}}\right)\right) \\ &= -\frac{1}{\bar{r}}\frac{\partial \bar{p}_{\mathrm{red}}}{\partial \varphi} - \mathrm{Pr}\,\frac{\bar{\mu}}{\bar{r}^2}\left(\bar{w} - 2\frac{\partial \bar{v}}{\partial \varphi}\right) \\ &- \bar{\rho}\,\frac{\overline{vw}}{\bar{r}} - 2\bar{\rho}\bar{v}\,\frac{L}{r_m}\cdot\mathrm{Re}\cdot\mathrm{Pr}\end{aligned} \tag{7}$$

$$\begin{aligned}\frac{\partial \bar{\rho}\bar{T}}{\partial \bar{t}} &+ \frac{1}{\bar{r}}\frac{\partial}{\partial \bar{x}}\left(\overline{\rho r u}\bar{T} - \frac{\bar{\lambda}\bar{r}}{\bar{c}_p}\frac{\partial \bar{T}}{\partial \bar{x}}\right) + \frac{1}{\bar{r}}\frac{\partial}{\partial \bar{r}}\left(\overline{\rho r v}\bar{T} - \frac{\bar{\lambda}\bar{r}}{\bar{c}_p}\frac{\partial \bar{T}}{\partial \bar{r}}\right) \\ &+ \frac{1}{\bar{r}}\frac{\partial}{\partial \varphi}\left(\bar{\rho}\bar{w}\bar{T} - \frac{\bar{\lambda}}{\bar{r}\bar{c}_p}\frac{\partial \bar{T}}{\partial \varphi}\right) = 0\end{aligned} \tag{8}$$

Herein Re appears within the Coriolis terms, while Ra is related to the buoyancy term. The dimensionless variables marked with an overbar are defined as:

$$u = \bar{u}\cdot\frac{a_0}{L};\quad p = \bar{p}\cdot\frac{\rho_0\cdot a_0^2}{L^2};\quad \rho = \bar{\rho}\cdot\rho_0;$$

$$T = \bar{T}\cdot\Delta T + T_m;\quad \lambda = \bar{\lambda}\cdot\lambda_0;\quad \mu = \bar{\mu}\cdot\mu_0;$$

$$c_p = \bar{c}_p\cdot c_{p0};\quad x = \bar{x}\cdot L;\quad r = \bar{r}\cdot L;\quad t = \bar{t}\cdot\frac{L^2}{a_0}$$

The fluid properties λ_0, a_0, ρ_0, μ_0, c_{p0} are evaluated for T_m as the reference temperature ($T_m = 0.5(T_h + T_c)$, see Fig. 2). They have also been used to calculate the values of Re, Ra, and Pr. To obtain the reduced pressure, defined as

$$p_{\mathrm{red}} = p - p_{SB},$$

the radial momentum equation for a rotating solid body at constant temperature is used:

$$-\frac{\partial p_{SB}}{\partial r} + \rho_{SB}\cdot\omega^2\cdot r = 0$$

$$\rho_{SB} = \frac{p_{SB}}{R\cdot T_m}$$

For the two-dimensional algorithm, the circumferential velocity component is still considered, while the circumferential derivations $\partial/\partial\varphi$ are neglected.

The Numerical Procedure. The system of coupled differential equations is solved numerically with a finite volume scheme. A nonuniform staggered grid is defined, with T and p being calculated at the main grid points and u, v, w being calculated at locations midway between the main grid points. In the employed "hybrid" approximation scheme upwind differencing is used for the convective terms when the cell Peclet number is greater than 2; otherwise central differencing is used for these terms (Patankar and Spalding, 1972).

Theoretical Results for the Closed Rotating Cavity. In Fig. 12 the temperature distribution and the flow pattern of a two-dimensional calculation for the closed rotating annulus with a pure co-axial heat flux are shown. The computation was carried out for air at $T_m = 317$ K, resulting in Pr of 0.6925 with $Ra = 2.261 \times 10^8$ and $Re = 6.57 \times 10^4$.

As described in Bohn et al. (1992) for a rotating cavity with $r_m/h = 4$, $Ra = 6.6 \times 10^6$ and $Re = 10^4$, an analogous flow situation occurs here. The fluid circulates around the walls in boundary layers, and nearly no motion occurs in the core region (see Fig. 12*b*). Due to the buoyancy force, the cold and heavy fluid at the cold side wall flows to the outer cylindrical wall. Passing this wall, the fluid is warmed up. When the fluid reaches the hot side wall, a large temperature gradient in the corner appears. Opposite temperature gradients are localized in that corner where the inner cylindrical wall meets the cold side wall. The physical mechanism is discussed more in detail in Bohn et al. (1994). Due to the theoretical investigations on the heat transfer in closed rotating annuli with pure co-axial heat flux done in the past, we proceeded with further computations using the two-dimensional version of the program code.

In Fig. 13 the comparison of the numerical results with experimental data is shown for a range $2 \times 10^8 < Ra < 10^{10}$. The result for Nu taken from the measurement is plotted with the variation given by the experimental apparatus.

It can be taken from this figure, that in case of $Ra < 2 \times 10^9$ the theoretical prediction of Nu matches well the Nu taken from experiment. Increasing Ra, the numerically predicted Nu differs more and more from Nu determined on the basis of experimental data. The reason for this is on one hand the supposition of a two-dimensional flow in the cavity and on the other hand the assumption of ideal adiabatic cylindrical side walls, which could not be realized in the experiment. Due to this it is obvious that in the experiments a mixture of an axial and a radially directed heat transfer occurs. Therefore, it is evident that the calculated Nu—based on a pure co-axial heat flux direction—must be greater than the Nu taken from experiment containing the heat losses throughout the cylindrical walls. The influence of these nonadiabatic cylindrical walls is shown in Fig. 14, where the temperature distributions along these walls are plotted.

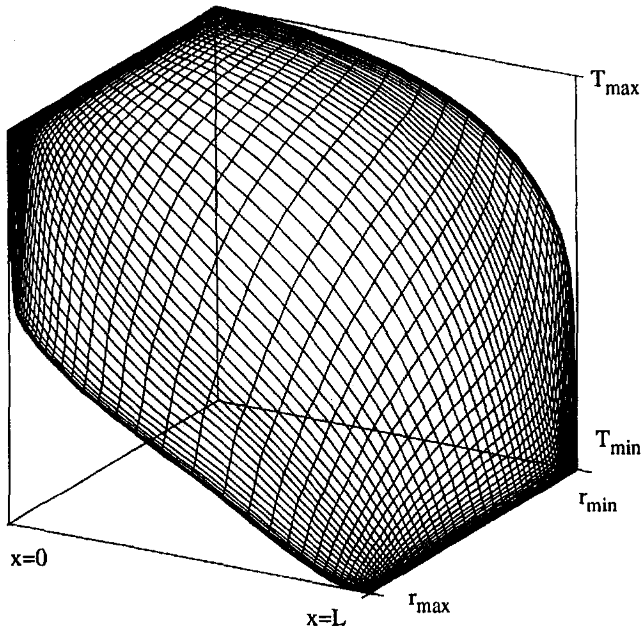

Fig. 12(*a*) Temperature distribution of a two-dimensional calculation, Re = 6.57×10^4, Ra = 2.261×10^8

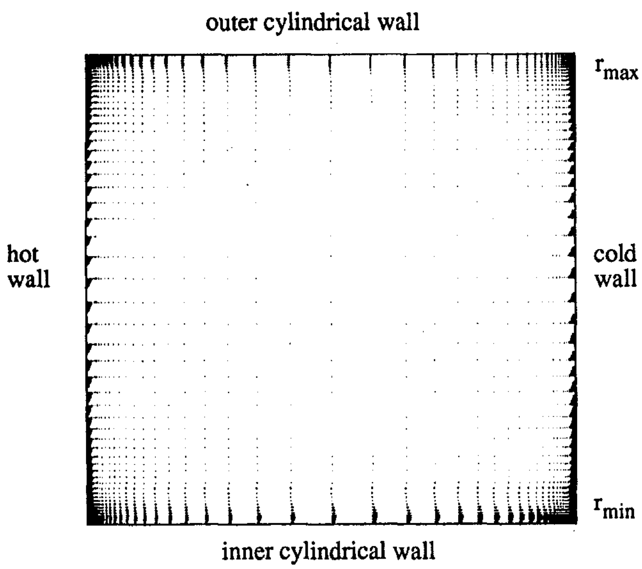

Fig. 12(*b*) Flow pattern of a two-dimensional calculation, Re = 6.57×10^4, Ra = 2.261×10^8

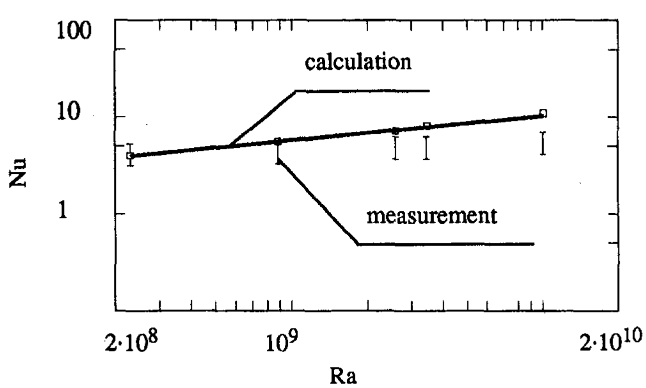

Fig. 13 Comparison of Nu obtained from experiment and two-dimensional calculation

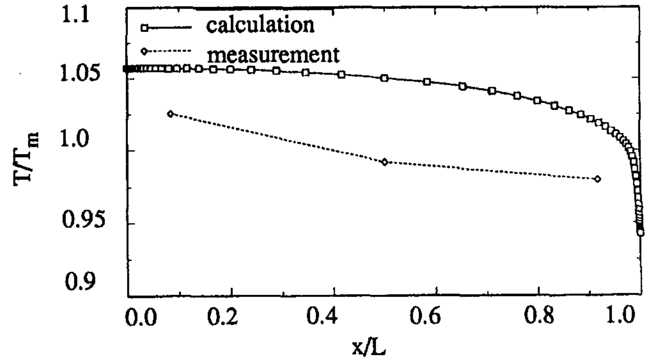

Fig. 14(*a*) Experimental and theoretical temperature distribution at the inner cylindrical wall

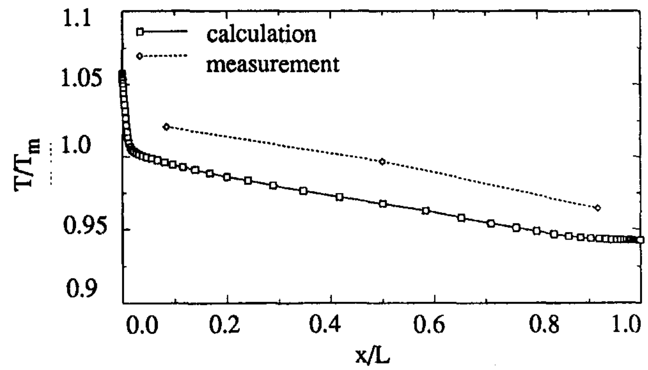

Fig. 14(*b*) Experimental and theoretical temperature distribution at the outer cylindrical wall

At the inner cylindrical wall, where the fluid flows from the hot to the cold side wall, the numerically predicted temperatures are somewhat greater than the measured ones. At the outer cylindrical wall, where the fluid flows from the cold to the hot wall, an analogous but opposite situation occurs. Due to the relatively small heat transfer throughout the cavity, the assumption of ideal adiabatic cylindrical side walls becomes significant on the overall Nu. As well known for other buoyancy-driven flows—see the Bénard problem—a critical Ra exists, at which the flow structure changes from a two-dimensional one to a three-dimensional one. To investigate such a complex flow phenomenon we used the three-dimensional code for the calculations.

The result obtained for $Nu_{3D} = 5.475$, calculated with Ra = 2.261×10^8 and Re = 6.57×10^4, differs strongly from the one taken from the two-dimensional calculation or experimental data, respectively.

In Fig. 15 results of the three-dimensional calculation for the temperature distribution are shown (for comparison see Fig. 12*a* for the two-dimensional calculation). It can be seen that the temperature distributions of both cases are similar, but in the region where the cold fluid reaches the hot wall (analogous to the region where the hot fluid reaches the cold wall) a significantly different temperature gradient occurs. In Fig. 16 the temperature distribution is plotted in an $r-\varphi$ plane for a medium axial position.

In the regions near the outer and inner cylindrical walls no circumferential temperature gradient exists. Between these regions an area with small circumferential temperature gradients occurs, indicating that another fluid motion takes place in this direction. This fluid motion may be another reason for the difference between the Nu values calculated with the two-dimensional and three-dimensional algorithms.

The difference between the results of the two-dimensional and three-dimensional calculations depends not only on Ra, but

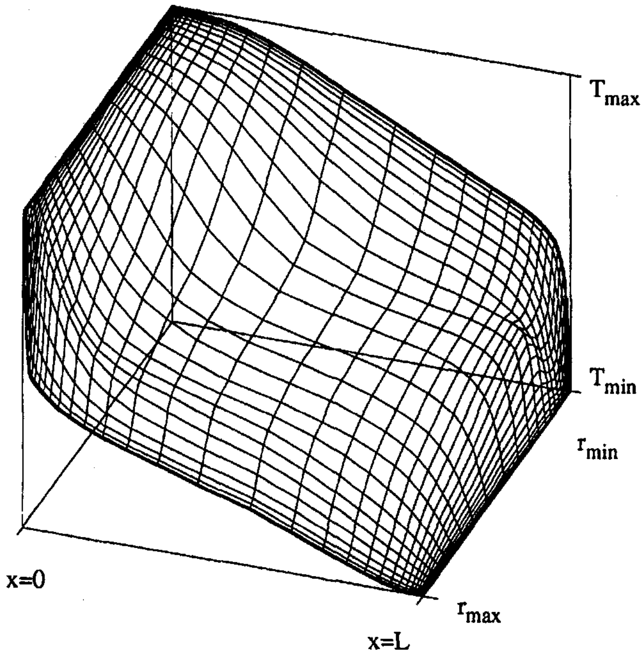

Fig. 15 Temperature distribution of a three-dimensional calculation, Re = 6.57 × 10⁴, Ra = 2.261 × 10⁸

is also influenced by the Coriolis forces, expressed by the size of Re. To point this out, further calculations were carried out for a smaller Re equal to 1.457×10^4, without changing the geometry of the cavity, so that the influence of the ratio r_m/h on the flow and the heat transfer is not changed. Due to the unexpectedly large calculation time (CPU time) for the three-dimensional calculations, we have not yet finished our theoretical study to find that critical Ra where the flow character changes completely. Table 1 gives an overview of the results obtained from performed calculations.

The predicted Nu of the two-dimensional and three-dimensional calculations are close together for a constant Re of Re

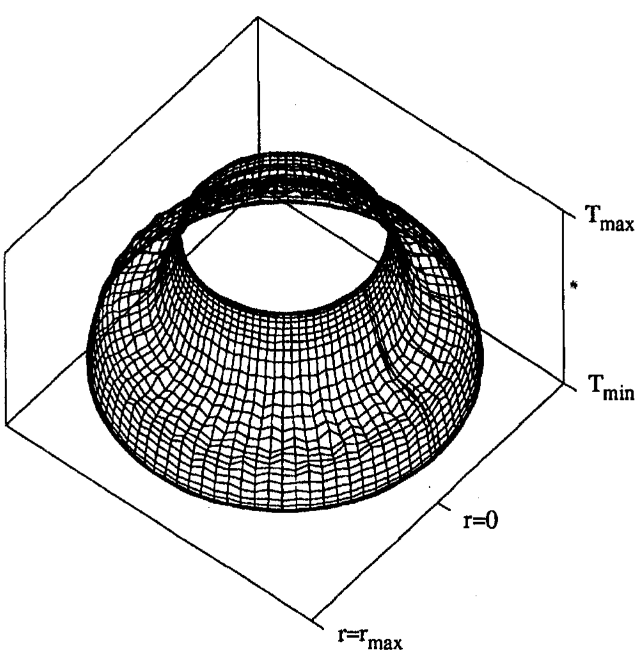

Fig. 16 Temperature distribution of a three-dimensional calculation, Re = 6.57 × 10⁴, Ra = 2.261 × 10⁸

Table 1 Comparison of the results from two-dimensional and three-dimensional calculations

$Re \cdot 10^4$	$Ra \cdot 10^7$	Nu_{2D}	Nu_{3D}
1.457	1.291	2.224	2.224
1.457	3.228	5.452	5.432

$= 1.457 \times 10^4$. Due to the damping influence of Re, an enlarged flow circulation between the cold and the hot wall is induced by decreasing Re more and more. At this situation Nu is increased. Increasing Re up to Re $= 6.57 \times 10^4$, an increasing fluid motion in the circumferential direction occurs, which cannot be calculated by a two-dimensional algorithm.

Summary and Conclusions

Investigations have been carried out on convective heat transfer in a closed annulus rotating around his horizontal axis. A pure axial heat flux throughout the cavity was applied by heating the axial side walls. All other walls of the annular cavities were thermally insulated.

Measurements have been performed varying Ra in a range usually encountered in the gas-filled cavities of gas turbine rotors ($2 \times 10^8 < Ra < 5 \times 10^{10}$). It can be concluded that in the case of an axially directed heat flux, the heat transfer depends strongly on Re. For the Re–Ra characteristics from the experimental apparatus, only a weak influence of Ra on the heat transfer occurs. With radially directed heat flux throughout the cavity, the heat transfer depends strongly on Ra but only weakly on Re.

Theoretical investigations for the basic case of isothermal side walls and adiabatic cylindrical walls have been made for the annular cavity. The calculations were carried out using two-dimensional and three-dimensional steady-state numerical algorithms. Due to Ra smaller than 2×10^9, the results taken from the two-dimensional algorithm match the experimental data. For increasing Ra the deviation enlarges between the two-dimensional numerical results and the experimental data. Two possible reasons for this difference were pointed out: On one hand the experimental setup could not achieve adiabatic cylindrical walls as assumed for the numerical calculations, and on the other hand the assumption of a two-dimensional flow inside the cavity may not be realistic.

Three-dimensional calculations were carried out for two different Re values. For small Re, i.e., Re $= 1.457 \times 10^4$, no difference to the two-dimensional results occurred. Increasing Re large differences between the results of the two-dimensional and three-dimensional calculations appeared.

Further investigations should work out instability conditions of the flow and show the influence of the thermal boundary conditions of the side walls on the flow and the heat transfer in the cavity. Especially, it has to be investigated by changing Re, at which size of Ra the flow field inside the cavity changes from a two-dimensional to a three-dimensional one.

Acknowledgments

The authors thank the Arbeitsgemeinschaft Hochtemperatur-Gasturbine (AG Turbo) for sponsoring the experimental research work. The AG Turbo is funded by German Gas Turbine Industry Companies and the Ministry of Research and Technology (BMFT).

References

Abell, S., and Hudson, J. L., 1975, "An Experimental Study of Centrifugally Driven Free Convection in a Rectangular Cavity," *Int. J. Heat Mass Transfer,* Vol. 18, pp. 1415–1423.

Bohn, D., Dibelius, G. H., Deuker, E., and Emunds, R., 1994, "Flow Pattern and Heat Transfer in a Closed Rotating Annulus," ASME JOURNAL OF TURBOMACHINERY, Vol. 116, pp. 542–547.

Bohn, D., and Gorzelitz, V., 1992, "Experimental Investigations of Heat Transfer in a Gas-Filled Rotating Annulus," presented at the International Symposium on Heat Transfer in Turbomachinery, Athens, Greece; to be published by Hemisphere Publishing Corporation, New York.

Bohn, D., Deuker, E., Emunds, R., and Gorzelitz, V., 1995, "Experimental and Theoretical Investigations of Heat Transfer in Closed Gas-Filled Rotating Annuli," ASME JOURNAL OF TURBOMACHINERY, Vol. 117, pp. 175–183.

Chew, J. W., 1985, "Computation of Convective Laminar Flow in Rotating Cavities," *J. Fluid Mech.,* Vol. 153, pp. 339–360.

Farthing, P. R., Long, C. A., Owen, J. M., and Pincombe, J. R., 1992, "Rotating Cavity With Axial Throughflow of Cooling Air: Heat Transfer," ASME JOURNAL OF TURBOMACHINERY, Vol. 114, pp. 229–236.

Harada, I., and Ozaki, N., 1975, "A Numerical Study of the Thermal Spin-up of a Stratified Fluid in a Rapidly Rotating Cylinder," *Lecture Notes in Physics,* Vol. 35, pp. 197–203.

Hignett, P., Ibbetson, A., and Killworth, P. D., 1981, "On Rotating Thermal Convection Driven by Non-uniform Heating From Below," *J. Fluid Mech.,* Vol. 109, pp. 161–187.

Kapinos, V. M., Pustovalov, V. I., and Rudko, A. P., 1981, "Effect of Stabilization in Free Convection of a Cylindrical Rotating Enclosure," *Energeticeskoe masinostroenie,* No. 32 [in Russian], pp. 76–79.

Lin, T. Y., and Preckshot, G. W., 1979, "Steady-State Laminar Natural Convection in a Rotating Annulus," *Studies in Heat Transfer: A Festschrift for E.R.G. Eckert,* Hemisphere Publishing Corporation, pp. 219–246.

Müller, M. R., and Burch, J. N., 1985, "An Experimental Study of the Behavior of Transient Isolated Convection in a Rigidly Rotating Fluid," *Experiments in Fluids,* Vol. 3, pp. 17–23.

Ong, C. L., and Owen, J. M., 1991, "Prediction of Heat Transfer in a Rotating Cavity With a Radial Outflow," ASME JOURNAL OF TURBOMACHINERY, Vol. 113, pp. 115–122.

Owen, J. M., Pincombe, J. R., and Rogers, R. H., 1985, "Source-Sink Flow Inside a Rotating Cylindrical Cavity," *J. Fluid Mech.,* Vol. 155, pp. 233–265.

Patankar, S. V., and Spalding, D. B., 1972, "A Calculation Procedure for Heat, Mass and Momentum Transfer in Three-Dimensional Parabolic Flows," *Int. J. Heat Mass Transfer,* Vol. 15, pp. 1787–1806.

Zysina-Molozhen, L. M., and Salov, N. N., 1977, "Heat Exchange and Flow Regime of Liquids in a Closed Rotating Annular Cavity," *Soviet-Aeronautics,* Vol. 20, No. 1, pp. 39–43.

DISCUSSION

A. Mirzamoghadam[1]

Investigation of the flow and heat transfer in a heated rotating cavity is of particular interest in our work, where we are generating thermal models to predict low-pressure turbine disk/rim metal temperatures in the interdisk cavity. The results reported in this paper suggest that natural convection induced by a heat flux directed radially is weakly sensitive to the rotational Reynolds number. However, previous studies (reference ASME Paper No. 93-GT-258) have reported a rather strong influence of rotational Re on Nu especially near the rim. Our three-dimensional CFD investigation leads us to believe that when the rim temperature is hotter than the mean disk temperature, the inflow motion of the core is enhanced by radial inflow natural convection, and there appears to be a distructive interference between the centrifugally driven upflow adjacent to the rotating disks and the strong inflow due to natural convection near the disk/rim corners. This observation will undoubtedly affect the Nusselt number variation along the hot rim, core, and the upper radii of the disks as the rotational Re is varied.

Authors' Closure

The authors thank Dr. Mirzamoghadam for his contribution, which mentions an interesting and important feature of the flow and heat transfer in rotating cavities with mainly *axial* throughflow.

However, in the case of heat transfer in a rotating annulus without the presence of axial throughflow motion, which was the subject of our investigation, the influence of the rotational Reynolds number on the overall Nusselt number is rather weak, if the heat flux is directed *radially* from the outer to the inner radius.

In the case of an axially directed heat flux, the Nusselt number is strongly affected by the Reynolds number through the damping influence of the Coriolis forces. This is clearly shown in Fig. 11 in our paper.

[1] Heat Transfer and Aerodynamics, BMW Rolls-Royce AeroEngines, Eschenweg, 15827 Dahlewitz, Federal Republic of Germany.

References

Abell, S., and Hudson, J. L., 1975, "An Experimental Study of Centrifugally Driven Free Convection in a Rectangular Cavity," *Int. J. Heat Mass Transfer,* Vol. 18, pp. 1415–1423.

Bohn, D., Dibelius, G. H., Deuker, E., and Emunds, R., 1994, "Flow Pattern and Heat Transfer in a Closed Rotating Annulus," ASME JOURNAL OF TURBOMACHINERY, Vol. 116, pp. 542–547.

Bohn, D., and Gorzelitz, V., 1992, "Experimental Investigations of Heat Transfer in a Gas-Filled Rotating Annulus," presented at the International Symposium on Heat Transfer in Turbomachinery, Athens, Greece; to be published by Hemisphere Publishing Corporation, New York.

Bohn, D., Deuker, E., Emunds, R., and Gorzelitz, V., 1995, "Experimental and Theoretical Investigations of Heat Transfer in Closed Gas-Filled Rotating Annuli," ASME JOURNAL OF TURBOMACHINERY, Vol. 117, pp. 175–183.

Chew, J. W., 1985, "Computation of Convective Laminar Flow in Rotating Cavities," *J. Fluid Mech.,* Vol. 153, pp. 339–360.

Farthing, P. R., Long, C. A., Owen, J. M., and Pincombe, J. R., 1992, "Rotating Cavity With Axial Throughflow of Cooling Air: Heat Transfer," ASME JOURNAL OF TURBOMACHINERY, Vol. 114, pp. 229–236.

Harada, I., and Ozaki, N., 1975, "A Numerical Study of the Thermal Spin-up of a Stratified Fluid in a Rapidly Rotating Cylinder," *Lecture Notes in Physics,* Vol. 35, pp. 197–203.

Hignett, P., Ibbetson, A., and Killworth, P. D., 1981, "On Rotating Thermal Convection Driven by Non-uniform Heating From Below," *J. Fluid Mech.,* Vol. 109, pp. 161–187.

Kapinos, V. M., Pustovalov, V. I., and Rudko, A. P., 1981, "Effect of Stabilization in Free Convection of a Cylindrical Rotating Enclosure," *Energeticeskoe masinostroenie,* No. 32 [in Russian], pp. 76–79.

Lin, T. Y., and Preckshot, G. W., 1979, "Steady-State Laminar Natural Convection in a Rotating Annulus," *Studies in Heat Transfer: A Festschrift for E.R.G. Eckert,* Hemisphere Publishing Corporation, pp. 219–246.

Müller, M. R., and Burch, J. N., 1985, "An Experimental Study of the Behavior of Transient Isolated Convection in a Rigidly Rotating Fluid," *Experiments in Fluids,* Vol. 3, pp. 17–23.

Ong, C. L., and Owen, J. M., 1991, "Prediction of Heat Transfer in a Rotating Cavity With a Radial Outflow," ASME JOURNAL OF TURBOMACHINERY, Vol. 113, pp. 115–122.

Owen, J. M., Pincombe, J. R., and Rogers, R. H., 1985, "Source-Sink Flow Inside a Rotating Cylindrical Cavity," *J. Fluid Mech.,* Vol. 155, pp. 233–265.

Patankar, S. V., and Spalding, D. B., 1972, "A Calculation Procedure for Heat, Mass and Momentum Transfer in Three-Dimensional Parabolic Flows," *Int. J. Heat Mass Transfer,* Vol. 15, pp. 1787–1806.

Zysina-Molozhen, L. M., and Salov, N. N., 1977, "Heat Exchange and Flow Regime of Liquids in a Closed Rotating Annular Cavity," *Soviet-Aeronautics,* Vol. 20, No. 1, pp. 39–43.

DISCUSSION

A. Mirzamoghadam[1]

Investigation of the flow and heat transfer in a heated rotating cavity is of particular interest in our work, where we are generating thermal models to predict low-pressure turbine disk/rim metal temperatures in the interdisk cavity. The results reported in this paper suggest that natural convection induced by a heat flux directed radially is weakly sensitive to the rotational Reynolds number. However, previous studies (reference ASME Paper No. 93-GT-258) have reported a rather strong influence of rotational Re on Nu especially near the rim. Our three-dimensional CFD investigation leads us to believe that when the rim temperature is hotter than the mean disk temperature, the inflow motion of the core is enhanced by radial inflow natural convection, and there appears to be a distructive interference between the centrifugally driven upflow adjacent to the rotating disks and the strong inflow due to natural convection near the disk/rim corners. This observation will undoubtedly affect the Nusselt number variation along the hot rim, core, and the upper radii of the disks as the rotational Re is varied.

Authors' Closure

The authors thank Dr. Mirzamoghadam for his contribution, which mentions an interesting and important feature of the flow and heat transfer in rotating cavities with mainly *axial* throughflow.

However, in the case of heat transfer in a rotating annulus without the presence of axial throughflow motion, which was the subject of our investigation, the influence of the rotational Reynolds number on the overall Nusselt number is rather weak, if the heat flux is directed *radially* from the outer to the inner radius.

In the case of an axially directed heat flux, the Nusselt number is strongly affected by the Reynolds number through the damping influence of the Coriolis forces. This is clearly shown in Fig. 11 in our paper.

[1] Heat Transfer and Aerodynamics, BMW Rolls-Royce AeroEngines, Eschenweg, 15827 Dahlewitz, Federal Republic of Germany.

Experimental Heat Transfer and Friction in Channels Roughened With Angled, V-Shaped, and Discrete Ribs on Two Opposite Walls

M. E. Taslim

T. Li

Department of Mechanical Engineering,
Northeastern University,
Boston, MA 02115

D. M. Kercher

GE Aircraft Engines,
General Electric Corporation,
Lynn, MA 01910

Experimental investigations have shown that the enhancement in heat transfer coefficients for air flow in a channel roughened with angled ribs is on the average higher than that roughened with 90 deg ribs of the same geometry. Secondary flows generated by the angled ribs are believed to be responsible for these higher heat transfer coefficients. These secondary flows also create a spanwise variation in heat transfer coefficient on the roughened wall with high levels of heat transfer coefficient at one end of the rib and low levels at the other end. In an effort basically to double the area of high heat transfer coefficients, the angled rib is broken at the center to form a V-shaped rib, and tests are conducted to investigate the resulting heat transfer coefficients and friction factors. Three different square rib geometries, corresponding to blockage ratios of 0.083, 0.125, and 0.167, with a fixed pitch-to-height ratio of 10, mounted on two opposite walls of a square channel in a staggered configuration, are tested in a stationary channel for 5000 < Re < 30,000. Heat transfer coefficients, friction factors, and thermal performances are compared with those of 90 deg, 45 deg, and discrete angled ribs. The V-shaped ribs are tested for both pointing upstream and downstream of the main flow. Test results show that: (a) 90 deg ribs represent the lowest thermal performance, based on the same pumping power, and is essentially the same for the 2:1 change in blockage ratio, (b) low-blockage-ratio ($e/D_h = 0.083$) V-shaped ribs pointing downstream produced the highest heat transfer enhancement and friction factors. Among all other geometries with blockage ratios of 0.125 and 0.167, 45 deg ribs showed the highest heat transfer enhancements with friction factors less than those of V-shaped ribs, (c) thermal performance of 45 deg ribs and the lowest blockage discrete ribs are among the highest of the geometries tested in this investigation, and (d) discrete angled ribs, although inferior to 45 deg and V-shaped ribs, produce much higher heat transfer coefficients and lower friction factors compared to 90 deg ribs.

Introduction

Heat transfer coefficient in a channel flow can be increased by roughening the walls of the channel. One such method, used over the past thirty years in internal cooling passages, is to mount rib-shape roughnesses on the channel walls. These ribs, also called turbulators, enhance the level of heat transfer coefficients by restarting the boundary layer after flow reattachment between ribs.

Geometric parameters such as channel aspect ratio (AR), rib height-to-passage hydraulic diameter or blockage ratio (e/D_h), rib angle of attack (α), the manner in which the ribs are positioned relative to one another (in-line, staggered, crisscross, etc.), rib pitch-to-height ratio (S/e) and rib shape (round versus sharp corners, fillets, rib aspect ratio (AR_r), and skewness toward the flow direction) have pronounced effects on both local and overall heat transfer coefficients. Some of these effects have been studied by different investigators such as Abuaf et al. (1986), Burggraf (1970), Chandra et al. (1988), Chandra and Han (1989), Han (1984), Han et al. (1978, 1992), Metzger et al. (1983), Taslim et al. (1988a, b, 1991a, b), Webb et al. (1971). Among those geometries close to the present investigation are the papers by Lau et al. (1990, 1992) and Han et al. (1991). These last two references deal with heat transfer characteristics of turbulent flow in a square channel with angled discrete ribs. Heat transfer performance of 30, 45, 60, and 90 deg discrete, parallel, and crossed ribs was investigated. The second investigation studied the augmentation of heat transfer in square channels roughened with parallel, crossed, and V-shaped ribs. While their rib pitch-to-height ratio of 10 was identical to that in this study, the rib height-to-channel hydraulic diameter was 0.0625 in both investigations, which is below the range tested in the present investigation (0.083–0.167). However, results of the smallest rib tested in this investigation are compared with those tested in the two above-mentioned references.

Test Sections

Figure 1 shows schematically the layout and cross-sectional area of a typical test section, while rib geometry details are

Contributed by the International Gas Turbine Institute and presented at the 39th International Gas Turbine and Aeroengine Congress and Exposition, The Hague, The Netherlands, June 13–16, 1994. Manuscript received by the International Gas Turbine Institute February 15, 1994. Paper No. 94-GT-163. Associate Technical Editor: E. M. Greitzer.

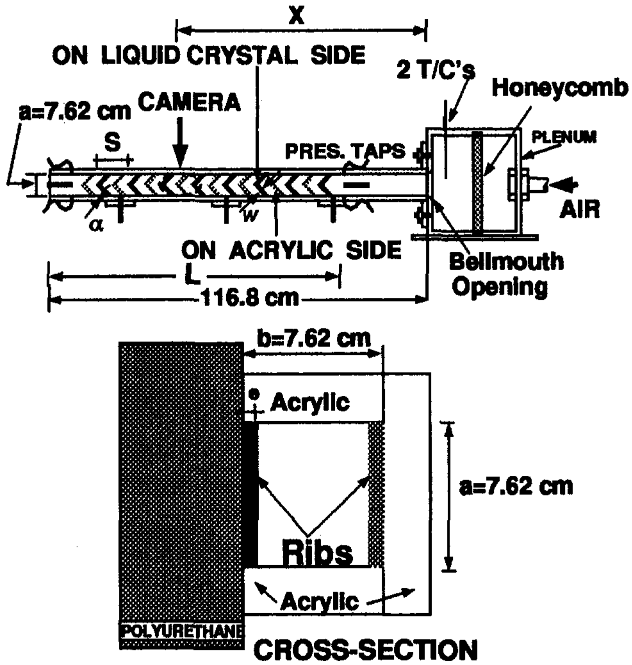

Fig. 1 Schematic of a typical test section

shown in Fig. 2. Table 1 contains the specifications of the 13 staggered rib geometries tested in this investigation. A liquid crystal technique was employed to measure the heat transfer coefficients between pairs of ribs in these test sections (Moffat, 1990). In this technique, the most temperature-sensitive color displayed by the liquid crystals is chosen as the reference color corresponding to a known temperature. By sensitive variation of the Ohmic power to a constant heat flux thin foil heater beneath the liquid crystals, the reference color is moved from one location to another such that the entire area between two ribs is eventually covered with the reference color at constant flow conditions. This process results in a series of photographs, each corresponding to a certain location of the reference color. The area covered by the reference color for each photograph is then measured and an area-weighted average heat transfer coefficient is calculated along with the iso-Nu contours. Details of this process are explained in the Procedure section. Among the advantages of liquid crystal thermography is the ability to depict the flow "footprints" and local values of heat transfer coefficient on the surface under investigation. This simultaneous "flow visualization" enhances the understanding of the underlying physics and helps the investigator in interpretation of the results. Furthermore, unexpected asymmetries in flow are revealed, as well as the slightest heat and flow leaks, nonuniformities in surface heat flux, imperfections associated with the attachment of the heater to the test section surface, and nonuniformities in wall material thermal conductivity.

Coolant air, supplied by a compressor to a 0.95 m^3 storage tank, was circulated through an air filter, to a water-to-air heat exchanger, and through a second air filter to remove any residual water vapor and oil. A pressure regulator downstream of the second filter was used to adjust the flow rate. The air then entered a critical venturimeter for mass flow measurement, to a plenum equipped with a honeycomb flow straightener, and then to the test section via a bellmouth opening.

All test sections, with a length of 116.8 cm, had a 7.62 cm × 7.62 cm square cross-sectional area. Three walls of these channels were made of 1.27-cm-thick clear acrylic plastic. The fourth wall, on which the heaters and liquid crystal sheets were attached and all measurements were taken, was made of a 5-cm-thick machinable polyurethane slab. This wall, for all cases tested, had a fixed width of 7.62 cm. Ribs were cut to length from commercially available acrylic plastic stock, in the form of square rods, and glued onto two opposite walls in a staggered arrangement.

The entrance region of all test sections was left smooth to produce well-established hydrodynamic and thermal boundary layers. Heat transfer measurements were performed for an area between a pair of ribs in the middle of the roughened zone corresponding to $X/D_h = 9.5-11.6$.

Four 7.62 cm × 27.94 cm custom-made etched-foil heaters with a thickness of 0.15 mm were placed on the polyurethane wall where measurements were taken using a special double-stick 0.05-mm-thick tape with minimal temperature deformation characteristics. A detailed construction sketch of the heaters is shown in El-Husayni (1991). The heaters covered the entire test section length including the smooth entry length. However, they did not extend over the actual rib surface nor on the acrylic plastic sidewalls. Thus the reported heat transfer coefficients are the averages over the wall surface area between a pair of ribs. The heat transfer coefficient on the rib surfaces are reported by other investigators, such as Metzger et al. (1988). As for having only one heated wall, it is noted that an experimental investigation by El-Husayni et al. (1992) on heat transfer in a rib-roughened channel with one, two, and four heated walls showed that, in a stationary roughened channel, the heat transfer coefficient is not significantly sensitive to the number of heated walls. Encapsulated liquid crystals sandwiched between a mylar sheet and a black paint coat, collectively having a thickness of 0.127 mm, were then placed on the heaters. Static pressure taps, located $\frac{1}{2}$-rib pitch upstream of the first rib and $\frac{1}{2}$-rib pitch downstream of the last rib, measured the pressure drop across the rib-roughened test section. The reported friction factor is the overall passage average, $\bar{f}$, and not just the roughened surfaces.

The test sections were covered on all sides by 5-cm-thick styrofoam sheets to minimize heat losses to the environment,

Nomenclature

a = channel height (Fig. 1)
A = cross-sectional area without ribs
b = channel width (Fig. 1)
AR = channel aspect ratio = b/a
AR_t = rib aspect ratio = e/w
D_h = hydraulic diameter based on the cross-sectional area without ribs = $4A/P$
e = rib height
$\bar{f}$ = Darcy friction factor = $(\Delta P(L/D_h))/\frac{1}{2}\rho U_m^2)$
$\bar{f}_s$ = Darcy friction factor in an all-smooth-wall channel
$\bar{h}_t$ = average heat transfer coefficient between a pair of ribs
k = air thermal conductivity
L = length of the roughened portion of the test section
$\overline{\mathrm{Nu}}$ = average Nusselt number between a pair of ribs $(\bar{h}_t D_h/k)$
$\overline{\mathrm{Nu}}_s$ = fully developed average Nusselt number in a smooth passage
P = channel perimeter without ribs
Re = Reynolds number = $\rho U_m D_h/\mu$
S = rib pitch (center-to-center)
T_f = film temperature = $0.5(T_s + T_m)$
T_m = air mixed mean temperature
T_s = surface temperature
U_m = air mean velocity
w = rib width
X = distance between camera and test section entrance
ΔP = pressure differential across the roughened portion of the test section
α = angle of attack
μ = air dynamic viscosity
ρ = air density

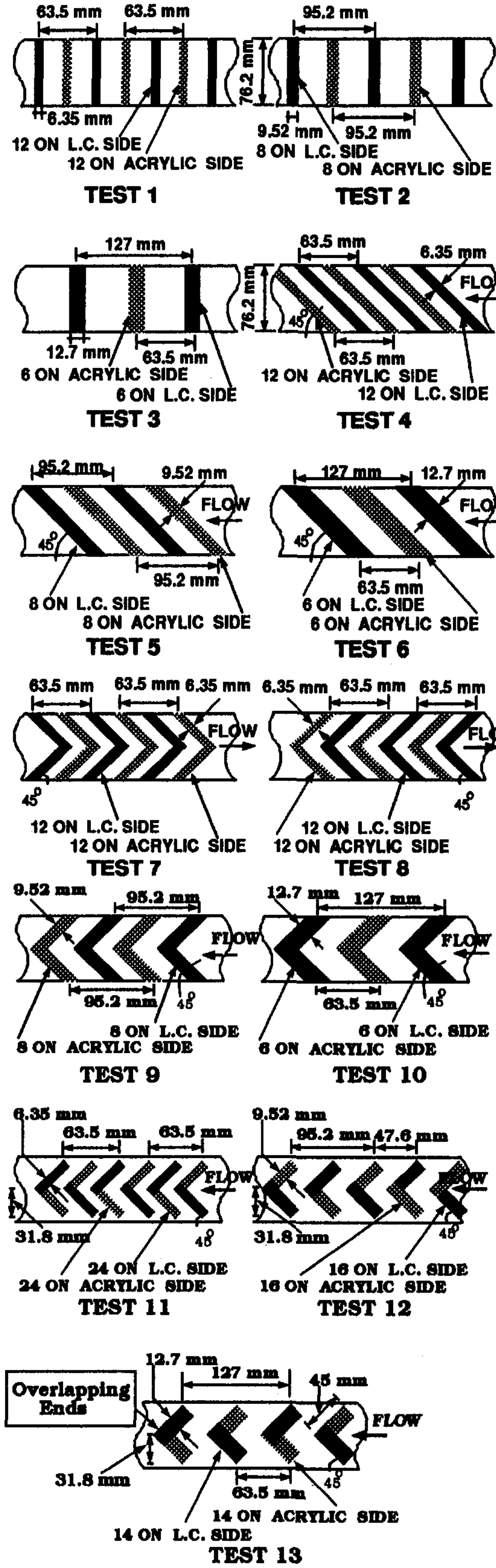

Fig. 2 Rib geometries

except for a small window on the opposite wall at the location where photographs of the liquid crystals were taken. The radiational heat loss from the heated wall to the unheated walls as well as losses to ambient air were taken into consideration when heat transfer coefficients were calculated. A 35 mm programmable SLR camera, in conjunction with proper filters and background lighting to simulate daylight conditions, was used to take photographs of isochrome patterns formed on the liquid crystal sheet. Surface heat flux in the test section was generated by the heaters through a custom-designed power supply unit. Each heater was individually controlled by a variable transformer.

Procedure

Before testing, the liquid crystal sheets were calibrated in a water bath to attain uniform isochromes on a small piece of the liquid crystal sheet used in this investigation. The temperature corresponding to each color was measured with a precision thermocouple and photographs were taken at laboratory conditions simultaneously to simulate closely the actual testing environment. A reference color along with its measured temperature of 36.9°C was chosen for the experiments. It should be noted that all possible shades of the selected reference color did not indicate a temperature variation more than 0.3°C. Therefore, the maximum uncertainty in wall temperature measurement was ±0.15°C.

A contact micromanometer with an accuracy of 0.025 mm of water column measured the pressure differential across the rib-roughened channel. A critical venturimeter, with choked flow for all cases tested, measured the total mass flow rate entering the test section. With the known surface heat flux along the test section and application of the energy balance from the test section inlet to the camera location, the air mixed mean temperature was calculated taking into account the small heat losses through the test section walls to ambient air.

For a typical test Reynolds number, at a constant mass flow rate, the lowest heat flux was induced by adjusting the heater power until the first band of reference color was observed on the liquid crystal sheet in the area of interest. Each heater was adjusted individually to insure a uniform heat flux over the entire tested surface. At thermal equilibrium a photograph was taken and data recorded. Power to the heaters was then increased such that the reference color moved to a location next to the previous one (higher heat transfer coefficient) and another photograph was taken. This procedure was repeated until the entire surface between a pair of ribs was covered by the reference color. The process was then repeated for the range of test Reynolds numbers. Each photograph was then digitized in order to measure the area covered by the reference color. This was done by using a magnetic tablet and a commercial software package running on an IBM-PC/AT. Once the areas were measured, an area-weighted average heat transfer coefficient was calculated.

For verification of the liquid crystal technique accuracy, an all-smooth-wall channel has been tested with heaters on one

Table 1 Specifications

TESTS	e (mm)	e/D_h	α	X (cm)	X/D	Remarks	
1	6.35	0.0633	90° Stag.	77.16	10.125	Straight Ribs	□
2	9.525	0.125	90° Stag.	77.16	10.125	Straight Ribs	×
3	12.7	0.167	90° Stag.	72.39	9.5	Straight Ribs	+
4	6.35	0.0633	45° Stag.	88.11	11.56	Straight Ribs	○
5	9.525	0.125	45° Stag.	76.52	10	Straight Ribs	✳
6	12.7	0.167	45° Stag.	72.39	9.5	Straight Ribs	◁
7	6.35	0.0633	45° Stag.	86.11	11.56	V-shape pointing downstream	▽
8	6.35	0.0633	45° Stag.	86.11	11.56	V-shape pointing upstream	△
9	9.525	0.125	45° Stag.	86.68	11.375	V-shape pointing downstream	◇
10	12.7	0.167	45° Stag.	85.1	11.16	V-shape pointing downstream	▷
11	6.35	0.0633	45° Stag.	78.74	10.33	Discrete Ribs	▼
12	9.525	0.125	45° Stag.	81.92	10.75	Discrete Ribs	◆
13	12.7	0.167	45° Stag.	78.74	10.33	Discrete Ribs	▶

AR=1 AR_t =1 S/e=10 for all geometries

symbols

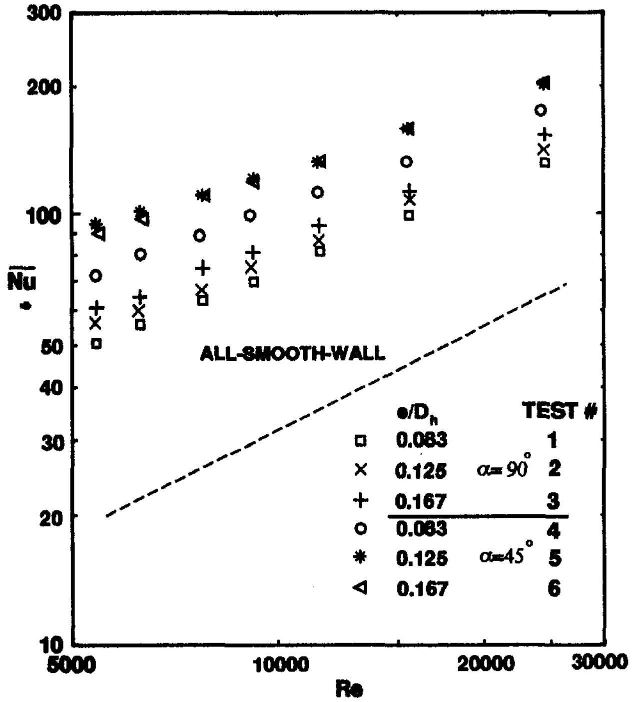

Fig. 3 Comparison of blockage ratio effects on surface average Nusselt number for 90 and 45 deg rib geometries

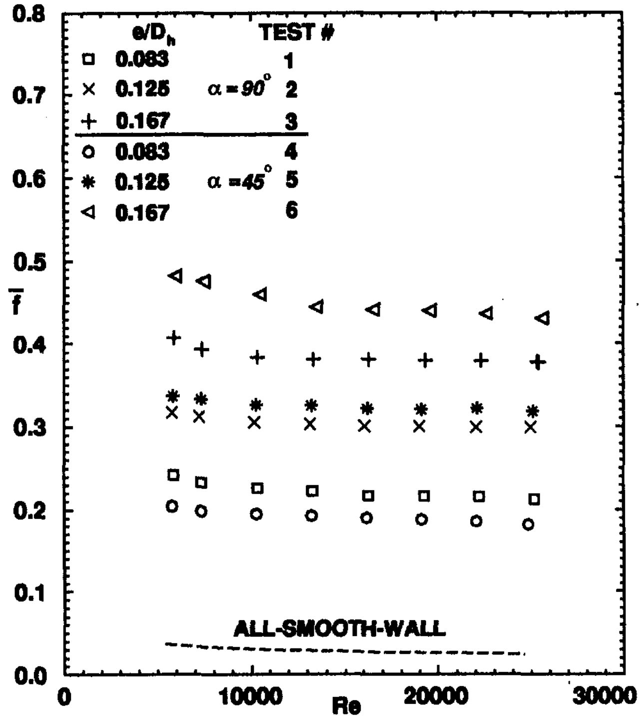

Fig. 4 Comparison of blockage ratio effects on channel average friction factor for 90 and 45 deg rib geometries

wall. The heat transfer coefficient results (Taslim, 1990) were within ±5 percent of the Dittus–Boelter (1930) correlation. Previous results (Taslim et al., 1991c) of various geometry roughened channels using the same technique compared favorably with those of Metzger et al. (1990). Experimental uncertainties, following the method of Kline and McClintock (1953), were estimated to be ±6% and ±8% for the heat transfer coefficient and friction factor, respectively.

Results and Discussion

Local average heat transfer coefficient results for an area between a pair of ribs corresponding to $X/D_h = 9.5-11.6$ for the 13 rib geometries are compared with the all-smooth-wall channel Dittus–Boelter (1930) correlation

$$\overline{\mathrm{Nu}_s} = 0.023\ \mathrm{Re}^{0.8}\ \mathrm{Pr}^{0.4}$$

in Figs. 3, 8, 10, 13, and 15. With this correlation, the enhancement in rib-roughened heat transfer coefficients can be readily evaluated as illustrated in Fig. 12. The thermal performance, based on the same pumping power, is given by

$$(\overline{\mathrm{Nu}}/\overline{\mathrm{Nu}_s})/(\bar{f}/\bar{f}_s)^{1/3}$$

(Han et al., 1985), where $\bar{f}_s$ is the all-smooth-wall friction factor from Moody (1944). Air properties for Nusselt and Reynolds number calculations are based on the local film temperature, T_f, for all cases.

90 and 45 deg Ribs. Heat transfer and friction factor results of the 45 and 90 deg ribs are shown in Figs. 3 and 4. As shown in Table 1 and Fig. 2, under otherwise identical conditions, the three 90 deg rib geometries representing three different blockage ratios will serve as a baseline against which other configurations will be compared.

As expected for 90 deg ribs, larger blockage ratios produced higher heat transfer coefficients as well as higher pressure losses. Some representative iso-Nu contours (contours of constant Nusselt number) for tests 1, 2, and 3 (Fig. 2) are shown in Fig. 5. The apparent change of scale from one test to another is due to the change of camera position to cover the area between a pair of ribs as they become farther apart. The shaded area represents the staggered rib on the opposite wall. It can be seen that the local heat transfer coefficient, starting from a relatively low value in the rib wake region, reaches its maximum near

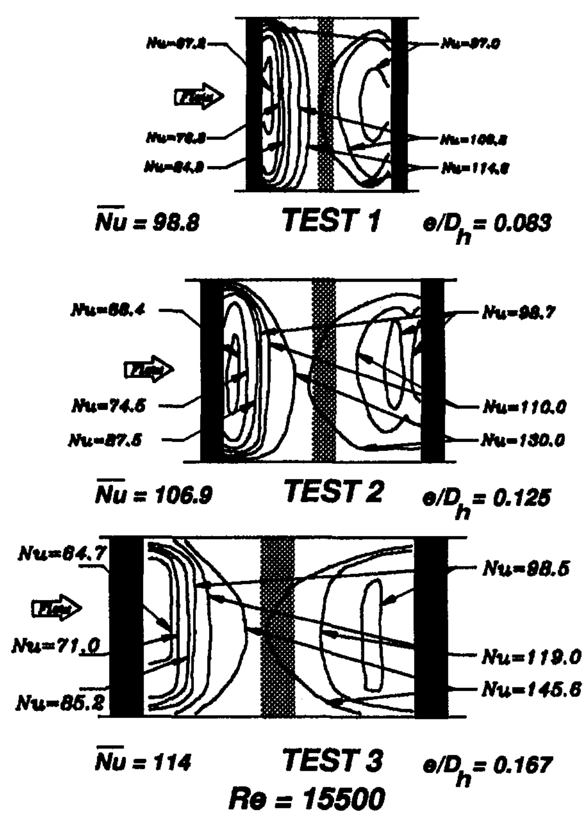

Fig. 5 Representative iso-Nu contours for the 90 deg ribs

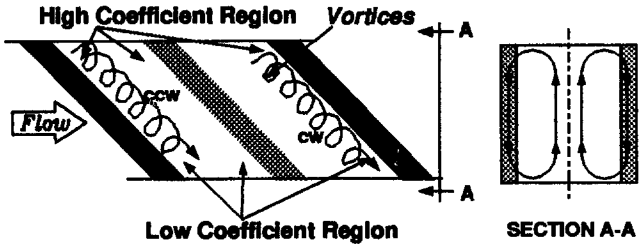

Fig. 6(*a*) Cell formation for 45 deg ribs

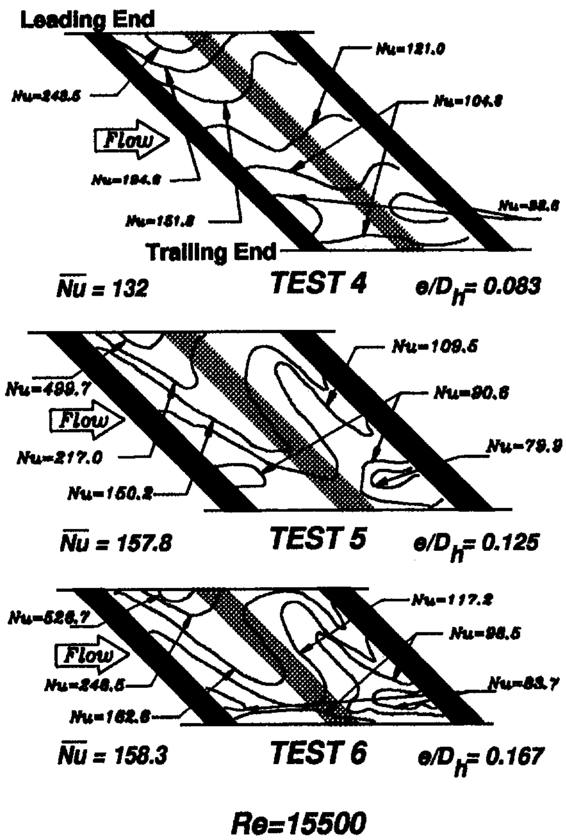

Fig. 6(*b*) Representative iso-Nu contours for 45 deg ribs

the point of flow reattachment and then decreases again close to the downstream rib.

To investigate the effects 45 deg angled ribs have on the heat transfer performance and pressure loss, test sections 4–6 (Fig. 2) were tested, which were identical to test sections 1–3 in all aspects except for the rib angle of attack, which was 45 deg to the flow direction. Spanwise, counterrotating, double-cell secondary flows created by the angling of ribs, as depicted in Fig. 6(*a*), appear to be responsible for the significant spanwise variation in heat transfer coefficient observed in Fig. 6(*b*). Formation of these rotating cells when ribs are angled is explained in detail by Metzger et al. (1990) and Fann et al. (1994). Whereas the two fluid vortices immediately upstream and downstream of a 90 deg rib are essentially stagnant (relative to the mainstream flow velocity), which raises the local fluid temperatures in the vortices and wall temperature near the rib resulting in low heat transfer coefficients, the vortices between 45 deg angled ribs are not stagnant but moving along the ribs and then join the mainstream (Fann et al., 1994). These moving vortices between staggered parallel angled ribs set up a strong double-cell counter-rotating secondary flow, which brings lower center-channel fluid temperatures near the angled ribs leading end regions, enhances the local heat transfer coefficients, and lowers the wall temperatures (Fann et al., 1994) at constant heat flux. Near the trailing end region of the ribs, the local fluid temperatures increase as the vortex secondary flow sweeps the floor between ribs shown in Fig. 6(*a*). This phenomenon appears to result in lower heat transfer coefficients in the rib

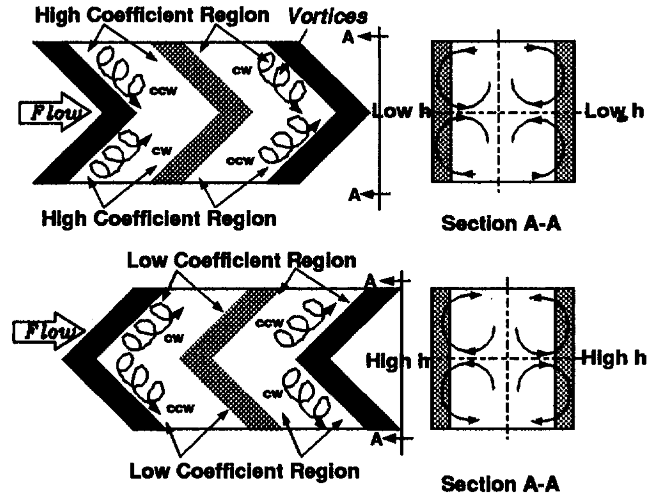

Fig. 7(*a*) Cell formation for V-shaped ribs

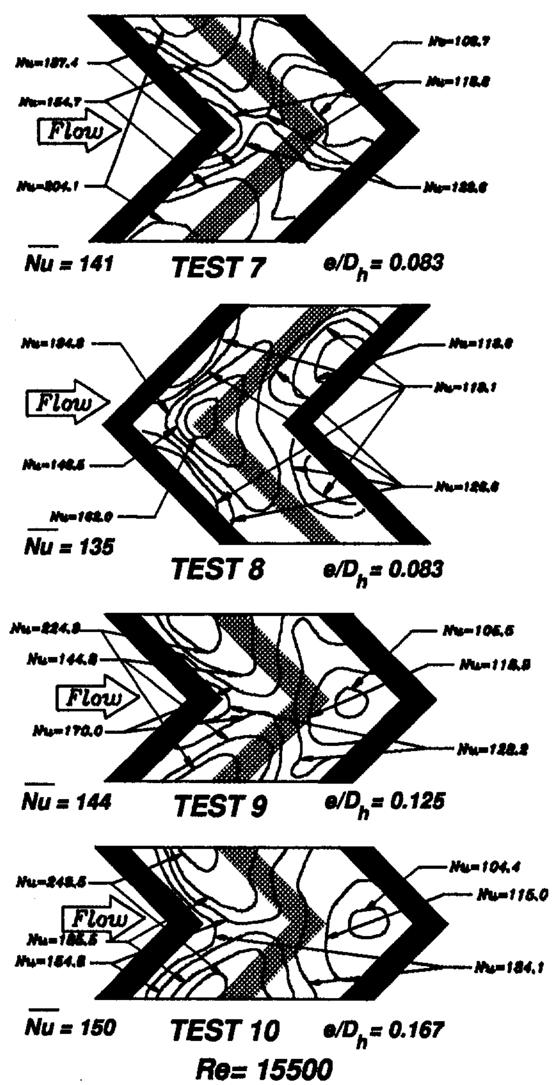

Fig. 7(*b*) Representative iso-Nu contours for the V-shaped ribs

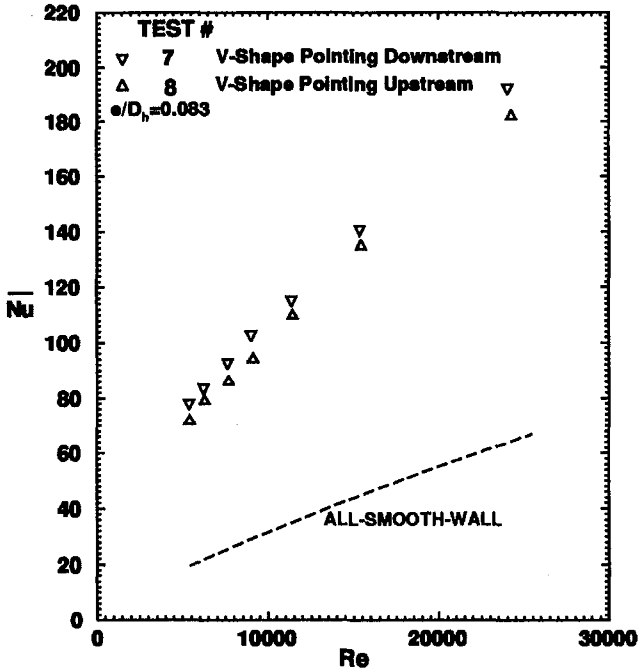

Fig. 8 Comparison of turbulator orientation on surface average Nusselt number for V-shaped rib geometries

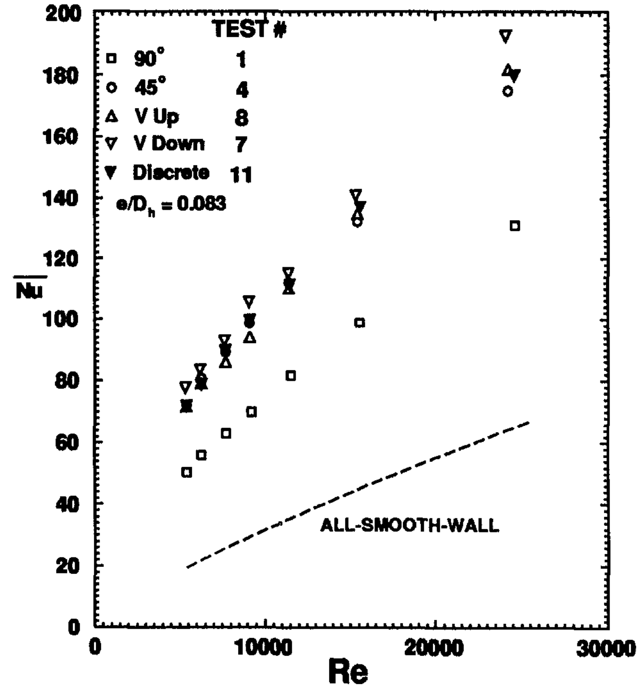

Fig. 10 Comparison of surface average Nusselt number for five rib geometries of 0.083 blockage ratio

leading end region, as indicated by measured results shown in Fig. 6(b). As shown in Fig. 3, the surface-averaged heat transfer coefficients for these geometries are higher than corresponding 90 deg ribs. In Fig. 4, the angled ribs with the lowest blockage ratio (0.083) produced less form drag, resulting in lower pressure losses compared to 90 deg ribs. The other two rib geometries produced slightly higher friction factors. The thermal performances for these two geometries, compared in Fig. 18 (combined Figs. 3 and 4), confirms the superiority of 45 deg angled ribs over the 90 deg ribs.

V-Shaped Ribs. The possibility of further increasing the wall heat transfer with V-shaped ribs is based on the observations made in Fig. 6(b). There exists a region downstream of the leading end of the angled rib where the heat transfer coefficient is maximum and a region downstream of the trailing end of the rib where the heat transfer coefficient is the lowest. To further enhance the average heat transfer coefficient, it was speculated that by breaking the 45 deg rib into two half ribs in a V shape, one basically doubles the high heat transfer coeffi-

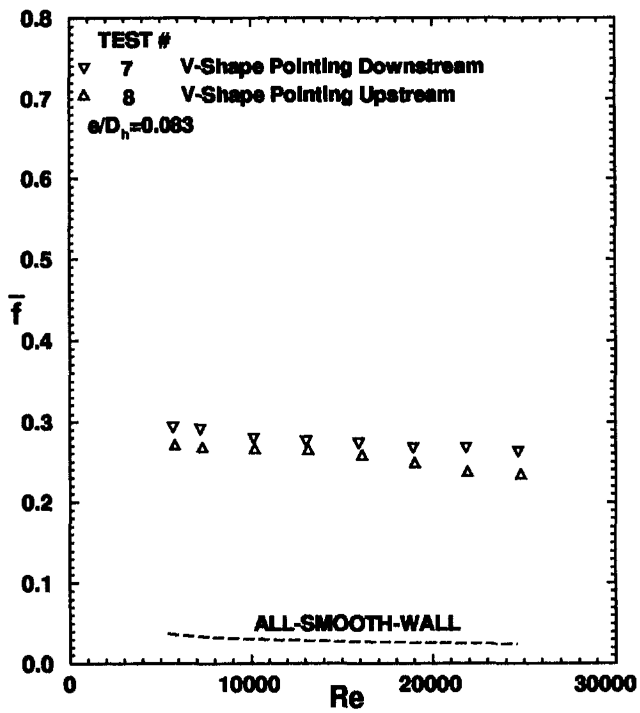

Fig. 9 Comparison of turbulator orientation on channel average friction factor for V-shaped rib geometries

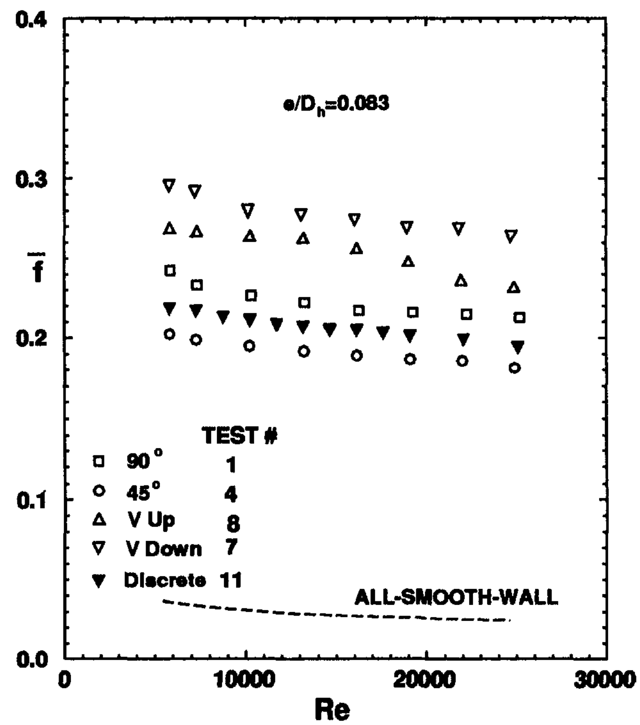

Fig. 11 Comparison of channel average friction factor for five rib geometries of 0.083 blockage ratio

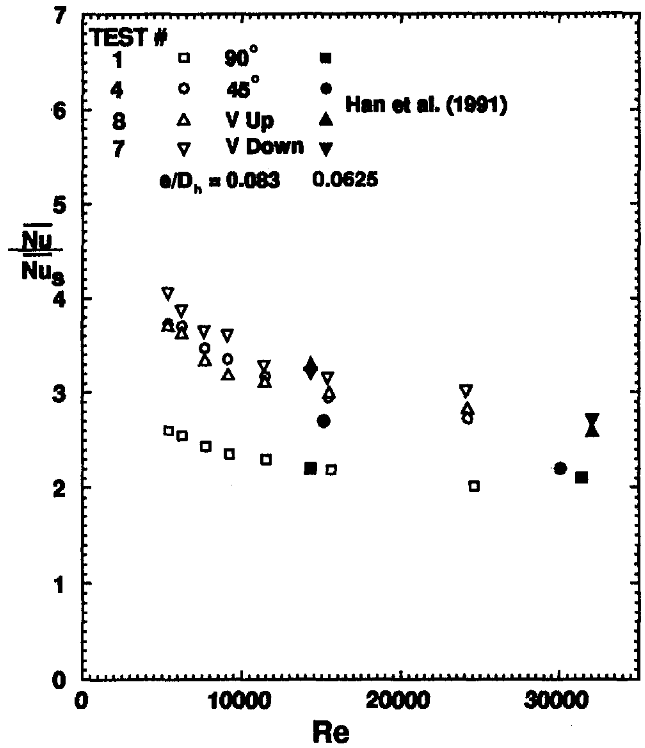

Fig. 12 Comparison of heat transfer enhancement for four rib geometries of 0.0625 and 0.083 blockage ratios

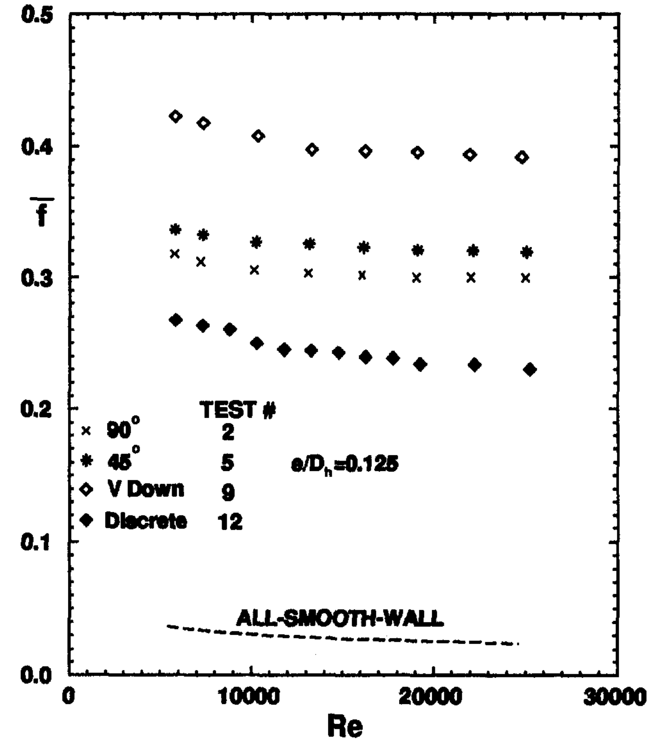

Fig. 14 Comparison of channel average friction factor for four rib geometries of 0.125 blockage ratio

cient area. It was also speculated that with the apex facing downstream, one would have higher overall heat transfer than facing upstream. This reasoning is based on the vortex characteristic change and the increase in the number of secondary flow cells formed by the V-shaped ribs relative to the 45 deg angled ribs. Whereas the 45 deg angled rib had a double-cell counterrotating secondary flow, the V-shaped rib vortices upstream and downstream of the ribs will generate two double-cell counterrotating secondary flow region when the rib apex is pointed downstream, as shown in Fig. 7(*a*). Again these rotations pump cooler center-channel air toward the leading end regions of the V-shaped ribs and warmer air toward the center of the ribs, as illustrated in Fig. 7(*a*). The increase in the number of cells to four and the corresponding changes in the secondary flow directions result in higher heat transfer coeffi-

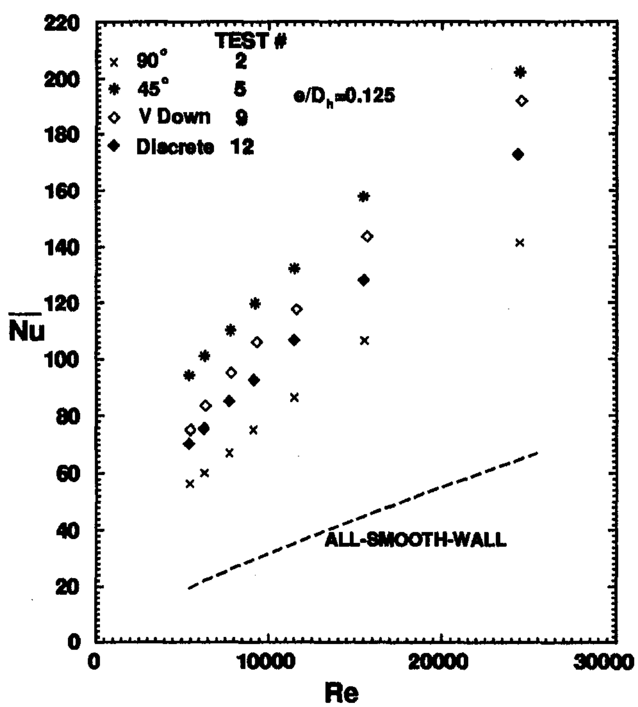

Fig. 13 Comparison of surface average Nusselt number for four rib geometries of 0.125 blockage ratio

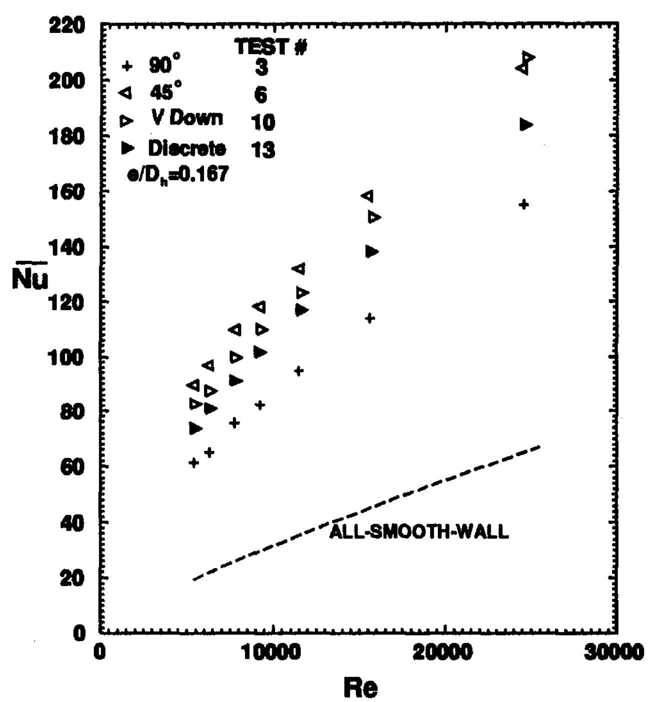

Fig. 15 Comparison of surface average Nusselt number for four rib geometries of 0.167 blockage ratio

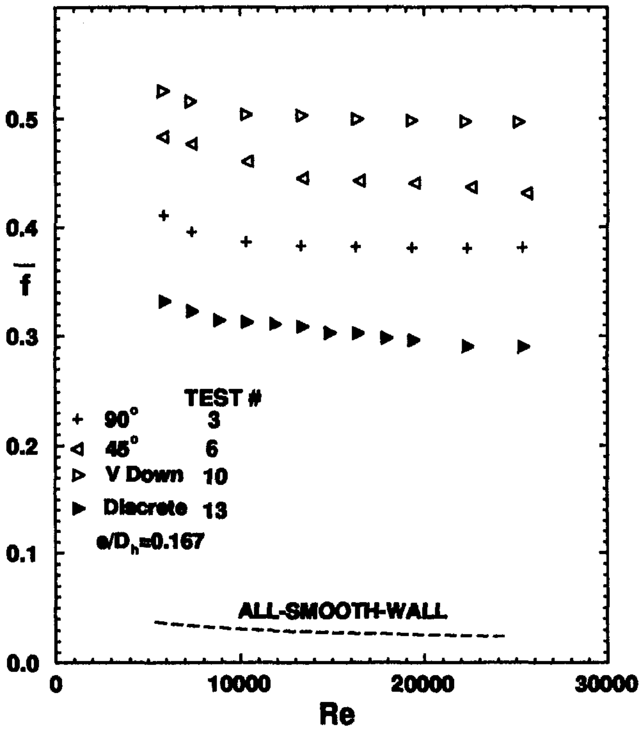

Fig. 16 Comparison of channel average friction factor for four rib geometries of 0.167 blockage ratio

cients near the leading ends and lower heat transfer coefficients near the center apex with a net increase in average heat transfer compared to the 45 deg angled ribs as later shown in Fig. 12.

For the rib apex facing upstream, it is reasoned that the change in the V-shaped rib orientation again creates two double-cell counterrotating vortices but in an opposite direction from the rib apex facing downstream as shown in Fig. 7(a). This results in warmer air being pumped into the rib leading end regions and cooler air being pumped into the rib center apex region. This should change the heat transfer coefficient distribution compared to the downstream pointed apex, i.e., increase the apex region coefficients and lower the leading end regions coefficients. Therefore, test sections 7 and 8, shown in Fig. 2, were tested.

The representative iso-Nu contours for these two low blockage ribs and two other higher blockage V-shaped ribs (test sections 9 and 10, downstream apex) are shown in Fig. 7(b). As expected, two symmetric leading end regions of high heat transfer coefficients and a center region of lower coefficients are formed, which contribute to a higher overall heat transfer coefficient for the V-shaped ribs when compared with the 45 deg angled ribs shown in Fig. 12. Comparing tests 7 and 8 in Fig. 7, iso-Nusselt-number contours further indicate that the distribution results compared well with the secondary flow speculation noted above, i.e., a reverse Nusselt number distribution exists for the upstream-facing apex ribs (Test 8) compared to Test 7. Furthermore, as shown in Figs. 8 and 9, the V-shaped ribs pointing downstream produce slightly higher heat transfer coefficients as well as friction factors than the ribs pointed upstream. Higher friction factor for those ribs pointing downstream is in line with the Colburn (1933) analogy between heat transfer coefficient and friction factor. From the thermal performance viewpoint, however, as shown in Fig. 18 the 45 deg angled ribs are still superior to V-shaped ribs.

Discrete Ribs. The next series of three test configurations deal with discrete angled ribs (test sections 11, 12, and 13 in Table 1 and Fig. 2) mounted on two opposite walls in a staggered array. Note that in Fig. 2, first, a gap between these ribs and the smooth walls and, second, the solid black ribs are mounted on the liquid crystal wall and the cross-hatched ribs are on the opposite acrylic wall with their overlapping leading edge on the channel centerline. For the two highest blockage ratios, the performance of these ribs was inferior to that of the V-shaped ribs in average heat transfer, as noted in Figs. 10, 13, and 15. This observation appears to be due to the presence of relatively large gaps between consecutive ribs on each wall and also between the ribs and smooth sidewalls (Fig. 2). These gaps allowed channeling of some local air with little interaction with the ribs, which results in lower center and endwall heat transfer coefficients as noted in Fig. 17, compared to the V-shaped iso-Nu distribution in Fig. 7. The surface-averaged heat transfer coefficients and friction factors for the 90 deg, 45 deg, V-shaped and discrete ribs of smallest blockage ratio (0.083) are compared in Figs. 10 and 11. Furthermore, as shown in Fig. 12, the heat transfer enhancement for these geometries compare favorably with those of Han et al. (1991) of otherwise identical geometries except for their blockage ratio of 0.0625.

The surface-averaged heat transfer coefficients and friction factors for the 90 deg, 45 deg, V-shaped, and discrete ribs of two higher blockage ratios (0.125 and 0.167) are compared in Figs. 13–16. First, it is observed that for these higher blockage ratios, compared with V-shaped ribs, 45 deg ribs result in higher average heat transfer coefficients with lower pressure losses. Secondly, discrete ribs of all tested blockage ratios have less pressure loss and higher heat transfer enhancements than 90 deg ribs. Representative iso-Nu contours for the discrete ribs are shown in Fig. 17. Again, considerable spanwise variations in heat transfer is observed due to the presence of secondary flows and the gap between the ribs.

As mentioned before, the thermal performance of all geometries tested are compared in Fig. 18. It is seen that 90 deg ribs represent the lowest thermal performance and their thermal performance does not change significantly with blockage ratio. The 45 deg ribs have the highest thermal performance and the

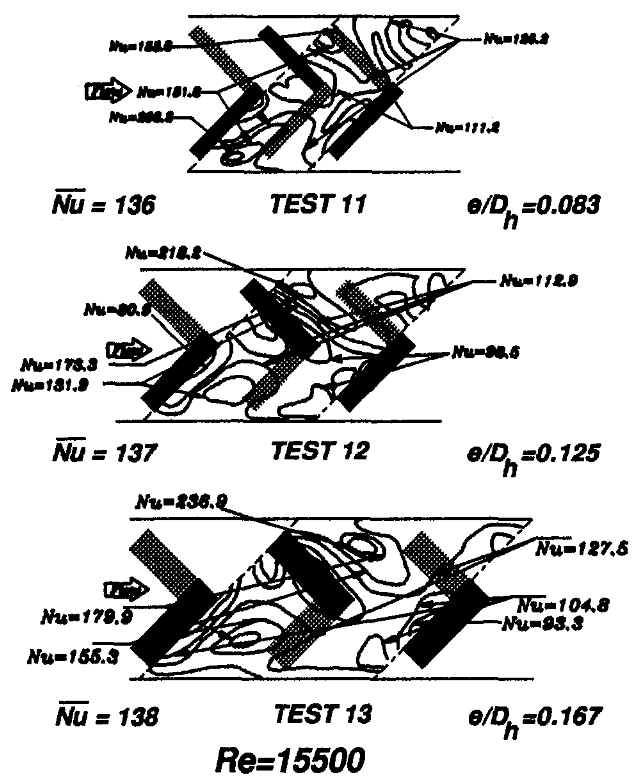

Fig. 17 Representative iso-Nu contours for the 45 deg discrete ribs

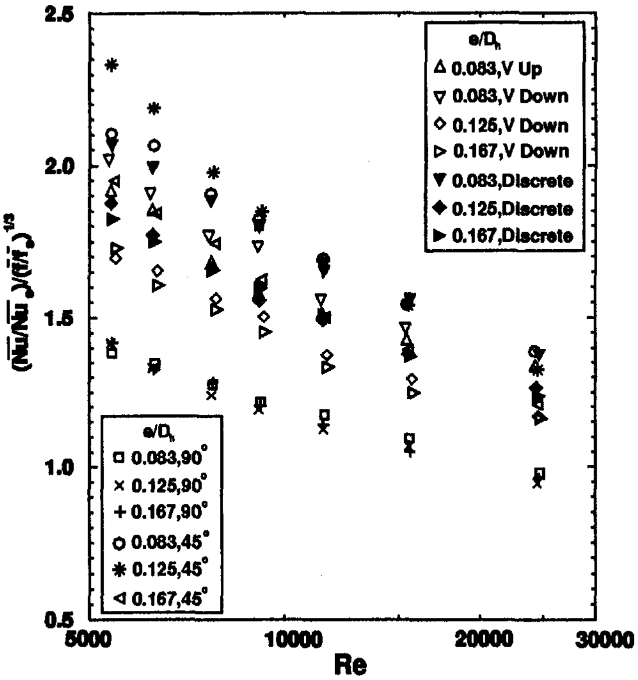

Fig. 18 Thermal performance of the 13 rib geometries

other two geometries (V-shaped and discrete ribs) fall in between with the discrete ribs producing a higher thermal performance than the V-shaped ribs.

Conclusions

A total of 13 rib geometries representing three blockage ratios in a practical range and four different configurations were tested for heat transfer and friction variations. From this study, it is concluded that:

1 The 45 deg ribs and the lowest blockage discrete ribs had thermal performance that was the highest among the geometries tested in this investigation.

2 The 90 deg ribs represent the lowest thermal performance and their thermal performance does not change significantly with blockage ratio.

3 Low-blockage-ratio ($e/D_h = 0.083$) V-shaped ribs pointing downstream produced the highest heat transfer enhancement and friction factors. Among all other geometries with blockage ratios of 0.125 and 0.167, 45 deg ribs showed the highest heat transfer enhancements with friction factors less than those of V-shaped ribs.

4 The discrete angled ribs, although inferior in average heat transfer coefficients to 45 deg and V-shaped ribs, produce much higher heat transfer coefficients and lower friction factors compared to 90 deg ribs.

Acknowledgments

The authors wish to express gratitude to Mr. James E. Hinds for his professional advice in preparing the final manuscript.

References

Abuaf, N., Gibbs, R., and Baum, R., 1986, "Pressure Drop and Heat Transfer Coefficient Distributions in Serpentine Passages With and Without Turbulence Promoters," *The Eighth International Heat Transfer Conference,* C. L. Tien, V. P. Carey, and J. K. Ferrel, eds., pp. 2837–2845.

Burggraf, F., 1970, "Experimental Heat Transfer and Pressure Drop With Two Dimensional Turbulence Promoters Applied to Two Opposite Walls of a Square Tube," *Augmentation of Convective Heat and Mass Transfer,* A. E. Bergles and R. L. Webb, eds., ASME, New York, pp. 70–79.

Chandra, P. R., Han, J. C., and Lau, S. C., 1988, "Effect of Rib Angle on Local Heat/Mass Transfer Distribution in a Two-Pass Rib-Roughened Channel," ASME Journal of Turbomachinery, Vol. 110, pp. 233–241.

Chandra, P. R., and Han, J. C., 1989, "Pressure Drop and Mass Transfer in Two-Pass Ribbed Channels," *AIAA J. Thermophysics,* Vol. 3, No. 3, pp. 315–319.

Colburn, 1933, "A Method of Correlating Forced Convection Heat Transfer Data and a Comparison With Fluid Friction," *Trans. AIChE,* Vol. 29, pp. 174–210.

Dittus, F. W., and Boelter, L. M. K., 1930, *Publications in Engineering,* University of California, Berkeley, CA, Vol. 2, p. 443.

El-Husayni, H., 1991, "An Experimental Investigation of Heat Transfer Coefficients in Stationary and Orthogonally Rotating Smooth and Turbulated Heated on One, Two and Four Walls," MS Thesis, Mechanical Engineering Department, Northeastern University, Boston, MA.

El-Husayni, H., Taslim, M. E., and Kercher, D. M., 1994, "Experimental Heat Transfer Investigation of Stationary and Orthogonally Rotating Asymmetric and Symmetric Heated Smooth and Turbulated Channels," ASME Journal of Turbomachinery, Vol. 116, pp. 124–132.

Fann, S., Yang, W. J., and Zhang, N., 1994, "Local Heat Transfer in a Rotating Serpentine Passage With Rib-Roughened Surfaces," *Int J. Heat Mass Transfer,* Vol. 37, No. 2, pp. 217–228.

Han, J. C., Glicksman, L. R., and Rohsenow, W. M., 1978, "An Investigation of Heat Transfer and Friction for Rib Roughened Surfaces," *Int J. Heat Mass Transfer,* Vol. 21, pp. 1143–1156.

Han, J. C., 1984, "Heat Transfer and Friction in Channels With Two Opposite Rib-Roughened Walls," ASME *Journal of Heat Transfer,* Vol. 106, pp. 774–781.

Han, J. C., Park, J. S., and Lei, C. K., 1985, "Heat Transfer Enhancement in Channels With Turbulence Promoters," ASME *Journal of Engineering for Gas Turbines and Power,* Vol. 107, pp. 628–635.

Han, J. C., Zhang, Y. M., and Lee, C. P., 1991, "Augmentated Heat Transfer in Square Channels With Parallel, Crossed, and V-shaped Angled Ribs," ASME *Journal of Heat Transfer,* Vol. 113, pp. 590–596.

Han, J. C., Zhang, Y. M., and Lee, C. P., 1992, "Influence of Surface Heat Flux Ratio on Heat Transfer Augmentation in Square Channels with Parallel, Crossed, and V-shaped Angled Ribs," ASME Journal of Turbomachinery, Vol. 114, pp. 872–880.

Kline, S. J., and McClintock, F. A., 1953, "Describing Uncertainty in Single-Sample Experiments," *Mechanical Engineering,* Vol. 75, Jan., pp. 3–8.

Lau, S. C., McMillin, R. D., and Han, J. C., 1990, "Heat Transfer Characteristics of Turbulent Flow in a Square Channel With Angled Discrete Ribs," ASME Journal of Turbomachinery, Vol. 111, pp. 117–123.

Lau, S. C., Kukreja, R. T., and McMillin, R. D., 1992, "Heat Transfer in a Square Channel With Staggered Discrete Ribs," *J. Thermophysics Heat Transfer,* Vol. 6, No. 1, pp. 171–173.

Metzger, D. E., Fan, C. S., and Pennington, J. W., 1983, "Heat Transfer and Flow Friction Characteristics of Very Rough Transverse Ribbed Surfaces With and Without Pin Fins," *Proc. ASME–JSME Thermal Engineering Joint Conference,* Vol. 1, pp. 429–436.

Metzger, D. E., Chyu, M. K., and Bunker, R. S., 1988, "The Contribution of On-Rib Heat Transfer Coefficients to Total Heat Transfer From Rib-Roughened Surfaces," *Transport Phenomena in Rotating Machinery,* J. H. Kim, ed., Hemisphere Publishing Co.

Metzger, D. E., Fan, C. S., and Yu, Y., 1990, "Effects of Rib Angle and Orientation on Local Heat Transfer in Square Channels With Angled Roughness Ribs," *Compact Heat Exchangers: A Festschrift for A. L. London,* Hemisphere Publishing Co., pp. 151–167.

Moody, L. F., 1944, "Friction Factors for Pipe Flow," *Trans. ASME,* Vol. 66, p. 671.

Moffat, R. J., 1990, "Experimental Heat Transfer," *Proc. 9th Int. Heat Transfer Conf.,* Vol. 1, pp. 187–204.

Taslim, M. E., and Spring, S. D., 1988a, "An Experimental Investigation of Heat Transfer Coefficients and Friction Factors in Passages of Different Aspect Ratios Roughened With 45° Turbulators," ASME HTD-Vol. 96.

Taslim, M. E., and Spring, S. D., 1988b, "Experimental Heat Transfer and Friction Factors in Turbulated Cooling Passages of Different Aspect Ratios, Where Turbulators Are Staggered," Paper No. AIAA-88-3014.

Taslim, M. E., 1990, "Application of Liquid Crystals in Heat Transfer Coefficient Measurement," *Proc. of IEEE ELECTRO/90,* Boston, MA.

Taslim, M. E., and Spring, S. D., 1991a, "An Experimental Investigation Into the Effects Turbulator Profile and Spacing Have on Heat Transfer Coefficients and Friction Factors in Small Cooled Turbine Airfoils," Paper No. AIAA-91-2033.

Taslim, M. E., Rahman, A., and Spring, S. D., 1991b, "An Experimental Investigation of Heat Transfer Coefficients in a Spanwise Rotating Channel With Two Opposite Rib-Roughened Walls," ASME Journal of Turbomachinery, Vol. 113, pp. 75–82.

Taslim, M. E., Bondi, L. A., and Kercher, D. M., 1991c, "An Experimental Investigation of Heat Transfer in an Orthogonally Rotating Channel Roughened With 45° Criss-Cross Ribs on Two Opposite Walls," ASME Journal of Turbomachinery, Vol. 113, pp. 346–353.

Webb, R. L., Eckert, E. R. G., and Goldstein, R. J., 1971, "Heat Transfer and Friction in Tubes With Repeated-Rib-Roughness," *Int J. Heat Mass Transfer,* Vol. 14, pp. 601–617.

Pressure Oscillations Occurring in a Centrifugal Compressor System With and Without Passive and Active Surge Control

W. M. Jungowski

M. H. Weiss

G. R. Price

Fluid Dynamics Group,
Novacor Research and
Technology Corporation,
Calgary, Alberta, Canada

A study of pressure oscillations occurring in small centrifugal compressor systems without a plenum is presented. Active and passive surge control were investigated theoretically and experimentally for systems with various inlet and discharge piping configurations. The determination of static and dynamic stability criteria was based on Greitzer's (1981) lumped parameter model modified to accommodate capacitance of the piping. Experimentally, passive control using globe valves closely coupled to the compressor prevented the occurrence of surge even with the flow reduced to zero. Active control with a sleeve valve located at the compressor was effective but involved a significant component of passive throttling which reduced the compressor efficiency. With an oscillator connected to a short side branch at the compressor, effective active control was achieved without throttling. Both methods of active control reduced the flow rate at surge onset by about 30 percent. In general, the experiments qualitatively confirmed the derived stability criteria.

Introduction

Centrifugal compressor systems exhibit various pressure oscillations, which depend on the internal compressor geometry, response of the connected piping system, and particular operating conditions. The characterization and control of these pressure perturbations is of considerable interest, since large-amplitude oscillations can seriously damage compressor components and even small-amplitude fluctuations may lead to noise and vibration problems in the associated piping. Pressure perturbations are generated mainly by blade passing and flow instabilities occurring, in particular, at reduced flow rates. The most commonly investigated instabilities are rotating stall within the impeller or radial diffuser and surge (Abdelhamid and Bertrand, 1979; Greitzer, 1981; Hansen et al., 1981; Boyce et al., 1983; Cumpsty, 1989; Seidel et al., 1991; Fink et al., 1992; Mizuki and Oosawa, 1992). Rotating stall represents a local instability, in contrast to surge, which represents the instability of the whole compression system. Mild surge occurs with the natural frequency of the system but deep surge with much lower frequency. A deep surge cycle is characterized by reversed flow and high pressure amplitudes. Compressors sometimes operate with axisymmetric stall near the inducer tips or with stationary nonaxisymmetric stall produced by the volute. However, this is acceptable because much of the pressure rise is produced by centrifugal effects, which are present even with separated flow. The rotating stall propagation speed primarily observed was in the range 0.25–0.75 of the impeller speed (Abdelhamid and Bertrand, 1979; Boyce et al., 1983; Ffowcs Williams et al., 1993; Mizuki and Oosawa, 1992). However, very low speeds below 0.1 occurred with a vaned diffuser (Seidel et al., 1991). The number of stall cells is typically 1 to 3, but Seidel et al. (1991) reported 4 to 7.

Contributed by the International Gas Turbine Institute and presented at the 39th International Gas Turbine and Aeroengine Congress and Exposition, The Hague, The Netherlands, June 13–16, 1994. Manuscript received by the International Gas Turbine Institute March 2, 1994. Paper No. 94-GT-133. Associate Technical Editor: E. M. Greitzer.

Many centrifugal compressor applications require a wide flow range and thus many efforts were made to extend the stable flow range of the compressor. For example, the installation of adjustable inlet guide vanes in some compressors can displace the surge line toward lower flow (Greitzer, 1981; Rodgers, 1991). Casing modifications at the rotor exit (Amann et al., 1975; Greitzer, 1981; Raw, 1986; Cumpsty, 1989) also delayed the surge onset. The most effective approach in eliminating surge, however, was close-coupled throttling (Dussourd et al., 1977; Greitzer, 1981), which produces a combined compressor characteristic with a negative slope even at a very low flow rate. For such a case, stable operation was possible at 40 percent of the normal surge flow, after which rotating stall occurred.

Active surge control, a concept whereby antiperturbations are generated to cancel the surge perturbations, was also tried. A typical active control system consists of a sensor monitoring the surge perturbations, a signal processor transforming the signal according to a predetermined algorithm, and an actuator controlled by the processed signal to produce the antiperturbation. The concept of active surge control has been developed considerably over the last six years, mainly at MIT and Cambridge University (Epstein et al., 1986; Huang, 1988; Pinsley, 1988; Gysling et al., 1991; Pinsley et al., 1991; Simon and Valavani, 1991; Ffowcs Williams et al., 1993; Simon et al., 1993). The theoretical considerations and experiments, however, were restricted to systems composed of a short duct and a plenum. For stability analysis, a lumped parameter model of compression system dynamics was used based on the following assumptions: one-dimensional, incompressible flow in the compressor duct; quasi-steady compressor operation; spatially uniform pressure in the plenum but varying in time; and quasi-steady throttle behavior.

In some of the experiments performed, pressure perturbations were sensed and antiperturbations were generated by varying the throttle area downstream of the plenum or by a loudspeaker inside the plenum (Epstein et al., 1986; Huang, 1988; Pinsley, 1988; Epstein et al., 1989; Ffowcs Williams and Huang, 1989; Pinsley et al., 1991). The maximum displacement of the surge line achieved was 25 and 30 percent, respectively. The system stability with a close-coupled control valve between the compressor and plenum was also analyzed (Simon and Valavani, 1991). In another study, the compression system in a working engine was stabilized by modulating a small extra air flow into the impeller eye (Ffowcs Williams et al., 1993) or into the plenum, i.e., combustion chamber (Ffowcs Williams and Graham, 1990). In addition to the examples cited above, it may be possible to utilize plenum heat transfer, variable inlet geometry, or fast inlet guide vanes as actuators to control surge (Simon et al., 1993). Sensors measuring not only pressure but also mass flow, velocity, or temperature can be implemented according to the selected actuation technique. For three actuators with four different sensors, Simon and Valavani (*1991*) have analytically derived open-loop transfer functions, closed-loop characteristic equations, as well as limitations on the compressor flow range increase using proportional control. The actuators considered were a close-coupled valve, a plenum bleed valve, and a movable wall, along with sensors of compressor mass flow, plenum pressure, compressor face total pressure, and compressor face static pressure. One more approach, namely surge control with tailored structures (Gysling et al., 1991), should be mentioned. This is rather a passive control technique but is closely related to active control, as it is based on the response to perturbations of a moveable plenum wall with an aerodynamic spring and damper. A 30 percent shift of the surge line toward lower flow was achieved with this technique.

This study was concerned with instabilities occurring in a small centrifugal compressor system without a plenum. The piping length as well as conditions within the inlet and discharge piping were varied. Active and passive surge control was investigated both theoretically and experimentally. For the theoretical considerations, Greitzer's (1981) lumped parameter model was modified somewhat to accommodate capacitance of the piping which enabled stability analysis. According to Greitzer's (1981) model with incompressible fluid in the pipe, the system without a plenum was always dynamically stable, which is obviously not the case for a compressible fluid. Active control was executed with a sleeve valve mounted in-line with the compressor piping or with an oscillator connected to a short side-branch at the compressor. Passive control utilized globe valves located close to the compressor.

Stability Analysis

Linear stability analysis was used to evaluate the stability criteria for several compressor configurations. The effect of active and passive devices on these criteria was investigated to determine their ability to enhance the stability of the system at reduced flow rates. The analysis is based on the linearized one-dimensional equations for mass and momentum conservation across a pipe accounting for perturbations from the mean flow variables. A lumped parameter approach was taken with bulk fluid properties set to the average value of the variables at the pipe ends. Additional elements were modeled by perturbation equations derived from continuity and steady pressure loss/rise equations. The results of the stability analysis for various compression systems are compiled in Table 1.

A detailed example of the stability analysis for a simple compression system, configuration 1 in Table 1, with a downstream pipe connected to a throttle valve, is presented in Appen-

Table 1 Static and dynamic stability criteria for various compression systems

No	CONFIGURATION	STATIC STABILITY	DYNAMIC STABILITY
1	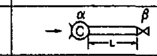	$\beta > \alpha$	$1 > \alpha\beta M^2$
2	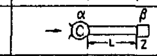	$\beta > \alpha(1+\beta\bar{\Phi}Z)$	$1+\beta\bar{\Phi}Z > \alpha\beta M^2$
3	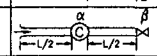	$\beta > \alpha$	$2 > \alpha\beta M^2$
4	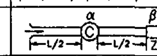	$\beta > \alpha(1+\beta\bar{\Phi}Z)$	$2(1+\beta\bar{\Phi}Z) > \alpha\beta M^2$
5	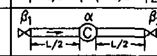	$\beta_1+\beta_2 > \alpha$	$2(1+\beta_1\beta_2 M^2) > \alpha(\beta_1+\beta_2) M^2$
6	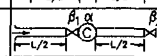	$\beta_1+\beta_2 > \alpha$	$2 + \beta_1\beta_2 M^2 > \alpha\beta_2 M^2$
7	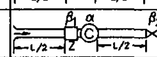	$\beta_1+\beta_2 > \alpha$	$2 + \beta_1\beta_2 M^2 + \beta_1\bar{\Phi}Z > \alpha\beta_2 M^2$
8	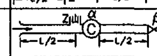	$\beta > \alpha$	NUMERICAL ANALYSIS
9	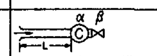	$\beta > \alpha$	STABLE
10		$\beta > \alpha$	$2 + (\beta-\alpha)M > \alpha\beta M^2$
11	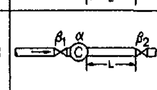	$\beta_1+\beta_2 > \alpha$	$2 + (\beta_1+\beta_2-\alpha)M + \beta_1\beta_2 M^2 > \alpha\beta_2 M^2$
12	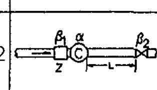	$\beta_1+\beta_2 > \alpha$	$2 + (\beta_1+\beta_2-\alpha)M + \beta_1\beta_2 M^2 + \beta_1\bar{\Phi}Z(1+\beta_2 M) > \alpha\beta_2 M^2$
13	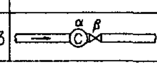	$\beta > \alpha$	STABLE

Nomenclature

a = sound speed = $\sqrt{(dp/d\rho)_s}$
A = pipe cross-sectional area
A_t = throttle area = $\bar{A}_t + A_t'$
$\bar{A}_t$ = time-mean throttle area
A_t' = throttle area increment
B = system parameter = $U/\omega L$
d = pipe diameter
i = unit imaginary number = $\sqrt{-1}$
L = total pipe length
m = instantaneous mass flow rate = $\bar{m} + m'$
$\bar{m}$ = time-mean flow rate
m' = flow rate perturbation
M = blade tip Mach number = U/a
n_1 = suction pipe/total pipe length = L_1/L
n_2 = discharge pipe/total pipe length = L_2/L
p = instantaneous pressure = $\bar{p} + p'$
$\bar{p}$ = time-mean pressure
p' = pressure perturbation
s = roots of system characteristic equation
$\bar{s}$ = normalized roots = s/ω
t = time
$\bar{t}$ = normalized time = $t\omega$
u = flow velocity
U = blade tip speed
Z = gain of throttle or speaker control = $|Z|\ \exp i\gamma$
α = slope of compressor characteristic = $d\bar{\psi}_c/d\bar{\phi}$
β = slope of throttle curve = $(\partial\bar{\psi}_t/\partial\bar{\phi})_{A_t}$
γ = phase angle between pressure disturbance and increment of throttle area or membrane velocity
Δp_c = compressor pressure rise
Δp_t = throttle pressure drop
ρ = gas density
$\bar{\rho}$ = time-mean gas density
ϕ = normalized instantaneous flow rate = $m/\rho UA$
$\bar{\phi}$ = normalized time-mean flow rate = $\bar{m}/\rho UA$
ϕ' = normalized flow rate perturbation = $m'/\rho UA$
ψ = normalized instantaneous pressure = $p/\rho U^2$
$\bar{\psi}$ = normalized time-mean pressure = $\bar{p}/\rho U^2$
ψ' = normalized pressure perturbation = $p'/\rho U^2$
ω = angular frequency

dix 1. The stability criteria for this simple compressor system without a plenum reveal that static stability requires $\beta > \alpha$, and dynamic stability $1 > \alpha\beta M^2$. Inclusion of the convective terms in the momentum equation across the pipe changed the stability criteria to $1 > \alpha\beta M^2 + (\alpha + \beta)\bar{\phi}M^2$. In reality, the maximum value of the additional term was below $0.065\ \alpha\beta M^2$; therefore, the convective terms were omitted for the other configurations. The speed of sound was assumed to be constant throughout the entire system, but differed by about 6 percent between the suction and discharge of the compressor. These simplifications appear to be acceptable when dealing with weak perturbations and linearized equations. They are generally applied in linear acoustics and should not distort the main conclusions from the stability analysis.

The criteria in Table 1 show that the dynamic stability of compression systems without a plenum depends on M, and not on B as it does with a plenum in Greitzer's (1981) model ($1 > \alpha\beta B^2$). For the latter case, substituting ω with the Helmholtz resonator frequency shows that B is proportional to M:

$$B = U/\omega L = M\sqrt{V/AL} \tag{1}$$

and when the plenum volume $V = AL$ it is equal to M.

A mathematical description of some system elements absent in the simple compression system, configuration 1, will be presented below. When the throttling valve is adjacent to the compressor on the suction or discharge side, i.e., configurations 6, 9, 11, and 13, the pressure perturbation equation becomes

$$\psi_2' - \psi_1' = (\alpha - \beta_1)\phi_1' \tag{2}$$

where the subscript 1 denotes upstream and 2 the downstream side.

With only one throttle valve, i.e., configurations 9 and 13, β should be used instead of β_1. With the sleeve valve as an active controller at the discharge, i.e., configurations 2 and 4, the pressure perturbation equation becomes

$$\psi_1' = \left[\frac{\beta}{(1 + \beta\bar{\phi}Z)}\right]\phi_1' \tag{3}$$

and at the compressor, i.e., configurations 7 and 12,

$$\psi_1'(1 + \beta\bar{\phi}Z) = \psi_2' - (\alpha - \beta)\,\phi_1' \tag{4}$$

With infinitely long piping, i.e., configurations 10 through 13, the anechoic conditions upstream yield

$$\psi_1' = -\phi_1'/M \tag{5}$$

and downstream

$$\psi_2' = \phi_2'/M \tag{6}$$

The system of linear algebraic and first-order ordinary differential equations that arises for a given compression system was reduced into a higher-order ordinary differential equation (O.D.E.) with a single perturbation variable. This was accomplished using Mathematica, a computer program that can render symbolic mathematics (Wolfram, 1991). Derivations of the stability criteria for four compression systems with variable upstream and downstream piping lengths are presented in Appendix II. After introducing equal upstream and downstream pipe lengths, i.e., $n_1 = n_2 = \frac{1}{2}$, they correspond to configurations 3, 5, 7, and 8 in Table 1.

The strongest criteria for static and dynamic stability are shown in Table 1. For the more complicated compression systems, application of the Routh–Hurwitz criterion results in several expressions/coefficients, which must remain positive to ensure stability. It was difficult to ascertain in some instances, which expressions embodied the static and dynamic stability, and of those which was the strongest criteria. In most cases, the expressions showed the condition for static stability was $\beta > \alpha$ or $\beta_1 + \beta_2 > \alpha$, depending on whether there are one or two valves in the configuration. However, in configurations 2 and 4, the expressions containing the static terms seemed to impose some limitation of the gain, Z, and therefore these results were included. With anechoic conditions applied to the pipe ends, i.e., configurations 10 through 13, the expressions also indicated that static stability was enhanced. These were ignored for lack of a physical meaning. Only the strongest requirements for dynamic stability were included. Comparison of configurations 1 through 7 and 9 show the stabilizing effects of: piping on both compressor sides, throttling with two valves, active control with the sleeve valve, and throttling at the compressor only. Configurations 10 through 13 show an additional stabilizing effect resulting from the anechoic boundary conditions. With the controlling oscillator on the side-branch, i.e., configuration 8, it was difficult to determine which expression controlled the stability of the system. A numerical analysis was performed and will be presented in the Discussion section.

Experimental Facilities

All experiments were performed on a single-stage 10 HP centrifugal compressor with an axial inlet and a vaneless diffuser volute outlet configuration. The 127-mm-dia unshrouded impeller consisted of 8 full blades and 8 splitter blades, all without back-sweep. An electric motor with a variable frequency controller was directly coupled to a high-speed gear box, which turned the impeller shaft. At the maximum rotational speed of 31,000 rpm, the impeller blade-tip Mach number was about 0.6 and a discharge-to-suction pressure ratio of 1.35 for the ambient inlet air could be achieved.

All piping for the numerous test configurations consisted of nominal 2-in-dia (52.5 mm) plastic pipe attached to the suction and discharge ports of the compressor. Standard 2 in. globe valves were used to throttle the flow at various locations. For the tests of passive control using close-coupled throttling, the same globe valves were implemented.

Basic instrumentation for compressor performance mapping was provided. Specifically, mean pressure across the compressor was measured with a Validyne differential pressure transducer connected to triple-T piezometer rings (Blake, 1976) at the inlet and discharge of the compressor. RTD probes were used to measure total temperature in the suction and discharge piping and the flow rate in the inlet piping was determined from venturi nozzles or a calibrated Pitot tube. The compressor speed was measured using an optical tachometer. In addition, flush-mounted Endevco dynamic pressure transducers were located close to the compressor inlet and discharge and TSI hot-film anemometer probes were mounted in the inlet piping. These dynamic transducers provided control signals for the active control systems. For the more detailed measurements of rotating stall, TSI hot-film anemometer probes or Endevco flush-mounted dynamic pressure transducers were located in the diffuser volute.

Two types of active control systems were tested. The first system consisted of a low-inertia rotary sleeve valve comprised of two sleeves, each with diametrically opposed windows. Rotation of the outer sleeve relative to the stationary inner sleeve established the degree to which the windows were aligned, which consequently determined the resistance to air flow. The absence of contact seals between the two sleeves prevented the valve from providing a positive seal when fully closed, although a close-tolerance annular gap did provide a large flow restriction. A valve position controller was designed to control the throttle area of the sleeve valve in response to a fluctuating pressure or velocity signal. The block diagram of this controller is given in Fig. 1 where the Infranor DC servomotor is shown connected directly to the outer rotating sleeve. An angular displacement transducer (RVDT) mounted on the rear of the servomotor determined the angular position of the motor shaft and

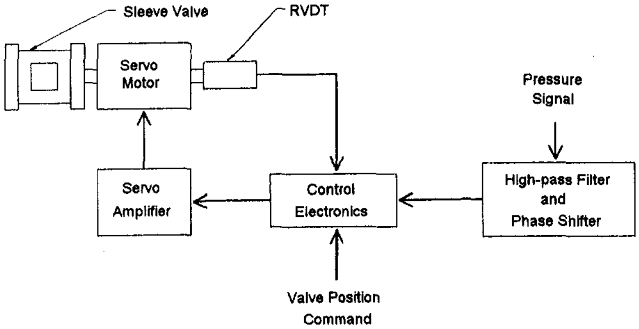

Fig. 1 Block diagram of sleeve valve active control system

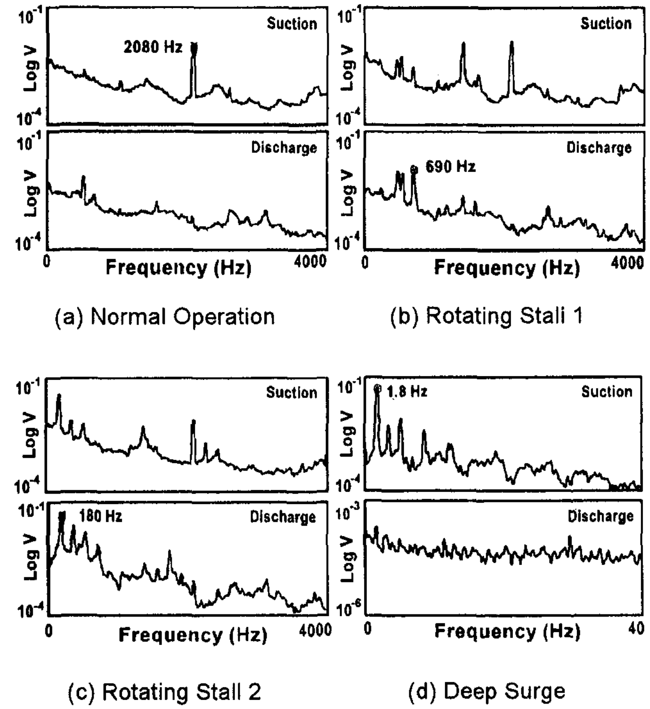

Fig. 3 Typical suction and discharge pressure spectra for various operational modes

thus the outer sleeve. The sleeve valve and motor control apparatus could be mounted in-line virtually anywhere in the inlet and discharge piping.

The second active control system is shown in Fig. 2 and consisted of either an electronic speaker or a speaker diaphragm mounted in a sealed enclosure and connected to the inlet piping with a tee fitting. Using an eccentric drive mechanism, the same servomotor and amplifier of the sleeve valve control system could be used to move the diaphragm. A somewhat different controller was designed that provided speed control of the diaphragm in response to a dynamic pressure signal. Unlike the sleeve valve system, this side branch oscillator did not introduce any passive or dynamic throttling into the system when in the active control mode.

Data for the compressor performance tests were acquired and processed using a personal computer. For the more detailed analysis of rotating stall, real-time FFT measurements were carried out with a two-channel dynamic analyzer.

Experimental Results

To begin with, the compressor performance was determined and several operating modes were defined. Next, the effect of throttling valve position on the compressor performance was investigated, followed by tests with two different active control systems. Detailed results of these experiments are described in this section. Due to the large number of test cases considered, the results are typically summarized in specific tables, which depict the test configurations and list the pertinent information.

Compressor Performance. Performance testing provided the compressor characteristic curve presented and analyzed in the Discussion section. In addition, performance testing exposed several modes of compressor operation in the low-flow region where each mode was associated with a characteristic pressure

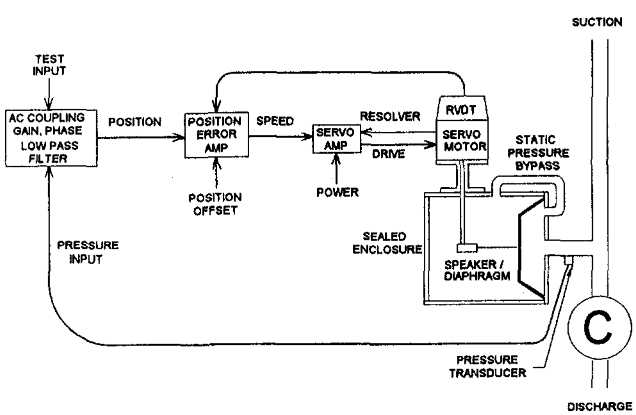

Fig. 2 Block diagram of side-branch oscillator active control system

spectrum (Fig. 3). *Normal operation* occurred at flow rates above the surge limit and was characterized by a dominant peak in the frequency spectrum that was four times that of the impeller frequency as shown in Fig. 3(*a*). This peak was due to four circumferentially located holes in the impeller, which were present to permit servicing of the compressor unit. Pressure oscillations for this mode were quite low. As the flow rate was decreased, a dominant frequency somewhat above the impeller frequency emerged and the level of pressure oscillation increased (Fig. 3(*b*)). This pattern characterized *rotating stall 1* for which phase angle measurements with sensors on the discharge volute indicated three stalled impeller cells propagating at 44 percent of the impeller speed. A further reduction of flow rate resulted in *rotating stall 2* with still larger pressure oscillations and a dominant peak in the pressure spectrum at about one-third of the impeller frequency (Fig. 3(*c*)). Phase measurements on the discharge volute indicated one stalled cell propagating at 35 percent of the impeller speed. With additional throttling, *mild surge* was observed followed by *deep surge.* Both mild and deep surge were characterized by large-amplitude oscillations of low frequency, although for deep surge larger amplitudes with flow reversals occurred and the frequencies were typically somewhat lower as shown in Fig. 3(*d*). At the maximum compressor speed for which M = 0.6, the normalized flow ranges, typical pressure oscillation levels, and dominant frequencies in the pressure spectrum for all five modes are summarized in Table 2.

Effect of Throttle Valve Position on Compressor Performance. The position of the throttling valve in a compressor system can influence the performance of the system, particularly if the valve is located very close to the compressor. For example, Dussourd et al. (1977) have demonstrated that a close-coupled resistance can substantially reduce the flow rate at which surge occurs. In the present study, various throttling positions with combinations of up to three valves were tested to observe the effects of throttling position on the compressor performance as flow was reduced to zero. The results are summarized in Table 3 in which the lowest flow operating mode for ten different

Table 2 Modes of compressor operation @ M = 0.6

	MODE				
	Normal Operation	Rotating Stall 1	Rotating Stall 2	Mild Surge	Deep Surge
$\bar{\phi}$	0.13-0.08	0.09-0.03	0.07-0.04	0.07-0.02	0.07-0.03
ψ'	0.002-0.009	0.004-0.007	0.011-0.024	0.02-0.05	0.04-0.16
Dominant Frequency	2080 Hz	690 Hz	180 Hz	10-12 Hz	2-4 Hz

cases is presented and where ψ_s' and ψ_d' represent the normalized fluctuating pressure amplitude at the compressor suction and discharge, respectively.

For case 1, the compressor with only a discharge globe valve and an inlet nozzle was tested. When the flow was reduced to zero, only rotating stall 2 was observed but surge did not occur. With the addition of piping on both the inlet and discharge of the compressor (case 2), deep surge occurred, although accurate measurements of mean flow rate could not be obtained in the presence of flow reversals. Essentially identical behavior occurred with the sleeve valve as the discharge throttling element (case 3), confirming that some fluid capacitance is necessary for surge to occur. Next, the globe valve was moved to the inlet side and located close to the compressor, as shown for case 4. In addition, the length of the inlet and discharge piping was doubled. Surge did not occur for this configuration since the close-coupled throttle valve interacts with the compressor, resulting in a combined characteristic, which provides stable operation even to the limit of no flow.

A second globe valve was located at the discharge end of the piping to provide throttling (case 5) and although the globe valve close to the compressor remained fully open, it inherently still provided some flow restriction. In this case deep surge did occur but the levels of pressure fluctuation were mitigated, probably due to the slight flow resistance of the fully open globe valve at the inlet to the compressor. When the inlet globe valve was also throttled, surge was again eliminated as shown in case 6. Replacing the inlet globe valve with the sleeve valve resulted in similar response (case 7).

Next a third globe valve was added to the system and located close to the compressor on the discharge side. Throttling was accomplished with one of the valves while the other two remained fully open. When the furthest downstream valve provided throttling (case 8), deep surge occurred, although again the levels of pressure fluctuation were reduced due to the additional flow restriction of the two valves close to the compressor. If either of the two valves located near the compressor were throttled, case 9 or case 10, surge was prevented. It is interesting to note that for case 6 the operating mode at zero flow is rotating stall 1, while in case 10 it is rotating stall 2. A closer comparison of the two cases indicates that additional throttling with a valve far away from the compressor somewhat enhances the stability of the system.

The results presented here confirmed that close-coupled resistance, in the form of a globe valve located near the compressor inlet or discharge, can extend the stable operating range of a centrifugal compression system. However, measurements indicate that this extended flow range is only achieved at the expense of a reduction in efficiency.

Active Control With Throttling Element (Sleeve Valve). The primary element of the first active control system tested consisted of a low-inertia rotary sleeve valve. Details of this system were provided earlier in the discussion of Fig. 1. The basic principle of this valve and control system was to provide variable throttling in response to a pressure disturbance signal from some point in the compressor piping. An inherent feature of the sleeve valve is that the slope of the throttling characteristic decreases dramatically as the valve is opened. As a consequence, for the relatively small angular valve displacements required for fast valve response, significant fluctuating flow restrictions are only possible when the valve is almost closed. This results in a significant passive throttling component during active control, the effect of which is difficult to distinguish from the purely active component of valve throttling. The findings previously summarized in Table 3 clearly indicate that passive throttling alone, especially when closely coupled to the compressor, can extend the stable operating range. Thus, in discussing the sleeve valve control system results summarized in Table 4, it should be kept in mind that the effectiveness of active control is due to a varying combination of both active and passive throttling. In Table 4, the effect of active control is illustrated by identifying the operating conditions during mild or deep surge without control in contrast to the resulting situation when control is activated.

Case 11 shows the effect of the sleeve valve when located at the end of the discharge piping. For this particular case, mild surge was induced by passively throttling the sleeve valve and then the control system was activated. Clearly, mild surge was eliminated, resulting in the rotating stall 2 mode with significantly reduced pressure oscillations. This demonstrates the effectiveness of active control throttling only since the sleeve valve was already almost closed to initiate surge. When a globe valve was added in series with the sleeve valve and throttled to induce mild surge (case 12), only marginal differences compared to the previous case were observed. Again the sole effect of active throttling was demonstrated. Next, the sleeve valve was moved closer to the compressor but was mounted as a venting side-branch, as shown in case 13, and not in-line as before. Since the sleeve valve did not have contact seals, flow was vented out through the valve even when it was fully closed. For this case, the induced mild surge was not as strong as in the previous cases and active control was able to restore the compressor to its normal operating condition.

The length of the inlet and discharge piping was doubled and the sleeve valve was mounted in-line with a globe valve at the end of the discharge piping (case 14). Note that for this case the sleeve valve was upstream of the globe valve rather than

Table 3 Effect of throttling position on compressor performance

CASE	CONFIGURATION	M	LOW FLOW LIMITING CONDITION				
			$\bar{\phi}$	$\bar{\psi}$	ψ_s'	ψ_d'	MODE
1	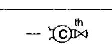	0.45	0.0	0.53	.019	.034	ROTATING STALL 2
		0.60	0.0	0.53	.018	.024	
2		0.45	0.06	0.61	0.02	0.02	MILD SURGE *
		0.60	0.07	0.63	0.03	0.03	
3		0.45	0.06	0.61	0.02	0.02	MILD SURGE *
		0.60	0.07	0.63	0.03	0.03	
4	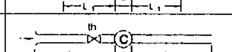	0.60	.036	.598	.003	.002	NORMAL OPERATION **
5	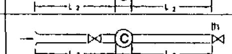	0.60	.027	0.51	0.06	0.05	DEEP SURGE
6	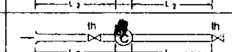	0.60	0.0	0.45	.007	.006	ROTATING STALL 1
7	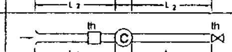	0.60	.046	0.60	.005	.005	ROTATING STALL 1
8	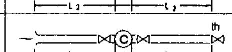	0.60	0.03	0.52	.049	.053	DEEP SURGE
9	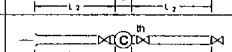	0.60	0.0	.476	.013	.017	ROTATING STALL 2
10		0.45	0.0	.496	.022	.033	ROTATING STALL 2
		0.60	0.0	.49	.013	.017	

* DEEP SURGE WAS OBSERVED BUT FLOW RATE WAS NOT MEASURED
** ROTATING STALL LIKELY OCCURRED AS FLOW DECREASED TO ZERO
L_1 =12m , L_2 =24m ⋈ GLOBE VALVE Ⓒ COMPRESSOR
□ SLEEVE VALVE th INDICATES THROTTLING

Table 4 Effect of active control using a sleeve valve throttling element

CASE	CONFIGURATION	M	NO CONTROL					WITH ACTIVE CONTROL				
			$\bar{\phi}$	$\bar{\psi}$	ψ'_s	ψ'_d	MODE	$\bar{\phi}$	$\bar{\psi}$	ψ'_s	ψ'_d	MODE
11	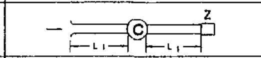	0.6	—	0.59	0.07	0.06	MILD SURGE	.063	.614	.012	.012	ROTATING STALL 2
12	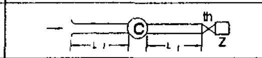	0.6	—	0.59	0.03	0.02	MILD SURGE	.063	0.61	0.01	.011	ROTATING STALL 2
13	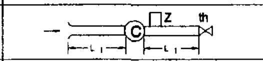	0.6	—	.622	.020	.019	MILD SURGE	.073	.629	.004	.004	NORMAL OPERATION
14	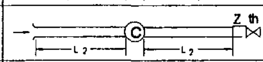	0.6	—	0.60	0.07	0.06	DEEP SURGE	.046	0.59	.006	.006	ROTATING STALL 1
15	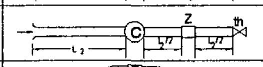	0.6	.056	0.57	.025	.044	MILD SURGE	.043	0.58	.004	.005	NORMAL OPERATION
16	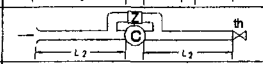	0.6			ACTIVE CONTROL INEFFECTIVE							
17	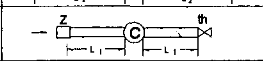	0.6	—	.455	.033	.012	MILD SURGE	.047	.488	.004	.003	NORMAL OPERATION
18	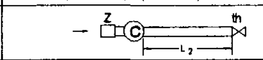	0.6	—	.489	.024	.016	MILD SURGE	—	.497	.011	.011	ROTATING STALL 2
19	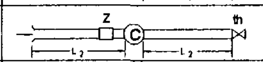	0.6	—	.527	0.07	0.07	DEEP SURGE	.021	.526	.003	.002	NORMAL OPERATION
20		0.6			ACTIVE CONTROL INEFFECTIVE							

L_1=12m , L_2=24m ⋈ GLOBE VALVE th INDICATES THROTTLING
□ SLEEVE VALVE z INDICATES ACTIVE CONTROL
ⓒ COMPRESSOR

downstream as in case 12. With this configuration deep surge was induced by the globe valve and completely suppressed by activating the sleeve valve. Moving the sleeve valve to the midpoint of the discharge line (case 15) resulted in equally effective control, although in this case the control of mild surge is illustrated. However, when the sleeve valve was mounted in a recycle loop, as shown in case 16, active control was ineffective. The ineffectiveness was due in part to the constant flow leakage around the compressor through the sleeve valve and the possible destabilizing effects of opposing pressure disturbances propagating to both the inlet and discharge sides of the compressor.

Several cases with the sleeve valve on the inlet side and a globe valve located at the end of the discharge were tested. With the shorter inlet and discharge piping length and the sleeve valve located at the inlet (case 17), active control was able to restore the compressor to normal operation from mild surge. Compared with case 11, the operating range was extended to lower flows but with a reduced pressure rise. For case 18, the inlet piping was eliminated, the discharge piping length doubled, and the sleeve valve located close to the compressor inlet. Control of mild surge was similar to the previous case, although the lack of inlet piping appeared to reduce the effectiveness of control. When inlet piping was added (case 19), even deep surge was controlled. For this case, the passive component of sleeve valve throttling contributed significantly to the effectiveness of surge suppression. However, by moving the sleeve valve to the beginning of the inlet piping, as shown in case 20, active control was ineffective. For this case, the long distance between the control element and the compressor resulted in a rather weak influence of active throttling.

Active Control With Side-Branch Oscillator. It is of considerable interest to determine if active control *without* throttling is possible. In order to test this idea, a second active control system was designed and tested. Some details of this system were described earlier in the discussion of the controller block diagram in Fig. 2, where the active element consisted of a speaker or speaker diaphragm in an enclosure mounted as a side branch. The active element drew air from the main piping or injected into it, thus providing a pressure disturbance in the main flow without introducing any throttling. A pressure equalization port, shown in Fig. 2, relieved the static pressure load on the speaker or diaphragm. The results for several variations of this active control system without throttling are summarized in Table 5. In the discussion that follows, the effect of active control is demonstrated through a comparison of the surge limit with and without active control. The surge limit is defined as the operating point just prior to the onset of mild surge. Specific performance data are listed in Table 5 along with schematics of the test configurations.

Initially, a low-wattage speaker (S1) was tested but at reduced compressor speeds due to performance limitations of the speaker. These results (case 21) indicated that active control without throttling was effective even with the limited speaker power as the operating range was extended to lower flow rates. A larger 1000 W speaker (S2) was installed, which provided some degree of control at higher compressor speeds, although performance at the maximum compressor speed was still restricted by speaker power limitations (see case 22). Finally, a robust speaker diaphragm was mounted in the enclosure, which was oscillated by a servomotor via an eccentric drive mechanism. This system is described in case 23, where the operational range was extended by as much as 30 percent at relatively high compressor speeds. At the maximum compressor speed, lowering of the flow range by more than a few percent was not possible due to flexibility of the diaphragm and insufficient power of the servomotor. When an additional globe valve was located close to the compressor discharge (case 24), the surge limit without control was lowered substantially, due to the close-coupled throttling. In this case, active control was able to extend the operating range by about 15 percent even at the maximum compressor speed. The following additional observation was made in the course of the measurements: When the diaphragm system was left to oscillate freely, surge onset was delayed and the fluctuating pressure levels were reduced on the inlet side of the compressor where the side-branch oscillator was mounted.

Table 5 Effect of active control using a side-branch oscillator

CASE	CONFIGURATION	M	SURGE LIMIT WITHOUT CONTROL					SURGE LIMIT WITH ACTIVE CONTROL				
			$\bar{\phi}$	$\bar{\psi}$	ψ'_s	ψ'_d	MODE	$\bar{\phi}$	$\bar{\psi}$	ψ'_s	ψ'_d	MODE
21	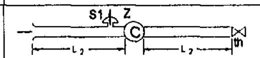	0.3	.046	0.59	.017	.018	ROTATING STALL 2	.029	0.55	0.02	.019	ROTATING STALL 2
		0.35	.042	0.60	.018	.017		.033	0.58	0.02	.018	
22	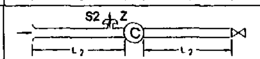	0.4	.068	0.63	.006	.008	ROTATING STALL 1 *	.042	0.54	.021	.013	ROTATING STALL 2
		0.5	.069	0.64	.006	.008		.058	0.62	.010	.014	
		0.6	.081	0.66	.005	.008		.073	0.65	.006	.011	
23	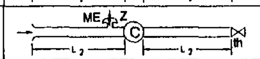	0.5	.079	0.65	.004	.007	ROTATING STALL 1	.057	0.62	.012	.021	**
		0.55	.088	0.65	.003	.005		.077	0.65	.004	.007	ROTATING STALL 1
		0.6	.081	0.65	.003	.005		.079	0.65	.003	.006	
24	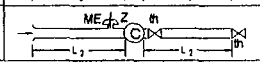	0.6	.025	0.54	.016	.019	ROTATING STALL 2	.021	0.54	.017	.020	ROTATING STALL 2

L_1=12m , L_2=24m

* ACTUAL LIMIT MAY HAVE BEEN AT SLIGHTLY LOWER FLOW RATES
** ROTATING STALL 2

⋈ GLOBE VALVE
SPEAKER/DIAPHRAGM
Ⓒ COMPRESSOR
th INDICATES THROTTLING
Z INDICATES ACTIVE CONTROL
S1,S2 ELECTRONICALLY ACTIVATED SPEAKER
ME MECHANICALLY ACTIVATED DIAPHRAGM

Thus the natural response of the diaphragm coupled to the mechanical drive and servomotor had a damping effect on surge.

Tests with purely active control, in the form of a side-branch oscillator, indicated that the operating range of centrifugal compressor systems can be extended to 30 percent lower flow rates without reducing the efficiency through throttling.

Discussion

All values of $\bar{\phi}$ and $\bar{\psi}$ acquired with maximum compressor speed (M = 0.6), various configurations, and three initial modes (normal operation, rotating stall 1 and 2), generating rather low pressure oscillations, were plotted in Fig. 4. Operation with active control and without was distinguished. The active control lowered slightly the pressure rise with higher flow rates. The experimental points were approximated with the function suggested by Ffowcs Williams and Huang (1989) and then the slope α was calculated as a function of ϕ.

The slope of the throttle curve was calculated with $\bar{\psi}_t = \bar{\psi}_c$, which means that pressure loss along the piping was combined with the pressure drop across the valve. The slopes α and β were plotted versus $\bar{\phi}$ in Fig. 5. Flow rates associated with surge were marked in Fig. 4: m = limit of operation without surge given by the compressor manufacturer ($\bar{\phi}$ = 0.13), t = dynamic stability limit for configuration 3 ($\bar{\phi}$ = 0.11), and e = experimental limit for operation without surge with that configuration. The numerical analysis of stability for configuration 8 was also based on slope values presented in Fig. 5. The coefficients of the array corresponding to Eq. (A70) were calculated and plotted versus $\bar{\phi}$ in Fig. 6 for optimum Z = 2.3. The system is stable when all of them are positive. Therefore, coefficients a_1, a_3, and b_3 determine the stability limit at $\bar{\phi}$ = 0.037 (Fig. 6). Figure 7 shows the dependence of that limit on gain for the symmetric case ($n_1 = n_2$). At optimum gain, $\bar{\phi}$ was reduced from 0.11 to 0.037, i.e., by about 66 percent. Clearly, the numerical stability analysis indicates a sensitive

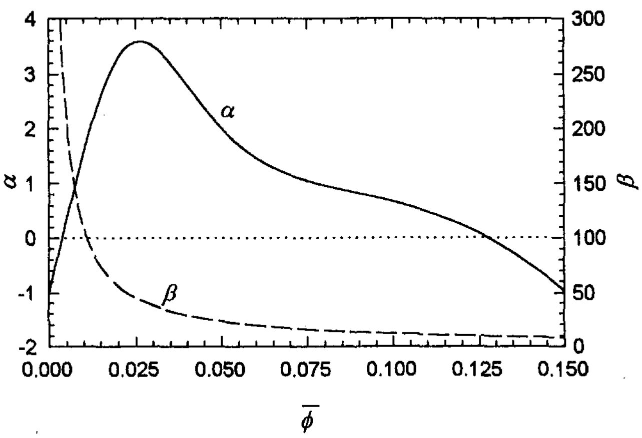

Fig. 5 Slope of the compressor characteristic α and the throttle curve β

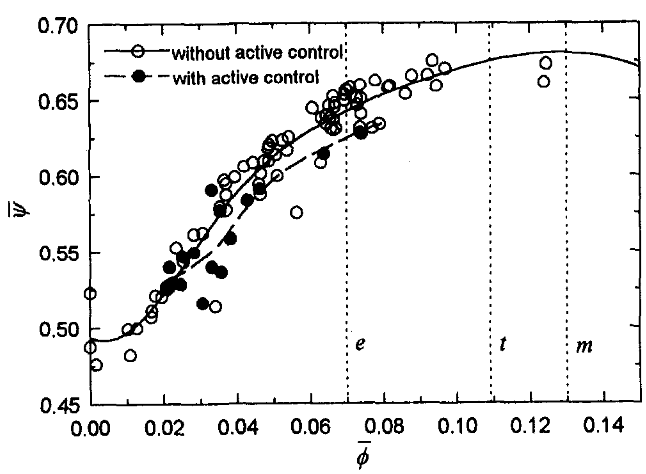

Fig. 4 Compressor characteristic with and without active surge control

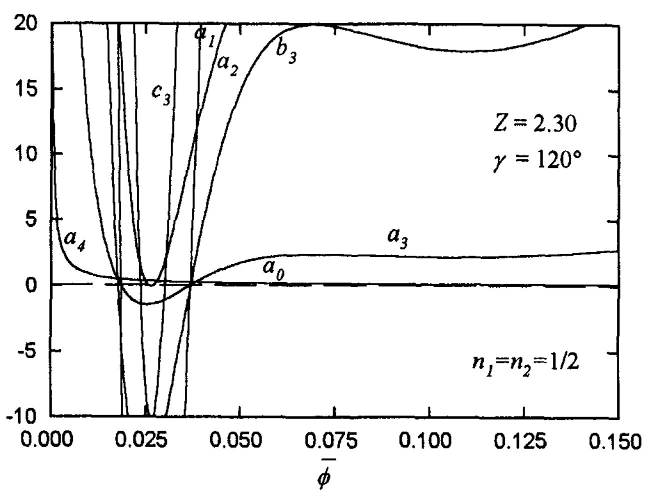

Fig. 6 Routh-Hurwitz coefficients with active control

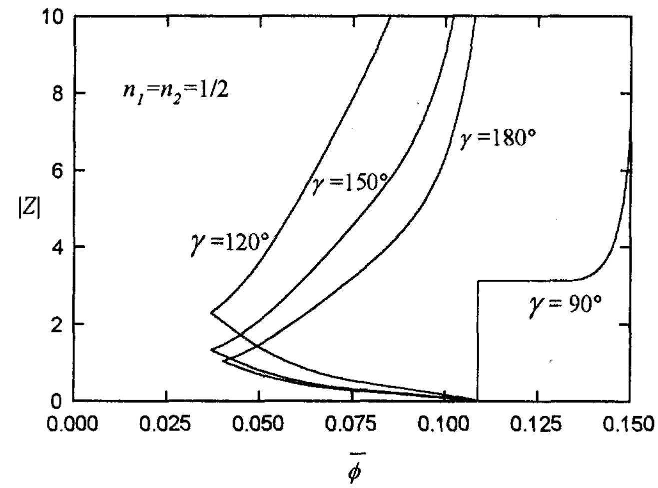

Fig. 7 Stability limit with side-branch oscillator

gain-phase relationship in the control of a system using a side-branch oscillator, which would explain the experimental difficulties encountered when tuning the active control system for cases 21 through 23 in Table 5.

In general, the experiments provided qualitative confirmation of the theoretically derived stability criteria. Several additional examples will be considered to illustrate the good agreement between experiment and theory. For instance, the dynamic stability criterion for configuration 3 in Table 1 indicates unstable operation if the throttling β becomes too large. The same experimental configuration is shown in Table 3, case 2, for which deep surge was indeed measured. When active control is applied (configuration 4, Table 1) stability of the system increases with gain Z. Experimental confirmation was again provided, as seen in case 11 of Table 4, where mild surge was moderated to rotating stall 2 using an actively controlled sleeve valve. Returning to passive control, the dynamic stability criterion given for configuration 6 in Table 1, indicates that when only the valve closest to the compressor is throttled (setting $\beta_2 = 0$), the system is always stable. This was confirmed experimentally in case 4 of Table 3, where surge was not observed even with the flow reduced to zero. Furthermore, when throttling with both β_1 and β_2, the stability of the system depends on the throttling ratio. This was also observed for case 6 of Table 3, where surge was only eliminated with significant throttling at β_1, i.e., the valve closest to the compressor. In the comparison of cases 18 and 19 of Table 4, it was noted that the presence of inlet piping had a stabilizing effect on the system so that even deep surge could be controlled. The same trend is found when comparing the dynamic stability criteria of configurations 1 and 3 in Table 1—the presence of inlet piping increases stability. In addition, the dynamic criteria of configuration 7 (Table 1) indicate that active control can stabilize the system, which was confirmed in case 19 of Table 4.

In reality, the systems tested were more stable than predicted theoretically. This trend is likely due to the effect of friction on the damping of perturbations, which was neglected in the theoretical analysis. Inherent simplifications in the model are also expected to introduce some differences. Furthermore, the dynamic stability is sensitive to the values of α and β obtained from the compressor characteristic. As such, any inaccuracies that arise in the determination of these values will affect the predicted stability.

Concluding Remarks

A stability analysis of several centrifugal compressor systems without a plenum showed that dynamic stability depends on Mach number M, and not on the system parameter B. Taking into account capacitance of the piping, the analysis indicated that surge can occur in a compression system without a plenum. Furthermore, anechoic end conditions have some stabilizing effect, while with throttling close to the compressor the system is always stable. The analysis also indicated that active control with the sleeve valve depends on passive throttling.

In general, qualitative confirmation of the theoretically derived stability criteria was provided by the experimental results. The present experiments confirmed that close-coupled throttling using globe valves at the compressor can prevent the occurrence of surge, even with the flow reduced to zero. Effective active control using a sleeve valve located within the compressor piping and with an oscillator connected to a short side branch near the compressor was demonstrated—both methods reduced the flow rate at surge onset by about 30 percent. Active control with a sleeve valve involved a significant component of passive throttling, which reduced the compressor efficiency; however, effective control was achieved with the valve at various locations within the compressor piping. With the side-branch oscillator, effective control was achieved without throttling.

Acknowledgments

The work presented here is based on a research project performed for NOVA Corporation of Alberta. Permission to publish the results is gratefully acknowledged. The authors are also grateful to Pete Tetreau for his contribution to the execution of the measurements and data processing, and to John Geerligs for his efforts in developing the electronic control systems.

References

Abdelhamid, A. N., and Bertrand, J., 1979, "Distinctions Between Two Types of Self Excited Gas Oscillations in Vaneless Radial Diffusers," ASME Paper No. 79-GT-58.

Amann, C. A., Nordenson, G. E., and Skellenger, G. D., 1975, "Casing Modification for Increasing the Surge Margin of a Centrifugal Compressor in an Automotive Turbine Engine," ASME *Journal of Engineering for Power*, Vol. 97, pp. 329–336.

Blake, K. A., 1976, "The Design of Piezometer Rings," *Journal of Fluid Mechanics*, Vol. 78, pp. 415–428.

Boyce, M. P., Bohannan, W. R., Gaston, J. R., Meier, R. H., Brown, R. N., Meher-Homji, C., and Pobanz, N. E., 1983, "Tutorial Session on Practical Approach to Surge and Surge Control," *Proceedings of the 12th Turbomachinery Symposium*, Texas A&M University, pp. 145–173.

Cumpsty, N. A., 1989, "Stall and Surge," in: *Compressor Aerodynamics*, Longman Scientific Technical, United Kingdom.

Dussourd, J. L., Pfannebecker, G. W., and Singhania, S. K., 1977, "An Experimental Investigation of the Control of Surge in Radial Compressors Using Close Coupled Resistances," ASME *Journal of Fluids Engineering*, Vol. 99, pp. 64–74.

Epstein, A. H., Ffowcs Williams, J. E., and Greitzer, E. M., 1986, "Active Suppression of Compressor Instabilities," AIAA Paper No. 86-1914.

Epstein, A. H., Ffowcs Williams, J. E., and Greitzer, E. M., 1989, "Active Suppression of Aerodynamic Instabilities in Turbomachines," *Journal of Propulsion and Power*, Vol. 5, pp. 204–211.

Ffowcs Williams, J. E., and Huang, X. Y., 1989, "Active Stabilization of Compressor Surge," *Journal of Fluid Mechanics*, Vol. 204, pp. 245–262.

Ffowcs Williams, J. E., and Graham, W. R., 1990, "An Engine Demonstration of Active Surge Control," ASME Paper No. 90-GT-224.

Ffowcs Williams, J. E., Harper, M. F. L., and Allwright, D. J., 1993, "Active Stabilization of Compressor Instability and Surge in a Working Engine," ASME JOURNAL OF TURBOMACHINERY, Vol. 115, pp. 68–75.

Fink, D. A., Cumpsty, N. A., and Greitzer, E. M., 1992, "Surge Dynamics in a Free-Spool Centrifugal Compressor System," ASME JOURNAL OF TURBOMACHINERY, Vol. 114, pp. 321–332.

Greitzer, E. M., 1981, "The Stability of Pumping Systems," ASME *Journal of Fluids Engineering*, Vol. 103, pp. 193–242.

Gysling, D. L., Dungundji, J., Greitzer, E. M., and Epstein, A. H., 1991, "Dynamic Control of Centrifugal Compressor Surge Using Tailored Structures," ASME JOURNAL OF TURBOMACHINERY, Vol. 113, pp. 710–732.

Hansen, K. E., Jorgensen, P., and Larsen, P. S., 1981, "Experimental and Theoretical Study of Surge in a Small Centrifugal Compressor," ASME *Journal of Fluids Engineering*, Vol. 103, pp. 391–395.

Huang, X. Y., 1988, "Active Control of Aerodynamic Instabilities," Ph.D. Thesis, Cambridge University, United Kingdom.

Mizuki, S., and Oosawa, Y., 1992, "Unsteady Flow Within Centrifugal Compressor Channels Under Rotating Stall and Surge," ASME JOURNAL OF TURBOMACHINERY, Vol. 114, pp. 312–320.

Pinsley, J. E., 1988, "Active Control of Centrifugal Compressor Surge," M.S. Thesis, Department of Aeronautics and Astronautics, Massachusetts Institute of Technology, Cambridge, MA.

Pinsley, J. E., Guenette, G. R., Epstein, A. H., and Greitzer, E. M., 1991, "Active Stabilization of Centrifugal Compressor Surge," ASME JOURNAL OF TURBOMACHINERY, Vol. 113, pp. 723–732.

Raw, J. A., 1986, "Surge Margin Enhancement by a Porous Throat Diffuser," *Canadian Aeronautics and Space Journal,* Vol. 32, pp. 54–60.

Rodgers, C., 1991, "Centrifugal Compressor Inlet Guide Vanes for Increased Surge Margin," ASME JOURNAL OF TURBOMACHINERY, Vol. 113, pp. 696–702.

Seidel, U., Chen, J., Haupt, U., Hasemann, H., Jin, D., and Rautenberg, M., 1991, "Rotating Stall Flow and Dangerous Blade Excitation of Centrifugal Compressor Impeller, Part 1 Phenomenon of Large-Number Stall Cells," ASME Paper No. 91-GT-102.

Simon, J. S., and Valavani, L., 1991, "A Lyapunov Based Nonlinear Control Scheme for Stabilizing a Basic Compression System Using a Close-Coupled Control Valve," *Proceedings of the 1991 American Control Conference,* Boston, MA, June 26–28, Vol. 3, pp. 2398–2406.

Simon, J. S., Valavani, L., Epstein, A. H., and Greitzer, E. M., 1993, "Evaluation of Approaches to Active Compressor Surge Stabilization," ASME JOURNAL OF TURBOMACHINERY, Vol. 115, pp. 57–67.

Wolfram, S., 1991, *Mathematica: A System for Doing Mathematics by Computer,* 2nd ed., Addison-Wesley Publishing Company, Inc., Redmond City, CA.

APPENDIX I

Stability of a Simple Compression System

The analysis is based on Greitzer's (1981) lumped parameter model, which has been extended to accommodate the pipe capacitance. This approach can be illustrated by application to a simple compression system composed of a centrifugal compressor, pipe, and throttling valve shown in Fig. A1. If the gas is considered as a compressible fluid, the mass flow entering a pipe may differ from that exiting, i.e., $m_2 \neq m_3$, which is, however, balanced by a change in the bulk density with time

$$m_2 - m_3 = AL\left(\frac{d\rho}{dt}\right) \tag{A1}$$

The bulk gas density can be replaced by the arithmetic mean at the pipe ends

$$m_2 - m_3 = \frac{AL}{2}\left(\frac{d\rho_2}{dt} + \frac{d\rho_3}{dt}\right) \tag{A2}$$

and ignoring temperature differences between the pipe ends,

$$a^2 = \frac{dp_2}{d\rho_2} = \frac{dp_3}{d\rho_3} \tag{A3}$$

the equation of mass conservation becomes

$$m_2 - m_3 = \frac{AL}{2a^2}\left(\frac{dp_2}{dt} + \frac{dp_3}{dt}\right) \tag{A4}$$

The equation of momentum conservation can be written as

$$p_2 - p_3 = L\rho\left(\frac{du}{dt}\right) + \rho_3 u_3^2 - \rho_2 u_2^2 \tag{A5}$$

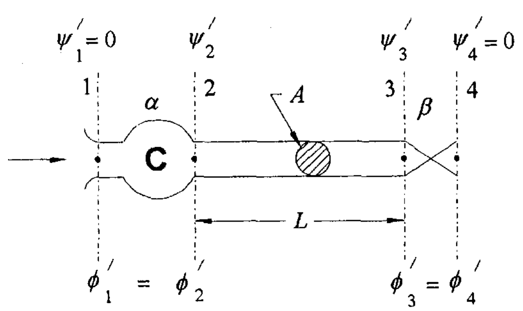

Fig. A1 Schematic of simple compression system

which after averaging the bulk properties is transformed into

$$p_2 - p_3 = \frac{L}{2}\left(\rho_2 \frac{du_2}{dt} + \rho_3 \frac{du_3}{dt}\right) + \rho_3 u_3^2 + \rho_2 u_2^2 \tag{A6}$$

and further to

$$p_2 - p_3 = \frac{L}{2A}\left(\frac{dm_2}{dt} + \frac{dm_3}{dt}\right) + \frac{1}{\rho_3 A^2} m_3^2 - \frac{1}{\rho_2 A^2} m_2^2 \tag{A7}$$

The capacitance and the inertance of the centrifugal compressor is neglected. Therefore, the mass entering the compressor equals that exiting

$$m_1 = m_2 \tag{A8}$$

and the pressure rise across the compressor can be expressed as a function of the upstream mass flow rate

$$\Delta p_c = p_2 - p_1 = F(m_1) \tag{A9}$$

Neglecting the capacitance and inertance of the throttle valve, mass conservation is simply

$$m_3 = m_4 \tag{A10}$$

and the pressure drop can be related to the mass flow through the valve by

$$\Delta p_t = p_3 - p_4 = \zeta \frac{\rho_3 u_3^2}{2} \tag{A11}$$

which is transformed to

$$\Delta p_t = p_3 - p_4 = \zeta \frac{m_3^2}{2\rho_3 A^2} \tag{A12}$$

Linearizing and normalizing Eqs. (A9), (A4), (A7), and (A12) results in:

$$\psi'_2 - \psi'_1 = \alpha\phi'_1 \tag{A13}$$

$$\phi'_2 - \phi'_3 = \frac{\mathrm{M}^2}{2B}\left(\frac{d\psi'_2}{d\bar{t}} + \frac{d\psi'_3}{d\bar{t}}\right) \tag{A14}$$

$$\psi'_2 - \psi'_3 = \frac{1}{2B}\left(\frac{d\phi'_2}{d\bar{t}} + \frac{d\phi'_3}{d\bar{t}}\right) + 2\bar{\phi}(\phi'_3 - \phi'_2) \tag{A15}$$

$$\psi'_3 - \psi'_4 = \beta\phi'_3 \tag{A16}$$

The last term in Eq. (A15), resulting from the net momentum flux, was initially included; however, subsequent calculations showed its effect on the dynamic stability criteria was small. Closure of the equations is achieved with ambient boundary conditions applied at the open ends of the system

$$\psi'_1 = \psi'_4 = 0 \tag{A17}$$

Elimination of three perturbations from the set of four equations results in a second-order ordinary differential equation

$$\mathrm{M}^2(\beta - \alpha)\frac{d^2\phi'_1}{d\bar{t}^2} + 4B(1 - \alpha\beta\mathrm{M}^2)\frac{d\phi'_1}{d\bar{t}} + 4B^2(\beta - \alpha)\phi'_1 = 0 \tag{A18}$$

The solution of Eq. (A18) is in the form $\phi'_1 = |\phi'_1| \exp \bar{s}\bar{t}$, resulting in a characteristic equation

$$a_2\bar{s}^2 + a_1\bar{s} + a_0 = 0 \tag{A19}$$

According to the Routh–Hurwitz criterion, the system is stable when all coefficients in Eq. (A19) and the coefficients in the first column of the array are positive

$$\begin{array}{c|cc} \bar{s}^2 & a_2 & a_0 \\ \bar{s}^1 & a_1 & 0 \\ \bar{s}^0 & b_1 & 0 \end{array} \qquad b_1 = \frac{(a_1 a_0 - a_0 . 0)}{a_1} = a_0 \tag{A20}$$

Thus, a_2 and a_0 determine the requirement for static stability $\beta > \alpha$, and a_1 for dynamic stability $1 > \alpha\beta M^2$.

APPENDIX II

Stability of Complex Compression Systems

Compressor With Downstream Throttle Valve. The approach described in Appendix I can be applied to more complicated compressor systems. Consider the compression system described in Appendix I with an additional length of pipe upstream of the compressor inlet as shown in Fig. A2. The overall piping length, L, in the system is made up of an upstream section of length $n_1 L$ and a downstream section of length $n_2 L$. Addition of the upstream and downstream length fractions, n_1 and n_2, respectively, equals unity.

The linearized and transformed equations for mass and momentum conservation can be expressed for the upstream pipe as

$$\phi_1' - \phi_2' = \frac{n_1 M^2}{2B}\left(\frac{d\psi_1'}{d\bar{t}} + \frac{d\psi_2'}{d\bar{t}}\right) \tag{A21}$$

$$\psi_1' - \psi_2' = \frac{n_1}{2B}\left(\frac{d\phi_1'}{d\bar{t}} + \frac{d\phi_2'}{d\bar{t}}\right) \tag{A22}$$

The perturbation equations across the centrifugal compressor are

$$\psi_3' - \psi_2' = \alpha\phi_2' \tag{A23}$$

$$\phi_3' = \phi_2' \tag{A24}$$

and for the downstream pipe

$$\phi_3' - \phi_4' = \frac{n_2 M^2}{2B}\left(\frac{d\psi_3'}{d\bar{t}} + \frac{d\psi_4'}{d\bar{t}}\right) \tag{A25}$$

$$\psi_3' - \psi_4' = \frac{n_2}{2B}\left(\frac{d\phi_3'}{d\bar{t}} + \frac{d\phi_4'}{d\bar{t}}\right) \tag{A26}$$

Lastly, across the throttle valve we have

$$\psi_4' - \psi_5' = \beta\phi_4' \tag{A27}$$

and subject to ambient conditions at the open ends

$$\psi_1' = \psi_5' = 0 \tag{A28}$$

Algebraic manipulation of Eqs. (A21)–(A28) reduces the number of equations to four first-order ordinary differential equations (O.D.E.'s). These four equations are assembled into matrix form as

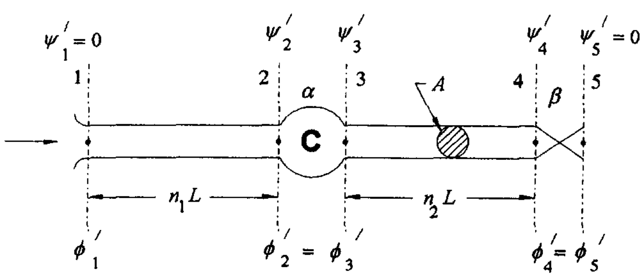

Fig. A2 Schematic of compressor with downstream throttle valve

$$\begin{bmatrix} a_{11} & a_{12} & a_{13} & a_{14} \\ a_{21} & a_{22} & a_{23} & a_{24} \\ a_{31} & a_{32} & a_{33} & a_{34} \\ a_{41} & a_{42} & a_{43} & a_{44} \end{bmatrix} \begin{bmatrix} d\phi_1'/d\bar{t} \\ d\phi_2'/d\bar{t} \\ d\phi_4'/d\bar{t} \\ d\psi_2'/d\bar{t} \end{bmatrix} = \begin{bmatrix} b_{11} & b_{12} & b_{13} & b_{14} \\ b_{21} & b_{22} & b_{23} & b_{24} \\ b_{31} & b_{32} & b_{33} & b_{34} \\ b_{41} & b_{42} & b_{43} & b_{44} \end{bmatrix} \begin{bmatrix} \phi_1' \\ \phi_2' \\ \phi_4' \\ \psi_2' \end{bmatrix} \tag{A29}$$

The matrix is inverted to obtain the time derivatives of the perturbations in terms of the linear variables

$$\begin{bmatrix} 1 & 0 & 0 & 0 \\ 0 & 1 & 0 & 0 \\ 0 & 0 & 1 & 0 \\ 0 & 0 & 0 & 1 \end{bmatrix} \begin{bmatrix} d\phi_1'/d\bar{t} \\ d\phi_2'/d\bar{t} \\ d\phi_4'/d\bar{t} \\ d\psi_2'/d\bar{t} \end{bmatrix} = \begin{bmatrix} c_{11} & c_{12} & c_{13} & c_{14} \\ c_{21} & c_{22} & c_{23} & c_{24} \\ c_{31} & c_{32} & c_{33} & c_{34} \\ c_{41} & c_{42} & c_{43} & c_{44} \end{bmatrix} \begin{bmatrix} \phi_1' \\ \phi_2' \\ \phi_4' \\ \psi_2' \end{bmatrix} \tag{A30}$$

The first row is re-arranged in terms of the perturbation to be eliminated, i.e., ψ_2'

$$\psi_2' = \frac{\dfrac{d\phi_1'}{d\bar{t}} - c_{11}\phi_1' - c_{12}\phi_2' - c_{13}\phi_4'}{c_{14}} \tag{A31}$$

Equation (A31) can be differentiated with respect to time

$$\frac{d\psi_2'}{d\bar{t}} = \frac{\dfrac{d^2\phi_1'}{d\bar{t}^2} - c_{11}\dfrac{d\phi_1'}{d\bar{t}} - c_{12}\dfrac{d\phi_2'}{d\bar{t}} - c_{13}\dfrac{d\phi_4'}{d\bar{t}}}{c_{14}} \tag{A32}$$

Substituting Eqs. (A31) and (A32) into the last three rows of matrix (A30) eliminates ψ_2'. This sequence is repeated to eliminate ϕ_2' and ϕ_4' and obtain the following fourth-order O.D.E. in terms of ϕ_1':

$$M^4 n_1^2 n_2^2(\beta - \alpha)\frac{d^4\phi_1'}{d\bar{t}^4} + 4BM^2 n_1 n_2(1 - n_1\alpha\beta M^2)\frac{d^3\phi_1'}{d\bar{t}^3} + 4B^2M^2[(n_1^2 + n_2^2)(\beta - \alpha) + 4n_1 n_2\beta]\frac{d^2\phi_1'}{d\bar{t}^2} + 16B^3 \times [1 - n_2\alpha\beta M^2]\frac{d\phi_1'}{d\bar{t}} + 16B^4(\beta - \alpha)\phi_1' = 0 \tag{A33}$$

The resulting characteristic equation is

$$a_4\bar{s}^4 + a_3\bar{s}^3 + a_2\bar{s}^2 + a_1\bar{s} + a_0 = 0 \tag{A34}$$

The system is stable when all coefficients of the characteristic equation and in the first column of the array are positive

$$\begin{array}{c|ccc} \bar{s}^4 & a_4 & a_2 & a_0 \\ \bar{s}^3 & a_3 & a_1 & 0 \\ \bar{s}^2 & b_3 & b_1 & 0 \\ \bar{s}^1 & c_3 & 0 & 0 \\ \bar{s}^0 & d_3 & 0 & 0 \end{array} \qquad \begin{aligned} b_3 &= \frac{(a_3 a_2 - a_4 a_1)}{a_3} \\ b_1 &= \frac{(a_3 a_0 - a_4 . 0)}{a_3} = a_0 \\ c_3 &= \frac{(a_1 b_3 - a_3 b_1)}{b_3} \\ d_3 &= \frac{(c_3 b_1 - b_3 . 0)}{c_3} = a_0 \end{aligned} \tag{A35}$$

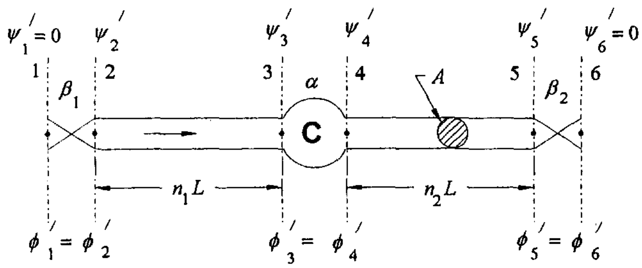

Fig. A3 Schematic of compressor with upstream and downstream throttle valves

When $n_1 = n_2 = \frac{1}{2}$, i.e., configuration 3 in Table 1, the compressor is connected to upstream and downstream pipes of equal length and the most stringent requirement for dynamic stability is $2 > \alpha\beta M^2$, while static stability remains as $\beta > \alpha$.

Compressor With Upstream and Downstream Throttle Valves. An additional throttle valve is positioned at the inlet of the upstream piping as shown in Fig. A3. The perturbation equations across the upstream valve are

$$\phi_1' = \phi_2' \tag{A36}$$

$$\psi_1' - \psi_2' = \beta_1\phi_1' \tag{A37}$$

Conservation of mass and momentum for the upstream pipe gives

$$\phi_2' - \phi_3' = \frac{n_1 M^2}{2B}\left(\frac{d\psi_2'}{d\bar{t}} + \frac{d\psi_3'}{d\bar{t}}\right) \tag{A38}$$

$$\psi_2' - \psi_3' = \frac{n_1}{2B}\left(\frac{d\phi_2'}{d\bar{t}} + \frac{d\phi_3'}{d\bar{t}}\right) \tag{A39}$$

across the centrifugal compressor

$$\phi_3' = \phi_4' \tag{A40}$$

$$\psi_4' - \psi_3' = \alpha\phi_3' \tag{A41}$$

and for the downstream pipe

$$\phi_4' - \phi_5' = \frac{n_2 M^2}{2B}\left(\frac{d\psi_4'}{d\bar{t}} + \frac{d\psi_5'}{d\bar{t}}\right) \tag{A42}$$

$$\psi_4' - \psi_5' = \frac{n_2}{2B}\left(\frac{d\phi_4'}{d\bar{t}} + \frac{d\phi_5'}{d\bar{t}}\right) \tag{A43}$$

Lastly, across the downstream throttle valve we have

$$\psi_5' - \psi_6' = \beta_2\phi_5' \tag{A44}$$

and subject again to ambient conditions at the open ends

$$\psi_1' = \psi_6' = 0 \tag{A45}$$

These equations are reduced to a single fourth-order O.D.E. in terms of ϕ_1':

$$M^4 n_1^2 n_2^2(\beta_1 + \beta_2 - \alpha)\frac{d^4\phi_1'}{d\bar{t}^4} + 4BM^2 n_1 n_2$$
$$\times [1 - n_1\alpha\beta_2 M^2 - n_2\alpha\beta_1 M^2 - \beta_1\beta_2 M^2]\frac{d^3\phi_1'}{d\bar{t}^3}$$
$$+ 4B^2M^2[(n_1^2 + n_2^2)(\beta_1 + \beta_2 - \alpha)$$
$$+ 4n_1n_2(\beta_1 + \beta_2 - \alpha\beta_1\beta_2 M^2)]\frac{d^2\phi_1'}{d\bar{t}^2}$$
$$+ 16B^3(1 - n_1\alpha\beta_1 M^2 - n_2\alpha\beta_2 M^2)\frac{d\phi_1'}{d\bar{t}}$$
$$+ 16B^4(\beta_1 + \beta_2 - \alpha)\phi_1' = 0 \tag{A46}$$

When $n_1 = n_2 = \frac{1}{2}$, i.e., configuration 5 in Table 1, the most stringent requirement for dynamic stability is $2(1 + \beta_1\beta_2 M^2) > \alpha(\beta_1 + \beta_2)M^2$ and static stability becomes $\beta_1 + \beta_2 > \alpha$.

Compressor With Upstream Sleeve Valve and Downstream Throttle Valve. A sleeve valve is located immediately upstream of the compressor as shown in Fig. A4. The resulting perturbation equations can be expressed as

$$\phi_1' - \phi_2' = \frac{n_1 M^2}{2B}\left(\frac{d\psi_1'}{d\bar{t}} + \frac{d\psi_2'}{d\bar{t}}\right) \tag{A47}$$

$$\psi_1' - \psi_2' = \frac{n_1}{2B}\left(\frac{d\phi_1'}{d\bar{t}} + \frac{d\phi_2'}{d\bar{t}}\right) \tag{A48}$$

$$\phi_2' = \phi_3' \tag{A49}$$

$$\psi_2' = \frac{\psi_3'\beta_1\phi_2'}{(1 + \beta_1\bar{\phi}Z)} \tag{A50}$$

$$\phi_3' = \phi_4' \tag{A51}$$

$$\psi_4' - \psi_3' = \alpha\phi_3' \tag{A52}$$

$$\phi_4' - \phi_5' = \frac{n_2 M^2}{2B}\left(\frac{d\psi_4'}{d\bar{t}} + \frac{d\psi_5'}{d\bar{t}}\right) \tag{A53}$$

$$\psi_4' - \psi_5' = \frac{n_2}{2B}\left(\frac{d\phi_4'}{d\bar{t}} + \frac{d\phi_5'}{d\bar{t}}\right) \tag{A54}$$

$$\psi_5' - \psi_6' = \beta_2\phi_5' \tag{A55}$$

$$\psi_1' = \psi_6' = 0 \tag{A56}$$

These equations are reduced to a single fourth-order O.D.E. in terms of ϕ_1'

$$M^4 n_1^2 n_2^2(\beta_1 + \beta_2 - \alpha)\frac{d^4\phi_1'}{d\bar{t}^4}$$
$$+ 4BM^2 n_1 n_2[1 - n_1\alpha\beta_2 M^2 + n_1\beta_1\beta_2 M^2 + n_2\beta_1\bar{\phi}Z]$$
$$\times \frac{d^3\phi_1'}{d\bar{t}^3} + 4B^2M^2[(n_1^2 + n_2^2)(\beta_1 + \beta_2 - \alpha)$$
$$+ 4n_1n_2\beta_2(1 + \beta_1\bar{\phi}Z)]\frac{d^2\phi_1'}{d\bar{t}^2}$$

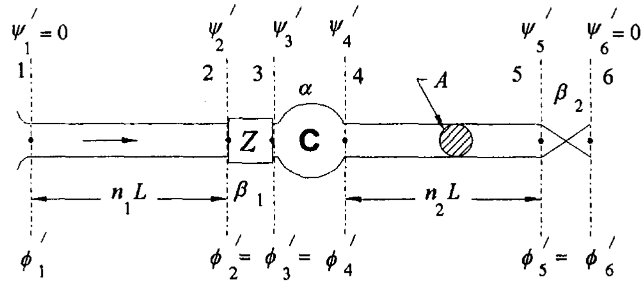

Fig. A4 Schematic of compressor with upstream sleeve valve and downstream throttle valve

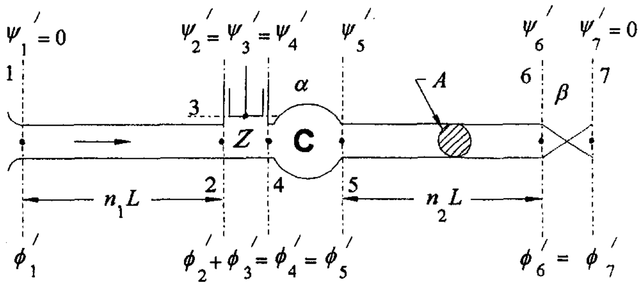

Fig. A5 Schematic of compressor with side-branch oscillator

$$+ 16B^3[1 - n_2\alpha\beta_2 M^2 + n_2\beta_1\beta_2 M^2 + n_1\beta_1\bar{\phi}Z]$$

$$\times \frac{d\phi_1'}{d\bar{t}} + 16B^4(\beta_1 + \beta_2 - \alpha)\,\phi_1' = 0 \quad \text{(A57)}$$

When $n_1 = n_2 = \frac{1}{2}$, i.e., configuration 7 in Table 1, the most stringent requirement for dynamic stability is $2 + \beta_1\beta_2 M^2 + \beta_1\bar{\phi}Z > \alpha\beta_2 M^2$ and for static stability $\beta_1 + \beta_2 > \alpha$.

Compressor With Side-Branch Oscillator. A side-branch oscillator is located immediately upstream of the compressor as shown in Fig. A5. The resulting perturbation equations can be expressed as

$$\phi_1' - \phi_2' = \frac{n_1 M^2}{2B}\left(\frac{d\psi_1'}{d\bar{t}} + \frac{d\psi_2'}{d\bar{t}}\right) \quad \text{(A58)}$$

$$\psi_1' - \psi_2' = \frac{n_1}{2B}\left(\frac{d\phi_1'}{d\bar{t}} + \frac{d\phi_2'}{d\bar{t}}\right) \quad \text{(A59)}$$

$$\phi_2' + \phi_3' = \phi_4' \quad \text{(A60)}$$

$$\psi_2' = \psi_4' \quad \text{(A61)}$$

$$\psi_3' = \psi_4' \quad \text{(A62)}$$

$$\phi_4' = Z\psi_3' \quad \text{(A63)}$$

$$\phi_4' = \phi_5' \quad \text{(A64)}$$

$$\psi_5' - \psi_4' = \alpha\phi_4' \quad \text{(A65)}$$

$$\phi_5' - \phi_6' = \frac{n_2 M^2}{2B}\left(\frac{d\psi_5'}{d\bar{t}} + \frac{d\psi_6'}{d\bar{t}}\right) \quad \text{(A66)}$$

$$\psi_5' - \psi_6' = \frac{n_2}{2B}\left(\frac{d\phi_5'}{d\bar{t}} + \frac{d\phi_6'}{d\bar{t}}\right) \quad \text{(A67)}$$

$$\psi_6' - \psi_7' = \beta\phi_6' \quad \text{(A68)}$$

$$\psi_1' = \psi_7' = 0 \quad \text{(A69)}$$

These equations are reduced to a single fourth-order O.D.E. in terms of ϕ_1'

$$M^4 n_1^2 n_2^2(\beta - \alpha)\frac{d^4\phi_1'}{d\bar{t}^4}$$

$$+ 4BM^2 n_1 n_2[1 - n_1\alpha\beta M^2 - n_2 Z(\beta - \alpha)]\frac{d^3\phi_1'}{d\bar{t}^3}$$

$$+ 4B^2M^2[(n_1^2 + n_2^2)(\beta - \alpha)$$

$$+ 4n_1 n_2(\beta - Z(1 - \alpha\beta M^2))]\frac{d^2\phi_1'}{d\bar{t}^2}$$

$$+ 16B^3[n_1\alpha\beta M^2 - n_1 Z(\beta - \alpha)]\frac{d\phi_1'}{d\bar{t}}$$

$$+ 16B^4(\beta - \alpha)\phi_1' = 0 \quad \text{(A70)}$$

When $n_1 = n_2 = \frac{1}{2}$, i.e., configuration 8 in Table 1, the following coefficients must be positive:

$$a_0 = 16B^4(\beta - \alpha) \quad \text{(A71)}$$

$$a_1 = 8B^3[2 - \alpha\beta M^2 - Z(\beta - \alpha)] \quad \text{(A72)}$$

$$a_2 = 2B^2M^2[3\beta - \alpha - 2Z(1 - \alpha\beta M^2)] \quad \text{(A73)}$$

$$a_3 = \frac{BM^2}{2}[2 - \alpha\beta M^2 - Z(\beta - \alpha)] \quad \text{(A74)}$$

$$a_4 = \frac{M^4}{16}(\beta - \alpha) \quad \text{(A75)}$$

$$b_3 = B^2M^2[5\beta - \alpha - 4Z(1 - \alpha\beta M^2)] \quad \text{(A76)}$$

$$c_3 = 32B^3 \times \frac{[\beta - Z(1 - \alpha\beta M^2)][2 - \alpha\beta M^2 - Z(\beta - \alpha)]}{[5\beta - \alpha - 4Z(1 - \alpha\beta M^2)]} \quad \text{(A77)}$$

An Experimental Investigation of Stator Induced Unsteadiness on Centrifugal Impeller Outflow

M. Ubaldi

P. Zunino

G. Barigozzi

A. Cattanei

Istituto di Macchine e Sistemi Energetici,
Università di Genova,
Genova, Italy

Detailed flow measurements were taken in a centrifugal turbomachine model to investigate the aerodynamic influence of the vaned diffuser on the impeller flow. The model consists of an unshrouded centrifugal impeller with backswept blades and a rotatable vaned diffuser, which enables a continuous variation of the vaned diffuser location with respect to the measuring points. Phase-locked ensemble-averaged velocity components have been measured with hot-wire probes at the impeller outlet for 30 different relative positions of the probe with respect to the diffuser vanes. The data also include the distribution of the ensemble-averaged static pressure at the impeller front end, taken by means of miniature fast response pressure transducers flush-mounted at the impeller stationary casing. By circumferentially averaging the results obtained for the different circumferential probe locations, the periodically perturbed impeller flow has been split into a relative steady flow and a stator-generated unsteadiness. The results for the different probe positions have also been correlated in time to obtain instantaneous flow field images in the relative frame, which provide information on the various aspects of the diffuser vane upstream influence on the relative flow leaving the impeller.

Introduction

Flow unsteadiness generated by rotor–stator aerodynamic interaction affects aerodynamic, thermal, and structural performance of turbomachinery components. Aerodynamic interaction takes place mainly through two distinct mechanisms: wake and potential flow effects (Dring et al., 1982).

The wake viscous effect originates from the impingement and the convection of wakes shed from the preceding row through the successive blade row in relative motion. The periodic striking of turbulent wake segments determines a complex unsteady flow field, which influences the onset of the boundary layer transition on the downstream blades (e.g., Pfeil et al., 1983; Hodson, 1985; La Graff et al., 1989; Liu and Rodi, 1992).

The potential flow effect is induced by the interaction of the inviscid flow fields generated by the adjacent blade rows in relative motion. It extends in both upstream and downstream directions, with a larger effect on the upstream row. However, the rate of decay of the potential perturbation is fast and the associated effect appears significant only in case of small gaps between adjacent rows.

Due to the important practical implications and the inherent complexity of the interaction phenomena, a large number of detailed experimental investigations are reported in the literature. Most of these efforts concern the analysis of wake-generated unsteady flows in axial turbomachines, either compressors (e.g., Zierke and Okiishi, 1982; Dunker, 1983; Suder et al., 1987; Hathaway et al., 1987; Poensgen and Gallus, 1990a, 1990b; Schulz et al., 1990) or turbines (e.g., Binder et al., 1985, 1989; Zeschky and Gallus, 1993). Dring et al. (1982) and Joslyn et al. (1983) have analyzed in detail both wake-generated and upstream potential flow effects in a large-scale, axial flow, turbine model.

Investigations dealing with rotor–stator interaction in centrifugal turbomachines are less numerous and, in general, concern both interaction mechanisms (e.g., Krain, 1981; Inoue and Cumpsty, 1984; Arndt et al., 1990). Since the mixing process that rotor blade wakes undergo is very fast and radial gaps between rotors and vaned diffusers are small, in centrifugal machines viscous and potential flow effects become comparable.

To study basic fluid dynamic phenomena, including aerodynamic rotor–stator interaction, a simplified model of centrifugal turbomachine with rotatable vaned diffuser has been designed and built. This paper reports results of an experimental investigation of the unsteadiness induced by the stator on the relative flow leaving the centrifugal impeller.

The unsteady flow field at the impeller outlet, which is not axisymmetric due to the upstream potential effect of the vaned diffuser, has been investigated with a constant-temperature hot-wire anemometer for several relative circumferential positions of the probe and the diffuser in order to reconstruct in great detail instantaneous pictures of the rotor outflow periodically perturbed by the diffuser vanes in relative motion. To gain more insight into the upstream propagation mechanism of the stator-induced unsteadiness, instantaneous static pressure at the front cover of the unshrouded impeller has also been measured using miniature fast-response pressure transducers and has been processed to get the images of the periodically perturbed pressure field within the centrifugal impeller passages.

Experimental Facility and Operating Conditions

A simplified model of centrifugal turbomachine, dedicated to basic fluid dynamic studies, has been utilized for the present experimental investigation. The model is shown in Fig. 1.

The model consists of a 420-mm-diam unshrouded centrifugal impeller and a rotatable radial vaned diffuser, which allows for continuous variation of the vaned diffuser circumferential location with respect to the measuring point. The impeller and the diffuser are shown in Fig. 2. The coordinates of the impeller blade and diffuser vane profiles are given in appendix.

The impeller, directly driven by an electric DC motor, has seven untwisted constant-thickness backswept blades with rounded-off leading and trailing edges. The blade camber angle with the radial direction varies continuously from 65 deg at the inlet ($D_1/D_2 = 0.57$) to 70 deg at the outlet, giving a geometric

Contributed by the International Gas Turbine Institute and presented at the 39th International Gas Turbine and Aeroengine Congress and Exposition, The Hague, The Netherlands, June 13–16, 1994. Manuscript received by the International Gas Turbine Institute January 31, 1994. Paper No. 94-GT-5. Associate Technical Editor: E. M. Greitzer.

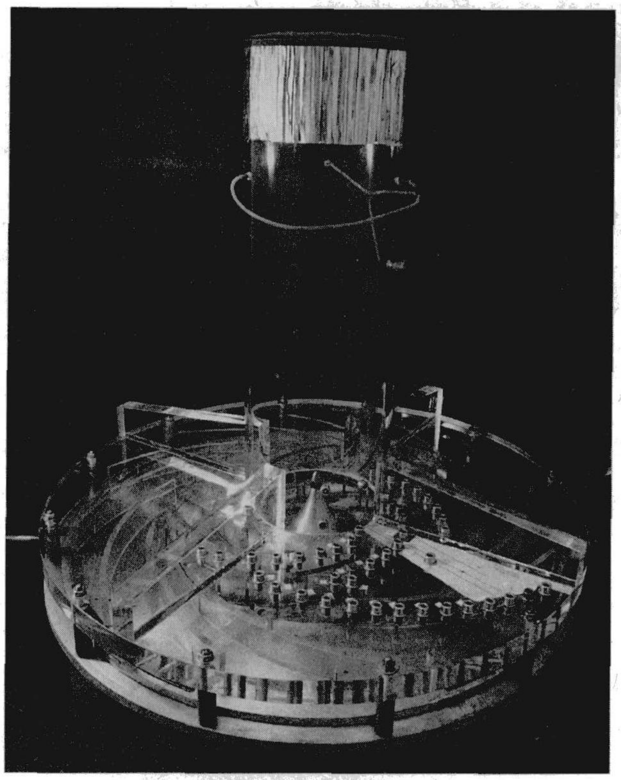

Fig. 1 Centrifugal turbomachine model

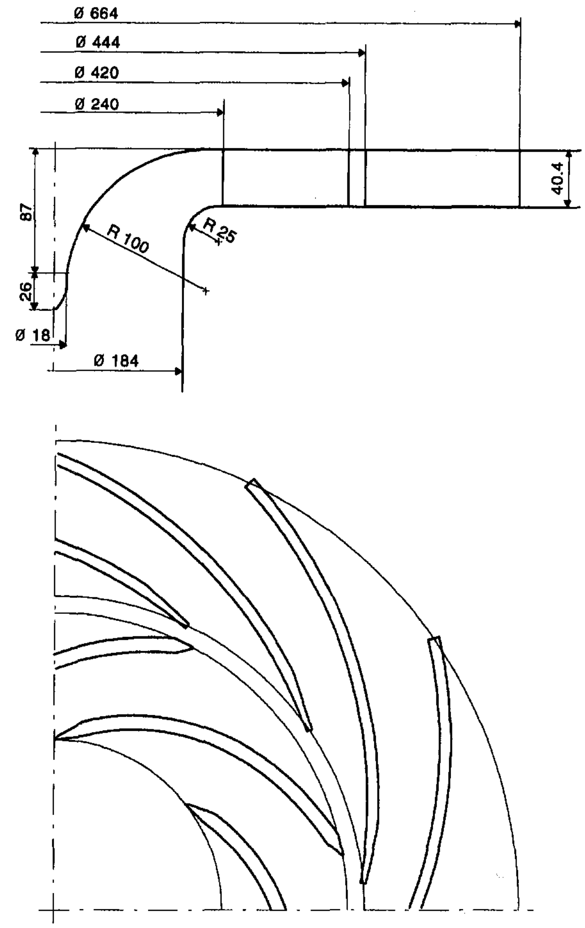

Fig. 2 Impeller and vaned diffuser geometry

diffusion ratio of 1.42. The diffuser is constituted by a disk with internal and external diameters 421 and 750 mm, respectively, supported by a bearing plane. The disk can be rotated with respect to the support by means of circumferential slits and protruding pins. Constant-thickness circular arc vanes can be used to construct several vaned diffusers with different vaneless radial gaps, stagger angles and number of vanes.

The diffuser used in the present investigation has 12 vanes and a 6 percent vaneless radial gap. The front cover of the model, which constitutes the impeller and diffuser casing, is made of perspex to allow for flow visualization and easy probe positioning. The cover is supported by the bearing plane through eight cylindrical holders. The holders' height can be varied to change the blade tip clearance. In the present investigation the tip clearance is set at its minimum value of 0.4 mm, to reduce tip leakage effects.

The model operates in an open circuit, with air being fed to the impeller through a long straight pipe and discharged into the atmosphere directly from the radial diffuser. The inlet pipe is equipped with a honeycomb, a cloth filtering element, and a

Nomenclature

b = impeller blade span
c = absolute velocity
C_p = static pressure coefficient = $2(p - p_0)/\rho U_2^2$
D_2 = impeller outlet diameter
G_i = impeller circumferential pitch
l = chord length
p = static pressure
p_t = total pressure
Q = flow rate
r = radial coordinate
R_n = meridional curvature radius
t = time
T_i = impeller blade passing period
u = peripheral velocity
U_2 = peripheral velocity at the impeller outlet
w = relative velocity
y_i = circumferential coordinate in the relative frame
z = axial coordinate
z_d = number of diffuser vanes
z_i = number of impeller blades
β = angle between the blade-to-blade relative velocity and the radial direction
β' = impeller blade angle with radial direction
γ = angle between the relative velocity and the blade-to-blade velocity
θ = angular coordinate
ν = kinematic viscosity
ρ = fluid density
φ = flow rate coefficient = $4Q/(U_2\pi D_2^2)$
ψ = total pressure rise coefficient = $2(p_{t4} - p_{t0})/\rho U_2^2$
ω = angular velocity

Subscripts

d = relative to the diffuser
i = relative to the impeller
m = relative to the measuring point
r = in the radial direction
u = in the tangential direction
z = in the axial direction
0 = in the suction pipe
1 = at the impeller leading edge
2 = at the impeller outlet
3 = at the diffuser inlet
4 = at the diffuser outlet

Superscripts

$'$ = unsteady quantity
$\sim$ = ensemble average
$-$ = circumferential average

throttling valve. The flow rate is measured by means of static pressure taps in the inlet pipe and a Pitot tube for the total pressure drop through the valve.

The experiment was conducted at the constant rotational speed of 2000 rpm, at the nominal operating condition (flow rate coefficient $\varphi = 0.048$, total pressure rise coefficient $\psi = 0.65$). At this operating condition the theoretical flow incidence on the impeller blades was 4 deg positive. The Reynolds number based on impeller tip speed and impeller blade chord was Re $= 6.5 \times 10^5$. The main geometric data of the model and the operating conditions are summarized in Table 1.

Instrumentation and Measuring Techniques

A constant-temperature hot-wire anemometer with single sensor probes and flush-mounted miniature fast response pressure transducers was used to measure the unsteady three-dimensional flow at the impeller outlet and the unsteady static pressure at the front cover facing the unshrouded impeller passages. To survey the impeller outflow, the hot-wire probe was introduced from the front cover at a radial distance 4 mm from the blade trailing edge ($D_m/D_2 = 1.02$) and 8 mm from the vane leading edge.

The probe was traversed in the axial direction to describe the impeller flow in the spanwise direction with 17 measuring points. The minimum distance from the walls was 2 mm. During the impeller revolutions the stationary fast response hot-wire probe senses an unsteady signal consisting of a periodic part and a random one. The former is due to the circumferential nonuniformity of the relative flow, the latter is associated with flow turbulence, trailing edge vortex shedding, separations and all the other unsteady phenomena not correlated with the impeller frequency. This apparent turbulence can more properly be defined as unresolved unsteadiness (Suder et al., 1987).

In order to separate the periodic signal from the unresolved unsteadiness, the phase-locked sampling and ensemble-average technique (Gostelow, 1977; Lakshminarayana, 1981) was applied to the hot-wire instantaneous signals. The once per revolution reference signal was provided by an optical device, which consists of a light source, a reflecting element glued on the shaft, and a receiving photocell. The ensemble averages were obtained by averaging 700 records of 160 data, corresponding to 160 circumferential positions in the rotor reference. The instantaneous signals were digitized at a frequency rate of 18.667 kHz by means of a 12 bit A/D converter board and a trigger alarm module (Burr Brown PCI 20019M and 200020M) and the data were stored in a personal computer. The selected sampling frequency provides a detailed description of an impeller passage by means of 80 circumferential points.

Table 1 Geometric data and operating conditions

Impeller			
inlet blade diameter	D_1	=	240 mm
outlet diameter	D_2	=	420 mm
blade span	b	=	40 mm
number of blades	z_i	=	7
inlet blade angle (with radial direction)	β_1'	=	-65 deg
outlet blade angle	β_2'	=	-70 deg
Diffuser			
inlet vane diameter	D_3	=	444 mm
outlet vane diameter	D_4	=	664 mm
vane span	b	=	40 mm
number of vanes	z_d	=	12
inlet vane angle	α_3'	=	-74 deg
outlet vane angle	α_4'	=	-68 deg
Operating conditions			
rotational speed	n	=	2000 rpm
flow rate coefficient	φ	=	0.048
total pressure rise coefficient	ψ	=	0.65
Reynolds number	Re	=	$U_2 l/\nu$ = $6.5\ 10^5$
Inlet air reference conditions			
temperature	T	=	298 K
air density	ρ	=	1.2 kg/m^3

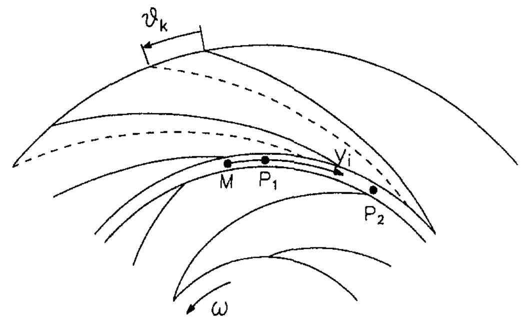

Fig. 3 Sketch of the radial rows of blades and reference coordinates

Miniature normal and slanted single sensor probes (Dantec 55P11 and 55P12) with tungsten wires of 1.25 mm length and 5 μm diameter were used to measure instantaneous velocities. The frequency response of the system exceeds 100 kHz. The probes were accurately calibrated for velocity magnitude and direction. The instantaneous cooling velocities were obtained from the sampled signals by numerical inversion of the calibration curve.

For each measuring point a set of 12 ensemble-averaged cooling velocities and 12 variances (9 for the slanted probe and 3 for the normal probe) were obtained by rotating the probe around the axis. The three ensemble-averaged velocity components and the six apparent Reynolds stress components associated with the unresolved flow unsteadiness were determined using the above-mentioned set of data and solving two overdetermined systems of algebraic equations. This experimental procedure is the same as the one used by Ubaldi et al. to measure the relative flow and turbulence characteristics downstream of a centrifugal impeller (1993a) and an axial flow rotor (1993b). The details of the hot-wire technique are given by Perdichizzi et al. (1990).

The instantaneous static pressure distributions at the front end of the unshrouded impeller were obtained at 10 radial measuring locations from the impeller inlet to the outlet, by combination of stationary and dynamic pressure measurements. The static pressure fluctuations were measured by means of a flush mounted semiconductor transducer (Entran Epil-203-013G) with a resonance frequency of 100 kHz. The time-averaged static pressures were measured by means of static pressure taps and a Betz micromanometer to avoid thermal zero drift effects on the miniature semiconductor pressure transducer output. The instantaneous static pressure distributions were ensemble averaged using the same procedure as the one applied to the hot wire signals.

From verification tests performed in a calibration wind tunnel, the following experimental uncertainties have been estimated:

Mean velocity ± 1 percent
Flow angles ± 1 deg
Apparent turbulence intensity ± 5 percent
Static pressure ± 2 percent of the reference inlet pressure
Probe position ± 0.1 mm

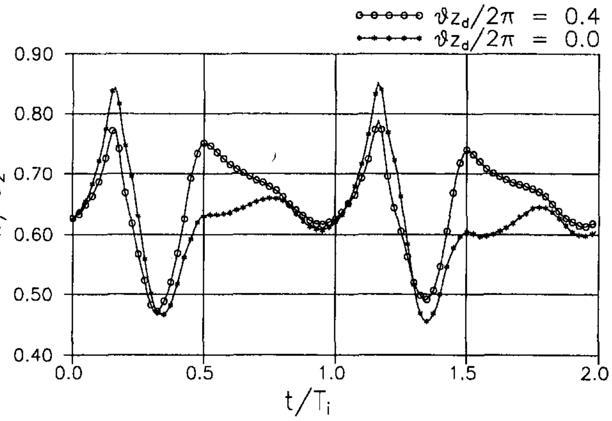

Fig. 4 Ensemble-averaged relative velocity distributions for two different circumferential locations of the probe, at the impeller outlet, midspan position

Data Reduction

The ensemble-averaging procedure enables the separation of the periodic unsteadiness at the blade passing frequency from the random unsteadiness, thus allowing to reconstruct the circumferential distribution of the impeller outflow velocity components in the relative frame, starting from the signal of a stationary probe. In case of a vaneless diffuser or a vaned diffuser with a large vaneless radial gap, the results are independent of the circumferential location of the probe. Reducing the radial distance between the probe and the vane leading edge lets the velocity distributions become sensitive to the probe circumferential location, as shown by Krain (1981) and by Inoue and Cumpsty (1984).

Evidence of the upstream potential flow effect generated by the vaned diffuser is given in Fig. 4. In the case of a vaned diffuser, a comprehensive description of the relative flow should account for information from several circumferential stationary points of view. In the present investigation, velocity and pressure measurements are taken at 30 circumferential locations distributed over one diffuser vane circumferential pitch, in such a way as to achieve an accurate description of the unsteady flow also in space.

In the present investigation the probe is maintained at a fixed position with respect to the absolute frame of reference and the various relative probe-diffuser vane positions have been obtained by rotation of the diffuser. Thus the temporal coordinate of the instantaneous signal for each diffuser position corresponds to the same circumferential coordinate in the rotating frame of reference, regardless of the diffuser position.

Therefore the instantaneous signal (for instance, the velocity c) is a function of time (t_j) or rotor circumferential coordinate, of the data record (n), of the stationary probe circumferential position with respect to the diffuser vane (θ_k), and of a further spatial coordinate (the axial coordinate (z) for the velocity measurements at the impeller outlet, the radial coordinate (r) for the pressure measurements at the impeller front end).

Omitting, for simplicity, the second spatial coordinate, the equations defining the ensemble average procedure are as follows:

Instantaneous velocity

$$c_{njk}(t_j, \theta_k) = \tilde{c}_{jk}(t_j, \theta_k) + c'_{njk}(t_j, \theta_k) \quad (1)$$

Ensemble-averaged velocity

$$\tilde{c}_{jk}(t_j, \theta_k) = \frac{1}{N} \sum_{n=1}^{N} c_{njk}(t_j, \theta_k) \quad (2)$$

Root mean square of the random unsteady fluctuations

$$\sqrt{\widetilde{c'^2_{jk}}(t_j, \theta_k)} = \sqrt{\frac{1}{N} \sum_{n=1}^{N} [c_{njk}(t_j, \theta_k) - \tilde{c}_{jk}(t_j, \theta_k)]^2} \quad (3)$$

where

n = 1 . . . N is the index of the sequence of records to be ensemble averaged ($N = 700$);
j = 1 . . . J is the index of the time coordinate t or the order of the sampled signal in the record ($J = 160$);
k = 1 . . . K is the index of the circumferential position θ of the probe ($K = 30$).

Inoue and Cumpsty (1984) for the case of a centrifugal compressor and Hathaway et al. (1987) for an axial compressor were able to divide the ensemble-averaged velocity $\tilde{c}_{jk}(t_j, \theta_k)$ into a steady-state velocity and a rotor-generated unsteadiness, by time averaging. This description has been proved to be effective in the study of the diffuser flow disturbed by the rotor wakes.

In the present study, concerning the upstream effect of the vaned diffuser on the rotor flow, the circumferential average over a diffuser vane pitch is performed instead of the time average. A representative picture of the impeller flow is provided in fact by the circumferential ensemble-averaged velocity, which is obtained by averaging the K distributions of the ensemble-averaged velocity:

$$\bar{\tilde{c}}_j(t_j) = \sum_{k=1}^{K} [\tilde{c}_{jk}(t_j, \theta_k)\Delta\theta_k] / \sum_{k=1}^{K} \Delta\theta_k \quad (4)$$

The ensemble-averaged velocity $\tilde{c}_{jk}(t_j, \theta_k)$ can be split into two components: the circumferential ensemble-averaged component $\bar{\tilde{c}}_j(t_j)$ and the circumferential distributed fluctuating component $\tilde{c}'_{jk}(t_j, \theta_k)$. The former is still a function of time or of the rotor circumferential coordinate and is no more dependent on the vane position. The latter is due to the upstream effect of the vaned diffuser on the steady, but not uniform in space, rotor relative flow.

$$\tilde{c}_{jk}(t_j, \theta_k) = \bar{\tilde{c}}_j(t_j) + \tilde{c}'_{jk}(t_j, \theta_k) \quad (5)$$

The root mean square of the circumferential distributed fluctuating component $\tilde{c}'_{jk}(t_j, \theta_k)$ represents the stator-induced unsteadiness on the impeller flow:

$$\sqrt{\overline{\tilde{c}'^2_j}(t_j)} = \sqrt{\sum_{k=1}^{K} [\tilde{c}_{jk}(t_j, \theta_k) - \bar{\tilde{c}}_j(t_j)]^2 \Delta\theta_k / \sum_{k=1}^{K} \Delta\theta_k} \quad (6)$$

The concept of stator-induced unsteadiness can be used to quantify the effects of the upstream propagation of the stator potential flow perturbation into the rotor flow. Furthermore, the procedure of splitting the instantaneous velocity into a steady-state velocity, a stator-induced unsteadiness, and an unresolved unsteadiness is suitable to be applied also to the Navier–Stokes equations in order to obtain an averaged form useful for simulating the steady-state turbulent rotor flow periodically perturbed by the downstream vanes.

Figure 5 shows the circumferential ensemble-averaged velocity and compares the stator-induced unsteadiness with the unresolved unsteadiness (rms normalized by the impeller tip speed).

A more impressive description of the periodically unsteady rotor flow can be achieved by correlating in both time and space each measurement, in such a way to obtain an instantaneous relative flow field pattern, which can be displayed over several rotor passages, as shown by Binder et al. (1985), or represented over one or two rotor pitches for different time instants corresponding to different relative positions between impeller blades and diffuser vanes, as shown by Inoue and Cumpsty (1984).

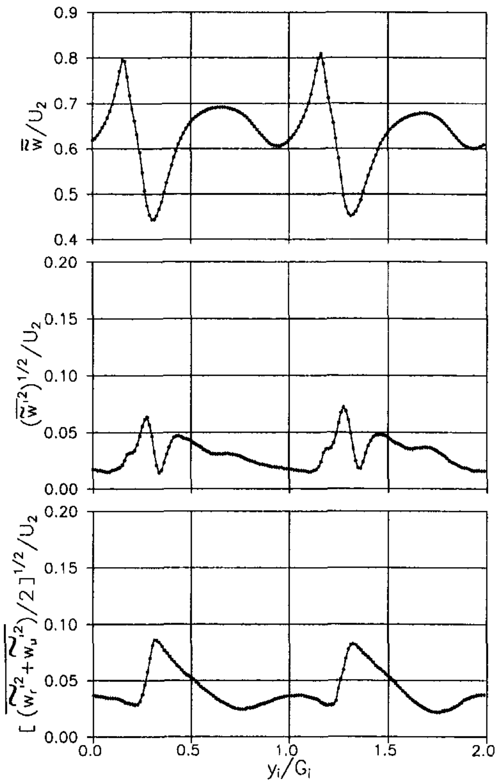

Fig. 5 Circumferential ensemble-averaged relative velocity, stator-generated unsteadiness, and unresolved unsteadiness at the impeller outlet, midspan position

In order to reconstruct the distribution of the ensemble-averaged velocity $\tilde{c}$ in function of the relative frame circumferential coordinate y_i at the time instant $\bar{t}$, it is necessary to reorder the information contained in the individual ensemble averaged signals obtained with the probe fixed in the point M for different circumferential positions θ_k of the diffuser.

Referring to Fig. 3, let P_m be the point in the mth diffuser passage, whose circumferential coordinate in the relative frame is defined by

$$y_i(P_m) = \omega r\bar{t} + r\theta_k + (m-1)\frac{2\pi r}{z_d}$$

then the value of $\tilde{c}$ in P_m at the time instant $\bar{t}$ can be obtained by interpolation of the function $\tilde{c}_{jk}(t_j, \theta_k)$ at the temporal coordinate

$$t = \bar{t} + \frac{\theta_k}{\omega} + (m-1)\frac{2\pi}{z_d\omega}$$

Figure 7 shows a typical result of the described procedure. The distribution of the radial velocity versus the rotor circumferential coordinate is perturbed in proximity to the diffuser vanes; both the vanes and the perturbations, felt by a relative observer, move jointly in time.

Results and Discussion

The results are given in terms of ensemble-averaged and circumferential ensemble-averaged velocity components and pressures, as well as of unresolved and stator generated unsteadiness distributions in space and time.

All the kinematic quantities are normalized with the rotor tip speed U_2. The circumferential rotor relative coordinate y_i and the axial coordinate z are made nondimensional by means of the rotor circumferential pitch $G_i = 2\pi r/z_i$ and the blade span at the rotor outlet b, respectively. The circumferential position of the probe with respect to the vane leading edge θ is normalized by the angular pitch of the diffuser $2\pi/z_d$. The time t is divided by the rotor blade passing period $T_i = 2\pi/\omega z_i$.

Ensemble-Averaged Velocity and Stator-Generated Unsteadiness. Figure 4 shows the ensemble-averaged relative velocity distributions versus time. These results were obtained at midspan, for $D_m/D_2 = 1.02$, with the stationary probe located in two different circumferential positions with respect to the rotatable diffuser. The probe senses in time sequence first the pressure side, then the wake, and finally the impeller passage from the suction to the pressure side. When the probe is set near midpitch ($\theta z_d/2\pi = 0.4$) the diagram shows a typical circumferential distribution of an unseparated outflow with clear evidence of blade wake velocity defects, velocity peaks at the pressure side blade trailing edges, and negative velocity gradient from suction to pressure side through the passage. The vane position has an important influence on the measurement results. When the probe is in proximity of the vane leading edge ($\theta z_d/2\pi = 0$), the pressure side peak is enhanced, whereas the velocity is depressed on the suction side and the impeller passage velocity gradient has completely altered.

The ensemble-averaged distributions corresponding to each of the 30 circumferential positions of the probe were circumferentially averaged, and the result is plotted on the top of Fig. 5 as a function of the normalized rotor circumferential coordinate. The resulting distribution looks very smooth and shows a good periodicity. It conserves the pressure side peaks and wake deficits already observed. The wake extends on the suction side more than on the pressure side and from the suction side the relative velocity continuously increases till midpassage, where a large smooth maximum is formed.

The same figure also reports the comparison of the stator-generated unsteadiness and the circumferentially averaged unre-

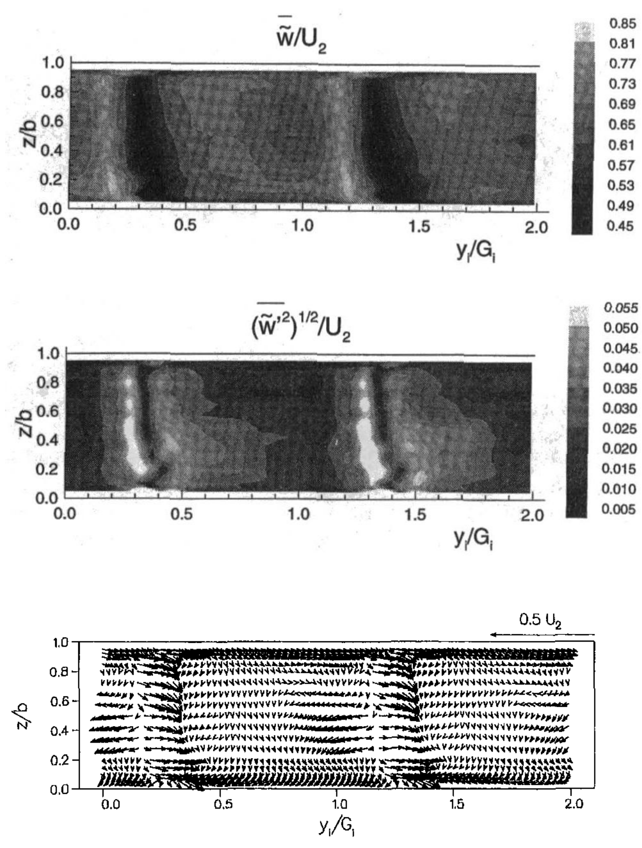

Fig. 6 Circumferential ensemble-averaged relative velocity, stator-generated unsteadiness, and circumferential-averaged relative secondary velocities at the impeller outlet

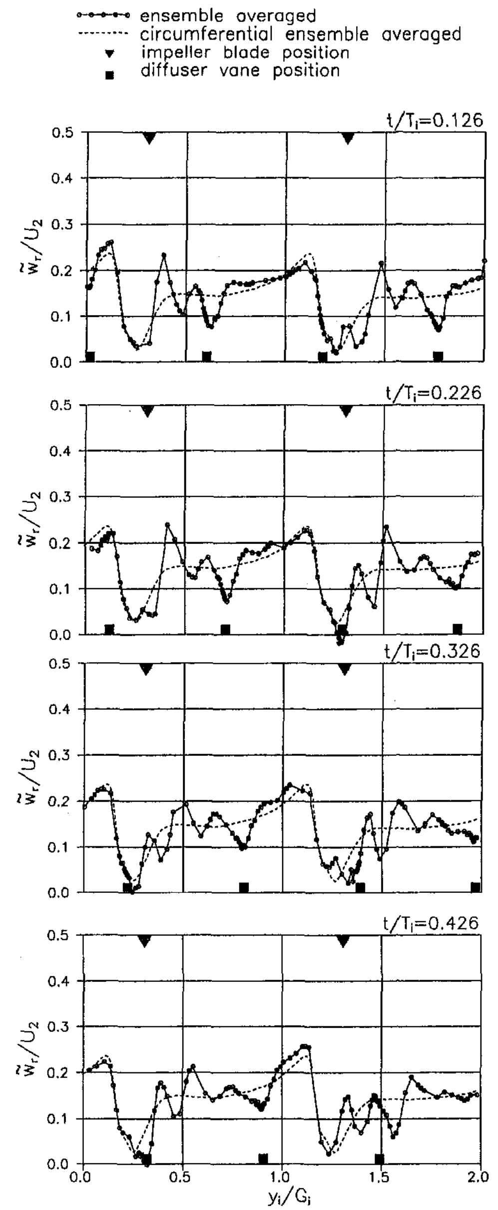

Fig. 7 Instantaneous distributions of the ensemble-averaged radial velocity at the impeller outlet, midspan position

solved unsteadiness. Both quantities are relevant and comparable. Peaks of 7 and 8 percent of the peripheral rotor speed are displayed by the stator-induced and the unresolved unsteadiness, respectively. Since the mean relative velocity is about 60 percent of the peripheral speed, these values correspond to apparent turbulence intensities larger than 10 percent. The unresolved unsteadiness presents a peak at the wake center position. From this point the unsteadiness decreases continuously through the suction side region to about a value of 2.5 percent. A minimum is located in correspondence with the pressure side velocity peak and from this position the unresolved unsteadiness has a steep increase, which gives rise to the wake peak.

The stator-generated unsteadiness shows a characteristic twin peak configuration in the wake region with a minimum at the wake center, in opposition to the unresolved unsteadiness maximum. The stator-generated unsteadiness decreases continuously through the impeller passage, from the suction to the pressure side regions, with values that vary from 5 to less than 2 percent. This result is rather interesting as it means that the center of the wake and the pressure side of the passages are nearly unaffected by stator-induced unsteadiness, implying that they represent a limit to the propagation of the stator-induced unsteadiness to adjacent rotor passages.

In order to have an overall representation of the mean unsteady flow field, the results obtained from the 17 spanwise measuring locations are used to construct area plots depicted over the cylindrical section of the model at the impeller outlet (Fig. 6). The physical scale of the frame is modified such that the vertical scale is three times the horizontal one. The impeller blades move from right to left.

The gray-filled contours of the circumferentially ensemble-averaged relative velocity, the contours of the stator-induced unsteadiness, and the circumferentially averaged relative secondary velocity vectors are shown in Fig. 6. Secondary velocity components are those in the plane perpendicular to the primary direction defined by the flow in the center of the passage ($\beta = -76$ deg, $\gamma = 0$ deg).

In the plot of the mean relative velocity, the two dark gray-filled area, representing the traces of the blade wakes, extend in the spanwise direction from hub to tip separating the individual impeller passages. Narrow light gray bands parallel to the wake traces show a relative velocity increase around the pressure side trailing edge region. The mean relative velocity increases continuously from the wake suction side toward midpassage.

The contours give also evidence of a core of rather low-momentum fluid, approximately located near midspan, halfway between the midpassage and the pressure side of the passage. This throughflow momentum wake, characteristic of unshrouded centrifugal impellers (e.g., Krain, 1987; Hathaway et al., 1993), is mainly due to the tip leakage action, which produces losses and convects them toward the pressure side, as also shown by results of calculations on a low-speed centrifugal compressor (Moore and Moore, 1993).

A second region of low-momentum fluid has been formed on the suction side/hub corner. In the present model, with the blades set in the wholly radial part of the impeller, the Rossby number $Ro = w/\omega R_n$, as defined by Johnson (1978), tends to zero. The centrifugal force defect acting on the blade boundary layers becomes negligible when compared with the Coriolis force effect on the hub endwall. This low-momentum fluid is convected into the suction side/hub corner by the passage vortex and this stable location for the wake is maintained.

Evidence of the passage and tip leakage vortices is given by the residual secondary velocities of the mean relative flow, which can be observed at the hub and casing endwalls respectively, in the vector plot of Fig. 6. The same vector plot also shows that, close to the wakes, relevant secondary slip velocities move against the rotor speed and feed fluid from the pressure side of the passage into the blade wake.

The unsteadiness generated by the stator on the impeller outflow is shown at the middle of Fig. 6. The narrow vertical dark gray bands extending from the hub to the casing in the center of the wakes constitute clean circumferential discontinuities in the stator generated unsteadiness distribution. This unsteadiness is large on both the pressure and suction sides of the wake, but low in the wake center. Within the impeller passage, the unsteadiness decreases from the suction to the pressure side and it is more intense between midspan and the hub endwall.

Instantaneous Distributions of the Ensemble-Averaged Velocity Components. Figure 7 shows the instantaneous circumferential distributions of the ensemble-averaged radial velocity at midspan, observed in the relative frame, for four different relative positions of the impeller blades and the diffuser vanes. For clarity the circumferential positions of blades and vanes are marked at the top and bottom of each frame, respectively. In the relative frame of reference, the impeller blade traces and the associated wakes have a fixed position in time, while the diffuser vanes are seen to move at the impeller peripheral speed, but in opposite direction, from left to right. To highlight the stator-induced unsteady disturbances, the circumferential ensemble-averaged radial velocity is plotted with dashed line over each instantaneous distribution.

The radial velocity distributions display well-defined minima on the pressure side of the wakes. The circumferential misalignment between the blade traces located in the center of the wakes and the radial velocity minima depends on the distribution of the relative flow angle, which has its minimum just on the pressure side of the wake. The diffuser-generated upstream potential flow effect is such that the radial velocity in proximity to each vane leading edge presents a local minimum. These minima rotate jointly with the diffuser vanes. The stagnation effect induces local reversals of the flow, whenever the impeller blade trailing edge and the diffuser vane leading edge are circumferentially aligned.

An interesting feature observable from the variations of the radial velocity distribution with time is the presence of a series of peaks and valleys, which originate on the suction side of the impeller passage and follow the leading minimum corresponding to the diffuser vane.

These disturbances propagate in the circumferential direction with a velocity of $-0.6\ U_2$, approximately equal to w_u, and reduce their amplitude with time. An explanation of this phenomenon has not yet been obtained, but the above-mentioned features suggest that they may be associated with the transit, in the measuring station, of flow that has been previously perturbed within the impeller by the passing diffuser vanes.

All the observed disturbances, correlated with the diffuser vane transit, reduce their amplitude from the suction to the pressure side of the impeller passage, in accordance with the previously shown stator induced unsteadiness distribution.

The instantaneous distributions of the ensemble-averaged relative velocity tangential component, given in Fig. 8, show variations through the blade wakes of about 35 percent of the peripheral speed U_2. The minimum, which is about $-0.8\ U_2$, is located on the pressure side, outside of the wake, where a peak of the relative velocity has been already observed. The maximum (about $-0.45\ U_2$) is aligned with the center of the wake.

The perturbations induced by the diffuser vanes are evidenced by tangential velocity variations on the vane sides. In fact the absolute streamlines tend to deflect around the vane leading edge, with an increase of the tangential velocity component on the suction side and a decrease on the pressure side of the diffuser vane leading edge. This effect was also observed by Inoue and Cumpsty (1984).

Instantaneous pictures of the ensemble-averaged velocity field at the impeller outlet, as seen by a relative observer, have been reconstructed from the data taken at the 17 axial measuring stations. The radial velocity distributions are shown in Fig. 9, as gray-filled contour plots. The impeller blades are fixed with time and the diffuser vanes appear to move past with circumferential speed $-U_2$. The radial velocity field is dominated by the presence of regions of very low velocity located on the pressure side of the blade traces and fixed with them in time. Depending on the relative positions of the vanes, the radial velocity on the suction side of the blade wakes changes with time from high to low values. For instance, when the diffuser vane is situated on the suction side of the impeller wake ($t/T_i = 0.326$, second blade from left), the defect in radial velocity becomes wider and the wake appears enlarged.

Looking at the central impeller passage, a well-defined deep velocity defect corresponding to the diffuser vane is evident. This interaction effect appears even more pronounced in the regions closer to the endwalls. As already observed, the main perturbation is followed by a series of smoother valleys and peaks moving from pressure to suction side with reduced speed and further perturbing the velocity field.

Since the potential effect of the vaned diffuser perturbs the instantaneous kinematic field at the impeller outlet, a remarkable

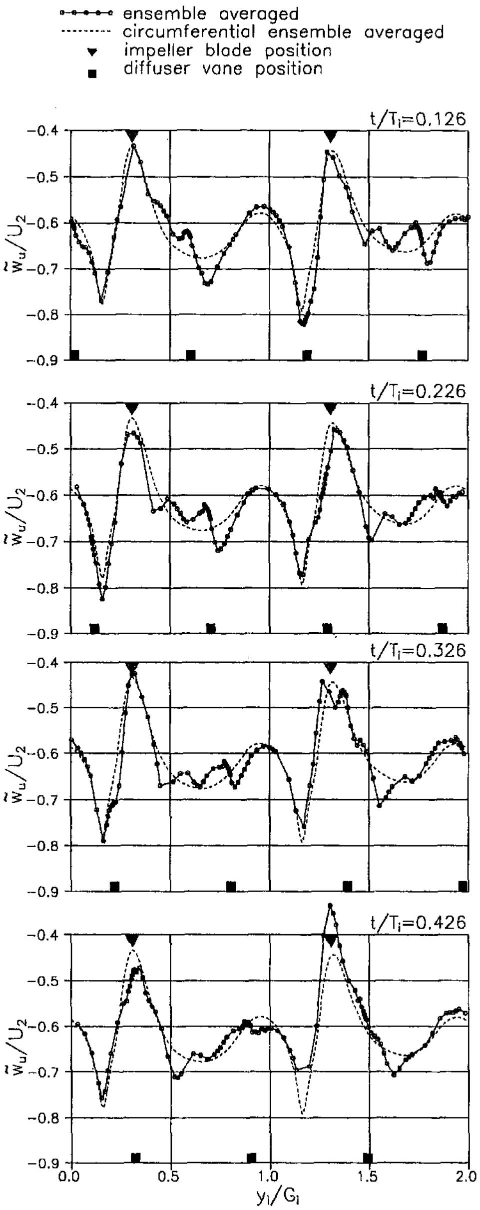

Fig. 8 Instantaneous distributions of the ensemble-averaged tangential relative velocity at the impeller outlet, midspan position

effect should also be expected on the moment of momentum of the fluid leaving the impeller. Figure 10 shows instantaneous pictures of the nondimensional quantity $\widetilde{c_r c_u}/U_2^2$, which is proportional to the moment of momentum of the mass flow rate leaving the impeller. This term represents an important contribution to the local rotor work exchange. In case of steady flow in the rotating frame and shrouded impeller, its integral over the exit area of the impeller is proportional to the impeller power input. When, as in the present case, the flow is unsteady in the relative frame and the impeller is unshrouded, the power loss due to viscous friction on the casing and the time rate of change of moment of momentum in the control volume should also be taken into account when calculating the impeller power (Lyman, 1993).

The plots of Fig. 10 show relevant circumferential and instantaneous variations of $\widetilde{c_r c_u}/U_2^2$. The energy exchange is very low on the pressure side of the impeller blades where both radial and tangential absolute velocities are low. On the contrary, the suction side of the wake and the core of low relative velocity,

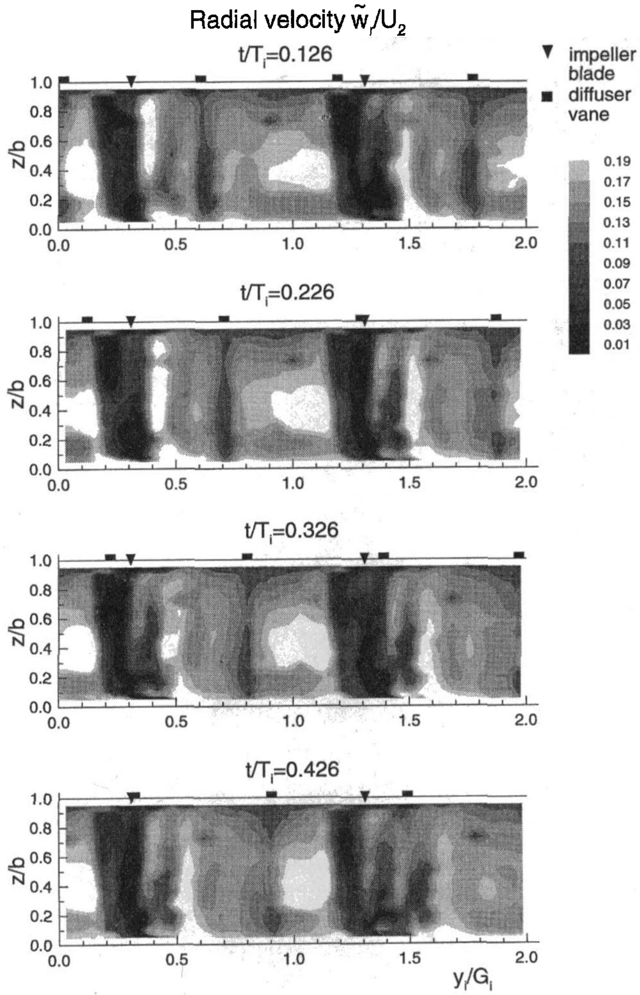

Fig. 9 Instantaneous pictures of the ensemble-averaged radial velocity at the impeller outlet

located near midspan, at the passage pressure side, are regions of large energy exchange.

The stator-generated unsteady effect continuously modifies the instantaneous flow pattern. The energy exchange is reduced at the pressure side of the diffuser vane due to the reduction of both radial and absolute tangential velocities in that region. As expected, this disturbance moves jointly with the vane. When the vane approaches the impeller pressure side from midpassage, the core of intense energy exchange, compressed between the vane and the pressure side of the wake, progressively reduces its area while its intensity tends to increase.

A further remarkable unsteady effect can be observed on the blade suction side region, which, at $t/T_i = 0.126$, shows the largest values of the local energy exchange, but at $t/T_i = 0.426$ presents local reductions of more than 30 percent.

Pressure Distributions. Unsteady pressure measurements at the unshrouded impeller front end were made for ten pressure taps from the impeller inlet to the outlet. Figure 11 shows the instantaneous distributions of the ensemble-averaged pressure coefficient $\tilde{C}_p$, measured at the same radial station ($D_m/D_2 = 1.02$) as the velocity. The instants chosen to describe the time evolution of the pressure are different from those chosen for the velocity, but the reference initial time ($t/T_i = 0$) is the same for all quantities. To point out the unsteady effects generated by the diffuser, the circumferential ensemble-averaged pressure distribution is added to each diagram.

The most striking feature of these distributions is the fact that the upstream disturbance induced by the diffuser vanes is not localized and does not rotate with the diffuser vane, as in the case of the velocity. On the contrary, it influences the whole pressure field limited by the two lateral pressure minima. In each impeller passage, the pressure fluctuates in time with a period of $T = 0.583\ T_i$, equal to the vane passing period, and an amplitude of about 8 percent of the dynamic pressure associated with the impeller speed U_2. This amplitude corresponds to pressure fluctuations as large as 25 percent of the impeller pressure rise with high and low pressure levels alternating in the same passage and from a passage to the adjacent one.

For each radial measuring location, the circumferential ensemble-averaged pressure coefficient $\overline{\tilde{C}_p}$ and stator-generated unsteady pressure coefficient $(\overline{\tilde{C}_p'^2})^{1/2}$ were calculated. The spatial distributions of the two pressure coefficients are given in Fig. 12, as color-filled contours depicted over the impeller passages. The impeller rotates counter clockwise.

Since impeller endwalls are straight, blade span is small compared with blade chord, and tip clearance is small too, the pressure measurements at the impeller front end are representative of the pressure distribution in the impeller passages (Gostelow, 1977).

As expected, the pressure increases along the impeller channel, showing characteristic potential flow features such as a remarkable blade aerodynamic loading, a stagnation effect on the pressure side of the leading edge region, a local minimum in the suction side region and, above all, an important pressure rise in the semi-vaneless region at the impeller outlet.

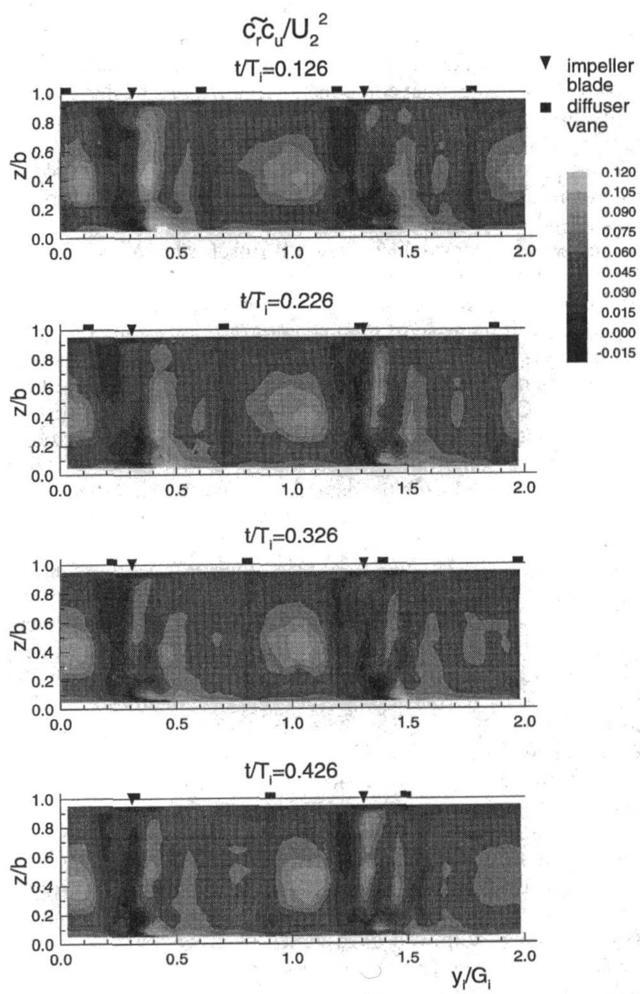

Fig. 10 Instantaneous pictures of the ensemble-averaged nondimensional moment of momentum of flow rate at the impeller outlet

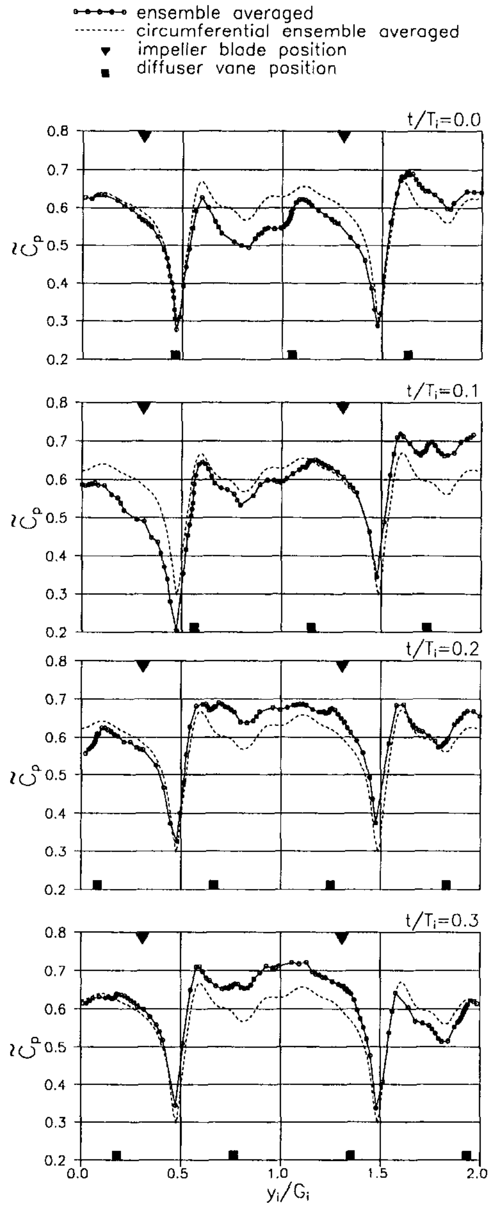

Fig. 11 Instantaneous distributions of the ensemble-averaged static pressure coefficient at the impeller outlet

The stator-induced pressure unsteadiness propagates into the impeller, undergoing progressive reduction nearly linear with the radial distance. At the impeller outlet the unsteady pressure coefficient takes values greater than 0.05, corresponding to an effective pressure unsteadiness of about 8 percent of the impeller pressure rise. At the impeller inlet, the unsteady pressure coefficient is reduced to less than 0.01.

The instantaneous pictures of the ensemble-averaged static pressure coefficient $\tilde{C}_p$ of Fig. 13 show remarkable variations with time in the semi-vaneless region at the impeller outlet. Referring to the central impeller passage, the pressure level is low at the instant $t/T_i = 0$, when the blade is approximately circumferentially centered in the diffuser passage. After a semiperiod of the diffuser vane passage, approximately corresponding to the time instant $t/T_i = 0.3$, the pressure level in the semi-vaneless region of the impeller and at the pressure side of the blade becomes high. In that instant the blade trailing edge and the vane leading edge are approximately aligned in the radial direction and their distance is minimum.

Conclusions

To study the upstream potential flow effect induced by the vaned diffuser on the impeller flow, detailed velocity and pressure measurements were performed with stationary fast response probes in a simplified model of centrifugal turbomachine.

The flow has been investigated for several relative circumferential positions of the probe with respect to the vaned diffuser. Data have been reduced and analyzed by means of ensemble-average and circumferential ensemble-average techniques in order to separate the periodic contribution due to steady nonuniform flow in the impeller from the unresolved and the stator-generated unsteadiness. This latter unsteady contribution has been calculated as the rms of the unsteady periodic fluctuations due to the diffuser vanes, which are in relative motion with respect to the impeller passages.

At the impeller outlet the unresolved and the stator-generated unsteadiness are comparable and present peaks of about 10 percent of the relative velocity. The stator-generated unsteady pressure coefficient at the impeller outlet is about 8 percent of the impeller pressure rise and propagates upstream into the impeller with a reduction proportional to the radial distance from the diffuser vanes.

By correlating in space and time the large amount of data taken, instantaneous pictures of the rotor outflow and of the impeller pressure distribution have been obtained. These pictures show the details of the flow periodically perturbed by the diffuser vanes.

Relevant local defects of radial velocity and streamline deflections are induced on the flow at the impeller outlet by the

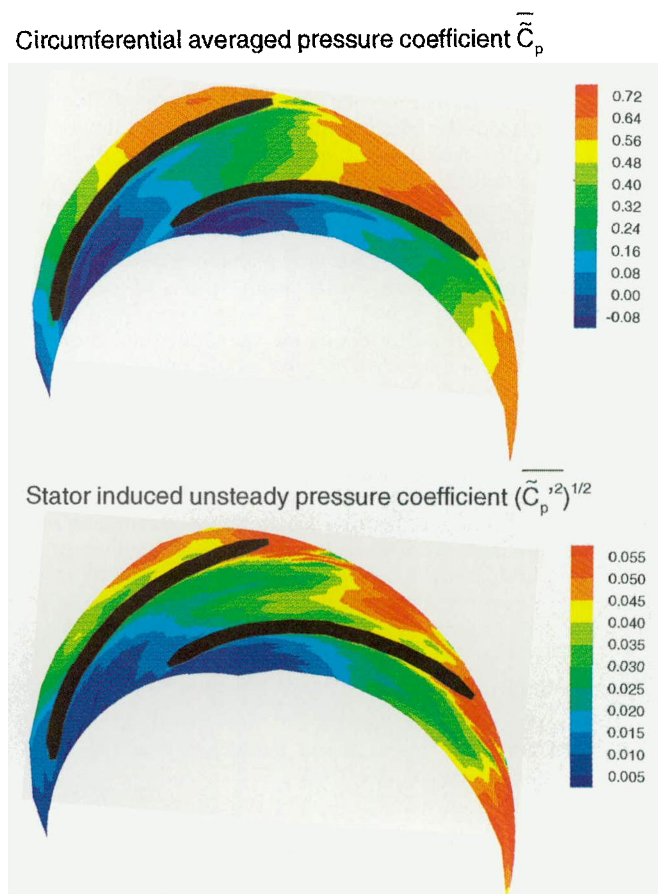

Fig. 12 Circumferential ensemble-averaged static pressure coefficient and stator-generated unsteady pressure coefficient at the impeller front end

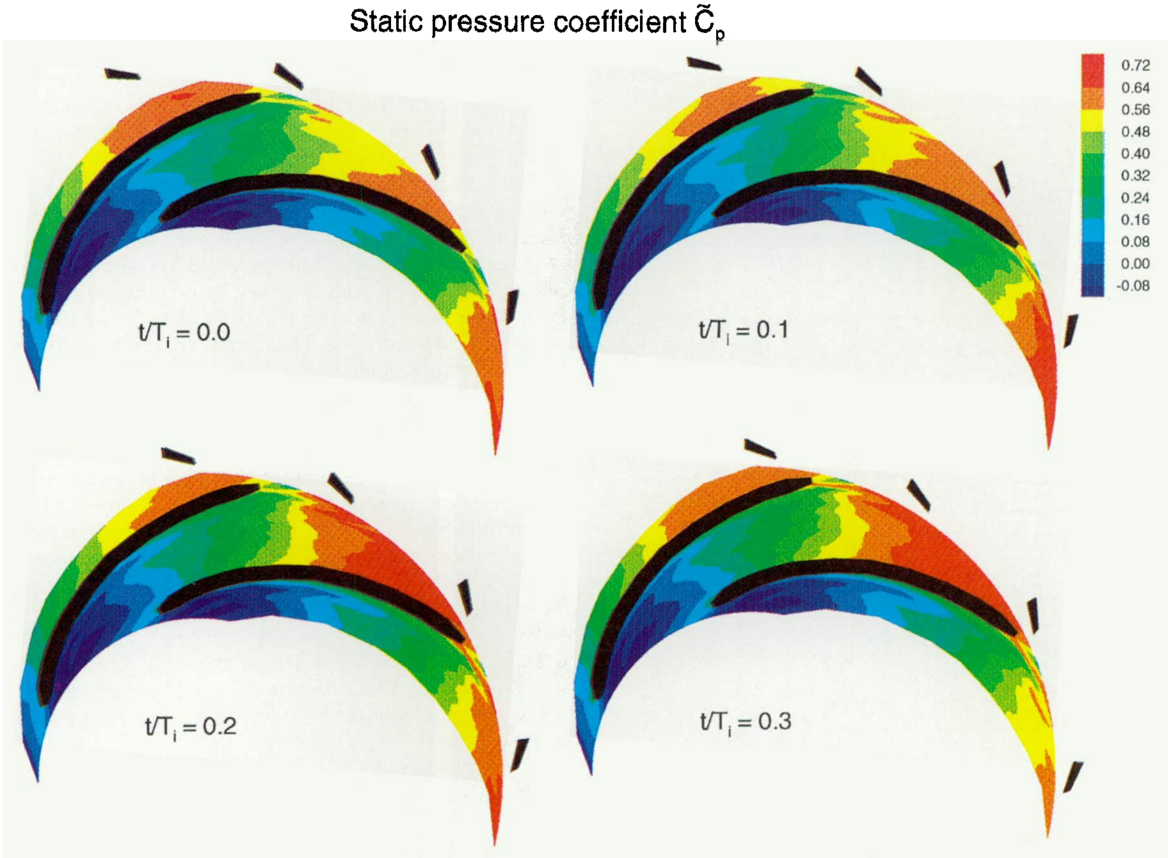

Fig. 13 Instantaneous pictures of the ensemble-averaged static pressure coefficient at the front end of the impeller

vaned diffuser. The diffuser vanes and the local perturbations move jointly from the suction side of the passage followed by further flow disturbances that propagate circumferentially in time with the tangential relative velocity.

The periodic interaction of the stator-generated flow perturbations with the local spatial nonuniformities of the impeller relative flow give rise to significant flow phenomena, such as periodic local reversed flow and instantaneous peaks of local work exchange.

The upstream diffuser effect on the static pressure results in a change of the pressure level in the whole impeller passage with time, rather than in a localized perturbation, as is the case for the velocity. Periodic pressure fluctuations as large as 25 percent of the impeller pressure rise affect the impeller passage and propagate to the adjacent passages.

The investigation has been limited to just one geometry and one flow condition and therefore quantitative information cannot be generalized. Nevertheless, these detailed results provide a better understanding of the potential flow interaction phenomena and give an estimation of the importance of the different effects induced by the vaned diffuser on the impeller flow.

Acknowledgments

This work has been carried out with the support of the Italian National Council of Research and the Ministry of University and Scientific Research.

References

Arndt, N., Acosta, A. J., Brennen, C. E., and Caughey, T. K., 1990, "Experimental Investigation of Rotor–Stator Interaction in a Centrifugal Pump With Several Vaned Diffusers," ASME JOURNAL OF TURBOMACHINERY, Vol. 112, pp. 98–108.

Binder, A., Forster, W., Kruse, H., and Rogge, H., 1985, "An Experimental Investigation Into the Effect of Wakes on the Unsteady Turbine Rotor Flow," ASME *Journal of Engineering for Gas Turbines and Power,* Vol. 107, pp. 458–466.

Binder, A., Schroeder, Th., and Hourmouziadis, J., 1989, "Turbulence Measurements in a Multistage Low-Pressure Turbine," ASME JOURNAL OF TURBOMACHINERY, Vol. 111, pp. 153–161.

Dring, R. P., Joslyn, H. D., Hardin, L. W., and Wagner, J. H., 1982, "Turbine Rotor–Stator Interaction," ASME *Journal of Engineering for Power,* Vol. 104, pp. 729–742.

Dunker, R. J., 1983, "Flow Measurements in the Stator Row of a Single-Stage Transonic Axial-Flow Compressor With Controlled Diffusion Stator Blades," *Proceedings of the 61th AGARD Specialists' Meeting of the Propulsion & Energetics Panel on Viscous Effects in Turbomachines,* Copenhagen, Denmark, Paper No. 23.

Gostelow, J. P., 1977, "A New Approach to the Experimental Study of Turbomachinery Flow Phenomena," ASME *Journal of Engineering for Power,* Vol. 99, pp. 97–105.

Hathaway, M. D., Okiishi, T. H., Suder, K. L., Strazisar, A. J., and Adamczyk, J. J., 1987, "Measurements of the Unsteady Flow Field Within the Stator Row of a Transonic Axial-Flow Fan II—Results and Discussion," ASME Paper No. 87-GT-227.

Hathaway, M. D., Chriss, R. M., Wood, J. R., and Strazisar, A. J., 1993, "Experimental and Computational Investigation of the NASA Low-Speed Centrifugal Compressor Flow Field," ASME JOURNAL OF TURBOMACHINERY, Vol. 115, pp. 527–542.

Hodson, H. P., 1985, "Measurements of Wake-Generated Unsteadiness in the Rotor Passages of Axial Flow Turbines," ASME *Journal of Engineering for Gas Turbines and Power,* Vol. 107, pp. 467–476.

Inoue, M., and Cumpsty, N. A., 1984, "Experimental Study of Centrifugal Impeller Discharge Flow in Vaneless and Vaned Diffusers," ASME *Journal of Engineering for Gas Turbines and Power,* Vol. 106, pp. 455–467.

Johnson, M. W., 1978, "Secondary Flows in Rotating Bends," ASME *Journal of Engineering for Power,* Vol. 100, pp. 553–560.

Joslyn, H. D., Dring, R. P., and Sharma, O. P., 1983, "Unsteady Three-Dimensional Turbine Aerodynamics," ASME *Journal of Engineering for Power,* Vol. 105, pp. 322–331.

Krain, H., 1981, "A Study on Centrifugal Impeller and Diffuser Flow," ASME *Journal of Engineering for Power,* Vol. 103, pp. 688–697.

Krain, H., 1988, "Swirling Impeller Flow," ASME JOURNAL OF TURBOMACHINERY, Vol. 110, pp. 122–128.

La Graff, J. E., Ashworth, D. A., and Schultz, D. L., 1989, "Measurement and Modeling of the Gas Turbine Blade Transition Process as Disturbed by Wakes," ASME JOURNAL OF TURBOMACHINERY, Vol. 111, pp. 315–322.

Lakshminarayana, B., 1981, "Techniques for Aerodynamic and Turbulence Measurements in Turbomachinery Rotors," ASME *Journal of Engineering for Power*, Vol. 103, pp. 374–392.
Liu, X., and Rodi, W., 1992, "Measurement of Unsteady Flow and Heat Transfer in a Linear Turbine Cascade," ASME Paper No. 92-GT-323.
Lyman, F. A., 1993, "On the Conservation of Rothalpy in Turbomachines," ASME JOURNAL OF TURBOMACHINERY, Vol. 115, pp. 520–526.
Moore, J., and Moore, J. G., 1993, discussion to the paper "Experimental and Computational Investigation of the NASA Low-Speed Centrifugal Compressor Flow Field," by Hathaway, M. D., Chriss, R. M., Wood, J. R., and Strazisar, A. J., ASME JOURNAL OF TURBOMACHINERY, Vol. 115, pp. 541–542.
Perdichizzi, A., Ubaldi, M., and Zunino, P., 1990, "A Hot Wire Measuring Technique for Mean Velocity and Reynolds Stress Components in Compressible Flow," *Proceedings of the 10th Symposium on Measuring Techniques for Transonic and Supersonic Flows in Cascades and Turbomachines*, VKI, Brussels, Belgium, Paper No. 8.
Pfeil, H., Herbst, R., and Schroeder, T., 1983, "Investigation of the Laminar-Turbulent Transition of Boundary Layers Disturbed by Wakes," ASME *Journal of Engineering for Power*, Vol. 105, pp. 130–137.
Poensgen, C., and Gallus, H. E., 1991a, "Three-Dimensional Wake Decay Inside of a Compressor Cascade and Its Influence on the Downstream Unsteady Flow Field. Part I: Wake Decay Characteristics in the Flow Passage," ASME JOURNAL OF TURBOMACHINERY, Vol. 113, pp. 180–189.
Poensgen, C., and Gallus, H. E., 1991b, "Three-Dimensional Wake Decay Inside of a Compressor Cascade and Its Influence on the Downstream Unsteady Flow Field. Part II: Unsteady Flow Field Downstream of the Stator," ASME JOURNAL OF TURBOMACHINERY, Vol. 113, pp. 190–197.
Schulz, H. D., Gallus, H. E., and Lakshminarayana, B., 1990, "Three-Dimensional Separated Flow Field in the Endwall Region of an Annular Compressor Cascade in the Presence of Rotor-Stator Interaction. Part 2—Unsteady Flow and Pressure Field," ASME JOURNAL OF TURBOMACHINERY, Vol. 112, pp. 679–690.
Suder, K. L., Hathaway, M. D., Okiishi, T. H., Strazisar, A. J., and Adamczyk, J. J., 1987, "Measurements of the Unsteady Flow Field Within the Stator Row of a Transonic Axial-Flow Fan I—Measurement and Analysis Technique," ASME Paper No. 87-GT-226.
Ubaldi, M., Zunino, P., and Cattanei, A., 1993a, "Relative Flow and Turbulence Measurements Downstream of a Backward Centrifugal Impeller," ASME JOURNAL OF TURBOMACHINERY, Vol. 115, pp. 543–551.
Ubaldi, M., Zunino, P., and Cattanei, A., 1993b, "Relative Flow and Turbulence Measurements Downstream of an Axial Flow Rotor," *Engineering Turbulence Modelling and Experiments 2*, W. Rodi and F. Martelli, eds., Elsevier Science Pub., pp. 795–804.
Zeschky, J., and Gallus, H. E., 1993, "Effects of Stator Wakes and Spanwise Nonuniform Inlet Conditions on the Rotor Flow of an Axial Turbine Stage," ASME JOURNAL OF TURBOMACHINERY, Vol. 115, pp. 128–136.
Zierke, W. C., and Okiishi, T. H., 1982, "Measurement and Analysis of Total-Pressure Unsteadiness Data From an Axial-Flow Compressor Stage," ASME *Journal of Engineering for Power*, Vol. 104, pp. 479–488.

APPENDIX

Diffuser Vane Profile Geometry

The diffuser vanes are thin constant thickness circular arc aerofoils. The geometry is defined by the following parameters:

- Radius of curvature of the camber line $R_c = 332$ mm.
- Angle between the camber line chord and the radial direction at the inlet $\lambda_{3'} = 101.65$ deg.
- Inlet and outlet radii of the camber line $R_{3'} = 223.94$ mm, $R_4 = 332$ mm.
- Constant thickness of the profile 8 mm.

Reduced thickness at the leading edge 4 mm, obtained by a linear cut of the airfoil on the pressure side from 13 percent of the camber line to the leading edge.

Impeller blade profile coordinates

Suction side		Pressure side	
R (mm)	θ (deg)	R (mm)	θ (deg)
120.00	0.00	120.00	0.00
120.48	1.61	122.76	1.16
121.06	3.21	124.91	2.79
121.74	4.79	126.76	4.10
122.50	6.36	128.71	5.40
123.36	7.91	130.77	6.69
124.31	9.43	132.95	7.96
128.31	13.62	137.43	11.86
132.58	17.67	141.73	15.98
136.86	21.65	146.03	20.04
141.13	25.60	150.33	24.05
145.40	29.50	154.63	28.03
149.67	33.37	158.92	31.96
153.94	37.21	163.22	35.86
158.22	41.01	167.52	39.72
162.49	44.79	171.81	43.54
166.77	48.52	176.11	47.33
171.05	52.22	180.40	51.06
175.33	55.87	184.69	54.75
179.61	59.47	188.98	58.39
183.89	63.02	193.27	61.97
188.17	66.52	197.56	65.49
192.45	69.95	201.85	68.95
196.74	73.31	206.13	72.34
201.02	76.61	210.42	75.66
203.83	77.59	210.34	77.00
206.67	78.52	210.36	78.23
209.53	79.42	210.47	79.33

DISCUSSION

Y. N. Chen[1]

The authors of the paper have presented very useful informations about the flow fields due to interaction between the impeller blades and the diffuser vanes.

The present discusser has discovered a special phenomenon of the secondary flow field, which may be of interest to the authors. The secondary flow field displayed in the lowest plot of Fig. 6 reveals a secondary vortex embedded just in the region, in which the throughflow momentum wake appears; see the upper plot of the same figure. This secondary vortex field is indicated by a circular curve L in Fig. 14(b).

The authors explained that the throughflow momentum wake is caused by the tip leakage action, which produces losses and convects them toward the pressure side.

However, if the secondary flow field mentioned is closely examined, the leakage flow of the tip clearance does not have any connection with this secondary vortex. Rather, this leakage flow meets the further secondary flow traveling in the opposite direction along the shroud. The meeting region of these two flows, as denoted by S in Fig. 14(b), must be a sink. As this region is situated within the dark area of the throughflow in the upper plot of Fig. 6, i.e., thus within the area of the lowest velocity, this sink therefore appears to guide the meeting flows in the reverse direction into the impeller. We then have a reverse flow along the corner "suction-surface/shroud" even at the normal operating point. This kind of reverse flow has been found by Chen et al. (1989) in their Fig. 5.

The upper plot of Fig. 5 of the present paper about the averaged total relative velocity (as transferred to Fig. 14a) shows that the curve rises to a peak along the pressure side of the impeller blade (cf. Fig. 8 about the tangential velocity component alone), drops sharply along the suction side to a minimum of the wake deficit. Afterward, the curve rises toward the pressure surface of the following impeller blade. This rising-up branch does not follow a uniform trend according to the potential theory, but rather a going-up and down pattern. The valley of this pattern is the throughflow momentum wake (as given in the upper plot of Fig. 6), which coincides with the secondary

[1] R & D, 1510, Sulzer Brothers Ltd., 8401 Winterthur, Switzerland.

Lakshminarayana, B., 1981, "Techniques for Aerodynamic and Turbulence Measurements in Turbomachinery Rotors," ASME *Journal of Engineering for Power*, Vol. 103, pp. 374–392.
Liu, X., and Rodi, W., 1992, "Measurement of Unsteady Flow and Heat Transfer in a Linear Turbine Cascade," ASME Paper No. 92-GT-323.
Lyman, F. A., 1993, "On the Conservation of Rothalpy in Turbomachines," ASME JOURNAL OF TURBOMACHINERY, Vol. 115, pp. 520–526.
Moore, J., and Moore, J. G., 1993, discussion to the paper "Experimental and Computational Investigation of the NASA Low-Speed Centrifugal Compressor Flow Field," by Hathaway, M. D., Chriss, R. M., Wood, J. R., and Strazisar, A. J., ASME JOURNAL OF TURBOMACHINERY, Vol. 115, pp. 541–542.
Perdichizzi, A., Ubaldi, M., and Zunino, P., 1990, "A Hot Wire Measuring Technique for Mean Velocity and Reynolds Stress Components in Compressible Flow," *Proceedings of the 10th Symposium on Measuring Techniques for Transonic and Supersonic Flows in Cascades and Turbomachines*, VKI, Brussels, Belgium, Paper No. 8.
Pfeil, H., Herbst, R., and Schroeder, T., 1983, "Investigation of the Laminar-Turbulent Transition of Boundary Layers Disturbed by Wakes," ASME *Journal of Engineering for Power*, Vol. 105, pp. 130–137.
Poensgen, C., and Gallus, H. E., 1991a, "Three-Dimensional Wake Decay Inside of a Compressor Cascade and Its Influence on the Downstream Unsteady Flow Field. Part I: Wake Decay Characteristics in the Flow Passage," ASME JOURNAL OF TURBOMACHINERY, Vol. 113, pp. 180–189.
Poensgen, C., and Gallus, H. E., 1991b, "Three-Dimensional Wake Decay Inside of a Compressor Cascade and Its Influence on the Downstream Unsteady Flow Field. Part II: Unsteady Flow Field Downstream of the Stator," ASME JOURNAL OF TURBOMACHINERY, Vol. 113, pp. 190–197.
Schulz, H. D., Gallus, H. E., and Lakshminarayana, B., 1990, "Three-Dimensional Separated Flow Field in the Endwall Region of an Annular Compressor Cascade in the Presence of Rotor-Stator Interaction. Part 2—Unsteady Flow and Pressure Field," ASME JOURNAL OF TURBOMACHINERY, Vol. 112, pp. 679–690.
Suder, K. L., Hathaway, M. D., Okiishi, T. H., Strazisar, A. J., and Adamczyk, J. J., 1987, "Measurements of the Unsteady Flow Field Within the Stator Row of a Transonic Axial-Flow Fan I—Measurement and Analysis Technique," ASME Paper No. 87-GT-226.
Ubaldi, M., Zunino, P., and Cattanei, A., 1993a, "Relative Flow and Turbulence Measurements Downstream of a Backward Centrifugal Impeller," ASME JOURNAL OF TURBOMACHINERY, Vol. 115, pp. 543–551.
Ubaldi, M., Zunino, P., and Cattanei, A., 1993b, "Relative Flow and Turbulence Measurements Downstream of an Axial Flow Rotor," *Engineering Turbulence Modelling and Experiments 2*, W. Rodi and F. Martelli, eds., Elsevier Science Pub., pp. 795–804.
Zeschky, J., and Gallus, H. E., 1993, "Effects of Stator Wakes and Spanwise Nonuniform Inlet Conditions on the Rotor Flow of an Axial Turbine Stage," ASME JOURNAL OF TURBOMACHINERY, Vol. 115, pp. 128–136.
Zierke, W. C., and Okiishi, T. H., 1982, "Measurement and Analysis of Total-Pressure Unsteadiness Data From an Axial-Flow Compressor Stage," ASME *Journal of Engineering for Power*, Vol. 104, pp. 479–488.

APPENDIX

Diffuser Vane Profile Geometry

The diffuser vanes are thin constant thickness circular arc aerofoils. The geometry is defined by the following parameters:

- Radius of curvature of the camber line $R_c = 332$ mm.
- Angle between the camber line chord and the radial direction at the inlet $\lambda_{3'} = 101.65$ deg.
- Inlet and outlet radii of the camber line $R_{3'} = 223.94$ mm, $R_4 = 332$ mm.
- Constant thickness of the profile 8 mm.

Reduced thickness at the leading edge 4 mm, obtained by a linear cut of the airfoil on the pressure side from 13 percent of the camber line to the leading edge.

Impeller blade profile coordinates

Suction side		Pressure side	
R (mm)	θ (deg)	R (mm)	θ (deg)
120.00	0.00	120.00	0.00
120.48	1.61	122.76	1.16
121.06	3.21	124.91	2.79
121.74	4.79	126.76	4.10
122.50	6.36	128.71	5.40
123.36	7.91	130.77	6.69
124.31	9.43	132.95	7.96
128.31	13.62	137.43	11.86
132.58	17.67	141.73	15.98
136.86	21.65	146.03	20.04
141.13	25.60	150.33	24.05
145.40	29.50	154.63	28.03
149.67	33.37	158.92	31.96
153.94	37.21	163.22	35.86
158.22	41.01	167.52	39.72
162.49	44.79	171.81	43.54
166.77	48.52	176.11	47.33
171.05	52.22	180.40	51.06
175.33	55.87	184.69	54.75
179.61	59.47	188.98	58.39
183.89	63.02	193.27	61.97
188.17	66.52	197.56	65.49
192.45	69.95	201.85	68.95
196.74	73.31	206.13	72.34
201.02	76.61	210.42	75.66
203.83	77.59	210.34	77.00
206.67	78.52	210.36	78.23
209.53	79.42	210.47	79.33

DISCUSSION

Y. N. Chen[1]

The authors of the paper have presented very useful informations about the flow fields due to interaction between the impeller blades and the diffuser vanes.

The present discusser has discovered a special phenomenon of the secondary flow field, which may be of interest to the authors. The secondary flow field displayed in the lowest plot of Fig. 6 reveals a secondary vortex embedded just in the region, in which the throughflow momentum wake appears; see the upper plot of the same figure. This secondary vortex field is indicated by a circular curve L in Fig. 14(b).

The authors explained that the throughflow momentum wake is caused by the tip leakage action, which produces losses and convects them toward the pressure side.

However, if the secondary flow field mentioned is closely examined, the leakage flow of the tip clearance does not have any connection with this secondary vortex. Rather, this leakage flow meets the further secondary flow traveling in the opposite direction along the shroud. The meeting region of these two flows, as denoted by S in Fig. 14(b), must be a sink. As this region is situated within the dark area of the throughflow in the upper plot of Fig. 6, i.e., thus within the area of the lowest velocity, this sink therefore appears to guide the meeting flows in the reverse direction into the impeller. We then have a reverse flow along the corner "suction-surface/shroud" even at the normal operating point. This kind of reverse flow has been found by Chen et al. (1989) in their Fig. 5.

The upper plot of Fig. 5 of the present paper about the averaged total relative velocity (as transferred to Fig. 14a) shows that the curve rises to a peak along the pressure side of the impeller blade (cf. Fig. 8 about the tangential velocity component alone), drops sharply along the suction side to a minimum of the wake deficit. Afterward, the curve rises toward the pressure surface of the following impeller blade. This rising-up branch does not follow a uniform trend according to the potential theory, but rather a going-up and down pattern. The valley of this pattern is the throughflow momentum wake (as given in the upper plot of Fig. 6), which coincides with the secondary

[1] R & D, 1510, Sulzer Brothers Ltd., 8401 Winterthur, Switzerland.

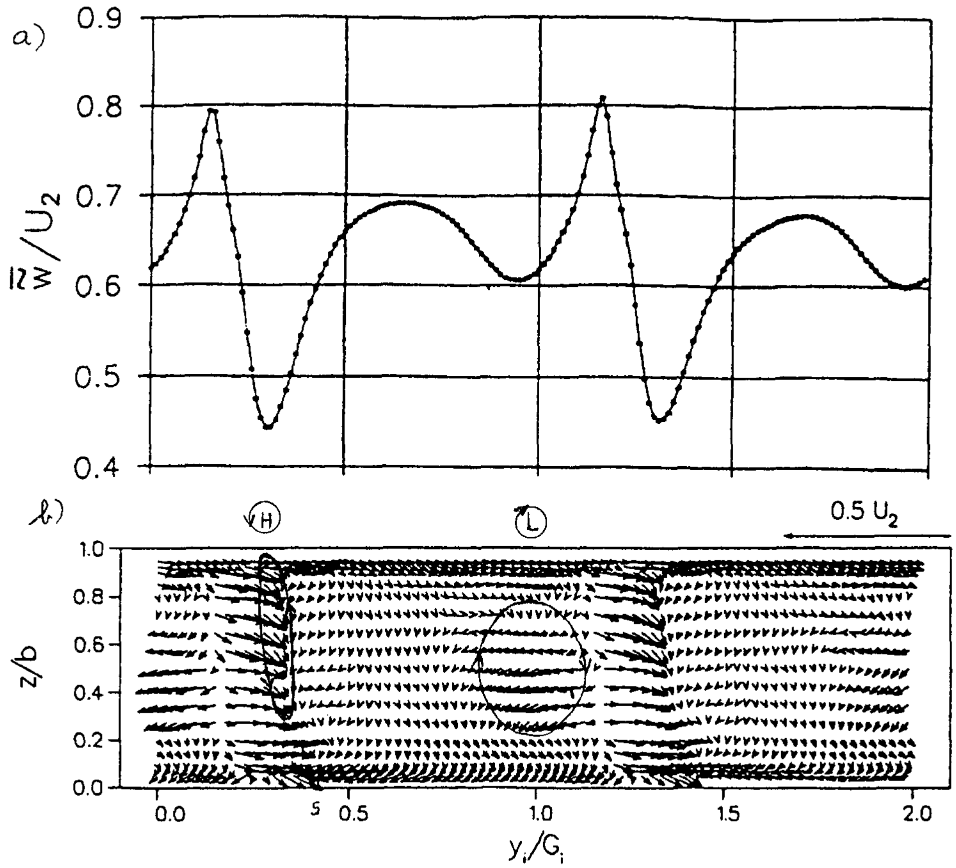

Fig. 14

vortex constructed in Fig. 14(b). Thus, this throughflow momentum wake is the core region of the secondary vortex. Only because the wake is protected by the vortex can it exist in the surroundings of the high velocities within the flow field of the blade channel of the impeller. The turbulence level therefore rises to a flat peak in this vortex region (see the lowest plot in Fig. 5).

Furthermore, if the secondary flow field in Fig. 14(b) is compared with the total-relative-velocity field in Fig. 14(a), the secondary flow field is divided by the trailing edge of the impeller blade into two regions: The one on the pressure side is deflected to the left and the other one on the suction side is deflected to the right. The deflection is the strongest in the region of the corner "suction-surface/hub," so that a secondary vortex H can be constructed. It is associated with a high throughflow as shown in the upper plot of Fig. 6. This secondary vortex has an opposite rotating sense compared to that of the throughflow momentum wake L.

Chen et al. (1991) have considered the secondary vortices in the blade channel as the developing Dean's type vortices of the curvature of the impeller. If the cross section No. 11 of the curvature in Fig. 15 is considered, the normal component Ω_n of the angular velocity Ω of the rotating axis acting on the cross section causes the secondary flow distributed over this section to rotate accordingly. The Dean vortex pair can be detected from the experimental data of Eckardt and Krain (1977), and Krain (1984) about the secondary flow field on a backswept impeller (Fig. 15). This vortex pair consists of a vortex "low (L)," rotating in the sense of Ω_n, and a vortex "high (H)," rotating against this sense.

The vortex "low" causes a radial flow toward its core (with the vortex stretching), which is familiar to the cyclone as a low in the atmosphere. This radial flow is then deflected into the axial direction and streams out of the core as an axial flow due to continuity law. The axial flow of the cyclone is directed upward from the high-pressure layer on the ground toward the low-pressure layer of the upper atmosphere. The axial flow of the vortex "low" of the impeller will thus also be directed

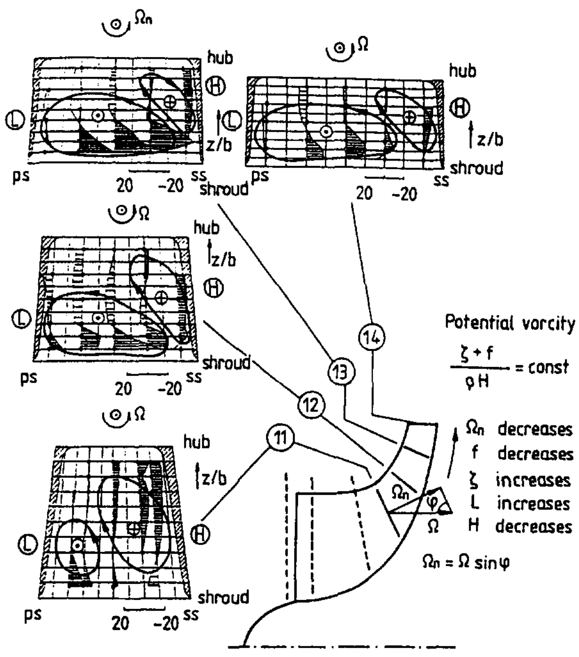

Fig. 15 Secondary flows over the cross sections of a back-swept impeller, normal component of the angular velocity $\Omega_n = \Omega \sin \varphi$

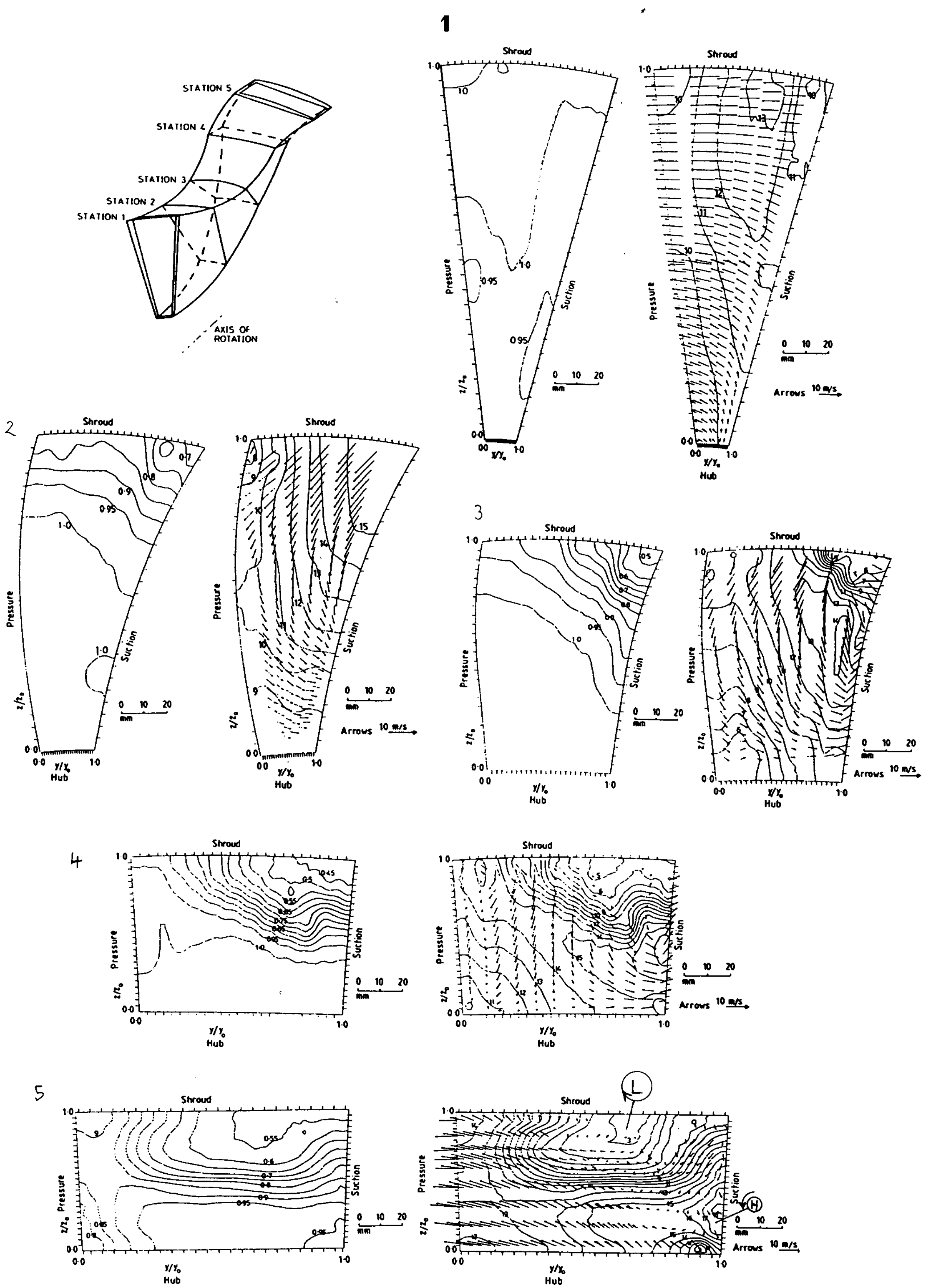

Fig. 16 Secondary flow fields across the sections of the blade channel at five stations, accompanied by the dimensionless rotary stagnation pressure (left diagram) and relative velocity contours in m/s (right diagram)

from its high-pressure layer of the outlet toward its low-pressure layer of the inlet. This axial flow is then a secondary backflow superimposed on the mean flow field: We have a strong throughflow momentum wake in the core region of the vortex "low."

The vortex "high" is associated with a radial flow out of the core, the same as the anticyclone. The axial flow through the core is directed from the low-pressure layer of the upper atmosphere toward the high-pressure layer on the ground. For the case of the impeller, this radial flow will come from the inlet through the core of the vortex "high" toward the outlet and spread out of it. We then have here a strong throughflow momentum jet along of the vortex "high" superimposed on the mean flow field.

The local Coriolis parameter $f = 2\,\Omega_n$ of the secondary flow over the cross section of the impeller-blade channel decreases downstream along the blade channel, while the pressure p increases at the same time.

According to the conservation law of the potential vorticity:

$$\Pi = \frac{\xi + f}{\rho H} = \frac{\xi + f}{p} = \text{const}$$

(Pedlosky, 1984), the relative vorticity ξ in the secondary flow will increase in this downstream direction. This indicates that the secondary vortex "low L" (with a positive sign of ξ) will strengthen and the secondary vortex "high H" (with a negative sign of ξ) will diminish along the blade channel in this downstream direction.

The derivation given above is verified by the experimental result given in Fig. 15 (Chen et al., 1991). The secondary vortex pair develops from the section 11 to the section 14 (i.e., the outlet) with the result that the vortex "low L" in the corner "pressure/shroud" becomes very huge in the outlet section 14, while the vortex "high H" in the corner "suction/hub" diminishes to a small intensity.

A further experimental result about the secondary flow of a backswept impeller obtained by Farge and Johnson (1990) is given in Fig. 16 along the blade channel in five stations. Each station consists of the secondary flows, in addition to the contours of the throughflow velocities (in the right diagram) and the dimensionless rotary stagnation pressure (in the left diagram).

At station 1 for the inlet of the blade channel, a passage vortex rotating against the rotational sense of the impeller forms the field of the secondary flow. This passage vortex keeps the absolute vorticity of the secondary flow at the zero value, because the throughflow has originated from the absolute frame with zero vorticity. This passage vortex is thus a huge "high H." The corresponding rotary stagnation pressure remains high at 0.95 to 1 with a very uniform distribution across the section of the inlet.

This very regular passage vortex then degenerates with the throughflow traveling downstream: A low-pressure center of 0.7 near the corner "section/shroud" at station 2, followed by 0.5 and 0.45 at stations 3 and 4, respectively. The low-pressure center of 0.55 becomes very broad at station 5, i.e., at the outlet section of the impeller, while the high-pressure center of 0.95 reduces to a smaller size in the corner region of the "suction/hub." The corresponding secondary velocity field is quite similar to that in Fig. 15.

The difference in the arrangements of the vortex pairs in the two experiments given in Figs. 15 and 16 is caused by the different shapes of the blade channels investigated. Thus these two experiments bear the evidence for the validity of the conservation of the potential vorticity along the blade channel.

The secondary vortices L and H in Fig. 14(b) correspond very well to those given in Figs. 15 and 16 over the outlet section of the impeller. Then, the vortex L is a pressure "low" centered on the throughflow momentum wake and the vortex H is a pressure "high" centered on the throughflow momentum jet, as given in Fig. 6.

References

Chen, Y. N., Haupt, U., and Rautenberg, M., 1989, "The Vortex-Filament Nature of Reverse Flow on the Verge of Rotating Stall," ASME JOURNAL OF TURBOMACHINERY, Vol. 111, pp. 450–461.

Chen, Y. N., Seidel, U., Haupt, U., and Rautenberg, M., 1991, "The Rossby Waves of Rotating Stall in Impellers, Part II: Application of the Rossby-Wave Theory to Rotating Stall," *Proceedings, 1991 Yokohama International Gas Turbine Congress,* pp. I/77–88.

Eckardt, D., and Krain, H., 1977, "Secondary Flow Studies in High-Speed Centrifugal Impellers," AGARD Conference "Secondary Flows in Turbomachines," Den Haag, AGARD CP 214, pp. 18/1–13.

Farge, T. Z., and Johnson, M. W., 1990, "The Effect of Backswept Blading on the Flow in a Centrifugal Compressor Impeller," ASME Paper No. 90-GT-231.

Krain, H., 1984., "Experimental Observation of the Flow in Impellers and the Diffusers," Lecture 1984-07, "Flow in Centrifugal Compressors," von Karman Institute for Fluid Dynamics.

Pedlosky, J., 1984, *Geophysical Fluid Dynamics,* Springer-Verlag, New York–Berlin–Heidelberg–Tokyo.

Authors' Closure

The authors wish to thank Dr. Chen for the comment and the kind attention to the results shown in the paper.

Dr. Chen has developed an original theory based on the analogy between geophysical and turbomachinery flows, which is useful to help interpret the complex secondary flow pattern in centrifugal turbomachinery rotors. Most secondary flow fields seem to be explainable in terms of a pair of counterrotating vortices, which verify the conservation law of the potential vorticity. The two vortices generate flow along their axis: One against the primary flow gives rise to the throughflow wake, the second in the opposite direction determines a momentum jet superimposed on the main flow field.

Compared with the cases mentioned in the discussion, the present impeller geometry represents a limiting case, as the blades are set in the wholly radial part of the meridional channel. In this case the component of the rotational speed vector normal to the inlet cross section tends to zero and therefore should not be responsible for the "low" vortex identified by Dr. Chen in the secondary flow field.

It is the authors' opinion that the position and the intensity of the low-momentum throughflow wake are strongly determined in the unshrouded impellers by the tip clearance effects. Evidence of that can be found in the experimental results and numerical predictions of Hathaway et al. (1993), in the computational investigation of Moore and Moore (1993) performed on the same impeller, without tip clearance and with different tip clearance gaps, and in the experimental data and computations of Hah and Krain (1990).

The authors are more familiar with secondary flow explanation based on the equilibrium of the fluid dynamic forces in the relative frame of reference and on the unbalance due to the presence of boundary layers near blades and endwall surfaces or to the tip clearance. However, they think that the two approaches are complementary and that the use of both may allow a more refined analysis and better understanding of the phenomena.

References

Hah, C., and Krain, H., 1990, "Secondary Flows and Vortex Motion in a High-Efficiency Backswept Impeller at Design and Off-Design Conditions," ASME JOURNAL OF TURBOMACHINERY, Vol. 112, pp. 7–13.

from its high-pressure layer of the outlet toward its low-pressure layer of the inlet. This axial flow is then a secondary backflow superimposed on the mean flow field: We have a strong throughflow momentum wake in the core region of the vortex "low."

The vortex "high" is associated with a radial flow out of the core, the same as the anticyclone. The axial flow through the core is directed from the low-pressure layer of the upper atmosphere toward the high-pressure layer on the ground. For the case of the impeller, this radial flow will come from the inlet through the core of the vortex "high" toward the outlet and spread out of it. We then have here a strong throughflow momentum jet along of the vortex "high" superimposed on the mean flow field.

The local Coriolis parameter $f = 2\,\Omega_n$ of the secondary flow over the cross section of the impeller-blade channel decreases downstream along the blade channel, while the pressure p increases at the same time.

According to the conservation law of the potential vorticity:

$$\Pi = \frac{\xi + f}{\rho H} = \frac{\xi + f}{p} = \text{const}$$

(Pedlosky, 1984), the relative vorticity ξ in the secondary flow will increase in this downstream direction. This indicates that the secondary vortex "low L" (with a positive sign of ξ) will strengthen and the secondary vortex "high H" (with a negative sign of ξ) will diminish along the blade channel in this downstream direction.

The derivation given above is verified by the experimental result given in Fig. 15 (Chen et al., 1991). The secondary vortex pair develops from the section 11 to the section 14 (i.e., the outlet) with the result that the vortex "low L" in the corner "pressure/shroud" becomes very huge in the outlet section 14, while the vortex "high H" in the corner "suction/hub" diminishes to a small intensity.

A further experimental result about the secondary flow of a backswept impeller obtained by Farge and Johnson (1990) is given in Fig. 16 along the blade channel in five stations. Each station consists of the secondary flows, in addition to the contours of the throughflow velocities (in the right diagram) and the dimensionless rotary stagnation pressure (in the left diagram).

At station 1 for the inlet of the blade channel, a passage vortex rotating against the rotational sense of the impeller forms the field of the secondary flow. This passage vortex keeps the absolute vorticity of the secondary flow at the zero value, because the throughflow has originated from the absolute frame with zero vorticity. This passage vortex is thus a huge "high H." The corresponding rotary stagnation pressure remains high at 0.95 to 1 with a very uniform distribution across the section of the inlet.

This very regular passage vortex then degenerates with the throughflow traveling downstream: A low-pressure center of 0.7 near the corner "section/shroud" at station 2, followed by 0.5 and 0.45 at stations 3 and 4, respectively. The low-pressure center of 0.55 becomes very broad at station 5, i.e., at the outlet section of the impeller, while the high-pressure center of 0.95 reduces to a smaller size in the corner region of the "suction/hub." The corresponding secondary velocity field is quite similar to that in Fig. 15.

The difference in the arrangements of the vortex pairs in the two experiments given in Figs. 15 and 16 is caused by the different shapes of the blade channels investigated. Thus these two experiments bear the evidence for the validity of the conservation of the potential vorticity along the blade channel.

The secondary vortices L and H in Fig. 14(b) correspond very well to those given in Figs. 15 and 16 over the outlet section of the impeller. Then, the vortex L is a pressure "low" centered on the throughflow momentum wake and the vortex H is a pressure "high" centered on the throughflow momentum jet, as given in Fig. 6.

References

Chen, Y. N., Haupt, U., and Rautenberg, M., 1989, "The Vortex-Filament Nature of Reverse Flow on the Verge of Rotating Stall," ASME JOURNAL OF TURBOMACHINERY, Vol. 111, pp. 450–461.

Chen, Y. N., Seidel, U., Haupt, U., and Rautenberg, M., 1991, "The Rossby Waves of Rotating Stall in Impellers, Part II: Application of the Rossby-Wave Theory to Rotating Stall," *Proceedings, 1991 Yokohama International Gas Turbine Congress,* pp. I/77–88.

Eckardt, D., and Krain, H., 1977, "Secondary Flow Studies in High-Speed Centrifugal Impellers," AGARD Conference "Secondary Flows in Turbomachines," Den Haag, AGARD CP 214, pp. 18/1–13.

Farge, T. Z., and Johnson, M. W., 1990, "The Effect of Backswept Blading on the Flow in a Centrifugal Compressor Impeller," ASME Paper No. 90-GT-231.

Krain, H., 1984., "Experimental Observation of the Flow in Impellers and the Diffusers," Lecture 1984-07, "Flow in Centrifugal Compressors," von Karman Institute for Fluid Dynamics.

Pedlosky, J., 1984, *Geophysical Fluid Dynamics,* Springer-Verlag, New York–Berlin–Heidelberg–Tokyo.

Authors' Closure

The authors wish to thank Dr. Chen for the comment and the kind attention to the results shown in the paper.

Dr. Chen has developed an original theory based on the analogy between geophysical and turbomachinery flows, which is useful to help interpret the complex secondary flow pattern in centrifugal turbomachinery rotors. Most secondary flow fields seem to be explainable in terms of a pair of counterrotating vortices, which verify the conservation law of the potential vorticity. The two vortices generate flow along their axis: One against the primary flow gives rise to the throughflow wake, the second in the opposite direction determines a momentum jet superimposed on the main flow field.

Compared with the cases mentioned in the discussion, the present impeller geometry represents a limiting case, as the blades are set in the wholly radial part of the meridional channel. In this case the component of the rotational speed vector normal to the inlet cross section tends to zero and therefore should not be responsible for the "low" vortex identified by Dr. Chen in the secondary flow field.

It is the authors' opinion that the position and the intensity of the low-momentum throughflow wake are strongly determined in the unshrouded impellers by the tip clearance effects. Evidence of that can be found in the experimental results and numerical predictions of Hathaway et al. (1993), in the computational investigation of Moore and Moore (1993) performed on the same impeller, without tip clearance and with different tip clearance gaps, and in the experimental data and computations of Hah and Krain (1990).

The authors are more familiar with secondary flow explanation based on the equilibrium of the fluid dynamic forces in the relative frame of reference and on the unbalance due to the presence of boundary layers near blades and endwall surfaces or to the tip clearance. However, they think that the two approaches are complementary and that the use of both may allow a more refined analysis and better understanding of the phenomena.

References

Hah, C., and Krain, H., 1990, "Secondary Flows and Vortex Motion in a High-Efficiency Backswept Impeller at Design and Off-Design Conditions," ASME JOURNAL OF TURBOMACHINERY, Vol. 112, pp. 7–13.

Experimental and Computational Results From the NASA Lewis Low-Speed Centrifugal Impeller at Design and Part-Flow Conditions

R. M. Chriss
NASA Lewis Research Center,
Cleveland, OH 44135

M. D. Hathaway
Vehicle Propulsion Directorate,
U.S. Army Research Laboratory,
Cleveland, OH

J. R. Wood
NASA Lewis Research Center,
Cleveland, OH 44135

The NASA Lewis Low-Speed Centrifugal Compressor (LSCC) has been investigated with laser anemometry and computational analysis at two flow conditions: the design condition as well as a lower mass flow condition. Previously reported experimental and computational results at the design condition are in the literature (Hathaway et al., 1993). In that paper extensive analysis showed that inducer blade boundary layers are centrifuged outward and entrained into the tip clearance flow and hence contribute significantly to the throughflow wake. In this report results are presented for a lower mass flow condition along with further results from the design case. The data set contained herein consists of three-dimensional laser velocimeter results upstream, inside, and downstream of the impeller. In many locations data have been obtained in the blade and endwall boundary layers. The data are presented in the form of throughflow velocity contours as well as secondary flow vectors. The results reported herein illustrate the effects of flow rate on the development of the throughflow momentum wake as well as on the secondary flow. The computational results presented confirm the ability of modern computational tools to model the complex flow in a subsonic centrifugal compressor accurately. However, the blade tip shape and tip clearance must be known in order to properly simulate the flow physics. In addition, the ability to predict changes in the throughflow wake, which is largely fed by the tip clearance flow, as the impeller is throttled should give designers much better confidence in using computational tools to improve impeller performance.

Introduction

The full potential of the centrifugal compressor is still not realized and its development lags that of its axial counterpart. Furthermore, the database containing flowfield measurements of centrifugal compressors is limited, and consists predominantly of two-dimensional measurements. Nevertheless, the measurements to date have greatly enhanced our understanding of the flow development in these machines. Some of the previous investigations involving flowfield measurements are discussed in the following.

Although detected and discussed earlier by Dean and Senoo (1960), Eckardt's laser measurements (1976) provided the first flowfield experimental evidence of the development of a "wake" of low-momentum fluid near the suction surface/shroud corner of the blade passage. Krain (1988), Krain and Hoffman (1989, 1990), and Sipos (1991), in a hot-wire investigation, drew conclusions about the secondary flow by looking at cross passage views of relative flow angle contours. However, their assumption of constant throughflow velocity tends to fail in the wake where the secondary flows are strongest. Krain and Hoffman (1989) have studied the effect of shroud contour shape on throughflow wake size and demonstrated that the position of the wake in the channel is strongly dependent upon the diffusion of the main flow in the impeller. Krain (1981) found only a weak influence of a vaned diffuser on the impeller flow albeit with a large diffuser leading edge radius ratio (1.1). He found large flow fluctuation levels far downstream at the diffuser throat.

Fagan and Fleeter (1990), in a low-speed mixed flow compressor, showed that wake location and momentum defect magnitude both changed with mass flow rate. Johnson and Moore (1983) studied a low-speed, shrouded impeller and found that the wake behaved as predicted by secondary flow theory (Cumpsty, 1989). Farge and Johnson (1990) made a detailed study of backswept shrouded impellers in a low-speed environment, which indicated wake formation at the shroud suction surface corner as predicted by theory.

Adler and Levy (1979), in a study of low-speed backswept shrouded impellers, and Rohne and Banzhaf (1990), in a study of high-speed backswept impellers, concluded that the output flow with backsweep yielded a more uniform and stable flow compared with radial bladed impellers. Ahmed and Elder (1990) made measurements inside a small high-speed backswept impeller with splitter blades at multiple speeds and flow rates. They found that the wake region moved toward the suction side as the flow rate was reduced and that their preliminary three-dimensional flow measurements indicated that three-dimensional effects were important.

In previously reported results from this compressor (Hathaway et al., 1993), extensive experimental and CFD analysis showed that the blade boundary layers in the inducer section are centrifuged outward and are entrained into the tip clearance flow, which forms the throughflow momentum wake, and that the wake is not a result of streamwise flow separation. The experimental and computational results presented herein were obtained at a lower mass flow condition for comparison with those previously reported results.

Contributed by the International Gas Turbine Institute and presented at the 39th International Gas Turbine and Aeroengine Congress and Exposition, The Hague, The Netherlands, June 13–16, 1994. Manuscript received by the International Gas Turbine Institute February 26, 1994. Paper No. 94-GT-213. Associate Technical Editor: E. M. Greitzer.

The data consist of three-dimensional laser velocimeter results upstream, inside, and downstream of the impeller. The purpose of the investigation is to compare results at the two flow conditions in order to study details of the flow physics as well as to provide data for CFD studies. In many locations data have been obtained in the blade boundary layers and endwall tip clearance flow. The data are presented in the form of throughflow velocity contours as well as secondary flow vectors.

Facility and Instrumentation

The Compressor. The test compressor is a backswept impeller (Fig. 1) with an exit corrected design tip speed of 153 m/s. The impeller has 20 full blades with a backsweep of 55 deg from the radial. The design mass flow rate is 30 kg/s (66 lbm/s) and the design corrected shaft speed is 1920 rpm. The inlet diameter is 870 mm and the inlet blade height is 218 mm. The exit diameter is 1524 mm and the exit blade height is 141 mm. The tip clearance between the impeller blade and the shroud is 2.54 mm and is constant from inlet to exit. This tip clearance is 1.8 percent of blade height at the impeller exit and 1.2 percent at the inlet. The blade surfaces are composed of straight-line elements from hub to tip. A vaneless diffuser was used for the laser anemometer investigation. This allows an axisymmetric boundary condition to be used in the numerical simulations. A complete description of the facility can be found in Wood et al. (1983) and Hathaway et al. (1992).

The operating conditions for both the computational and experimental efforts are mass flow rates of 30.0 kg/s (66 lbm/s) and 23.6 kg/s (52 lbm/s) representing design and part flow conditions. For both conditions the corrected speed was fixed at 1862 rpm. The performance map is shown in Fig. 2. The differing symbols represent different downstream diffuser configurations as well as different spatial resolutions in the aerodynamic surveys. The uncertainty bars in the figure are based on mass flow and torque measurement limitations as well as a 0.6 K (1 R) thermocouple uncertainty.

In order to characterize the flow in the impeller with some relevant design parameters, a one-dimensional analysis of the impeller flow was undertaken. The results show that the diffusion ratio (given as the exit relative velocity divided by the inlet tip relative velocity) at the design flow, part flow, and unstable condition was 0.75, 0.65, and 0.6, respectively. The absolute flow angle into the diffuser significantly influences the amount of pressure recovery that can be sustained by the diffuser. The diffuser entry flow angle from the radial for the three flow conditions was 67, 74, and 77 deg, respectively.

Instrumentation. A two-component laser fringe anemometer operating in on-axis backscatter mode was used in this investigation. An argon ion laser was used to produce the 514.5 nm (green) and 488 nm (blue) wavelengths for two orthogonal fringe systems. Frequency shifting was used for both fringe systems to provide directional sensitivity for all velocity measurements. Due to the size of the compressor, a relatively long focal length of 733 mm was used. The final focusing lens aperture was 155 mm. In addition, beam expansion (3.75×) was used to enhance the system signal-to-noise ratio.

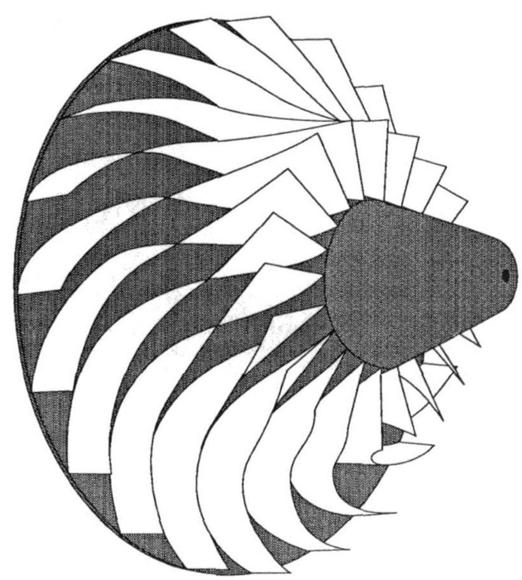

Fig. 1 The large low-speed impeller

The probe volume length was 2.96 mm with a diameter of 98.6 μm. The fringe spacings for the blue and green systems were 8.22 μm and 8.67 μm, respectively.

In order to obtain all three velocity components, two sets of measurements were obtained, each at a different orientation to the flow. The resulting four measured velocity components were then combined with a least-squares fit in order to obtain the three components of velocity.

Polystyrene latex (PSL) spheres, manufactured using the process developed by Nichols (1987), were used as the seed material. The mean size of the seed particles varied from 0.80 μm to 0.95 μm.

Data Reduction. The station numbers given in Table 1 are the streamwise indices of the body-fitted grid at which the laser measurements were taken. The survey planes and their spanwise extent are shown in Fig. 3.

All the data are ensemble-averaged across the 20 blade channels to yield a single "representative" blade passage. This pas-

Nomenclature

$\hat{e}$ = unit vector
$\hat{g}$ = streamwise grid unit vector
$\hat{g}_M$ = meridional grid unit vector = $(g_r\hat{e}_r + g_z\hat{e}_z)/\sqrt{g_r^2 + g_z^2}$
ΔH = total enthalpy rise
J = streamwise station index
$\dot{m}$ = mass flow rate
m/m_s = nondimensional shroud meridional distance (percent chord)
N = number of laser anemometer realizations
N_B = number of blades
PS = pressure surface
Δp = blade static pressure differential
q = relative dynamic pressure = $\frac{1}{2}\rho W^2$
r = radial position
r/r_e = radius normalized by impeller exit tip radius
SS = suction surface
U_t = corrected impeller exit tip speed
$\mathbf{V}$ = absolute velocity vector
$\mathbf{V}_M$ = meridional velocity vector = $V_r\hat{e}_r + V_z\hat{e}_z$
$\mathbf{V}_T$ = throughflow velocity = $(V_M \cdot \hat{g}_M)\hat{g}_M$
$\mathbf{W}_{sec}$ = relative secondary velocity vector = $\hat{g} \times (W \times \hat{g})$
$\mathbf{W}$ = relative velocity vector
z_c = statistical confidence coefficient
ρ = density
σ = local standard deviation
ω = impeller rotational speed

Superscripts

$-$ = ensemble average
$'$ = instantaneous value

Subscripts

r = radial component
z = axial component
θ = tangential component

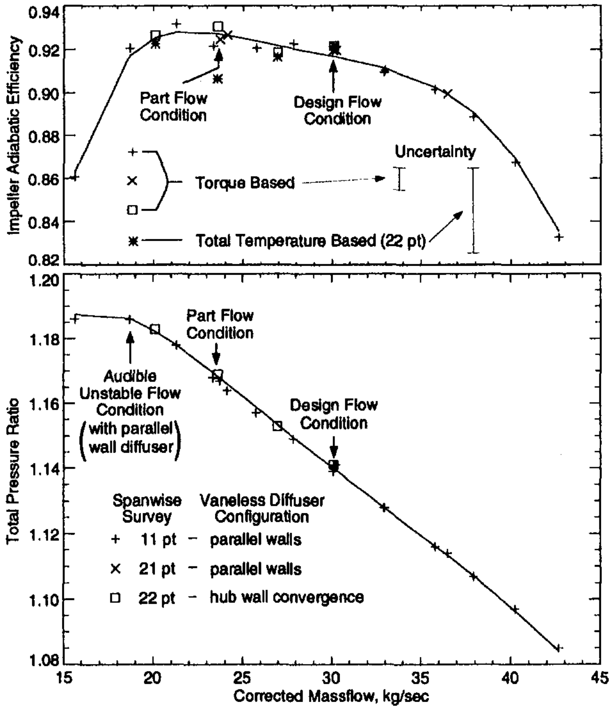

Fig. 2 Performance map for the large low-speed centrifugal impeller

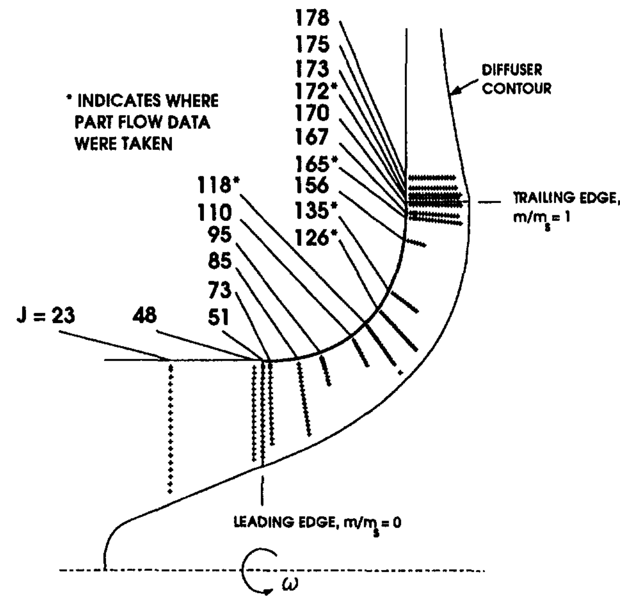

Fig. 3 Laser anemometer survey station locations

sage is divided into 1000 equal arc lengths or window "bins." For presentation purposes, these bins are usually averaged down to 200 measurement locations across the blade passage. To clarify the secondary flow vectors further, only every third vector is presented in the results below. This results in 66 vectors across a passage in the secondary flow results. Further details of the philosophy and the method used to obtain and average the data can be found in Strazisar et al. (1989).

Table 1 Survey station meridional locations

leading edge: J = 51; trailing edge: J = 171

Station (J)	m/m_s (%)
23	-39.7
48	-3.8
51	0.0
73	3.0
85	14.9
95	24.8
110	39.6
118*	47.5
126*	55.5
135*	64.4
156	85.2
165*	94.1
167	96.0
170	99.0

Diffuser:

Station (J)	r/r_e
172*	1.010
173	1.019
175	1.037
178	1.065

* Denotes where part flow data were taken.

Measurement Uncertainties. An estimate of the uncertainty in the calculated results was made from the least-squares fit calculations. Throughout most of the impeller passage, the uncertainty is estimated to be ± 1.5 m/s, which is about 2 percent of the throughflow velocity.

The measurements are susceptible to distortions of the probe volume due to window curvature effects. Due to the geometry of the laser system, the spanwise velocity component is the most sensitive to measurement uncertainty. This is analogous to the difficulties in measuring the on-axis velocity component in a wind tunnel situation.

Large levels of uncertainty in the throughflow velocity exist in some isolated throughflow wake regions. Uncertainty levels approaching 15 percent were found to exist near some of the wake core regions.

The CFD Analysis

The computational results for the LSCC flow field were obtained using the Reynolds-averaged Navier–Stokes code developed by Dawes (1988). The code solves the equations of motion in cylindrical coordinates in integral conservation form using six-sided control volumes formed by a simple H-mesh. The basic algorithm as described by Dawes (1988) is similar to a two-step Runge–Kutta method plus residual smoothing. A combined second and fourth derivative artificial viscosity model with pressure gradient switching is used to eliminate spurious "wiggles" and to control shock capturing. The eddy viscosity is obtained using the Baldwin–Lomax (1970) mixing length model. Tip clearance is handled by gradually decreasing the thickness of the blade to zero at the blade tip and enforcing periodicity in the tip gap.

In previous calculations (Hathaway et al., 1993), it was assumed that the impeller blade tips were sharp and that in order to obtain the correct flow through the tip gap (a prime factor when considering the impact of the clearance flow on impeller aerodynamic performance) the tip clearance flow area used in the calculations would have to be reduced to account for the expected "vena contracta" produced by a sharp-edged entry.

Assuming that a sharp-edged blade tip existed on the LSCC, a contraction coefficient of 0.6 was used in the previous calculations. That is, the grid in the gap was modified to reduce the flow area to 60 percent of the physical clearance.

The blade tips of the LSCC were inspected at the end of the test program and were not found to be sharp, as expected, but instead were rounded. For a rounded tip a contraction coefficient of one would be more appropriate (Heyes et al., 1992), i.e., the flow would be expected to fill the entire physical clearance gap. The results presented here were calculated with this assumption. These calculations show much better agreement with the experimental results than previous calculations with the reduced tip gap. It is important to note, however, that the choice of using the full tip clearance in the present calculations was not based upon the experimental results but based upon the results from the blade inspection.

In addition to inspecting the blade tips of the LSCC, inspections were made of two high-speed impellers and an axial core compressor rotor for comparison. These were: a small, 6:1 pressure ratio titanium impeller; a small 4:1 pressure ratio aluminum impeller; and a 2:1 pressure ratio transonic axial flow core rotor made of maraging steel. When scaled the same, the tip profiles were very similar. We conclude, therefore, that the rounding of the LSCC blade tips is not unique and should be expected in high-speed, in-service hardware. Our results show that the tip shape must be taken into account when modeling the tip clearance flow. This is true whether the tip clearance is modeled with the simplified approach of Dawes or whether the tip clearance gap is gridded with a separate blocked grid.

The grid used in the present analysis was identical to that used by Hathaway et al. (1993), with the exception that the upstream boundary was moved from 84 percent shroud chord upstream of the leading edge to a position on the spinner 42 percent of the shroud chord upstream. The boundary condition necessary for the absolute tangential velocity was obtained from a previous solution that included that particular position on the

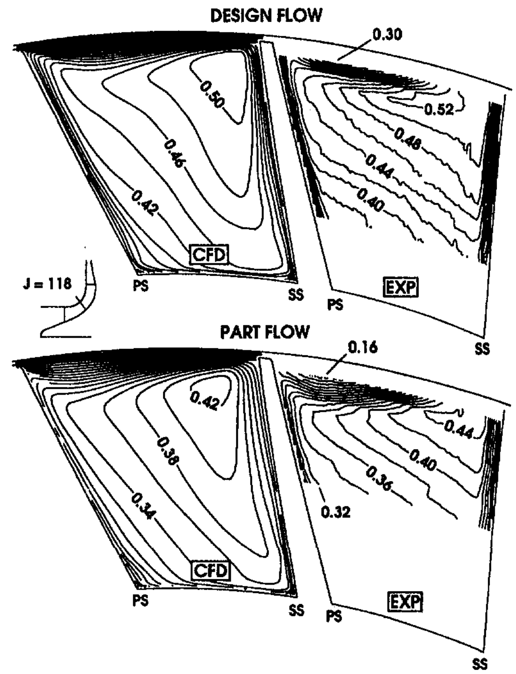

Fig. 5 Distribution of throughflow velocity at station 118 normalized by the corrected exit tip speed (153 m/s)

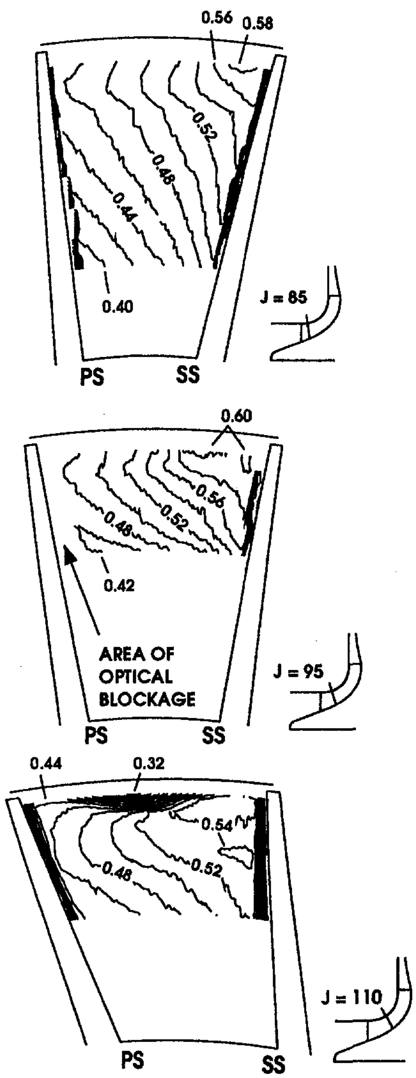

Fig. 4 Distribution of experimental results of throughflow velocity component in the inducer at the design flow normalized by the corrected exit tip speed (153 m/s)

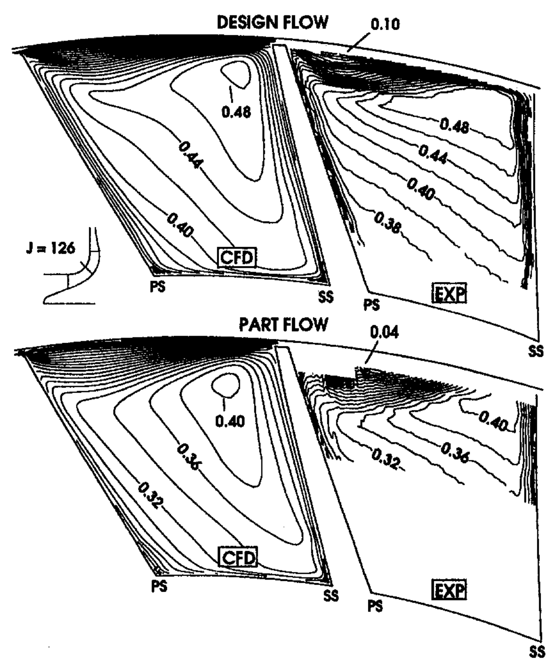

Fig. 6 Distribution of throughflow velocity at station 126 normalized by the corrected exit tip speed (153 m/s)

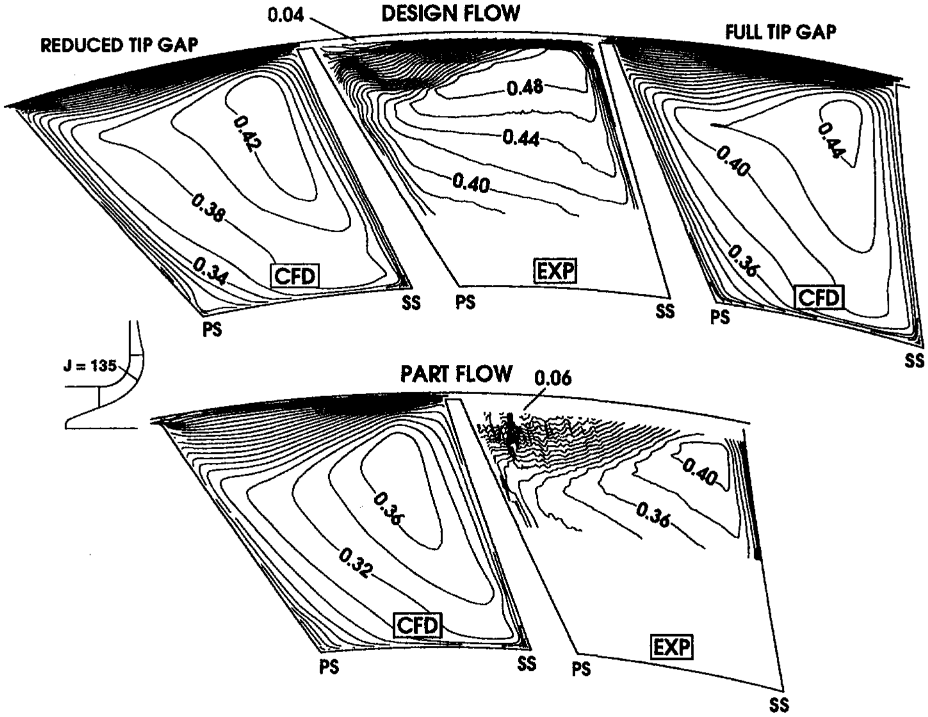

Fig. 7 Distribution of throughflow velocity at station 135 normalized by the corrected exit tip speed (153 m/s)

spinner as part of the computational domain. Also, the downstream extent of the grid was reduced from a radius 50 percent greater than the impeller exit radius to one that was 15 percent greater than the exit radius. The grid had 41 points in the pitchwise direction, 71 in the spanwise direction (4 cells from blade tip to shroud), 75 points on the blade in the streamwise direction, 26 points upstream of the blade, and 17 points downstream of the blade.

For the part-flow calculation, the grid locations near the solid surfaces produced Y-plus values for the first cell-center ranging on the hub from 9 to 113 with an average of 53; on the shroud from 2.3 to 117 with an average of 66; on the suction surface from 35 to 211 with an average of 106; and on the pressure surface from 20 to 251 with an average of 92. The maximum for the suction surface occurred near the trailing edge at 75 percent span and on the pressure surface at the leading edge at 97 percent span. Consequently, over almost all of the computational domain the wall-function formulation of Dawes was being used to obtain wall shear stress. The amount of flow crossing the blade tips was calculated for both the design and part-flow condition and was 9.4 and 11.1 percent of inlet mass flow, respectively.

Results

The selected results below are divided into four sections: (1) throughflow development; (2) secondary flow development; (3) unusual characteristics found at station 165; and (4) the throughflow wake size and location. The part-flow data were taken at five stations from the knee region to impeller exit, so

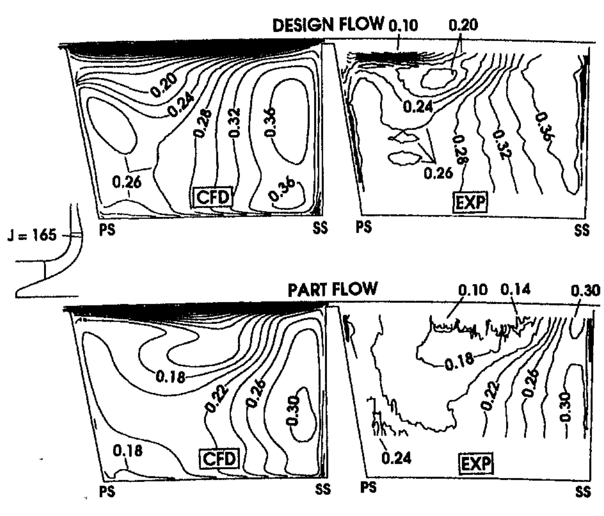

Fig. 8 Distribution of throughflow velocity at station 165 normalized by the corrected exit tip speed (153 m/s)

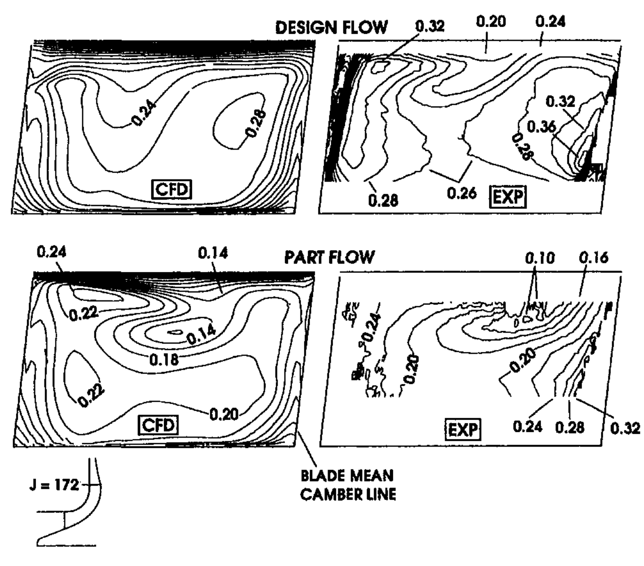

Fig. 9 Distribution of throughflow velocity at station 172 normalized by the corrected exit tip speed (153 m/s); looking downstream

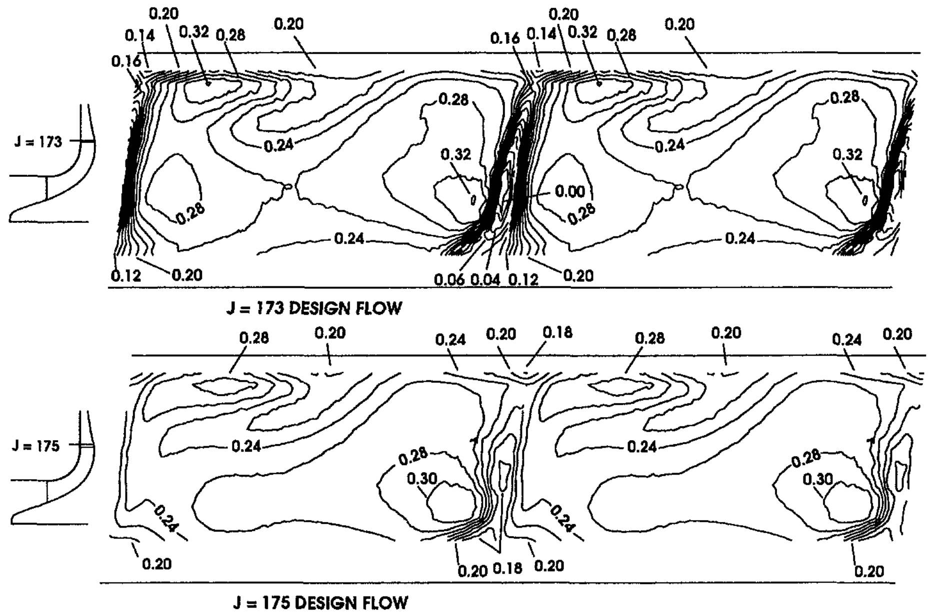

Fig. 10 Distribution of experimental results of throughflow velocity with duplicate passages at stations 173 and 175, normalized by the corrected exit tip speed (153 m/s); looking downstream

that no comparison of part flow with the design condition is possible in the inducer and diffuser regions.

Throughflow Development. The throughflow velocity vector, $\mathbf{V}_T$, also called quasi-meridional velocity, is defined here as the projection of the meridional velocity vector in the local meridional streamwise grid direction.

In Hathaway et al. (1993), extensive analysis of the CFD results using flow traces showed that the throughflow wake is fed primarily by the tip clearance flow. In addition, it was shown that the inducer blade boundary layers are centrifuged outward and entrained into the tip clearance flow and thereby contribute significantly to the throughflow wake.

Inducer Region at Design Flow Rate. Selected results from the inducer region at stations 85, 95, and 110 are shown in Fig. 4. The tip clearance flow is not evident in the results until station 110. The overall appearance in the inducer region is similar to that found in shrouded impellers until station 110 is reached.

The results from the CFD analysis (not shown) at the design flow condition indicate that the tip clearance flow penetration as a percent of span is 97.6, 96.7, and 94 percent for stations 85, 95, and 110, respectively. This indicates why the wake does not appear in the first two stations, since the measurements were taken up to 95 percent span for stations 85 and 95 and up to 97 percent span for station 110. The pitchwise location of the wake at station 110 agrees well with that predicted by the CFD analysis with the experiment showing the wake at approximately 55 percent pitch from the suction surface and the analysis showing it at about 62 percent pitch.

Design and Part-Flow CFD and Experiment. The CFD and experimental throughflow results at the design and part-flow conditions are shown in Figs. 5–9. At the part-flow condition, for stations 118, 126, and 135, the greater influence of the tip clearance flow on the core flow can be seen in both CFD and experiment. At station 165 the shape and level of the velocity contours are in good agreement between the experiment and CFD. At station 172 (1.01 exit radius ratio) the contours are generally in good agreement, except near the suction surface, where the experimental values peak near the blade wake.

This difference is probably due to the trailing edge CFD grid shape, which tapers to zero, whereas the actual trailing edge is blunt. At these stations the throughflow wake has migrated nearer the suction surface at the part-flow condition than in the design condition, as expected from secondary flow theory.

The results from station 135, Fig. 7, show a comparison of the CFD results using two different tip gaps based on different contraction coefficients in the "vena contracta" tip clearance flow model. The CFD results on the left were obtained with a contraction coefficient of 0.6, with the initial assumption of a sharp-edged blade tip (as presented in Hathaway et al., 1993). The results on the right were obtained with a contraction coefficient of 1.0, which is representative of the actual tip shape. These results show the sensitivity of wake size to a change in flow rate through the tip clearance gap.

Diffuser at Design. Experimental throughflow results for stations 173 and 175 at the design condition are shown in Fig. 10. A high degree of mixing takes place in the blade wake region between these two stations. This was shown in Hathaway et al. (1993), in terms of the change in absolute flow angle. The high shear in the blade wake produces intense mixing from the trailing edge to station 175, at which location the gradients in the blade wake and throughflow wake become similar and mixing is greatly reduced. From station 175 (r/r_e = 1.037) to station 178, not shown (r/r_e = 1.065), there is little additional mixing of the flow, which would indicate that placing diffuser vanes at a radius ratio greater than about 4 percent of the impeller exit radius would do little to provide a more uniform flow into the diffuser. Other conditions such as pressure perturbations from diffuser vanes upon the impeller exit flow, which may produce deeper blade wakes, could moderate this conclusion.

Comparison of Secondary Flow Development. Secondary flow in this paper is defined as the departure of the local relative velocity vector from the local streamwise grid direction. The secondary flow vector is given by $\mathbf{W}_{\text{sec}} = \hat{g} \times (\mathbf{W} \times \hat{g})$. The spanwise and pitchwise components of the secondary velocity vector are the projections of the secondary velocity vector in the local spanwise and pitchwise grid directions.

The secondary flow vector results are especially sensitive to uncertainties in the measured velocities. Areas that show chaotic appearance of the secondary vectors, therefore, are suspect in that they are areas where flow unsteadiness or passage-to-pas-

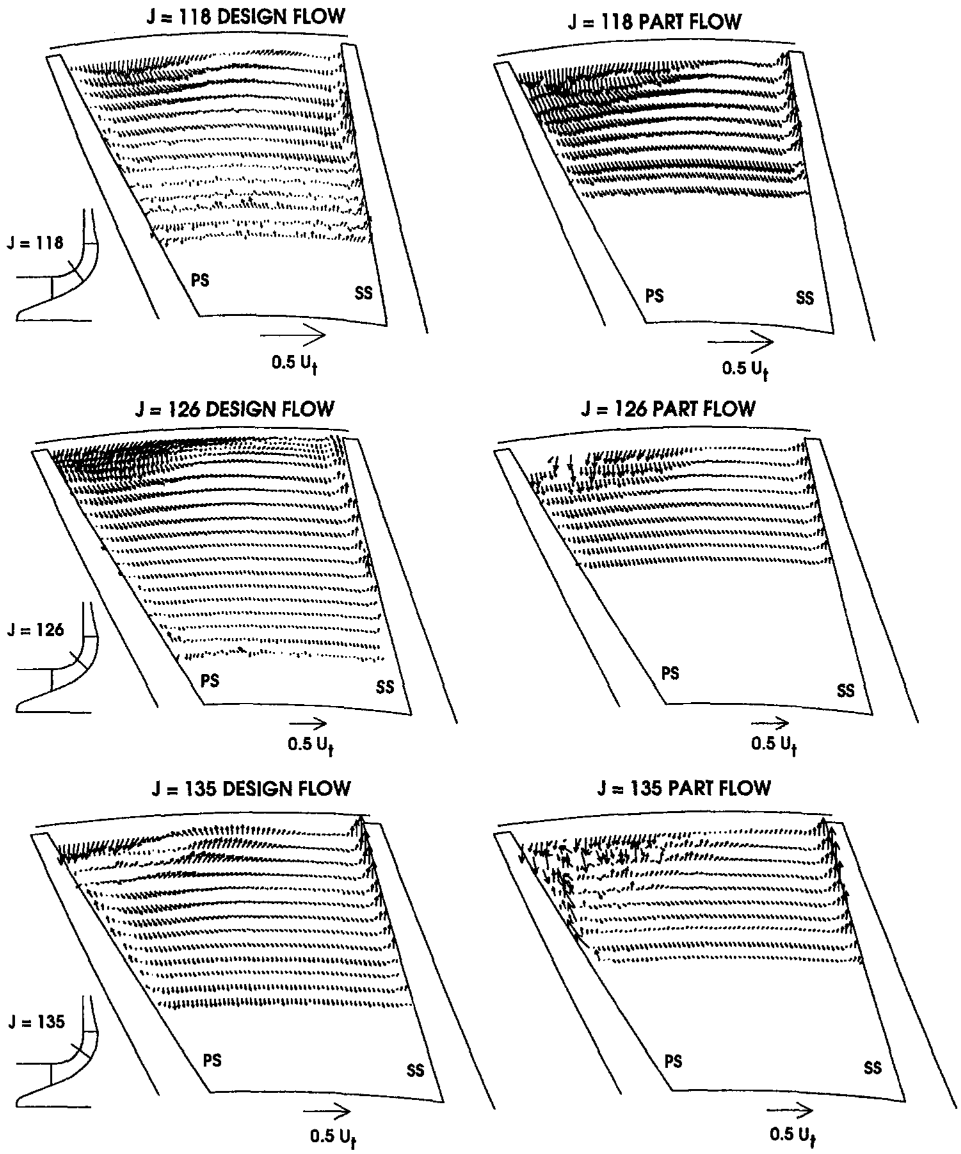

Fig. 11 Measured secondary flow vectors in the knee region at design and part-flow conditions

sage variations are possible. It has been our experience that in wake-type regions, measurement uncertainty cannot be decreased significantly by increasing the number of measurements. The results presented herein have been ensemble-averaged, and thus the contributions of flow unsteadiness and passage-to-passage variations to measurement uncertainty cannot be separated out. However, we have inspected the measurements in numerous locations and found that the contribution from passage-to-passage variations is generally very small. Therefore, we generally attribute large values of uncertainty in wake regions to flow unsteadiness.

Similar secondary flow development for both flow rates is evident at stations 118 through 135 (Fig. 11). CFD particle traces (not shown here) confirm that the tip clearance flow penetrates across the channel and impinges on the pressure surface for both flow conditions. However, greater spanwise penetration is exhibited at the part-flow condition.

It is evident from these figures that the throughflow wake development occurs earlier in the impeller at the part-flow condition relative to the design condition, e.g., the flow at station 118 at part flow appears similar to that of 126 at design flow. This is noted also in the CFD results, which are not shown here.

The unusual flow pattern at station 165 (Fig. 12) begins development at station 156 (not shown) and is dissipating by station 167 (also not shown). The origins of this flow structure are at present unknown. Some evidence for flow unsteadiness is noted in the part-flow case near the hub pressure surface corner at station 165. This is discussed further in the following section.

Station 165 Wake Fluctuations. Considerable effort has been expended in order to investigate the secondary flow vector results at station 165 for both the design and part-flow conditions. At the design condition the unusual bifurcation pattern near the throughflow wake sparked interest, as did the results at part flow near the pressure side/hub corner. These investigations are described in the following.

Design. In Hathaway et al. (1993), it was shown in the design flow case that the flow pattern at 165 would look similar to the pattern at 172 if the *mode* of the measurements was used in the determination of each velocity component as opposed to the *mean,* which is normally used. The mode is by definition what the flow is doing "most of the time," i.e., it is the most probable value. This leads one to believe that some unsteadiness of unknown origin may be present at station 165.

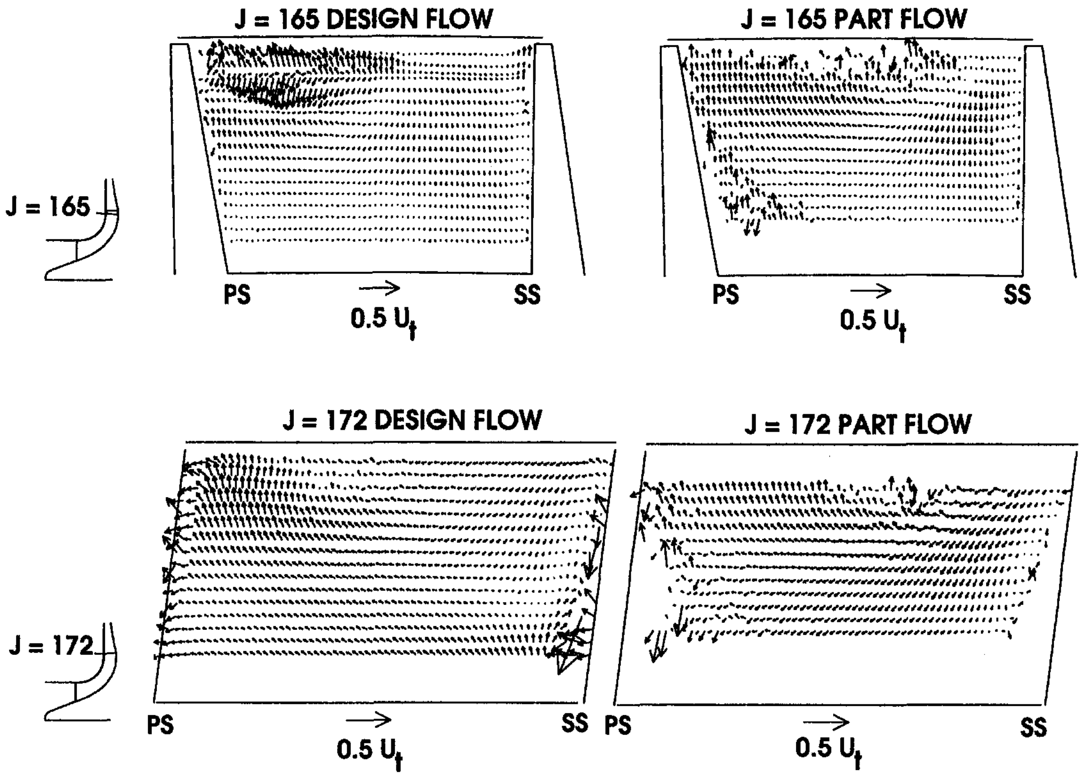

Fig. 12 Measured secondary flow vectors near the impeller exit at design and part-flow conditions; looking downstream

In an attempt to determine the origin of this possible unsteadiness, a set of measurements was acquired such that the tangential and throughflow components were measured directly while in the "coincident" data acquisition mode. The coincident mode insures that velocity measurements from each of the two laser anemometer channels arise from the same particle. This raises the statistical confidence in the $V_T'V_\theta'$ correlation, which will be described further below.

These results were ensemble-averaged onto a representative "revolution," or all twenty passages, rather than a single passage (as is done for the other results in this paper). If there were geometric variations contributing to the uncertainty, they would be detected as a passage-to-passage variation in this average.

No significant variation from passage to passage could be detected. In addition, the $V_T'V_\theta'$ correlation showed that the fluctuations could not be attributed to any organized flow pumping in either the throughflow or tangential directions. That is, if V_T' and V_θ' were positively correlated, it would indicate fluctuations primarily in magnitude with minimal fluctuations in absolute flow angle. If they were negatively correlated it would indicate (because of the local velocity triangle) that flow angle fluctuations were greater than fluctuations in magnitude.

Without any indication of an organized fluctuation in the throughflow–tangential plane, we therefore conclude that the variation in the secondary vectors in the throughflow wake region is primarily associated with fluctuations in the spanwise component of velocity. This could be precipitated by wandering or kinking of the clearance vortex as noted in axial flow pump research by Straka and Farrell (1992) and Zierke et al. (1993).

Part Flow. In the secondary flow results at station 165, some indication of flow unsteadiness is noted in the chaotic behavior of the vectors near the hub, pressure surface corner, and in the wake. The secondary flow vector results are very sensitive to fluctuations in any of the velocity component measurements. An investigation similar to that described above was undertaken in order to look for stalled passages (i.e., passage-to-passage variation).

No stalled passages were found in the analysis. Moreover, line plots of the throughflow velocity (shown in Fig. 13), along with uncertainty limits (based on a 95 percent confidence level), show no indication of a flow separation, although the fluctuation levels in this region were very high (30 percent of the mean flow levels). Note that the regions of high uncertainty correspond to regions of chaotic behavior in the secondary flow vectors of Fig. 12.

Wake Size and Location. Hathaway et al. (1987) and Suder et al. (1987) observed that the strength of the velocity fluctuations, which are uncorrelated with the fundamental rotor rotational frequency (e.g., velocity fluctuations due to turbulence, vortex shedding, etc.), can be used as an effective marker to locate the wakes within turbomachinery. The strength of these uncorrelated velocity fluctuations (denoted by Hathaway as "unresolved unsteadiness") is measured by the local (relative to the rotor) standard deviation of the laser velocimeter measurements. The wake regions shown in Fig. 14(a) were determined from contour plots of the standard deviation of one of the laser velocimeter channels. The wake boundary is arbitrarily defined here as 50 percent of the peak standard deviation outside of the blade boundary layers in each of the cross-channel planes. The wake location given in Fig. 14(b) is the approximate wake center determined by inspection of Fig. 14(a).

Relative to the design flow results, the part-flow results show a slight increase in wake size up to station 135 and a decrease in wake size near the impeller exit. The CFD results support the observed wake size behavior in the experiment between the two flow rates. A comparison of the CFD distribution of the clearance flow for both flow conditions is given in Fig. 15(a). The cumulative clearance flow is plotted versus meridional distance and shows that the clearance flow for the part-flow case exceeds that for the design flow case until about 65 percent

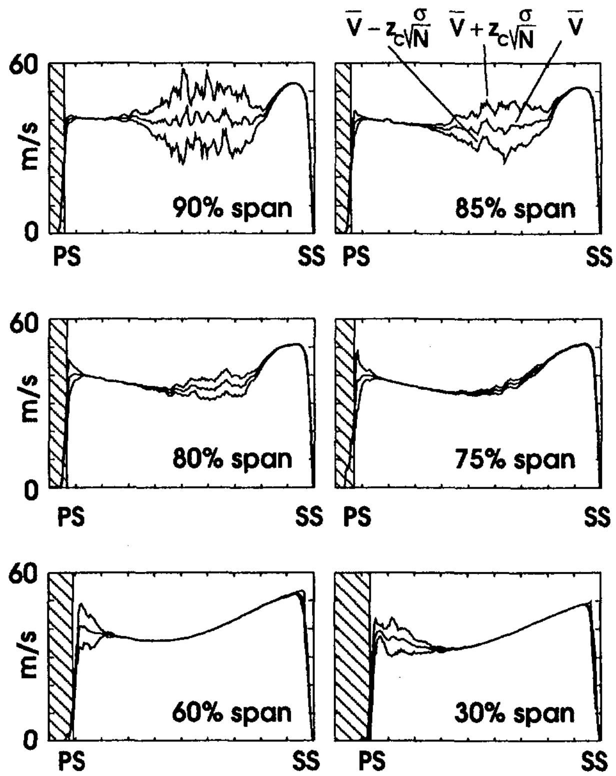

Fig. 13 Plots of throughflow mean velocity component with local uncertainty limits at station 165 at part flow. The uncertainty is given by $z_c(\sigma/\sqrt{N})$ where $z_c = 1.96$ for a 95 percent confidence level.

chord, which corresponds to station 135 in the laser measurements. After 65 percent chord the clearance flow for the part-flow case becomes less than for the design flow case until it is lower by 17 percent at impeller exit. This corresponds well to the qualitative distribution of the wake size shown in Fig. 14(a). A detailed look at the clearance flow per unit chord along the meridional direction is shown in Fig. 15(b). The clearance flow per unit chord for the part-flow case exceeded that for the design flow up to 8 percent chord, after which it was less than for the design flow case.

A comparison of the CFD predicted and experimentally measured blade pressure loadings revealed that the leading edge region for the part-flow case is more heavily loaded than for the design flow case due to increased incidence, but that the rest of the blade pressure loading is less than for the design flow case. Consequently, we can conclude that the wake size increase in the inducer region is due to increased incidence at part flow and that the apparent smaller wake size in the exit region is a result of decreased pressure difference across most of the blade, which results in a decrease in clearance flow per unit chord over the aft 92 percent of the blade.

A reduction in blade pressure loading with increased overall pressure rise for the part-flow case is not intuitively obvious, but it can be easily shown from the tangential momentum equation for near radial flow in an impeller that the pressure difference across the channel is given by

$$\Delta p = \frac{2\pi}{N_B}(2V_rV_\theta)\rho .$$

In the radial portion of the impeller, the radial velocity varies with the mass flow rate and, thus, it is clear that the reduction in blade pressure loading with reduced flow rate is a logical consequence. Noting this and the results of the measured wake location from Fig. 14(b), it is clear that an increase in cross-channel pressure loading cannot be responsible for the movement of the wake closer to the suction surface for the part-flow condition as one might intuitively expect.

Morris and Kenny (1971) proposed using $\Delta p/2q$ as a measure of blade loading and hence propensity for secondary flow development. This is the ratio of the cross-channel pressure gradient to the dynamic head and is similar to the rotation number (ratio of Coriolis acceleration to inertial acceleration). The expression can be simplified for a radial impeller to

$$\frac{\Delta p}{2q} = \frac{4\pi r\omega}{N_B V_r} .$$

For a radial bladed impeller this is a measure of the imbalance in forces that occur on a low-velocity fluid when subjected to a transverse pressure gradient set up by a higher velocity mainstream. We conclude that the free-stream dynamic head decreases faster than the blade pressure loading as the flow rate decreases so that the net result is for the low-velocity wake fluid to exit the impeller closer to the suction surface.

To insure that the measured and CFD blade pressure loadings versus mass flow rate characteristic is not unique to this impeller, we compared the variation in blade pressure loading based upon overall experimentally measured quantities for the present impeller to that of two high pressure ratio impellers. These impellers had pressure ratios of 6:1 and 4:1. From overall power

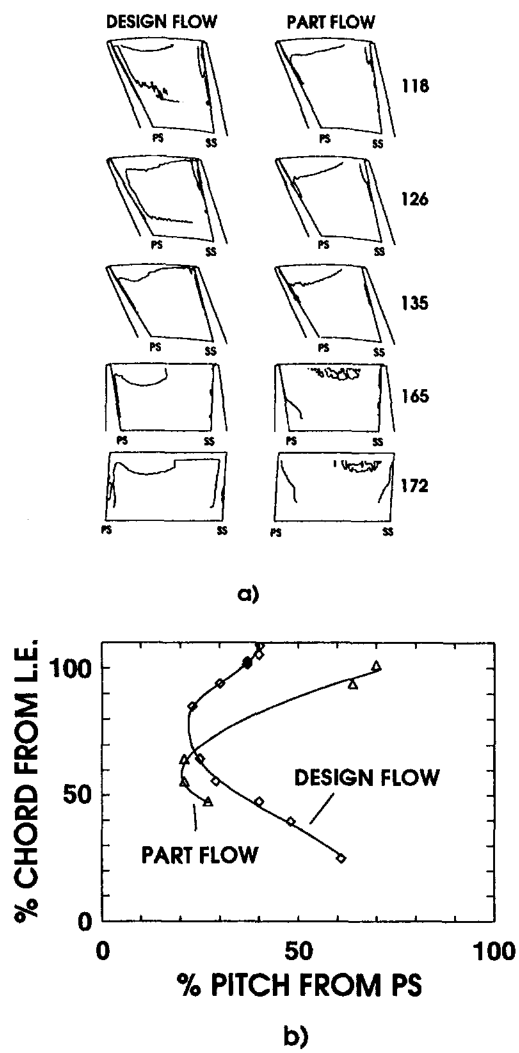

Fig. 14 (a) Wake boundary contours shown are at 50 percent of the peak value outside of the blade boundary layers. (b) Approximate throughflow wake location as a function of chord for both the design and part-flow conditions.

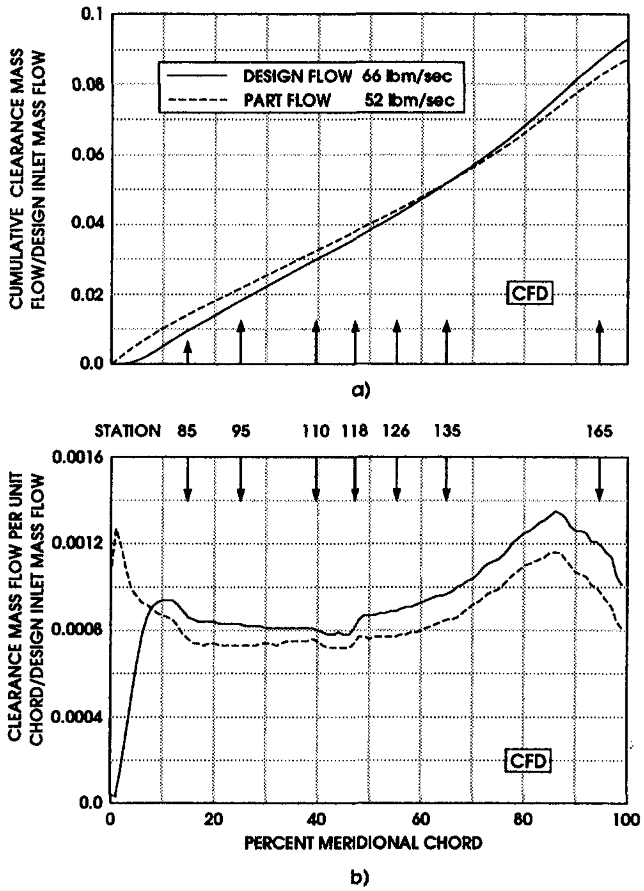

Fig. 15 CFD results of tip clearance mass flow: (*a*) Cumulative mass flow. (*b*) Clearance mass flow per unit chord.

input the blade pressure loading can be related to overall performance through

$$\Delta p \propto \dot{m} \frac{\Delta H}{\omega}.$$

The same trend of reduced blade loading with decreasing flow rate was found in both high pressure ratio impellers for flow rates below about 96–98 percent of choking flow. Near choke the total enthalpy rise decreases at constant mass flow rate so that the trend does not hold.

Conclusions

Detailed measurements and three-dimensional viscous calculations of the LSCC velocity field at two different flow rates have demonstrated the ability of modern computational tools to simulate the flow reasonably in a centrifugal compressor that contains no large streamwise separation. The tip clearance flow, which constitutes a large portion of the throughflow wake, impinges upon the pressure surface sooner and then moves farther toward the suction surface as the flow rate is reduced. It was shown that the movement of the throughflow wake closer to the suction surface as the flow was reduced from design flow to part flow was not a result of an increased pressure difference across the blade channel. Both CFD and experiment showed that the cross-channel pressure difference decreased as flow was reduced. The movement of the throughflow wake toward the suction surface is consistent with well-known nondimensional factors used to characterize the migration of low-velocity fluid subjected to transverse pressure gradients imposed by a higher velocity free-stream fluid. These features are accurately captured by the computations. The throughflow wake at the impeller exit was slightly smaller at the lower flow rate, which was consistent with the clearance flows obtained from the CFD analysis.

The importance of accurately knowing not only the tip clearance gap but the physical shape of the blade tip (whether due to in-service wear or initial manufacture) was demonstrated and emphasizes further the importance of adequately knowing the "as-tested" geometry when predicting impeller aerodynamic performance.

The computational results presented confirm the ability of modern computational tools to model the dynamics of a subsonic centrifugal compressor impeller accurately when such pertinent geometric parameters as tip clearance and blade tip shape are accurately known. The ability to predict development of the throughflow wake, which is largely fed by the tip clearance flow as the impeller is throttled, should give designers much better confidence in using computational tools to improve impeller performance.

References

Adler, D., and Levy, Y., 1979, "A Laser-Doppler Investigation of the Flow Inside a Backswept, Closed, Centrifugal Compressor," *Journal of Mechanical Engineering Science*, Vol. 21, No. 1.

Ahmed, N. A., and Elder, R. L., 1990, "Flow Investigation in a Small High Speed Impeller Passage Using Laser Anemometry," ASME Paper No. 90-GT-233.

Baldwin, B., and Lomax, H., 1970, "Thin Layer Approximation and Algebraic Model for Separated Turbulent Flows," AIAA Paper No. 78-257.

Cumpsty, N. A., 1989, *Compressor Aerodynamics*, Longman Scientific and Technical, United Kingdom.

Dawes, W. N., 1988, "Development of a 3-D Navier–Stokes Solver of Application to All Types of Turbomachinery," ASME Paper No. 88-GT-70.

Dean, R., and Senoo, Y., 1960, "Rotating Wakes in Vaneless Diffusers," ASME *Journal of Basic Engineering*, Vol. 82, pp. 563–574.

Eckardt, D., 1976, "Detailed Flow Investigations Within a High-Speed Centrifugal Compressor Impeller," ASME *Journal of Fluids Engineering*, Vol. 98, pp. 390–402.

Fagan, J. R., and Fleeter, S., 1990, "Impeller Flow Field Measurement and Analysis," ASME JOURNAL OF TURBOMACHINERY, Vol. 113, pp. 670–679.

Farge, T. Z., and Johnson, M. W., 1990, "The Effect of Backswept Blading on the Flow in a Centrifugal Compressor Impeller," ASME Paper No. 90-GT-231.

Hathaway, M. D., Suder, K. L., Okiishi, T. H., Strazisar, A. J., and Adamczyk, J. J., 1987, "Measurements of the Unsteady Flow Field Within the Stator Row of a Transonic Axial-Flow Fan, Part II—Results and Discussion," ASME Paper No. 87-GT-227.

Hathaway, M. D., Wood, J. R., and Wasserbauer, C. W., 1992, "NASA Low Speed Centrifugal Compressor for 3-D Viscous Code Assessment and Fundamental Flow Physics Research," ASME JOURNAL OF TURBOMACHINERY, Vol. 114, pp. 295–303.

Hathaway, M. D., Chriss, R. M., Wood, J. R., and Strazisar, A. J., 1993, "Experimental and Computational Investigation of the NASA Low-Speed Centrifugal Compressor Flow Field," ASME JOURNAL OF TURBOMACHINERY, Vol. 115, pp. 527–542.

Heyes, F. J. G., Hodson, H. P., and Dailey, G. M., 1992, "The Effect of Blade Tip Geometry on the Tip Leakage Flow in Axial Turbine Cascades," ASME JOURNAL OF TURBOMACHINERY, Vol. 114, pp. 643–651.

Johnson, M. W., and Moore, J., 1983, "The Influence of Flow Rate on the Wake in a Centrifugal Impeller," ASME *Journal of Engineering for Power*, Vol. 105, pp. 33–39.

Krain, H., 1981, "A Study on Centrifugal Impeller and Diffuser Flow," ASME *Journal of Engineering for Power*, Vol. 103, pp. 688–697.

Krain, H., 1988, "Swirling Impeller Flow," ASME JOURNAL OF TURBOMACHINERY, Vol. 110, No. 1.

Krain, H., and Hoffmann, W., 1989, "Verification of an Impeller Design by Laser Measurements and 3D-Viscous Flow Calculations," ASME Paper No. 89-GT-159.

Krain, H., and Hoffmann, W., 1990, "Centrifugal Impeller Geometry and Its Influence on Secondary Flows," in: *Secondary Flows in Turbomachines*, AGARD.

Morris, R. E., and Kenny, D. P., 1971, "High Pressure Ratio Centrifugal Compressors for Small Gas Turbine Engines," in: *Advanced Centrifugal Compressors*, R. C. Dean, ed., ASME, New York.

Nichols, C. E., 1987, "Preparation of Polystyrene Microspheres for Laser Velocimetry in Wind Tunnels," NASA TM 89163.

Rohne, K. H., and Banzhaf, M., 1990, "Investigation of the Flow at the Exit of an Unshrouded Centrifugal Impeller and Comparison With the Classical Jet-Wake Theory," ASME JOURNAL OF TURBOMACHINERY, Vol. 113, pp. 654–659.

Sipos, G., 1991, "Secondary Flow Loss Distribution in a Radial Compressor With Untwisted Backswept Vanes," ASME JOURNAL OF TURBOMACHINERY, Vol. 113, pp. 686–695.

Straka, W. A., and Farrell, K. J., 1992, "The Effect of Spatial Wandering on Experimental Laser Velocimeter Measurements of the End-Wall Vortices in an Axial Flow Pump," *Experiments in Fluids*, Vol. 13, No. 2, pp. 163–170.

Strazisar, A. J., Wood, J. R., Hathaway, M. D., and Suder, K. L., 1989, "Laser Anemometer Measurements in a Transonic Axial-Flow Fan Rotor," NASA TP-2879.

Suder, K. L., Hathaway, M. D., Okiishi, T. H., Strazisar, A. J., and Adamczyk, J. J., 1987, "Measurements of the Unsteady Flow Field Within the Stator Row of a Transonic Axial-Flow Fan, Part I—Measurement and Analysis Technique," ASME Paper No. 87-GT-226.

Wood, J. R., Adam, P. W., and Buggele, A. E., 1983, "NASA Low-Speed Centrifugal Compressor for Fundamental Research," NASA TM 83398.

Wood, J. R., Strazisar, A. J., and Hathaway, M. D., 1990, "E/C0-2 Single Transonic Fan Rotor," AGARD AR-275.

Zierke, W. C., Straka, W. A., and Taylor, P. D., 1993, "The High Reynolds Number Flow Through an Axial-Flow Pump," The Pennsylvania State University, Applied Research Laboratory, TR-93-12.

Experimental and Numerical Investigation of a Shock Wave Within a Swept Shrouded Propfan Rotor

K. Helming[1]
DLR, Institute for Propulsion Technology,
Cologne, Federal Republic of Germany

Laser velocity measurements are conducted in a swept propfan rotor in order to investigate the local transonic flow region on the suction surface at high subsonic inlet Mach numbers. The velocity measurements are accompanied by a three-dimensional Navier–Stokes calculation for a selected operating point. The good agreement between computed and measured flow field gives some confidence to study the local three-dimensional passage shock on the suction surface by using the numerical procedure. Apart from the computed three-dimensional shock, structure is investigated in detail. By considering streamlines, it is concluded whether the shock wave is normal or oblique. The results are compared with the one-dimensional shock conditions.

Introduction

Shock losses significantly influence the efficiency of transonic and supersonic compressor rotors. Improvements in rotor design tend in one respect to swept blades in order to obtain oblique shocks in the spanwise direction with lower losses. Possible reduction of shock losses can be illustrated by a theoretical study of total pressure losses for several shock angles. The loss coefficient ratios of the oblique shock to the normal shock are plotted versus the preshock Mach number in Fig. 1. The diagram demonstrates the considerable reduction of shock losses in the case of oblique shocks. For example, for a preshock Mach number of 1.15 and a shock angle of 76°, the shock losses of the normal shock are reduced to 50 percent. However, up to now, it could not be finally clarified in transonic compressor rotors to what extent oblique passage shock waves do exist.

Many investigations deal with detection and analysis of three-dimensional flow in the blade-to-blade plane. It has been found that the flow does not fulfill the normal shock relations.

Prince (1980) summarized investigations of three-dimensional shock structures at that time for transonic and supersonic compressor rotors. He gave some quotations of remarkable shock investigations as, for example, Wuerker et al. (1974): "The pressure increase in the normal shock does not agree with the theoretical value of a one-dimensional supersonic flow," and Wisler (1977): "It is recognized that the velocity jump across the normal shock does not follow the classical normal shock relations."

Although comparisons between three-dimensional calculations and flow field measurements were presented by many researchers, for example, Strazisar and Chima (1980), Chima and Strazisar (1983), Pierzga and Wood (1985), Hah and Wennerstrom (1990), Rabe et al. (1991), and Copenhaver et al. (1993), the question has not been adequately answered to what extent an oblique shock exists in respect to the streamlines in three-dimensional transonic rotor flows. Attempts to describe physical phenomena of three-dimensional shock waves in compressor rotors were undertaken by Miller et al. (1961) and Wennerstrom and Puterbaugh (1984) who constructed a shock loss model, the latter one for three-dimensional applications. Epstein et al. (1979) pointed out by a simple model that the jump conditions across passage shocks are able to produce a radial disequilibrium with large radial pressure gradients.

The purpose of this paper is to investigate the three-dimensional shock shape in a swept propfan rotor and to describe the shock relations. The investigation was conducted on a propfan rotor model (CRISP[2]) developed by MTU. Experiments were performed in an axial compressor test facility at DLR, Cologne. "Laser-2-Focus" (L2F) velocity measurements are carried out in detail between 75 and 94 percent relative blade height in order to detect the local supersonic region on the suction side. The experimental results are compared with a three-dimensional Navier–Stokes calculation. The good agreement in quantity as well as in quality gives some confidence in using the numerical results for further analyses.

Propfan Rotor and Experiment

The tip diameter of the tested propfan rotor is 400 mm and the hub-to-tip ratio is 0.25. The gap/chord ratio is about 2.4 at rotor tip. Details of the propfan aerodynamic design and of experimental results are given by Dupslaff et al. (1989).

The laser anemometer system used in this investigation is a "Laser-2-Focus" velocimeter (L2F) developed by Schodl (1986) at DLR. This kind of velocimeter measures the velocity magnitude and its direction in the axial/tangential plane.

The laser anemometer measurements were obtained for a relative rotor tip Mach number just below 1.00. The measurement locations are shown in a meridian view of the rotor in Fig. 2. Laser anemometer measurements are made on cylindrical surfaces. The axial spacing of the measurement points varies from 25 percent axial chord length upstream of the rotor to about 8 percent in the shock region. The spacing in tangential direction is about 3.1 percent of a blade gap. The selected measurement planes for shock analysis are located at 92.8, 89.5, and 86.2 percent relative blade height.

Grid of Three-Dimensional Calculation

A three-dimensional Navier–Stokes code developed by Dawes (1987) is employed to calculate the propfan rotor. The generated H-grid consists of 59 nodes in the blade-to-blade

[1] Current address: BMW Rolls-Royce Aeroengines, Eschenweg 11, 15827 Dahlewitz, Federal Republic of Germany.

Contributed by the International Gas Turbine Institute and presented at the 39th International Gas Turbine and Aeroengine Congress and Exposition, The Hague, The Netherlands, June 13–16, 1994. Manuscript received by the International Gas Turbine Institute February 18, 1994. Paper No. 94-GT-221. Associate Technical Editor: E. M. Greitzer.

[2] CRISP: Counter Rotating Integrated Shrouded Propfan.

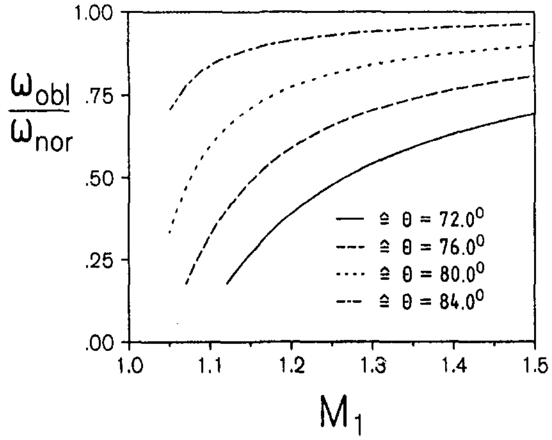

Fig. 1 Pressure loss coefficient of oblique shocks

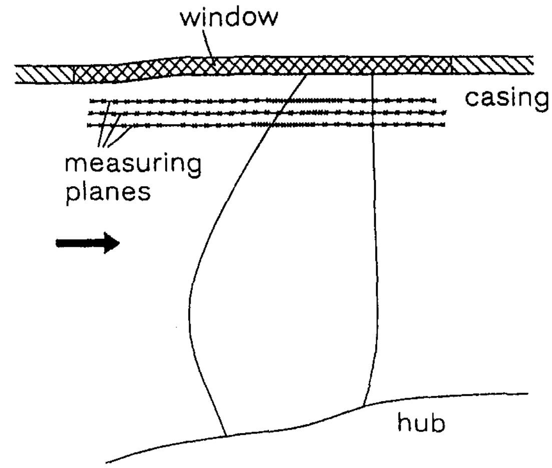

Fig. 2 Meridian view of a model of the propfan CRISP, rotor 1

direction, 97 nodes in the streamwise direction, and 59 nodes in the spanwise direction. One third of the cells are located in the blade area.

Attention is given to the grid generation on the surfaces due to the strong influence of boundary layer and tip leakage flow on the shock structure. The grid refinement in the radial direction is about 0.20 percent relative blade height and in the circumferential direction about 0.14 percent of the blade passage. The tip clearance is assumed to be constant with 2.5 percent of tip chord length and is modeled with three nodes in the spanwise direction. The assessment of the grid was done by comparing each computed result of several grid configurations with the laser velocimeter measurements.

Comparison of Results

In order to use the numerical results for the analysis of the shock wave, the agreement of the calculated values with the measured values in quality and quantity as well has to be guaranteed. Distributions of the relative Mach number are compared with those calculated in Figs. 3–5. The experimental Mach number contours are smoothed for better identification. Figure 3 shows a good agreement of the calculated relative Mach number contours at 89.5 percent relative blade height with the measured contours. The flow on the suction surface accelerates to a maximum preshock Mach number of approximately 1.17. The measured and calculated shock locations are defined as the line where the flow passes from the supersonic region into the subsonic region. This line will be further called "shock line." The shock, extrapolated to the suction surface, is located at about 0.40 relative chord length. The postshock Mach number is found to be approximately 0.96. Under the assumption of a nearly normal shock wave, the postshock Mach number is obviously too high relative to the normal shock relations.

The relative Mach number contours at 92.8 and 86.2 percent blade height are shown in Figs. 4(a, b) and 5(a, b). The agreement between calculation and measurement is also very good. The measured and calculated shock waves agree in strength and position. Near the suction side (Fig. 4) the flow seems to be re-accelerated behind the shock wave due to a three-dimensional interaction of the flow with the blade surface boundary layer, casing boundary layer, and the tip leakage flow. Obviously, this re-acceleration is mainly influenced by the tip leakage flow and the endwall boundary layer because this interaction region decreases at smaller radii. A numerical analysis of the tip leakage flow in that rotor was done by Melake (1992). Strong tip leakage flow and possible boundary-layer separation are indicated by the fact that L2F measurements above 93 percent relative blade height could not be conducted due to very high turbulence levels in that area. The extent of the supersonic region decreases on the lower radius (Fig. 5) and the maximum Mach number is just under 1.15. On the outer radius (Fig. 4) the preshock Mach number reaches a value above of 1.20.

For a quantitative comparison of the experimental and numerical results, the relative Mach number and relative circumferential flow angle distributions from blade to blade on 89.5 percent relative blade height will be considered next. The axial positions are sketched by dotted lines in Fig. 3(a). The experimental and calculated curves of the relative Mach number are compared in Fig. 6. The relative Mach numbers of the experiment are calculated from the measured velocity values using the assumption of constant rothalpy. For all three cases the curves deduced from experiment agree well with the computed curves. The supersonic region is to be found at 16.3 and 29.0 percent relative chord length at the suction surface. At the axial position of 41.8 percent relative chord length, the flow is completely subsonic. So, this axial position is located just downstream of the shock wave.

The distributions of the relative circumferential flow angle are shown in Fig. 7 for the same positions as for the relative Mach numbers. Considering the fine scale division, it becomes obvious that the measured and calculated curves differ from each other by not much more than one degree. The agreement of both curves is very good near the suction side at 29.0 and 41.8 percent relative chord length.

Nomenclature

h = relative blade height
M = Mach number
m = mass-flow rate
u = circumferential velocity of the rotor
w = relative velocity
β = relative circumferential flow angle
γ = meridian angle
Θ = shock angle
ω = relative total pressure loss coefficient

Subscripts

nor = normal
obl = oblique
ps = pressure side
r = relative
ss = suction side
t = total
1 = preshock
2 = postshock

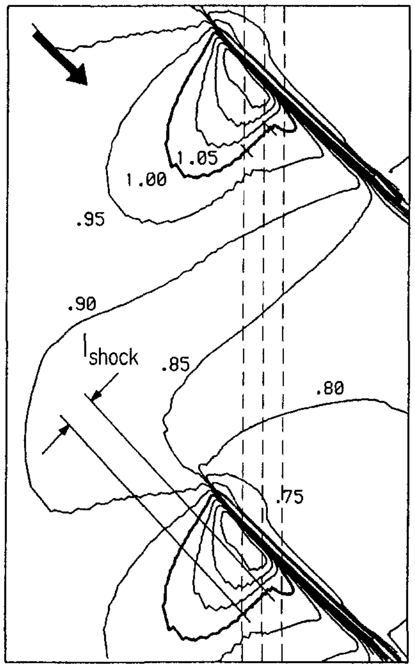

Fig. 3(*a*) Calculated relative Mach number contours at h = 89.5 percent

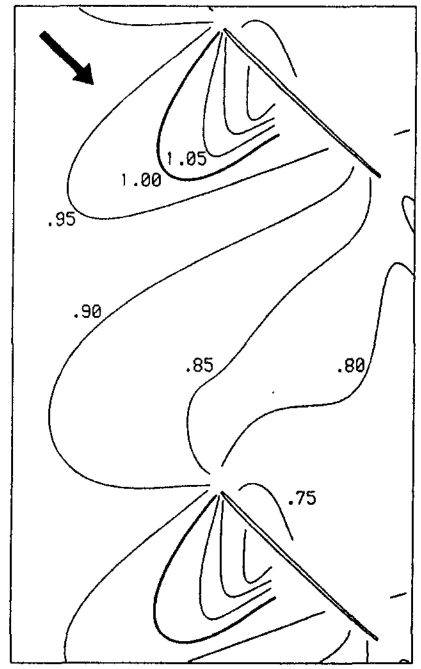

Fig. 3(*b*) Measured relative Mach number contours at h = 89.5 percent

Measurement Error. As shown above, the experimental and numerical results agree very well in quality and quantity. The magnitude and influence of measurement errors will now be regarded to confirm the reliability of the L2F measurements. The absolute velocity is measured with an uncertainty of 0.7 percent and the absolute flow angle with ±0.5°. The relative Mach number deduced from measurements is a calculated value and therefore the reliability does not only depend on the measured velocity and angle, but also on other parameters as:

- Total temperature, measured upstream of the rotor
- Determination of the exact radius
- Constancy of the circumferential velocity of the rotor

It can be assumed that the total temperature is measured with an error of ±0.5 K. The radius of the laser focus point is determined with an error of ±0.5 mm and the circumferential velocity of the rotor has an uncertainty of 0.5 percent in the worst case. The relatively high error in determining the radial position mainly depends on the accuracy in measuring a known radial point as reference. Considering these determined errors, the maximum variation of the relative Mach number is ±0.0012.

Another error source for velocity measurements is the capability of the seeding particles to follow the flow across the shock

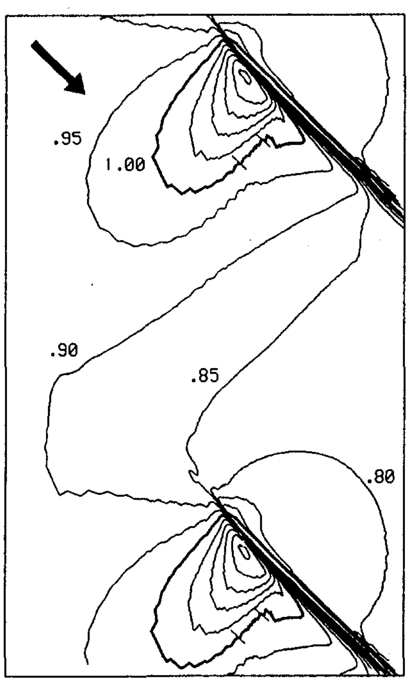

Fig. 4(*a*) Calculated relative Mach number contours at h = 92.8 percent

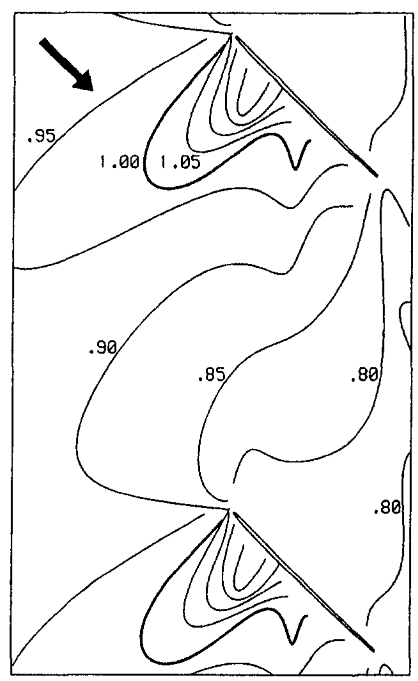

Fig. 4(*b*) Measured relative Mach number contours at h = 92.8 percent

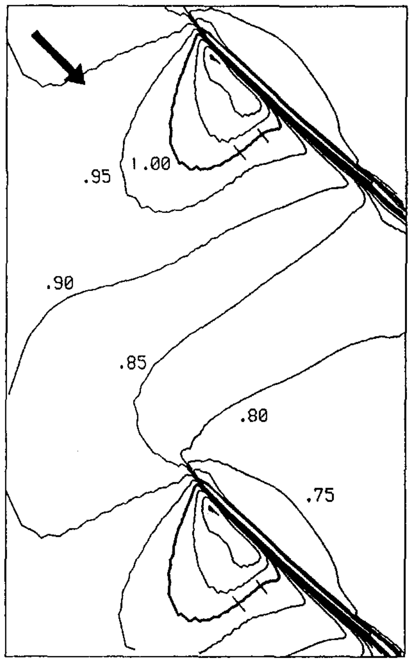

Fig. 5(*a*) Calculated relative Mach number contours at h = 86.2 percent

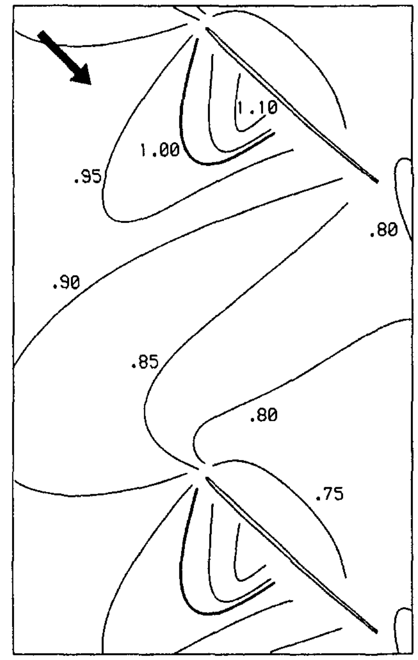

Fig. 5(*b*) Measured relative Mach number contours at h = 86.2 percent

wave. An assessment of the particle lag can be done with known preshock velocity values and the magnitude of the velocity jump. In this case the absolute preshock velocity is about 270 m/s. The velocity is decelerated by the shock wave to 220 m/s. It can be derived from an investigation about the particle lag by Melling (1986) that the 0.5 μm particles used here reach the flow velocity about 1 mm behind the shock wave.

Numerical Analysis of the Passage Shock

On the basis of the good agreement between measured and calculated data, the investigation of the shock wave is done by using the numerical result. The analysis focuses on the question, whether the shock is normal or oblique in respect to the flow direction. This problem will be attached by comparing the preshock velocity vector of a streamline with a vector perpendicular to the shock surface.

For determining the three-dimensional shock surface, shock sections are defined on the shock line at several radii. The selected sections are marked by cross lines on the shock lines in the Mach number contours of Figs. 3(*a*)–5(*a*). Due to the numerically caused wiggles in the flow field, the separate shock sections have to be smoothed. The sections are aligned in the radial direction, and with that result in a continuous three-dimensional surface of the shock. The vector perpendicular to this surface now can be constructed at each point of the shock surface. A meridian view of the rotor tip area with a shock line is shown in Fig. 8 giving an impression of the radial shock extension. The meridian plane is located at 13.7 percent pitch from the suction side. Here the shock wave has an inclination relative to the radial direction. The angle is about half of the meridian sweep angle.

Streamlines are obtained by the means of particle tracing, whereby the particles are numerically introduced in front of the leading edge. Aerodynamic flow values are interpolated along the streamlines. Figures 9–11 show distributions of relative Mach number, relative flow angle, and meridian flow angle along one streamline. This streamline is located in the shock area at 15.2 percent pitch from the suction side at 89.5 percent relative blade height. Figure 9 demonstrates that the shock is approximately smeared over 15 percent chord length due to the insufficient capability of the used pressure adaptive artificial viscosity scheme presenting a shock over fewer than five computational cells. The distribution of the relative circumferential flow angle in Fig. 10 shows a continuous deflection, which obviously is not being influenced by the shock wave. The distribution of the meridian angle in Fig. 11 shows an increasing flow deflection toward the hub upstream of the leading edge. This deflection is caused by the increasing radial pressure gradient with increasing rotor sweep (Helming, 1994). Basic effects of sweep are studied, for example, by Smith and Yeh (1963). Within the blade row the deflection decreases from the leading edge to the end of the shock wave due to a changed radial pressure gradient. The difference of the relative circumferential and meridian flow angles to those of other investigated streamlines is about 2 deg. The shapes of these distributions are similar.

With the relative circumferential and meridian flow angles, the three-dimensional flow vector is calculated at that point where the streamline passes the shock wave. The shock angle is subsequently determined with the above-mentioned vector perpendicular to the shock wave.

The calculated shock angles are plotted in Fig. 12 over the length of the considered shock sections (Fig. 3). For all three cases the shock angle is obviously less than 90 deg and indicates an oblique shock. The obliquity is mainly due to the radial inclination of the shock wave (Fig. 8). Parameters influencing the radial shock position are mainly the sweep of the rotor blade and the radial distribution of the back pressure. Sweep in itself has the effect of forming a shock wave parallel to the leading edge. Different back pressures shift a local shock wave on the blade surface in the axial direction. The shock wave is located closer to the leading edge for high back pressure than for low back pressure. So the radial inclination of the investigated shock wave differs from the leading edge inclination due to the radial distribution of the back pressure. In this way the more acute shock angle on 92.8 percent relative blade height (Fig. 12) can be explained by a reduced pressure ratio requirement.

The shock angle decreases toward the pressure side due to a three-dimensional effect of the decreasing shock strength. This will be explained in a sketch (Fig. 13) of two radial blade sections, where the phenomenon is exaggeratedly shown in contrast to the small differences of the real shock wave. The upper

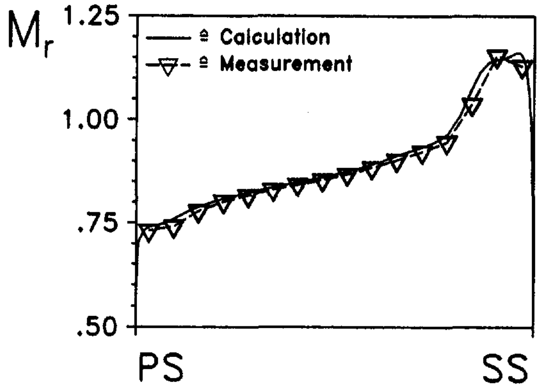

Fig. 6(*a*) Comparison of measured and calculated relative Mach numbers at 16.3 percent chord length, *h* = 89.5 percent

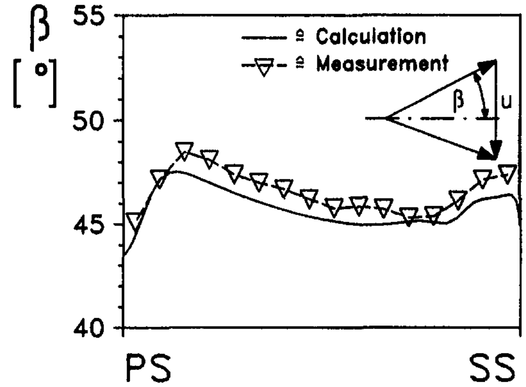

Fig. 7(*a*) Comparison of measured and calculated relative circumferential flow angles at 16.3 percent chord length, *h* = 89.5 percent

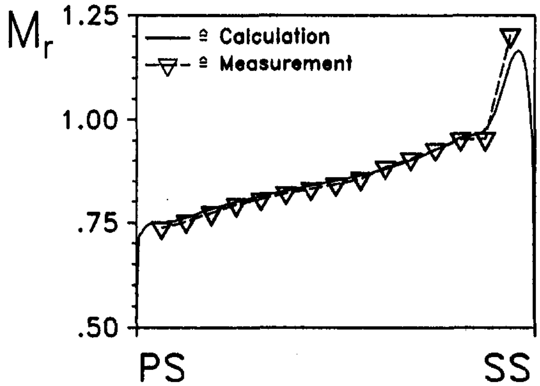

Fig. 6(*b*) Comparison of measured and calculated relative Mach numbers at 29.0 percent chord length, *h* = 89.5 percent

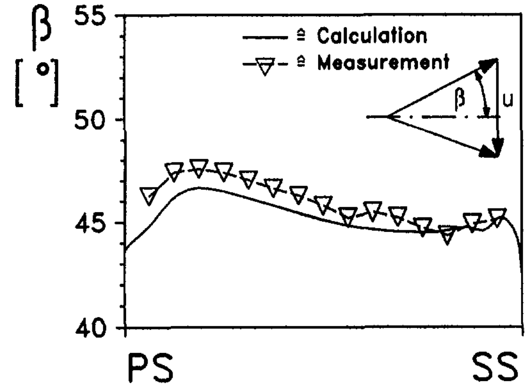

Fig. 7(*b*) Comparison of measured and calculated relative circumferential flow angles at 29.0 percent chord length, *h* = 89.5 percent

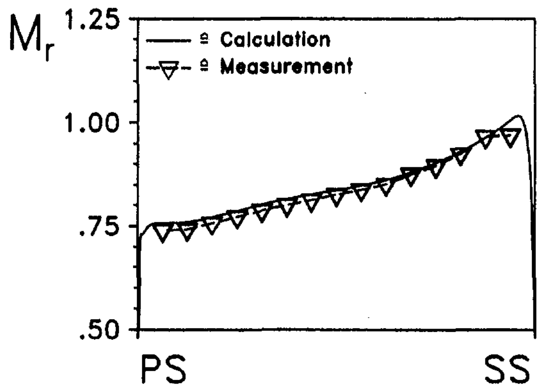

Fig. 6(*c*) Comparison of measured and calculated relative Mach numbers at 41.8 percent chord length, *h* = 89.5 percent

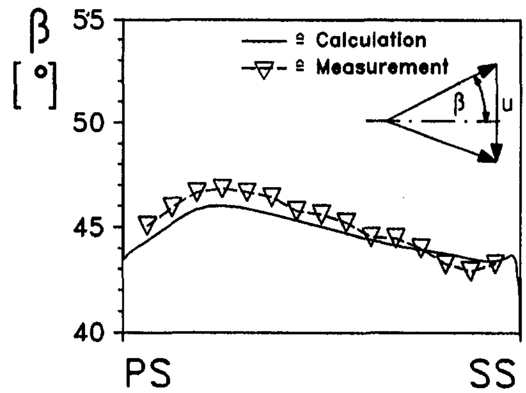

Fig. 7(*c*) Comparison of measured and calculated relative circumferential flow angles at 41.8 percent chord length, *h* = 89.5 percent

blade section can be identified with the greater stagger angle of the profile and the larger extension of the supersonic region. The radial inclination of the shock wave is indicated by shifting the shock wave at different positions on the blade surface. Thereby, the hatched area between both shock lines is a measure of the radial inclination of the shock wave. The hatched area increases in pressure side direction due to the different extension and shape of the shock wave on both radii. Therefore, the radial inclination of the shock wave increases and the shock angle decreases.

At the suction side (Fig. 12), the shock angle decreases at higher radii. This is due to the above-mentioned re-acceleration area, which is accompanied by a low pressure level. At higher radii the re-acceleration area grows in strength and shifts the shock wave downstream due to lower back pressures. So the shock wave gets a higher radial inclination at the suction side than outside of this area. This effect explains the decrease in the shock angle.

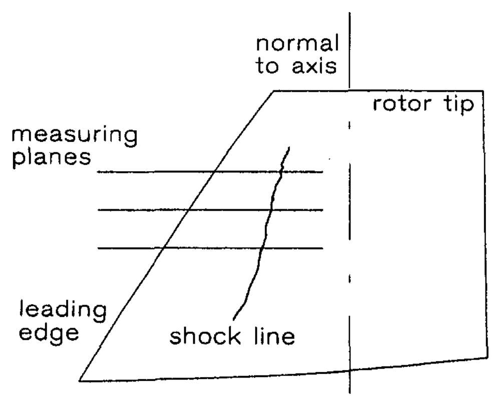

Fig. 8 Meridian view of the rotor tip area with a shock line at 13.7 percent pitch from the suction side

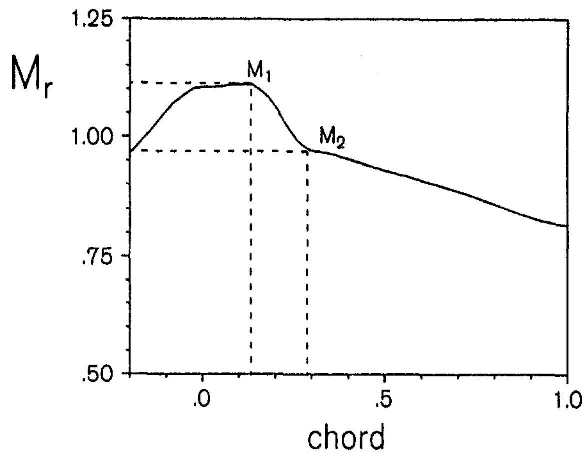

Fig. 9 Relative Mach number along a streamline at 15.2 percent pitch and 89.5 percent relative blade height

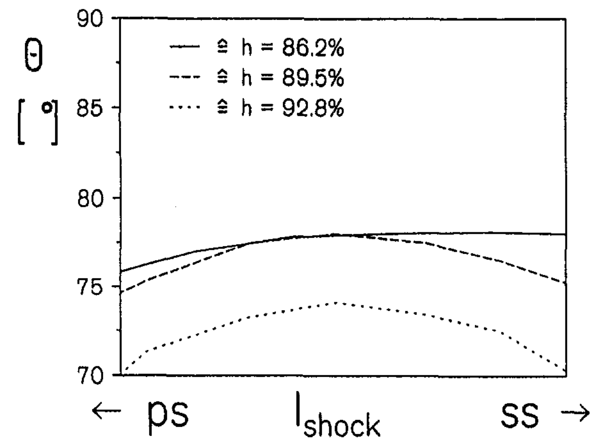

Fig. 12 Shock angle along the separate shock sections

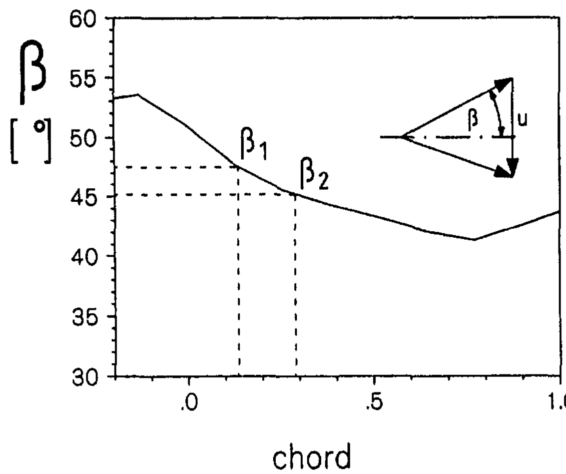

Fig. 10 Relative circumferential flow angle along a streamline at 15.2 percent pitch and 89.5 percent relative blade height

postshock Mach numbers resulting from the three-dimensional calculation are compared to the theoretical Mach numbers with normal and oblique shock conditions. In the case of the oblique shock the shock angle is taken from the determined angle shown in Fig. 12.

The figures show that the postshock Mach numbers of the three-dimensional calculation are higher in all three cases than for a normal shock. The difference between both is too large to be explained by uncertainties or errors as discussed above. However, one explanation of this difference can be the existence of an oblique shock. This is shown by calculating the postshock Mach number with the determined shock angles. The comparison of the three-dimensional calculation and the theoretical oblique shock wave shows that the postshock Mach numbers

Now the question will be discussed whether the observed obliquity of the shock wave is a possible reason for the high postshock Mach numbers. Figures 14–16 show three distributions of postshock Mach numbers in relation to the distribution of preshock Mach number at the regarded sections. The

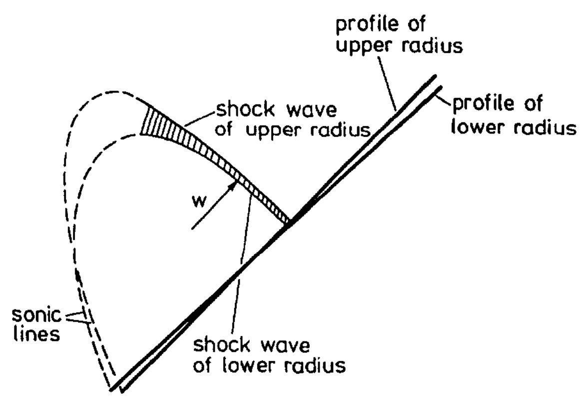

Fig. 13 Sketch of two radial blade sections with local shock waves

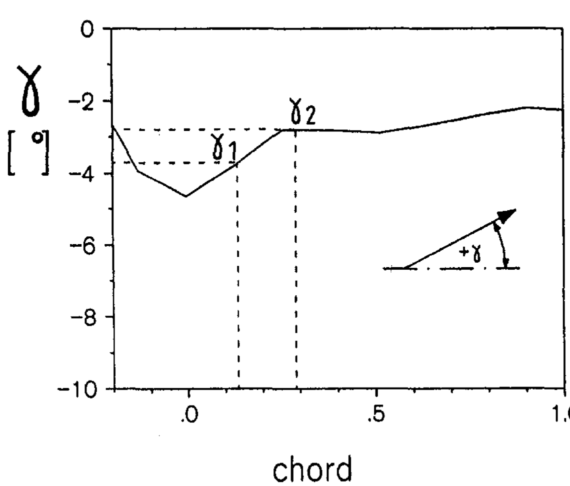

Fig. 11 Meridian angle along a streamline at 15.2 percent pitch and 89.5 percent relative blade height

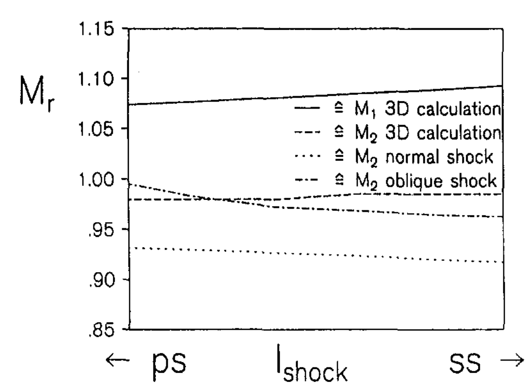

Fig. 14 Postshock Mach numbers of the three-dimensional calculation and of theoretical normal and oblique shocks at h = 86.2 percent

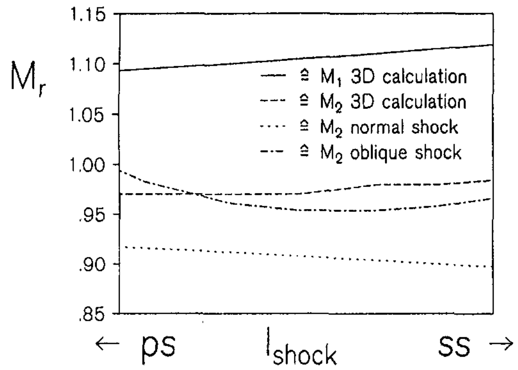

Fig. 15 Postshock Mach numbers of the three-dimensional calculation and of theoretical normal and oblique shocks at h = 89.5 percent

are on the same level. Differences between the postshock Mach numbers are mainly due to the fact that the postshock Mach number of the theoretical oblique shock is determined assuming one-dimensional shock conditions. The flow across a shock wave in a transonic compressor rotor is additionally influenced by three-dimensional effects as for example changes of streamtube areas and radial pressure gradients.

Conclusion

An experimental and numerical investigation is conducted on a high subsonic swept propfan rotor in order to analyze the three-dimensional passage shock. The comparison of the experimental and numerical results shows a good agreement in quantity as well as in quality. So the three-dimensional shock surface is analyzed using the numerical data. Shock normal vectors are calculated at several points on this surface. By means of particle tracing, streamlines are determined that cross the shock wave at these points. The three-dimensional shock angle is obtained by comparing the flow vector of the streamlines with the shock normal vector. The study shows that an oblique shock exists with a radial inclination. The angle is about half of the meridian sweep angle. The shock angles are further used to explain the high postshock Mach numbers. The results show that the postshock Mach numbers of the theoretical oblique shock are on the same level as those of the three-dimensional calculation. Differences are mainly due to the one-dimensional shock conditions, which do not consider three-dimensional effects in a transonic rotor flow field. So, a further investigation could be on the study of the influence of streamtube areas and radial pressure gradients on the three-dimensional shock behavior in transonic rotors.

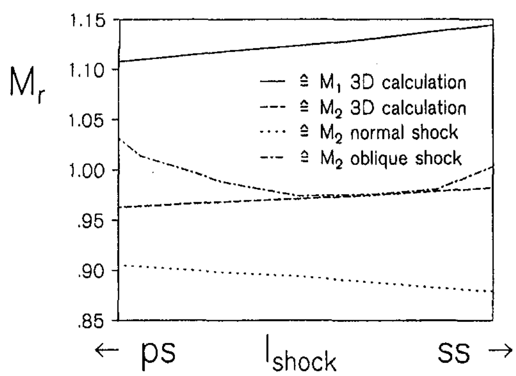

Fig. 16 Postshock Mach numbers of the three-dimensional calculation and of theoretical normal and oblique shocks at h = 92.8 percent

Acknowledgments

The author wishes to thank MTU for conducting and publishing the present investigation of a CRISP rotor model. Grateful thanks is also extended to the test crew, and to Mr. Peter Schimming and Dr. Hans Starken for their general help while preparing this paper.

References

Chima, R. V., and Strazisar, A. J., 1983, "Comparison of Two- and Three-Dimensional Flow Computations With Laser Anemometer Measurements in a Transonic Compressor Rotor," ASME *Journal of Engineering for Power,* Vol. 105, pp. 596–605.

Copenhaver, W. W., Hah, C., and Puterbaugh, S. L., 1993, "Three-Dimensional Flow Phenomena in a Transonic, High-Throughflow, Axial-Flow Compressor Stage," ASME JOURNAL OF TURBOMACHINERY, Vol. 115, pp. 240–248.

Dawes, W. N., 1987, "A Numerical Analysis of the Three-Dimensional Viscous Flow in a Transonic Compressor Rotor and Comparison With Experiment," ASME JOURNAL OF TURBOMACHINERY, Vol. 109, pp. 83–90.

Dupslaff, M., Wehlitz, P., and Schimming, P., 1989, "Propfan Technology," DGLR/AAAf/RAES European Forum: The Evaluation of Regional Aircraft Technologies and Certification, Apr.

Epstein, A. H., Kerrebrock, J. L., and Thompkins, W. T., Jr., 1979, "Shock Structure in Transonic Compressor Rotors," *AIAA Journal,* Vol. 17, No. 4, pp. 375–379.

Hah, C., and Wennerstrom, A. J., 1991, "Three-Dimensional Flowfields Inside a Transonic Compressor With Swept Blades," ASME JOURNAL OF TURBOMACHINERY, Vol. 113, pp. 241–251.

Helming, K., 1994, "Numerical Analysis of Sweep and Dihedral Effects in Propfan Rotors," presented at AIAA/ASME/SAE/ASEE Joint Propulsion Conference and Exhibit, June 27–29, Indianapolis, IN.

Melake, A., 1992, "Numerical Flow Simulation and Analysis of a Shrouded Propfan Rotor," AIAA Paper No. 92-3773.

Melling, A., 1986, "Seeding Gas Flows for Laser Anemometry," Advanced Instrumentation for Aero Engine Components, AGARD CP-399.

Miller, G. R., Lewis, G. W., and Hartmann, M. J., 1961, "Shock Losses in Transonic Compressor Blade Rows," ASME *Transactions,* Vol. 83, No. 3, pp. 235–242.

Pierzga, M. J., and Wood, J. R., 1985, "Investigation of the Three-Dimensional Flow Field Within a Transonic Fan Rotor: Experiment and Analysis," ASME *Journal of Engineering for Gas Turbines and Power,* Vol. 107, pp. 437–449.

Prince, D. C., Jr., 1980, "Three Dimensional Shock Structures for Transonic/Supersonic Compressor Rotors," *Journal of Aircraft,* Vol. 17, No. 1, pp. 28–37.

Rabe, D., Hoying D., and Koff S., 1991, "Application of Sweep to Improve Efficiency of a Transonic Fan: Part II. Performance and Laser Test Results," AIAA Paper No. 91-2544.

Schodl, R., 1986, "Laser-Two-Focus Velocimetry," *Advanced Instrumentation for Aero Engine Components,* AGARD-CP-399, Paper 7, Philadelphia, PA.

Smith, L. H., Jr., and Yeh, Hsuan, 1963, "Sweep and Dihedral Effects in Axial-Flow Turbomachinery," ASME *Journal of Basic Engineering,* Vol. 85, pp. 401–416.

Strazisar, A. J., and Chima, R. V., 1980, "Comparison Between Optical Measurements and a Numerical Solution of the Flow Field Within a Transonic Axial-Flow Compressor Rotor," AIAA Paper No. 80-1078.

Wennerstrom, A. J., and Puterbaugh, S. L., 1984, "A Three-Dimensional Model for the Prediction of Shock Losses in Compressor Blade Rows," ASME *Journal of Engineering for Gas Turbines and Power,* Vol. 106, No. 2, pp. 295–299.

Wisler, D. C., 1977, "Shock Wave and Flow Velocity Measurement in a High-Speed Fan Rotor Using the Laser Velocimeter," ASME *Journal of Engineering for Power,* pp. 181–188.

Wuerker, R. F., Kobayashi, R. J., Heflinger, L. O., and Ware, T. C., 1974, "Application of Holography to Flow Visualization Within Rotating Compressor Blade Row," NASA CR 121264.

W. M. König[1]

D. K. Hennecke

Department of Flight Propulsion,
Technical University of Darmstadt,
Darmstadt, Federal Republic of Germany

L. Fottner

Institute for Jet Propulsion,
German Armed Forces
University of Munich,
Neubiberg, Federal Republic of Germany

Improved Blade Profile Loss and Deviation Angle Models for Advanced Transonic Compressor Bladings: Part I—A Model for Subsonic Flow

New blading concepts as used in modern transonic axial-flow compressors require improved loss and deviation angle correlations. The new model presented in this paper incorporates several elements and treats blade-row flows having subsonic and supersonic inlet conditions separately. In the first part of this paper two proved and well-established profile loss correlations for subsonic flows are extended to quasi-two-dimensional conditions and to custom-tailored blade designs. Instead of a deviation angle correlation, a simple method based on singularities is utilized. The comparison between the new model and a recently published model demonstrates the improved accuracy in prediction of cascade performance achieved by the new model.

Introduction

The performance of a new compressor can be predicted by calculation methods that approximate the pressure losses, the deviation angles, and the secondary flow effects on the basis of the aerodynamic data at the cascade inlet and some characteristic parameters for the cascade geometry and the blade shape. In order to adapt theoretically deduced values to cascade measurements (e.g., Lieblein et al., 1953; Lieblein, 1957), to compressor measurements (e.g., Çetin et al., 1987; Miller and Wright, 1991) or even to systematic calculations for cascade flows (Koch and Smith, 1976), these correlations incorporate empirical correction factors. Usually, their data base is bound to bladings of special, in most cases older, profile types or to investigations focusing on the influence of selected aerodynamic parameters and limit the scope of the deduced correlation.

These facts gave the impetus to improve existing correlations for profile losses and to propose a singularity method to estimate reliable deviation angles for transonic axial-flow compressors with custom-tailored bladings.

Experimental Data Base

Extensive measurement data of eight cascades were available to improve existing profile loss correlations and to adapt a singularity calculation method to obtain corrected outlet-flow angles. Since the blade shapes of the cascades are substantially different, correction factors refering to any specific blade geometry were excluded.

Figure 1 shows the blade shape for each cascade and catalogues its design Mach number. Additionally, references describing the experimental investigations of the individual cascades are noted. König (1992) compiles the cascade geometries and the aerodynamic test parameters, and briefly describes the design goals. Both of the two L030-cascades designed for supersonic cascade inlet-flows were investigated also in detail at high subsonic Mach numbers. The double-circular-arc cascade DCA-V2, the cascade with a NACA-65-blading NACA 65-(12)06 and the cascade with the British circular-arc profile 9C7/32.5C50 were investigated in the high velocity cascade wind tunnel at its former location at DLR Braunschweig. The measurement data of all other cascades were taken in the transonic cascade wind tunnel at DLR-Cologne.

All cascades were investigated at high Reynolds numbers (4×10^5 to 11×10^5) and low turbulence levels (Tu $\approx$ 1 percent). Although no explicit values are documented, the surface quality of the blades is presumed as hydraulically smooth.

Blade Profile Losses in Subsonic Range

The correlations for the minimum or design losses and for the off-design losses presented in this paper depend on the

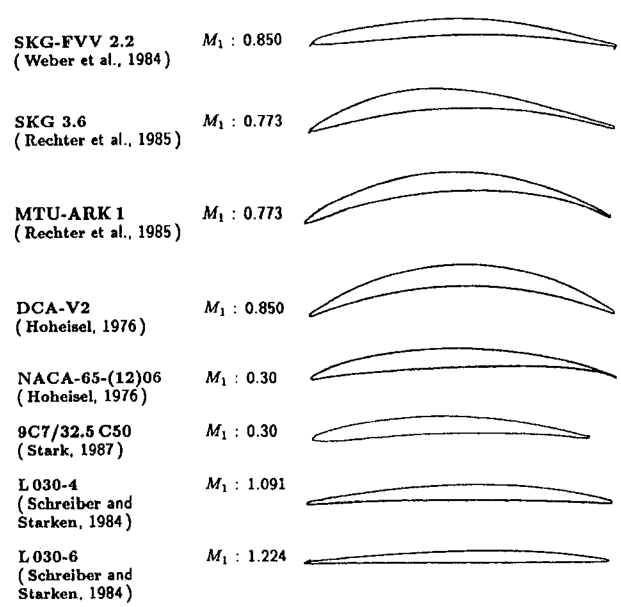

Fig. 1 Blade shapes of the cascades investigated with subsonic inlet-flow and their design Mach numbers

[1] Current affiliation: ABB Power Generation Ltd., Dept. KWDT4, CH 5400 Baden, Switzerland.

Contributed by the International Gas Turbine Institute and presented at the 39th International Gas Turbine and Aeroengine Congress and Exposition, The Hague, The Netherlands, June 13–16, 1994. Manuscript received by the International Gas Turbine Institute March 2, 1994. Paper No. 94-GT-335. Associate Technical Editor: E. M. Greitzer.

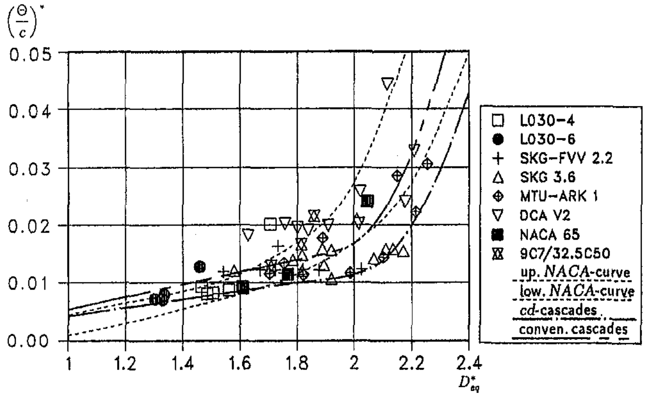

Fig. 2 Momentum loss thickness versus the equivalent diffusion ratio for cascade inlet flow with lowest pressure losses

relationship between the momentum loss thickness in the blade wake and the velocity diffusion along the suction surface of a compressor blade element. This velocity diffusion is expressed by the equivalent diffusion ratio D_{eq} for compressible, quasi-two-dimensional cascade flow as follows:

$$D_{eq} = \frac{v_{\max}}{v_2} = \frac{1}{\Omega} \cdot \frac{\rho_2}{\rho_1} \cdot \frac{\sin \beta_2}{\sin \beta_1} \cdot \frac{v_{\max}}{v_1} \quad (1)$$

Equation (1) implicits the streamtube contraction ratio Ω. The appendix summarizes the equations for the loss estimation and details the deduction of the velocity ratio on the blade suction side for cascades with various blade shapes operating in compressible flow with streamtube contraction.

Correlation for Minimum Losses. The velocity ratios on the suction surfaces of the cascade blades were first determined for incompressible cascade flows and later transformed back to compressible conditions according to the method described in the appendix. The diffusion ratios were obtained from Eq. (1). Figure 2 presents the dependency of the momentum loss thickness on the velocity diffusion for various inlet-flow Mach numbers and incidence angles causing lowest total pressure losses. Figure 14 of Lieblein et al. (1953) shows the same relationship for NACA-65 and British C4 cascades in two-dimensional, incompressible flow. The lower and upper boundary lines of his data scatter were determined and drawn into Fig. 2 as NACA curves. The bulk of the evaluated data falls in between these two boundary lines and coincides with the range of Lieblein's data. It is important to notice that the Reynolds numbers of the evaluated cascade data exceed by far the Reynolds numbers of Lieblein's data, which lay at about 2.5×10^5.

The cascades MTU-ARK1 and SKG3.6 achieve a remarkable loss reduction at higher diffusion ratios and seem to be less affected by boundary-layer separations since their values deviate distinctly from the lower NACA curve.

Lieblein (1959) succeeded in correlating the wake-momentum loss thickness to the equivalent diffusion ratio with fixed boundary-layer parameters over its entire range. Since these values vary even for one type of blade shape, and more markedly for cascades with various types of blading, this concept appears to be questionable. Consequently, two equations, each valid in a specified range of the diffusion ratio, are proposed for cascades with modern bladings.

A curve for this relationship is illustrated in Fig. 2.

$$1 \le D^*_{eq} \le 2,0 \quad : \quad \left(\frac{\Theta}{c}\right)^* = 0.0071 D^*_{eq} - 0.0029 \quad (2)$$

$$2,0 < D^*_{eq} \quad :$$

$$\left(\frac{\Theta}{c}\right)^* = 0.1786 D^{*2}_{eq} - 0.7071 D^*_{eq} + 0.7111 \quad (3)$$

Loss Estimation at Off-Design Incidence Angles. The velocity diffusion ratio at off-design incidence angles is strongly influenced by the individual blade shape of the cascade under consideration. Çetin et al. (1987), investigating loss correlations for off-design incidence angles, stated that the correlation of Swan (1961), which is limited to blade rows of DCA profiles, achieves the best comparison with measurement data of transonic axial-flow compressors. Swan's concept relates the differences of wake-momentum loss thickness to the differences of diffusion ratios:

$$\left(\frac{\Theta}{c}\right) - \left(\frac{\Theta}{c}\right)^* = K(D_{eq} - D^*_{eq})^2 \quad (4)$$

First of all, the evaluated measurement data in Figs. 3 and 4 for the cascades SKG-FVV 2.2 and MTU-ARK 1 confirm, as examples for all investigated cascades, the square-type dependency expressed by Eq. (4). Moreover, an increasing Mach number causes a rising slope of the parabolic curves, i.e., the parabolic factor K takes higher values for higher inlet-flow Mach numbers.

In order to refine Swan's correlation to comprehend cascades with arbitrary blade shapes, the parabolic factor K in Eq. (4) should incorporate the effect of the individual cascade blade

Nomenclature

c, d = constants in Eq. (5) for the K factor
c = chord length (Fig. 17)
c_A = lift coefficient (Eq. (10))
D_{eq} = equivalent diffusion ratio (Eq. (1))
K = parabolic factor in Eq. (4) for differences in wake-momentum loss thicknesses
$K_{1,2}$ = constants in Eq. (13) for velocity ratio
M = Mach number
p = static pressure
v = velocity
w_{cl} = height of camber line (Fig. 17)
w_{Seff} = effective height of blade suction surface (Fig. 7)
β = flow angle measured normal to axial direction (Fig. 17)
β_s = stagger angle (Fig. 17)
Γ' = circulation parameter (Eq. (14))
δ = deviation angle (Eq. (8))
Θ = wake-momentum loss thickness
κ = ratio of specific heats
σ = solidity, ratio of chord to spacing (Fig. 17)
ρ = mass density
$\Psi_{a,b}$ = boundary-layer parameters (Eq. (9))
ω = total-pressure-loss coefficient (Eq. (17))
Ω = streamtube contraction ratio (axial-velocity-density ratio) (Eq. (1))

Subscripts

0 = total value
1 = cascade inlet
2 = cascade outlet
∞ = mean value of the cascade inlet and outlet values
inc = incompressible
cor = determined by correlation
m = measured data
max = maximum value
v = corrected for viscous effects
ref = reference value

Superscripts

* = value for minimum losses

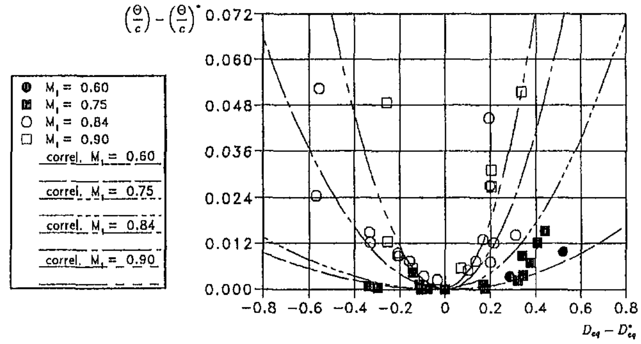

Fig. 3 Variation of wake-momentum loss thickness with equivalent diffusion ratio at off-design incidence angles for cascade SKG-FVV 2.2

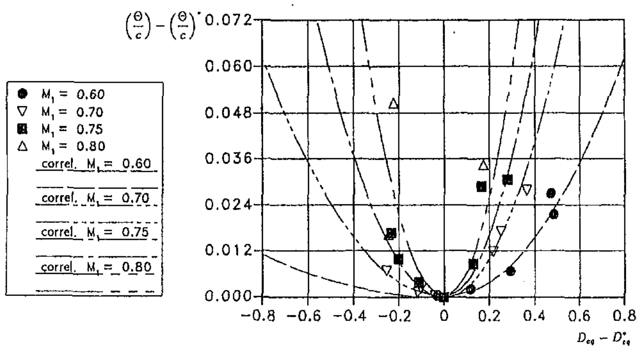

Fig. 4 Variation of wake-momentum loss thickness with equivalent diffusion ratio at off-design incidence angles for cascade MTU-ARK1

shape additionally to the inlet-flow Mach number. A sole parameter was sought to represent best the blade geometry, and it was found to be the suction side curvature of the blade shape. The following approach was taken to define its relation to the parabolic factor K:

First, values for the parabolic factor K were determined for various inlet-flow Mach numbers of all cascades. Care was taken to reduce data scatter due to measurement errors. This was accomplished by selecting measurement data having significant differences in diffusion ratios. Figures 5 and 6 show the values for the positive and negative diffusion ratios.

A cascade having a less cambered blade suction surface (MCA-blading) achieves the same value of K factor at a higher inlet-flow Mach number, as a cascade with a more cambered blade suction surface at a lower inlet-flow Mach number (DCA- or CD-blading). The K factor seems to take a certain minimum value for all cascades at low inlet-flow Mach numbers regardless

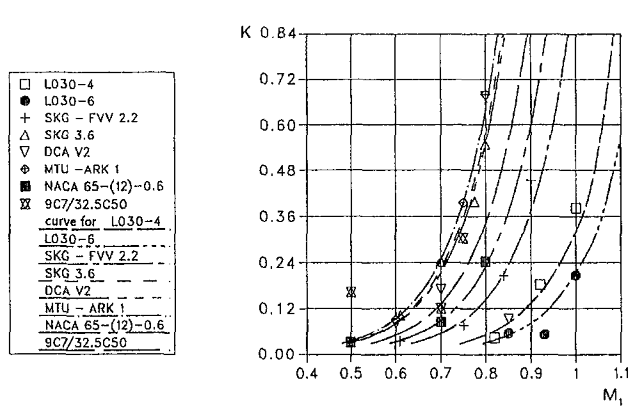

Fig. 5 Parabolic factor K versus Mach number at the cascade entrance for positive differences of diffusion ratios

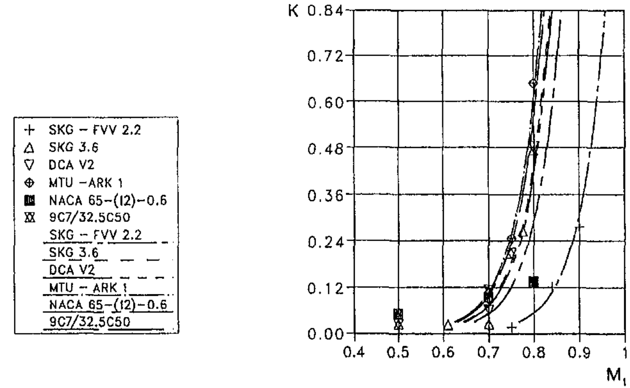

Fig. 6 Parabolic factor K versus Mach number at the cascade entrance for negative differences of diffusion ratios

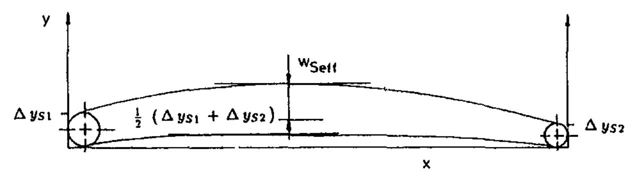

Fig. 7 Effective suction side height w_{Seff} of a blade shape

of the individual blade shape. However, the K factor rises at a particular Mach number, which depends on the blade geometry of each cascade, and it will be called in the following passages the "blade-reference-Mach number" M_{ref}. Second, an exponential function was selected to describe the parabolic factor:

$$K = c \cdot e^{d(M_1 - M_{ref})} \tag{5}$$

The constant c is the minimum value of the K factor at low inlet-flow Mach numbers and was determined to be 0.032 for the positive range of diffusion ratio differences and 0.016 for the negative range. The exponent d in Eq. (5) is a measure for the rise of the K factor and was found to be $d = 10.109$ for the positive range, and $d = 16.864$ for the negative range.

Finally, the blade-reference Mach numbers were related to the effective suction side heights w_{Seff} of the cascade blades illustrated in Fig. 7. w_{Seff} denotes the maximum camber height of the blade suction side measured from the mean values of the ordinates (y_{S1} and y_{S2}) where the suction side contour intersects with the leading edge and the trailing edge circle. Thus, it is in relation with the possible flow turning on the blade suction side.

Figure 8 indicates a linear relationship between the reference Mach number and the square root of the effective suction side

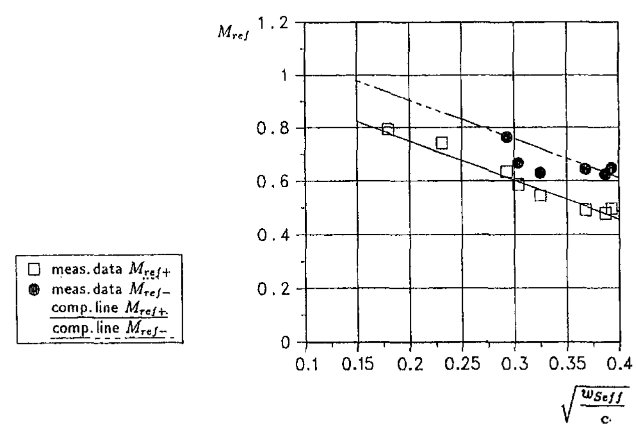

Fig. 8 Empirical relationship between the square roots of related suction side heights and blade-reference Mach numbers

height for all cascade blades. This relationship is described best by the following equations for the range of negative and positive differences of diffusion ratios:

$$\Delta D_{eq} < 0 \quad : \quad M_{ref} = -1.464\sqrt{\frac{w_{Seff}}{c}} + 1.043 \qquad (6)$$

$$\Delta D_{eq} > 0 \quad : \quad M_{ref} = -1.464\sqrt{\frac{w_{Seff}}{c}} + 1.198 \qquad (7)$$

The reference Mach numbers M_{ref} were approximated by Eq. (6) and (7) for the known effective suction side heights of all cascade blades. The K factors were determined subsequently for the inlet-flow Mach numbers. Finally, the differences of momentum loss thickness were obtained by Eq. (4) and drawn as parabolic curves into Figs. 3 and 4. As can be seen by these graphs for two cascades, the parabolic curves approach quite well the evaluated measurement data for all investigated cascades. König (1992) shows the same relationship for two more cascades.

Deviation Angles in Subsonic Range

Demand for a New Approach. Performance prediction methods commonly approximate flow angles at the blade row exits either by use of the correlation of Carter and Hughes (1946) or of Lieblein's correlation (1960). These semi-empirical relationships yield the deviation angle between the blade camber line and the outlet-flow direction instead of the real outlet-flow angle:

$$\delta = \beta_2 - \beta_{cl2} \qquad (8)$$

Since Lieblein established his correlation in the middle of the 50s, no significant improvement has been elaborated. The data sets available for the present report are equally not suited for a general revision of one of the original deviation angle correlations. In view of the capacities of modern computers, a potential blade-to-blade calculation method has become a reasonable alternative to the use of a deviation angle correlation. The singularity method presented originally by Schlichting (1955) and extended by Stark (1987) for cascade flows with streamtube contraction was selected because of its simplicity and uncomplicated applicability. Since the singularities are arranged along the blade chord instead of along the camberline, this method is restricted to compressor blades with small to medium camber ($w_{cl}/c \leq 0.15$).

Measured and Calculated Deviation Angles. The deviation angles were calculated by the modified Schlichting method, for the same cascades considered before, and compared with the corresponding measured values. The entire data set for each cascade was first categorized by the criteria of a nearly uniform Mach number at the cascade inlet and an approximately constant streamtube contraction ratio. The scatter for the Mach numbers as well as for the streamtube contraction ratios was permitted to stay within ±0.015. Each sub-data set should cover a broad range of inlet-flow angles. The camber-lines of modern blade shapes were determined by connecting the centers of circles fit in between their pressure and suction side contours.

Figures 9 to 11 present the measured and calculated deviation angles for cascades with different blade shapes but in each graph an uniform streamtube contraction ratio Ω in the range of 1.05 to 1.20. The deviation angles estimated with the original correlation of Carter and Hughes (1946) for strictly two-dimensional cascade flow are drawn into the graphs as "NGTE correlation." No influence of the cascade inlet-flow Mach number, on the curve shapes of the measured deviation angles, can be detected, at least until the critical Mach number of the cascade is reached. This result corroborates the observation made by several other authors, e.g., Stark (1987).

The streamtube contraction ratio has a weak influence on the measured as well as on the calculated results, especially for cascades with high solidities. This fact is illustrated in Fig. 9 for the cascade NACA 65-(12)06. Moreover, the difference between the measured and the calculated deviation angles obtained by the inviscid singularity method, for a specific cascade and a fixed streamtube contraction ratio, increases as expected remarkably only in the range of high positive incidence angles. At design inlet-flow angles this difference is influenced by the blade shape, as lower cambered blades have smaller differences than higher cambered blades.

The curves for the NGTE or Carter correlation, included in the figures, agree better with the measured than with the calculated deviation angles for most of the cascades. Only for cascades of the L 030-type shown in Fig. 10 do these curves approach the calculated data. While the curves for the Carter correlation compare quite well with the measured deviation angles of cascade SKG-FVV 2.2 in Fig. 11, they exceed the measured values of the cascades MTU-ARK 1 and SKG 3.6 by nearly 3 deg. For this reason, Carter's correlation, which neglects any streamtube contraction effects, seems to be not suited for cascades with highly cambered modern blade shapes.

In contrast, the modified Schlichting method yields deviation angles that are generally smaller than the measured values and, thus, afford a correction for viscous effects and for the arrangement of the singularities.

Influence of Surface Friction. Although the deviation angles increase slightly more in the range of positive than in the range of negative incidence angles (Fig. 11 for cascade SKG-FVV 2.2), this effect was neglected and only the deviation

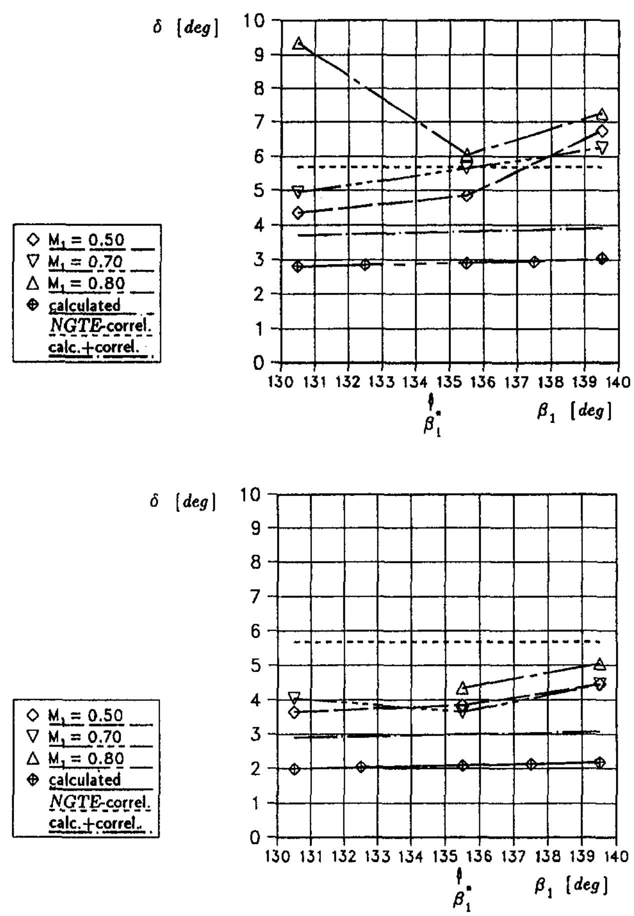

Fig. 9 Deviation angles of cascade NACA 65-(12)06 versus cascade inlet-flow angles β_1 for the streamtube contraction ratios Ω = 1.05 (top) and Ω = 1.20 (bottom)

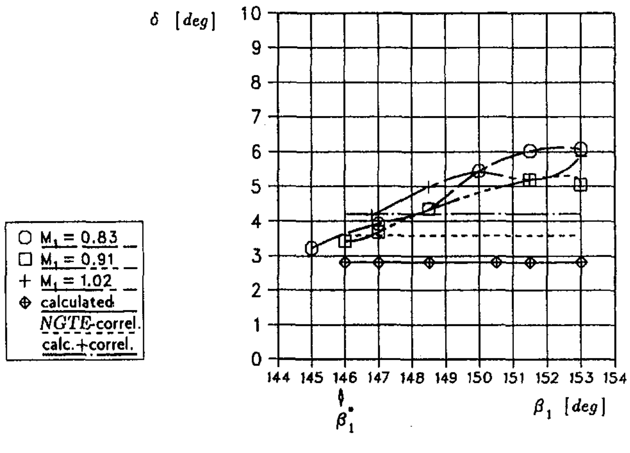

Fig. 10 Deviation angles of cascade L 030-4 versus cascade inlet-flow angles β_1 for the streamtube contraction ratio $\Omega = 1.13$

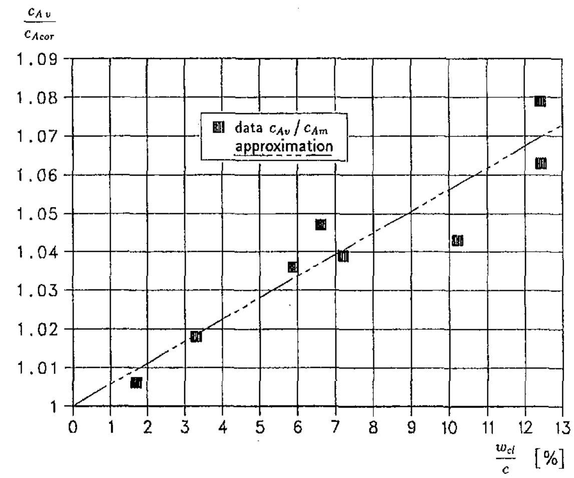

Fig. 12 Ratios of calculated and measured lift coefficients c_{Av}/c_{Am} versus heights of the camberlines related to chord-lengths w_{cl}/c

angles for minimum losses were considered. A mixing calculation with boundary-layer parameters at the trailing edges of flat-plate cascades is proposed in order to quantify losses approximately by surface friction and wake mixing downstream of the cascades. According to Scholz (1965), the momentum equations in axial direction and normal to axial direction were formulated for the wake region of the cascades. Finally, they yielded the outlet-flow angle β_2 for a uniformly mixed-out flow at a distance of about one chord length downstream of the cascade exit. As Gustafson (1975) proposes, the portion of the streamtube contraction ratio for the wake region was estimated to be 20 percent of its total value. The outlet-flow angle β_{2v} for the mixed-out, viscous flow was computed as follows:

$$\cot \beta_{2v} = \frac{1}{\Omega^{0.2}} \cdot \frac{1 - \Psi_a - \Psi_b}{(1 - \Psi_a)^2} \cdot \cot \beta_2 \tag{9}$$

The index v symbolizes the viscous effects of the wake flow. The boundary-layer parameters, Ψ_a and Ψ_b, which were introduced by Scholz (1965), include the displacement thickness and the wake-momentum loss thickness. These values were computed first for flat plates with plate thicknesses corresponding to the diameters of the trailing-edge circles of the blade shapes. The cascade flow was assumed to be incompressible and turbulent and to have a velocity distribution in the boundary-layers according to the "1/7"-power-law.

Second, the values Ψ_a and Ψ_b were computed by use of the correlation of Koch and Smith (1976). Since the results of both methods differed at maximum by 0.3 deg and for most of the considered cascades less than 0.1 deg, the relations for flat-plates were applied to the new model.

Influence of Camberline. The arrangement of the singularities along the blade chord by the Schlichting method leads in fact to more of an overestimation of the velocities at the suction side surfaces the larger the camber angle of the cascade blades is. Thus, the outlet-flow angles, obtained by the Schlichting method and corrected first to account for viscous effects, require a second correction. This can be accomplished by a correlation for the lift coefficients due to the camberline heights. For this reason, the lift coefficients c_A for the cascade geometries were determined with the measured outlet-flow angles as well as with the calculated and corrected outlet-flow angles by the following equations with respect to the angle convention (Fig. 17):

$$c_A = \frac{2}{\sigma} \sin \beta_\infty \cdot \left(\frac{2}{1 + \Omega} \cdot \frac{\rho_\infty}{\rho_1} \cot \beta_1 \right) - \frac{2}{\sigma} \sin \beta_\infty \cdot \left(\frac{2\Omega}{1 + \Omega} \cdot \frac{\rho_\infty}{\rho_2} \cot \beta_2 \right) \tag{10}$$

The mean angle β_∞ is defined as follows:

$$\cot \beta_\infty = \frac{\cot \beta_1 + \Omega \dfrac{\rho_1}{\rho_2} \cot \beta_2}{1 + \Omega \dfrac{\rho_1}{\rho_2}} \tag{11}$$

When the solidity σ, the inlet-flow angle β_1, and the lift coefficient c_A are given, Eqs. (10) and (11) yield the unknown outlet-flow angle β_2. The ratios of the calculated to the measured lift coefficients c_{Av}/c_{Am} were subsequently set up and drawn into Fig. 12 versus the heights of the camberlines related to the chord-lengths w_{cl}/c.

The following equation was found for a line that approximates the lift ratios best:

$$\frac{c_{Av}}{c_{A\text{cor}}} = 1 + 0.562 \frac{w_{cl}}{c} \tag{12}$$

Finally, the computed outlet-flow angles, which had been previously corrected for viscous effects, were now corrected by use of relationship (12). The angles obtained are drawn into Figs. 9 to 11 as "calculated and corrected" curves. They differ at maximum from the measured data by twice the value of the measurement inaccuracy, which is assumed to be 0.3 deg.

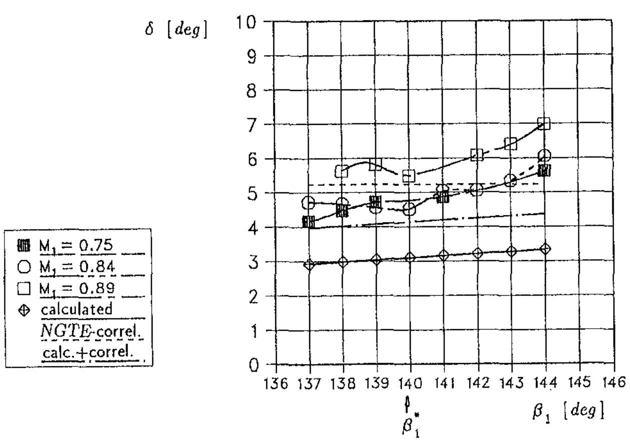

Fig. 11 Deviation angles of cascade SKG-FVV 2.2 versus cascade inlet-flow angles β_1 for the streamtube contraction ratio $\Omega = 1.10$

Application of the New Model

In order to demonstrate the accuracy and the reliability of the new correlation model, it was compared with the correlation

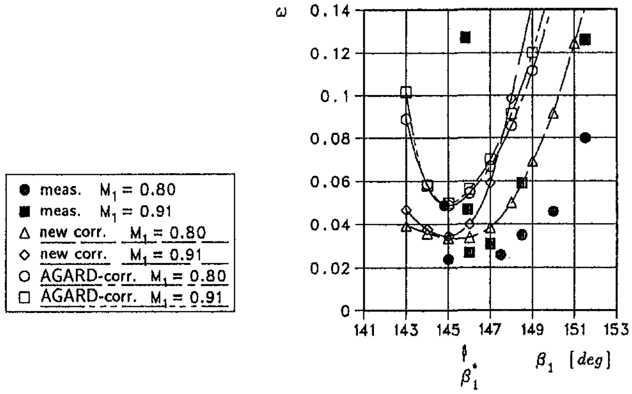

Fig. 13 Total-pressure losses of cascade L 030-4 in compressible subsonic flow

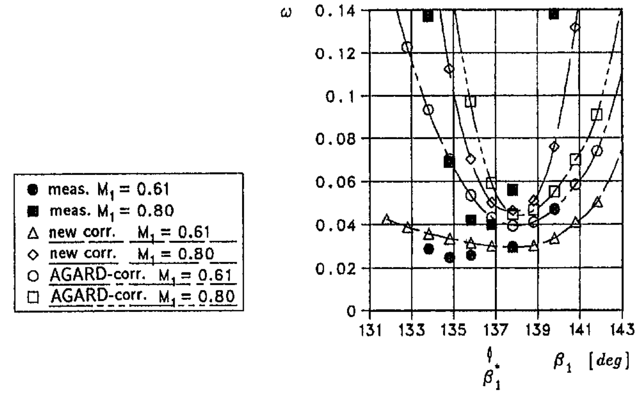

Fig. 15 Total-pressure losses of cascade SKG 3.6 in compressible subsonic flow

model of Çetin et al. (1987) established on the basis of transonic compressor measurement data and the cascade data itself. The correlations of Çetin et al. (1987) will be called in the following sections AGARD correlations with regard to their first publication. Two features especially suit them for a comparison with the new model:

First, they were established on the basis of data from rig compressors instead of cascade data. These NASA and Pratt & Whitney rig compressors were designed with DCA and MCA bladings during the 70s.

Second, the flow mechanisms are interpreted differently by this model in comparison to the new model. The authors expect cumulative effects to take place in the flow fields of transonic turbomachinery. For this reason, they combine the flow mechanisms at off-design conditions, and treat the blade losses, shock losses, and secondary-flow losses as a unit. In contrast, the new model leans on the assumption of their additive superposition, which allows their separate computation.

Incidence Angle Correlation. The AGARD model determines the incidence angles at minimum losses with the correlation of Lieblein (1960), which was modified to reflect Mach number influences observed in compressor flow fields. Since these effects could not be proved for the evaluated cascade data, this modification was removed again. By adding the specific factors for cascades with NACA-65 or British C-type bladings, the original incidence angle correlation of Lieblein was restored. Although this correlation refers to strictly two-dimensional cascade flow, it had to be used for the new correlation model. However, it should be emphasized that it is not able to reflect any effects of streamtube contraction.

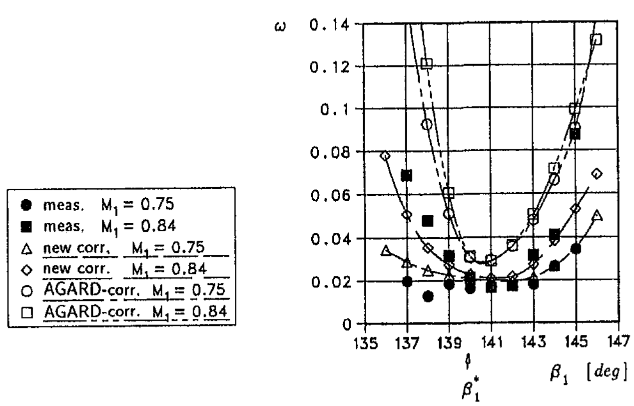

Fig. 14 Total-pressure losses of cascade SKG-FVV 2.2 in compressible subsonic flow

Lieblein (1960) established his correlation with measurement data of cascades with 10 percent thick NACA-65 blade shapes. He introduced two special factors, $(K_i)_{sh}$ and $(K_i)_t$, to apply his correlation to cascades with DCA bladings and to cascades with other maximum thicknesses than the 10 percent value related to the chord length. Now the question arose how to define appropriately the values for those cascades considered in the present paper that are outside the scope of Lieblein's correlation, i.e., the cascades with controlled diffusion bladings, SKG-FVV 2.2 and SKG 3.6 and the cascade MTU-ARK 1. This aspect is discussed in full length by König (1992).

Since the thickness distributions of these blade shapes are apparently more similar to the thickness distributions of NACA-65 profiles than of DCA profiles, the factor $(K_i)_{sh}$ was set to unity. The factor for the correction of the maximum thickness, $(K_i)_t$, was chosen for cascade SKG-FVV-2.2 from the relationship for NACA-65-blades and for the other two cascades from the relationship for DCA-profiles. The incidence angles for minimum losses calculated by this method exceed by 1.5 deg the angles measured for cascade SKG 3.6 in Fig. 15 as well as for cascade MTU-ARK 1. In contrast, good comparison was achieved for cascade SKG-FVV 2.2.

Measurement and Calculation. Both the AGARD model and the new model require necessarily detailed information about the cascade outlet-flow angels before the subsonic cascade losses can be calculated. The authors of the AGARD model just adapted the relationship for the minimum loss case outlined by Carter and Hughes (1946) to their available compressor data. Since a previous chapter broadly compared the calculation method of the new model with the original correlation of Carter and Hughes, only the most important results obtained with the AGARD model are mentioned here.

The modified NGTE correlation incorporated in the AGARD model clearly overestimates the deviation angles and yields overly high cascade outlet-flow angles. Since it includes only the factor for circular arc camberlines, this overestimation is evident especially for bladings with remarkably different camberlines as outlined by König (1992).

Comparison of Total Pressure Losses. Both models treat separately minimum losses and off-design losses with different correlations. Figures 13–16 present the calculated and the measured losses for the highest and lowest Mach numbers, which had been adjusted during the wind-tunnel investigations of each cascade. The measured data are distinguished in the graphs by filled symbols, while the calculated values are connected with *spline* curves. The minimum or design pressure losses are predicted by both models for the major part of the investigated cascades in good accordance with the measured losses. For the cascade L 030-4 in Fig. 13, the AGARD model yields values

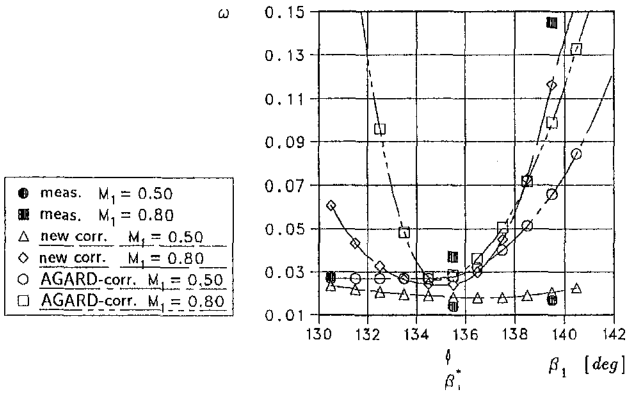

Fig. 16 Total-pressure losses of cascade NACA-65-(12)06 in compressible subsonic flow

that lie remarkably above the measured data. The explanation for this difference is clearly seen by analyzing the basis of the correlation of Koch and Smith (1976).

This correlation, which is used by the AGARD model, presumes a velocity distribution of the rooftop type for the calculation of the suction side boundary-layers. The salient point is that such a velocity distribution is more typical for controlled diffusion blades at high subsonic Mach numbers than for supersonic blades like the MCA-type blades of the L 030 cascades.

The correlation presented by Koch and Smith overestimates the minimum pressure losses for these cascades. In the off-design range the AGARD model achieves at lower Mach numbers too strong increases for the total pressure losses for both positive and negative incidence angles. In contrast, the predicted results compare satisfactorily for higher Mach numbers with the measurement data. The new model treats the spread of the loss curves due to the inlet-flow Mach numbers correctly. Even for negative incidence angles at low inlet-flow Mach numbers an accurate increase of the losses is predicted. However, chocking occurs with rising velocities at the inlets of the L 030 cascades and limits the range of negative incidence angles (Fig. 13).

While the off-design loss correlation of the AGARD-model yields an almost correct loss increase when the chocking limit is approached, the new model requires an additional equation to match this situation.

The conclusion can be drawn that the AGARD-model achieves correct total pressure losses at off-design incidence angles and high subsonic Mach numbers for cascades with a DCA or MCA blading. But on the other hand, it overestimates the minimum or design pressure losses for cascades with these blading types. The new model estimates the total pressure losses for the design and the off-design case in good accordance with the measurement data independent of the cascade blade shapes and the inlet-flow Mach numbers. The reliability of the new model for the loss prediction at transonic and supersonic speeds is presented in the second part of this report.

Conclusions

The scope of proved and well-established loss correlations for compressor cascades in subsonic flows is extended to match the requirements of application to compressors with modern blade designs and typical turbomachinery flow conditions. A simple singularity method is proposed to estimate the cascade deviation angles instead of a correlation. The correlations and the singularity method are combined with a well-known incidence angle correlation to form a new correlation model. This model is demonstrated to be superior in comparison to a recently published model referring to older blade designs.

An important result of the investigations is the statement that the accuracy of the pressure losses at off-design conditions depends significantly not only on the reliability of the off-design loss correlation but on the quality of the selected incidence angle, deviation angle, and even on the selected design loss correlation. Thus, the four correlations necessary for the loss estimation in subsonic cascade flow, have to be looked upon as a whole system. A revision of a single correlation, for example of the design loss correlation, leads probably only to a poor improvement if the other influencing correlations are not accordingly adapted.

Acknowledgments

The authors wish to thank H. Starken and H. A. Schreiber from DLR Köln as well as H. Hoheisel from DLR-Braunscweig and U. Stark from T. U. Braunschweig for providing extensive measurement data and the kind permission for publication.

References

Carter, A. D. S., and Hughes, H. P., 1946, "A Theoretical Investigation Into the Effect of Profile Shape on the Performance of Aerofoils in Cascade," A. R. C. Rep. and Mem. No. 2384.

Çetin, M., Uçer, A. S., Hirsch, Ch., and Serovy, G. K., 1987, "Application of Modified Loss and Deviation Correlations to Transonic Axial Compressors," AGARD Report No. 745.

Gustafson, B. A., 1975, "A Simple Method for Supersonic Compressor Cascade Performance Prediction," Chalmers Univ. of Techn., Dept. for Turbomachinery; also ASME Paper No. 76-GT-64.

Hoheisel, H., 1976, "Ergebnisse der Untersuchungen an ebenen Verdichterschaufelgittern in kompressibler Unterschallströmung bei Variation der axialen Stromdichte," VDI-Bericht No. 264, VDI-Verlag, Düsseldorf, Germany.

Hoheisel, H., and Seyb, N. J., 1986, "The Boundary Layer Behaviour of Highly Loaded Compressor Cascades at Transonic Flow Conditions," AGARD Conference Proceedings 401, pp. 4.1–4.17.

Koch, C. C., and Smith, L. H., Jr., 1976, "Loss Sources and Magnitudes in Axial-Flow Compressors," ASME *Journal of Engineering for Power*, Vol. 98, pp. 411–424.

König, W. M., 1992, "Korrelationen für die Kennfeldrechnung transsonischer Axialverdichter," *Fortschrittberichte VDI*, Reihe 7, No. 217, VDI-Verlag, Düsseldorf, Germany.

Lieblein, S., Schwenk, F. C., and Broderick, R. L., 1953, "Diffusion Factor for Estimating Losses and Limiting Blade Loadings in Axial-Flow Compressor Blade Elements," NACA RM E53D01.

Lieblein, S., 1957, "Analysis of Experimental Low-Speed Loss and Stall Characteristics of Two-Dimensional Compressor Blade Cascade," NACA RM E57A28.

Lieblein, S., 1959, "Loss and Stall Analysis of Compressor Cascades," ASME *Journal of Basic Engineering*, Vol. 81, pp. 387–400.

Lieblein, S., 1960, "Incidence and Deviation-Angle Correlations for Compressor Cascades," ASME *Journal of Basic Engineering*, Vol. 82, pp. 575–587.

Miller, D. C., and Wright, P. I., 1991, "An Improved Compressor Performance Prediction Model," Institute for Mechanical Engineering, Pap. 432/028, London.

Rechter, H., Steinert, W., and Lehmann, K., 1985, "Comparison of Controlled Diffusion Airfoils With Conventional NACA-65 Airfoils Developed for Stator Blade Application in a Multistage Axial Compressor," ASME *Journal of Engineering for Power*, Vol. 107, pp. 494–498.

Schlichting, H., 1955, "Berechnung der reibungslosen, inkompressiblen Strömung für ein vorgegebenes ebenes Schaufelgitter," *VDI-Forschungsheft*, Vol. 447, VDI-Verlag, Braunschweig, Germany.

Scholz, N., 1965, *Aerodynamik der Schaufelgitter I*, Verlag G. Braun, Karlsruhe, Germany.

Schreiber, H. A., and Starken, H., 1984, "Experimental Cascade Analysis of a Transonic Compressor Rotor Blade Section," ASME *Journal of Engineering for Power*, Vol. 106, pp. 288–294.

Stark, U., 1987, "Ebene Verdichtergitter in quasi-zweidimensionaler Unterschallströmung," *VDI-Forschungsheft*, No. 641/87, VDI-Verlag, Braunschweig, Germany.

Swan, W. C., 1961, "A Practical Method for Predicting Transonic-Compressor Performance," ASME *Journal of Engineering for Power*, Vol. 83, pp. 322–330.

Weber, A., Rechter, H., and Starken, H., 1984, "Entwicklung eines Entwurfsverfahrens für verlustarme superkritische Verdichtergitter," *FVV-Vorhaben*, No. 266, Heft 344-2, Germany.

APPENDIX

Extended Diffusion Concept

The diffusion concept established by Lieblein (1953, 1957) was extended in order to apply it to cascades with arbitrarily designed blade shapes operating in compressible flow with

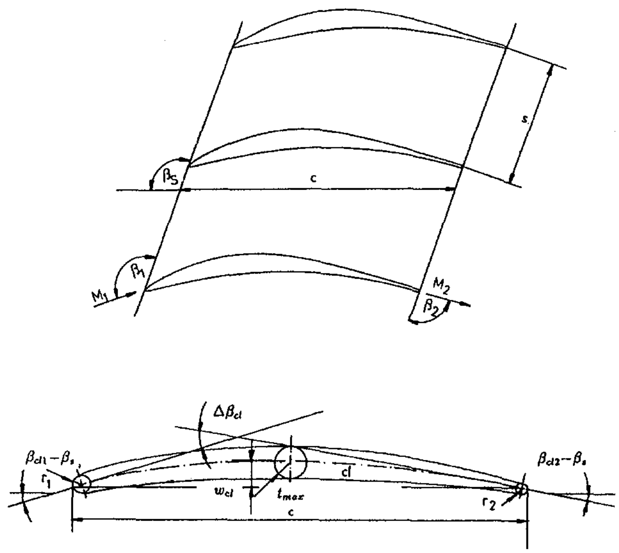

Fig. 17 Cascade and blade element nomenclature and sign conventions

streamtube contraction. Figure 17 illustrates the definition of the flow angles and the notation selected for this paper.

The equivalent diffusion ratio D_{eq} in Eq. (1) is expressed with use of the maximum velocity on the blade suction surfaces related to the velocity at the cascade inlet $v_{\max}/v_1$. Since this ratio is usually unknown particularly at the time of a performance calculation, it has to be determined by correlation. König (1992) analyzes in full length the velocity ratios of the cascades considered in this paper at various inlet-flow Mach numbers and incidence angles at design and off-design conditions. After he had transformed the geometric and the aerodynamic parameters of the cascade data by the Prandtl–Glauert rule, and the velocities by the Kármán–Tsien rule to incompressible flow conditions, he confirmed the dependency of the related maximum velocities on Lieblein's circulation parameter. Cascades with stronger cambered blades, especially older profile types, still corroborate the validity of the linear relationship deduced by Lieblein (1957):

$$\left(\frac{v_{\max}}{v_1}\right)^*_{\text{inc}} = K_1 + K_2 \cdot \Gamma'_{\text{inc}} \tag{13}$$

The constants $K_1 = 1.12$ and $K_2 = 0.61$ take the same values as found by Lieblein (1957).

The circulation parameter Γ'_{inc} at design conditions is defined as follows:

$$\Gamma'_{\text{inc}} = \frac{2}{\sigma} \sin^2 \beta_1^* \left(\Omega \frac{\rho_1}{\rho_2} \cot \beta_2^* - \cot \beta_1^* \right) \tag{14}$$

In contrast to this linear dependency, a parabolic relation was detected for the transformed velocity ratios of cascades with blade profiles having less cambered suction sides at the front portions, i.e., cascades of MCA-type or controlled diffusion bladings, in the range of $\Gamma^*_{\text{inc}} \leq 0.2$:

$$\left(\frac{v_{\max}}{v_1}\right)^*_{\text{inc}} = -1.180\Gamma^{*2}_{\text{inc}} + 1.446\Gamma^*_{\text{inc}} + 1.000 \tag{15}$$

In the off-design range both the linear and the parabolic relationships are shifted due to the incidence angle as found by Lieblein, according to the term $a \cdot (\beta - \beta^*)^b$. The two constants $a = 0.0117$ and $b = 1.43$ for cascades with NACA-65 profiles proved to be valid for all cascade bladings under consideration.

After the value for the velocity ratio $(v_{\max}/v_{1\text{inc}})$ in incompressible cascade flow had been determined, it was transformed back to the real compressible flow situation. The relationship between the momentum thickness in the wakes and the total-pressure losses is derived according to Lieblein (1957) for compressible, quasi-two-dimensional flow:

$$\frac{\Theta}{c} \approx \frac{\omega}{2} \cdot \frac{1}{\Omega^2} \cdot \frac{1}{\sigma} \cdot \frac{\sin^3 \beta_2}{\sin^2 \beta_1} \cdot \frac{\rho_2}{\rho_1} \left(1 + \frac{\kappa - 1}{2} M_2^2 \right)^{1/(1-\kappa)} \tag{16}$$

with ω defined as the total-pressure loss coefficient:

$$\omega = \frac{p_{o1} - p_{o2}}{p_{o1} - p_1} \tag{17}$$

W. M. König[1]

D. K. Hennecke

Department of Flight Propulsion,
Technical University of Darmstadt,
Darmstadt, Federal Republic of Germany

L. Fottner

Institute for Jet Propulsion,
German Armed Forces University of Munich,
Neubiberg, Federal Republic of Germany

Improved Blade Profile Loss and Deviation Angle Models for Advanced Transonic Compressor Bladings: Part II—A Model for Supersonic Flow

New blading concepts as used in modern transonic axial-flow compressors require improved loss and deviation angle correlations. The new model presented in this paper incorporates several elements and treats blade-row flows having subsonic and supersonic inlet conditions separately. The second part of the present report focuses on the extension of a well-known correlation for cascade losses at supersonic inlet flows. It was originally established for DCA bladings and is now modified to reflect the flow situation in blade rows having low-cambered, arbitrarily designed blades including precompression blades. Finally, the steady loss increase from subsonic to supersonic inlet-flow velocities demonstrates the matched performance of the different correlations of the new model.

Introduction

For several years blade shapes for advanced axial-flow compressors have been designed individually to match specific inlet-flow conditions and to exchange energy with reduced pressure losses. Bladings for the supersonic flow range have extremely low curvature in the front region of the suction side to reduce the strength of compression shocks at cascade entrance and to lower the risk of a shock induced boundary-layer separation. The wedge-type blade shapes designed by Fottner and Lichtfuss (1983), or the extreme case of precompression blade with even a concave shape investigated by Tweedt et al. (1988) show this design trend.

Since the supersonic cascade flow with these blade shapes is remarkably different from the flow situation in cascades having older bladings, a well-conditioned shock-loss model has to be established. The simple shock-loss model of Miller et al. (1961), which is still in widespread use, predicts shock losses of bladings with older DCA blade shape with good agreement with measurement data. Investigations of blade rows with modern profile types detect the shortcomings and the oversimplification of this model to describe accurately the real flow characteristics and to yield reliable shock losses for modern bladings.

However, when comparing shock-loss models published in the available literature, the two-shock model of Gustafson (1975) simulated best the actual flow situation at supersonic cascade inlet flow. Although Gustafson established his two-shock model for cascades having DCA bladings, his model was taken as a basis, which was revised for the application to advanced supersonic compressor blade rows with low-cambered or concave blade shapes.

Experimental Data Base

Measurement data sets from eight cascades with various supersonic blade shapes were evaluated to modify the original two-shock model of Gustafson. Figure 1 shows the profile shapes of the investigated cascades together with their design Mach numbers. König (1992) presents the geometries and the aerodynamic parameters of these cascades and reports briefly the design goals.

All cascades were investigated in the transonic cascade wind-tunnel facility of DLR-Cologne with the exception of cascade ARL-2 DPC. Since the design inlet-flow Mach number of this cascade lies in a higher range, its measurement data were taken in the supersonic cascade wind-tunnel facility of the same organization and are partly documented by Tweedt et al. (1988). A portion of the measurement data of the two L 030-cascades described by Schreiber (1988) was used in the first part of this paper. The three cascades of the MTU series with wedge-type profiles are presented by Fottner and Lichtfuss (1983).

Schlieren pictures allowed a qualitative assessment of the cascade flow characteristics. These pictures were available in addition to the pressure distributions for all cascades but the cascades DCA-A3 and MCA-A4, which represent two blade sections of the rotor blade designed by Weyer and Strinning (1974). Nevertheless, the number and the positions of the shock waves occurring at these cascades could be reconstructed with acceptable accuracy by use of their pressure distributions. The existence of two compression shocks, one standing at the entrance of the blade passage and the other one positioned close to its exit, could be clearly detected for all investigated cascades.

Modified Two-Shock Model

Gustafson (1975) simplified the complex flow situation for cascades with DCA blade shape operating close to their design point. He observed two compression shocks and a completely separated boundary layer on the blade suction side between both shock waves. In order to emphasize clearly the modifications explained below, the main features of the original two-shock model should be briefly recalled:

- deceleration of the cascade inlet-flow by an oblique shock-wave, which is detached from the (blunt) blade leading edge
- supersonic acceleration along the (convex) blade suction side from the leading edge to the entrance of the blade passage

[1] Current affiliation: ABB Power Generation Ltd., Dept. KWDT4, CH 5400 Baden, Switzerland.

Contributed by the International Gas Turbine Institute and presented at the 39th International Gas Turbine and Aeroengine Congress and Exposition, The Hague, The Netherlands, June 13–16, 1994. Manuscript received by the International Gas Turbine Institute March 2, 1994. Paper No. 94-GT-336. Associate Technical Editor: E. M. Greitzer.

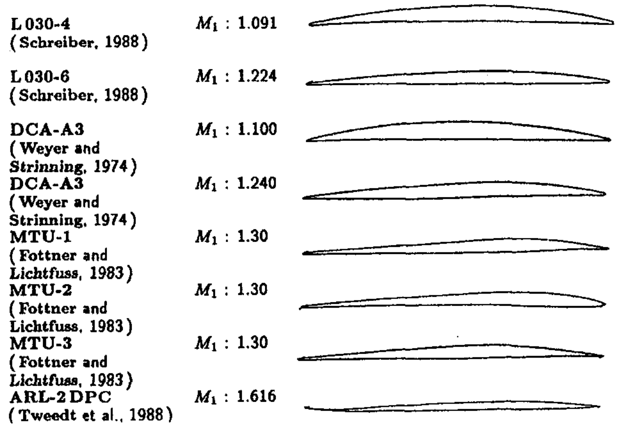

Fig. 1 Blade shapes of the cascades investigated with supersonic inlet-flow and their design Mach number

- first normal shock standing in front of the blade passage with the shape of a λ shock being the result of a strong interaction with the suction side boundary layer
- entire separation of the suction side boundary layer from the blade passage entrance to the trailing edge; the displacement of the passage flow leads to an acceleration back to supersonic velocities
- deceleration of the passage flow to subsonic velocities by a second normal shock located close to the exit of the blade passage
- mixing out of the detached boundary layer and the passage flow, which is regarded as inviscid downstream of the cascade exit

The most important characteristic of the original two-shock model is the assumption of a boundary-layer separation at the blade suction side downstream of the passage shock, since the static pressure is presumed to remain constant in the blade passage. Whereas this effect applies to cascades with blades having a strongly curved front region of the suction side, especially the older DCA blades, the design of modern supersonic cascades tends to avoid this boundary-layer separation at design point operation. The pressure distributions of the cascades investigated in this paper indicate no extended regions with constant static pressure along the blade suction side with the exception of the data of cascade DCA-A3. Cascade ARL-2 DPC is the only cascade that shows an oblique shock at the entrance of the blade passage. The first shock of all the other cascades is a normal shock having a λ shape, which strongly influences the suction side boundary layer with increasing inlet-flow Mach numbers.

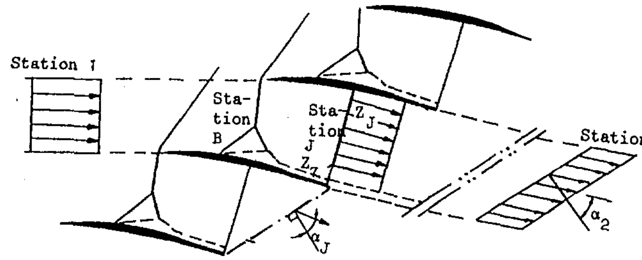

Fig. 2 Simplified flow situation of the modified two-shock model

The two-shock model had to be modified in several aspects to be applicable to supersonic compressor cascades with modern blade shapes. Since the leading edge of these blades is extremely thin, the detachment of the oblique shock ahead of it was neglected. A normal shock with at most a local boundary-layer separation at the blade passage entrance was presumed for cascades with wedge-type blades or low-cambered MCA blades. The first shock in a cascade with precompression blades was assumed to be formed as an oblique shock. Since only local separation regions were presumed to occur, the static pressure along the blade suction side varied along the blade passage. The mixing relation of the original two-shock model is still used, but the assumption for the flow angle at the blade passage exit had to be changed. Figure 2 shows the features of the modified two-shock model.

Equations for the Modified Two-Shock Model

First Shock Wave for Cascades With MCA and Wedge-Type Profiles. The shift of the stagnation streamline and the associated change of the inlet-flow Mach number ahead of the cascade entrance was neglected for supersonic compressor cascades with thin leading edges. Thus, a mean Mach number M′ upstream of the first shock wave was obtained from the inlet-flow Mach number M_1 and the Mach number $M_{B'}$ at the suction surface ahead of the shock wave:

$$M' = \frac{1}{2}(M_1 + M_{B'}) \tag{1}$$

The position x_B/c of the blade passage entrance and, thus, of the first shock wave was approximated using the cascade solidity σ and the stagger angle β_s:

$$\frac{x_B}{c} = -\frac{1}{\sigma}\cos\beta_s \tag{2}$$

If the front part of the suction side is curved, the incoming flow changes its direction from the leading edge to the position B at the cascade entrance by an angle Θ:

$$\Theta = \beta_1 - \beta_s - \gamma_B \tag{3}$$

Nomenclature

A = cross section of flow path
c = chord length
C_{ar} = constant in Eq. (10) for cross-sectional ratios
M = Mach number
p = static pressure
P_c = correction factor in Eq. (5) for static pressure rise over shock wave
s = spacing
T = static temperature
x = coordinate in chord direction
Z = width of blade passage (Fig. 2)
Z_δ = boundary-layer thickness at cascade exit (Fig. 2)
α_J = flow direction at cascade exit (Fig. 2)
β = flow angle measured from tangential direction
β_s = stagger angle
γ = angle between a tangent to the blade contour and chord line (Eq. (3))
Θ = flow turning along front part of suction side (Eq. (3))
κ = ratio of specific heats
ν = angle of Prandtl–Meyer function
σ = solidity, ratio of chord to spacing
ω_s = shock-loss coefficient
Ω = streamtube contraction ratio (axial-velocity-density ratio)

Subscripts

0 = total value
1 = upstream of cascade inlet
2 = downstream of cascade outlet
B = position of first shock wave
D = pressure side
J = position of second shock wave
S = suction side

Superscripts

′ = just upstream of shock wave
″ = just downstream of shock wave

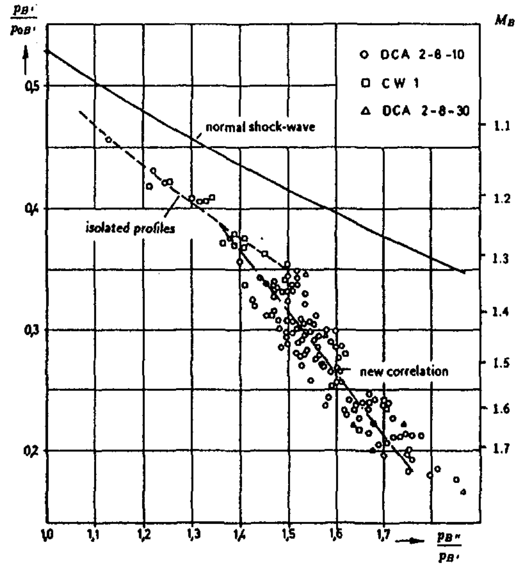

Fig. 3 Static pressure ratios over a compression shock interacting with a surface boundary layer (Starken, 1971)

The angle γ_B between a tangent to the suction side shape at position B and the chord direction is determined immediately for blade geometries specified in detail. Otherwise, it can be calculated with help of a substitute profile geometry if the blade shape is only approximately known as reported by König (1992). The Prandtl–Meyer angle ν_1 for a given inlet-flow Mach number M_1 was calculated at first with the well-known Prandtl–Meyer function. Afterward this function yielded by iteration the Mach number $M_{B'}$ at the root of the shock wave for the angle ν_B:

$$\nu_B = \nu_1 + \Theta \tag{4}$$

The static pressure ratio over the first shock-wave was correlated with the Mach number $M_{B'}$ at the suction surface ahead of the shock wave with use of Fig. 3. Starken (1971) observed an incipient separation when the local upstream Mach number $M_{B'}$ exceeded the value of 1.27. When its value lay below the observed limit Mach number of 1.27 for a local boundary-layer separation, the relationship found by Sinnot for single aerofoils was chosen. In contrast, a relationship based on the cascade data of Starken was deduced for local Mach numbers in the range of 1.27 to 1.60.

The extension of the shock-induced separation zone remains small in this region and lies in the order of magnitude of several lengths of the upstream boundary-layer thickness (Delery and Marvin, 1986). For this reason, a correction factor P_c was introduced into the equation for the normal shock to reflect the weakening of the static pressure rise by the shock–boundary-layer interaction:

$$\frac{p_{B''}}{p_{B'}} = 1 + \frac{2\kappa}{\kappa + 1}(M_{B'}^2 - 1)\cdot P_c \tag{5}$$

Evidently, this correction factor P_c varies with the upstream Mach number in the range $1.0 \leq M_{B'} \leq 1.6$ according to the equation:

$$P_c = -0.5\cdot(M_{B'} - 1) + 0.64 \tag{6}$$

The equations for a normal shock wave were used to calculate the total pressure ratio $p_{0B''}/p_{0B'}$ over the shock wave and the downstream Mach number $M_{B''}$, while the mean Mach number M' was taken for the Mach number ahead of the shock wave.

First Shock Wave for Precompression Blades. Cascades with precompression blades, i.e., blades with a concave shape of the suction side from the leading edge to the blade passage entrance, reduce the strength of the first compression shock by nearly isentropic compression wave fans. This effect was reflected by a change of the inlet-flow direction ahead of the first shock wave as follows:

$$\Theta = \beta_1 - \beta_S - 2\gamma_{1S} \tag{7}$$

The Schlieren pictures of cascade ARL-2 DPC investigated by Tweedt et al. (1988) show clearly an oblique shock wave instead of a normal shock wave standing at the entrance of the blade passage. Preliminary calculations assuming a normal shock wave resulted in loss values for only the first shock wave, which exceeded even the measured total losses of the cascades. These two indications suggested the assumption of an oblique shock wave at the blade passage entrance for cascades with precompression blades. After the static pressure ratio had been determined by Eqs. (5) and (6), the unknown angle of shock obliquity ϑ, the total pressure ratio $p_{0B''}/p_{0B'}$ over the shock wave and, finally, the Mach number behind the oblique shocks $M_{B''}$ were computed with the equations for oblique shocks.

The first compression shock turns the flow by an angle δ toward the suction surface. A second oblique shock wave aligns it parallel to the surface again. Generally, since the second shock is weaker than the first shock wave, its corresponding total-pressure losses and changes in Mach number can be neglected.

The pressure ratio $p_{0B''}/p_{B''}$ behind the first shock wave can be expressed for cascades of all blade shapes by:

$$\frac{p_{0B''}}{p_{B''}} = \frac{p_{0B''}}{p_{0B'}}\cdot\frac{p_{B'}}{p_{B''}}\cdot\frac{p_{0B'}}{p_{B'}} \tag{8}$$

Blade Passage Flow. In contrast to the original two-shock model by Gustafson, no separation of the boundary layer on the suction side of the blades and, thus, no constant static pressure inside the blade passage was presumed. Since the passage flow was regarded as isentropic, the total pressure remains constant:

$$p_{0J'} = p_{0B''} \tag{9}$$

Since a second compression shock wave close to the exit of the blade passage occurs, the blade passage flow, which had reached subsonic velocities, must have been reaccelerated back to supersonic velocities. The thickening of the boundary layer as the result of the shock–boundary-layer interaction explains this acceleration. The modified two-shock model treats separately passage flows with subsonic and with supersonic inlet conditions. For the first case with an incoming subsonic flow the blade passage contours are substituted by a convergent–divergent nozzle (Laval nozzle). Otherwise a strictly divergent nozzle is considered in order to accelerate an incoming supersonic flow further on.

Figure 4 presents the substitute contours for the flow paths in the blade passage. An investigation of computational results

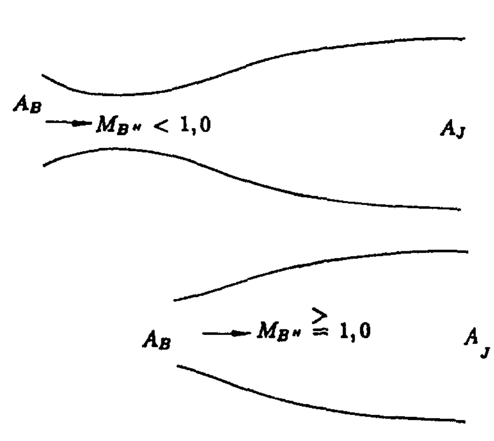

Fig. 4 Assumptions for the blade passage contours due to the regime of inlet-flow Mach number at blade passage entrance

and their comparison with the available measurement data led to the establishment of the following exit-to-entrance area ratio for the blade passage:

$$\frac{A_J}{A_B} = 0.4993\mathrm{M}_{B''} + 0.5007 + C_{ar} \tag{10}$$

The constant C_{ar} takes a value of 0.0774 for cascades having an MCA or wedge-type blading and a value of 0.0351 for cascade ARL-2 DPC having a precompression blading.

When the Mach number $\mathrm{M}_{B''}$ behind the first shock wave lies in the subsonic range, then the *critical* flow area A^* has to be calculated with the equations for compressible gas theory. The subsequent blade passage is assumed to be strictly divergent with a Mach number $\mathrm{M}_{B''} = 1$ at the entrance having a flow cross section $A_{B''} = A^*$. The equations of continuity and the relations for isentropic flow variations describe the interior inviscid flow inside the Laval-nozzle. The Mach number ahead of the second shock wave at the nozzle's exit has to be determined by iteration, since it is due to the ratios of the passage areas, those of the total pressures, and those of the total temperatures as follows:

$$\frac{\left(1 + \frac{\kappa - 1}{2}\mathrm{M}_{J'}^2\right)^{(\kappa+1)/2(\kappa-1)}}{\mathrm{M}_{J'}} = \frac{\left(1 + \frac{\kappa - 1}{2}\mathrm{M}_{B''}^2\right)^{(\kappa+1)/2(\kappa-1)}}{\mathrm{M}_{B''}} \cdot \frac{A_J}{A_B} \cdot \frac{p_{0J'}}{p_{0B''}} \sqrt{\frac{T_{0B''}}{T_{0J'}}} \tag{11}$$

The effect of a radial shift of the streamlines likely to occur in compressor rotors is described by Gustafson (1976).

Second Shock Wave. Available Schlieren pictures showing the investigated cascades with supersonic inlet and subsonic outlet flow clearly identify the second shock wave at the blade passage exit to be a normal shock. The ratio of the static pressure rise over this shock was therefore determined with Eqs. (5) and (6) due to the Mach number $\mathrm{M}_{J'}$ in front of it. The second shock wave decelerates the passage flow from supersonic to subsonic velocities. Thus, the Mach number $\mathrm{M}_{J''}$ behind the second shock wave was not computed due to the weakened static pressure rise but due to the static pressure rise of a normal shock.

Equation (12) yields the ratio of the total pressures at station 1 upstream of the cascade entrance and at the blade passage exit, station J. The shock-loss coefficient of the cascades was then determined by Eq. (13):

$$\frac{p_{0J''}}{p_{01}} = \frac{p_{0J''}}{p_{0J'}} \frac{p_{0J'}}{p_{0B''}} \frac{p_{0B''}}{p_{0B'}} \tag{12}$$

$$\omega_S = \frac{1 - \dfrac{p_{0J''}}{p_{01}}}{1 - \dfrac{p_1}{p_{01}}} \tag{13}$$

Mixing of Blade Wakes. The blade passage flow, which was computed inviscidly, and the blade wakes mix out downstream of the cascade exit plane. Approaching station 2 behind the cascade, a uniform exit flow is achieved. The portion of the streamtube contraction in the wake region was assumed to be about 20 percent as in the original model. The flow quantities of the mixed-out flow at station 2 were computed in the same way as described in the first part of the present paper for the correction of the potentially obtained cascade outlet-flow angles. This method is based on the equations of continuity and momentum in the axial and circumferential directions, which are formulated for the control volume reaching from the passage exit plane, station J, to station 2. It is emphasized that the passage exit area A_J, which was determined fictitiously, should not be considered as the cascade exit. The blade shapes of the investigated cascades are similar to flat plates and justify the assumption $A_J = A_B$ for the mixing calculations. The blade passage height at the location of the second shock Z_J/c is expressed by:

$$\frac{Z_J}{c} = \frac{A_B}{A_1} \cdot \frac{1}{\sigma} \sin \beta_1 \Omega^{0.8} \tag{14}$$

The sine rule gives the boundary-layer thickness Z_δ/c at the passage exit:

$$\frac{Z_\delta}{c} = \frac{1}{\sigma} - \frac{Z_J}{c} \cdot \frac{\sin(\beta_s - \alpha_J)}{\sin \beta_s} \tag{15}$$

As Gustafson (1975) recommends, three constants were introduced to the equations of continuity and momentum in order to simplify the calculation of the aerodynamic values at station 2.

The flow direction at the cascade exit downstream of the second shock has to be determined previously to the mixing calculation and has a significant influence on the result of it. Gustafson discusses reasons to fix the exit flow angle either parallel to the blade suction or to the pressure side. Although his model is based on the assumption of a complete boundary-layer separation at the blade passage entrance, he finally selects a flow direction parallel to the blade suction surface at the trailing edge. Preliminary mixing calculations were conducted with this assumption and resulted in excessively high mixing losses and flow angles at station 2, which differed by about 15 deg from the angles at the cascade exit. The effect was most pronounced for cascades with a strong curvature of the rear portions of the blade suction surface, for instance for the cascades MCA-A4 and MTU-2. A boundary-layer separation likely occurs at the position of the second shock for these blade shapes. Thus, the mean flow direction at the cascade exit plane seems to be aligned rather parallel to the contour of the blade pressure side:

$$\alpha_J = \beta_S - 90° + \gamma_{2D} \tag{16}$$

The flow angle α_J at the cascade exit is measured from the axial direction of the cascade to intensify clearness in contrast to the angle convention utilized in this report. Angle γ_{2D} represents the angle between the chord direction and a tangent to the pressure side shape.

When the flow direction at the cascade exit plane was specified according to this assumption, mixing losses of the expected order were obtained. Figures 5 and 6 demonstrate the good agreement of the calculated cascade outlet-flow direction of the mixed-out flow at station 2 and the measured outlet-flow angle for the cascades MCA-A4 and MTU-1.

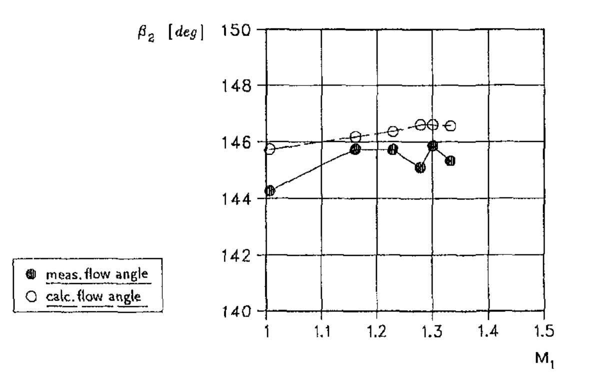

Fig. 5 Measured and calculated outlet-flow angles of cascade MCA-A4

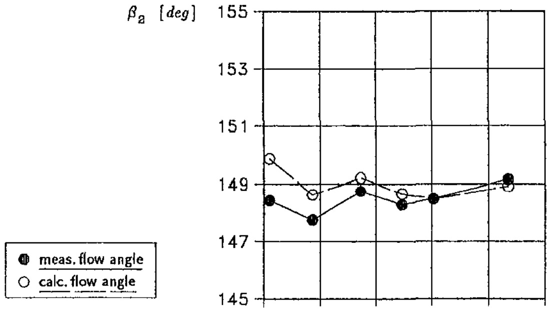

Fig. 6 Measured and calculated outlet-flow angles of cascade MTU-1

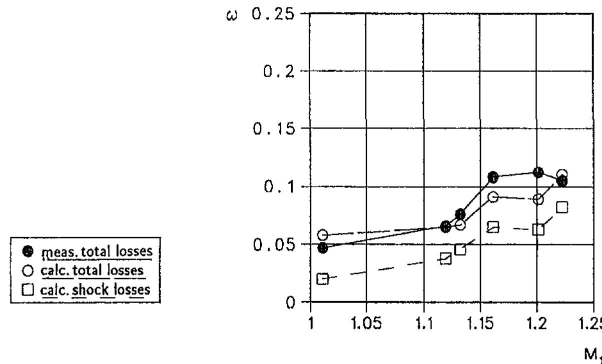

Fig. 7 Calculated and measured losses of cascade L 030-6 for supersonic inlet flow

Limits of Validity. The modified two-shock model calculates the flow acceleration inside the blade passage back to supersonic velocities with a correlation. Since it supports measured data of only some cascades with defined geometries, the limits of its validity have to be checked.

A strong shock–boundary-layer interaction at the foot of the first shock wave at the blade passage entrance provokes a blockage of the passage height and, thus, a flow acceleration. The blockage evidently depends on the ratio of the blade passage height and the chord length. For the considered cascades, these values varied within small limits between 0.33 for cascade MTU-1 and 0.37 for cascade DCA-A3.

In contrast to the assumption of a full boundary-layer separation made by Gustafson, the modified two-shock model presumes the reattachment of the boundary layer downstream of the first shock wave. Delery and Marvin (1986) observed local boundary-layer separations induced by normal shocks having the extension of only some boundary-layer thicknesses ahead of the shock waves. The Mach number ahead of the foot of the shock waves approached values in the order of 1.5. The cascades considered in this paper have blade suction sides with low curvature where separation regions might exist, but they are small in their extensions.

In order to achieve an overexpansion of the blade passage flow, the modified two-shock model assumes a fictitious widening of the passage cross section due to the inlet-flow Mach number at the passage entrance. In the case of a subsonic inlet flow ($M_{B''} < 1$), the exit area is assumed to be identical with the area of the blade passage entrance. The overexpansion starts at the critical flow area where sonic conditions are just reached. König (1992) determined the smallest area ratio A^*/A_B to be 0.98 since the static pressure rise over the shock-waves is estimated by the correlation. On the other side he found an area ratio of $A_J/A_B = 1.15$ for supersonic inlet-flow at the blade passage entrance and an inlet-flow Mach number of $M_{B'} = 1.50$.

However, when applying the modified two-shock model to predict shock losses of modern supersonic compressor cascades, these limits should be respected.

Comparison of Calculation and Measurements. The accuracy of the modified two-shock model is demonstrated with the comparison of the calculated shock and total-pressure losses and the measured total-pressure losses of the considered cascades at high back pressures. This operating condition corresponds to the design-point operation of supersonic compressor bladings. Measurement data with an approximately uniform streamtube contraction ratio in the range of 1.05 to 1.15 were selected for the verification of the model. Figures 7 to 9 show the variations of the calculated and measured losses for the cascades L 030-6, MTU-2, and ARL-2 DPC.

The parallel alignment of the curves for the calculated shock losses and the measured total losses indicates that the blade surface friction and wake-mixing losses are independent of the Mach number for supersonic cascade inlet flow at least for high back pressures. Furthermore, this fact justifies the addition of the shock losses and the losses caused by surface friction and by wake mixing as suggested for other shock-loss models (Miller et al., 1961; Swan, 1961).

The level of the shock losses and the slope of these losses due to the Mach number of the cascade inlet flow is almost identical for the cascades of the MTU-series, those of the L 030-types, and cascade MCA-A4. Cascade DCA-A3 achieves remarkably higher shock and wake-mixing losses as described by König (1992). In contrast, the loss increase of cascade ARL-2 DPC in Figure 9 with precompression blades is shifted to higher inlet-flow Mach numbers by about $\Delta M \approx 0.3$ as a consequence of the almost isentropic compression in front of its blade passages. This can be seen when the shock-loss levels of cascade MTU-2 with wedge-type blades in Fig. 8 and those of cascade ARL-2 DPC in Fig. 9 are compared. Since positive incidence angles lead to supersonic expansions along the front

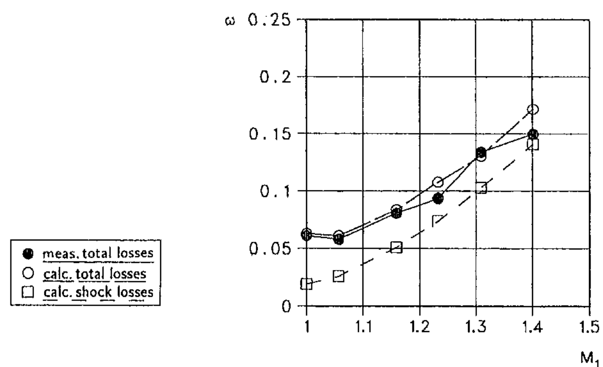

Fig. 8 Calculated and measured losses of cascade MTU-2 for supersonic inlet flow

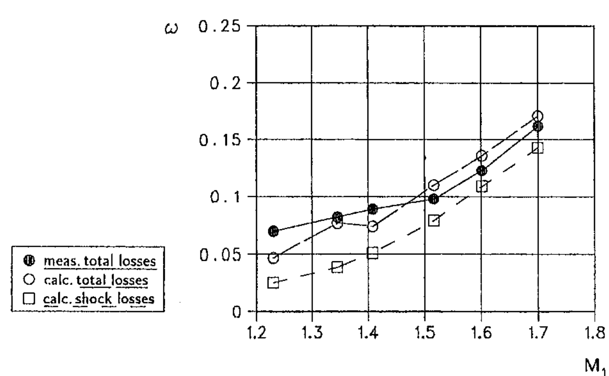

Fig. 9 Calculated and measured losses of cascade ARL-2 DPC for supersonic inlet flow

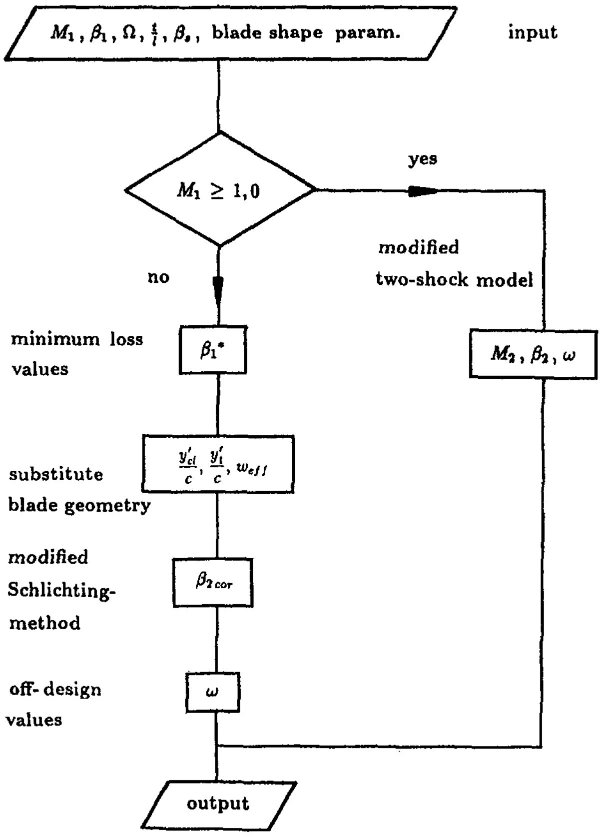

Fig. 10 ***Structure of the performance prediction program***

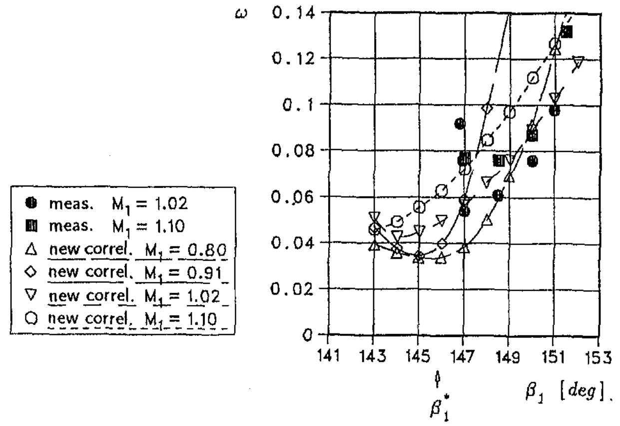

Fig. 11 Total-pressure losses of cascade L 030-4 at inlet flow with high subsonic and low supersonic Mach numbers

part of the blade suction sides, shock losses are computed even at just sonic inlet-flow conditions for most of the cascades.

A critical examination of the differences between the calculated and the measured total losses demonstrates the reliability of the mixing calculation. The modified two-shock model yields slightly low mixing losses for cascade DCA-A3, cascade MCA-A4, and cascade L 030-6 in Fig. 7. The reason for this underprediction is the assumption of the flow angle α_J at the cascade exit to be parallel to the blade pressure side close to the trailing edge. However, the calculated outlet-flow angles β_2 at station 2, which are also influenced by the exit angles α_J, agree quite well with the measured angles for these cascades.

Miller et al. (1961) stated a shock-loss contribution of 35 to 55 percent to the total losses for their measurement data. The Mach number level of the transonic compressors investigated by them lay in the range of 1.0 to 1.3, like most of the cascade measurement data available for the present paper. As can be seen in Figs. 7–9, the portion of the shock losses to the total losses takes values of about 50 percent or, as in the case of the cascades with wedge-type blades of the MTU series, exceeds this value distinctively for the considered range of inlet-flow Mach numbers.

Transition From Subsonic to Supersonic Flow

The equations of the modified two-shock model were programmed and incorporated as a subroutine in the correlation subprogram presented in the first part of this report. Figure 10 shows the structure of the entire subprogram described in more detail by König (1992) for the performance prediction of transonic axial-flow compressors with modern blade designs. A comparison between the AGARD model (Çetin et al., 1987) and the new correlation model as made in Part I of this paper is not included here.

Since the AGARD model incorporates the correlation for the minimum losses established by Koch and Smith (1976), it adds the shock losses to the losses caused by blade surface friction and wake mixing when the Mach number at cascade inlet passes the speed of sound. This method yields a steady loss increase across the sonic border. In contrast, the new correlation model treats the losses for subsonic and supersonic range separately according to the flow scheme in Fig. 10. This concept will probably lead to some discontinuities when the Mach number of the inlet flow transits the sonic line. For this reason, the results of the new model for rising cascade inlet-flow Mach numbers passing from subsonic to supersonic velocities are analyzed.

In order to examine this conjecture, the variations of the total losses were calculated with the new model and compared in Figs. 11 and 12 to the measured values of both L 030 cascades for two inlet-flow Mach numbers closely beneath and above the sonic line.

The modified two-shock model predicts the level of the minimum total losses in the supersonic range just as accurately as the correlations for the subsonic flow range. However, a comparison of the curves yields a difference of about 2 deg between the estimated inlet-flow angles with minimum losses for supersonic inlet-flow Mach numbers and the inlet-flow angles (marked in the graphs as β_1^*) obtained by the cascade investigations with subsonic inlet flows. At off-design incidence angles, the modified two-shock model predicts a slightly weaker loss increase than indicated by the measured data. The presumed flow situation with high back pressures at the cascade outlets, which corresponds to design conditions, causes this deviation. If this is realized, the good approximation of the measured data in the off-design range is indeed satisfactory.

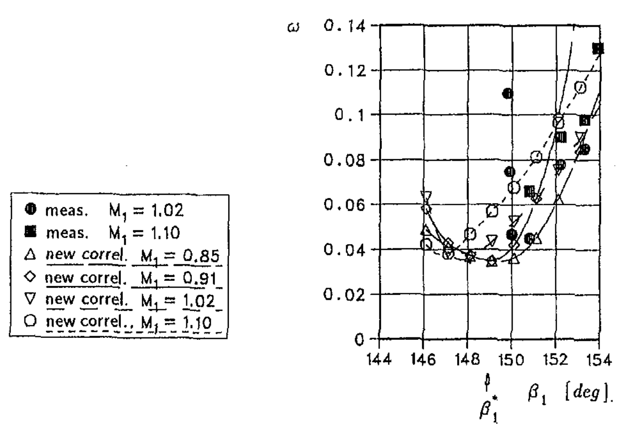

Fig. 12 Total-pressure losses of cascade L 030-6 at inlet flow with high subsonic and low supersonic Mach numbers

The incidence angles that can be attained for supersonic cascade inlet-flows lie in a limited range. This range contracts with rising inlet-flow Mach numbers and leads to a direct link between the incidence angles and the inlet-flow Mach numbers (unique incidence condition) at even moderate supersonic cascade inlet flows. Thus, several loss values were taken for the same inlet-flow angle in Figs. 11 and 12. This effect cannot be reflected by the new model and has to be kept in mind when the variation of the total pressure losses due to the incidence angles is judged for the L 030-cascades.

Conclusions

The second part of the present paper describes a correlative model to estimate the total-pressure losses and the deviation angles of compressor blade rows having supersonic inlet-flow Mach numbers. Thus, it completes the presentation of a new correlation model started in Part I with a model for subsonic flows. The outlined model is based on the assumption of two shock waves and an attached boundary layer on the blade suction side inside the blade passage. It reflects by a simple but still realistic concept the flow situation in supersonic compressor cascades with modern bladings, including precompression bladings. The comparison of the computed values with the measured data of eight different cascades demonstrates the accuracy of the prediction for shock losses as well as those for surface friction and wake-mixing losses. Finally, the subsonic correlations and the modified two-shock model achieve a continuous transition of the loss curves from subsonic to supersonic inlet conditions. Now, a correlation model is available to predict accurately and reliably the losses that have to be expected for axial-flow compressor blade rows with contemporary blade designs.

Acknowledgments

The authors are indebted to H. Starken and to H. A. Schreiber from DLR Köln for the provision of extensive cascade measurement data and the kind permission for publication.

References

Çetin, M., Üçer, A. S., Hirsch, Ch., and Serovy, G. K., 1987, "Application of Modified Loss and Deviation Correlations to Transonic Axial Compressors," AGARD Report No. 745.

Delery, J., and Marvin, J. G., 1986, "Shock-Wave Boundary-Layer Interactions," AGARDograph No. 280, pp. 8–50.

Fottner, L., and Lichtfuss, H. J., 1983, "Design of Transonic Compressor Cascades for Minimal Shock Losses and Comparison With Test Results," AGARD CP No. 351, pp. 4.1–4.22.

Gustafson, B. A., 1975, "A Simple Method for Supersonic Compressor Cascade Performance Prediction," Chalmers Univ. of Techn., Dept. for Turbomachinery; also ASME Paper No. 76-GT-64.

Koch, C. C., and Smith, L. H., Jr., 1976, "Loss Sources and Magnitudes in Axial-Flow Compressors," ASME *Journal of Engineering for Power,* Vol. 98, pp. 411–424.

König, W. M., 1992, "Korrelationen für die Kennfeldrechnung transsonischer Axialverdichter," *Fortschrittberichte VDI,* Reihe 7 No. 217, VDI-Verlag, Düsseldorf, Germany.

Miller, G. R., Lewis, G. W., Jr., and Hartmann, M. J., 1961, "Shock Losses in Transonic Compressor Blade Rows," ASME *Journal of Engineering for Power,* Vol. 83, pp. 235–241.

Schreiber, H. A., 1988, "Shock Losses in Transonic and Supersonic Compressor Cascades," VKI-Lecture Series 1988-03, Von-Kármán Institute for Fluid Dynamics, Brussels.

Starken, H., 1971, "Untersuchung der Strömung in ebenen Überschallverzögerungsgittern," DLR FB 71-99, Diss. RWTH Aachen, Germany.

Swan, W. C., 1961, "A Practical Method for Predicting Transonic-Compressor Performance," ASME *Journal of Engineering for Power,* Vol. 83, pp. 322–330.

Tweedt, D. L., Schreiber, H. A., and Starken, H., 1988, "Experimental Investigation of the Performance of a Supersonic Compressor Cascade," ASME Journal of Turbomachinery, Vol. 110, pp. 456–466.

Weyer, H., and Strinning, P., 1974, "Auslegung und Nachrechnung einer transsonischen Axialverdichterstufe," *1. Zwischenbericht,* FVV-Vorhaben No. 136, Heft 158, Germany.

J. J. Adamczyk
NASA Lewis Research Center,
Brook Park, OH 44135

M. L. Celestina
Department of Aeromechanics,
Sverdrup Technology, Inc.,
Brook Park, OH 44135

Jen Ping Chen
NSF Engineering Research Center,
Mississippi State University,
Mississippi State, MS 39762

Wake-Induced Unsteady Flows: Their Impact on Rotor Performance and Wake Rectification

The impact of wake-induced unsteady flows on blade row performance and the wake rectification process is examined by means of numerical simulation. The passage of a stator wake through a downstream rotor is first simulated using a three-dimensional unsteady viscous flow code. The results from this simulation are used to define two steady-state inlet conditions for a three-dimensional viscous flow simulation of a rotor operating in isolation. The results obtained from these numerical simulations are then compared to those obtained from the unsteady simulation both to quantify the impact of the wake-induced unsteady flow field on rotor performance and to identify the flow processes which impact wake rectification. Finally, the results from this comparison study are related to an existing model, which attempts to account for the impact of wake-induced unsteady flows on the performance of multistage turbomachinery.

Introduction

Turbomachinery is able either to impart or to remove energy from a flow stream because the flow within is inherently unsteady. This simple fact is overlooked by many researchers for this reason: When analyzing the flow through an isolated rotating blade row, the dependence on time may be eliminated by transforming to a coordinate system fixed to the blade row. However, as soon as one attempts to address the flow through more than one blade row, the role of time becomes self-evident. As an example, time appears explicitly in the form of a local time derivative of pressure in the equation governing the time rate of change of the total enthalpy of a fluid particle. For multiblade row configurations, this term can not be removed by a trivial transformation of coordinates.

A procedure for grouping, according to flow processes, the unsteady terms that impact the performance of blade rows within single and multistage turbomachinery was developed by Adamczyk (1985). This grouping procedure was based on the closure terms, which account for the presence of neighboring blade rows in his average-passage equation system. These equations govern the time-average flow field of a typical passage of a blade row. Within this equation system, the surrounding blade rows make their presence known through a system of body forces, a number of energy sources or sinks, a set of velocity correlations similar in form to the Reynolds stresses, and a correlation involving both the unsteady total enthalpy field and the unsteady velocity field. These terms serve as "mail boxes" in which to place (and hence group) the various unsteady flow processes occurring within multiblade row turbomachinery.

In this paper, the topic of wake-induced unsteady flows as it affects the performance of a rotor of an axial flow compressor will be addressed. Specifically, the need to account for the wake-induced unsteady flows set up by an upstream stator in predicting rotor performance will be examined. In addition, the related topic of wake rectification will also be addressed. The various flow processes associated with the unsteady processes will be related to the closure terms in the average-passage equation system. The study will be undertaken using the results from a series of numerical simulations.

Atkins and Smith (1982) argued that mixing brought about by secondary flows had a significant impact on the radial distribution of the axisymmetric flow properties in multistage axial flow compressors. Included in the definition of the secondary flow field was the effect of the wakes. In the Atkins and Smith (1982) model, the mixing within a blade row is the result of a superpositioning of the secondary flow generated by the blade row itself plus that generated by all the blade rows upstream. The major contributor to this mixing process was the secondary flow set up by the blade row immediately upstream. Hence, the mixing process Atkins and Smith (1982) are modeling is unsteady and comes about by the interaction between the incoming unsteady secondary flow field and the downstream blade row.

The first publication on the topic of wake rectification as a result of circumferential mixing was that of Kerrebrock and Mikolajczak (1970). They showed that wakes from a rotor are rectified as they pass through a downstream stator, yielding an increase in total temperature on the pressure surface of the stator, which is another form of wake blade row interaction. This work has been used by compressor aerodynamicists as a diagnostic tool for estimating the performance of a rotor. Kerrebrock and Mikolajczak (1970) used the results of their analysis to infer the performance of a rotor from measurements taken downstream of a stator. However, they make no attempt to relate their findings to the performance of the stator. Very recently their analysis has been used by Butler et al. (1989) as well as others in the study of thermal loads generated by hot streaks in turbines.

We begin the present study by addressing the importance of including the effects of wake-induced unsteady flows in the description of the time-averaged flow field across a rotor operating downstream of a stator. If no significant reason can be given for including these effects, then one may seriously question their impact on the interrotor blade row flow field. This part of the present work is intended to demonstrate at the very minimum the need to include the radial mixing process de-

Contributed by the International Gas Turbine Institute and presented at the 39th International Gas Turbine and Aeroengine Congress and Exposition, The Hague, The Netherlands, June 13–16, 1994. Manuscript received by the International Gas Turbine Institute February 18, 1994. Paper No. 94-GT-219. Associate Technical Editor: E. M. Greitzer.

scribed by Atkins and Smith (1982) in the modeling of the time-averaged three-dimensional flow field within a typical passage of a blade row embedded within a multistage configuration. This study will be followed by an analysis of the stator wake rectification.

The stator configuration used in this study has a corner separation at the junction of the hub and the suction surface. This separation leads to a very thick wake, which is acted upon by the lower portion of the downstream rotor. The thick wake helps to accentuate the effects of the unsteady deterministic flow field associated with the wake on the rotor performance. The numerical codes used in this study are three dimensional, compressible, and viscous, with the effects of turbulence introduced through the model proposed by Baldwin and Lomax (1978). The shear force acting on solid surfaces is modeled using wall functions. In addition, these surfaces are assumed to be adiabatic. One of the codes solves for the time-averaged flow field surrounding a blade row embedded in a multistage configuration and has been reported upon by Adamczyk et al. (1990). The other is a recently developed time-dependent code, which simulates the passage of a wake through a blade row, and is reported upon by Chen et al. (1994). This unsteady code uses an implicit integration scheme to advance the solution in time and is second-order accurate in both space and time. Using the results from a temporal accuracy study reported in Chen et al., a time step of one-fourth of a wake passing cycle was used in the unsteady simulation. In all the simulations, a common grid was used consisting of 31 radial points, 31 circumferential points, and 31 points distributed along the chord of each blade row. Based on previous simulations of similar configurations, this grid density was deemed adequate for the purpose of this study. However, this grid density requires the use of wall functions to establish the shear force acting on solid surfaces.

Performance of an Embedded Blade Row

The impact of the unsteady flow field generated by a blade row on the performance of a downstream blade row is investigated through numerical experimentation. As stated earlier, the geometry is that of a compressor stage consisting of a stator followed by a rotor. These blade rows are subsonic and are representative of embedded blade rows within a multistage axial flow compressor. The first simulation executed used the average-passage code. The output from this simulation was used to define the inlet conditions in an unsteady simulation of the rotor flow field. By comparing the results of this time-dependent simulation to that in which the rotor is modeled as an isolated blade row, the effects of the unsteady deterministic flow field on the rotor's performance can be quantified. This exercise could have been undertaken using the average-passage code if the value of the closure terms as modeled in this code were identical to those derived from the unsteady simulation. However, because the physics associated with wake cutting and intrablade row transport is not accounted for in the current closure model, any conclusions drawn from the results of the average-passage code could be questioned. From the rotor unsteady flow simulation, the axial, absolute tangential, and radial velocity components, as well as the absolute total temperature and pressure, were averaged over time and circumference to define the radial distribution of the time-averaged yaw and pitch angle, in addition to the absolute total temperature and pressure of the flow entering the rotor. These flow quantities were further averaged over span and used to establish the corrected flow to the rotor. In this work, these averaged flow quantities are used to define the inlet conditions to the rotor as if it were operating in isolation. The grid for this simulation is identical to that used in the unsteady flow simulation. Figure 1 shows the radial distribution of the circumferential average of the product of density and axial velocity, density and absolute tangential velocity, and density and radial velocity from the isolated rotor simulation compared to that derived from the unsteady simulation at the common inlet plane. Also presented are the resulting inlet total pressure distributions. Because the two inlet total temperature distributions are identical, both being uniform across the span and equal to the total temperature at the stator inlet, they are not presented. As can be seen in the figure, the inlet conditions for the isolated rotor simulation very nearly match those derived from the unsteady simulation. Note that all the flow variables in this figure and in all subsequent figures are normalized with respect to the total conditions upstream of the stator.

Figure 1 also includes a plot of the radial distribution of the circumferential average of the pressure from the unsteady and isolated rotor simulation at the common inlet plane. The unsteady distribution is also averaged over time. Note the difference between the two curves, which at the hub amounts to 20 percent of the inlet flow dynamic head. This difference, which is not negligible, is related to the magnitude of the time variation of the inlet dynamic head. This term is equal to one half the sum of the diagonal elements of the temporal velocity correlation tensor.

Figure 2 shows plots of the mass-averaged radial distribution of the absolute total temperature and pressure at the common exit plane for both simulations. The unsteady simulation results are also mass-averaged over time. Since the inlet absolute total temperature specified in the isolated rotor simulation is identical to its unsteady counterpart, the differences seen are once again the result of an unsteady incoming flow field to the rotor. The absolute total temperature curves show the energy input to the flow to be larger in the case of the isolated rotor. The total pressure plots show a similar behavior. The last plot of this figure shows the efficiency as derived from the simulation of the isolated rotor and the unsteady case. The efficiency is evaluated from the respective inlet and exit mass-averaged total pressure and temperature distributions. In the hub region, the efficiency of the isolated rotor is far greater than that of the rotor operating downstream of the stator. Outboard of 35 percent of span, the efficiency of the isolated rotor is less than that of the rotor downstream of the stator. The differences in the hub region result from there being far more radial and circumferential movement of fluid particles in the unsteady simulation than is occurring in the isolated rotor simulation. The reversal between the two efficiency plots outboard of 35 percent of span is associated with the unsteady interaction between the incoming stator wake and the pressure field. This interaction will be discussed in the section dealing with wake rectification.

Based on the work of Stewart (1959), Dring and Spear (1991) and also Dawes (1992) suggested that a blade row within a multistage machine could be modeled as an isolated blade row, provided that the inlet conditions were those derived from passing the unsteady flow exiting the upstream blade row through a mixing plane. Across this mixing plane the mass flux, axial impulse, flux in tangential and radial momentum, and flux in total enthalpy are conserved. This mixing plane model assumes that there is little if any impact of the unsteady intrablade row flow processes on performance. Hence, this model is unable to account for the mixing process outlined by Atkins and Smith (1982). Following the work of Dring and Spear (1991), the output from the average-passage simulation of the stator was used in conjunction with a mixing plane analysis to extract the required inlet conditions for simulating the downstream rotor. The results of this analysis are presented in a format identical to that used for Figs. 1 and 2. Figure 3 shows plots of the radial distribution of the product of axial velocity and density, absolute tangential velocity and density, radial velocity and density, absolute total pressure, and pressure at the inlet plane. To generate these plots, the results from the mixing plane model were averaged over the circumferential direction. In the case of the unsteady results, they were also averaged over time. The corrected weight flow per unit area upstream of

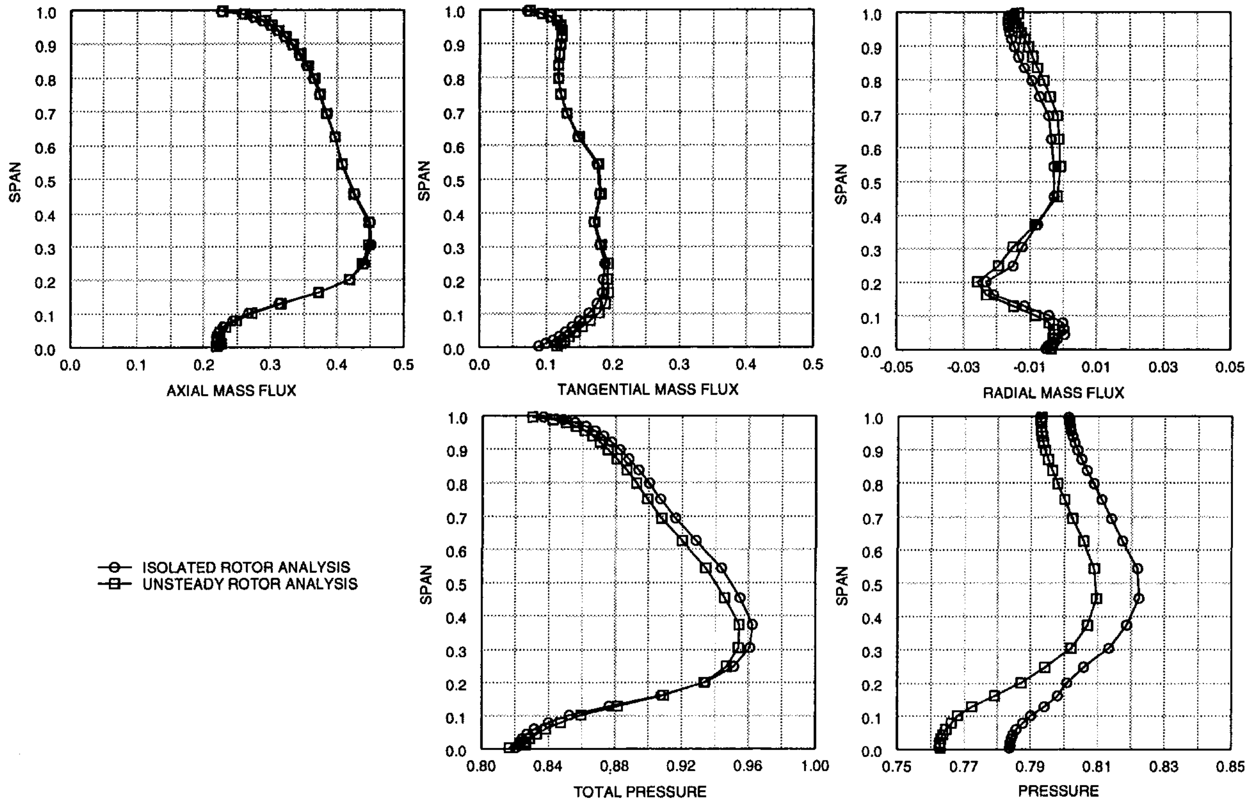

Fig. 1 Inlet flow conditions to isolated rotor analysis versus time-average inlet flow conditions derived from unsteady rotor analysis

the mixing plane matches that of the rotor in the unsteady simulation.

Figure 3 shows that a significant difference exists between the profiles of tangential and radial velocity as derived from the mixing plane model and their respective counterparts derived from the unsteady simulation. This difference is a direct measure of the magnitude of the temporal correlation involving the product of the axial and tangential velocities in the one case and the product of the axial and radial velocities in the other. These correlations account for the transport of axial momentum in the tangential and radial directions associated with the unsteady flow entering the rotor. The differences in the magnitude of the velocity components also imply differences in the yaw and pitch angle of the fluid entering the rotor. The two curves of absolute total pressure show that the mixing model yields values "higher" than those derived from the unsteady simulation. This result is unexpected, for one would argue that in an irreversible mixing process there should be a loss in total pressure rather than a gain. This odd result is easily explained by noting that what is being plotted in the case of the unsteady simulation is the time-averaged total pressure entering the rotor as opposed to its mass-averaged value as is needed to estimate the loss due to mixing. Had the mass-averaged total pressure distribution associated with the unsteady simulation been plotted, one would indeed see that there was a loss in total pressure as a result of the modeled mixing process. We chose not to present the mass-weighted total pressure curve associated with the unsteady simulation to dramatize the fact that the unsteady flow is not mixed out prior to entering the rotor and thus the wake mixing is taking place within the rotor passage under conditions that are not accounted for by the mixing plane model. Finally, note that the inlet plane pressure distributions are also

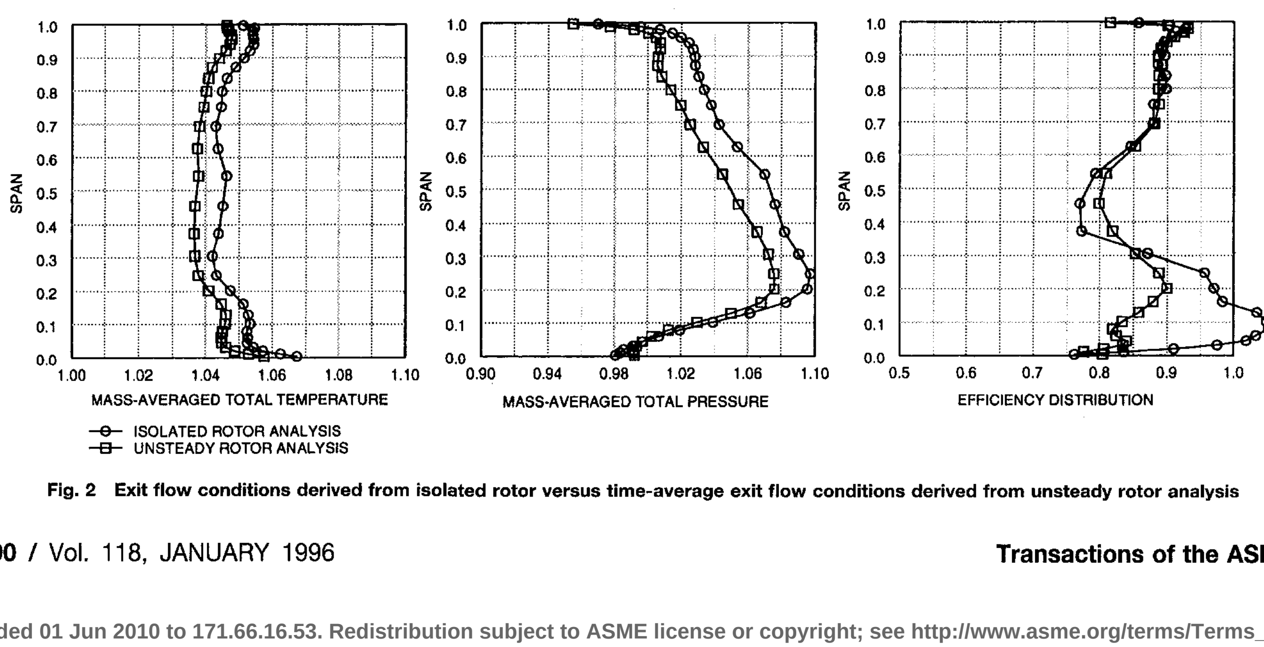

Fig. 2 Exit flow conditions derived from isolated rotor versus time-average exit flow conditions derived from unsteady rotor analysis

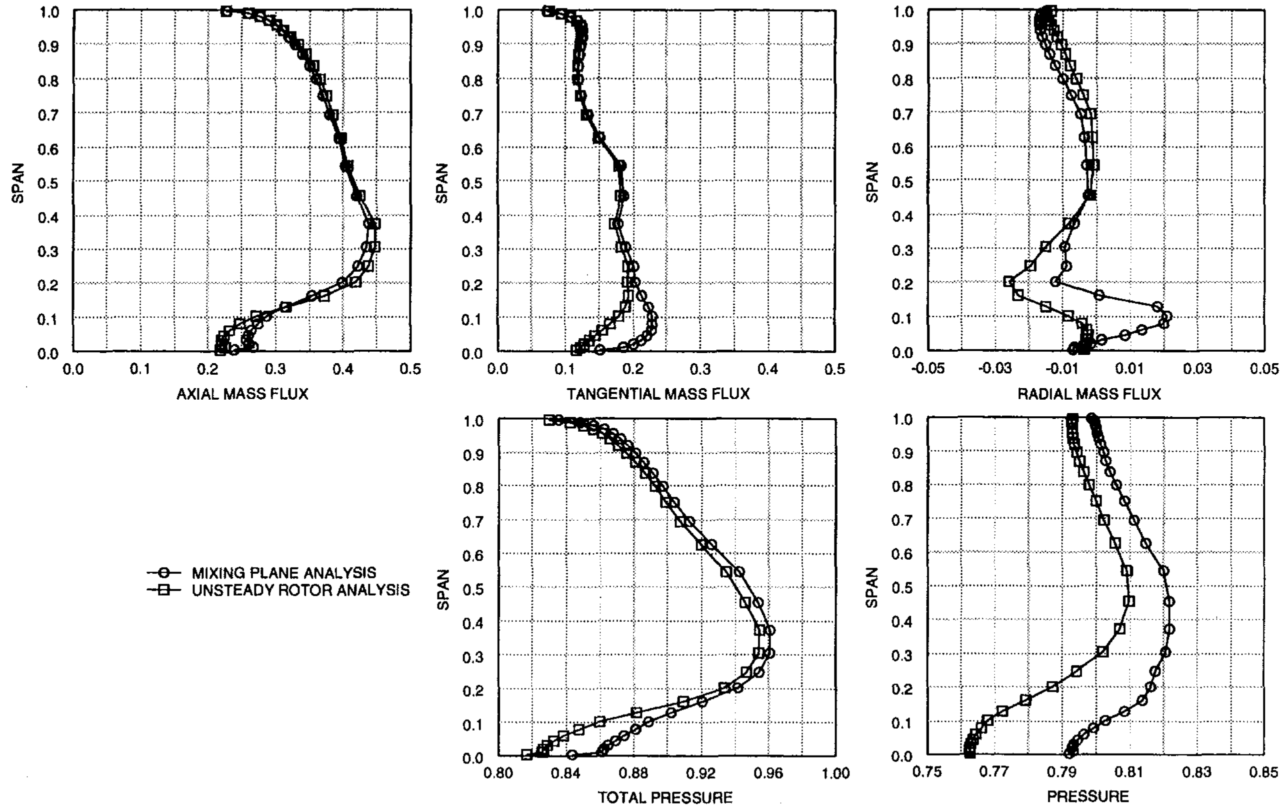

Fig. 3 Inlet flow conditions derived from mixing plane analysis versus time-average inlet flow conditions derived from unsteady rotor analysis

different and that, as previously stated, this difference is caused by the unsteady flow generated by the stator.

Figure 4 shows plots of the absolute total temperature and pressure, mass-averaged circumferentially, as a function of span at the exit plane. The results from the unsteady rotor simulation (as in Fig. 2) were also mass-averaged over time. Since the total temperature of the flow stream entering the rotor is identical for both cases, the total temperature plot also indicates the energy input to the flow stream by the rotor. It appears that the rotor operating downstream of the mixing plane is putting more energy into the flow than it would in the unsteady flow environment. The total pressure plots show a similar behavior. The difference between the results from the unsteady simulation and those from the mixing plane model increases with distance from the hub. This difference between the two sets of results appears to be caused by the larger radial movement of fluid particles in the unsteady simulation.

The last plot of Fig. 4 shows the efficiency derived from total pressure and temperature distributions aft and forward of the mixing plane. For comparison purposes the efficiency as derived from the unsteady rotor simulation is also shown and is identical to that presented in Fig. 2. The efficiency as derived from the flow condition downstream of the mixing plane is greater than that derived from the unsteady simulation over most of the span. This difference occurs because no account has been taken of the loss in total pressure across the mixing plane. If one uses the flow conditions upstream of the mixing plane to establish the efficiency of the rotor, the agreement between that derived from the unsteady simulation and that from the mixing plane simulation is considerably improved. However, by doing so

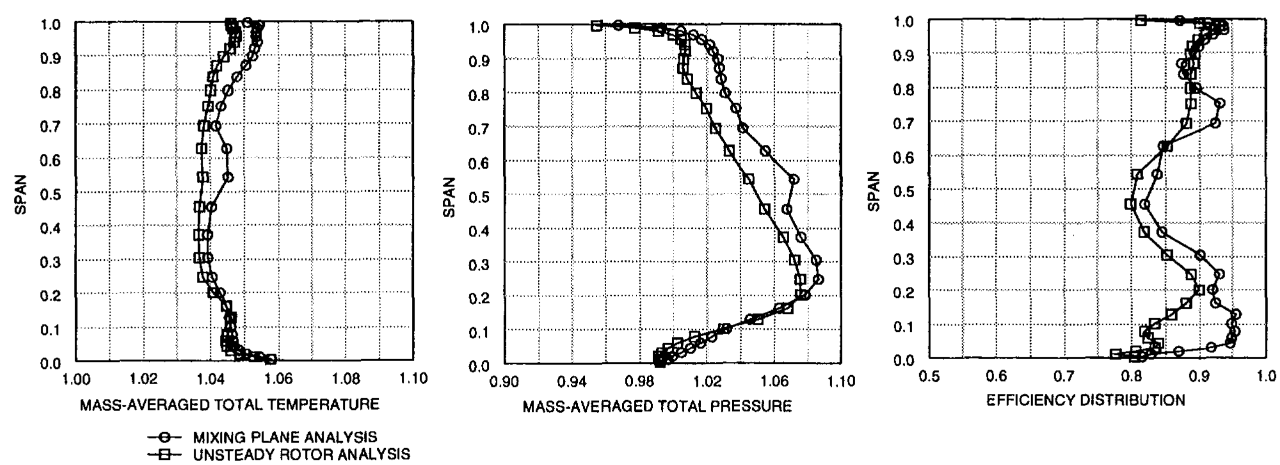

Fig. 4 Exit flow conditions derived from mixing plane analysis versus time-average exit flow conditions derived from unsteady rotor analysis

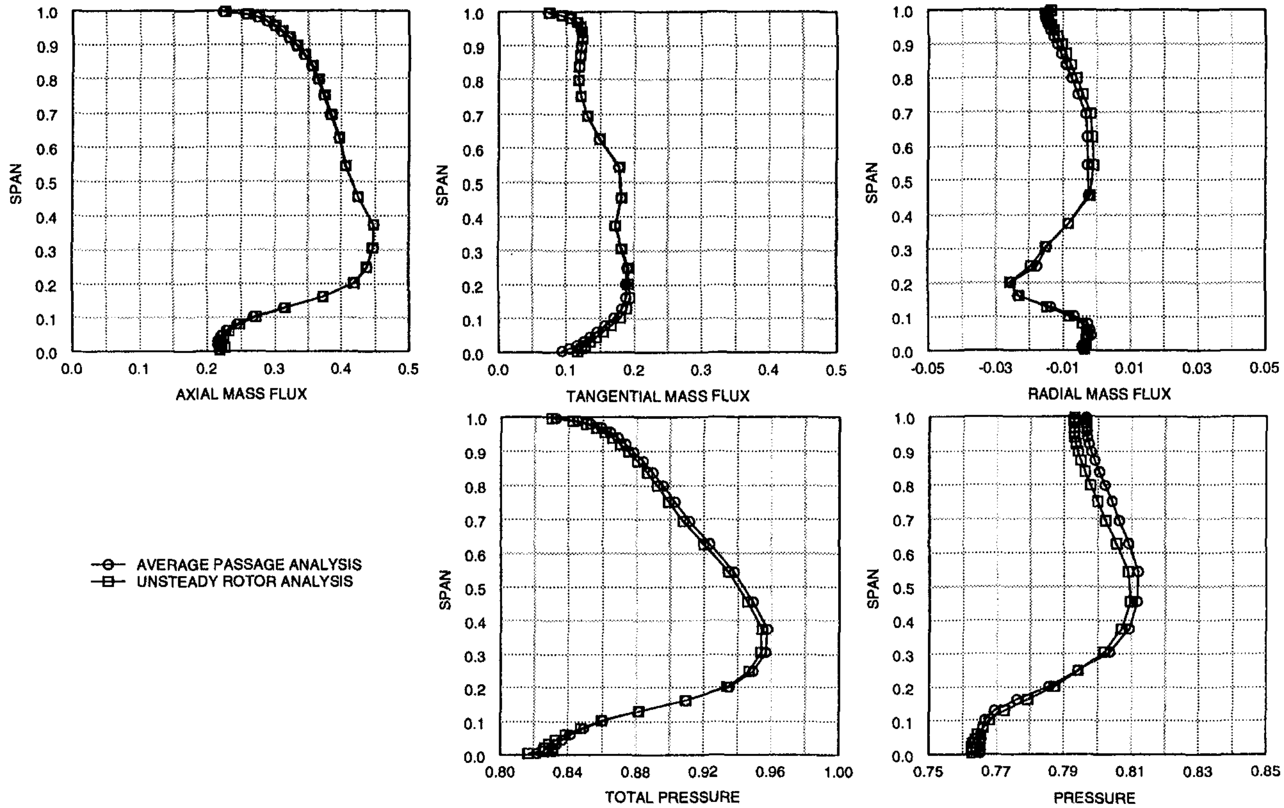

Fig. 5 Inlet flow conditions derived from average-passage analysis versus time-average inlet flow conditions derived from unsteady rotor analysis

we raise the following question: Which component should be charged with the mixing loss, the stator that generated the wake or the rotor through which the wake passes?

The last set of results is from the average-passage model. As stated previously, the results derived from this model of multistage turbomachinery flows should be identical to those derived from an unsteady model averaged over time. Any differences between the average-passage results and those from the unsteady rotor simulation are due to the inadequacy of the current closure models to account for the effects of the incoming unsteady flow field. Further note that the results from the average-passage simulation would be identical to an isolated rotor simulation, which incorporated the unsteady deterministic stress used in the average-passage simulation of the rotor, with inlet conditions that match the time average mass flux, the time average absolute tangential velocity, the time average radial velocity, and the time-averaged absolute total temperature of the unsteady simulation.

Figure 5 shows plots of the product of velocity field and density, as well as the absolute total pressure and pressure field from the rotor average-passage simulation at an axial plane corresponding to the inlet plane in the rotor unsteady simulation. Also shown in these plots are the results obtained from the rotor unsteady simulation. The agreement between the two sets of results is very good. It indicates that the unsteady flow entering the rotor is being accounted for by the existing closure models. Furthermore, one should note that the average-passage flow model gives a reasonable estimate not only of the time-averaged flow conditions to the rotor but also of the time-averaged axial impulse and the momentum flux in both the radial and tangential directions. Thus the average-passage flow model provides a correct representation of the time-averaged flow field to the rotor.

Figure 6 shows plots of the radial distribution of the mass-averaged absolute total temperature and pressure at the exit plane of the rotor as well as the predicted rotor efficiency. For comparison purposes the corresponding results derived from the unsteady rotor simulation are also shown. The agreement between the two simulations is not as good as that shown in Fig. 5. The total temperature from the average-passage simulation outboard of 40 percent of span is overpredicted, implying more energy is being added to the flow stream relative to that deduced from the unsteady simulation. It should be noted that both the isolated blade row simulation and the mixing plane simulation overpredicted the total temperature rise over the entire span. The average-passage total pressure plot reflects the added energy addition. The efficiency plots show the average-passage result to be in good agreement with the unsteady result to 20 percent of span, to be greater than the unsteady result between 20 and 38 percent of span, and to be lower from there on. This behavior is believed to be tied to the mixing of the stator wakes as they pass through the rotor and is associated with the modeling of the wake rectification and recovery process. In general, the results from the average-passage model are in reasonable agreement with the results from the unsteady simulation. The average-passage results also suggest that accounting for the unsteady flow within the rotor passage by means of the current closure models yields results that are in far better agreement with the results from the unsteady simulation as compared to that obtained using the mixing plane model. However, as mentioned previously, there is also a clear need to improve the closure models further.

Wake Rectification

In examining data taken downstream of a high-speed fan stage, Kerrebrock and Mikolajczak (1970) noted a circumferential nonuniformity in the total temperature field. Based on a kinematic model, they were able to show that this nonuniformity was the result of the rotor wake fluid piling up on the stator

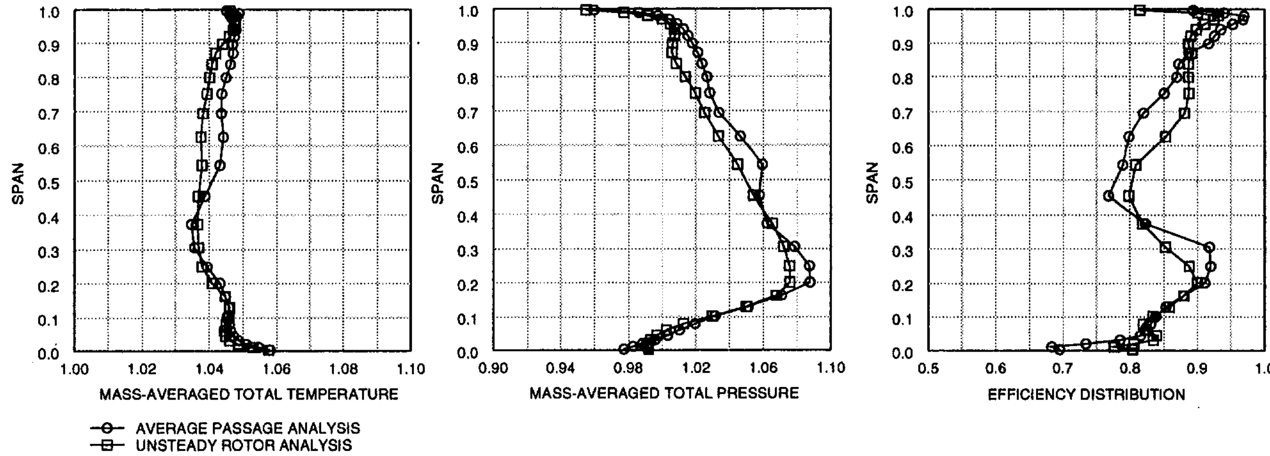

Fig. 6 Exit flow conditions derived from average-passage analysis versus time-average exit flow conditions derived from unsteady rotor analysis

pressure surface. They argued that because of the difference between the velocity of a wake fluid particle and that of a fluid particle in the free stream, a drift velocity exists, which causes the wake fluid to migrate toward the pressure surface of the downstream blade. Upon impact, the component of the drift velocity normal to the blade pressure surface is lost, causing the path of a wake particle to become tangent to the pressure surface. The total temperature of a wake particle is assumed to remain constant during this process, which results in the formation of a circumferential gradient in the time-averaged total temperature at the pressure surface. For the case of a rotor, its time-averaged flow field will have a circumferential gradient in rothalpy at the pressure surface caused by the rectification of the upstream stator wake.

The results from the unsteady rotor simulation showed that, in addition to the kinematic process described by Kerrebrock and Mikolajczak (1970), there is another process by which wake rectification may occur. The process is dynamic and is the result of the interaction between the wake and the unsteady pressure field generated as the wake encounters the leading edge of a blade. For the case of a stator wake passing through a rotor, the flow physics associated with this process can be explained by referring to the inviscid nonconducting form of the equation for the rothalpy of a fluid particle. The mathematical form of this equation is

$$DI/Dt = (1/\rho)\partial p/\partial t \qquad (1)$$

where I is the rothalpy of a fluid particle, D/Dt is the time rate of change following a fluid particle, ρ is the density, p is the pressure, and $\partial/\partial t$ is the local time rate of change. As the wake encounters the leading edge of the rotor, the component of the wake velocity normal to the rotor surface causes the pressure field to undergo a change in time and space. According to Eq. (1), the change of pressure with time will cause a change in the rothalpy of a fluid particle. The phasing in time between the rothalpy of a wake fluid particle and the unsteady pressure will cause the time-averaged rothalpy field to become spatially nonuniform. This process, as well as that described by Kerrebrock and Mikolajczak (1970), is accounted for in the average-passage model through a term, which is equal to the divergence of the temporal correlation between the unsteady rothalpy and the unsteady velocity field.

The new scenario for wake rectification is illustrated by means of a series of plots, which show the instantaneous contours of entropy and rothalpy as derived from the unsteady simulation of the rotor. Shown in Figs. 7 and 8 are five contour plots of the instantaneous entropy and rothalpy on a blade-to-blade surface of revolution approximately 20 percent from the hub. The time increments are equally spaced over a cycle of the wake passing period. From these plots we see that the entropy is convected toward the pressure surface of the rotor as described by Kerrebrock and Mikolajczak (1970). In addition, note that from the inlet plane to near midchord, the wakes are distinct and the entropy contours associated with the wakes are maintained as the wakes move down the inlet plane. Between the inlet plane of the computational domain and the inlet plane to the rotor, and perhaps as far downstream as the quarter-chord plane, the unsteady flow features associated with the wake are primarily the result of inviscid flow processes. These inviscid flow features are associated with the new rectification process and are adequately resolved by the chosen numerical grid.

Figure 8 shows the rothalpy associated with the wakes. Forward of quarter chord, one observes a clear periodic change with time of the rothalpy contours associated with the wakes as they move down the inlet plane. As stated previously, the corresponding wake entropy contours are not changing with time. This change with time of the wake rothalpy contours is brought about by the unsteady pressure field as discussed above. This unsteady interaction between the pressure field and the wake leads to the rectified or time-averaged rothalpy field shown as the sixth contour plot in Fig. 8. In their experimental study of rotor–stator aerodynamic interactions, Hathaway et al. (1987) observed many of the features seen in these figures.

The rectification process being described is nearly isentropic, hence associated with the increase in rothalpy is a corresponding increase in the rotary total pressure. It may be possible to control and harness this increase in the rotary total pressure to enhance the performance of a rotor. One may also expect to observe a similar rectification process within stator passages, which may also be controllable and lead to an increase in stator performance. These issues are beyond the scope of the current research, but it is hoped that they will be addressed in a future publication.

Summary and Conclusion

In this work we have conducted a series of numerical simulations to assess the need for introducing models of the effect of the unsteady deterministic flow field into simulations of the time-averaged flow field associated with a blade row embedded in a multistage machine. The first study examined the impact of this unsteady flow field on the flow across a rotor located downstream of a stator. From this numerical investigation, it was concluded that a major difference exists between the performance of the rotor operating in isolation and the same rotor operating downstream of the stator at the same time-averaged inlet flow conditions. Furthermore, it was shown that the use of a mixing plane located between the trailing edge of the stator and the leading edge of the rotor to wash out the time-varying flow exiting the stator yielded results that were in better agreement with the results derived from the unsteady rotor simulation than those obtained by completely ignoring the existence of the unsteady flow state. Finally, the rotor results obtained from the average-passage model were presented. The results from the average-passage model are equivalent to those that would be obtained from an isolated rotor simulation that incorporated the deterministic stress field of the average-passage rotor simulation, with inlet conditions deduced from the average-passage simulation of the stator. The results from the average-passage simulation of the rotor were found to be in far better agreement with those from the unsteady simulation as compared to the results from the mixing plane model, especially at the inlet to the rotor. However, there is still need for further improvements in the closure models to portray the unsteady intrablade row flow processes more accurately.

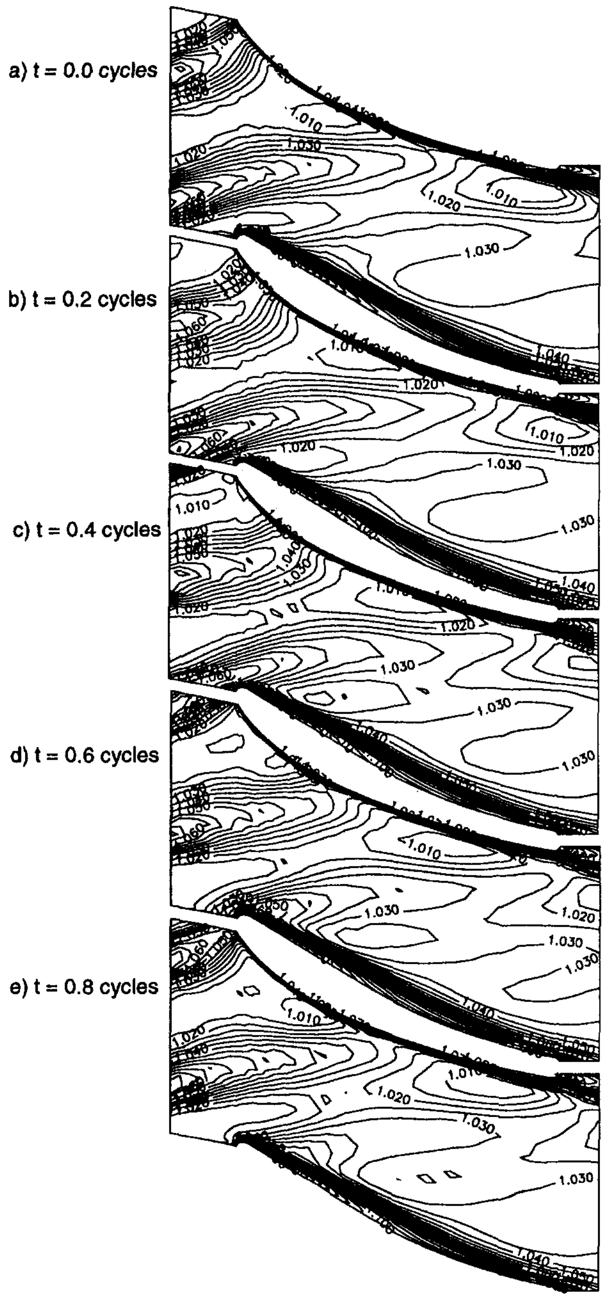

Fig. 7 Instantaneous contours of entropy

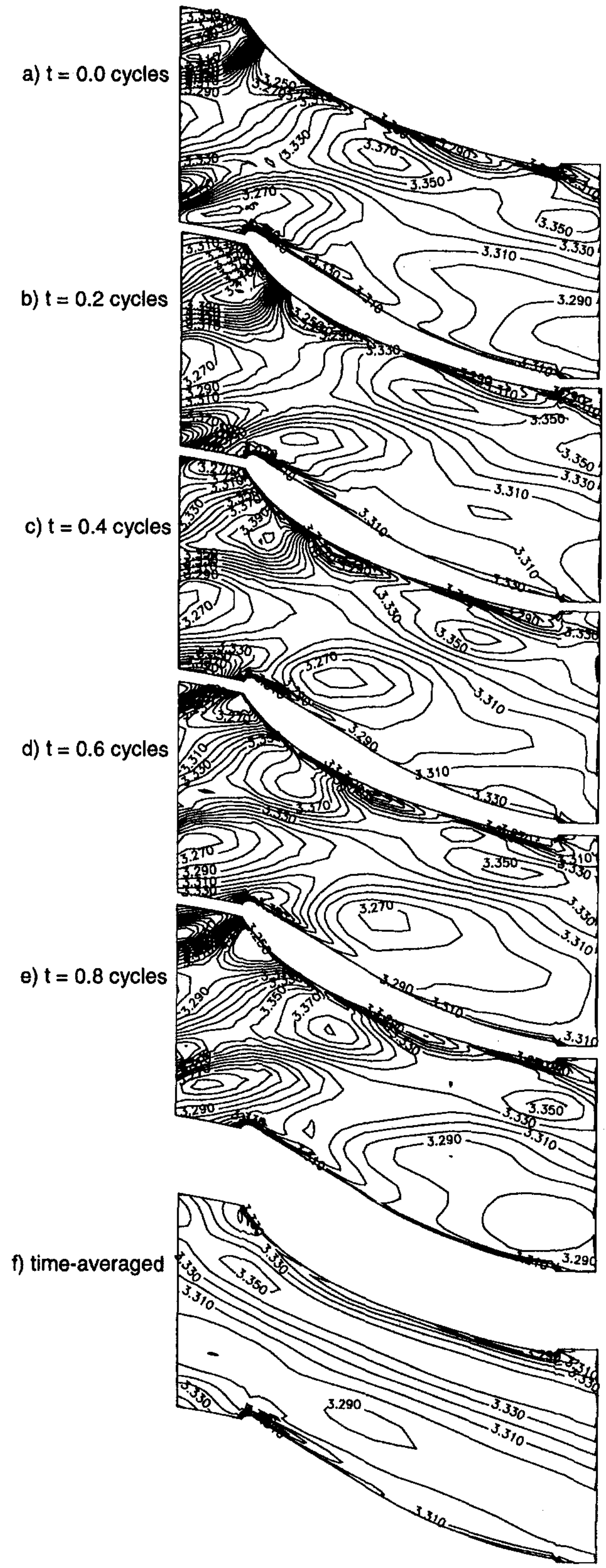

Fig. 8 Contours of rothalpy

Finally, a new scenario was found leading to wake rectification. It was shown that the unsteady flow field generated as the wake created by an upstream stator blade convects past the leading edge of the downstream rotor can lead to a rectification of the rothalpy field. This unsteady process is dynamic, as opposed to the kinematic process identified by Kerrebrock and

Mikolajczak (1970). The resulting rectified rothalpy field produces a rectified rotary total pressure field, which may be harnessed to enhance rotor performance. It is speculated that a similar rectification process may occur within stators. Further investigation of the observed rectification process is warranted.

References

Adamczyk, J. J., 1985, "Model Equation for Simulating Flows in Multistage Turbomachinery," ASME Paper No. 85-GT-226.

Adamczyk, J. J., Celestina, M. L., Beach, T. A., Barnett, M., 1990, "Simulation of Three Dimensional Viscous Flow Within a Multistage Turbine," ASME JOURNAL OF TURBOMACHINERY, Vol. 112, pp. 370–376.

Atkins, G. G., Jr., and Smith, L. H., Jr., 1982, "Spanwise Mixing in Axial-Flow Turbomachines," ASME *Journal of Engineering for Power,* Vol. 104, pp. 97–110.

Baldwin, B. S., and Lomax, H., 1978, "Thin Layer Approximation and Algebraic Model for Separated Turbulent Flows," AIAA Paper No. 78-257.

Butler, T. L., Sharma, O. P., Joslyn, H. D., and Dring, R. P., 1989, "Redistribution of an Inlet Temperature Distortion in an Axial Flow Turbine Stage," AIAA *J. of Propulsion and Power,* Vol. 5.

Chen, J. P., Celestina, M. L., and Adamczyk, J. J., 1994, "A New Procedure for Simulating Unsteady Flows Through Turbomachinery Blade Passages," ASME Paper No. 94-GT-151.

Dawes, W. N., 1992, "Toward Improved Throughflow Capability: The Use of Three-Dimensional Viscous Flow Solvers in a Multistage Environment," ASME JOURNAL OF TURBOMACHINERY, Vol. 114, pp. 8–17.

Dring, R. P., and Spear, D. A., 1991, "The Effect of Wake Mixing on Compressor Aerodynamics," ASME JOURNAL OF TURBOMACHINERY, Vol. 113, No. 4.

Hathaway, M. D., Suder, K. L., Okiishi, T. H., Strazisar, A. J., and Adamczyk, J. J., 1987, "Measurements of the Unsteady Flow Field Within the Stator Row of a Transonic Axial-Flow Fan II," ASME Paper No. 87-GT-227.

Kerrebrock, J. L., and Mikolajczak, A. A., 1970, "Intra-stator Transport of Rotor Wakes and Its Effect on Compressor Performance," ASME *Journal of Engineering for Power,* Vol. 92A, pp. 359–368.

Stewart, W. L., 1959, "Analysis of Two-Dimensional Flow Loss Characteristics Downstream of Turbomachine Blade Rows in Terms of Basic Boundary Layer Characteristics," NACA TN 3515.

Computation and Simulation of Wake-Generated Unsteady Pressure and Boundary Layers in Cascades: Part 1—Description of the Approach and Validation

S. Fan
Graduate Assistant.
Mem. ASME

B. Lakshminarayana
Evan Pugh Professor of
Aerospace Engineering.
Fellow ASME

Center for Gas Turbines and Power,
Pennsylvania State University,
University Park, PA 16802

The unsteady pressure and boundary layers on a turbomachinery blade row arising from periodic wakes due to upstream blade rows are investigated in this paper. A time-accurate Euler solver has been developed using an explicit four-stage Runge–Kutta scheme. Two-dimensional unsteady nonreflecting boundary conditions are used at the inlet and the outlet of the computational domain. The unsteady Euler solver captures the wake propagation and the resulting unsteady pressure field, which is then used as the input for a two-dimensional unsteady boundary layer procedure to predict the unsteady response of blade boundary layers. The boundary layer code includes an advanced $k-\epsilon$ model developed for unsteady turbulent boundary layers. The present computational procedure has been validated against analytic solutions and experimental measurements. The validation cases include unsteady inviscid flows in a flat-plate cascade and a compressor exit guide vane (EGV) cascade, unsteady turbulent boundary layer on a flat plate subject to a traveling wave, unsteady transitional boundary layer due to wake passing, and unsteady flow at the midspan section of an axial compressor stator. The present numerical procedure is both efficient and accurate in predicting the unsteady flow physics resulting from wake/blade-row interaction, including wake-induced unsteady transition of blade boundary layers.

Introduction

The flow in a turbomachinery stage is essentially unsteady. Most of the unsteadiness is due to the combination of circumferential nonuniform flow field in each blade row and the relative motion between the rotor and stator blade rows. Three different sources have been identified as being responsible for generating the majority of the unsteadiness in the flow field. Viscous wakes from the proceeding stator or rotor blade row pass through the succeeding rotor or stator blade row, generating unsteady pressure, surface heat transfer, and boundary layers. This is called wake/blade-row interaction. Unsteadiness is also generated due to the relative motion between the rotor and stator pressure fields, known as potential interaction. In a turbomachinery stage, three-dimensional interactions arise due to the transport of secondary flows, tip leakage flows, and skewed end wall boundary layers, etc., through the subsequent blade row. Unsteadiness also arises from unsteady separation, trailing edge vortex shedding, transition and random turbulence fluctuation, etc. The purpose of the present work is to investigate the effects of viscous wakes on the unsteady pressure and turbulent boundary layers on the subsequent blade row.

Many attempts have been made to predict rotor/stator interactions by solving the unsteady Navier–Stokes equations. The numerical schemes used range from explicit schemes (Jorgensen and Chima, 1988; Lewis et al., 1989; Giles and Haimes, 1993) to implicit schemes (Rai, 1989; Ho and Lakshminarayana, 1993; Chen and Whitfield, 1993). Ideally, the solution of the Navier–Stokes equations with an adequate turbulence model and enough grid resolution is capable of fully resolving the unsteady flow due to rotor/stator interaction. In practice, however, most of the above-mentioned Navier–Stokes solutions can only provide accurate prediction of the unsteady pressure field. One of the major concerns is the grid resolution of unsteady viscous layers, and/or the computing cost for the Navier–Stokes solutions.

It is well known that the length scales in an unsteady cascade flow due to rotor/stator interaction are quite different from those in a steady cascade flow. In a steady flow of high Reynolds number, typical length scale for the potential flow region is comparable to the pitch or chord of the blade and the one for the near-wall viscous region is the boundary layer thickness. In an unsteady cascade flow, however, at least two more length scales are also important. The first one is the width of the incoming wake, which affects the solution in the core flow region. The second one is the length scale of the unsteady viscous shear wave. Since the typical width of a wake is smaller than the pitch or chord of the blade, and the wake is constantly passing through the blade passage, a much finer and more uniform grid (compared to corresponding grid for steady computation) is necessary in order to capture the unsteady transport of wakes accurately. This is also true for the accurate prediction of unsteady pressure waves resulting from rotor/stator interaction. As an example, Giles (1988) used a grid of 400×50 to predict an inviscid wake/blade-row interaction accurately in a flat plate cascade. In the meantime, the ratio of the thickness of the steady boundary layer to that of the unsteady viscous

Contributed by the International Gas Turbine Institute and presented at the 39th International Gas Turbine and Aeroengine Congress and Exposition, The Hague, The Netherlands, June 13–16, 1994. Manuscript received by the International Gas Turbine Institute February 9, 1994. Paper No. 94-GT-140. Associate Technical Editor: E. M. Greitzer.

shear layer increases with the reduced frequency ($\omega x/\bar{u}_e$ for laminar boundary layer and $\omega\nu/\bar{u}_\tau^2$ for turbulent boundary layer) for an unsteady free-stream velocity condition of $\tilde{u}_e(t) = \bar{u}_e[1 + D \sin(\omega t)]$, where D is the ratio of the wave amplitude to the mean free-stream velocity. Based on the unsteady turbulent boundary layer measurements of Menendez and Ramaprian (1989) on a flat plate, an estimate shows that the thickness of the blade boundary layer is much larger than that of the unsteady viscous shear layer near the trailing edge of the blade. The fact that the unsteady viscous shear layer could be much thinner than the steady boundary layer means many more computational grid points are required in the near-wall viscous region in order to capture both the steady and the unsteady boundary layers accurately. A study by Giles and Haimes (1993) indicates that with the typical number of grid points used, most Navier–Stokes calculations of unsteady flow barely resolve the details of the unsteady viscous flow in the lower part of the boundary layer. An accurate prediction of unsteady blade surface boundary layers from a Navier–Stokes solver is not practical at the present time due to enormous computational resources required.

At high Reynolds number, the majority of the flow region in the blade passage can be treated as inviscid. The investigation by Hodson (1985) indicates that many of the phenomena associated with wake/blade-row interactions are dominated by inviscid effects. Hence, an inviscid scheme is sufficient to predict the transport of wakes through the blade passages and the resulting unsteady pressure field. This approach has been adopted by many other researchers to predict wake/blade-row interactions (Giles, 1988; Liu and Sockol, 1989; Korakianitis, 1992).

The near-wall viscous flow region can be adequately described using a boundary layer model, with the unsteady edge conditions provided by the inviscid solution. Power et al. (1991) used an unsteady boundary layer solver to predict heat transfer on the rotor and stator blade surfaces of a low-speed turbine. The unsteady pressure was obtained from the experimental data. Tran and Taulbee (1992) solved the unsteady Euler equation to obtain the time-dependent surface pressure and used it as input to predict the unsteady heat transfer on the blade surface of a turbine rotor. A similar approach was also used by Korakianitis et al. (1993) to predict turbine rotor heat transfer.

In the present study, a time-accurate Euler solver has been developed based on a steady Navier–Stokes code (RKCC) developed earlier by Kunz and Lakshminarayana (1992). An explicit four-stage Runge–Kutta scheme is used to integrate the unsteady Euler equations. The two-dimensional unsteady nonreflecting boundary condition developed by Giles (1990) has been implemented in the present Euler code. Unsteady boundary layer solutions are obtained using a modified unsteady boundary layer code originally developed by Power et al. (1991). The modified boundary layer code includes a $k-\epsilon$ model developed by Fan et al. (1993) for unsteady turbulent boundary layers.

This paper presents the numerical approach and validations of the computational procedures. Detailed analysis of the results and a numerical study of the effects of various design parameters on the unsteady blade boundary layers is presented in Part 2.

Unsteady Euler Procedure

Governing Equations. The compressible two-dimensional unsteady Euler equations are written in generalized coordinates and in conservative form as:

$$\frac{\partial \hat{Q}}{\partial t} + \frac{\partial \hat{E}}{\partial \xi} + \frac{\partial \hat{F}}{\partial \eta} = 0 \tag{1}$$

Nomenclature

c = chord length/speed of sound
c_x = axial chord length
c_1, c_2, c_3, c_4 = characteristic variables
C_f = skin friction coefficient $= \tau_w/(0.5\rho_{is}q_{is}^2)$
C_p = pressure coefficient $= (p - p_{\rm ref})/0.5\rho_{is}q_{is}^2$
D = artificial dissipation operator/amplitude of nondimensional wake velocity defect
e = total energy per unit mass, Eq. (6)
f = frequency, Hz
E, F = flux vectors
G_1, G_2 = contravariant velocity components
H = total enthalpy/shape factor
J = Jacobian of curvilinear transformation
k = turbulence kinetic energy $= 0.5((u')^2 + (v')^2 + (w')^2)$
k_4 = fourth-order artificial dissipation constant
L = nominal length of the flat plate
n_w, n_b = number of rotor wakes, number of stator blades
p, p_o = static pressure, stagnation pressure
$p_{\rm ref}$ = static pressure on the casing at inlet
Pr, $\Pr_t$ = molecular and turbulent Prandtl numbers
P_w, P_b = rotor wake pitch, stator blade pitch
q_{is} = total steady velocity at inlet to the blade row
q_n = maximum unsteady inlet velocity in the wake normal to q_{is}
Q = primary transport variable vector/wave traveling speed
R = residual vector/gas constant
Re = Reynolds number based on chord
Re_θ = Reynolds number based on momentum thickness
Re_x = Reynolds number based on x
$\mathrm{Re}_t, \mathrm{Re}_y$ = turbulent Reynolds numbers; Re_t: $k^2/\nu\epsilon$, Re_y: $\sqrt{k}y/\nu$
$S_{4\xi}, S_{4\eta}$ = artificial dissipation scale factors
t = time
T = static temperature/blade passing period
T_u = turbulence intensity $= [((u')^2 + (v')^2 + (w')^2)/3]^{0.5}/\bar{u}_e$
u, v = velocity components in x, y directions
u_τ = friction velocity, $\sqrt{\tau_w/\rho}$
U = wake traverse speed
w = dimensionless wake width parameter, Eq. (41)
x, y = Cartesian coordinates/surface coordinates in boundary layer equations
x_c = distance along the chord
y^+ = inner variable, $u_\tau y/\nu$
α = stator inlet absolute flow angle (counterclockwise from axial direction)
β = rotor outlet relative flow angle (clockwise from axial direction)
γ = specific heat ratio/intermittency factor $= (H - H_l)/(H_t - H_l)$
δ, θ = boundary layer thickness, momentum thickness
$\delta_{\xi\xi\xi\xi}, \delta_{\eta\eta\eta\eta}$ = central fourth-order-difference operators
Δt = time step
Δp = $p_s - p_p$, normalized by unsteady dynamic head $\rho q_s q_r$.
ϵ = dissipation rate of turbulent kinetic energy
μ, μ_t = molecular and turbulent eddy viscosity
ν = kinematic viscosity

where

$$\hat{Q} = \frac{1}{J}\begin{Bmatrix} \rho \\ \rho u \\ \rho v \\ \rho e \end{Bmatrix}, \quad \hat{E} = \frac{1}{J}\begin{Bmatrix} \rho G_1 \\ \rho u G_1 + \xi_x p \\ \rho v G_1 + \xi_y p \\ (\rho e + p) G_1 \end{Bmatrix},$$

$$\hat{F} = \frac{1}{J}\begin{Bmatrix} \rho G_2 \\ \rho u G_2 + \eta_x p \\ \rho v G_2 + \eta_y p \\ (\rho e + p) G_2 \end{Bmatrix} \tag{2}$$

$$G_1 = \xi_x u + \xi_y v, \quad G_2 = \eta_x u + \eta_y v \tag{3}$$

$$J = \xi_x \eta_y - \eta_x \xi_y \tag{4}$$

$$\xi_x = \frac{\partial \xi}{\partial x}, \quad \xi_y = \frac{\partial \xi}{\partial y}, \quad \eta_x = \frac{\partial \eta}{\partial x}, \quad \eta_y = \frac{\partial \eta}{\partial y} \tag{5}$$

where ρ, u, v, p, e are the density, velocity components in x, y directions, pressure, and total internal energy. The total energy is defined as

$$e = \frac{R}{\gamma - 1} T + \frac{1}{2}(u^2 + v^2) \tag{6}$$

where γ is the specific heat ratio and R is the gas constant. For a perfect gas, $p = \rho RT$.

Numerical Solution Procedure. The standard four-stage Runge–Kutta scheme is used to discretize the governing equations:

$$\hat{Q}^1 = \hat{Q}^n + \tfrac{1}{4}\Delta t \hat{R}(\hat{Q}^n) \tag{7}$$

$$\hat{Q}^2 = \hat{Q}^n + \tfrac{1}{3}\Delta t \hat{R}(\hat{Q}^1) \tag{8}$$

$$\hat{Q}^3 = \hat{Q}^n + \tfrac{1}{2}\Delta t \hat{R}(\hat{Q}^2) \tag{9}$$

$$\hat{Q}^{n+1} = \hat{Q}^n + \Delta t \hat{R}(\hat{Q}^3) \tag{10}$$

where R is defined as:

$$\hat{R} = -\left(\frac{\partial \hat{E}}{\partial \xi} + \frac{\partial \hat{F}}{\partial \eta}\right) \tag{11}$$

The scheme is fourth-order accurate in time. Central differences are used to discretize the spatial derivatives in Eq. (11).

Fourth-order artificial dissipation is needed to stabilize the Runge–Kutta scheme. The residual with artificial dissipation becomes:

$$\hat{R} = -\left(\frac{\partial \hat{E}}{\partial \xi} + \frac{\partial \hat{F}}{\partial \eta}\right) + S_{4\xi}\delta_{\xi\xi\xi\xi}Q + S_{4\eta}\delta_{\eta\eta\eta\eta}Q \tag{12}$$

The eigenvalue scaling of the artificial dissipation terms proposed by Martinelli (1987) is used:

$$S_{4\xi} = \frac{k_4}{J}\left[\frac{1}{\Delta t_{c\xi}}\left(1 + \frac{\Delta t_{c\xi}}{\Delta t_{c\eta}}\right)^{\alpha}\right] \tag{13}$$

$$S_{4\eta} = \frac{k_4}{J}\left[\frac{1}{\Delta t_{c\eta}}\left(1 + \frac{\Delta t_{c\eta}}{\Delta t_{c\xi}}\right)^{\alpha}\right] \tag{14}$$

Here, $\Delta t_{c\xi}$, $\Delta t_{c\eta}$ are the time steps required for stability of the inviscid one-dimensional problem in each direction:

$$\Delta t_{c\xi} = \frac{\mathrm{CFL}}{|G_1| + c\sqrt{\nabla \xi \cdot \nabla \xi}} \tag{15}$$

$$\Delta t_{c\eta} = \frac{\mathrm{CFL}}{|G_2| + c\sqrt{\nabla \eta \cdot \nabla \eta}} \tag{16}$$

in which c is the speed of sound. The empirical coefficient α in Eqs. (13) and (14) is chosen between $\frac{1}{2}$ and $\frac{2}{3}$.

Boundary Conditions. At the wall boundaries, normal velocity is set to zero and the adiabatic wall conditions are used.

Periodic boundary conditions are used in the pitchwise direction as in a steady solution. If the rotor and stator have the same number of blades, the unsteady computation can be carried out by solving a single blade passage. When the blade count differs between the rotor and the stator, a multipassage solution is generally necessary. The coding technique in the present program allows for the solution to be carried out for an arbitrary number of blade passages.

At the inlet and outlet boundaries, conventional boundary conditions (total pressure, total temperature, and flow angle at the inlet boundary, static pressure at the outlet boundary) are used for the steady computation. For the unsteady computation, the two-dimensional unsteady nonreflecting boundary conditions developed by Giles (1990) are used. For the inlet boundary, the boundary conditions are split into two parts. The first part is a specified unsteady inlet flow determined through a wake profile. The second part is a perturbation over and above the specified wake profile, corresponding to the incoming and outgoing unsteady characteristic waves.

The inlet wake profile can be obtained from wake models, experimental measurements, and Navier–Stokes solution for the preceding blade row. Following the work of Giles (1988), the wake is assumed to be parallel, with uniform static pressure and total enthalpy across the wake in the blade frame. The wake

Nomenclature (cont.)

σ_k, σ_ϵ = turbulent Prandtl numbers for k and ϵ
ξ, η = curvilinear coordinates
ρ = density
τ_w = wall shear stress
ω = wake passing frequency = $2\pi U/P_w$
Ω = reduced frequency = $\omega c_x/u_{is}$

Superscripts and Subscripts

c = chord
e = free-stream quantity
inl = prescribed inlet variables in the blade frame of reference
is = inlet steady values in the blade frame of reference
iw = inlet wake values in the wake frame of reference
l = laminar quantity
os = outlet steady values in the blade frame of reference
p = pressure surface
s = stator/steady-state/suction surface
sw = inlet steady values in the wake frame of reference
t = turbulence quantity
w = wake quantity/quantity at the wall
∞ = free-stream/reference quantity
$\hat{}$ = quantity scaled by metric Jacobian
$-$ = time-averaged quantity
$\sim$ = ensemble-averaged quantity
$'$ = turbulent fluctuating quantity
amp[ ] = amplitude of the first Fourier component
phs[ ] = phase angle of the first Fourier component

density, velocity, and static pressure are given in the blade frame as:

$$p_{iw} = p_{sw} \tag{17}$$

$$u_{iw} = q_{sw}[1 - f(\eta)] \cos(\alpha_{sw}) \tag{18}$$

$$v_{iw} = q_{sw}[1 - f(\eta)] \sin(\alpha_{sw}) \tag{19}$$

$$\rho_{iw} = \frac{\gamma}{\gamma - 1} \frac{p_{sw}}{[H_{sw} - 0.5(u_{iw}^2 + v_{iw}^2)]} \tag{20}$$

where the subscript sw stands for the steady values and iw denotes the wake values at the inlet boundary in the wake/rotor frame of reference. α_{sw} is the wake flow angle, $f(\eta)$ is the nondimensional wake profile function and η is the local wake coordinate.

According to Giles (1990), the transformation to and from the one-dimensional characteristic variables can be written as

$$\begin{pmatrix} c_1 \\ c_2 \\ c_3 \\ c_4 \end{pmatrix} = \begin{pmatrix} -c^2 & 0 & 0 & 1 \\ 0 & 0 & \rho c & 0 \\ 0 & \rho c & 0 & 1 \\ 0 & -\rho c & 0 & 1 \end{pmatrix} \begin{pmatrix} \delta\rho \\ \delta u \\ \delta v \\ \delta p \end{pmatrix}$$

$$\begin{pmatrix} \delta\rho \\ \delta u \\ \delta v \\ \delta p \end{pmatrix} = \begin{pmatrix} -1/(c^2) & 0 & 1/(2c^2) & 1/(2c^2) \\ 0 & 0 & 1/(2\rho c) & -1/(2\rho c) \\ 0 & 1/(\rho c) & 0 & 0 \\ 0 & 0 & 1/2 & 1/2 \end{pmatrix} \begin{pmatrix} c_1 \\ c_2 \\ c_3 \\ c_4 \end{pmatrix} \tag{22}$$

where $\delta(\ ) = (\ ) - (\ )_{inl}$ at the inlet boundary (the subscript inl denotes the prescribed inlet variables in the blade frame of reference), and $\delta(\ ) = (\ ) - (\ )_{os}$ at the outlet boundary (the subscript os denotes the steady outlet values in the blade frame of reference). The four characteristic variables c_1, c_2, c_3, c_4 correspond to the entropy wave, the downstream going pressure wave, the vorticity wave, and the upstream going pressure wave.

At the inlet boundary, the outgoing characteristic variable c_4 is extrapolated from the interior flow solution, the three incoming characteristic variables c_1, c_2, c_3 are determined from the following equation:

$$\frac{\partial}{\partial t}\begin{pmatrix} c_1 \\ c_2 \\ c_3 \end{pmatrix} + \begin{pmatrix} v & 0 & 0 & 0 \\ 0 & v & (c+u)/2 & (c-u)/2 \\ 0 & (c-u)/2 & v & 0 \end{pmatrix} \times \frac{\partial}{\partial y}\begin{pmatrix} c_1 \\ c_2 \\ c_3 \\ c_4 \end{pmatrix} = 0 \tag{23}$$

At the outlet boundary, the three outgoing characteristic variables c_1, c_2, c_3 are extrapolated from the interior solution, the one incoming characteristic variable is determined by the following equation:

$$\frac{\partial c_4}{\partial t} + (0 \quad u \quad 0 \quad v)\frac{\partial}{\partial y}\begin{pmatrix} c_1 \\ c_2 \\ c_3 \\ c_4 \end{pmatrix} = 0 \tag{24}$$

Equations (23) and (24) are transformed into the generalized coordinates and solved using the same integration scheme for the Euler equations. Central difference is used to discretize the pitchwise derivative. A fourth-order artificial dissipation term, similar in form and magnitude to those for the Euler equation, is found to be necessary to remove odd-even decoupling of the solution due to the use of the central difference. At each time step, the pitch-averaged incoming characteristic variables are set to zero, as is required by Eqs. (23) and (24).

Boundary Layer Procedure

The unsteady two-dimensional compressible boundary layer procedure and the code were originally developed by Power et al. (1991) using a mixing length turbulence model. A low-Reynolds-number form $k-\epsilon$ model has been developed and implemented in this code by Fan et al. (1993). The unsteady boundary layer equations and the $k-\epsilon$ equations are given as:

$$\frac{\partial\tilde{\rho}}{\partial t} + \frac{\partial(\tilde{\rho}\tilde{u})}{\partial x} + \frac{\partial(\tilde{\rho}\tilde{v})}{\partial y} = 0 \tag{25}$$

$$\tilde{\rho}\frac{\partial\tilde{u}}{\partial t} + \tilde{\rho}\tilde{u}\frac{\partial\tilde{u}}{\partial x} + \tilde{\rho}\tilde{v}\frac{\partial\tilde{u}}{\partial y} = -\frac{\partial\tilde{p}}{\partial x} + \frac{\partial}{\partial y}\left[(\mu + \mu_t)\frac{\partial\tilde{u}}{\partial y}\right] \tag{26}$$

$$\tilde{\rho}\frac{\partial\tilde{H}}{\partial t} + \tilde{\rho}\tilde{u}\frac{\partial\tilde{H}}{\partial x} + \tilde{\rho}\tilde{v}\frac{\partial\tilde{H}}{\partial y} = \frac{\partial\tilde{p}}{\partial t} + \frac{\partial}{\partial y}\left[\mu\left(1 - \frac{1}{\mathrm{Pr}}\right)\tilde{u}\frac{\partial\tilde{u}}{\partial y} + \left(\frac{\mu}{\mathrm{Pr}} + \frac{\mu_t}{\mathrm{Pr}_t}\right)\frac{\partial\tilde{H}}{\partial y}\right] \tag{27}$$

$$\tilde{\rho}\frac{\partial k}{\partial t} + \tilde{\rho}\tilde{u}\frac{\partial k}{\partial x} + \tilde{\rho}\tilde{v}\frac{\partial k}{\partial y} = \frac{\partial}{\partial y}\left[\left(\mu + \frac{\mu_t}{\sigma_k}\right)\frac{\partial k}{\partial y}\right] + \mu_t\left(\frac{\partial\tilde{u}}{\partial y}\right)^2 - \tilde{\rho}\epsilon \tag{28}$$

$$\tilde{\rho}\frac{\partial\epsilon}{\partial t} + \tilde{\rho}\tilde{u}\frac{\partial\epsilon}{\partial x} + \tilde{\rho}\tilde{v}\frac{\partial\epsilon}{\partial y} = \frac{\partial}{\partial y}\left[\left(\mu + \frac{\mu_t}{\sigma_\epsilon}\right)\frac{\partial\epsilon}{\partial y}\right] + C_{\epsilon1}f_1\frac{\epsilon}{k}\mu_t\left(\frac{\partial\tilde{u}}{\partial y}\right)^2 - \tilde{\rho}C_{\epsilon2}f_2\frac{\epsilon^2}{k} \tag{29}$$

where

$$\mu_t = \rho C_\mu f_\mu k^2/\epsilon \tag{30}$$

and k, ϵ are the ensemble-averaged turbulent kinetic energy and dissipation rate.

The values of the model constants are $C_\mu = 0.09$, $\sigma_k = 1.0$, $\sigma_\epsilon = 1.3$, $C_{\epsilon1} = 1.4$, $C_{\epsilon2} = 1.8$. The near-wall and low-Reynolds-number functions f_μ, f_1, f_2 are given by

$$f_\mu = 0.4\frac{f_w}{\sqrt{\mathrm{Re}_t}} + \left(1 - 0.4\frac{f_w}{\sqrt{\mathrm{Re}_t}}\right)\left[1 - \exp\left(-\frac{\mathrm{Re}_y}{42.63}\right)\right]^3 \tag{31}$$

$$f_1 = 1.0 \tag{32}$$

$$f_2 = \left\{1.0 - \frac{0.4}{1.8}\exp\left[-\left(\frac{\mathrm{Re}_t}{6}\right)^2\right]\right\}f_w^2 \tag{33}$$

where

$$f_w = 1 - \exp\left\{-\frac{\sqrt{\mathrm{Re}_y}}{2.30} + \left(\frac{\sqrt{\mathrm{Re}_y}}{2.30} - \frac{\mathrm{Re}_y}{8.89}\right) \times \left[1 - \exp\left(-\frac{\mathrm{Re}_y}{20}\right)\right]^3\right\} \tag{34}$$

The boundary layer equations and the $k-\epsilon$ equations are transformed using a modified Levy–Lees transformation. A

Table 1 Flat plate cascade parameters, from Giles (1988)

Pitch/Chord (P_y/c)	0.5
Stagger angle (steady flow angle)	30°
Mach number (steady flow)	0.7
Wake number n_w/n_h	1.0
Wake inflow angle (rotor outlet flow angle)	30°
Wake velocity defect	5%
Reduced frequency (Ω)	12.57

fully implicit numerical scheme is used to solve the transformed equations (see Power et al., 1991, for detailed description of the solution procedure).

The boundary conditions for k and ϵ are: $k = 0$, $\partial\epsilon/\partial y = 0$ at the solid wall surface. The free-stream turbulence is determined by solving the following equations at the outer edge of the solution domain:

$$\frac{\partial k_e}{\partial t} + \tilde{u}_e \frac{\partial k_e}{\partial x} = -\epsilon_e \tag{35}$$

$$\frac{\partial \epsilon_e}{\partial t} + \tilde{u}_e \frac{\partial \epsilon_e}{\partial x} = -C_{\epsilon 2}\frac{\epsilon_e^2}{k_e} \tag{36}$$

The temporal history of the free-stream turbulence quantities at the first streamwise station can be deduced from experimental measurements or Navier–Stokes solutions of the flow in the preceding blade row using a $k-\epsilon$ model.

The profiles of k and ϵ in the normal direction at the initial streamwise station are prescribed as

$$k = k_e(\tilde{u}/\tilde{u}_e)^2 \tag{37}$$

$$\epsilon = 0.1k(\partial\tilde{u}/\partial y) \tag{38}$$

Validation of Numerical Procedures

The code is validated against the following analytical and/or experimental results:

1 Inviscid wake/blade-row interaction in a flat-plate cascade;
2 Inviscid wake/blade-row interaction in a compressor EGV cascade;
3 Unsteady turbulent boundary layer subject to traveling wave disturbance;
4 Steady and unsteady boundary layer transition;
5 Wake/blade-row interaction in an axial compressor stator cascade.

These are described in detail below.

1 Inviscid Wake/Blade-Row Interaction in a Flat Plate Cascade. In order to validate the unsteady Euler solver described above, a flat-plate cascade flow subject to the influence of unsteady incoming wakes is computed. This case has been used by Giles (1988) to validate the nonlinear Euler code. A sinusoidal function is chosen for the incoming wake shape. The magnitude of the wake velocity defect used is 5 percent of the inlet steady velocity. The geometric and flow parameters for this cascade are listed in Table 1. Since there is no steady load and the amplitude of the unsteadiness is small, the linear analytic solution by Whitehead (1970, LINSUB) is expected to be accurate and therefore used to validate the code.

An H grid is used for the unsteady Euler solution. Fifty-one grid points are used in the pitchwise direction and 151 grid points are used in the streamwise direction. Of the 151 streamwise grid points, 40 are distributed between the inlet and the leading edge, 80 are distributed on the blade surface. The time-accurate solution starts from a steady-state solution, which, in this case, is a uniform flow. One thousand time steps are used for each blade passing period. The time step is chosen to be smaller than the minimum limiting time steps among all the grid points for the steady solution.

The pressure difference between the suction surface and the pressure surface at the leading edge, 50 percent chord, and the trailing edge, as well as the lift and moment coefficients, are used to determine the convergence of the solution. For this test case, all the unsteady pressures are normalized by the product of the mean density, the mean speed, and the maximum wake defect velocity normal to the steady inlet flow ($\rho_{is}q_{is}q_n$). For the periodic solution considered, the residue is defined as the difference between the solutions in two consecutive periods. For the flat-plate cascade case, 20 wake passing periods were computed to converge the lift and moment coefficients within 1 percent. Figure 1 shows the convergence history of the leading edge, 50 percent chord, trailing edge pressure differences. The nonperiodic residue approaches zero as the number of blade passing periods increases.

In Fig. 2, the computed unsteady blade surface pressure difference across the blade is compared with the linear analytic solution from LINSUB, which is given by Giles (1988). For convenience, the phase angle at the leading edge is set to zero. The computed amplitude and phase angle agree very well with the analytic solution.

2 Inviscid Wake/Blade-Row Interaction in a Compressor EGV Cascade. To validate the present code for a more realistic cascade flow, including the effects of camber and thickness, the flow in a compressor exit guide vane (EGV) cascade subjected to an incoming vorticity wave is computed. The unsteady response of the EGV cascade to the vorticity wave was obtained by Verdon et al. (1991) by solving the linearized potential equations. For this flow case, the computation by Dorney (1992), using the code originally developed by Rai (1989), showed very good agreement between the linearized inviscid

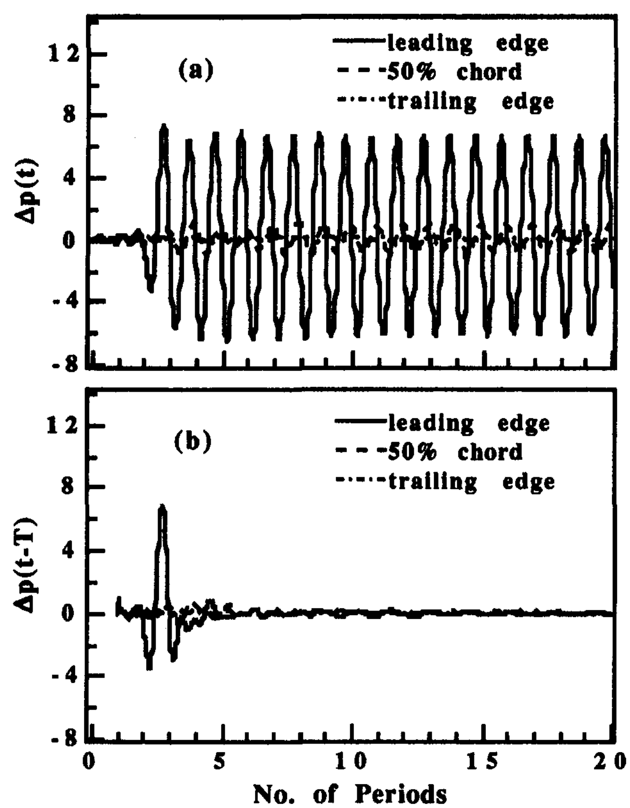

Fig. 1 Convergence history: (*a*) periodic solution, (*b*) nonperiodic residue

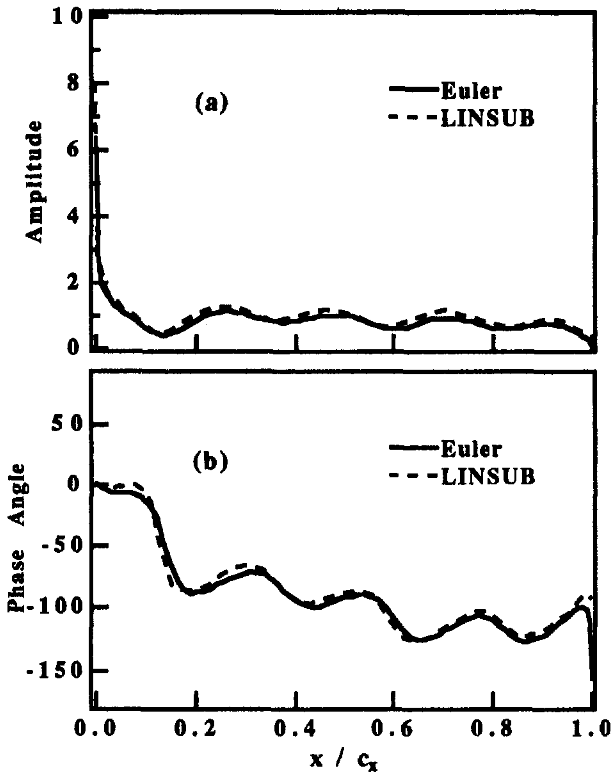

Fig. 2 Unsteady pressure difference for flat-plate cascade: (*a*) amplitude, (*b*) phase angle

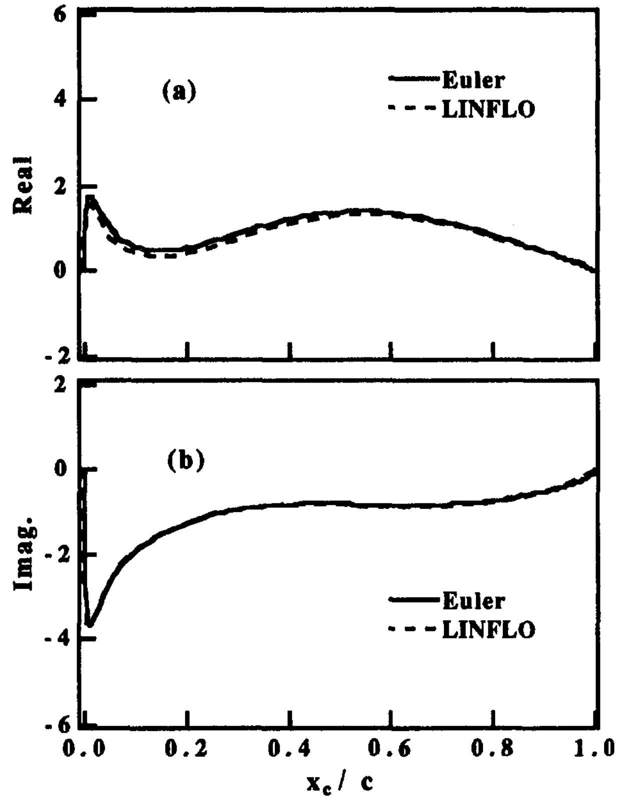

Fig. 3 Unsteady pressure difference for EGV cascade: (*a*) real, (*b*) imaginary

solution, the nonlinear Euler solution and the Navier–Stokes solution. The present prediction is compared with the linearized inviscid solution of Verdon et al. (1991).

The geometric and flow parameters of the EGV cascade are listed in Table 2. Details on specifying the inlet vorticity wave can be found in Verdon et al. (1991), and are not repeated here for brevity. Sixty-one grid points are used in the pitchwise direction and 261 grid points are used in the streamwise direction. Of the 261 streamwise grid points, 90 points are distributed between the inlet and the leading edge, 100 points on the blade surface. For the case computed, the pitch of the vorticity wave is twice as large as the pitch of the cascade. Therefore, two blade passages are solved simultaneously in order to satisfy the periodic boundary conditions. The time-accurate computation starts from a steady flow solution. A constant time step deduced from the steady-state solution is used for the time accurate solution. In this case, the frequency and the steady Mach number are rather small. Twenty-four hundred time steps are used within each blade passing period.

The computed unsteady pressure difference across the blade is compared with the results from the linearized inviscid theory (LINFLO) in Fig. 3. For this test case, all the unsteady pressures are normalized by the product of the mean density, the mean speed, and the maximum wake defect velocity normal to the inlet flow ($\rho_{is}q_{is}q_n$). The first harmonic of unsteady pressure difference is given in the form of real (in phase) part and imaginary (out of phase) part. The computed unsteady pressure agrees very well with the linearized inviscid solution.

Table 2 Compressor EGV cascade parameters, from Verdon et al. (1991)

Pitch/Chord (P_y/c)	0.6
Stagger angle	15°
Steady inflow angle	30°
Mach number (steady flow)	0.3
Wake number n_w/n_b	0.5
Wake inflow angle (rotor outlet flow angle)	-12.3°
Fractional wake velocity defect	5%
Reduced frequency (Ω)	5.58

The in-phase components of the first harmonic of the unsteady pressure field, predicted from the unsteady Euler solution and the linearized inviscid solution (LINFLO), are compared in Fig. 4. Very good agreement is shown between the unsteady pressure contours from these two predictions. Despite the use of the two-dimensional nonreflecting boundary conditions, a small amount of pressure wave reflection still remains at the inlet and the outlet boundaries. Detailed comparisons have shown that the intensity of the reflections is much smaller (with the two-dimensional unsteady nonreflecting boundary conditions) than with the one-dimensional unsteady nonreflecting boundary conditions of Giles (1988). The remaining reflections are due to the use of reflective boundary conditions for the steady flows. The small reflections are found to have no significant effects on the prediction of the unsteady pressure on the blade surfaces.

3 Unsteady Turbulent Boundary Layer Subject to Traveling Wave Disturbance

The unsteady turbulent boundary layer subject to an oscillatory free stream in the form of a traveling wave, measured by Patel (1977), is used to validate the boundary layer code. The free-stream velocity is given as

$$\tilde{u}_e = \bar{u}_e\{1 + D \sin [2\pi f(t - x/Q)]\}$$

where D is the ratio of the wave amplitude to the mean free-stream velocity, Q is the convection velocity of the traveling

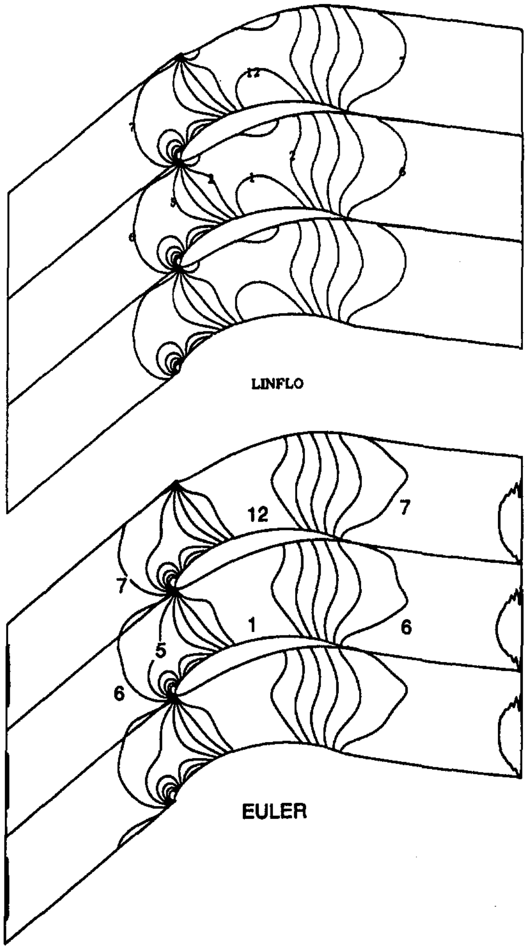

Fig. 4 In-phase component of unsteady pressure $(p - \bar{p})/\rho_{is}q_{is}q_n$ for EGV cascade

wave. For the case computed, $\bar{u}_e = 19.8$ m/s, $D \approx 11$ percent, $f = 4$ Hz, $Q/\bar{u}_e = 0.77$.

Excellent agreement is obtained (not shown) between the measured and predicted time-averaged boundary layer profile and chordwise distribution of time-averaged displacement and momentum thickness. The prediction of the unsteady boundary layer velocity profile is shown in Fig. 5. The first harmonic of the unsteady velocity profile is given in the form of amplitude and phase angle. Comparisons are made at three different streamwise locations of the boundary layer. The agreement between the predicted and the measured distributions of amplitude and phase angle of unsteady velocity is generally very good at all three streamwise locations. The velocity amplitude is slightly underpredicted in the inner portion of the boundary layer at the first two streamwise locations, which is similar to the predictions by Lam (1990).

One important feature of the unsteady velocity profiles is the large phase lag between the oscillatory velocity in the boundary layer and that in the free stream. For a standing wave type of free-stream disturbance, a phase lead up to 45 deg has been observed from both the measurements and the computation (see Menendez and Ramaprian, 1989; Fan and Lakshminarayana, 1993, for example). In the present case, the phase lag of the unsteady boundary layer profile is due to the much slower wave speed of the free-stream unsteady velocity.

4 Steady and Unsteady Boundary Layer Transition

For steady flow, a number of investigators have successfully used the low-Reynolds-number form two-equation models to simulate the transition from laminar to turbulent flows under the influence of free-stream turbulence, (see Rodi and Scheuerer, 1985; Schmidt and Patankar, 1991, for example). The reason a low-Reynolds-number $k-\epsilon$ model can predict the boundary layer transition, as described by Schmidt and Patankar (1991), lies in the correspondence between the near-wall cross-stream regions in a fully turbulent boundary layer, and the progressive stages through which developing boundary layers pass in the streamwise direction. The low-Reynolds-number functions play a key role in transition modeling.

The transition predicted for the steady boundary layer by the present $k-\epsilon$ model, as indicated by the distribution of skin friction coefficient, is shown in Fig. 6(a) at different free-stream turbulence intensities. The computations are made for a flat-plate boundary layer without pressure gradient. Earlier transition is predicted at higher free-stream turbulence intensities. This trend is in agreement with the experimental observations. The momentum Reynolds numbers at the start and the end of transition are compared with the correlation of Abu-Ghannam and Shaw (1980) in Fig. 6(b). Following Schmidt and Patankar (1991), the beginning and the end of transition are defined as the point of minimum and maximum skin friction coefficient, respectively. The beginning of transition predicted from the present $k-\epsilon$ model agrees quite well with the correlation. However, the length of the transition region predicted by the $k-\epsilon$ model is typically shorter than the one given by the correlation. It is expected that this deficiency will have no significant consequence in compressor applications, where transition length is usually short due to the effects of adverse pressure gradient. Improvement to the model is necessary for turbine applications, where transition length is usually longer due to the effects of favorable pressure gradient.

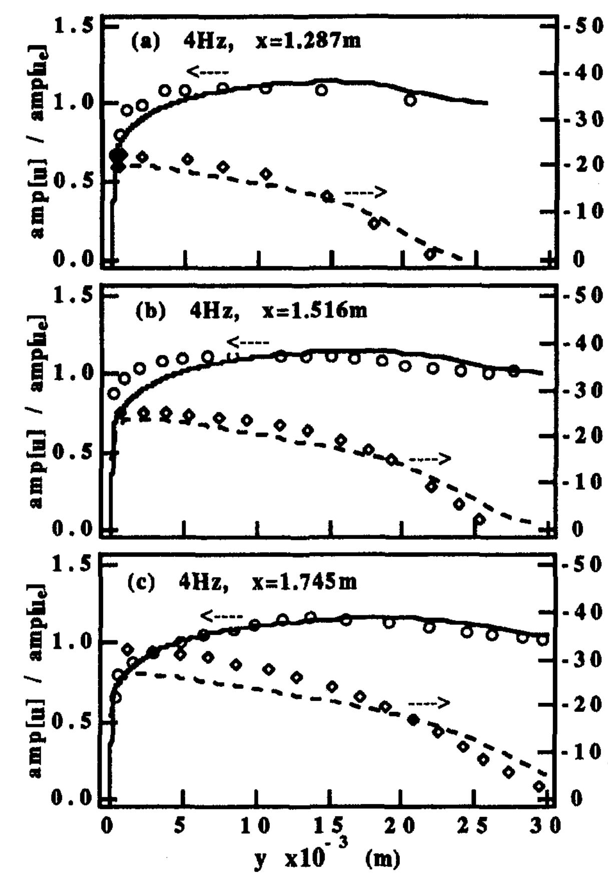

Fig. 5 First Fourier component of velocity profile for unsteady turbulent boundary layer; symbols: data of Patel (1977), lines: prediction

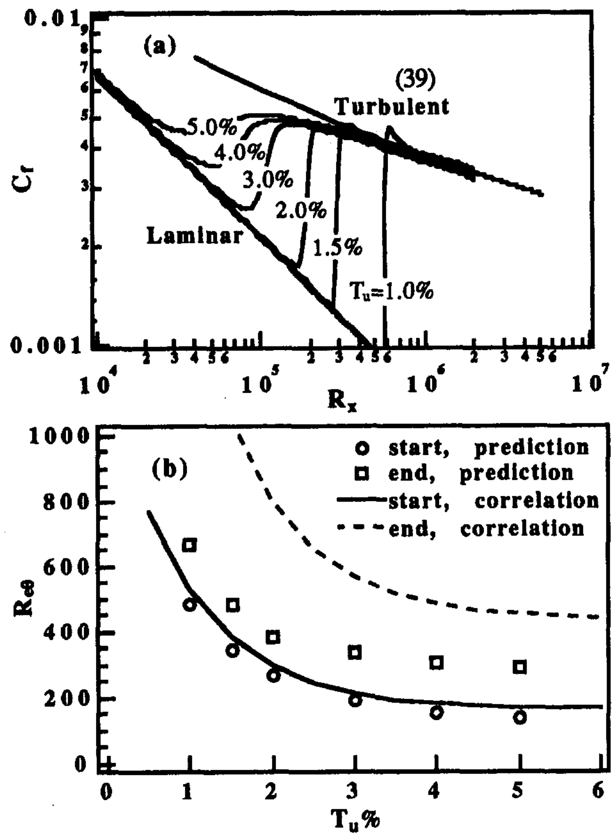

Fig. 6 Transition in steady boundary layer: (*a*) skin friction coefficient, (*b*) start and end of transition locations; correlation from Abu-Ghannam and Shaw (1980)

The unsteady transition in a boundary layer resulting from a passing wake with high turbulence intensity has been investigated experimentally by Pfeil and Herbst (1979), Doorly and Oldfield (1985), Addison and Hodson (1990), Liu and Rodi (1991), and others, (see Mayle, 1991; Hodson, 1991, for detailed reviews). These experimental studies show that the forced transition due to wake turbulence is dominated by the formation and transport of transitional patches. Following the passage of a turbulent wake in the free stream, a highly turbulent region or transitional patch is formed in the boundary layer underneath the wake. The location where the transitional patch starts to form depends on the turbulence level in the wake and the Reynolds number. Following its formation, the transitional patch is transported downstream. The leading edge of the patch is observed to propagate at about the free-stream speed, while the trailing edge propagates at about half of the free-stream speed. The difference between the propagation speed of the leading edge and the trailing edge of the transitional patches results in the spreading of the patch. Between two patches, the boundary layer stays nearly laminar. The transition is completed when two patches merge or when they reach the natural/background transition point. The process described above can be well illustrated by the space–time contour plot of intermittency factors measured in the suction surface boundary layer of a large scale turbine rotor, shown in Fig. 7(*a*), taken from Hodson (1991).

To explore the capability of the $k-\epsilon$ model to predict the wake-induced unsteady transition, the unsteady transitional boundary layer measured by Pfeil and Herbst (1979) is computed. In this experiment, a laminar boundary layer on a flat plate is subjected to unsteady wake passing. The upstream turbulent wakes are generated using a cage of rotating cylinder bars. The number of bars was varied from 0 to 90. Unsteady transition of the boundary layer is induced due to the high turbulence intensity in the passing wakes. The profile of turbulence intensity distribution near the leading edge of the plate is modeled using a Gaussian distribution:

$$T_u = T_{ub} + T_{uw} \exp[-0.5(tu_e/Lw)^2] \qquad (40)$$

where T_u is the turbulence intensity, T_{ub} (=0.6 percent) is the background turbulence intensity in the free stream, T_{uw} is the maximum value of additional turbulence intensity due to the wake (over and above the background turbulence intensity value), t is the time, L (=0.5 m) is the nominal length of the boundary layer, w is a wake width parameter, u_e (=18 m/s) is the velocity in the free stream. The values of T_{uw} and w for the primary wakes were 5.4 percent and 0.016, respectively. The value of T_{uw} is chosen such that the averaged turbulence intensity in the wake is about 4 percent, which is suggested by Hodson (1991) for this case. For the secondary wakes generated by the returning bars, the values of T_{uw} and w are estimated to

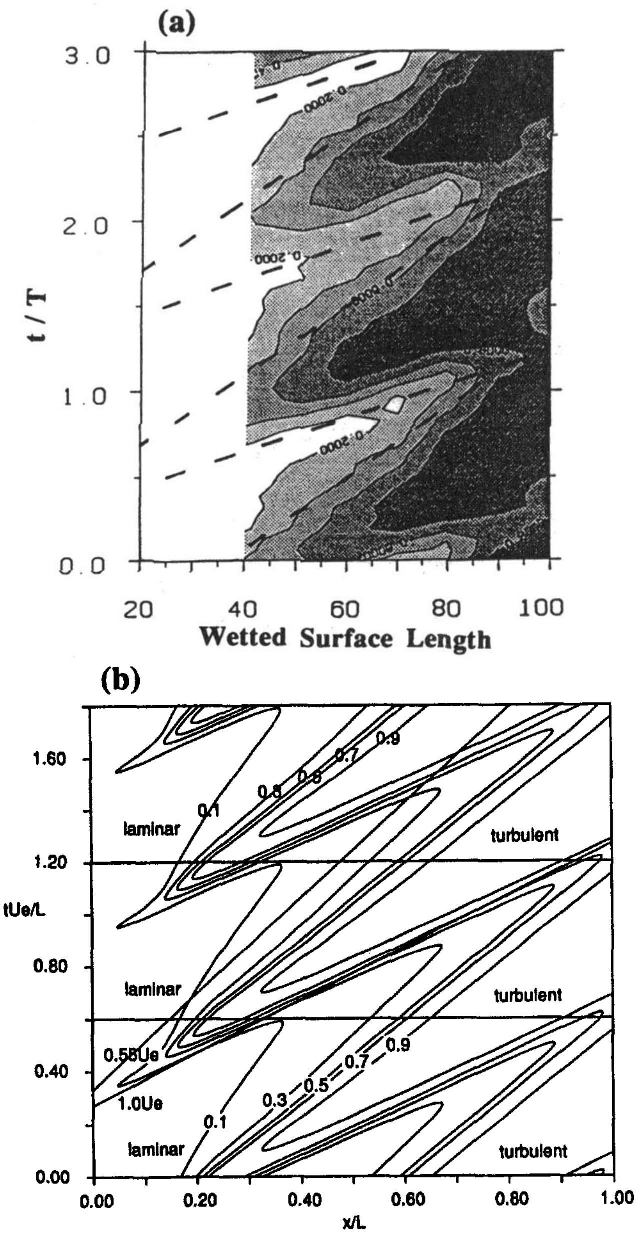

Fig. 7 Instantaneous intermittency factors: (*a*) measurement in turbine blade boundary layer (Hodson, 1991); (*b*) prediction for boundary layer subjected to wake passing, 9 bars. The numbers are intermittency factor γ.

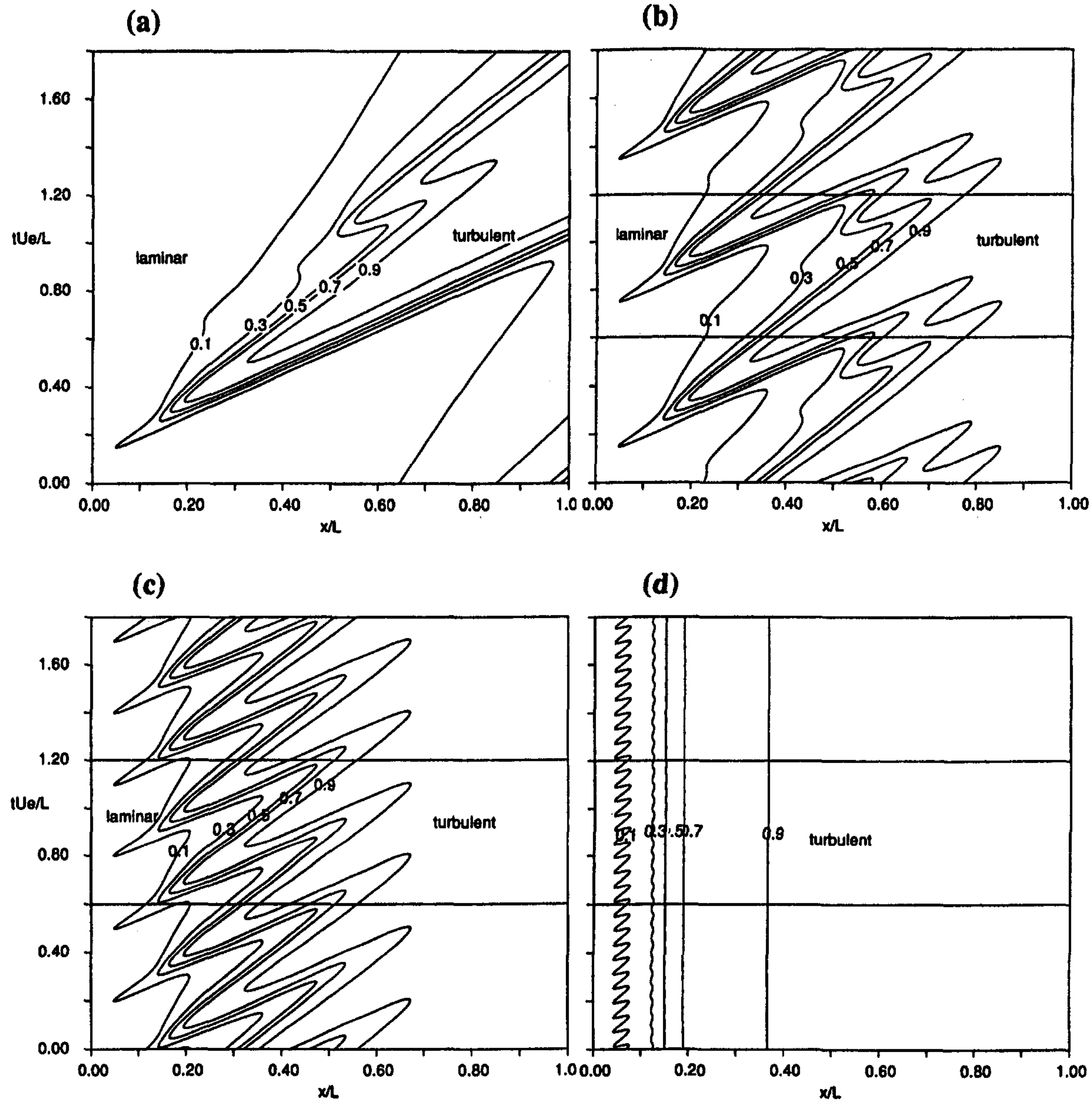

Fig. 8 Space–time contours of instantaneous intermittency factor γ in unsteady transitional boundary layer: Number of bars: (*a*) 3, (*b*) 9, (*c*) 18, (*d*) 90

be 2.2 percent and 0.044, respectively, using a wake decay model.

Figure 7(*b*) shows the space-time contours of the predicted intermittency factor with nine cylinder bars. The intermittency factor γ is defined as $(H - H_l)/(H_t - H_l)$ in this case, where H is the shape factor of the boundary layer, H_l and H_t are the shape factors in laminar and turbulent boundary layers, respectively. The effects of wakes from the returning bars are not included in this figure for clarity. It is clear from Fig. 7(*b*) that the dominant physical processes in the wake induced unsteady transition, namely the formation and transport of transitional patches, are captured well by the $k-\epsilon$ model. The predicted distribution of instantaneous intermittency factor in the flat plate boundary layer shows strong similarity to the measured one shown in Fig. 7(*a*) for the turbine blade boundary layer.

The predicted distributions of instantaneous intermittency factor are plotted in Fig. 8 for different number of bars varying from 3 to 90, resulting in a variation of reduced frequencies from 3.5 to 105. As the number of bars/reduced frequency increases, the boundary layer at a certain axial location in the transition region is occupied by the transitional patches for a larger fractional time in a period. As a result, the time-averaged intermittency factor increases with an increase in the number of bars/reduced frequency. For the case with 90 bars, the wakes merge before reaching the plate. The unsteady transition process almost returns to a steady transition. The predicted time-averaged intermittency factors are plotted in Fig. 9 and compared with the experimental data. The increase in the time-averaged intermittency factor with an increase in the number of bars/reduced frequency is clearly indicated by the data. The distributions of time-averaged intermittency factor with different number of bars/reduced frequencies are captured very well by the present $k-\epsilon$ model.

The ability of the low-Reynolds-number form $k-\epsilon$ model to predict the formation and propagation of the unsteady transitional patches has been demonstrated. Surprisingly good performance of the $k-\epsilon$ model in predicting wake-induced unsteady transition can be attributed to the transport nature of the $k-\epsilon$ equations. Since the turbulence in the transitional patch grows

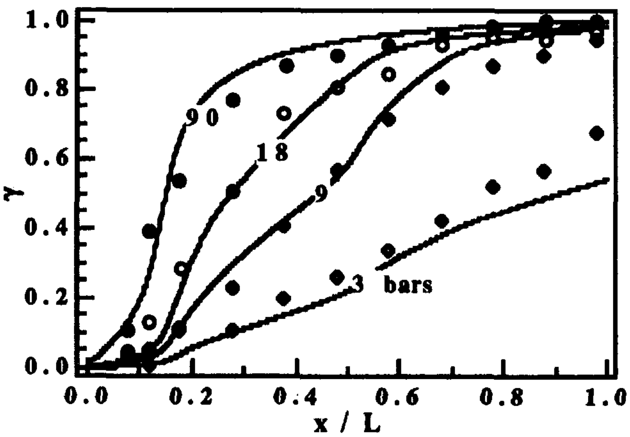

Fig. 9 Time-averaged intermittency in unsteady transitional boundary layer; lines: prediction; symbols: data of Pfeil and Herbst (1979)

in a quasi-steady fashion, it poses no extra difficulty for the turbulence model.

5 Wake/Blade-Row Interaction in an Axial Compressor Stator Cascade

The unsteady flow at the midspan section of an axial flow compressor stator is computed using the Euler/boundary layer procedure described earlier. Steady and unsteady measurements of the flow in the stator have been reported by Schulz et al. (1990). The incoming wakes are generated using a cascade of rotating bars, which are used to simulate the effects of rotor-wake/stator interaction in an actual compressor stage. The geometric and flow parameters of this cascade are given in Table 3. The following Gaussian distribution is used to model the wake velocity defect and turbulence intensity profiles generated by the rotating bars:

$$f(\eta) = D\exp(-\eta^2/2w^2) \tag{41}$$

$$T_u = T_{ub} + T_{uw}\exp(-\eta_t^2/2w^2) \tag{42}$$

where D is the nondimensional velocity defect at the center of the wake, $\eta = y/P_w$, $\eta_t = t/T$, P_w is the pitch of the wake, T is the wake passing period, w is a wake width parameter, T_u is the turbulence intensity, T_{ub} (=5 percent) is the background turbulence intensity in the free stream, T_{uw} (=8 percent) is the maximum value of additional turbulence intensity due to the wake (over and above the background turbulence intensity value). Notice that in applying these two equations, it is implied that the pitchwise phase speed of the wake unsteadiness is constant, and is equal to the rotating speed of the wake. This model has been found by the authors to be very accurate in reproducing the velocity and turbulence intensity profiles of the incoming wake measured by Schulz et al. (1990). When applying Eq. (41), the pitch-averaged value of $f(\eta)$ is subtracted to keep the time-averaged mass flow at the inlet the same as in a steady flow. In the computation, the temporal turbulence intensity profile is synchronized with the wake passing by matching the maximum turbulence intensity with the maximum unsteady entropy in the wake.

Table 3 Compressor stator cascade parameters, from Schulz et al. (1990)

Pitch/Chord (P_b/c)	0.78
Stagger angle	29°
Steady inflow angle	49.2°
Inlet Mach number (steady flow)	0.293
Reynolds number based on chord	0.405x10^6
Wake number n_w/n_b	1.0
Wake inflow angle (rotor outlet flow angle)	-15.55°
Fractional wake velocity defect	28.3%
Wake width parameter (w)	0.095
Reduced frequency (Ω)	6.12

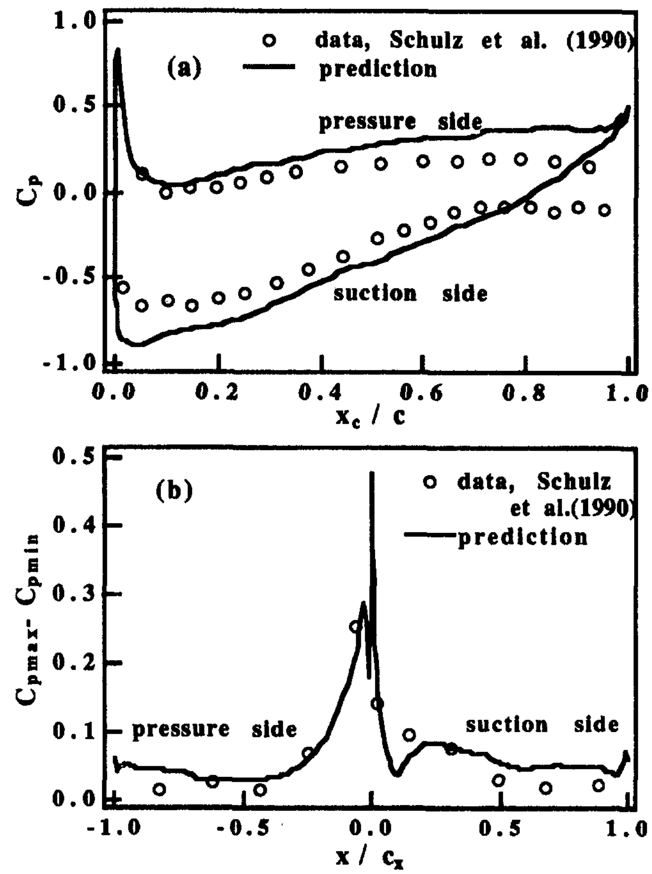

Fig. 10 Pressure coefficient on the blade for compressor cascade: (*a*) time-averaged pressure, (*b*) magnitude of unsteady pressure

Sixty-one grid points are used in the pitchwise direction and 241 grid points are used in the streamwise direction. Of the 241 streamwise grid points, 80 points are distributed between the inlet and the leading edge, 90 points on the blade surface. Sixteen hundred time steps are used within each blade passing period. For the boundary layer solution, 120 streamwise stations and 121 grid points normal to the boundary layer are used. Each wake passing period is divided into 100 time steps and three periods are found necessary for a converged boundary layer solution. The total CPU time for the computations, including one unsteady Euler solution and unsteady boundary layer solutions on both surfaces, is about 30 minutes on the NASA Lewis Cray-YMP supercomputer.

The predicted time-averaged pressure distribution is shown in Fig. 10(*a*). The pressure difference between the suction and pressure surfaces predicted by the Euler solution is slightly larger than the measured values. This difference is due to the viscous effects in the real cascade flow. At about 85 percent of the chord, the measured pressure on the suction surface starts to decrease and then flattens out, indicating separation of the suction surface boundary layer. Figure 10(*b*) shows the predicted and measured magnitude of unsteady pressure coefficient ($C_{p\max} - C_{p\min}$). Near the leading edge of the blade, both the prediction and the data show large magnitude of unsteady pressure. The magnitude of unsteady pressure is much smaller away

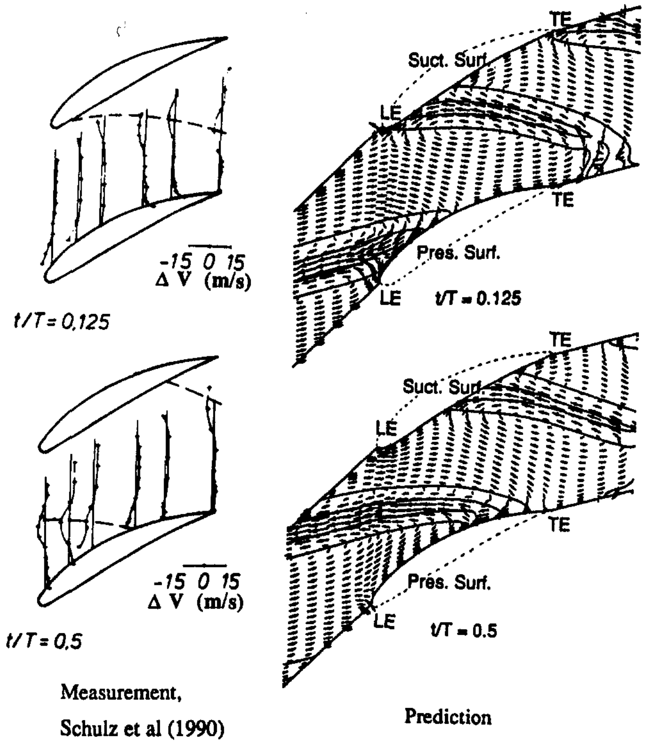

Fig. 11 Unsteady velocity in blade passage

from the leading edge region. Notice that the predicted unsteady pressure does not monotonically decrease from the leading edge to the trailing edge. Local maxima and minima exist on the unsteady surface pressure profile. The unsteady pressure profiles for previous cases showed a similar trend (see Figs. 2–3). The predictions agree well with the data at most locations, including the leading edge.

The predicted unsteady velocity is compared with the measurement in Fig. 11. The comparison is made at two different time instants: $t = \frac{1}{8}$ and $\frac{1}{2}$ of the period. The steady velocity has been subtracted from the instantaneous velocity for clarity. Also, entropy contours have been included in the velocity vector plots to identify the position of the wake. The unsteady flow field and the trajectory of the wake predicted from the Euler solution are in good agreement with the measured ones. However, due to the limited spatial resolution of the experimental data, the comparison is qualitative.

Due to the relative motion between the rotor and the stator, the wake from the rotor blade is perceived as a negative jet in the stator frame of reference. This can be clearly seen from the unsteady Euler simulation shown in Fig. 11. Once the wake enters the blade passage, it is chopped into segments by the leading edges of the blade row. Near the leading edge, the higher local speed on the suction surface results in a larger wake segment width than that near the pressure surface. This can be clearly seen in Fig. 11. This difference in wake segment width quickly diminishes as the wake segment is convected beyond the midchord, where the width of the wake segment near the pressure side is actually larger due to the migration of wake fluid from the suction surface to the pressure surface. The unsteady flow inside the blade passage is characterized by the formation of counterrotating recirculating-flow patterns. The recirculating-flow pattern on the leading side of a wake segment is shown as a clockwise rotating vortex, while the one on the trailing side of the wake segment forms a counterclockwise rotating vortex. The formation of recirculating-flow pattern due to wake/blade-row interaction has been well documented. A detailed discussion of this phenomenon is given by Korakianitis (1992).

The predicted unsteady velocity profiles are shown in Fig. 12 for the suction surface boundary layer. The profiles of the first Fourier component of the unsteady velocity are plotted for three different axial locations. The amplitude profile of the unsteady velocity in the boundary layer is characterized by a small overshoot in the boundary layer. The phase angle profiles show a rather large velocity phase lag compared with the free-stream velocity. The magnitude of phase lag increases with an increase in the distance from the leading edge. The characteristics of the unsteady velocity profiles discussed above indicate that a traveling wave type of disturbance has an important influence on the development of unsteady blade boundary layers in a wake/blade-row interaction. Comparison with measurement is not available for the unsteady velocity profiles due to the lack of data. The predicted amplitude and phase angle profiles are very similar to the ones measured in a turbulent boundary layer subjected to passing wakes by Evans and Yip (1988).

The predicted chordwise distributions of unsteady boundary layer momentum thickness and the skin friction coefficients are shown in Figs. 13 and 14. The information shown includes the time-averaged value, the maximum and the minimum values within each period and the steady-state value, which is the predicted value without the incoming wake. The boundary layer on the suction surface is known to separate at about 85 percent of the chord. Since the boundary layer code is incapable of predicting separated boundary layer, no attempt has been made to predict the boundary layer beyond the separation point. The pressure surface boundary layer is not separated. Figure 13 shows the distribution of boundary layer momentum thickness. The magnitude of unsteady boundary layer momentum thickness ($\theta_{\max} - \theta_{\min}$) grows with the streamwise distance. Significant instantaneous departure from the time-averaged values is shown for the boundary layer momentum thickness. Another important feature shown in Fig. 13 is that the time-averaged momentum thickness of the unsteady boundary layer grows faster than the steady boundary layer. This has direct engineering significance since the increased momentum thickness at the trailing edge results in increased profile loss. The predicted time-averaged boundary layer thickness and the range of periodic variation in the boundary layer thickness are generally

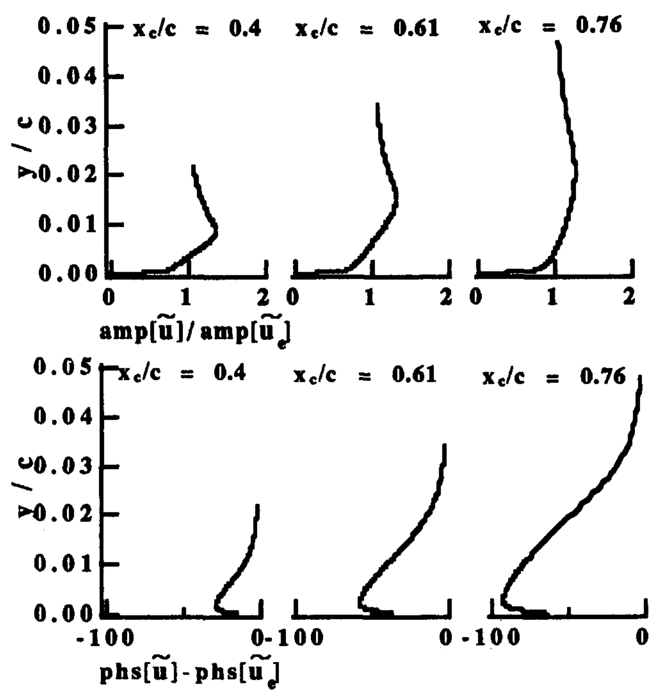

Fig. 12 Predicted unsteady boundary-layer velocity profiles on suction surface

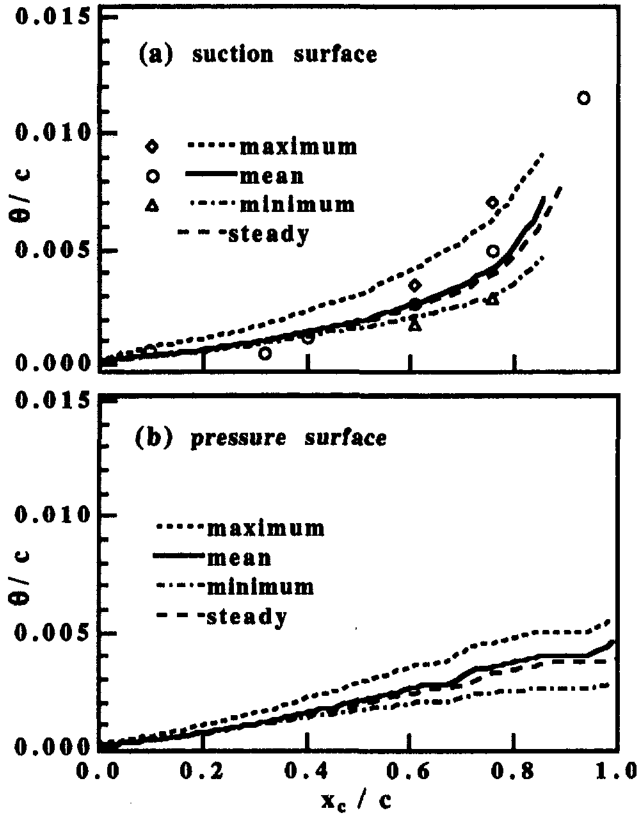

Fig. 13 Momentum thickness of blade boundary layers for compressor cascade: symbols: data of Schulz et al. (1990); lines: prediction

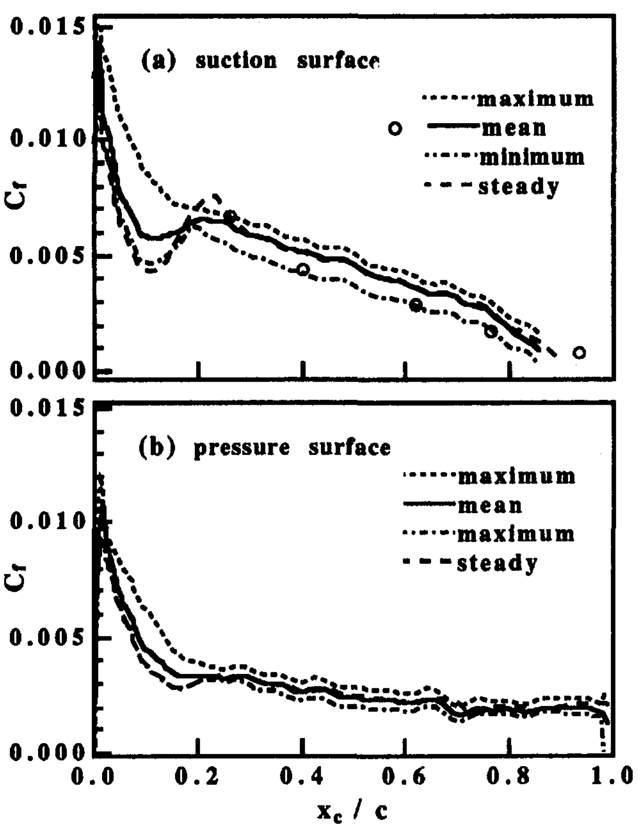

Fig. 14 Skin friction of blade boundary layers for compressor cascade: symbols: data of Schulz et al. (1990); lines: prediction

in good agreement with the experimental data, which is only available for the suction surface boundary layer.

Figure 14 shows the skin friction coefficient for the suction and pressure surfaces. It can be clearly seen that the influence of the upstream wake on the skin friction is quite different from that on the boundary layer thickness. Large periodic variations in the skin friction coefficient exist up to quarter chord point on both sides of the blade, followed by a relatively smaller and constant periodic variation on the rest of the blade surface. The time-averaged and steady skin friction coefficients differ only up to about 25 percent of chord length from leading edge, where the transition from the laminar to the turbulent boundary layer occurs. The difference is a strong indication that the laminar to turbulent transition in the boundary layer has been affected by the unsteady wake passing. The time-averaged transition of the boundary layer, as indicated by the distribution of the skin friction coefficient, starts earlier and has a smoother transition curve than the corresponding one in the steady boundary layer. The time-averaged skin friction coefficients agree well with the measured values, which are only available for the suction surface boundary layer.

Detailed simulation and discussion of the influence of the wake passing on the transition and development of unsteady blade boundary layers will be given in Part 2 of the paper.

Concluding Remarks

An efficient inviscid/viscous procedure has been developed for the prediction of unsteady flows in a turbomachinery blade row due to wake interaction. A time-accurate two-dimensional Euler solver is developed to predict the transport of viscous wakes and the resulting unsteady pressure and flow fields. The development of blade boundary layers is predicted using an unsteady boundary layer code with an advanced $k-\epsilon$ model developed for unsteady turbulent flows. The present computational procedure has been extensively validated. The predicted unsteady surface pressure distributions, unsteady velocity field, and unsteady blade boundary layers agree very well with the corresponding results from the analytic solution/experimental data.

The applicability of the $k-\epsilon$ turbulence model for the prediction of unsteady boundary layer transition resulting from the wake passing has been demonstrated. The $k-\epsilon$ model has been shown to be capable of simulating the formation and transport of unsteady transitional patches, which are the major physical processes associated with the wake-induced unsteady transition.

The time-averaged momentum thickness of the unsteady blade boundary layer, resulting from wake interaction, is found to be larger than that of the corresponding steady boundary layer without the wake interaction. The boundary layer transition process is affected strongly by the unsteady wake passing, resulting in significant differences in the distributions of the local skin friction coefficient in the transition region between the steady and the time-averaged boundary layers.

Acknowledgments

This work was supported by National Aeronautics and Space Administration (NASA) through the contract, NAG 3-1168, with Dr. P. Sockol as the technical monitor. The authors wish to acknowledge NASA for providing the supercomputing resources at NASA Lewis Research Center and NASA Ames Research Center.

References

Abu-Ghannam, B. J., and Shaw, R., 1980, "Natural Transition of Boundary Layers—The Effects of Turbulence, Pressure Gradient and Flow History," *Journal of Mechanical Engineering Science*, Vol. 22, No. 5, pp. 213–228.

Addison, J. S., and Hodson, H. P., 1990, "Unsteady Transition in an Axial-Flow Turbine: Part 1—Measurements on the Turbine Rotor, Part 2—Cascade

Measurements and Modeling," ASME JOURNAL OF TURBOMACHINERY, Vol. 112, pp. 206–221.

Chen, J. P., and Whitfield, D., 1993, "Navier–Stokes Calculation for the Unsteady Flow Field of Turbomachinery," AIAA Paper No. 93-0676.

Doorly, D. J., and Oldfield, M. L. G., 1985, "Simulation of the Effects of Shock Wave Passing on a Turbine Rotor Blade," ASME JOURNAL OF ENGINEERING FOR GAS TURBINES AND POWER, Vol. 107, pp. 998–1006.

Dorney, D. J., 1992, "Numerical Simulations of Unsteady Flows in Turbomachines," Ph.D. Thesis in Aerospace Engineering, Pennsylvania State Univ., University Park, PA.

Evans, R. L., and Yip, R. S. K., 1988, "An Experimental Investigation of Unsteady Wake-Boundary Layer Interaction," *Journal of Fluids and Structures,* Vol. 2, pp. 313–322.

Fan, S., Lakshminarayana, B., and Barnett, M., 1993, "A Low-Reynolds-Number $K-\epsilon$ Model for Unsteady Turbulent Boundary Layer Flows," *AIAA Journal,* Vol. 31, No. 10, pp. 1777–1784.

Fan, S., and Lakshminarayana, B., 1993, "A Simplified Reynolds Stress Model for Unsteady Turbulent Boundary Layers," AIAA Paper No. 93-0204.

Giles, M. B., 1988, "Calculation of Unsteady Wake/Rotor Interaction," AIAA *Journal of Propulsion and Power,* Vol. 4, No. 4, pp. 356–362.

Giles, M. B., 1990, "Non-reflecting Boundary Conditions for Euler Equation Calculations," *AIAA Journal,* Vol. 28, No. 12, pp. 2050–2058.

Giles, M., and Haimes, R., 1993, "Validation of a Numerical Method for Unsteady Flow Calculations," ASME JOURNAL OF TURBOMACHINERY, Vol. 115, pp. 110–117.

Ho, Y.-H., and Lakshminarayana, B., 1993, "Computation of Unsteady Viscous Flow Using an Efficient Algorithm," *AIAA Journal,* Vol. 31, p. 2232.

Hodson, H. P., 1985, "A Blade-to-Blade Prediction of a Wake-Generated Unsteady Flow," ASME *Journal of Engineering for Gas Turbines and Power,* Vol. 107, pp. 337–344.

Hodson, H. P., 1991, "Aspects of Unsteady Blade-Surface Boundary Layers and Transition in Axial Turbomachines," VKI-LS-1991-06, in: *VKI Boundary Layers in Turbomachines.*

Jorgensen, P. C. E., and Chima, R. V., 1988, "An Explicit Runge–Kutta Method for Unsteady Flows," AIAA Paper No. 88-0049.

Korakianitis, T., 1992, "On the Prediction of Unsteady Forces on Gas Turbine Blades, Part 1: Description of the Approach; Part 2: Analysis of the Results," ASME JOURNAL OF TURBOMACHINERY, Vol. 114, pp. 114–131.

Korakianitis, T., Papagiannidis, P., and Vlachopoulos, N. E., 1993, "Unsteady-Flow/Quasi-Steady Heat Transfer Computations on a Turbine Rotor and Comparison With Experiments," ASME Paper No. 93-GT-145.

Kunz, R. F., and Lakshminarayana, B., 1992, "Explicit Navier–Stokes Computation of Cascade Flows Using the $k-\epsilon$ Turbulence Model," *AIAA Journal,* Vol. 30, No. 1, pp. 13–22.

Lam, C. Y., 1990, "Turbulent Boundary Layers Under Small Harmonic Progressive Oscillations of the Free Stream," *Aeronautical Journal,* Aug.–Sep., pp. 251–259.

Lewis, J. P., Delaney, R. A., and Hall, E. J., 1989, "Numerical Prediction of Turbine Vane-Blade Aerodynamic Interaction," ASME JOURNAL OF TURBOMACHINERY, Vol. 111, pp. 387–393.

Liu, J., and Sockol, P., 1989, "Unsteady Euler Cascade Analysis," AIAA Paper No. 89-0322.

Liu, X., and Rodi, W., 1991, "Experiments on Transitional Boundary Layers With Wake-Induced Unsteadiness," *Journal of Fluid Mechanics,* Vol. 231, pp. 229–256.

Martinelli, L., 1987, "Calculation of Viscous Flows With Multigrid Methods," Ph.D. Thesis, MAE Department, Princeton University, Princeton, NJ.

Mayle, R. E., 1991, "The Role of Laminar-Turbulent Transition in Gas Turbine Engines," ASME JOURNAL OF TURBOMACHINERY, Vol. 113, pp. 509–537.

Menendez, A. N., and Ramaprian, B. R., 1989, "Experimental Study of a Periodic Turbulent Boundary Layer in Zero Mean Pressure Gradient," *Aeronautical Journal,* June–July, pp. 195–206.

Patel, M. H., 1977, "On Turbulent Boundary Layers in Oscillatory Flow," *Proceedings of the Royal Society, London, A* Vol. 353, pp. 121–144.

Pfeil, H., and Herbst, R., 1979, "Transition Procedure of Instationary Boundary Layers," ASME Paper No. 79-GT-128.

Power, G. D., Verdon, J. M., and Kousen, K. A., 1991, "Analysis of Unsteady Compressible Viscous Layers," ASME JOURNAL OF TURBOMACHINERY, Vol. 133, No. 4, pp. 644–653.

Rai, M., 1989, "Three Dimensional Navier–Stokes Simulation of Turbine-Stator Interaction, Part 1—Methodology; Part 2—Results," *Journal of Propulsion,* May–June, pp. 305–311.

Rodi, W., and Scheuerer, G., 1985, "Calculation of Heat Transfer to Convection-Cooled Gas Turbine Blades," ASME *Journal of Engineering for Gas Turbines and Power,* Vol. 107, pp. 620–627.

Schmidt, R. C., and Patankar, S. V., 1991, "Simulating Boundary Layer Transition With Low-Reynolds-Number $k-\epsilon$ Turbulence Models: Part 1—An Evaluation of Prediction Characteristics; Part 2—An Approach to Improving the Predictions," ASME JOURNAL OF TURBOMACHINERY, Vol. 113, pp. 10–26.

Schultz, H. D., Gallus, H. E., and Lakshminarayana, B., 1990, "Three-Dimensional Separated Flow Field in the End Wall Region of an Annular Compressor Cascade in the Presence of Rotor–Stator Interaction, Part 1: Quasi-Steady Flow Field and Comparison With Steady-State Data, Part 2: Unsteady Flow and Pressure Field," ASME JOURNAL OF TURBOMACHINERY, Vol. 112, pp. 669–690.

Tran, L. T., and Taulbee, D. B., 1992, "Prediction of Unsteady Rotor-Surface Pressure and Heat Transfer From Wake Passing," ASME JOURNAL OF TURBOMACHINERY, Vol. 114, pp. 807–817.

Verdon, J. M., Barnett, M., Hall, K. C., and Ayer, T. C., 1991, "Development of Unsteady Aerodynamic Analyses for Turbomachinery Aeroelastic and Aeroacoustic Applications," NASA CR 4405.

Whitehead, D. S., 1970, "Vibration and Sound Generation in a Cascade of Flat Plate in Subsonic Flow," British Aeronautical Research Council, R&M 3685, London.

Computation and Simulation of Wake-Generated Unsteady Pressure and Boundary Layers in Cascades: Part 2—Simulation of Unsteady Boundary Layer Flow Physics

S. Fan
Graduate Assistant.
Mem. ASME

B. Lakshminarayana
Evan Pugh Professor of Aerospace Engineering.
Fellow ASME

Center for Gas Turbines and Power,
Pennsylvania State University,
University Park, PA 16802

The unsteady pressure and boundary layers on a turbomachinery blade row arising from periodic wakes due to upstream blade rows are investigated in this paper. Numerical simulations are carried out to understand the effects of the wake velocity defect and the wake turbulence intensity on the development of unsteady blade boundary layers. The boundary layer transition on the blade is found to be strongly influenced by the unsteady wake passing. Periodic transitional patches are generated by the high turbulence intensity in the passing wakes and transported downstream. The time-dependent transition results in large unsteadiness in the instantaneous local skin friction coefficient and a smoother time-averaged transition curve than the one observed in the steady boundary layer. A parametric study is then carried out to determine the influence of wake parameters on the development of the unsteady blade boundary layers. It is shown that the unsteadiness in the blade boundary layer increases with a decrease in the axial gap, an increase in wake/blade count ratio, or an increase in the wake traverse speed. The time-averaged boundary layer momentum thickness at the trailing edge of the blade is found to increase significantly for higher wake/blade count ratio and larger wake traverse speed. Increase of the wake/blade count ratio also results in higher frictional drag of the blade.

Introduction

An understanding of the flow physics associated with the wake/boundary layer interaction in turbomachinery and the ability of the computer codes to predict its effects on the blade row performance is essential for eventual integration of the unsteady effects into the design process.

A large body of experimental data exists on the wake/boundary layer interactions. The investigations include influence of moving wakes on flat-plate boundary layers (Pfeil et al., 1983; Liu and Rodi, 1991; Orth, 1993), on two-dimensional compressor or turbine cascades (Wittig et al., 1987; Ashworth et al., 1989; Dong and Cumpsty, 1990; Dullenkopf et al., 1991; Ladwig and Fottner, 1993) as well as interactions in three-dimensional rotor or stator blades (Hodson, 1985; Addison and Hodson, 1990; Schulz et al., 1990). The most significant finding in these investigations is that the boundary layer transition process is strongly influenced by the unsteady wake passing (Pfeil et al., 1983; Addison and Hodson, 1990). The unsteady transition, resulting mainly from the high turbulence intensity in the wake, has been found to change the profile loss and the time-averaged surface heat transfer rate significantly (Hodson, 1990; Dullenkopf et al., 1991). The magnitude of the wake velocity defect, turbulence intensity, wake passing frequency, wake incidence angle as well as the Reynolds number are among the major factors influencing the wake/boundary layer interaction.

Contributed by the International Gas Turbine Institute and presented at the 39th International Gas Turbine and Aeroengine Congress and Exposition, The Hague, The Netherlands, June 13–16, 1994. Manuscript received by the International Gas Turbine Institute February 9, 1994. Paper No. 94-GT-141. Associate Technical Editor: E. M. Greitzer.

In Part 1 of this paper (Fan and Lakshminarayana, 1996), an inviscid/viscous procedure has been developed for the prediction of unsteady flows due to wake/blade row interaction. The unsteady transport of wakes through the blade passage is simulated using a time-accurate Euler solution. An unsteady boundary layer solution is then used to predict the effects of unsteady pressure and turbulence intensity on the development of the blade boundary layers. Both these codes were validated using analytical solution and the experimental data.

Systematic numerical simulations are carried out in this paper to study the development and physics of unsteady boundary layers resulting from the wake/blade interaction. The first set of simulations is designed to improve an understanding of the dynamic process of wake/boundary layer interaction. This is accomplished through isolation of each source of unsteadiness, such as wake velocity defect and the wake turbulence intensity level. A parametric study is then carried out to investigate the influence of wake parameters on the development of unsteady blade boundary layer.

Influence of Upstream Wake on the Blade Boundary Layers

The wake-stator blade configuration described in Part 1 of this paper (Fan and Lakshminarayana, 1996) is used for additional numerical simulation to understand the flow physics associated with the wake/blade-row interaction (see Schulz et al., 1990, for detailed description of the compressor stage). In Part 1 of this paper, the stator with 49 deg inlet flow angle (5 deg incidence) was used to validate the numerical procedure since this is the only flow case for which boundary layer data are available. The suction surface boundary layer separated at about

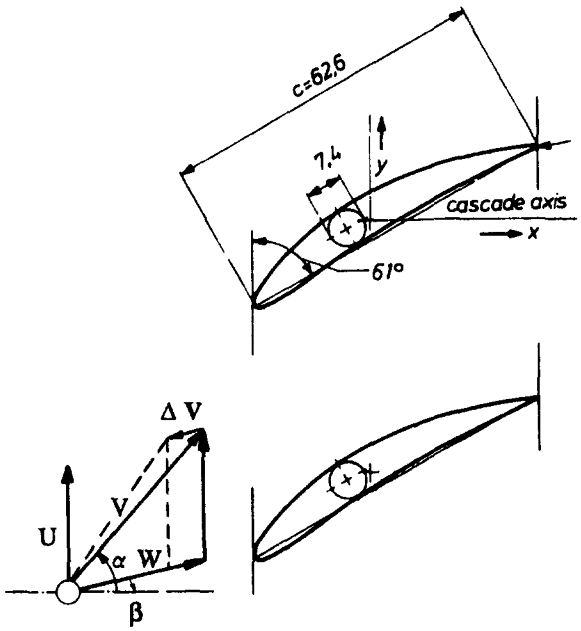

Fig. 1 Geometric configuration and velocity triangle of compressor stator cascade (Schulz et al., 1990); length unit: millimeter; velocity triangle in the wake is shown in dotted line

85 percent of the chord. For the present simulation, the flow with a 44 deg inlet angle (zero degree incidence) is used. It will be shown that better surface pressure distribution and smaller separation region are predicted for this flow case. The blade geometry and the velocity triangle at the inlet to the stator cascade of Schulz et al. are shown in Fig. 1. Also shown is the velocity triangle in the wake (dotted line) simulated by the rotating rods.

Due to the relative motion between the rotor and the stator, the nonuniformity in the rotor wake is perceived in the stator as a negative jet (see Fig. 11 in Part 1 of this paper). Interaction between a cascade of negative jets with the stator blade row results in unsteady pressure on the surface of the blade, which in turn affects the development of the turbulent blade boundary layers. In addition, the high turbulence intensity in the wake affects the transition and the development of the unsteady boundary layers.

The effects of unsteady pressure and the wake turbulence on the development of blade boundary layers are studied through a series of numerical simulations. As discussed in Part 1, the following expressions for the velocity defect and the turbulence intensity profiles are used:

$$f(\eta) = D\exp(-\eta^2/2w^2) \tag{1}$$

$$T_u = T_{ub} + T_{uw}\exp(-\eta_t^2/2w^2) \tag{2}$$

where D is the nondimensional velocity defect at the center of the wake, $\eta = y/p_w$, $\eta_t = t/T$, p_w is the pitch of the wake, T is the wake passing period, w is the wake width parameter, T_u is the turbulence intensity, T_{ub} is the background turbulence intensity in the free stream undisturbed by the wake, and T_{uw} is the maximum value of additional turbulence intensity due to the wake (over and above the background turbulence intensity). Equation (1) is used at the inlet of the Euler solution domain to describe the shape of the wake velocity profile. Equation (2) is used at the first streamwise station of the boundary layer solution to specify the periodic free-stream turbulence intensity profile. In applying these two equations, it is implied that the pitchwise phase speed of the wake unsteadiness is constant, and is equal to the rotating speed of the wake. Equations (1) and (2) have been found to represent accurately the velocity and turbulence intensity profiles of the incoming wake measured by Schulz et al. (1990). When applying Eq. (1), the pitch-averaged value of $f(\eta)$ is subtracted to keep the time-averaged mass flow at the inlet the same as in a steady flow. At this inlet flow angle, the characteristic wake parameters are $D = 0.28$, $T_{ub} =$ 5 percent, $T_{uw} = 8$ percent, $w = 0.093$, based on the measured data. The reduced frequency is $\Omega = 5.7$.

The prediction of unsteady blade surface pressure will first be discussed. This will be followed by four simulation cases (Cases A through D) designed to understand the wake/boundary layer interaction. The wake parameters for the four cases are listed in Table 1.

Unsteady Surface Pressure. The predicted time-averaged pressure and magnitude of the unsteady pressure on the blade surfaces are compared with the experimental data of Schulz et

Nomenclature

- c = chord length
- c_x = axial chord length
- C_f = skin friction coefficient = $\tau_w/(0.5\rho_{is}q_{is}^2)$
- C_p = pressure coefficient = $(p - p_{\text{ref}})/0.5\rho_{is}q_{is}^2$
- d = axial distance between blade leading edge and rotor trailing edge
- D = amplitude of nondimensional wake velocity defect
- D_f^* = frictional drag of the blade, normalized by the steady-state value
- n_w, n_b = number of rotor wakes, number of stator blades
- p = static pressure
- p_{ref} = static pressure on the casing at inlet
- P_w, P_b = rotor wake pitch, stator blade pitch
- q_{is} = total steady velocity at inlet to the blade row
- q_n = maximum unsteady inlet velocity in the wake normal to q_{is}
- Re = Reynolds number based on chord
- t = time
- T = blade passing period
- T_u = turbulence intensity = $[\frac{1}{3}((\widetilde{u'})^2 + (\widetilde{v'})^2 + (\widetilde{w'})^2)]^{0.5}/\overline{u_e}$
- u_{is} = steady axial velocity at the inlet of blade row
- U = wake traverse speed (wheel speed)
- V = total velocity in stator frame
- w = dimensionless wake width parameter, Eq. (1)
- W = total velocity in rotor frame
- x, y = Cartesian coordinates (axial and tangential)
- x_c = distance along the chord
- α = stator inlet absolute flow angle (counterclockwise from axial direction, Fig. 1)
- β = rotor outlet relative flow angle (clockwise from axial direction, Fig. 1)
- ΔV = difference between instantaneous and steady velocities
- θ = boundary layer momentum thickness
- θ^* = total momentum thickness at the trailing edge, normalized by its steady value
- ρ = density
- ω = wake passing frequency = $2\pi U/P_w$
- Ω = reduced frequency = $\omega c_x/u_{is}$

Superscripts and Subscripts

- e = free-stream quantity
- is = steady-state inlet values to the blade
- w = wake quantity, quantity at the wall
- $-$ = time-averaged quantity
- $\sim$ = ensemble-averaged quantity
- $'$ = turbulent fluctuating quantity

Table 1 Wake parameters used for the simulation

Wake Parameter	D	T_{nh}	T_{uw}
Case A	0.28	13%	0%
Case B	0.28	5%	0%
Case C	0.00	5%	8%
Case D	0.28	5%	8%

al. (1990) in Fig. 2. The predicted time-averaged pressure agrees well with the data, except on the last 10 percent of chord near the trailing edge. This is due to flow separation on the suction surface visualized by Schulz et al. (1990). The boundary layer prediction also indicates an onset of separation at about 90 percent blade chord on the suction surface.

The predicted magnitude of unsteady surface pressure coefficient ($C_{p\max} - C_{p\min}$) shows good agreement with the data. The profile is characterized by a large peak near the leading edge and a nearly uniform distribution on the rear part of the blade, with a minimum value in between. The distribution of unsteady pressure suggests that different mechanisms are responsible for the generation of unsteady pressure near the leading edge and on the rest of the blade surface. This can be clearly seen in the space–time (S–T) contour plot of the unsteady pressure on the suction surface (mean pressure being subtracted) shown in Fig. 3.

In Fig. 3(a), the wake center reaches the leading edge at about $t/T = 0.23$, where a minimum unsteady pressure occurs in the leading edge area on the suction surface. This is due to an increase in the local incidence angle near the leading edge as a result of the unsteady velocity component in the wake, which results in a decrease in the static pressure on the suction surface of the blade and an increase in static pressure on the pressure surface. As shown in Fig. 11 of Part 1, the unsteady component of velocity between the wakes is in the opposite direction to the flow in a wake. It acts to decrease the local incidence angle near the leading edge, hence to increase the pressure on the suction surface and decrease the pressure on the pressure surface. The maximum amplitude of the pressure variation occurs near the leading edge, where the cutting of wakes by the blade results in rapid change in momentum of the wake fluid. The magnitude of unsteady pressure variation decays rapidly with distance from the leading edge, caused by the guidance of the flow by the blade. In the leading edge area, the relationship between the steady velocity and the steady static pressure (the steady Bernoulli equation) is no longer valid for unsteady flow. In fact, a decrease in streamwise velocity is predicted in the leading edge area on the suction surface with the arrival of the wake, corresponding to an increase in the local incidence angle and a decrease in the static pressure. This phenomenon is confirmed by the experimental measurement by Schulz et al. (1990).

As shown in Fig. 11 of Part 1, recirculating-flow patterns are generated once the unsteady wake is cut by the blade. Once the unsteady recirculating-flow pattern, or unsteady vortices, are generated, they strongly affect the generation of unsteady pressure on the blade, while the direct effect of normal velocity in the wake segments is of higher order significance. On the suction surface, the clockwise-rotating vortex on the leading side of the wake tends to decrease the local velocity and increase the static pressure on the blade suction surface, while the counterclockwise rotating vortex on the trailing side of the wake tends to increase the local velocity and decrease the static pressure. In addition, due to the orientation of the wake with respect to the blade surface, the streamwise unsteady velocity of the wake is in the opposite direction to the mean stream. This amplifies the effects of the clockwise-rotating vortex and cancels the effects of the counterclockwise-rotating vortex, resulting in a pressure peak on the suction surface following the passage of the wake.

As the unsteady recirculating vortices leave the trailing edge, the induced velocity changes the instantaneous outlet flow angle near the trailing edge. This in turn results in a periodic variation of the static pressure near the trailing edge of the blade surfaces, which is clear from Fig. 3(a). The low pressure in the regions centered at $x_c/c = 0.4$ and $t/T = 0.2$, 1.2 in Fig. 3(a) is a result of the periodic pressure field originating from the pressure surface (mostly in the leading edge area) of the adjacent blade (counting from bottom to top in Fig. 1). The interference between the periodic pressure field from the adjacent pressure surface and the convective unsteady pressure (following the convection of the wake on the suction surface) results in amplification or suppression of unsteady pressure at certain locations on the blade. The interference pattern is not very clear in Fig. 3(a) due to the small reduced frequency ($\Omega = 5.7$). The interference pattern can be very clearly identified in Fig. 3(b) at the higher reduced frequency ($\Omega = 11.4$). This explains the typical distribution of the amplitude profiles of unsteady surface pressure at higher reduced frequencies shown earlier in Fig. 2(a) of Part 1 and later in this paper.

This discussion shows that the unsteady pressure distribution on the surface of the blade can be explained as the combined effects of three different mechanisms. The first is the wake cutting by the blade leading edge, which generates strong periodic pressure in the area close to the leading edge. The second is the change in streamwise velocity near the surface by the counterrotating vortices and the wake segment, which results in a convective unsteady pressure pattern. The last is the unsteady pressure generated by the periodic variation of the instantaneous outflow angle due to the counterrotating vortices. In addition, interference between pressure fields on the neighboring blades

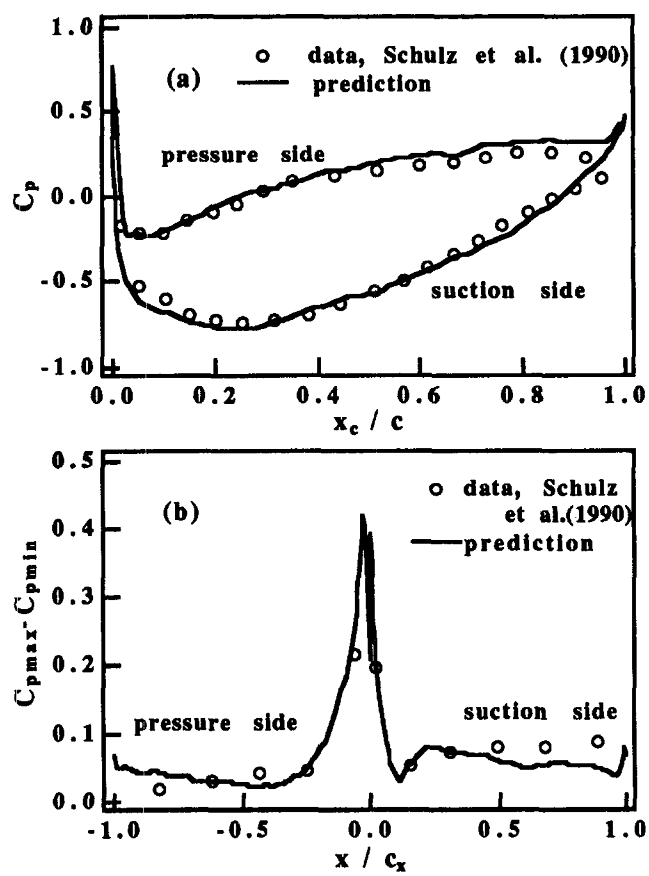

Fig. 2 Prediction of pressure coefficient on stator blade, $\Omega = 5.7$: (a) time-averaged pressure, (b) magnitude of unsteady pressure

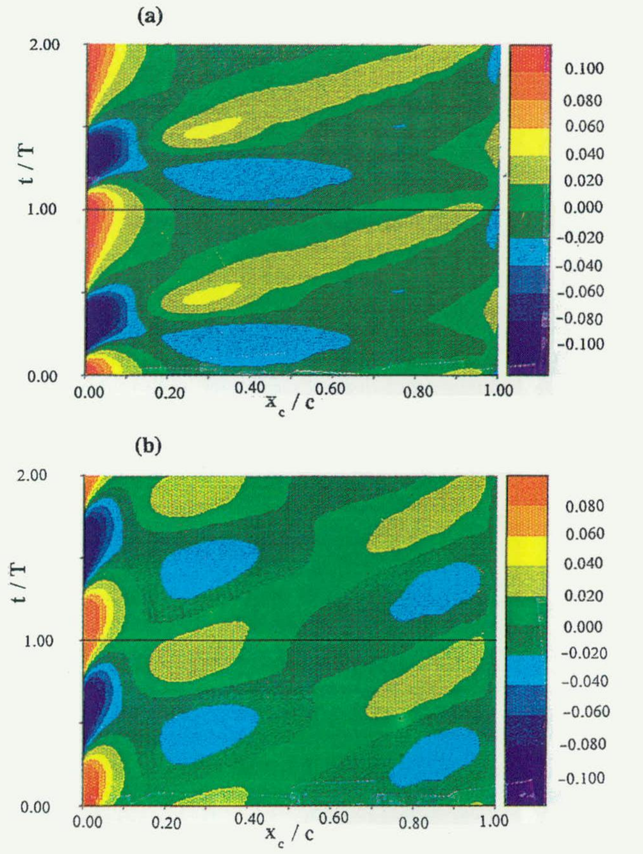

Fig. 3 Space-time contour of unsteady pressure coefficient, $C_p - \overline{C_p}$, on the suction surface: (*a*) $\Omega = 5.7$, (*b*) $\Omega = 11.4$

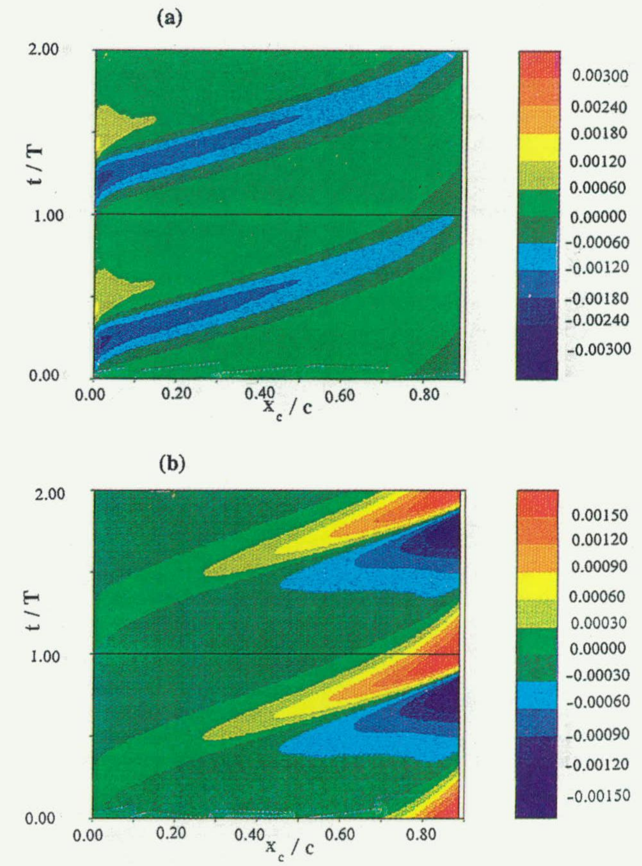

Fig. 4 Space-time contour of unsteady boundary layer quantities on the suction surface, $\Omega = 5.7$, Case A: (*a*) $C_f - \overline{C_f}$ (*b*) $(\theta - \overline{\theta})/c$

produces an interference pattern in unsteady surface pressure distribution.

Case A: Effects of Wake Velocity Defect on Fully Turbulent Boundary Layer. The purpose of this and the subsequent simulations is to isolate the effects of wake velocity defect and the wake turbulence intensity on the development of unsteady boundary layers on the blade. High turbulence intensity (which is equal to the peak turbulence intensity measured in the wake) is prescribed over the entire pitch/period (see Table 1 for other parameters), which results in a time-independent transition very close to the leading edge. The effects of laminar/turbulent transition are insignificant in this simulation.

Figure 4 shows the unsteady skin friction coefficient and the momentum thickness (mean values have been subtracted) on the suction surface boundary layer. It is clear from Fig. 4(*a*) that the instantaneous skin friction is reduced following the trajectory of the wake. In between two wakes, the skin friction is slightly higher than the mean value. The reduction in skin friction coefficient following the passage of the wake is mainly caused by the decrease in free-stream velocity at the edge of the boundary layer due to the wake passing.

The S–T contour of the unsteady momentum thickness (Fig. 4(*b*)) shows a decrease in the momentum thickness on the leading side of the wake and an increase in the momentum thickness on the trailing side of the wake. This is more pronounced beyond midchord. The development of momentum thickness is closely related to the unsteady pressure field shown in Fig. 3(*a*). Large pressure variation in the leading edge area does not cause a significant variation in unsteady momentum thickness. This is because the mean boundary layer is experiencing a favorable pressure gradient in this part of the blade surface and the time-averaged boundary layer thickness is very small. Away from the leading edge area, the unsteady pressure distri-

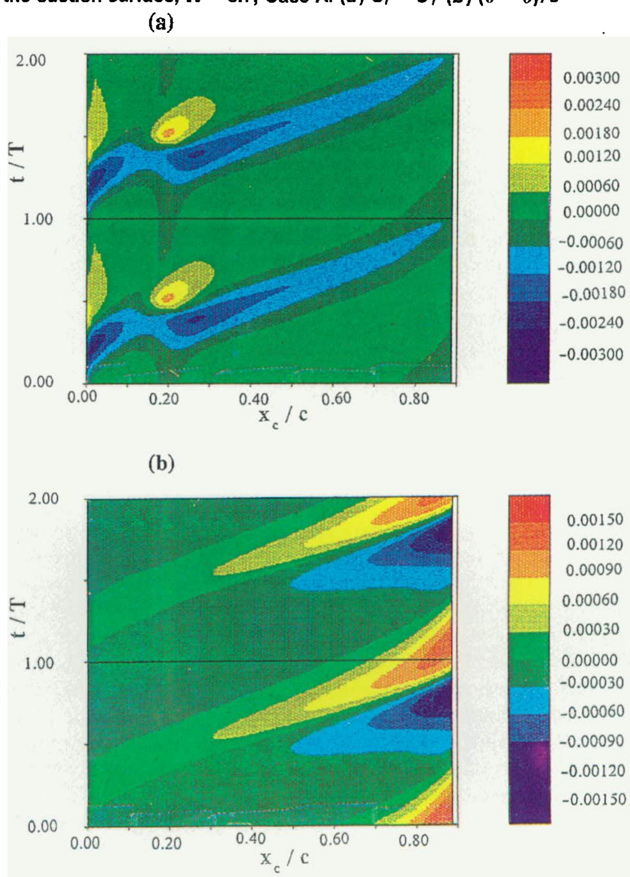

Fig. 6 Space-time contour of unsteady boundary layer quantities on the suction surface, $\Omega = 5.7$: Case B: (*a*): $C_f - \overline{C_f}$, (*b*) $(\theta - \overline{\theta})/c$

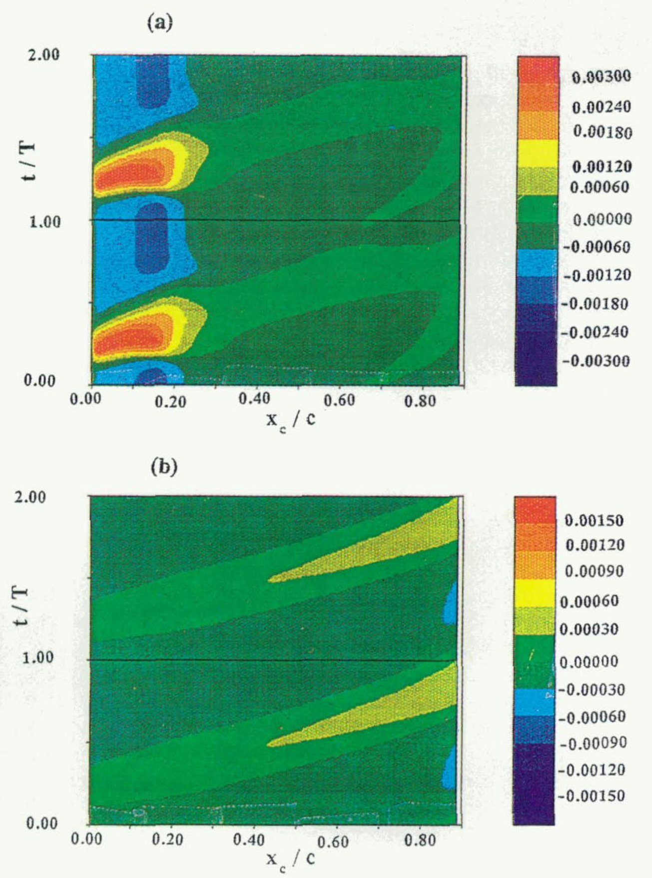

Fig. 8 Space–time contour of unsteady boundary layer quantities on the suction surface, $\Omega = 5.7$: Case C: (a) $C_f - \overline{C_f}$, (b) $(\theta - \overline{\theta})/c$

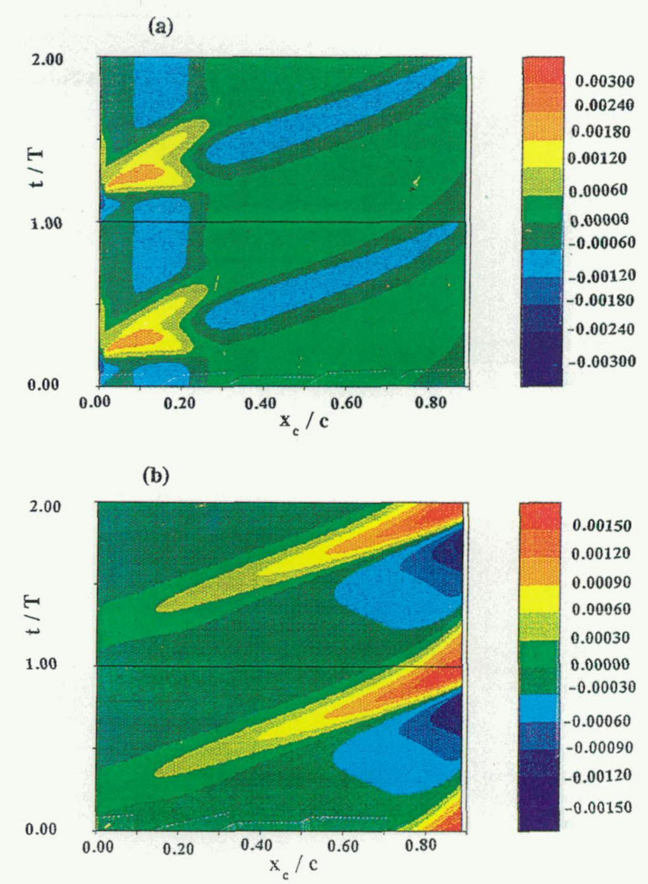

Fig. 10 Space–time contour of unsteady boundary layer quantities on the suction surface, $\Omega = 5.7$: Case D: (a) $C_f - \overline{C_f}$, (b) $(\theta - \overline{\theta})/c$

bution is characterized by a pressure peak following the trajectory of the wake. As a result of this distribution, an instantaneous favorable unsteady streamwise pressure gradient (over and above the mean pressure field) is generated on the leading side of the wake and an instantaneous adverse unsteady pressure gradient is generated on the trailing side of the wake. The unsteady favorable pressure gradient tends to suppress the growth of the boundary layer while the unsteady adverse pressure gradient tends to increase the growth of the boundary layer. The combination of these two pressure gradients results in a decrease in the momentum thickness on the leading side of the wake and an increase in the momentum thickness on the trailing side of the wake.

Figure 5 shows the distribution of time-averaged skin friction coefficient and the momentum thickness on the suction surface. The time-averaged skin friction coefficient and momentum thickness are nearly the same as the steady state. The magnitude of the unsteady skin friction coefficient is nearly uniform over the blade chord. The magnitude of the unsteady momentum thickness grows rapidly with distance. As discussed earlier, this is because the unsteady momentum thickness is generated by the cumulative and history effects of unsteady pressure gradient.

Case B: Effects of Wake Velocity Defect on Transitional Boundary Layer. In this simulation, the background turbulence intensity is prescribed as the measured value (5 percent), and it is assumed to be the same in the wake also. The main difference between this simulation case and the previous one (case A) is that the boundary layer is transitional in this case, and the effect of wake velocity defect is isolated from the effect of wake turbulence.

The predicted boundary layer skin friction coefficient and the momentum thickness are shown in Figs. 6 and 7. The unsteady

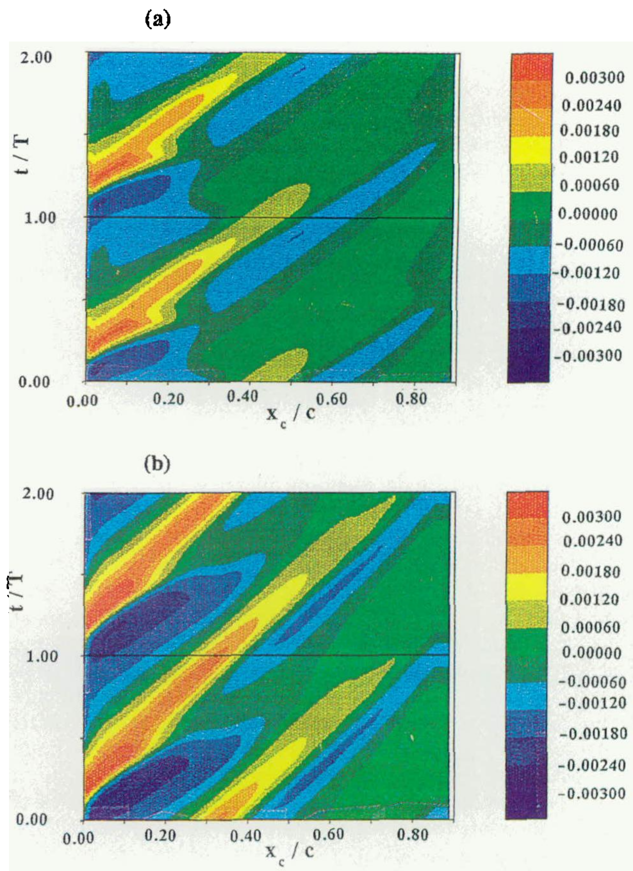

Fig. 16 Space–time contour of unsteady skin friction coefficient at different wake traverse speeds: (a) $U/u_{is} = 1.61$, (b) $U/u_{is} = 2.43$

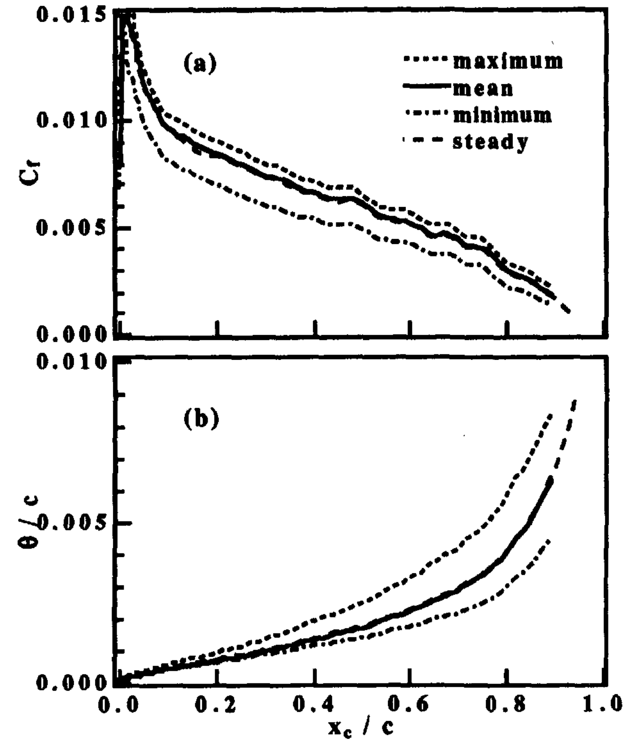

Fig. 5 Time-averaged and unsteady boundary layer development on the suction surface, at Ω = 5.7: Case A: (*a*) skin friction coefficient, (*b*) momentum thickness

skin friction coefficient contour (Fig. 6(*a*)) for the transitional boundary layer shows some unique features between 10 to 30 percent blade chord. Compared with the previous case (Fig. 4(*a*)), the line of minimum skin friction is twisted at about 20 percent chord and a high skin friction region occurs at 20 percent chord and $t/T = 0.5$. Since these features do not exist in a fully turbulent boundary layer, a logical assumption is that the transition process has been affected by the unsteady velocity/pressure at the edge of the boundary layer. This phenomenon can be clearly seen in Fig. 7(*a*). The transition region in steady boundary layer is predicted to occur between 17 to 25 percent chord. The Reynolds number based on momentum thickness is 159, which is close to the estimated value of 146 using the correlation by Mayle (1991). With the unsteady pressure due to wake/blade interaction, the earliest transition recorded by the upper envelope of skin friction coefficient starts at about 14 percent chord and ends at about 20 percent chord. The lower envelope shows an early start of transition but a delayed completion of transition.

The time-dependent transition process is closely related to the instantaneous local momentum thickness. It is clear from Figs. 6 and 7(*a*) that the location where the earliest transition starts in a period (centered at $x_c/c \approx 0.14$, $t/T \approx 0.4$, characterized by an increase in the unsteady skin friction coefficient compared with the distribution in Fig. 4(*a*)), coincides with the peak position of momentum thickness shown in Fig. 6(*b*) at the same axial location. Although the absolute value of the unsteady momentum thickness is small, the ratio of the peak value to the time-averaged momentum thickness is significant (about 1.2 at the above-mentioned location). The instantaneous momentum Reynolds number reaches 171 at the maximum point, which exceeds the predicted value of 159 at the transition starting point in the steady boundary layer. In the present case, the turbulence intensity does not vary with time. Other factors, such as the pressure gradient, are expected to have small effect on the onset of transition at the relatively high turbulence level (5 percent). The inception of the unsteady transition in the S–T plane depends mainly on the value of momentum Reynolds number. The region in the S–T plane with high momentum thickness has an earlier transition than the one with the lower momentum thickness. This effect results in a periodic unsteady motion of the transition location.

As a result of the unsteady transition process, the time-averaged skin friction coefficient no longer equals the steady values in the transition region. The time-averaged transition curve is smoother than the steady one. The relative magnitude of unsteady momentum thickness and the time-averaged momentum thickness are not significantly changed by the unsteady transition. For the Reynolds number and free-stream turbulence intensity value used here, the interaction between the unsteady surface pressure/velocity (through the unsteady momentum thickness) and the boundary layer transition does not have significant effect on the global development of the blade boundary layer.

Case C: Effects of Wake Turbulence on the Transitional Boundary Layer. In this simulation, the unsteady velocity and pressure due to wake/blade interaction is removed in order to isolate the effects of wake turbulence. The turbulence intensity in the wake is specified using Eq. (2), with $T_{ub} = 5$ percent and $T_{uw} = 8$ percent. The peak turbulence level is 13 percent at the center of the wake. The mean flow in the free stream is assumed to be steady ($D = 0$).

The predicted skin friction coefficient and momentum thickness are shown in Figs. 8 and 9. The S–T contours (Fig. 8(*a*)) show a dramatic increase in skin friction coefficient near the leading edge of the blade following the passage of the high turbulence "wake." Comparison with Fig. 9(*a*) indicates that the high skin friction patch in Fig. 8(*a*) corresponds to the accelerated transition process promoted by the high turbulence intensity level in the wake. With such a high turbulence intensity, transition occurs very close to the leading edge following the passage of the wake center. The unsteadiness in skin friction coefficient decreases rapidly after about 25 percent blade chord where the boundary layer undisturbed by the wake turbulence

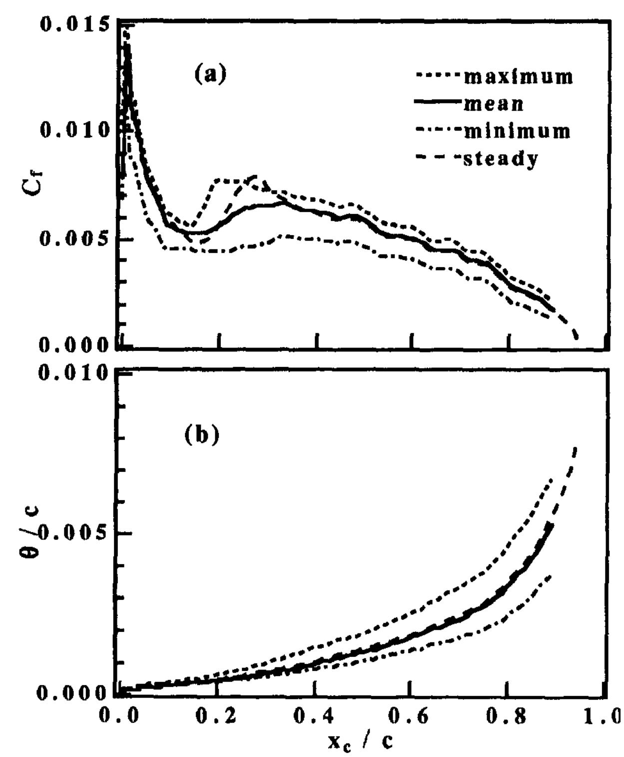

Fig. 7 Time-averaged and unsteady boundary layer development on the suction surface, at Ω = 5.7: Case B: (*a*) skin friction coefficient, (*b*) momentum thickness

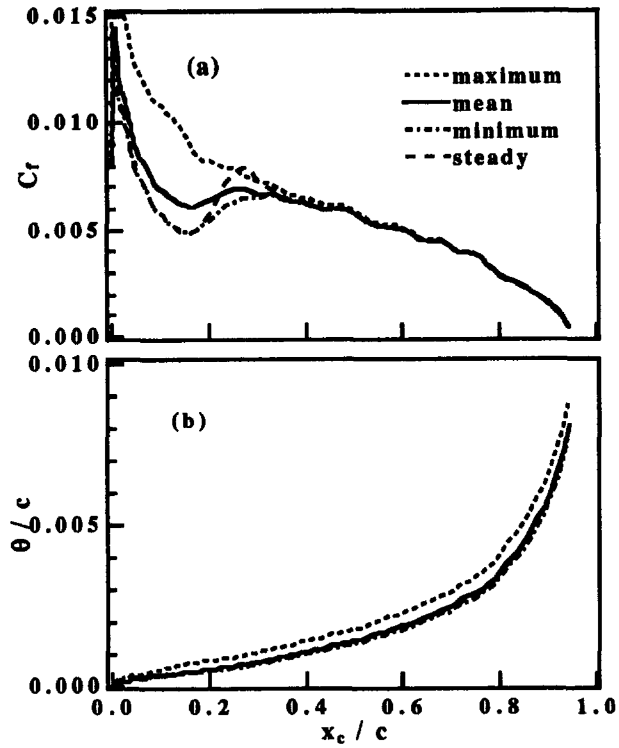

Fig. 9 Time-averaged and unsteady boundary layer development on the suction surface, at Ω = 5.7: Case C: (*a*) skin friction coefficient, (*b*) momentum thickness

completes its transition. It is clear from Fig. 8(*a*) that the leading edge (bottom line) of the high skin friction patch, or transitional patch, has a smaller slope than the trailing edge (top line), indicating a faster traveling speed for the leading edge of the transitional patch. As a result, the width of the transitional patch increases as it propagates downstream.

After the trailing edge of the transition patch passes through, the boundary layer is predicted to relaminarize. As shown in Fig. 9(*a*), the lower envelope of the skin friction coefficient is identical to that of the steady boundary layer before the start of the transition. Since in this case the lower envelope reflects the boundary layer undisturbed by the wake turbulence, the above-mentioned fact clearly indicates that the state of the boundary layer is mainly laminar between two wakes. For the boundary layer in between two passing wakes, Fig. 9(*a*) shows a transition starting point, which is nearly the same as the steady boundary layer. The rate of increase in skin friction coefficient after the transition point, however, is slower than that in the steady boundary layer. This indicates that the production of turbulence in the boundary layer between two transition patches is suppressed compared with the steady boundary layer. The time-averaged transition starts at an earlier streamwise location and has a smoother transition curve. As a result, the time-averaged skin friction coefficient is significantly different from the steady-state value in the transition region.

The time-dependent transition due to the convection of wake turbulence also results in a periodic increase in momentum thickness. Unlike the one caused by the unsteady pressure gradient, the magnitude of unsteady momentum thickness resulting from the turbulence-induced unsteady transition appears to be relatively small. The unsteady transition tends to increase the time-averaged momentum thickness due to the increased area of turbulent boundary layer on the S–T plot. In the present case, increase in the time-averaged momentum thickness is not very significant due to the short laminar region in the steady boundary layer. This is the result of the relatively high background turbulence level.

Case D: Combined Effects. In this simulation case, the combined effects of both the velocity defect (Case B) and the turbulence profile (Case C) in the wake are considered. The distribution of unsteady skin friction coefficient shown in Fig. 10(*a*) is best understood through comparison of the results for cases B and C shown in Figs. 6(*a*) and 8(*a*), respectively. Within the transition region on the blade ($x < 20$ percent chord), the effect of wake velocity defect reduces the instantaneous skin friction coefficient, while the earlier transition due to the wake turbulence increases the skin friction coefficient. The combination of these two effects still results in an increase in skin friction coefficient, but with a smaller magnitude. The effect of the unsteady transition caused by the periodic variation of momentum thickness is found (in Fig. 10(*a*)) to modify the transitional patch produced by wake turbulence. The unsteady transition has little effect on the skin friction coefficient in the fully turbulent region. The time-averaged skin friction coefficient differs from the steady value only in the transition region (Fig. 11(*a*)). The time-averaged transition, as indicated by the skin friction coefficient distribution, is smoother than the one in the corresponding steady boundary layer.

The unsteady momentum thickness due to the unsteady pressure and the unsteady wake-induced transition are nearly in phase with each other. As a result, the two effects combine to produce a larger magnitude of unsteady momentum thickness. This can be seen in Figs. 10(*b*) and 11(*b*). Figure 11(*b*) also shows a small net increase in the time-averaged momentum thickness resulting from the combined effects of wake velocity defect and the wake turbulence intensity.

The effects of wake/boundary layer interaction on the pressure surface boundary layer are very similar to that observed on the suction surface boundary layer. The major difference is the unsteady pressure, which is out of phase with the unsteady pressure on the suction surface. The magnitude of unsteady pressure is also different. A larger increase in the time-averaged momentum thickness over the steady value is observed on the pressure surface as a result of the combined effects of velocity

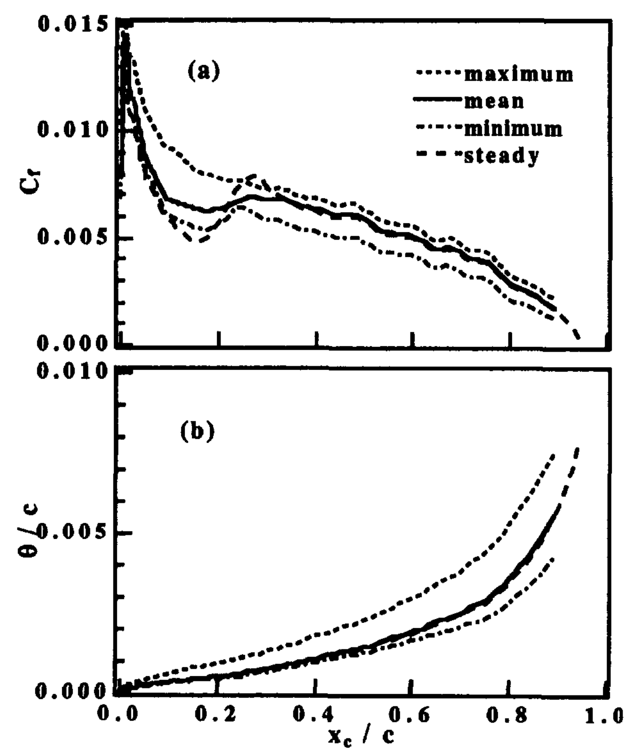

Fig. 11 Time-averaged and unsteady boundary layer development on the suction surface, at Ω = 5.7: Case D: (*a*) skin friction coefficient, (*b*) momentum thickness

defect and the turbulence profile in the wake. This might be due to the fact that the unsteady transition process on the pressure surface (near the leading edge) occurs with an adverse pressure gradient (see Fig. 2(*a*)) whereas the one on the suction surface occurs with a favorable pressure gradient.

Effects of Wake Parameters on Unsteady Pressure and Blade Boundary Layers

As demonstrated by Korakianitis (1992), the unsteady pressure on the surface of a blade due to rotor/stator interaction is mainly affected by the axial gap (spacing) between the blade rows, the wake/blade count ratio and the wake inflow angle (rotor outflow angle). In this paper, the effects of these parameters are studied in the context of unsteady boundary layer development on the blade surface. The reference conditions and the blade geometry used for this study are the same as the one simulated in the previous section, with $d/c = 0.6$, $n_w/n_b = 1.0$, $U/u_{is} = 0.81$, and $D = 0.28$, $T_{ub} = 5$ percent, $T_{uw} = 8$ percent, $w = 0.093$, $\Omega = 5.7$, $\beta = 44$ deg. Series of computations are carried out in which systematic variations of the wake parameters (d/c_x, n_w/n_b, U/u_{is}) are made one at a time. Due to the absence of a real rotor cascade, no attempt has been made to account for the effects of changes in rotor loading on the inlet wake characteristics.

Effects of Axial Gap. In an axial turbomachinery stage, the wake from the rotor blade decays as it progresses through the axial gap between the rotor and the stator blade. By the time it reaches the stator blade, the amplitude of the wake is reduced and the width increased. Direct simulation of the wake decay is not possible from the unsteady Euler procedure. However, the effect of the wake decay in the axial gap can be approximated using a wake decay model or it can be simulated by a steady Navier–Stokes solver. In the present study, the wake decay model developed by Raj and Lakshminarayana (1973) has been used to estimate the decay of rotor wake in the axial gap.

In this simulation, three different axial gaps are considered, $d/c_x = 0.3$, 0.6, 0.9. The corresponding wake amplitudes and wake width parameters in Eqs. (1) and (2) are $D = 0.39$, 0.28, 0.23 and $w = 0.066$, 0.093, 0.114. The additional turbulence intensity at the center of the wake is estimated to be $T_{uw} = 10$ percent, 8 percent, 7 percent. The predicted unsteady and time-averaged pressure distributions on the suction surface are compared in Fig. 12. Figure 12(*a*) shows the time-averaged value. Figures 12(*b*) and 12(*c*) show the amplitude of the first and the second Fourier components. The same format applies to Figs. 13 and 15, which will not be repeated each time.

The mean blade pressure distributions shown in Fig. 12(*a*) indicate that the variation in the axial gap had no effect on the time-averaged surface pressure distribution, and they are identical to the steady-state value. The fact that the time-averaged pressure distribution is identical to the steady pressure distribution indicates that the inviscid wake/blade interaction is basically a linear process for the cases computed. Although the nondimensional wake velocity defect in the rotor frame is quite large ($D = 0.39$, 0.28, 0.23), the maximum nondimensional crossflow velocity in the stator frame is relatively small ($q_n/q_{is} = 0.16$, 0.12, 0.11). Hence, nonlinear interaction in the inviscid flow is small. In all the computations, identical values are maintained for the time-averaged velocity or the mass flow. This is essential for accurate assessment of the effects of wake variables on unsteady performance of the stator blade row.

The first and the second Fourier components of the amplitudes of the unsteady pressure at various axial gaps are compared in Figs. 12(*b*) and 12(*c*), respectively. Notice that a smaller scale is used in these figures for clarity in comparison. The second Fourier amplitude is about half the magnitude of the first Fourier amplitude. The relatively large amplitude for the second Fourier component should not be interpreted as an indication of nonlinear interaction. Instead, this is a result of the assumed Gaussian shape of the wake profile, which contains both the low and the high Fourier components. The amplitude of unsteady pressure increases as the axial gap decreases. The influence is much stronger on the second Fourier component than the first Fourier component. As the axial gap becomes smaller, the velocity defect at the center of the wake increases while the width of the wake decreases. The reduction in wake width results in a shift of energy from the first Fourier component to higher Fourier components. This explains the larger increase in the second Fourier amplitude for the unsteady surface pressure as the gap is reduced.

The predicted time averaged and unsteady skin friction coefficients are compared in Fig. 12. Except for very small differences in the transition region, the mean skin friction coefficients are nearly identical for all the axial gaps. This indicates that the time-averaged boundary layer is not significantly affected by the change in the axial gap. The variation of the first Fourier amplitude of C_f, shown in Fig. 12(*b*), indicates differences in the trend observed in the transition region and the rest of the boundary layer. As discussed earlier, the wake velocity defect tends to reduce the instantaneous local skin friction coefficient. This effect becomes stronger at smaller axial gap. Since this is the dominant mechanism affecting the unsteady skin friction coefficient beyond the transition region, the amplitude of unsteadiness in skin friction coefficient increases (instantaneous C_f value decreases) with a reduction in the axial gap. This is clearly seen from the data for $x_c/c > 0.25$. Within the transition region, there are opposing mechanisms in play. The transitional patch due to the wake turbulence increases the instantaneous skin friction coefficient. The amount of increase is compensated by the effect of wake velocity defect, which tends to decrease the instantaneous skin friction coefficient. The decrease in axial gap amplifies the latter, hence reduces the amplitude of the first Fourier component in the transition region. The influence of the axial gap on the second Fourier component of C_f is similar to the behavior of the first harmonic outside the transition region. Unlike the first Fourier component, the amplitude of the second Fourier component in the transition region increases with a decrease in the axial gap. This is the result of a narrower and stronger wake turbulence profile, which results in a shift of unsteadiness from the first Fourier component to higher Fourier components.

The distributions of momentum thickness are compared in Fig. 12. Axial gap has no significant influence on the time-averaged momentum thickness. The amplitudes of both the Fourier components show a consistent increase in the momentum thickness with a decrease in the axial gap. This is because the unsteady momentum thickness is mainly influenced by the unsteady pressure gradient. The larger effect of axial gap on the second Fourier component of the momentum thickness is also consistent with the trend observed in unsteady pressure (Fig. 12*c*).

Effects of Wake/Blade Count Ratio. In the aerodynamic and acoustic design of a compressor stage, one important variable is the wake/blade count ratio. The effects of wake/blade count ratio on the wake/blade interaction effects are investigated in this simulation. Three different blade count ratios are considered, with $n_w/n_b = 0.5$, 1.0, and 2.0. This is achieved through the variation of the number of wakes per stator. The geometry of the stator remains the same. For the case $n_w/n_b = 0.5$, two stator blade passages are computed in the Euler solution. The predicted results for the suction surface are shown in Fig. 13.

It is clear from Fig. 13(*a*) that the time averaged pressure distribution is not influenced by the change in the wake/blade count ratio. As the wake/blade count ratio increases, the reduced frequency for the stator also increases ($\Omega = 2.9$, 5.7,

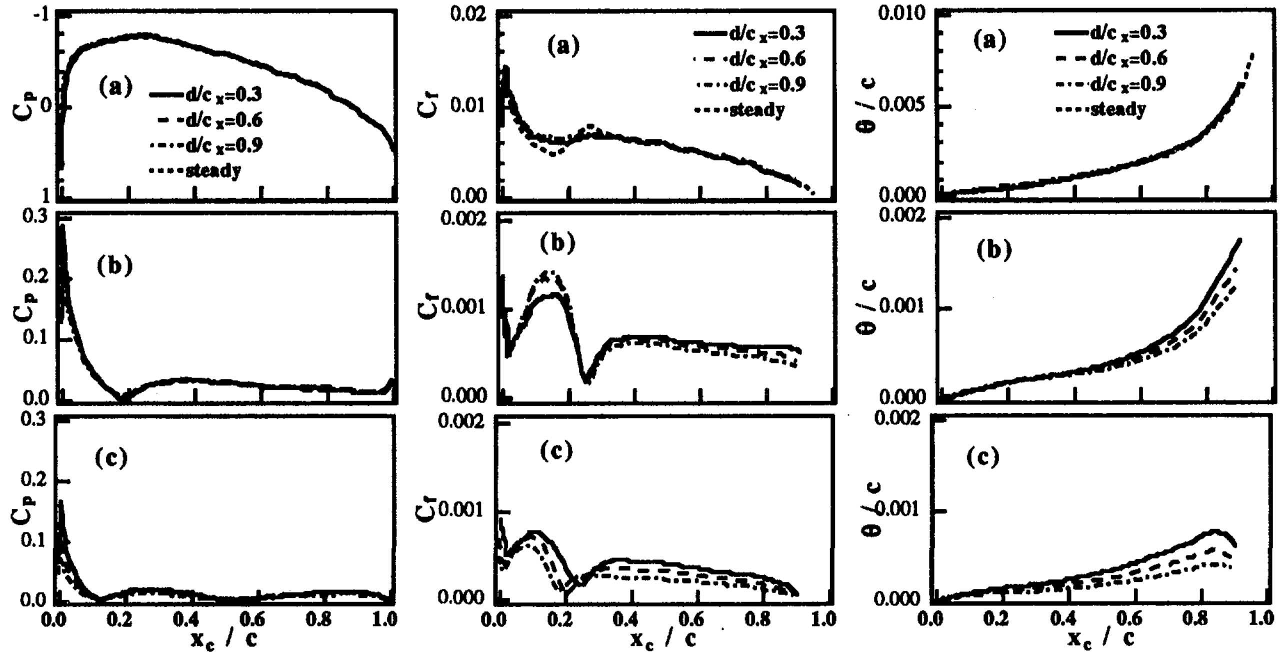

Fig. 12 Distribution of pressure coefficient, skin friction coefficient and momentum thickness on suction surface. Effect of axial gap, n_w/n_b = 1.0, U/u_{is} = 0.81: (*a*) mean value, (*b*) amplitude of first Fourier component, (*c*) amplitude of second Fourier component.

11.4). The variation in the unsteady pressure distribution shown in Fig. 13(*b*) results mainly from an increase in the reduced frequency. An increase in the reduced frequency results in an increase in the axial wave number of the incoming wakes. As discussed earlier, stronger interference between the unsteady pressure field from the adjacent pressure surface and the unsteady pressure on the suction surface occurs at higher reduced frequencies or axial wave numbers. As shown in Figs. 13(*b*) and 13(*c*), more lobes exist on the distribution of unsteady pressure amplitude at higher wake/blade count ratios as a result of stronger pressure wave interaction. In this simulation, the pitch of the wake is reduced for a higher n_w/n_b value, while the absolute wake width is kept constant. As a result, the relative wake width compared to the wake pitch increases for an increase in n_w/n_b value. The effect of this is a shift of energy from the higher Fourier components to the first Fourier component. This is the reason for the decrease in the second Fourier amplitude for higher wake/blade count ratio shown in Fig. 13(*c*).

Figure 13(*a*) shows an increase in time-averaged C_f on the first quarter chord of the blade with an increase in the wake/blade count ratio or reduced frequency. This is an indication of faster transition in the boundary layer. As the number of wakes increases, a larger fraction of the area on the S–T plane is occupied by the transitional patches. As a result, the time-

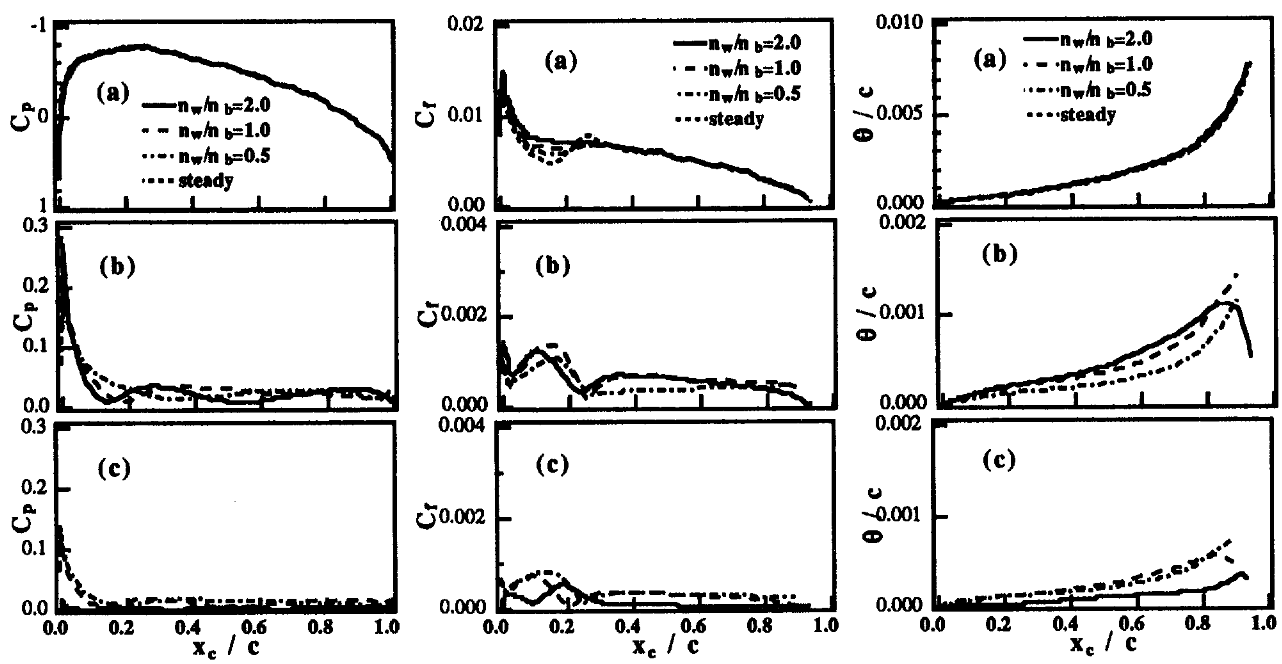

Fig. 13 Distribution of pressure coefficient, skin friction coefficient and momentum thickness on suction surface. Effect of wake/blade count ratio, d/c_x = 0.6, U/u_{is} = 0.81: (*a*) mean value, (*b*) amplitude of first Fourier component, (*c*) amplitude of second Fourier component.

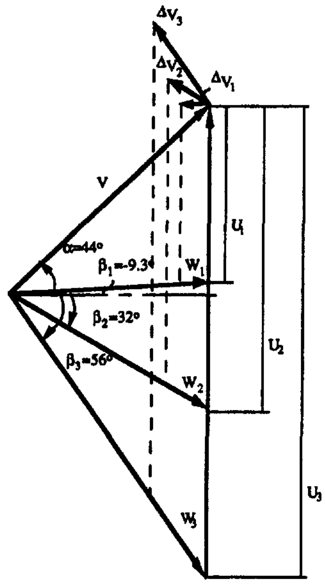

Fig. 14 Velocity triangles at different wake traverse speeds (wake inflow angles)

averaged intermittency factor increases in the unsteady transition region. This trend has been experimentally observed by many authors (Pfeil et al., 1983) and demonstrated computationally in Part 1 of this paper.

The effect of increased wake/blade count ratio on the Fourier components is characterized by a shift of energy from the higher Fourier components to the first Fourier component. As discussed above, this is due to an increase in the relative wake width at higher wake/blade count ratio. The variation of the harmonics of the skin friction coefficient is consistent with that observed for the pressure coefficient (Fig. 13). At a higher wake/blade count ratio, the second Fourier component of C_f becomes insignificant beyond 20 percent of the chord.

Figure 13(a) shows a consistent increase in the time-averaged momentum thickness with an increase in the wake/blade count ratio. This is partly due to the accelerated time-averaged transition as indicated by the time-averaged skin friction coefficient. Following the trend in unsteady pressure, shown in Fig. 13, the first Fourier component of the unsteady momentum thickness shows a general increase in the amplitude with an increase in the wake/blade count ratio, while the second Fourier component shows a decline. The nonmonotonic development of unsteady boundary layer thickness shown in Figs. 13(b) and 13(c) is a result of the unsteady pressure pattern shown in Figs. 13(b) and 13(c).

Effects of Wake Traverse Speed. Depending on the velocity triangle of the compressor stage, the inflow angle of the rotor wake in the relative frame may show large variation from design to design. In an actual stage, the stator inlet flow angle usually depends on the design of the rotor. For simplicity, the stator inlet flow angle is maintained the same in these simulations. The wake traverse speed is increased to provide different wake inflow angles (rotor exit flow angles). In this simulation, series of computations are made with three different wake traverse speeds $U/u_{is} = 0.81, 1.61, 2.43$, resulting in three different wake inflow angles, $\beta = -9.3$, 32, and 56 deg as shown in Fig. 14. This also increases the reduced frequency. The corresponding reduced frequencies are 5.7, 11.3, and 17.1. The velocity triangle for all these cases are shown in Fig. 14. It is difficult to estimate the wake parameters for rotor blades with different loading without a prior knowledge of the rotor flow. For simplicity, the same wake profiles are used for all the three simulations. The decay of the wake in the axial gap is estimated using the wake decay model due to Raj and Lakshminarayana (1973). The emphasis in this simulation is on the effects of the orientation of the wake and the reduced frequency. The results are shown in Fig. 15.

Figure 15 shows the predicted pressure distribution on the suction surface of the stator blade. The time-averaged pressure distributions are essentially the same as the steady-state pressure distribution. The magnitude and distribution of the first Fourier component of the unsteady pressure show a strong dependency on the wake traverse speed. Both the reduced frequency and the wake inflow angle increase with an increase in the wake traverse speed. As discussed in the previous simulation, more lobes appear on the chordwise distribution of unsteady surface pressure at a higher reduced frequency due to the pressure wave interference. Increase in the relative angle between the wake flow and the mean flow results in much higher maximum nondimensional crossflow velocities ($q_n/q_{is} = 0.12$, 0.22, and 0.27), which in turn result in an increase in the magnitude of the unsteady pressure on the blade surface. The effect of wake traverse speed on the second Fourier component is mainly an effect of the change in the reduced frequency.

As shown in Fig. 15(a), the time-averaged skin friction coefficient increases in the transition region and decreases slightly in the fully turbulent region as the wake traverse speed increases. The overall change on the entire blade surface is insignificant. The major influence of the change in wake traverse speed is on the first Fourier component. Figure 15(b) shows that as the wake traverse speed is increased, the amplitude of first Fourier component increases dramatically up to 40 percent of blade chord. This trend has not been observed previously and needs more detailed explanation.

In the cases discussed earlier, the relative angle between the wake and the blade surface is small and the effect of wake velocity defect is to reduce the unsteady skin friction. In the transition region, this effect is found to compensate the high skin friction coefficient caused by the early transition induced by the wake turbulence. These two effects occur at nearly the same location in the S–T plan and the net result is an increase in skin friction coefficient of smaller magnitude. This is no longer the case at higher wake inflow angles. As the angle between the wake and the blade surface increases, the low skin friction region in the S–T plot moves downstream and no longer coincides with the transitional patch. As shown in Fig. 16, the increase in the skin friction within the transitional patch is no longer canceled by the effect due to the wake velocity defect. At the largest wake inflow angle (corresponding to the highest wake traverse speed), the two effects discussed above start adding to (instead of canceling) each other, producing a large increase in the magnitude of unsteady skin friction, shown in Fig. 15(b).

The time-averaged momentum thickness shown in Fig. 15(a) indicates a significant effect of wake traverse speed on the time-averaged momentum thickness. The time-averaged boundary layer momentum thickness grows more rapidly at higher wake traverse speeds. A substantial increase in the amplitude of the first Fourier component is also predicted for higher wake traverse speeds. This is a result of large unsteady surface pressure, shown in Fig. 15. The nonmonotonic distribution of the unsteady momentum thickness in the rear part of the boundary layer is a result of the increased reduced frequency, which has been discussed earlier. No substantial increase in the second Fourier component is predicted. Verdon et al. (1991) computed the response of a flat plate boundary layer to unsteady pressure waves. A substantial increase in the time-averaged boundary layer thickness is also observed in their simulation, especially for unsteady pressure waves with larger amplitude and higher frequency. Upstream-traveling pressure waves were found to have a stronger influence on the time-averaged boundary layer thickness than downstream-traveling pressure waves. This is

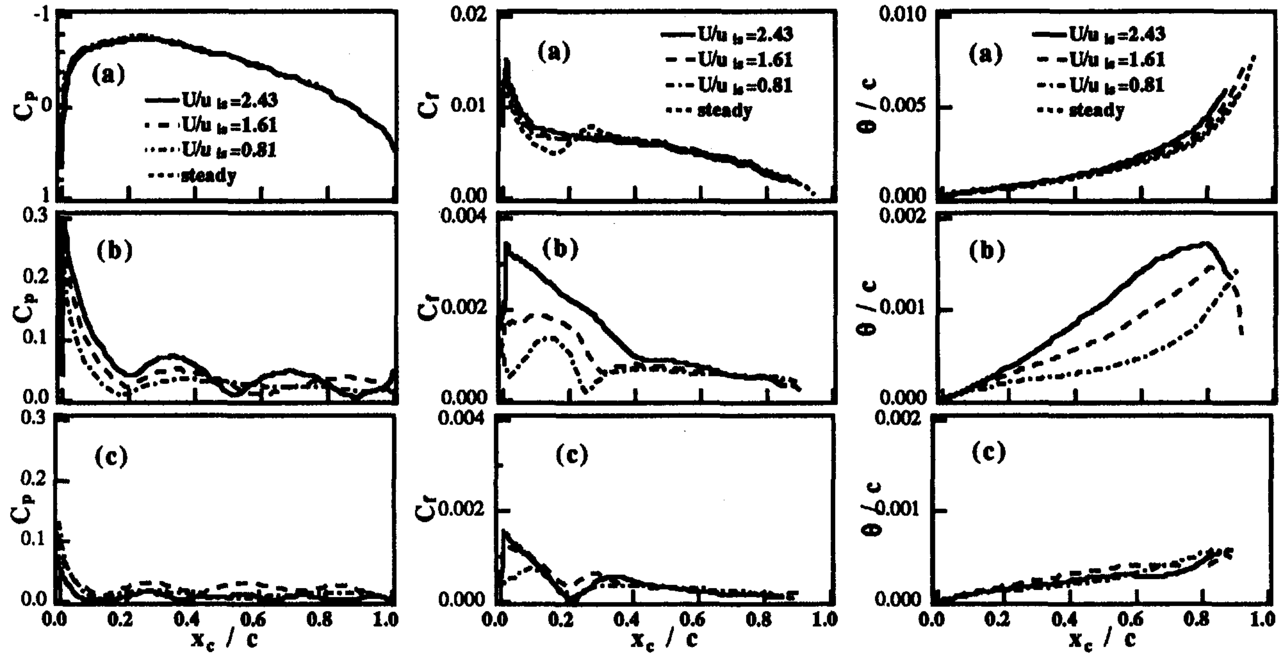

Fig. 15 Distribution of pressure coefficient, skin friction coefficient and momentum thickness on the suction surface. Effect of wake traverse speed, d/c_x = 0.6, n_w/n_b = 1.0: (*a*) mean value, (*b*) amplitude of first Fourier component, (*c*) amplitude of second Fourier component

believed to be a result of nonlinear response of the boundary layer to the unsteady pressure gradient.

This discussion is concerned with the development of unsteady boundary layer on the suction surface of the blade. The development of the pressure surface boundary layer is found to be similar to that observed on the suction surface. For the cases studied, the parametric influence is similar on both the surfaces.

Effects on Performance. Since the time-averaged profile loss of the blade row is proportional to the trailing edge momentum thickness, the effects of various parameters affecting the wake/blade-row interaction on the profile loss can be studied by analyzing the predicted boundary layer momentum thickness at the trailing edge. In the following discussion, two parameters are defined. The first one is the total time-averaged boundary layer at the trailing edge divided by its steady-state value,

$$\theta^* = (\theta_s + \theta_p)_{te}/(\theta_s + \theta_p)_{te}^{ss} \tag{3}$$

where the superscript *ss* denotes the steady-state value, the subscript *te* denotes the value at the trailing edge. θ^* gives an indication on the ratio of time-averaged profile loss to the steady state profile loss. The second parameter is defined as

$$D_f^* = \int_0^c (C_{fs} + C_{fp})dx_c \bigg/ \int_0^c (C_{fs}^{ss} + C_{fp}^{ss})dx_c \tag{4}$$

where D_f^* is a measure of the increased frictional drag over the steady-state value.

Figure 17 compares the overall effects of the axial gap, the wake/blade count ratio, and the wake traverse speed on the stator blade boundary layers. The two parameters defined above are used for performance comparison. In the present computation, the boundary layers separate at around 90 percent chord on the suction side and 98 percent on the pressure side. Nominal trailing edges (90 percent chord on suction side, 98 percent chord on pressure side) are used to calculate θ^* and D_f^*.

It is clear from Fig. 17(*a*) that the unsteady wake/blade interaction has an appreciable influence on the trailing edge momentum thickness. Nearly 10 percent increase in profile loss (over steady-state value) is observed at the smallest axial gap. The time-averaged profile loss decreases slightly as the axial gap is increased. The dependency of the time-averaged frictional drag of the blade row on the axial gap is weak over the range considered.

Significant influence of the wake/blade count ratio, on both the time-averaged momentum thickness and frictional drag, is clearly shown in Fig. 17(*b*). As the wake/blade count ratio increases, the profile losses as well as the frictional drag of the stator increase. Additional numerical simulations of the fully turbulent blade boundary layers for the case n_w/n_b = 2 show that the momentum thickness increase is about 8 percent over the steady-state value. This suggests that the contribution of the unsteady transition and the unsteady pressure to the profile loss is comparable in this case.

As shown in Fig. 17(*c*), increasing the wake traverse speed results in a substantial increase in the time-averaged profile loss. Additional numerical simulations of fully turbulent blade boundary layers show a comparable percentage increase, which

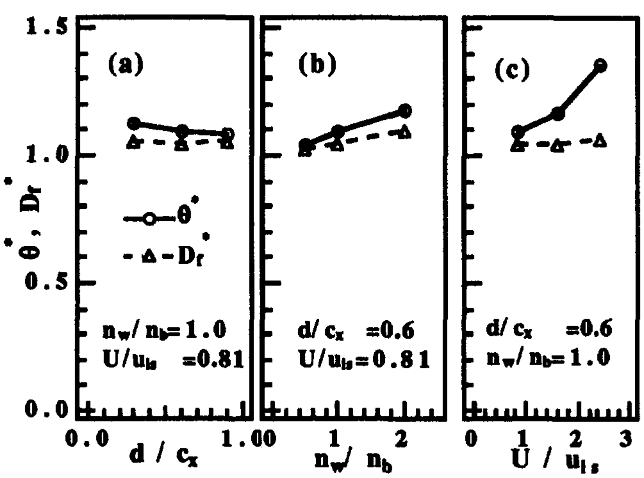

Fig. 17 Variation of momentum thickness parameter θ^* and frictional drag parameter D_f^*: (*a*) effect of axial gap, (*b*) effect of wake/blade count ratio, (*c*) effect of wake traverse speed

indicates that the unsteady pressure has a stronger influence on the increase in profile loss at higher wake traverse speeds.

Conclusions

The following conclusions can be drawn based on the simulation study of unsteady cascade flow due to wake/blade interaction.

The combined effects of three different mechanisms are found to be responsible for the generation of unsteady pressure on the blade surface with a wake/blade-row interaction: the wake cutting by the blade leading edge, the change in streamwise velocity near the surface caused by the counterrotating vortices, and the wake velocity defect, the periodic variation of the instantaneous outflow angle induced by the counterrotating vortices.

In the transitional blade boundary layer subjected to wake velocity gust, the onset of transition changes periodically due to temporal variation of local boundary layer momentum thickness. The time-dependent transition caused by the wake velocity defect does not have a significant effect on the global development of the blade boundary layers.

The transition on the blade is strongly influenced by the high turbulence intensity in the wake. Periodic transitional patches are generated by the high turbulence intensity in the passing wakes and transported downstream. The time-dependent transition results in large unsteadiness in the instantaneous local skin friction coefficient and a smoother time-averaged transition curve than the one observed in the steady boundary layer.

Both the wake velocity defect and the wake turbulence are found to have a significant influence on the unsteady blade boundary layers. The wake velocity defect has stronger influence on the magnitude of unsteady momentum thickness, while the wake turbulence is mainly responsible for the large magnitude of unsteady skin friction coefficient in the transition region.

A decrease in axial gap results in an increase in the amplitude of unsteady surface pressure and unsteady momentum thickness. The amplitude of the unsteady skin friction coefficient increases outside the transition region.

At higher reduced frequencies, more lobes appear on the chordwise distribution of unsteady surface pressure. This results in nonmonotonic increase in the chordwise distribution in the amplitude of the unsteady momentum thickness.

An increase in the reduced frequency and the wake inflow angle due to higher wake traverse speed results in a rapid increase in the magnitude of unsteady surface pressure, skin friction coefficient, and the boundary layer momentum thickness.

Unsteady wake/blade interaction has an appreciable influence on the profile loss. The time-averaged profile loss decreases slightly as the axial gap is increased. Increase in the wake/blade count ratio results in significant increase in both the time-averaged profile loss and the frictional drag. Increase in wake traverse speed could result in appreciable increase in the time averaged profile loss.

The results presented in this paper are subject to the performance of the turbulence model, the wake decay model and the simplifications in wake specification procedure (change in rotor blade loading has not been considered, for example). Further improvements in the turbulence model and more accurate wake specification procedure are necessary to improve the accuracy of the numerical procedure.

Acknowledgments

This work was supported by National Aeronautics and Space Administration (NASA) through contract No. NAG 3-1168, with Dr. P. Sockol as the technical monitor. The authors wish to acknowledge NASA for providing the supercomputing resources at NASA Lewis Research Center and NASA Ames Research Center.

References

Addison, J. S., and Hodson, H. P., 1990, "Unsteady Transition in an Axial-Flow Turbine: Part 1—Measurements on the Turbine Rotor; Part 2—Cascade Measurements and Modeling," ASME JOURNAL OF TURBOMACHINERY, Vol. 112, pp. 206–221.

Ashworth, D. A., Lagraff, J. E., and Schultz, D. L., 1989, "Unsteady Interaction Effects on a Transitional Turbine Blade Boundary Layer," ASME JOURNAL OF TURBOMACHINERY, Vol. 111, pp. 162–168.

Dong, Y., and Cumpsty, N. A., 1990, "Compressor Blade Boundary Layers, Part 1: Test Facility and Measurements With No Incident Wakes; Part 2: Measurements With Incident Wakes," ASME JOURNAL OF TURBOMACHINERY, Vol. 112, pp. 222–240.

Dullenkopf, K., Schulz, A., and Wittig, S., 1991, "The Effect of Incident Wake Conditions on the Mean Heat Transfer of an Airfoil," ASME JOURNAL OF TURBOMACHINERY, Vol. 113, pp. 412–418.

Fan, S., and Lakshminarayana, B., 1996, "Computation and Simulation of Wake-Generated Unsteady Pressure and Boundary Layers in Cascades: Part 1—Description of Approach and Validation," ASME JOURNAL OF TURBOMACHINERY, Vol. 118, this issue, pp. 96–108.

Hodson, H. P., 1985, "Boundary-Layer Transition and Separation Near the Leading Edge of a High-Speed Turbine Blade," ASME *Journal of Engineering for Gas Turbines and Power*, Vol. 107, pp. 127–134.

Hodson, H. P., 1990, "Modeling Unsteady Transition and Its Effects on Profile Loss," ASME JOURNAL OF TURBOMACHINERY, Vol. 112, pp. 691–701.

Korakianitis, T., 1992, "On the Prediction of Unsteady Forces on Gas Turbine Blades. Part 1: Description of the Approach; Part 2: Analysis of the Results," ASME JOURNAL OF TURBOMACHINERY, Vol. 114, pp. 114–131.

Ladwig, M., and Fottner, L., 1993, "Experimental Investigations of the Influence of Incoming Wakes on the Losses of a Linear Turbine Cascade," ASME Paper No. 93-GT-394.

Liu, X., and Rodi, W., 1991, "Experiments on Transitional Boundary Layers With Wake-Induced Unsteadiness," *Journal of Fluid Mechanics*, Vol. 231, pp. 229–256.

Mayle, R. E., 1991, "The Role of Laminar-Turbulent Transition in Gas Turbine Engines," ASME JOURNAL OF TURBOMACHINERY, Vol. 113, pp. 509–537.

Orth, U., 1993, "Unsteady Boundary-Layer Transition in Flow Periodically Disturbed by Wakes," ASME JOURNAL OF TURBOMACHINERY, Vol. 115, pp. 707–713.

Pfeil, H., Herbst, R., and Schroder, T., 1983, "Investigation of the Laminar-Turbulent Transition of Boundary Layers Disturbed by Wakes," ASME *Journal of Engineering for Power*, Vol. 105, pp. 131–137.

Raj, R., and Lakshminarayana, B., 1973, "Characteristics of the Wake Behind a Cascade of Airfoils," *Journal of Fluid Mechanics*, Vol. 61, Part 4, pp. 707–730.

Schulz, H. D., Gallus, H. E., and Lakshminarayana, B., 1990, "Three-Dimensional Separated Flow Field in the End Wall Region of an Annular Compressor Cascade in the Presence of Rotor-Stator Interaction, Part 1: Quasi-Steady Flow Field and Comparison With Steady-State Data; Part 2: Unsteady Flow and Pressure Field," ASME JOURNAL OF TURBOMACHINERY, Vol. 112, pp. 669–690.

Verdon, J. M., Barnett, M., Hall, K. C., and Ayer, T. C., 1991, "Development of Unsteady Aerodynamic Analyses for Turbomachinery Aeroelastic and Aeroacoustic Applications," NASA CR 4405.

Wittig, S., Dullenkopf, K., Schulz, A., and Hestermann, R., 1987, "Laser-Doppler Studies of the Wake-Effected Flow Field in a Turbine Cascade," ASME JOURNAL OF TURBOMACHINERY, Vol. 109, pp. 170–176.

DISCUSSION

N. A. Cumpsty[1]

These are interesting and useful papers. The ability to predict the behavior of the unsteady flow inside the passages is impressive and I believe it will prove very helpful in calculating the interaction of wakes with blade boundary layers and improving our understanding. My grounds for caution relate to the second paper, which refers specifically to the *physics* of the boundary layer flow. The problem goes beyond what is normally described as turbulence modeling.

Experiments were performed some years ago by Dong (1988) and Li (1990) with traveling wakes disturbing the boundary layers on the surfaces of compressor blades. These measurements demonstrated that the flow physics is not quite how it is assumed in most treatments of the flow, including the present one of Fan and Lakshminarayana. (Some of the results obtained by Dong were reported by Dong and Cumpsty, 1990.) After a turbulent patch or spot passes, there is a period of calmed flow,

[1] Director, Whittle Laboratory, University of Cambridge, Madingley Rd., Cambridge, CB3 ODY United Kingdom.

indicates that the unsteady pressure has a stronger influence on the increase in profile loss at higher wake traverse speeds.

Conclusions

The following conclusions can be drawn based on the simulation study of unsteady cascade flow due to wake/blade interaction.

The combined effects of three different mechanisms are found to be responsible for the generation of unsteady pressure on the blade surface with a wake/blade-row interaction: the wake cutting by the blade leading edge, the change in streamwise velocity near the surface caused by the counterrotating vortices, and the wake velocity defect, the periodic variation of the instantaneous outflow angle induced by the counterrotating vortices.

In the transitional blade boundary layer subjected to wake velocity gust, the onset of transition changes periodically due to temporal variation of local boundary layer momentum thickness. The time-dependent transition caused by the wake velocity defect does not have a significant effect on the global development of the blade boundary layers.

The transition on the blade is strongly influenced by the high turbulence intensity in the wake. Periodic transitional patches are generated by the high turbulence intensity in the passing wakes and transported downstream. The time-dependent transition results in large unsteadiness in the instantaneous local skin friction coefficient and a smoother time-averaged transition curve than the one observed in the steady boundary layer.

Both the wake velocity defect and the wake turbulence are found to have a significant influence on the unsteady blade boundary layers. The wake velocity defect has stronger influence on the magnitude of unsteady momentum thickness, while the wake turbulence is mainly responsible for the large magnitude of unsteady skin friction coefficient in the transition region.

A decrease in axial gap results in an increase in the amplitude of unsteady surface pressure and unsteady momentum thickness. The amplitude of the unsteady skin friction coefficient increases outside the transition region.

At higher reduced frequencies, more lobes appear on the chordwise distribution of unsteady surface pressure. This results in nonmonotonic increase in the chordwise distribution in the amplitude of the unsteady momentum thickness.

An increase in the reduced frequency and the wake inflow angle due to higher wake traverse speed results in a rapid increase in the magnitude of unsteady surface pressure, skin friction coefficient, and the boundary layer momentum thickness.

Unsteady wake/blade interaction has an appreciable influence on the profile loss. The time-averaged profile loss decreases slightly as the axial gap is increased. Increase in the wake/blade count ratio results in significant increase in both the time-averaged profile loss and the frictional drag. Increase in wake traverse speed could result in appreciable increase in the time averaged profile loss.

The results presented in this paper are subject to the performance of the turbulence model, the wake decay model and the simplifications in wake specification procedure (change in rotor blade loading has not been considered, for example). Further improvements in the turbulence model and more accurate wake specification procedure are necessary to improve the accuracy of the numerical procedure.

Acknowledgments

This work was supported by National Aeronautics and Space Administration (NASA) through contract No. NAG 3-1168, with Dr. P. Sockol as the technical monitor. The authors wish to acknowledge NASA for providing the supercomputing resources at NASA Lewis Research Center and NASA Ames Research Center.

References

Addison, J. S., and Hodson, H. P., 1990, "Unsteady Transition in an Axial-Flow Turbine: Part 1—Measurements on the Turbine Rotor; Part 2—Cascade Measurements and Modeling," ASME JOURNAL OF TURBOMACHINERY, Vol. 112, pp. 206–221.

Ashworth, D. A., Lagraff, J. E., and Schultz, D. L., 1989, "Unsteady Interaction Effects on a Transitional Turbine Blade Boundary Layer," ASME JOURNAL OF TURBOMACHINERY, Vol. 111, pp. 162–168.

Dong, Y., and Cumpsty, N. A., 1990, "Compressor Blade Boundary Layers, Part 1: Test Facility and Measurements With No Incident Wakes; Part 2: Measurements With Incident Wakes," ASME JOURNAL OF TURBOMACHINERY, Vol. 112, pp. 222–240.

Dullenkopf, K., Schulz, A., and Wittig, S., 1991, "The Effect of Incident Wake Conditions on the Mean Heat Transfer of an Airfoil," ASME JOURNAL OF TURBOMACHINERY, Vol. 113, pp. 412–418.

Fan, S., and Lakshminarayana, B., 1996, "Computation and Simulation of Wake-Generated Unsteady Pressure and Boundary Layers in Cascades: Part 1—Description of Approach and Validation," ASME JOURNAL OF TURBOMACHINERY, Vol. 118, this issue, pp. 96–108.

Hodson, H. P., 1985, "Boundary-Layer Transition and Separation Near the Leading Edge of a High-Speed Turbine Blade," ASME *Journal of Engineering for Gas Turbines and Power,* Vol. 107, pp. 127–134.

Hodson, H. P., 1990, "Modeling Unsteady Transition and Its Effects on Profile Loss," ASME JOURNAL OF TURBOMACHINERY, Vol. 112, pp. 691–701.

Korakianitis, T., 1992, "On the Prediction of Unsteady Forces on Gas Turbine Blades. Part 1: Description of the Approach; Part 2: Analysis of the Results," ASME JOURNAL OF TURBOMACHINERY, Vol. 114, pp. 114–131.

Ladwig, M., and Fottner, L., 1993, "Experimental Investigations of the Influence of Incoming Wakes on the Losses of a Linear Turbine Cascade," ASME Paper No. 93-GT-394.

Liu, X., and Rodi, W., 1991, "Experiments on Transitional Boundary Layers With Wake-Induced Unsteadiness," *Journal of Fluid Mechanics,* Vol. 231, pp. 229–256.

Mayle, R. E., 1991, "The Role of Laminar-Turbulent Transition in Gas Turbine Engines," ASME JOURNAL OF TURBOMACHINERY, Vol. 113, pp. 509–537.

Orth, U., 1993, "Unsteady Boundary-Layer Transition in Flow Periodically Disturbed by Wakes," ASME JOURNAL OF TURBOMACHINERY, Vol. 115, pp. 707–713.

Pfeil, H., Herbst, R., and Schroder, T., 1983, "Investigation of the Laminar-Turbulent Transition of Boundary Layers Disturbed by Wakes," ASME *Journal of Engineering for Power,* Vol. 105, pp. 131–137.

Raj, R., and Lakshminarayana, B., 1973, "Characteristics of the Wake Behind a Cascade of Airfoils," *Journal of Fluid Mechanics,* Vol. 61, Part 4, pp. 707–730.

Schulz, H. D., Gallus, H. E., and Lakshminarayana, B., 1990, "Three-Dimensional Separated Flow Field in the End Wall Region of an Annular Compressor Cascade in the Presence of Rotor-Stator Interaction, Part 1: Quasi-Steady Flow Field and Comparison With Steady-State Data; Part 2: Unsteady Flow and Pressure Field," ASME JOURNAL OF TURBOMACHINERY, Vol. 112, pp. 669–690.

Verdon, J. M., Barnett, M., Hall, K. C., and Ayer, T. C., 1991, "Development of Unsteady Aerodynamic Analyses for Turbomachinery Aeroelastic and Aeroacoustic Applications," NASA CR 4405.

Wittig, S., Dullenkopf, K., Schulz, A., and Hestermann, R., 1987, "Laser-Doppler Studies of the Wake-Effected Flow Field in a Turbine Cascade," ASME JOURNAL OF TURBOMACHINERY, Vol. 109, pp. 170–176.

DISCUSSION

N. A. Cumpsty[1]

These are interesting and useful papers. The ability to predict the behavior of the unsteady flow inside the passages is impressive and I believe it will prove very helpful in calculating the interaction of wakes with blade boundary layers and improving our understanding. My grounds for caution relate to the second paper, which refers specifically to the *physics* of the boundary layer flow. The problem goes beyond what is normally described as turbulence modeling.

Experiments were performed some years ago by Dong (1988) and Li (1990) with traveling wakes disturbing the boundary layers on the surfaces of compressor blades. These measurements demonstrated that the flow physics is not quite how it is assumed in most treatments of the flow, including the present one of Fan and Lakshminarayana. (Some of the results obtained by Dong were reported by Dong and Cumpsty, 1990.) After a turbulent patch or spot passes, there is a period of calmed flow,

[1] Director, Whittle Laboratory, University of Cambridge, Madingley Rd., Cambridge, CB3 ODY United Kingdom.

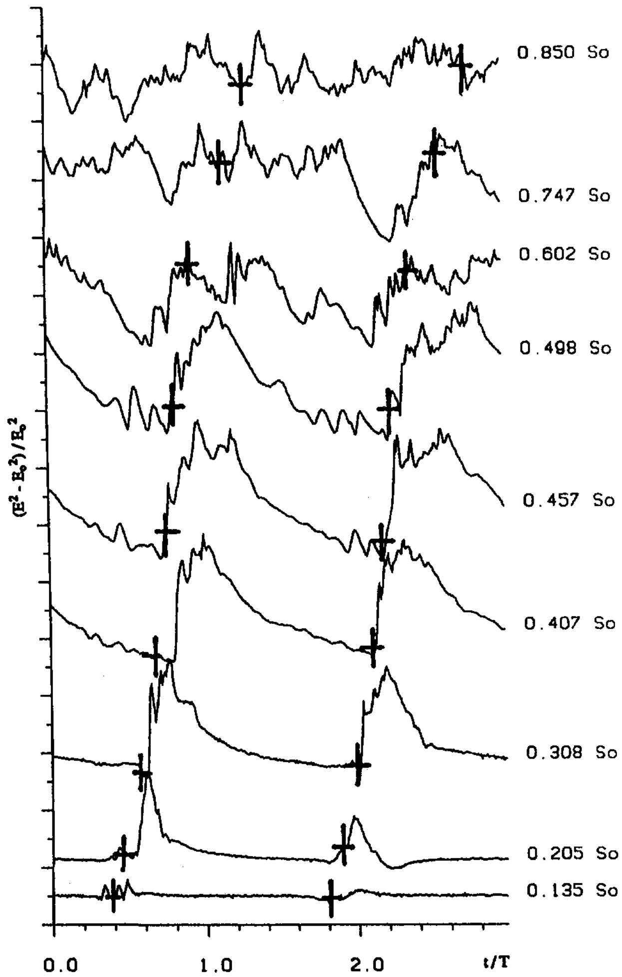

Fig. 18 Raw traces from a hot-film gage at positions on the suction surface of a rotor blade passing through wakes from upstream

and for compressor blades this lasts for a time comparable to the time for the free-stream flow to travel the length of the blade passage. Although the flow in the calmed region is laminar, the properties of this calmed region are quite unlike those of a conventional laminar boundary layer. The calmed region was first reported by Schubauer and Klebanoff (1955), but it has received little study of consideration since.

The importance of the calmed region is illustrated in Fig. 18 with results taken from Li (1990). The data are from a hot-film gage attached to the suction surface of a C4 rotor blade at midspan, operating in the presence of wakes created by stationary radial rods upstream. The incidence for this test was 2 deg, close to optimum for the blade. Figure 18 shows raw (i.e., *not* ensemble-averaged) traces from a *single* hot-film gage attached at different chordwise positions on a rotor blade, each position expressed as a fraction of the total suction surface length s_0. The ordinate in Fig. 18 is chosen to give an approximate value for the instantaneous skin friction. The abscissa is time, nondimensionalized by the blade passing period. Each of the traces is started at the same time relative to the passing of wakes; the times at which each wake reaches a position are shown by the bold crosses. From a distance back from the leading edge of around $0.205s_0$ a recognizable turbulent patch is produced (different in each realization in this raw data). What is even more marked is the calm region following each patch of turbulence; there are patches of calm flow right back to $0.850s_0$. In the calmed flow the skin friction is not small, as it would be in a conventional laminar boundary layer, but at the start of each calmed region it is equal to the skin friction in the preceding turbulent patch. With the passage of time the calm laminar region relaxes back to a conventional laminar boundary layer.

A paper by Cumpsty, Dong, and Li, illustrating the phenomenon of a wake interacting with a blade boundary layer more fully, and attempting to explain some aspects of the flow, has been presented at the ASME International Gas Turbine and Aeroengine Congress and Exposition in Houston (Paper No. 95-GT-443).

References

Dong, Y., 1988. "Boundary Layers on Compressor Blades," PhD Dissertation, University of Cambridge, United Kingdom.

Dong, Y., and Cumpsty, N. A., 1990, "Compressor Blade Boundary Layers: Part 2—Measurements With Incident Wakes," ASME JOURNAL OF TURBOMACHINERY, Vol. 112, pp. 231–240.

Li, Y. S., 1990, "Mixing in Axial Compressors," PhD Dissertation, University of Cambridge, United Kingdom.

Schubauer, G. B., and Klebanoff, P. S., 1955, "Contributions on the Mechanics of Boundary Layer Transition," NACA TN 3489.

Authors' Closure

We would like to thank Dr. Cumpsty for his valuable comments. Dr. Cumpsty's discussion points us to the very important issue of modeling the effects of the calmed flow region observed in a transitional boundary layer following the passage of a turbulent spot. The characteristics of the calmed region have been summarized most recently by Halstead et al. (1995). Within the calmed region, the shear stress relaxes from a turbulent to a laminar level. The boundary layer profile in this region is more stable and tends to suppress flow instabilities, both from Tollmien–Schlichting waves and the bypass transition process.

The modeling effort described in the present papers simulates the transitional boundary layer in an ensemble-averaged sense. A description of individual turbulent spot and the calmed region associated with it is beyond the capability of the present approach. It is found that the k–ϵ model does a reasonably good job in simulating the generation and transport of the ensemble-averaged transitional patches. Although no special treatments or assumptions were made for the calmed region, the model does predict a boundary layer recovery region, which bears close resemblance to the experimentally observed calmed region behind an ensemble-averaged transitional patch.

This region can be clearly seen in Fig. 7(b) of Part 1. In this figure, the intermittency factor γ defined from the shape factor, $(H - H_l)/(H_t - H_l)$, can be used as a measure for the difference in boundary layer profiles between a conventional laminar boundary layer and a turbulent boundary layer, with a zero for a conventional laminar boundary layer and unity for a conventional turbulent boundary layer on a flat plate. In Fig. 7 (b), conventional laminar boundary layer regions (say $\gamma < 0.1$) occupy relatively small area close to the leading edge in the space–time contours. No conventional laminar boundary layer exists beyond 36 percent plate length from the leading edge. The (predominantly turbulent) transitional patches, which assume a wedge shape in the space–time contours, start from about 14 percent blade length and extend to the trailing edge. The triangular regions (on the left) bounded by a conventional laminar boundary layer region and two consecutive transitional patches (from top and bottom) closely resemble the experimentally observed calmed region. The boundary layer in these regions is characterized by the recovery from a turbulent boundary layer profile to a conventional laminar boundary layer profile. Upstream of the point $x/L = 0.36$, the boundary layer after the passage of a transitional patch is able to relax to a conventional laminar profile. Downstream of the point $x/L = 0.36$, the next transitional patch catches up and forces it into turbulent before the boundary layer relaxes to a conventional laminar profile. It is interesting to notice that the convecting velocity deduced from the $\gamma = 0.1$ contour is about 0.33 of the free-stream velocity. This is close to the observed trailing edge convecting

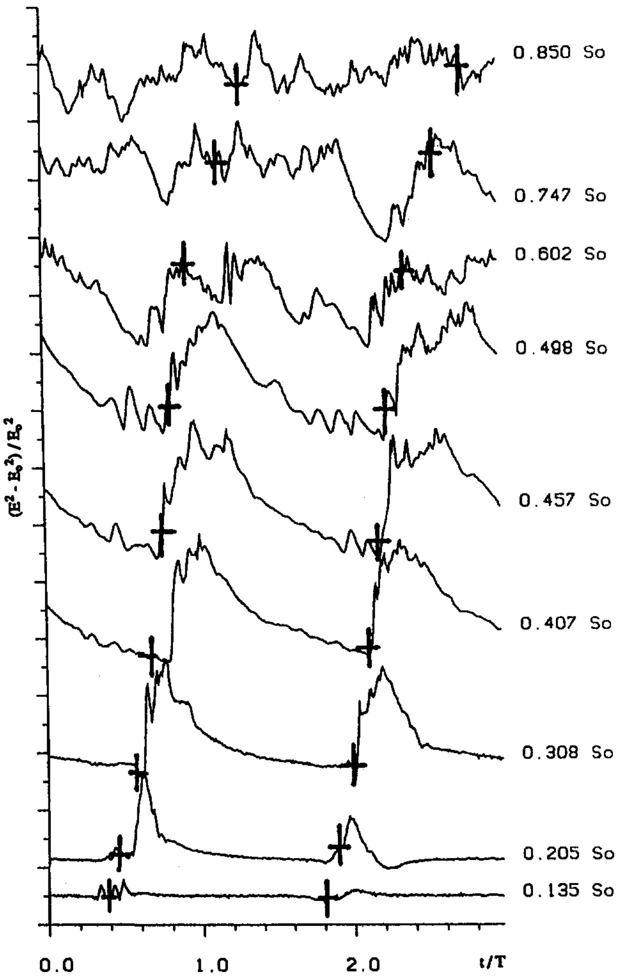

Fig. 18 Raw traces from a hot-film gage at positions on the suction surface of a rotor blade passing through wakes from upstream

and for compressor blades this lasts for a time comparable to the time for the free-stream flow to travel the length of the blade passage. Although the flow in the calmed region is laminar, the properties of this calmed region are quite unlike those of a conventional laminar boundary layer. The calmed region was first reported by Schubauer and Klebanoff (1955), but it has received little study of consideration since.

The importance of the calmed region is illustrated in Fig. 18 with results taken from Li (1990). The data are from a hot-film gage attached to the suction surface of a C4 rotor blade at midspan, operating in the presence of wakes created by stationary radial rods upstream. The incidence for this test was 2 deg, close to optimum for the blade. Figure 18 shows raw (i.e., *not* ensemble-averaged) traces from a *single* hot-film gage attached at different chordwise positions on a rotor blade, each position expressed as a fraction of the total suction surface length s_0. The ordinate in Fig. 18 is chosen to give an approximate value for the instantaneous skin friction. The abscissa is time, nondimensionalized by the blade passing period. Each of the traces is started at the same time relative to the passing of wakes; the times at which each wake reaches a position are shown by the bold crosses. From a distance back from the leading edge of around $0.205s_0$ a recognizable turbulent patch is produced (different in each realization in this raw data). What is even more marked is the calm region following each patch of turbulence; there are patches of calm flow right back to $0.850s_0$. In the calmed flow the skin friction is not small, as it would be in a conventional laminar boundary layer, but at the start of each calmed region it is equal to the skin friction in the preceding turbulent patch. With the passage of time the calm laminar region relaxes back to a conventional laminar boundary layer.

A paper by Cumpsty, Dong, and Li, illustrating the phenomenon of a wake interacting with a blade boundary layer more fully, and attempting to explain some aspects of the flow, has been presented at the ASME International Gas Turbine and Aeroengine Congress and Exposition in Houston (Paper No. 95-GT-443).

References

Dong, Y., 1988. "Boundary Layers on Compressor Blades," PhD Dissertation, University of Cambridge, United Kingdom.

Dong, Y., and Cumpsty, N. A., 1990, "Compressor Blade Boundary Layers: Part 2—Measurements With Incident Wakes," ASME JOURNAL OF TURBOMACHINERY, Vol. 112, pp. 231–240.

Li, Y. S., 1990, "Mixing in Axial Compressors," PhD Dissertation, University of Cambridge, United Kingdom.

Schubauer, G. B., and Klebanoff, P. S., 1955, "Contributions on the Mechanics of Boundary Layer Transition," NACA TN 3489.

Authors' Closure

We would like to thank Dr. Cumpsty for his valuable comments. Dr. Cumpsty's discussion points us to the very important issue of modeling the effects of the calmed flow region observed in a transitional boundary layer following the passage of a turbulent spot. The characteristics of the calmed region have been summarized most recently by Halstead et al. (1995). Within the calmed region, the shear stress relaxes from a turbulent to a laminar level. The boundary layer profile in this region is more stable and tends to suppress flow instabilities, both from Tollmien–Schlichting waves and the bypass transition process.

The modeling effort described in the present papers simulates the transitional boundary layer in an ensemble-averaged sense. A description of individual turbulent spot and the calmed region associated with it is beyond the capability of the present approach. It is found that the k–ϵ model does a reasonably good job in simulating the generation and transport of the ensemble-averaged transitional patches. Although no special treatments or assumptions were made for the calmed region, the model does predict a boundary layer recovery region, which bears close resemblance to the experimentally observed calmed region behind an ensemble-averaged transitional patch.

This region can be clearly seen in Fig. 7(b) of Part 1. In this figure, the intermittency factor γ defined from the shape factor, $(H - H_l)/(H_t - H_l)$, can be used as a measure for the difference in boundary layer profiles between a conventional laminar boundary layer and a turbulent boundary layer, with a zero for a conventional laminar boundary layer and unity for a conventional turbulent boundary layer on a flat plate. In Fig. 7 (b), conventional laminar boundary layer regions (say $\gamma < 0.1$) occupy relatively small area close to the leading edge in the space–time contours. No conventional laminar boundary layer exists beyond 36 percent plate length from the leading edge. The (predominantly turbulent) transitional patches, which assume a wedge shape in the space–time contours, start from about 14 percent blade length and extend to the trailing edge. The triangular regions (on the left) bounded by a conventional laminar boundary layer region and two consecutive transitional patches (from top and bottom) closely resemble the experimentally observed calmed region. The boundary layer in these regions is characterized by the recovery from a turbulent boundary layer profile to a conventional laminar boundary layer profile. Upstream of the point $x/L = 0.36$, the boundary layer after the passage of a transitional patch is able to relax to a conventional laminar profile. Downstream of the point $x/L = 0.36$, the next transitional patch catches up and forces it into turbulent before the boundary layer relaxes to a conventional laminar profile. It is interesting to notice that the convecting velocity deduced from the $\gamma = 0.1$ contour is about 0.33 of the free-stream velocity. This is close to the observed trailing edge convecting velocity (0.3 of the free-stream velocity) for a calmed region. The agreement between the trailing edge convecting velocity also indicates the similarity between the predicted recovering region and an experimentally observed calmed region.

The predicted effect of the calmed region or recovering region on bypass transition of the boundary layer between wake-induced transitional patches can be identified from the results shown in Figs. 8(a) and 9(a) of Part 2. An interesting phenomenon has been observed from the discussion of results shown in Fig. 9(a), namely the transition process along the minimum skin friction path is substantially slower than the one for the steady boundary layer. Since the steady boundary layer is subjected to the background free-stream turbulence only, its transitional process is representative of the region between two transitional patches, where the boundary layer is not disturbed by the patches and the calmed regions following them. The fact that there exists a path on the space–time contours (see Fig. 8(a)) along which the boundary layer transition is slower than that in the region completely undisturbed by the patches is beyond the conventional explanation. Examination of the space–time contours of skin friction in Fig. 8(a) shows that between 14 and 34 percent blade chord, where transition occurs for boundary layer between wake-induced transitional patches, the location of minimum skin friction immediately follows the trailing edge of the wake-induced transitional patches, instead of lying midway between two transitional patches. The location coincides with the recovery region following the transitional patch. The explanation is that the special boundary layer profile in the recovery region tends to suppress turbulence production in the transition region and results in a slower bypass transition than the boundary layer completely unaffected by the transitional patch. The tendency of the predicted recovering region to suppress additional transition further supports its resemblance to the experimentally observed calmed region.

This discussion shows that the present modeling approach did capture some of the ensemble-averaged characteristics of the calmed region. The underlying mechanism in the $k-\epsilon$ model that works to mimic this phenomenon is not yet clear, nor is its quantitative capability. Further investigations into these issues are necessary before we can predict this phenomenon with confidence. This is also true for other modeling issues, such as the performance of the model in adverse pressure gradients and control of turbulent production rate to simulate the correct length of transition, etc.

References

Halstead, D. E., Wisler, D. C., Okiishi, T. H., Walker, G. J., Hodson, H. P., and Shin, H.-Y., 1995, ''Boundary Layer Development in Axial Compressors and Turbines: Part 1 of 4—Composite Picture,'' ASME Paper No. 95-GT-461; accepted for publication in the ASME JOURNAL OF TURBOMACHINERY.

Impact of Rotor–Stator Interaction on Turbine Blade Film Cooling

R. S. Abhari [1]
The Ohio State University,
Columbus, OH 43210

The goal of this study is to quantify the impact of rotor–stator interaction on surface heat transfer of film cooled turbine blades. In Section I, a steady-state injection model of the film cooling is incorporated into a two-dimensional, thin shear layer, multiblade row CFD code. This injection model accounts for the penetration and spreading of the coolant jet, as well as the entrainment of the boundary layer fluid by the coolant. The code is validated, in the steady state, by comparing its predictions to data from a blade tested in linear cascade. In Section II, time-resolved film cooled turbine rotor heat transfer measurements are compared with numerical predictions. Data were taken on a fully film cooled blade in a transonic, high pressure ratio, single-stage turbine in a short duration turbine test facility, which simulates full-engine nondimensional conditions. Film cooled heat flux on the pressure surface is predicted to be as much as a factor of two higher in the time average of the unsteady calculations compared to the steady-state case. Time-resolved film cooled heat transfer comparison of data to prediction at two spanwise positions is used to validate the numerical code. The unsteady stator–rotor interaction results in the pulsation of the coolant injection flow out of the film holes with large-scale fluctuations. The combination of pulsating coolant flow and the interaction of the coolant with this unsteady external flow is shown to lower the local pressure side adiabatic film effectiveness by as much as 64 percent when compared to the steady-state case.

Motivation and Background

The mainstream flow in a turbine is inherently unsteady, in particular around the rotor blade. Of particular interest is the impact of periodic unsteadiness on the heat transfer distribution around a film cooled turbine blade. The impact of rotor–stator interaction on airfoil heat transfer has been actively studied in recent years. Experimental studies of the surface heat transfer on high-pressure-ratio rotating turbine blades without film cooling have been reported by Dunn (1990) and Guenette et al. (1989). These studies have shown that the amplitude of the unsteady surface heat transfer is comparable to the time-averaged levels. By using fast response Kulite transducers, Dietz and Ainsworth (1992), Dunn (1990), and Dunn et al. (1990) measured the unsteady surface pressure on rotating turbine blades. The measurements showed large-scale fluctuation of the surface pressure, particularly near the leading edge. By comparing details of the time-resolved heat transfer data to unsteady numerical calculations, Abhari et al. (1992) showed that the fluctuations of the surface heat flux could be explained by the multiple passage of the shock and wake structures from the upstream NGVs. Dunn et al. (1990) and Tran and Taulbee (1992) made the same observation in their respective numerical work.

Rigby et al. (1990) and Mehendale et al. (1994) investigated the impact of upstream moving shocks and wakes from rotating bars on the film effectiveness and heat transfer distribution of film cooled turbine blades in linear cascades. Three detailed experimental measurements of film cooling on rotating turbine blades are available in the open literature. By utilizing a mass–heat transfer analogy, Dring et al. (1980) measured the time-averaged film cooling effectiveness on the rotor blade of a low-speed turbine stage. Takeishi et al. (1992) also used a similar mass–heat transfer analogy to measure the film cooling effectiveness on the rotor blade of a cold air turbine. Abhari and Epstein (1994) measured the time-resolved heat transfer distribution around a high-pressure-ratio rotating turbine blade under fully scaled engine conditions. All three studies concluded that film cooling on the suction surface provides good surface protection, while on the pressure surface the results are mixed.

It has long been recognized that the flow just downstream of the discrete film holes is fundamentally three dimensional and any two-dimensional computational method must be modified to account for this three-dimensional interaction accurately. Crawford et al. (1980) developed a boundary layer code with an algebraic turbulence model in which the mixing length was "augmented" at the injection site to simulate the enhanced local mixing. Tafti and Yavuzkurt (1987) also developed a model of the injection process in which the three-dimensional mixing of the coolant and the boundary layer was accounted for through an "entrainment fraction." The entrainment fraction was correlated to experimental data and incorporated into a boundary layer code, which was shown to be successful in the prediction of film cooling effectiveness in multirow film cooling configurations (Tafti and Yavuzkurt, 1990). In another approach, Schönung and Rodi (1987) used a three-dimensional elliptic calculation to obtain "dispersion terms," which describe the enhanced mixing at the injection location. These dispersion terms were then incorporated in a boundary layer code. Haas et al. (1992) modified this approach by arguing that the dynamics of the interaction of the coolant with the boundary layer is better characterized by the momentum ratio as opposed to the blowing ratio. Their modification of the general approach improved the comparison between the data and the predictions. Leylek and Zerkle (1994) used a three-dimensional CFD code to predict the flow and the adiabatic film effectiveness. The computational grid extended into the holes and the coolant plenum to model the elliptic nature of the flow at the film hole exit plane. The predicted results clearly illustrated the three-dimensionality of flow within and in the near hole region.

[1] Previously at former Textron Lycoming, (now Allied Signal Engines) Stratford, CT 06497.

Contributed by the Heat Transfer Division for publication in the JOURNAL OF TURBOMACHINERY. Manuscript received by the Heat Transfer Division April 20, 1994. Associate Technical Editor: M. G. Dunn.

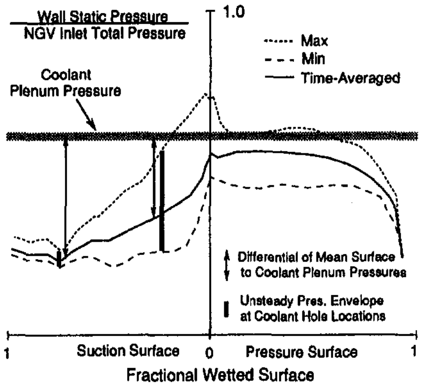

Fig. 1 Midspan rotor surface pressure predicted by the unsteady multiblade row, viscous CFD code

The design of turbine blade film cooling is generally achieved using steady-state conditions of the main and coolant gases, without accounting for the flow unsteadiness. A prediction of the maximum, the minimum, and the time-average of the surface pressure distribution for a typical high-pressure stage turbine blade are shown in Fig. 1. The mean coolant plenum pressure for the film cooled test at design condition is also shown. At the position of the coolant holes on the suction surface, the mean pressure differentials across the holes and the magnitude of the peak-to-peak pressure fluctuations are also identified. When the magnitude of the peak-to-peak fluctuation is much smaller than the mean pressure differential, the influence of unsteadiness is small. It is seen that for the front half of the suction surface and almost entire pressure surface, the peak-to-peak unsteady surface pressure variation is of the same order of magnitude as the mean coolant plenum-to-surface differential pressure, and as such, unsteadiness could be important. Abhari and Epstein (1994) also showed that the unsteady rotor–stator interaction results in the pulsation of the film cooling out of the holes. The resolution of the impact of this unsteady blowing on the time-averaged surface heat flux provides the motivation for the present study.

The present study consists of two separate sections. In Section I, a time-accurate multiblade row viscous CFD code is enhanced by incorporating an injection model. In a single blade row steady-state mode, the code is used to calculate the film cooling performance around a linear cascade airfoil reported by Camci (1989). Reasonably good comparisons between the code prediction and the test data are presented as the validation of the code in steady state. In Section II, the impact of rotor–stator interaction generated flow unsteadiness on turbine blade film cooling process is quantified. By using a short duration turbine test facility, time-resolved and time-averaged heat transfer measurements have been obtained on a fully film cooled transonic turbine blade (Abhari, 1991). Rotor blade surface heat transfer data at two spanwise positions and at two different turbine operating points are presented. Predictions from the code are compared to both time-resolved and time-averaged data. The computational code is then used as a numerical experiment to quantify the impact of the external flow unsteadiness and coolant pulsation on blade heat transfer.

Section I: Analytical Modeling

Numerical Method. The numerical procedure used to model this flow is a two-dimensional, Reynolds-averaged, unsteady multiblade row Navier–Stokes code, UNSFLO, developed by Giles (1988). This is a coupled viscous/inviscid code in which the thin shear layer Navier–Stokes equations are solved on a body-fitted boundary layer grid using an implicit algorithm, while the Euler equations are solved on an outer inviscid grid using an explicit algorithm. The interface between the two regions is handled in a manner in which mass, momentum, and energy are fully conserved. Quasi-three-dimensional effects are included through the specification of a stream-tube thickness variation in the third dimension. Here, the Euler equations are solved using a generalization of Ni's Lax–Wendroff algorithm (Ni, 1981). Full second-order accuracy is achieved. The inviscid grid can be a structured or an unstructured mesh composed of an arbitrary mix of quadrilateral and triangular cells. The viscous grid is an O-type mesh about each blade for which an ADI (alternating-direction-implicit) method with Roe's flux-difference splitting gives third-order upwinding for the residual operator and first-order upwinding for the implicit operator. The Baldwin–Lomax (1978) algebraic turbulence model is used in the viscous part of the solution with the location of the boundary layer transition specified. For all the calculations presented herein, transition was assumed at the leading edge. For the unsteady rotor–stator interaction calculations presented in Section II, the code utilizes an innovative space–time coordinate transformation, "time-tilting" (Giles, 1988), to permit arbitrary rotor–stator pitch ratios. Many more details on UNSFLO and its verification may be found in Giles and Haimes (1993) and Abhari et al. (1992).

For the calculations presented in Section II, both the mid and hub section geometries of the stage are modeled. Coordinates for the midsection of the blade are given by Ashworth (1987). Unfortunately, the exact design coordinates of the hub section

Nomenclature

α_0 = film hole chordwise angle to surface shown in Fig. 2
b = film hole pitch
C = true chord
C_{ax} = axial chord
d = film hole diameter
ϵ = heat transfer coefficient augmentation, defined in Eq. (5a)
h = heat transfer coefficient
η_{ad} = adiabatic film effectiveness
I = momentum ratio = $(\rho U^2)_c/(\rho U^2)_e$
k = defined in Eq. (3a)
M = blowing ratio = $(\rho U)_c/(\rho U)_e$
M_{eff} = effective injection ratio, defined in Eq. (3b)
Nu = Nusselt number based on C_{ax}, inlet blade relative total temperature, T_w, and main gas thermal conductivity at the wall
P = pressure
θ = nondimensional coolant temperature = $(T_r - T_c)/T_r - T_w)$
ρ = density
S = surface length from the stagnation point
T = temperature
U = velocity
X = axial distance
ξ = orthogonal coordinate normal to jet centerline, shown in Fig. 2
Ψ = nondimensional unsteady pressure parameter, defined in Eq. (6)
y_{cl} = centerline penetration of the coolant jet

Subscripts

0 = without film cooling
1 = first harmonic
ad = adiabatic with film cooling
c = coolant
cl = center line
e = external flow
fc = film cooled
j = integrated within the coolant jet cross section
r = recovery condition
s = static
tc = coolant stagnation condition
w = wall

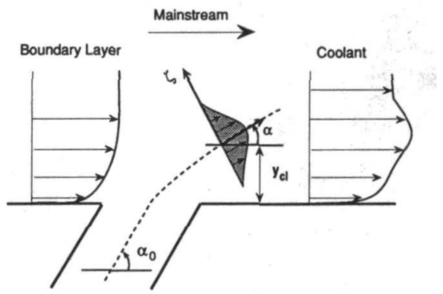

Fig. 2 Illustration of the coolant injection model

were not available to the author. The hub section geometry was reconstructed from photographs and drawings available in the public domain (Abhari, 1991; Norton et al., 1990; Guenette et al., 1989). Aerodynamic boundary conditions for the numerical simulations at different test conditions are obtained from Abhari (1991). Streamtube height distribution through the stage (input to the code) is derived from a streamline curvature calculation (Norton, 1987).

Injection Modeling. The injection model incorporated into UNSFLO approximates the three-dimensional fluid dynamics at the film holes. This model is an extension of the model proposed by Tafti and Yavuzkurt (1990) for a two-dimensional boundary layer code. At every injection site, an equivalent plane jet is distributed into the viscous computational domain. This distribution of the coolant accounts for the penetration of the jet into the boundary layer, the spreading of the injected jet, and the entrainment of boundary layer fluid by the coolant fluid. In the time-resolved predictions, instantaneous conditions at the injection location are used to predict the coolant behavior. It is hypothesized that the details of the mixing at the injection site are quasi-steady, even though the rest of the flow is fully unsteady. In this mode, all the fluxes out of the coolant holes are recalculated and updated at each time step.

In the present model, the specified coolant flow parameters are the values of total pressure and temperature, and the specific heat ratio. The coolant fluxes out of the holes are calculated by assuming that the coolant flow is isentropically expanded (up to choking) to the surface pressure at the injection site. For shaped holes, the mean coolant velocity is scaled by the ratio of the exit area to the throttling area of the hole. The discharge coefficients from the holes are calculated by using a previously developed correlation (Abhari, 1993), which accounted for the change in momentum flux ratios. In cases where the hole discharge coefficient or the coolant mass flux has been measured, the internal correlation is bypassed and the measured value of the discharge coefficient is directly used. It was observed that rapid local changes in surface pressure (prior to convergence) result in oscillatory coolant injection behavior. After some experimentation, it was determined that the solution is stabilized by spatial averaging of wall static pressure from three diameters upstream to three diameters downstream of the injection sites. The model of the coolant injection is illustrated in Fig. 2. Similar to Tafti and Yavuzkurt (1990), the coolant jet profile is assumed to be of the form;

$$\frac{U_j}{U_{cl}} = \{1 - (9\xi/10\xi^*)^{1.5}\}^2 \qquad (1)$$

where $U_{cl} = 1.43\ U_e$, $\xi^* = 0.7\ \pi d/(4b/d)$, and ξ is the jet coordinate orthogonal to its trajectory shown in Fig. 2. The jet temperature is assumed to be uniform and equal to the coolant total temperature. The coolant penetration of the external flow is modeled by a jet trajectory model (Abramovich, 1960), which is of the form

$$\frac{y_{cl}}{d} = \frac{2}{k}\left\{\left(k\frac{x}{d} + \cot^2\alpha_0\right)^{1/2} - \cot\alpha_0\right\} \qquad (2)$$

where

$$k = \frac{40\ \rho_j(b/d)}{\pi M_{\text{eff}}^2 \rho_e \sin\alpha_0} \qquad (3a)$$

$$M_{\text{eff}} = (\rho U)_c/(\rho U)_j \qquad (3b)$$

The parameter M_{eff} is an effective injection ratio and is calculated by the ratio of the density times velocity of the coolant to that of the main flow, integrated over the modeled jet cross-sectional area. After the extent of the jet penetration and spreading is determined, the distribution of the injected coolant in each computational cell at the injection site is calculated. By conserving mass, momentum, and enthalpy of the injected jet, the added fluxes are integrated over each cell surface and the contributions distributed at the cell nodes. In order to account for the effect of three-dimensional entrainment on the temperature profile, Tafti and Yavuzkurt (1990) introduced a source term into the energy equation. The parameters that characterized this source term were Γ and I_{ent}, defined as the "entrainment fraction" and the "entrainment enthalpy," respectively. Entrainment fraction accounts for the entrainment of the boundary layer fluid by the three-dimensional coolant jet. Entrainment enthalpy is the mass-averaged enthalpy of the upstream boundary layer from the wall to the outer edge of the injected jet. The same approach is also used in the present model.

Here, the overall energy conservation is obtained by adding a sink term to the energy equation at the outer edge of the boundary layer to account for the sum of the entrainment source terms. The entrainment fraction correlation reported by Tafti and Yavuzkurt (1987) is found to be ill-suited for the cases where the ratio of the coolant-to-main flow densities is large (about 2) or the external flow is compressible. To obtain the dependence of the entrainment fraction on the flow conditions and the coolant hole geometries, an extensive number of flat plate simulations were performed and matched to their corresponding experiments. The resultant correlation for the value of Γ *is a function of the film hole diameter-to-pitch ratio*, injection angle, and the ratio of the dynamic heads of the coolant flow (based on P_w) to that of the main flow at the edge of the boundary layer.

To capture the mixing of the coolant close to the injection sites better, the computational grid is locally packed in the streamwise direction. A grid-independent solution is obtained by refining the computational grid to the point where further refinement does not alter the solution. A typical result of this grid refinement for a flat plate test case is presented in Fig. 3. In this figure, the predictions using a coarse grid, a fine grid, and a locally packed grid are compared to the film cooled heat transfer data. Spacing of the coarse grid is approximately four times the diameters of the hole (d) and the fine grid corresponds to a spacing of $\frac{1}{2}\ d$ throughout the domain. The locally packed grid has a spacing of $\frac{1}{2}\ d$ locally at the injection site extending to 4 d away from the hole location. Considerable computational efficiency is realized by utilizing the grid packing compared to a fine grid approach while achieving comparable solution accuracies. In the simulations of film cooled transonic airfoils, where surface pressure varies rapidly, grid packing is found to be important to predict the film hole exit pressure, and hence coolant fluxes, accurately.

Steady-State Validation. The experimental study of Camci (1989) performed at VKI on a film cooled linear cascade is chosen as the steady-state test case, where the spanwise averaged heat transfer coefficients on the suction surface of a blade under near engine simulated conditions were measured. The test model represents a typical high-pressure turbine blade with

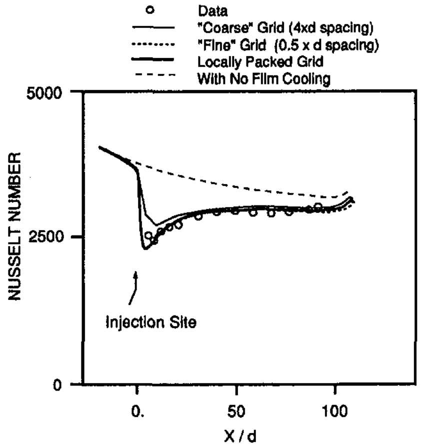

Fig. 3 Comparison between data and the predictions of film cooled heat transfer for three different computational grids (coarse, fine, and locally packed)

about 100 deg of turning and an isentropic exit Mach number of 0.9. Two staggered rows of conical shaped holes angled at 37 and 43 deg to the surface are located at approximately 16 and 18.5 percent of the suction surface wetted surface. The two rows have a pitch-to-diameter ratio of 2.8 and a row spacing-to-hole diameter of 2.6. The test model also had leading edge showerhead holes, which were internally blocked, and tripped the boundary layer very close to the leading edge. The computational grid used in the present study is shown in Fig. 4(*a*). Enlarged details of the local mesh packing at the injection site are shown in Fig. 4(*b*). The grid is a combination of unstructured triangular cells in the inviscid region coupled to an O-grid wrapped around the blade.

The surface Nusselt number distributions with film cooling, nondimensionalized by the no-film cooling values, are plotted in Fig. 5 for three blowing ratios. The comparison between the prediction and the measurements for the suction rows are shown; in Fig. 5(*a*) for the lowest local blowing ratio of 0.37, in Fig. 5(*b*) for the blowing ratio of 0.62, and in Fig. 5(*c*) for the blowing ratio of 0.99. The coolant-to-gas density ratio is 2.0, which is near representative of modern operating conditions. In the near-hole region, the heat flux appears to be overpredicted particularly at the middle blowing ratio. Away from the holes, the predictions closely follow the measurements for all three test cases. The comparisons between the present predictions and the data for the coolant-to-gas density ratio of 1.39 are shown in Fig. 6. Three different test blowing ratios are simulated with the results being shown in Fig. 6(*a*) for a blowing ratio of 0.44, in Fig. 6(*b*) for a blowing ratio of 0.57, and in Fig. 6(*c*) for a blowing ratio of 0.93. Again, the code seems to overpredict the heat flux near the injection site. Away from the hole, the code does a reasonably good job of predicting the influence of film cooling. A possible physical reason for the near-hole overprediction is that the boundary layer fluid entrainment by the coolant jet evolves over a certain length-scale downstream of the holes. In the present model, the sum of three-dimensional boundary layer entrainment by the coolant jet is added at the injection plane. This lumped boundary layer entrainment, represented by Γ, would be expected to raise the predicted local heat transfer near the injection site when compared to data.

Section II: Unsteady Rotor–Stator Interaction

Experimental Technique. These experiments were conducted in a short duration (0.3 s) blowdown turbine test facility at MIT, which simulates full-engine-scale Reynolds number, Mach number, Prandtl number, gas-to-wall and coolant-to-mainstream temperature ratios, specific heat ratios, and flow geometry (Epstein et al., 1986). The corrected speed and weight flow were kept constant to better than 0.5 percent over the test time. The turbulent intensity at the nozzle guide vane inlet was less than 1 percent. For the tests reported herein, a coolant injection system was added to the facility (Abhari, 1991). Coolant-to-main flow mass flux ratio (the blowing ratio) remained constant (± 2 percent) over the test time. An argon/freon gas mixture was used for the coolant in order to match the ratio of specific heats of engine coolant (1.36). Details of the turbine test conditions are reported by Abhari (1991).

Of interest here is the measurement of the time-resolved heat flux distribution about the rotor blade. Heat flux is measured with thin-film heat flux gages (Epstein et al., 1986) distributed about the blade profile. The frequency response of these instruments extends from d.c. to 100 kHz. The gages are individually calibrated and relative gage calibrations are accurate to better than 5 percent. Absolute calibration accuracy is about 10 percent. Uncertainty was evaluated for each transducer and is noted in the subsequent figures. For the data presented herein, the signals from the heat flux gauges were digitized at a 200 kHz sampling rate (33 times blade passing). For the time-resolved data, the digital signal was then ensemble-averaged for 360 vane passing periods.

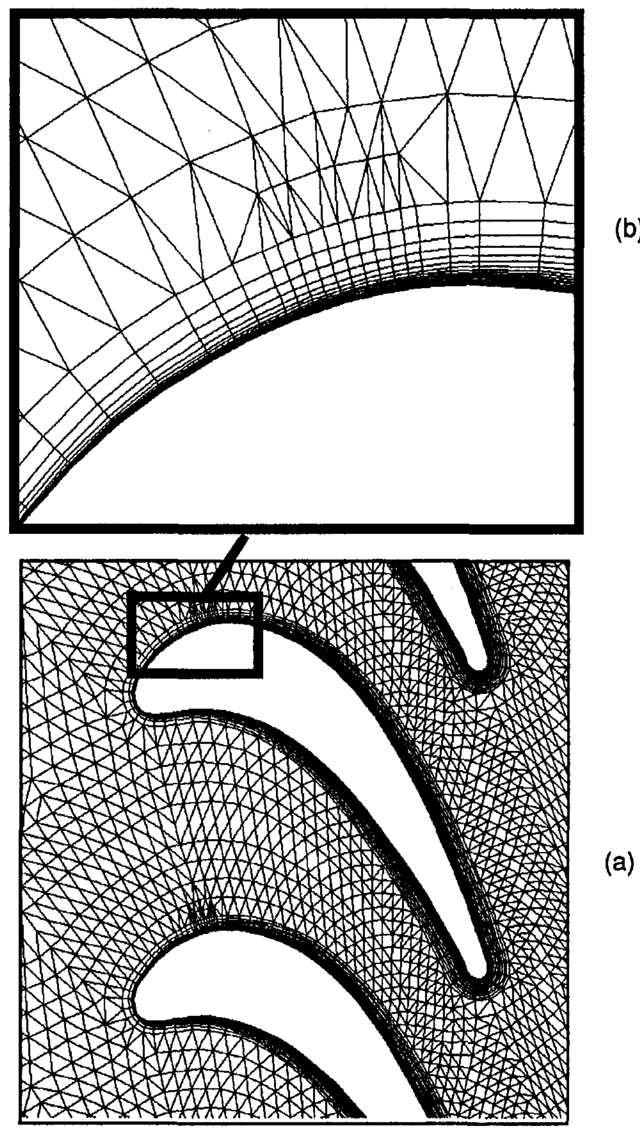

Fig. 4 Computational grid for VKI blade calculations: (*a*) full domain, (*b*) enlarged view of local packing at injection site

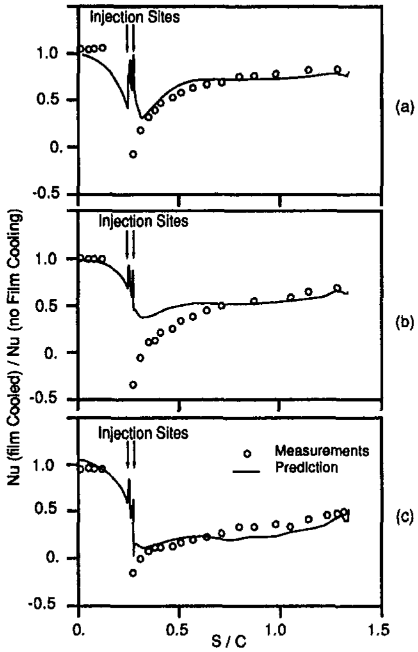

Fig. 5 Comparison of the VKI blade film cooled heat transfer predictions and data (Camci, 1989), coolant-to-gas total density ratio of 2.0, blowing ratios of: (*a*) 0.37, (*b*) 0.62, and (*c*) 0.99

The 0.5-m-diam turbine tested (Fig. 7) was a single-stage, 4:1 pressure ratio transonic machine. This turbine geometry has been extensively studied in cooled and uncooled cascades (Ashworth, 1987), an uncooled stage (Abhari et al., 1992) and fully cooled stage (Abhari and Epstein, 1994). For the present cooled rotor tests, thin walled nozzle guide vanes (NGVs) were used with slot injection near the pressure surface trailing edge sized to pass the flow of a fully cooled NGV. Solid rotor blading was used for the uncooled tests. For the cooled testing, two coolant supply plenums were drilled out of the solid aluminum blades. The coolant hole internal diameters (0.5 mm) were 2

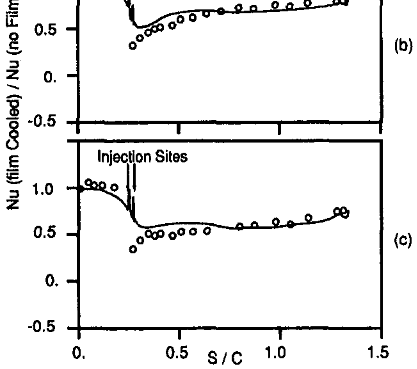

Fig. 6 Comparison of the VKI blade film cooled heat transfer predictions and data (Camci, 1989), coolant-to-gas total density ratio of 1.39, blowing ratios of: (*a*) 0.44, (*b*) 0.57, and (*c*) 0.93

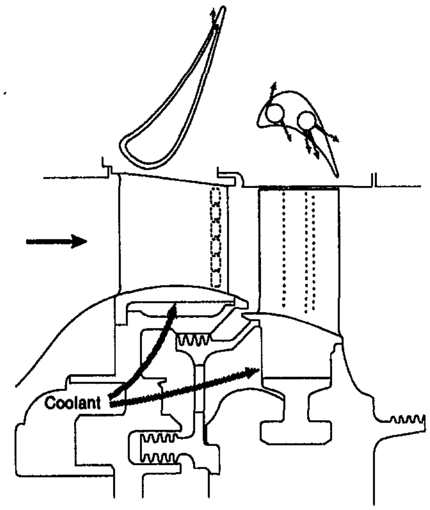

Fig. 7 Turbine geometry and cooling arrangement

percent of axial chord. All rows had circular exit areas except for the suction surface row near the leading edge, which was diffusion shaped. Coolant hole and heat flux gage locations are shown in Fig. 8. The design coolant to main mass flow rates were at 3 percent for the NGV trailing edge slots and 6 percent for the blade. The middle chordwise row will be referred to as midspan, and the bottom as the hub gages. These locations were chosen so as to elucidate the spanwise variation in the flow insofar as possible without intruding into the endwall flow region (Norton, 1987). Unfortunately, several of the gages failed over the course of the testing (especially on the pressure surfaces), so not all measurement locations yielded data at all test conditions. All data taken during each test are reported.

Time-Averaged Results. The computational grid for the present time steady and unsteady numerical simulations is shown in Fig. 9. The inviscid computational grid consists of an H-type structured grid around the vanes and an unstructured mesh composed of an arbitrary mix of quadrilateral and triangular cells around the rotor blades. The viscous grid is an O-type mesh about each blade, with grid packing at the injection region (Fig. 9(*b*)) to capture the enhanced local mixing. Streamwise mesh spacing at the injection sites are less than half the hole diameters. The computational grid (Fig. 9(*a*)) utilizes 18 points across the viscous layer in the O-grid. A total of 14,000 mesh points are used in the computational domain.

In this section, the time-averaged film cooled heat transfer measurements at two spanwise positions and at two different turbine operating conditions are presented. These measurements are compared to the steady state and the time average of unsteady predicted heat flux with and without film cooling. The term uncooled measurements would be used to represent the

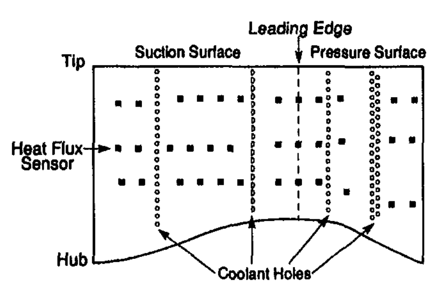

Fig. 8 Composite of heat flux gages and coolant hole positions on the projected blade surface with each of the three chordwise rows of gages on a separate blade

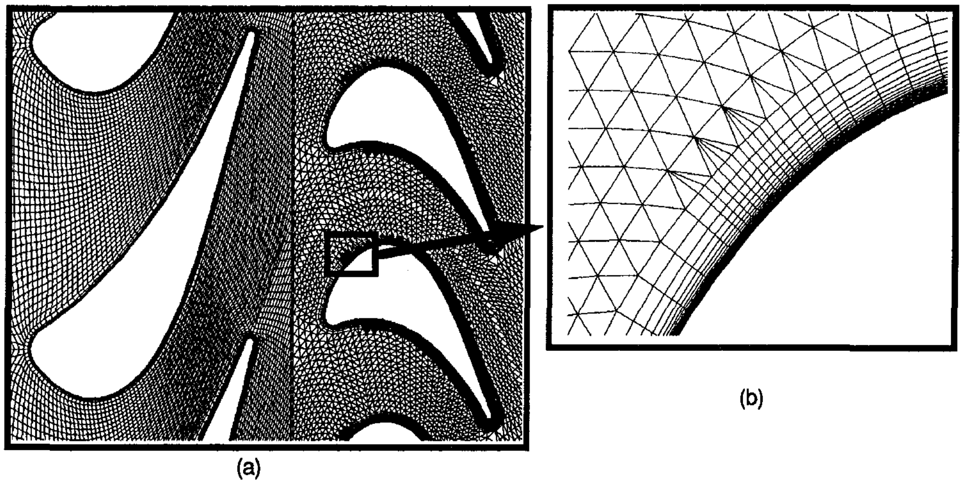

Fig. 9 Computational grid for midspan, used in both the steady and unsteady stator-rotor calculations: (*a*) full domain, (*b*) enlarged view of local packing at an injection site

test data with no rotor film cooling. For all the measurements and the predictions presented here, the NGVs are cooled with coolant injection from the back of the pressure surface. The comparisons are presented for two operating conditions of the turbine stage, corresponding to different turbine reaction and rotor relative flow angles. All the cases correspond to the 120 percent nominal Reynolds number condition.

In Fig. 10(*a*), the measured midspan film cooled Nusselt number distribution is plotted against the surface length for the design condition. In the same figure, the time average of the unsteady prediction with and without film cooling as well as the film cooled steady-state prediction are plotted. These results illustrate that film cooling is a very effective method of lowering the surface heat flux, particularly on the suction surface. The influence of film cooling on the pressure surface heat flux is not as pronounced as on the suction surface where the steady-state prediction is close to the time average of the unsteady calculation. On the pressure surface, however, the time average of the unsteady Nusselt number distribution is as much as 230 percent greater than the steady-state prediction. The comparison of the measurement and the predictions for the hub section is presented in Fig. 10(*b*), which shows the same trends as the midspan.

For the −10 deg incidence test case, the comparison of data and calculations for the hub section is presented in Fig. 11. The two sets of data presented in Fig. 11 correspond to two separate tests, at the same operating condition, taken two months apart to check for the repeatability of the experiment. The same trends as the design condition are observed, with the exception of the front of the pressure surface, where the steady-state film cooled prediction is seen to be very close to the time average of the unsteady uncooled prediction. The surface pressure in the steady-state prediction is in fact very close to (slightly higher than) the plenum pressure and no coolant was discharged. In the unsteady prediction, the surface fluctuation resulted in intermittent coolant injection. Therefore, unlike all other conditions, in this case the predicted steady-state film cooled heat transfer was higher than the average of the unsteady film cooled heat flux on the hub pressure surface between the first and second rows.

In the original design of the experiment, steady-state CFD codes were used to predict the surface pressure distribution without simulating the influence of the coolant injection, estimating that the plenum pressure will be always higher than the

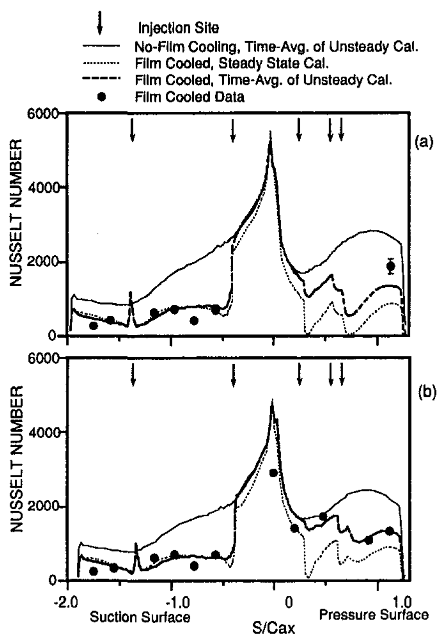

Fig. 10 Comparison of measured heat transfer data against the film cooled steady-state prediction, and the time average of unsteady prediction with and without film cooling at design test condition: (*a*) midspan, (*b*) hub section

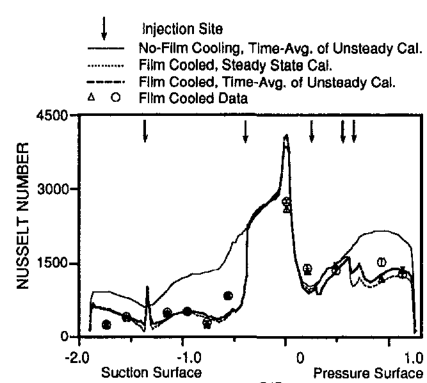

Fig. 11 Comparison of measured heat transfer data (two tests illustrating level of repeatability) against the film cooled steady-state prediction, and the time average of unsteady prediction with and without film cooling at −10 deg incidence condition at hub section

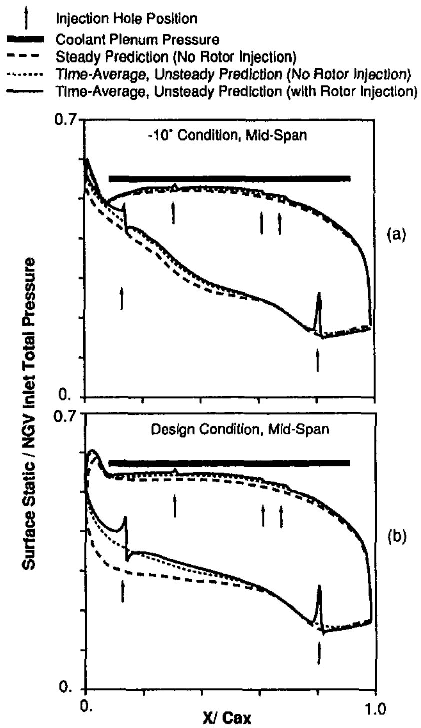

Fig. 12 Midspan comparison of surface pressure distribution between the predictions of steady-state flow without film cooling, the time average of unsteady flow without film cooling, and the time average of the unsteady flow with film cooling: (*a*) −10 deg incidence, and (*b*) design test cases

surface pressure even on the hub section. For the design test condition, the calculated midspan surface pressure distribution around the airfoil for the steady state, time average of unsteady with no film cooling, and the time average of the unsteady pressure with film cooling are plotted in Fig. 12(*b*). The same comparison for the midspan of the −10 deg incidence test condition is also presented in Fig. 12(*a*). It is observed that the time average of the unsteady surface pressure with no film cooling is always higher than the steady-state value. The unsteady interaction of the turbine rotor blade with the NGV wake and NGV injected coolant flow results in a higher interblade row pressure than in the steady state case. When comparing the time average with and without film cooling, it is observed that the surface pressure is locally altered by the addition of the coolant. The addition of the coolant results in the deceleration of the flow upstream of the injected site followed by a rapid acceleration after the hole position. At the back of the suction surface, the solution shows the formation of a weak shock at the hole site. On the suction surface, the impact of the coolant injection on the static pressure seems to be very sensitive to the local isentropic Mach number. For the design test condition, it is observed that the injection on the front of the suction surface resulted in the unloading of the airfoil with the subsequent increase of the surface static pressure many hole diameters upstream of the injection. Without accounting for the interaction of the film and the main flow, the prediction of the coolant mass flow from the holes in high Mach number regions using uncooled surface pressure prediction could overestimate the injected mass flux.

Time-Resolved Comparisons. In recent studies, it has been recognized that the rotor blade heat transfer is highly unsteady (Abhari et al., 1992). To understand the form of this unsteadiness and validate the predictive capabilities of the present numerical code, time-resolved predictions of film cooled heat transfer around the airfoil are compared to the measurements. The comparison of data and prediction for the −10 deg incidence at the hub section is shown in Fig. 13. It is observed that the heat flux with film cooling is unsteady and the numerical code predicts the general shape and the relative phase of the surface heat flux. The same comparison for the midspan suction surface at design condition is shown in Fig. 14. In this figure, the measured surface heat flux with no film cooling (when available) is also plotted for comparison. It is observed that the film cooling has reduced the mean level of heat flux when compared to the no-film cooling case and introduced a phase shift in the unsteady waveform. This characteristic is most pronounced at the crown of the suction surface (shown in Fig. 14(*a*)) where the present calculation seems to have well predicted both the phase shift and the reduction in the amplitude of the heat transfer due to film cooling. From this accurate prediction of the amplitude and phase of the surface heat transfer, it is concluded that for this test case, the details of the mixing of the coolant and the main flow at the injection plane can be considered quasi-steady. This quasi-steady nature suggests that the characteristic time scale of the locally three-dimensional mixing of the coolant with the boundary layer, represented by the entrainment fraction, is much smaller than the vane passing time-scale.

Influence of Unsteadiness. The widespread use of steady-state cascade measurements to develop film cooling correlations has generated a considerable database for cooling design of turbine blades. The reduction in the surface heat flux achieved by the film cooling at engine conditions has generally been estimated by utilizing these correlations as well as numerical simulations. Abhari and Epstein (1994) have shown that the flow unsteadiness generated by the relative motion of rotor and stator blades results in the unsteady coolant blowing from the film holes, which could impact the time-averaged heat load. In this section, the impact of this flow unsteadiness on the mass flow rate and the effectiveness of the cooling for the present turbine blade is quantified.

Effectiveness and Augmentation. The conventional method of accounting for the reduction in the heat flux due to film cooling is to take advantage of the linearity of the energy equation for a constant property fluid on an isothermal wall. The ratio of the heat load with and without the film cooling can then be written as

$$\frac{\mathrm{Nu}_{fc}}{\mathrm{Nu}_0} = \epsilon(1 - \theta\eta_{ad}) \tag{4}$$

where

$$\epsilon = \frac{h_{fc}}{h_0} \tag{5a}$$

$$\eta_{ad} = \left(\frac{T_r - T_{ad}}{T_r - T_c}\right) \tag{5b}$$

Prediction of the adiabatic film effectiveness (η_{ad}) and the heat transfer augmentation factor (ϵ) requires the knowledge of the adiabatic recovery temperature without film cooling (T_r), the film cooled adiabatic surface temperature (T_{ad}), the heat flux without film cooling (Nu_0), and heat flux with film cooling (Nu_{fc}). To calculate these parameters, four separate numerical simulations are performed. To calculate the distribution of T_r around the airfoil, the blade wall boundary condition is specified to be adiabatic with no film cooling in the first simulation. The distribution of T_{ad} around the airfoil is calculated by specifying an adiabatic blade wall boundary condition with film cooling in the second simulation. The distribution of Nu_0 is predicted by specifying an isothermal wall temperature of T_w without film cooling in the third simulation. The distribution of Nu_{fc} is predicted by specifying the same isothermal wall temperature (T_w), with film cooling in the fourth simulation. In all these

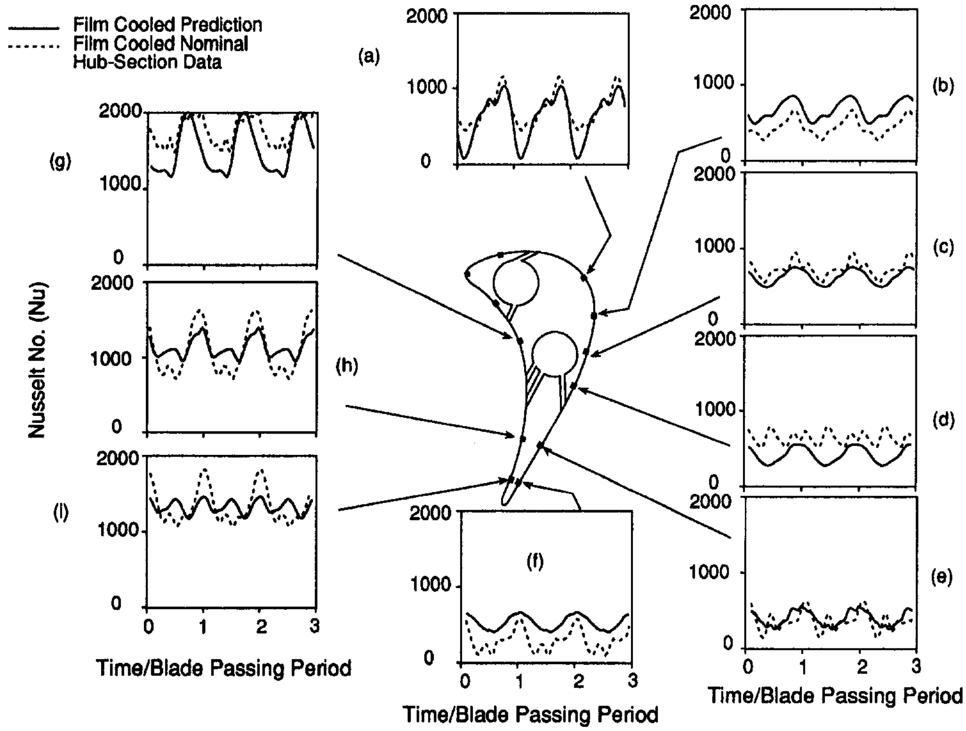

Fig. 13 Time-resolved film cooled rotor blade heat transfer measurements on the hub section at the −10 deg incidence condition compared to the film cooled predictions

four simulations, the NGVs are specified to be isothermal with pressure side coolant injection to correctly simulate the rotor relative incoming flow conditions. In this manner, any change in the adiabatic film effectiveness as result of variation in the blade recovery temperature due to interaction with the incoming cold shear layer is removed.

The code was used in a "steady-state" rotor–stator mode. In this type of simulation, the flow about each blade row is calculated in steady state and the mean fluxes at the interface of the NGVs and the rotor blades are balanced. At each spanwise section, these four simulations are first performed under steady-state conditions. The steady-state adiabatic film effectiveness and augmentation factor distributions are then calculated. The same four simulations are performed under unsteady conditions with rotor–stator interaction. By using the time average of the unsteady surface temperatures and heat fluxes, the time-averaged adiabatic film effectiveness and augmentation factors are calculated.

The time average of unsteady and the steady-state adiabatic film effectiveness for the midspan at the design test condition are compared in Fig. 15(a). This comparison shows that on the pressure surface, the steady-state effectiveness is as much as 64 percent higher than the time-averaged prediction. On the suction surface, the steady-state effectiveness is as much as 11 percent lower near the front row and 10 percent higher near the back row than the time average of the unsteady prediction. The same comparison for the augmentation factor at the design condition is shown in Fig. 15(b). The steady-state augmen-

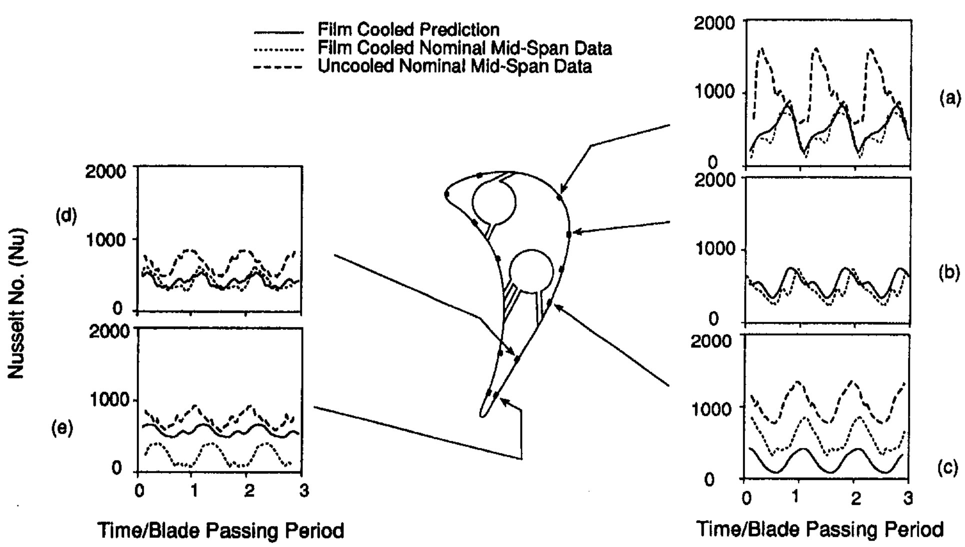

Fig. 14 Time-resolved film cooled rotor blade suction surface heat transfer measurements on the midspan at design condition compared to the uncooled data and the film cooled predictions

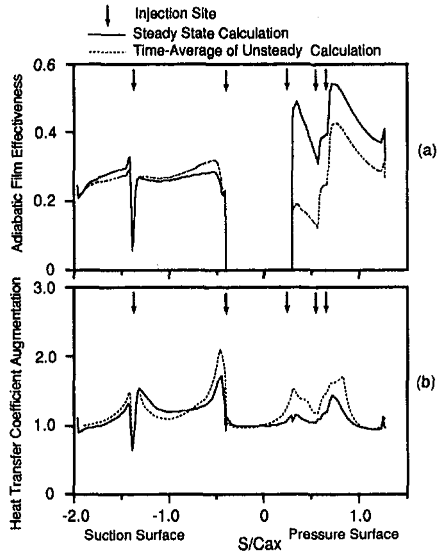

Fig. 15 Comparison between the steady-state prediction and the time average of unsteady: (*a*) adiabatic film effectiveness, (*b*) heat transfer augmentation, midspan at design condition

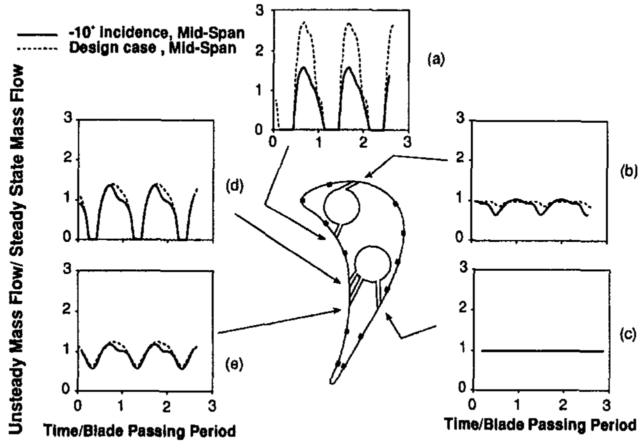

Fig. 17 Predicted levels of coolant pulsation from the coolant holes, nondimensionalized by the mean value at midspan for the design and −10 deg incidence test conditions

tation is seen to be generally higher than the time-averaged prediction by as much as 23 percent at the injection site with the two predictions converging together rapidly downstream of the injection site. At the back of the suction surface injection site, where the main flow is supersonic, narrow spikes in the values of both η_{ad} and ϵ are predicted. These spikes are due to the influence of weak local compression and expansion waves, which appear due to the blockage of the injected fluid in the supersonic flow.

The steady state and the time average of unsteady predictions of the η_{ad} and ϵ at the −10 deg incidence test condition are respectively presented in Figs. 16(*a*) and 16(*b*). It is seen that with the exception of the pressure surface film effectiveness, the influence of unsteadiness is less than 10 percent of the steady-state value. Similar to the previous test condition, the predicted pressure surface steady-state adiabatic film effectiveness is as much as 104 percent greater than the time average of the unsteady value. In subsequent predictions at many different test conditions, the same trend of lower pressure surface film effectiveness was observed. This sizable reduction in the pressure surface film effectiveness could be caused by a reduction of the mean coolant flux in the unsteady prediction or the enhanced mixing out of the coolant fluid with the unsteady main flow.

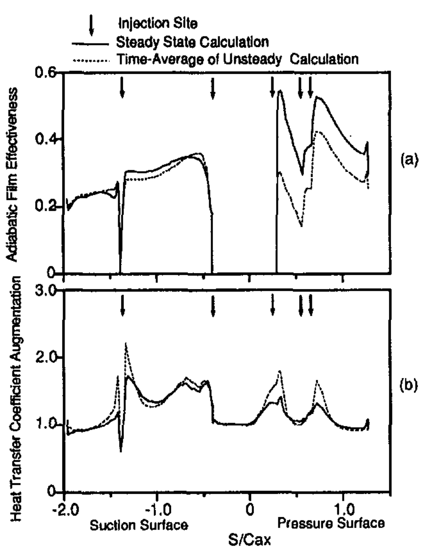

Fig. 16 Comparison between the steady-state prediction and the time average of unsteady: (*a*) adiabatic film effectiveness, (*b*) heat transfer coefficient augmentation, at midspan for −10 deg incidence test condition

Coolant Mass Pulsation. The large pressure fluctuations around the airfoil results in a pulsating injection of the coolant fluid from the holes. In Fig. 17, the calculated time-resolved mass flux nondimensionalized by the steady-state mass flow for the five film cooling rows at the design and −10 deg test conditions are plotted versus time. The row on the front of the pressure surface (Fig. 17(*a*)) exhibits the largest fluctuations of mass flow, with peaks at 2.7 times (at design condition) the steady level and troughs with no flow lasting around 30 percent of the period. The design condition seem to exhibit a greater level of unsteadiness on the pressure surface than the −10 deg test condition. The waveforms of the pulsating mass flow from the film holes at the back of the pressure surface (Figs. 17(*b*) and 17(*c*)) exhibit undulation of the order of the steady-state mass flux. Under steady-state conditions, the front suction row (Fig. 17(*d*)) is choked for the design condition and at 88 percent of choked value for the −10 deg condition. In the unsteady predictions, this row of holes unchokes with the greatest deviation from the steady value of 36 percent seen at the design test condition. The row at the back of the suction surface is choked in the steady-state simulations and remained so throughout all test conditions. The steady-state mass flow from the front pressure side row (Fig. 17(*a*)) is 17 percent higher at the design condition and is 43 percent lower than at −10 deg condition when compared to the time average of the unsteady prediction.

Within a design process, it is important to determine when the flow unsteadiness alters the mean coolant flux from the film holes. A proposed measure of the significance of unsteadiness on the pulsating coolant flux is the parameter ψ, defined by the ratio of the amplitude of the first harmonic of the pressure divided by the difference between the coolant plenum and the surface static pressure.

$$\psi = \frac{|P_{1(S)}|}{P_{tc} - \bar{P}_{(S)}} \tag{6}$$

ψ corresponds to the change in the surface static pressure relative to the pressure head available to push the coolant through the holes, and $\bar{P}_{(S)}$ is the time average of the unsteady surface static pressure. It also directly corresponds to the level of the coolant fluctuation in the absence of choking. For the cases where the value of ψ is much less than unity, the amplitude of

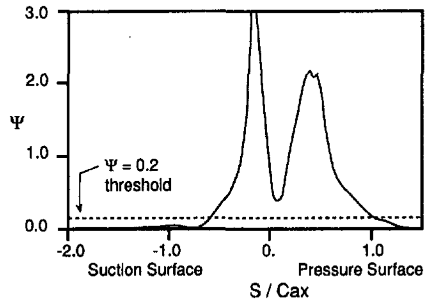

Fig. 18 Calculated distribution of the pressure parameter Ψ (Eq. (6)) around the airfoil midspan, −10 deg incidence condition

the pulsating mass flow is much less than the mean magnitude. To calculate ψ, the predicted static pressure fluctuation around the airfoil is Fourier analyzed and the amplitude of the fundamental periodic frequency around the airfoil is calculated. For the -10 deg test conditions, ψ is calculated and plotted in Fig. 18. From a practical point of view, for conditions under which the value of ψ is less than some level, say 0.2, the influence of pulsation on the time-averaged coolant flux may be neglected. On the suction surface, ψ drops below 0.2 after the first 30 percent of the wetted surface. On the pressure surface, however, ψ remains above 0.2 over 85 percent of the surface length, suggesting that the unsteady pulsation is important for almost any coolant hole placement. In another area of particular interest to the designers, the leading edge showerhead region would also experience significant pulsation of the coolant flow.

To minimize the magnitude of pulsation, the value of ψ could be reduced by raising the coolant discharge pressure. For the present turbine at the design operating condition, the coolant supply pressure would have to be 30 percent greater than the relative total pressure to keep ψ below 0.2 over most of the surface. For the turbine reported by Dunn et al. (1990), if film cooled, the coolant plenum pressure needs to be approximately 40 percent higher than the relative total pressure by the same guideline. This high coolant supply pressure is generally not attainable for propulsion applications. Even if this high coolant pressure becomes available, it would result in very high values of blowing ratio elsewhere on the blade.

A matter of interest is to determine if the change in the time average of film effectiveness is due to the reduction in the time-averaged coolant flux or due to the nonlinear (in time) of unsteady mixing. To address this question, the input coolant plenum pressure in the steady-state prediction was changed in such a manner to match the time-averaged mass flux from the unsteady simulation. The adiabatic film effectiveness from this "matched" simulation for the -10 deg incidence test condition is presented in Fig. 19. This adjustment of the mean coolant flux accounts for 55 percent of the difference between the steady state and the time average of the unsteady adiabatic film effectiveness, as shown in Fig. 15(a). It is concluded that both adjustment of the mean coolant flux and unsteady mixing of the coolant flow should be accounted for in the prediction of film cooling performance.

Summary and Conclusions. An existing two-dimensional unsteady, multiblade row, coupled Euler/Navier–Stokes CFD code is enhanced by the addition of coolant injection. The injection is added into the computational domain through a penetration, spreading and entrainment model. A new correlation of the boundary layer fluid entrainment by the injected coolant is developed and implemented into the code. The computational grid consists of an unstructured grid in the inviscid region and an O-grid in the viscous region. To capture the coolant mixing without the use of large mesh sizes, local packing of the grid at the injected regions is used. Comparisons of data and predictions from the present code for a blade in a linear cascade are presented. This test case provides data for representative airfoil geometry and cooling configurations at simulated flow conditions. The greatest deviation between the calculations and the measurements occurs at the injection region. The results show that the present code does a reasonably good job of predicting the influence of film cooling on the surface heat flux, except in the regions immediately downstream of the injection rows. This study provides the validation of the present CFD code with injection under steady-state conditions.

Time-resolved heat transfer measurements and calculations for a fully cooled turbine blade have been compared at two operating points. The numerical prediction accurately predicts the amplitude and the phase of the surface heat flux in the presence of surface film cooling in both cases. It is concluded that for the present turbine blade conditions, the mixing of the coolant and the main flow at the injection plane can be considered quasi-steady. This quasi-steady nature is exhibited only at the injection planes, and the rest of the flow around the rotor blade is fully unsteady. It is concluded that the present computational approach is applicable for time-accurate prediction of flow in a film cooled turbine blade.

In this particular turbine, stator coolant injection changes the time-averaged pressure distribution around the downstream blades. This change is exhibited as an unloading of the blade suction surface. Injection of film cooling on the blade surface also affects the mean surface pressure distribution. These changes on the surface pressure distribution could have a substantial effect on the film cooling design, particularly on the pressure surface where the back-flow margin (difference between internal to surface static pressure) is small. The code is then used in both time-resolved and steady-state modes to calculate the flow at two different turbine operating conditions. The time average of the unsteady calculations is shown to predict the time-averaged surface heat transfer measurements of a rotating film cooled turbine blade accurately. Comparing the steady state against the time average of the unsteady calculations, it is observed that on the suction surface, the two results are similar. On the pressure surface, however, the time average of the unsteady surface heat flux is as much as 230 percent greater than the steady-state prediction. By performing a series of numerical simulations, it is determined that a large reduction in the adiabatic film effectiveness (by as much as 64 percent) is the primary cause of the enhanced pressure surface heat transfer with

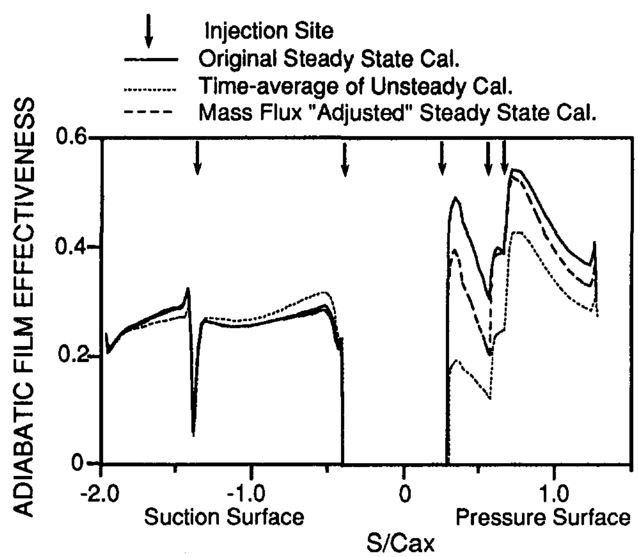

Fig. 19 Comparison of the predicted adiabatic film effectiveness at the steady state, the time average of unsteady, and the "adjusted" steady-state conditions. Adjusted condition corresponds to the case in which the individual mass flow rates from each hole have been changed to match the time average of the unsteady values.

flow unsteadiness. The reduction in the adiabatic film effectiveness is shown to be attributed to both the change in the time-averaged mass flux out of the film holes as well as the interaction of the coolant with the unsteady external flow.

The large-scale fluctuations of the instantaneous static pressure around the rotor airfoil are shown to result in considerable pulsation of the coolant from the film holes. In certain circumstances, choking and unchoking of the film holes is observed. This pulsation affects the time average of the mass, momentum, and enthalpy fluxes from the coolant holes. Depending on the details of the film hole design (including hole placement) and the turbine operating condition, the unsteady pressure fluctuations could decrease or increase the time-averaged coolant fluxes from the holes. The greatest impact of unsteady rotor–stator interaction on the film cooling of turbine blades would occur on the front portion of the suction surface, the leading edge (showerhead area), and the entire pressure surface. A measure of the significance of unsteadiness on the pulsating coolant fluxes (ψ) was proposed. This parameter allows the designers to minimize (or utilize) the impact of flow unsteadiness on their film cooling designs. The main conclusion of the present study is that unsteady rotor–stator interaction significantly influences the film cooling performance. The impact of flow unsteadiness on the pressure surface adiabatic film effectiveness is shown to be substantial, reducing the mean level by as much as 64 percent.

Acknowledgments

The modeling part of the work was sponsored by Textron Lycoming, whose permission to publish this work is acknowledged. The stimulating comments of Dr. M. Giles and Dr. K. Poon are also greatly appreciated. The experimental part of this work was performed at the Gas Turbine Lab. at MIT, and was supported by the Wright Laboratories, USAF, Dr. C. MacArthur, program monitor, and Rolls-Royce Inc., Dr. R. J. G. Norton, technical monitor. The generous assistance of Drs. A. Epstein, G. R. Guenette, and R. J. G. Norton in the experimental portion of this work is greatly appreciated.

References

Abhari, R. S., 1991, "An Experimental Study of the Unsteady Heat Transfer Process in a Film Cooled Fully Scaled Transonic Turbine Stage," Ph.D. Dissertation, Massachusetts Institute of Technology, Cambridge, MA.

Abhari, R. S., Guenette, G. R., Epstein, A. H., and Giles, M. B., 1992, "Comparison of Time-Resolved Turbine Rotor Blade Heat Transfer Measurements and Numerical Calculations," ASME JOURNAL OF TURBOMACHINERY, Vol. 114, pp. 818–827.

Abhari, R. S., 1993, internal communication, Textron Lycoming.

Abhari, R. S., and Epstein, A. H., 1994, "An Experimental Study of Film Cooling in a Rotating Transonic Turbine," ASME JOURNAL OF TURBOMACHINERY, Vol. 116, pp. 63–70.

Abramovich, G. M., 1960, *The Theory of Turbulent Jets,* MIT Press.

Ashworth, D. A., 1987, "Unsteady Aerodynamics and Heat Transfer Processes in a Transonic Turbine Stage," D. Phil. Thesis, Oxford University, United Kingdom.

Baldwin, B. S., and Lomax, H., 1978, "Thin Layer Approximation and Algebraic Model for Separated Turbulent Flows," AIAA Paper No. 78-257.

Camci, C., 1989, "An Experimental and Numerical Investigation of Near Cooling Hole Heat Fluxes on a Film Cooled Turbine Blade," ASME JOURNAL OF TURBOMACHINERY, Vol. 111, pp. 63–70.

Crawford, M. E., Kays, W. M., and Moffat, R. J., 1980, "Full-Coverage Film Cooling, Part II: Heat Transfer Data and Numerical Simulation," ASME *Journal of Engineering for Power,* Vol. 102, pp. 1006–1012.

Dietz, A. J., and Ainsworth, R. W., 1992, "Unsteady Measurements on the Rotor of a Model Turbine Stage in a Transient Flow Facility," ASME Paper No. 92-GT-156.

Dring, R. P., Blair, M. F., and Joslyn, H. D., 1980, "An Experimental Investigation of Film Cooling on a Turbine Rotor Blade," ASME *Journal of Engineering for Power,* Vol. 102, pp. 81–87.

Dunn, M. G., 1990, "Phase and Time-Resolved Measurements of Unsteady Heat Transfer and Pressure in a Full-Stage Rotating Turbine," ASME JOURNAL OF TURBOMACHINERY, Vol. 112, pp. 531–538.

Dunn, M. G., Bennett, W., Delaney, R., and Rao, K., 1990, "Investigation of Unsteady Flow Through a Transonic Turbine Stage: Part II—Data/Prediction Comparison for Time-Averaged and Phase Resolved Pressure Data," AIAA Paper No. 90-2409.

Epstein, A. H., Guenette, G. R., Norton, R. J. G., and Yuzhang, C., 1986, "High Frequency Response Heat Flux Gauge," *Review of Scientific Instruments,* Vol. 75, No. 4, pp. 639–649.

Giles, M. B., 1988, "UNSFLO: A Numerical Method for Unsteady Inviscid Flow in Turbomachinery," MIT Gas Turbine Laboratory Report No. 195.

Giles, M. B., and Haimes, R., 1993, "Validation of a Numerical Method for Unsteady Flow Calculations," ASME JOURNAL OF TURBOMACHINERY, Vol. 115, pp. 110–117.

Guenette, G. R., Epstein, A. H., Giles, M. B., Haimes, R., and Norton, R. J. G., 1989, "Fully Scaled Transonic Turbine Rotor Heat Transfer Measurements," ASME JOURNAL OF TURBOMACHINERY, Vol. 111, pp. 1–7.

Haas, W., Rodi, W., and Schönung, B., 1992, "The Influence of Density Difference Between Hot and Cold Gas on Film Cooling by a Row of Holes: Predictions and Experiments," ASME JOURNAL OF TURBOMACHINERY, Vol. 114, pp. 747–755.

Leylek, J. H., and Zerkle, R. D., 1994, "Discrete-Jet Film Cooling: A Comparison of Computational Results With Experiments," ASME JOURNAL OF TURBOMACHINERY, Vol. 116, pp. 358–368.

Mehendale, A. B., Han, J.-C., Ou, S., and Lee, C. P., 1994, "Unsteady Wake Over a Linear Turbine Blade Cascade With Air and CO_2 Film Injection: Part II—Effect on Film Effectiveness and Heat Transfer Distributions," ASME JOURNAL OF TURBOMACHINERY, Vol. 116, pp. 730–737.

Ni, R.-H., 1981, "A Multiple Grid Scheme for Solving the Euler Equations," *AIAA Journal,* Vol. 20, No. 11, pp. 1565–1571.

Norton, R. J. G., 1987, private communications, Rolls Royce Inc.

Norton, R. J. G., Forest, A. E., White, A. J., Epstein, A. H., Schultz, D. L., and Oldfield, M. L. G., 1990, "Turbine Cooling Design, Vol. 1," Wright Patterson Airforce Report, WRDC-TR-89-2109.

Rigby, M. J., Johnson, A. B., and Oldfield, M. L. G., 1990, "Gas Turbine Rotor Blade Film Cooling With and Without Simulated NGV Shock Waves and Wakes," ASME Paper No. 90-GT-78.

Schönung, B., and Rodi, W., 1987, "Prediction of Film Cooling by a Row of Holes With a Two-Dimensional Boundary Layer Procedure," ASME JOURNAL OF TURBOMACHINERY, Vol. 109, pp. 579–587.

Tafti, D. K., and Yavuzkurt, S., 1987, "Two-Dimensional Turbulence Modeling for Flat Plate and Turbine Airfoil With Discrete Film Cooling," RFQ:YC 69359, Final Report submitted to Textron Lycoming.

Tafti, D. K., and Yavuzkurt, S., 1990, "Prediction of Heat Transfer Characteristics for Discrete Hole Film Cooling for Turbine Blade Applications," ASME JOURNAL OF TURBOMACHINERY, Vol. 112, pp. 504–511.

Takeishi, K., Aoki, S., Sato, T., Tsukagoshi, K., 1992, "Film Cooling on a Gas Turbine Rotor Blade," ASME JOURNAL OF TURBOMACHINERY, Vol. 114, pp. 828–834.

Tran, L. T., and Taulbee, D. B., 1992, "Prediction of Unsteady Rotor-Stator Pressure and Heat Transfer From Wake Passing," ASME JOURNAL OF TURBOMACHINERY, Vol. 114, pp. 807–817.

Compressor Blade Forced Response Due to Downstream Vane-Strut Potential Interaction

H.-W. D. Chiang

M. G. Turner

GE Aircraft Engines,
Cincinnati, OH 45215

A blade forced response prediction system has been developed using an implicit two-dimensional CFD solver to model the rotor blade forced response due to the static pressure distortion (potential disturbance) from the downstream stator vanes and struts. The CFD solver predicts the static pressure distortion upstream of the stator vanes and struts, which is used to calculate the induced velocity perturbation at the rotor inlet. Using the velocity perturbation and the blade's natural frequencies and mode shapes from a finite element model, the unsteady aerodynamic modal forces and the aerodynamic damping are calculated. A modal response solution is then performed. The results show that the stator vanes cause a significant amplification of the potential disturbances due to the struts. Effects of strut and vane modifications are examined using the analysis. A vane modification with an ''optimized'' flow angle distribution shows that the disturbance can be greatly reduced. Recent testing of the strut modification shows exceptional correlation with the prediction.

Introduction

Turbomachinery blades are susceptible to nonuniform flows generated by inlet distortion, wakes, and pressure disturbances from adjacent blade rows. Large unsteady aerodynamic loads can be experienced by the blades when they pass through these flow nonuniformities or flow defects. When the frequency of these unsteady aerodynamic loads matches the blade natural frequency, blade failures can result.

The three primary types of flow defect that cause forced response problems in turbomachinery blading are: inlet distortion, wake disturbances, and potential disturbances. This paper describes an investigation of compressor blade response due to potential disturbances from downstream stator vanes and frame struts. Figure 1 is a schematic of the blades along with the downstream stator vanes and struts. Based on the axial distance between the rotor and the struts, the potential disturbance from the strut reaching the rotor was expected to be minimal. However, experience has surprisingly shown that there can be a significant blade response. A forced response prediction system was developed to analyze the blade response. The analysis shows that the stator vanes between the rotor and the strut cause a significant amplification of the potential disturbance from the struts.

The blade forced response prediction system was extended from a previously developed system (Chiang and Kielb, 1993), which consists of three parts: (1) flow defect modeling, (2) unsteady aerodynamics for gust response and aerodynamic damping, and (3) aeroelastic modal solution for blade response. The flow chart for the system is shown in Fig. 2.

Static pressure distortions can be reasonably modeled using inviscid CFD methods or they can be measured in a test. Unlike inlet distortions and wake disturbances, which always come from upstream, potential disturbances can propagate either upstream or downstream. Potential disturbances have been modeled either with classical small disturbance theory (Kemp and Sears, 1953; Osborne, 1973; Taylor and Ng, 1987; Korakianitis, 1988) or with CFD methods using potential, Euler, and Navier–Stokes solutions (O'Brien et al., 1985). In this paper, potential disturbances from downstream stator vanes and struts were modeled using an implicit two-dimensional CFD solver, which incorporates a finite volume form of the continuity equation, and an integral form of the cross-stream momentum equation. It was formulated to ensure an accurate spatial representation of entropy and stagnation enthalpy.

The predicted static pressure distortion upstream of the stator vanes and struts at the rotor exit plane was assumed to be at the rotor inlet to calculate the induced velocity perturbation. Using the velocity perturbation, and the blade's natural frequencies and mode shapes from a finite element model, the unsteady aerodynamic modal forces and the aerodynamic damping are calculated. The unsteady aerodynamic models for gust response and aerodynamic damping are based on Kirsch's (1990) classical two-dimensional kernel function approach for subsonic flows. This method is similar to that of Whitehead (1970) and uses the ''frozen gust'' assumption.

A modal aeroelastic model was utilized to simulate the three-dimensional aeroelastic effects by calculating the unsteady aerodynamic loads on two-dimensional strips, which are stacked along the span of the blade from hub to tip. This model assumes a ''tuned'' rotor such that all the blades in the rotor have identical frequencies and mode shapes (i.e., no mistuning effects are included). The system predicts the blade modal response and the vibratory blade stress for comparison with measured data.

This paper provides a basic description of the system, which includes: (1) CFD model for the pressure disturbance, (2) a kernel function solution technique for unsteady aerodynamics, and (3) a modal aeroelastic solution using strip theory. This analysis technique was then used to study the effects of strut and vane variations, which resulted in a vane modification that greatly reduced the potential disturbance.

Forced Response Modeling

The forced response prediction system was based on an earlier system developed by Chiang and Kielb (1993), which can model blade forced response due to inlet distortion and wake/shock excitation from upstream. In this paper, this system was extended to incorporate a CFD solver to model the static pressure distortion from downstream.

The system starts with the well-known dynamic equations of motion, which can be expressed as a system of equations for the n degrees of freedom of the system:

Contributed by the International Gas Turbine Institute and presented at the 38th International Gas Turbine and Aeroengine Congress and Exposition, Cincinnati, Ohio, May 24–27, 1993. Manuscript received at ASME Headquarters March 10, 1993. Paper No. 93-GT-287. Associate Technical Editor: H. Lukas.

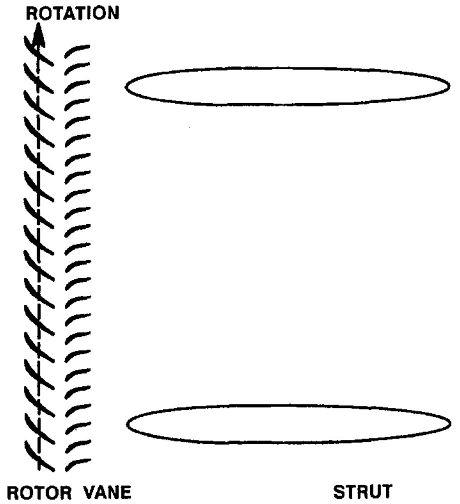

Fig. 1 Schematic of rotor with vanes and struts

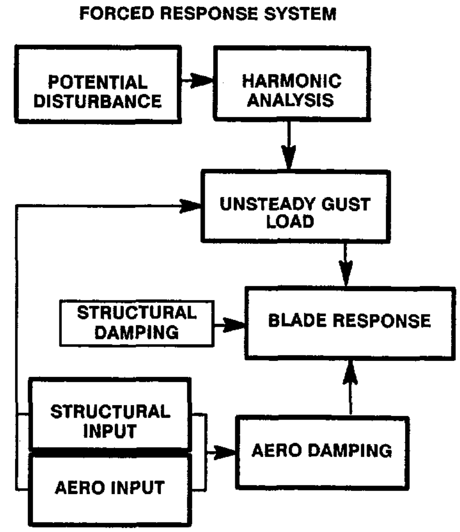

Fig. 2 Forced response system flow chart

$$[M]\{\ddot{X}\} + [G]\{\dot{X}\} + [K]\{X\} = \{F_m(t)\} + \{F_g(t)\}. \quad (1)$$

The $[M]$, $[G]$, and $[K]$ matrices represent the mass, damping, and stiffness properties of the blade with $\{X\}$ being the n degree-of-freedom displacements. The forcing terms on the right-hand side of Eq. (1) represent the motion-dependent unsteady aerodynamic forces $\{F_m(t)\}$ and the gust response unsteady aerodynamic forces $\{F_g(t)\}$.

As shown by Chiang and Kielb (1993), Eq. (1) can be converted into a modal coordinate system using the modal displacement $\{\bar{Q}\}$ defined by

$$\{X(t)\} = [\phi]\{\bar{Q}\}e^{i\omega t}, \quad (2)$$

where $[\phi]$ and ω are, respectively, the mode shape and frequency. The resulting modal equation of motion becomes

$$-\omega^2[M_m]\{\bar{Q}\} + i\omega[G_m]\{\bar{Q}\} + [K_m]\{\bar{Q}\} = [\phi]^T([A]\{\bar{Q}\} + \{\bar{F}_g\}), \quad (3)$$

where $[A]$ can be obtained using the unsteady aerodynamic program with input of mode shapes and frequencies provided by a finite element vibratory analysis. The gust response $\{\bar{F}_g\}$ is calculated using the same unsteady aerodynamic program with input from a flow defect model.

Flow Defect Model

To predict dynamic stress levels, flow fields must be identified and analyzed to formulate proper definition of relevant flow defects. In this paper, the potential disturbance due to downstream stator vanes and struts is considered, and is modeled using an implicit two-dimensional CFD solver. The CFD solver had been developed to solve the quasi-three-dimensional (two-dimensional with area variations in the third dimension) flow field in an aircraft engine fan frame including the OGVs, and is described in detail by Turner and Keith (1985). The geometry of the OGV fan-frame configuration is very similar to the vane-strut problem analyzed in this paper. However, in the fan-frame problem, variations in total pressure, total temperature, and angle are determined from a rotor characteristic and the circumferential variations in static pressure at the fan trailing edge plane. The flow solver can therefore solve rotational flow fields, although the analysis shown in this paper is for potential flow fields.

The solver is essentially a fixed grid analog of the streamline curvature method. The streamline curvature is made up of the grid curvature and one of the derivatives of velocity. This derivative of velocity is actually an unknown in the equation system along with the two velocity components.

The equation system includes a finite volume form of the continuity equation, an integral form of the cross-stream momentum equation, a spline-like equation that relates a velocity component with its derivative, and the boundary conditions. The streamwise momentum equation and energy equation are solved by convecting total pressure and total temperature along streamlines. This equation system is then solved implicitly using Newton's method, which provides fast convergence and allows for many options in boundary condition treatment.

To analyze a flow field with many airfoils and passages in a timely manner, the solver needs to predict the flow details accu-

Nomenclature

AF = amplification factor
b = blade semichord
C_P = specific heat at constant pressure
$\{F_m(t)\}$ = motion-dependent unsteady aerodynamic forces
$\{F_g(t)\}$ = gust response unsteady aerodynamic forces
$[G]$ = blade damping matrix
$[G_m]$ = generalized damping matrix
$[K]$ = blade stiffness matrix
$[K_m]$ = generalized stiffness matrix
k = reduced frequency = $\omega b/U$
M = Mach number
$[M]$ = blade mass matrix
$[M_m]$ = generalized mass matrix
P = pressure
$\{Q(t)\}$ = modal displacement
T = temperature
U = uniform mean flow relative velocity
V = flow velocity
$\{X\}$ = physical displacements
a = flow angle
β = interblade phase angle
γ = specific heat ratio
ϱ = air density
$[\phi]$ = $n \times m$ mode shape matrix
ω = blade natural frequency

Subscripts

1 = leading edge of actuator disk
2 = trailing edge of actuator disk
T = total property

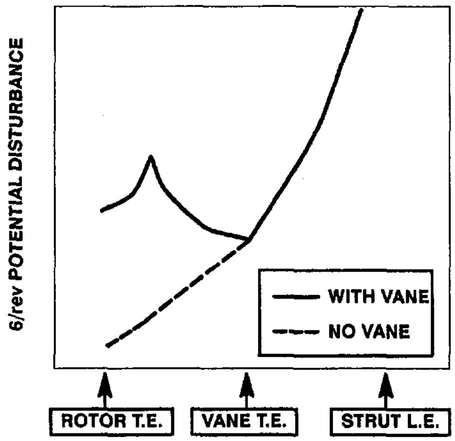

Fig. 3 Potential disturbance amplification

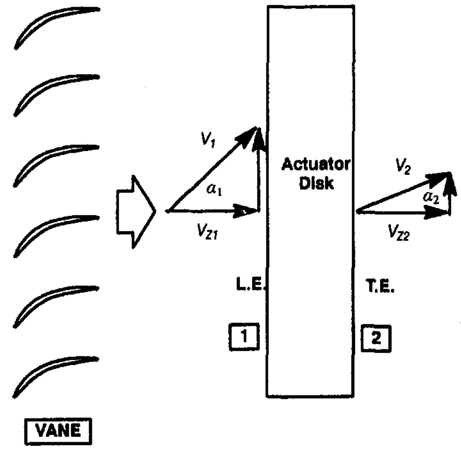

Fig. 4 Stator vane modeled as actuator disk

rately with a relatively coarse mesh. This is achieved with the current solver for the following reasons:

1 The streamline curvature, including the curvature along the blade surface, is calculated with high-order-accurate cubic splines and directly integrated in the cross-stream momentum equation. This allows much coarser grids to represent the curvature than a finite differences approach would. Also, the integration is a combination of analytical and numerical integration, which provides more accurate results than a purely numerical approach.
2 Entropy and rothalpy are conserved along streamlines. This eliminates the requirement of fine leading edge grid resolution.
3 The numerics are second-order-accurate for uniform and nonuniform grids.
4 No artificial viscosity or damping terms are required in subsonic flow regions. However, "artificial compressibility" is used to stabilize the algorithm and capture shocks in supersonic regions.

The implicit approach has allowed for many different boundary conditions to be applied including a "design option" mode for which results are presented later in the paper. At the inlet, rather than specifying a prescribed flow angle, the circumferential average flow angle is specified along with the specification that the static pressure at this inlet plane is uniform (this is the desired property to minimize distortion). The flow angle that meets this specification is then calculated. A stator vane row can be designed to approximate this flow angle distribution, which has the effect of nearly eliminating the static pressure distortion.

Analytical Model of Pressure Disturbance Amplification

In this study, the axial distance between the blade trailing edge and the strut leading edge is about two chord lengths of the blade, as shown in Fig. 1. With this axial distance, the potential disturbance from the strut reaching the rotor was expected to be minimal, assuming an exponential decay. However, as demonstrated by the flow defect analyses, the stator vane between the rotor and the strut actually amplifies the potential disturbance from the strut as shown in Fig. 3. The amplification factor can be defined as:

$$AF = \frac{6/\text{REV potential disturbance @ Stator L.E.}}{6/\text{REV potential disturbance @ Stator T.E.}}. \quad (4)$$

This amplification phenomenon can be explained using a simplified analytical model.

Although the use of a CFD solver can provide answers for complicated geometry, physical mechanisms are often understood better if the problem is simplified. Further understanding can result if the mechanism is reduced to a pure analytical formulation. In this analytical model, the problem is simplified by treating the row of stator vanes as an actuator disk, and determining the amplification factor first for incompressible flow, and then accounting for compressibility.

The stator vane row is treated as an actuator disk, as shown in Fig. 4. The actuator disk concept assumes there are an infinite number of infinitesimal blades which all turn the flow to an angle of a_2. A loss mechanism can be prescribed, but for this case it will be assumed that the total pressure is constant across the actuator disk. Essentially a downstream strut imposes a disturbance in pressure at the trailing edge of the stator. The pressure at station 2 is then

$$P_2 = \overline{P_2} + P_2'. \quad (5)$$

If the pressure at station 1 can be determined such that

$$P_1 = \overline{P_1} + P_1', \quad (6)$$

then the amplification factor across the actuator disk is

$$AF = \frac{dP_1'}{dP_2'}. \quad (7)$$

Incompressible Flow. Bernoulli equation relates the pressure and velocity at each station:

$$P_1 = P_T - \frac{\varrho V_1^2}{2}, \quad (8)$$

$$P_2 = P_T - \frac{\varrho V_2^2}{2}. \quad (9)$$

The continuity equation is

$$V_{Z1} = V_{Z2} \quad (10)$$

or

$$V_1 \cos a_1 = V_2 \cos a_2. \quad (11)$$

If Eqs. (5), (6), (8), and (9), are differentiated, the following expression can be obtained:

$$\frac{dP_1'}{dP_2'} = \frac{V_1}{V_2}\frac{dV_1}{dV_2}. \quad (12)$$

If Eq. (11) and its derivative are substituted into Eq. (12), then

$$\frac{dP'_1}{dP'_2} = \left(\frac{\cos a_2}{\cos a_1}\right)^2 . \quad (13)$$

This result demonstrates that for incompressible flow, the amplification factor is strictly a function of the inlet and exit angles. For an outlet guide vane where $a_2 = 0$ deg and $a_1 = 30$ deg, $AF = 1.3333$. From this derivation, it can be seen that it is the nonlinearity of the pressure–velocity relation and conservation of mass that cause the disturbance amplification.

Compressible Flow. Compressibility complicates the analysis somewhat because density is no longer constant, and a closed-form solution is no longer possible. However, a similar derivation can proceed using numerical solutions to the equations and numerical differentiation to produce a graphic result.

For compressible flow, the energy equation is needed. Since there is no work done, the total temperature is uniform. The static temperature is related to the velocity squared:

$$T_1 = T_T - \frac{V_1^2}{2C_P} , \quad (14)$$

$$T_2 = T_T - \frac{V_2^2}{2C_P} . \quad (15)$$

The Mach number is defined as

$$M_1 = \frac{V_1}{\sqrt{\gamma R T_1}} , \quad (16)$$

$$M_2 = \frac{V_2}{\sqrt{\gamma R T_2}} . \quad (17)$$

The pressure is related to the Mach number and total pressure by

$$P_1 = \frac{P_T}{\left(1 + \frac{\gamma - 1}{2} M_1^2\right)^{\gamma/\gamma-1}} , \quad (18)$$

$$P_2 = \frac{P_T}{\left(1 + \frac{\gamma - 1}{2} M_2^2\right)^{\gamma/\gamma-1}} . \quad (19)$$

The density is defined by the ideal gas law:

$$\varrho_1 = \frac{P_1}{RT_1} , \quad (20)$$

$$\varrho_2 = \frac{P_2}{RT_2} . \quad (21)$$

The continuity equation is

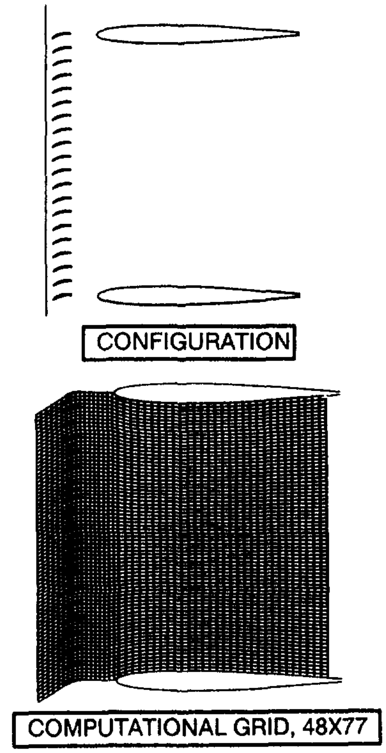

Fig. 6 Vane–strut configuration and grid

$$\varrho_1 V_1 \cos a_1 = \varrho_2 V_2 \cos a_2 . \quad (22)$$

A procedure was set up, which for a given M_2, a_1, and a_2, then P_2, P_1, and M_1 would be determined iteratively using the equations shown. The same procedure was run for $M_2 + \delta M_2$ so the changes δP_1 and δP_2 could be determined numerically. The amplification factor is then

$$AF = \frac{\delta P_1}{\delta P_2} . \quad (23)$$

Figure 5 shows these amplification factors for $P_T = 14.7$ psi, $T_T = 560R$, $\gamma = 1.4$, $a_2 = 0$ deg a_1 varying between 10 and 50 deg, and as a function of the inlet Mach number M_1. As the inlet Mach number goes to 0, these results are the same as the analytic incompressible results presented previously.

For the case presented in the paper, the amplification factor using this analysis would be 1.6. However, from the CFD calculation, it was determined to be 1.33 across the stator. This shows that the actuator disk theory can demonstrate the mechanism,

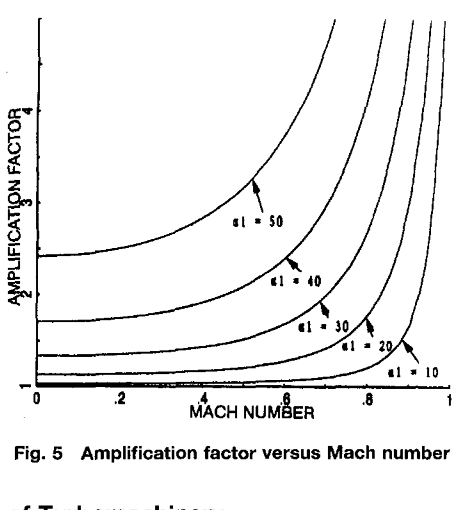

Fig. 5 Amplification factor versus Mach number

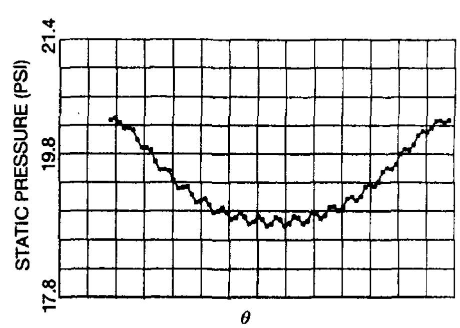

FFT		
6/Rev	12/Rev	18/Rev
0.66 psi	0.16 psi	0.05 psi

Fig. 7 Rotor TE static pressure distortion

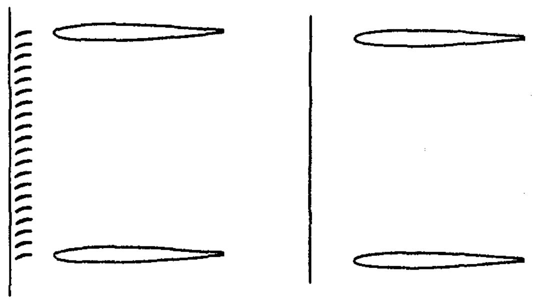

Fig. 8(*a*) With and without vane configurations

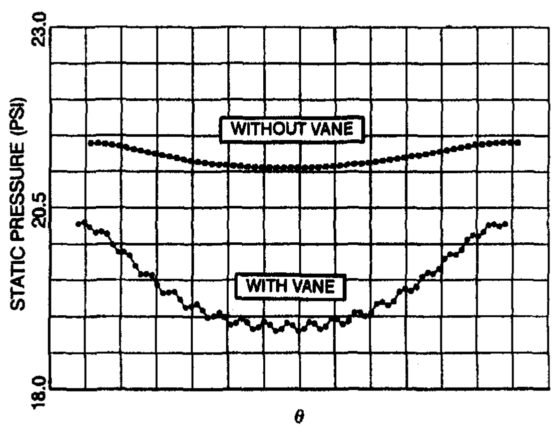

Fig. 8(*b*) With and without vane disturbance

but overpredicts the amplification factor because some attenuation can occur since the chord is finite and the solidity is not infinite.

Unsteady Aerodynamics

Once the circumferential flow defects are obtained, they are transformed into the rotating blade coordinate system and Fourier transformed for the desired harmonic. In particular, the predicted static pressure distortion upstream of the stator vanes and struts, which is at the rotor exit plane, is assumed to be at the rotor inlet and then transformed into the rotating blade coordinate system. With the static pressure distortion data as input, a harmonic analysis program is run to Fourier transform the distortion into unsteady velocity perturbations for the harmonic components of interest. The unsteady velocity perturbation (gust) is then calculated and input to an unsteady aerodynamic program, which calculates the gust-induced unsteady aerodynamic forces acting on the blade row, i.e., the unsteady aerodynamic loading.

Both the unsteady aerodynamic loading $\{\bar{F}_g\}$ and the aerodynamic damping $[A]$ are calculated utilizing classical two-dimensional kernel functions in a strip theory calculation for subsonic flows (Kirsch, 1990). With the velocity perturbation provided by flow defect models, and the blade mode shapes and frequencies provided by a finite element model, the system calculates the modal unsteady aerodynamic loading due to the flow defects as well as the aerodynamic damping. For the unsteady aerodynamic loading, the unsteady aerodynamic model assumes the velocity perturbation (gust) is convected by the free stream and is not deformed by the blade row (i.e., the frozen gust assumption).

Modal Aeroelastic Solution

The structural damping $[G_m]$ can be determined from previous experience or with measured data. With the unsteady aerodynamic loading given above $\{\bar{F}_g\}$, the motion-dependent unsteady aerodynamic forces $[A]$, and the structural damping $[G_m]$ as input, the blade modal response can be calculated using Eq. (3):

$$\{\bar{Q}\} = [-\omega^2[M_m] + i\omega[G_m] + [K_m] - [\phi]^T[A]]^{-1}[\phi]^T\{\bar{F}_g\}. \quad (24)$$

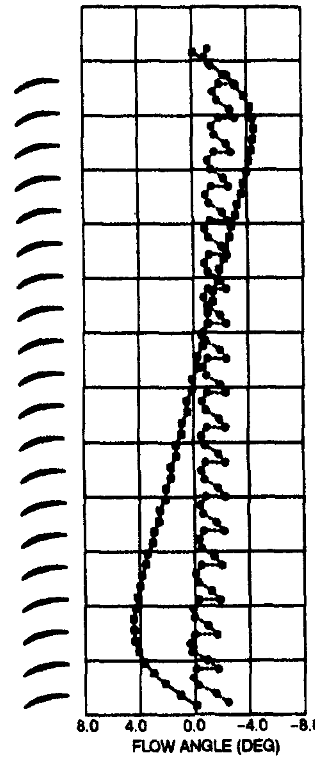

Fig. 9(*a*) Optimized and baseline flow angles

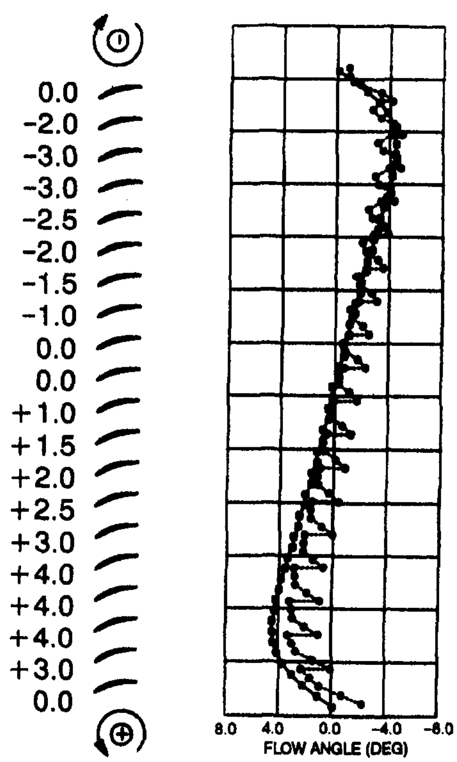

Fig. 9(*b*) Optimized and resulting flow angles

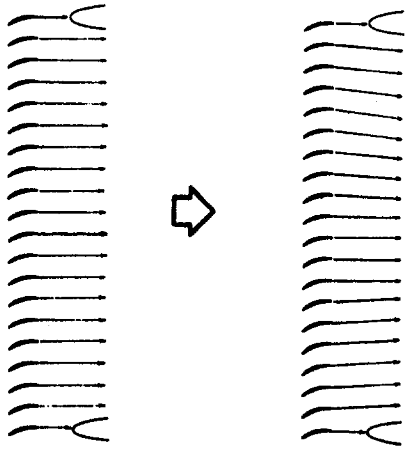

Fig. 10(*a*) Baseline and optimized configurations

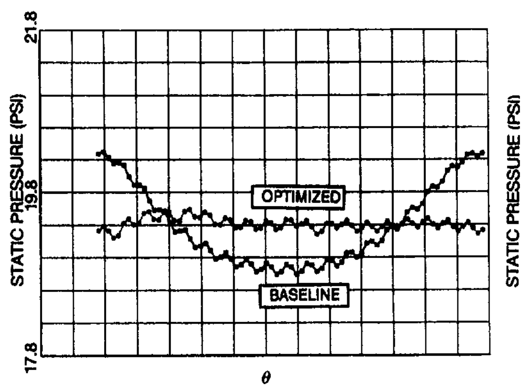

Fig. 10(*b*) Baseline and optimized disturbances

The blade modal response $\{\bar{Q}\}$ can be used to calculate the vibratory blade stress using the modal stress information.

Results

This forced response prediction system was applied to investigate a compressor rotor in which the first flex mode of the rotor blade was excited by the six downstream struts at the 6/rev crossing speed.

Baseline Potential Disturbance. The implicit two-dimensional CFD solver was used to model the static pressure distortion reaching the rotor trailing edge from the stator vanes and the struts. This was accomplished by considering both the stator vanes and the struts without the rotor. The stator vane row has 114 vanes and there are six struts (one "king" strut and five nominal struts). By assuming six nominal struts to simplify the case further, the CFD solver was used to model a 60 deg sector, which consists of one nominal strut and 19 stator vanes. The stator vane and strut configuration and the computational grid are shown in Fig. 6. The vertical line in Fig. 6 is the rotor trailing edge location. The CFD solver was run at the resonant speed where the flow is subsonic. The circumferential static pressure distribution at the rotor trailing edge was generated and Fourier decomposed as shown in Fig. 7. The 6/rev component of 0.66 psi is significant enough to excite the rotor blade at resonance.

Stator Vane Effects. The stator vane effects are demonstrated by running the CFD solver with and without the stator vanes, and also by imposing different inlet conditions to simulate the vane inlet and strut inlet conditions. These vane configurations are shown in Fig. 8(*a*). Both circumferential static pressure distributions at the rotor trailing edge are presented in Fig. 8(*b*). As can be seen, the stator vanes cause a significant amplification of the pressure disturbances due to the frame struts. The Fourier decomposition shows that a fourfold increase in the 6/rev strut potential disturbance is caused by the stator vanes.

Stator Vane Modifications. The CFD solver has an option to determine the flow angle distribution entering the struts, which will minimize the potential disturbance propagating upstream. This is done by running the CFD solver without the stator vanes and determining the flow angle distribution at the strut inlet, which yields a uniform static pressure at this plane. This "optimum" flow angle distribution is compared with the baseline actual flow angle distribution in Fig. 9(*a*). According to the optimized flow angle distribution, it appears that it is necessary to guide the flow around the struts. Therefore, each stator vane was rotated (i.e., the stagger angle modified) from −3 to +4 deg trying to match the optimized flow angle distribution. The resulting flow angle distribution was obtained by running the CFD solver using the rotated stator vanes, and compares well with the optimized flow angle distribution, as seen in Fig. 9(*b*). The baseline and optimized configurations are shown in Fig. 10(*a*). The resulting circumferential static pressure distribution at the rotor trailing edge for the rotated vane case was compared with the baseline case in Fig. 10(*b*), which shows the 6/rev component reduced by 92 percent from the baseline. Figure 11 shows the axial static pressure distributions along the stator vane surface grid lines for the rotated stator vane case and the baseline case. As can be seen, the loading on the modified stator vanes was much more uniform from vane to vane than the baseline stator vanes and therefore has much less circumferential pressure variation or potential disturbance.

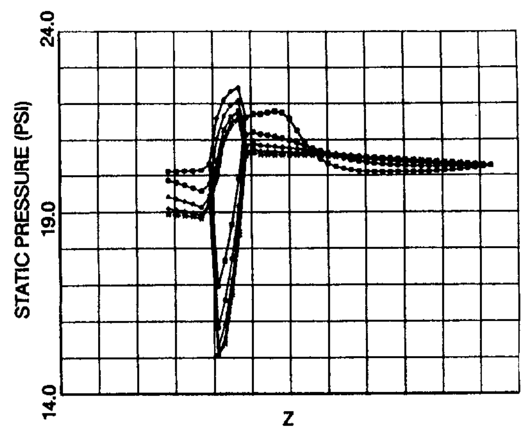

Fig. 11(*a*) Baseline stator vane pressure

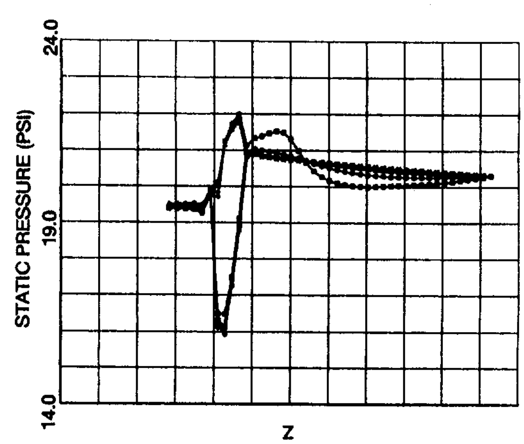

Fig. 11(*b*) Optimized stator vane pressure

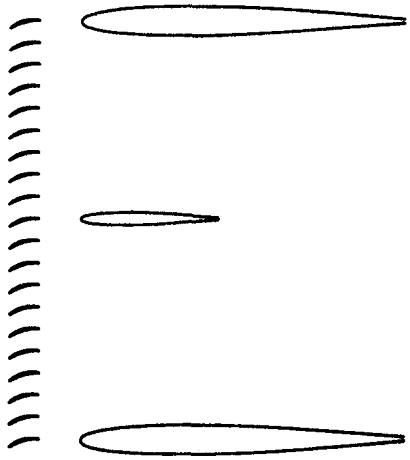

Fig. 12(*a*) Splitter configuration

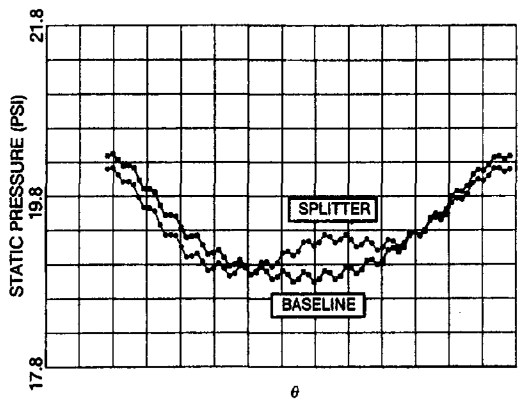

Fig. 12(*b*) Splitter potential disturbance

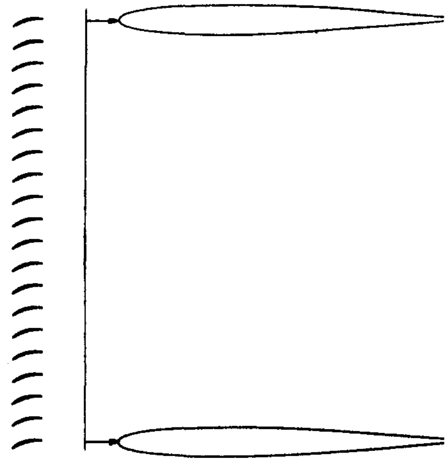

Fig. 13(*a*) Cut-back configuration

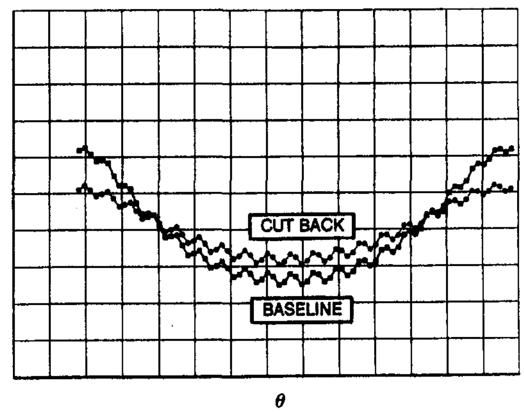

Fig. 13(*b*) Cut-back potential disturbance

Splitter Effects. As shown in Fig. 12(*a*), a 42 percent scaled strut was added between the nominal struts to make a 12-strut configuration. The purpose of adding a splitter is to reduce the 6/rev potential disturbance. The resulting circumferential static pressure distribution at the rotor trailing edge with the splitter was compared with the baseline case. Fig. 12(*b*) shows that the 6/rev component is reduced by 33 percent from the baseline. However, as expected, it increased the 12/rev component from 0.16 psi to 0.26 psi.

Strut Cut-Back Effects. To simulate the strut cut-back effects, the axial distance between the stator vanes and the struts was increased by 75 percent from the baseline case as shown in Fig. 13(*a*). Shown in Fig. 13(*b*) is the calculated circumferential static pressure distribution at the rotor trailing edge for the strut cut-back case compared with the baseline case. As a result of the strut cut-back, the 6/rev component was reduced by 42 percent from the baseline.

Flow Defect Study Summary. Table 1 summarizes all these strut/vane modifications as potential methods to reduce the 6/rev potential disturbance.

Finite Element Model. The finite element model is shown in Fig. 14. The Campbell diagram of this blade in Fig. 15(*a*) shows how the first flex mode crosses 6/rev at resonant speed. The first flex mode shape as shown in Fig. 15(*b*) and the blade natural frequency are input to the motion-dependent unsteady aerodynamic program to calculate the resulting aerodynamic damping.

Unsteady Aerodynamics. The flow field for the rotor blade is subsonic. The reduced frequency is 0.24 to 0.25 for the first flex mode and the interblade phase angle is 331.6 deg for the 6/rev backward-traveling wave mode.

With the velocity perturbation provided by the flow defect model and the blade mode shape and frequency provided by the finite element model, the unsteady aerodynamic program calculates the modal unsteady aerodynamic loading due to the flow defects as well as the aerodynamic damping.

Blade Response. The blade modal response was calculated for the baseline condition. The modal response was then combined with the finite element dynamic stress solution to predict the blade stresses at the strain gage locations for the baseline case. The predicted response was compared with the strain gage data to calculate the structural damping.

Strut Cut-Back Test. To verify the analysis prediction, a strut cut-back test was run to provide data. A pretest analysis was performed to predict the stress reduction due to the strut cut back. With the circumferential static pressure distribution as input, the forced response analysis predicted a 25 percent

Table 1 Flow defect study summary

Option	Fourier Decomposition			6/Rev
	6/Rev	12/Rev	18/Rev	Reduction
Baseline	0.66 psi	0.16 psi	0.05 psi	0%
Vane Modification	0.05 psi	0.04 psi	0.04 psi	92%
Splitter	0.44 psi	0.26 psi	0.03 psi	33%
Strut Cut Back	0.38 psi	0.05 psi	0.01 psi	42%

stress reduction. Testing shows a 27 percent stress reduction, which is an excellent correlation with the prediction.

Summary and Conclusions

An analysis system developed to predict compressor rotor blade forced response due to downstream stator vanes and struts has been presented. The forced response prediction system is an extension of a system developed earlier, which incorporates an implicit CFD solver to model static pressure distortion from downstream. The description of the potential disturbance flow defect is obtained from the CFD model. The finite element method is used to provide the mode shapes and frequencies for the blade motion. With structural damping determined from previous data, the system predicts the blade forced response.

The results showed that the stator vanes cause a significant amplification of the pressure disturbances from the frame struts. Effects of strut and vane modifications were examined using the analysis. A vane modification with an "optimized" flow angle distribution shows the disturbance can be greatly reduced. Recent testing of the strut modification shows exceptional correlation with the analysis prediction.

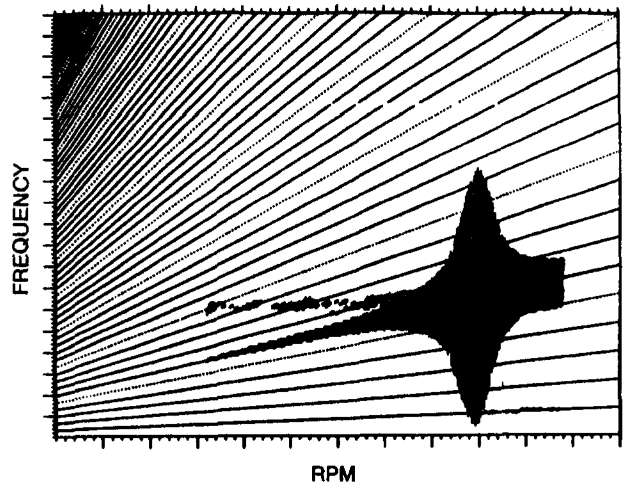

Fig. 15(*a*) Rotor Campbell diagram

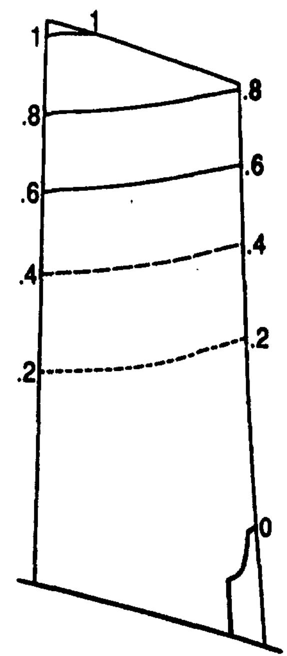

Fig. 15(*b*) Rotor first flex mode shape

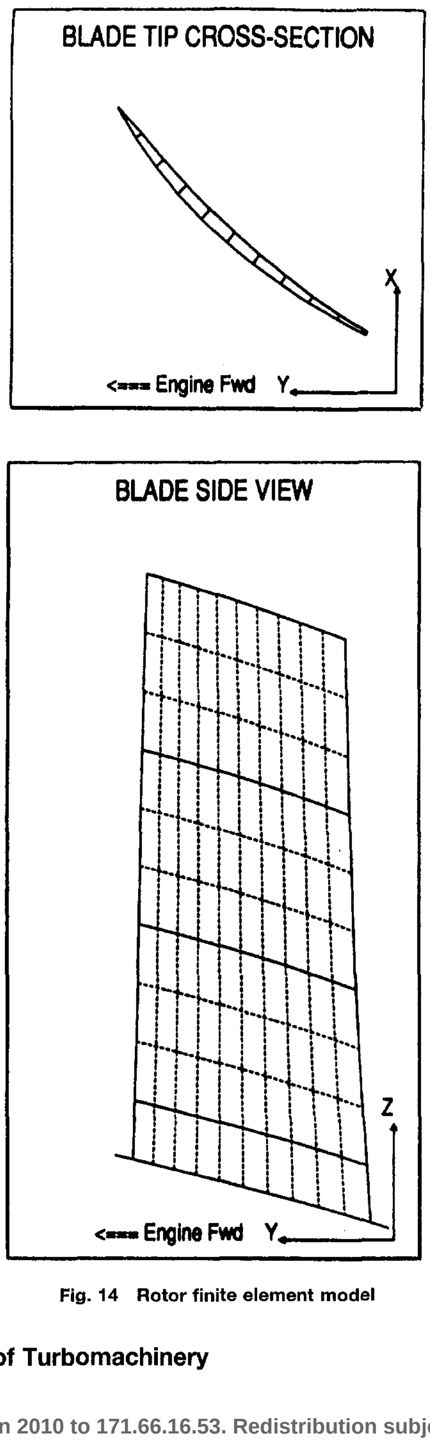

Fig. 14 Rotor finite element model

Acknowledgments

The authors would like to thank Dr. Ron Fost and Dr. Robert Kielb for their suggestions for the corrections and revisions in this paper and to General Electric Aircraft Engines for permission to publish this paper.

References

Chiang, H. D., and Kielb, R. E., 1993, "An Analysis System for Blade Forced Response." ASME JOURNAL OF TURBOMACHINERY, Vol. 115, pp. 762–770.

Kaza, K. R. V., and Kielb, R. E., 1984, "Flutter of Turbofan Rotors With Mistuned Blades," *AIAA Journal,* Vol. 22, No. 11, pp. 1618–1625.

Kaza, K. R. V., and Kielb, R. E., 1985, "Vibration and Flutter of Mistuned Bladed-Disk Assemblies," AIAA *Journal of Propulsion and Power,* Vol. 1, No. 5, pp. 336–344.

Kemp, N. H., and Sears, W. R., 1953, "Aerodynamic Interference Between Moving Blade Rows," *J. Aeronaut. Sci.,* Vol. 20, no. 9, pp. 585–597.

Kirsch, A. A., 1990, General Aeroelastic Program—GE Proprietary Analysis.

Korakianitis, T. P., 1988, "On the Prediction of Unsteady Forces on Gas-Turbine Blades," ASME Paper No. 88-GT-89.

O'Brien, W. F., Ng, W., and Richardson, S. M., 1985, "Calculation of Unsteady Fan Rotor Response Caused by Downstream Flow Distortions," *Journal of Propulsion and Power,* Vol. 1, No. 6, pp. 464–469.

Osborne, C., 1973, "Compressible Unsteady Interactions Between Blade Rows," *AIAA Journal,* Vol. 11, No. 3, pp. 340–346.

Taylor, A. C., and Ng, W. F., 1987, "Analytical Prediction of the Unsteady Lift on a Rotor Caused by Downstream Struts," ASME Paper No. 87-GT-145.

Turner, M. G., and Keith, J. S., 1985, "An Implicit Algorithm for Solving 2D Rotational Flow in an Aircraft Engine Fan Frame," Paper No. AIAA-85-1534.

Whitehead, D. S., 1970, "Vibration and Sound Generation in a Cascade of Flat Plates in Subsonic Flow," Aeronautical Research Council, Reports and Memoranda 3865.

Computed Eccentricity Effects on Turbine Rim Seals at Engine Conditions With a Mainstream

Z. Guo

D. L. Rhode

F. M. Davis

Department of Mechanical Engineering,
Turbomachinery Laboratory,
Texas A&M University,
College Station, TX 77843

A previously verified axisymmetric Navier–Stokes computer code was extended for three-dimensional computation of eccentric rim seals of almost any configuration. All compressibility and thermal/momentum interaction effects are completely included, and the temperature, pressure, and Reynolds number of the mainstream, coolant stream, and turbine wheel are fixed at actual engine conditions. Regardless of the seal eccentricity, both ingress and egress are found between $\theta = -30$ and 100 deg, which encompasses the location of maximum radial clearance at $\theta = 0$ deg. All other θ locations within the rim seal show only egress, as does the concentric base case for all circumferential locations. Further, the maximum ingress occurs near $\theta = 30$ deg for all eccentricities. This is found to produce a blade root/retainer temperature rise from the concentric case of 390 percent at 50 percent eccentricity and a 77 percent rise at 7.5 percent eccentricity. In addition, the nature of an increased eccentricity causing a decreased seal effectiveness is examined, along with the corresponding increase of cavity-averaged temperature.

Introduction

The wheel spaces in gas turbine engines are typically sealed with a rim seal and are cooled by purge air bled from the compressor. In modern engines, the total coolant being bled approaches 20 percent of the throughflow. Clearly, this is a major penalty on the thermal efficiency and power output. Naturally a considerable amount of effort is being devoted toward using the bleed air in a more efficient manner. It is known that a considerable number of turbines are operated with the full awareness that hot gas ingestion into the wheelspace occurs in the downstream stages. Therefore, designers are greatly interested in obtaining an enhanced understanding of the phenomena affecting this ingestion and heating of the turbine blade root retainer region of the wheel.

The present investigation builds on recent numerical developments (Ko and Rhode, 1991). For computational economy reasons, that study considered the axisymmetric subproblem of a generic rotor–stator cavity at actual engine temperature, pressure, and Reynolds number of the cooling and main streams as well as the disk. This earlier work illuminated the presence and significance of a gap recirculation zone (GRZ) located slightly inward of a rim seal having a stator shroud. Specifically, it was shown how the GRZ is responsible for a large portion of the heat transport from the mainstream to the outer portion of the wheelspace. The presence of the GRZ in that study has been corroborated by measurements (Elovic, 1991) and by independent CFD computations revealed by Hendricks (1993) and Ivey (1991). The present investigation provides an enhanced understanding of the effects of rim seal eccentricity on cavity and blade root/retainer thermal phenomena. Of particular interest is the effect of seal eccentricity on: (a) circumferential distribution of mainstream ingress and egress, (b) seal effectiveness, (c) cavity-averaged temperature and pressure, (d) location and temperature of rotor and stator hot spots, and (e) circumferential distribution of blade root/retainer temperature.

Contributed by the International Gas Turbine Institute and presented at the 39th International Gas Turbine and Aeroengine Congress and Exposition, The Hague, The Netherlands, June 13–16, 1994. Manuscript received by the International Gas Turbine Institute February 4, 1994. Paper No. 94-GT-31. Associate Technical Editor: E. M. Greitzer.

Although numerous simple algebraic models exist for estimating $C_{w,\min}$ without the interaction with the mainstream, there are apparently very few for estimating the ingress including mainstream effects. This situation is attributed to the complexity of: (a) the momentum/thermal flow field and (b) the geometric layout of wheelspace cavities. Perhaps the first algebraic model for estimating ingress with a mainstream is that by Chew (1991). He proposed a model that combines the momentum-integral equations for cavity flows with a very simple seal model. Some of the basic seal mechanisms were not included, however, such that this model has uncertain applicability to various situations. Very recently Hamabe and Ishida (1992) assessed their algebraic ingress model by making gas concentration measurements in the wheelspace of a shrouded rotor–stator system with a nonaxisymmetric main flow. The asymmetry of the circumferential pressure distribution in the mainstream is the only three-dimensional effect on the turbine rim seal, and the rotor–stator cavity has been idealistically treated as being totally axisymmetric. It was found that the sealing effectiveness largely depends on the shape of the circumferential pressure distribution in the mainstream.

More sophisticated models using the Navier–Stokes equations have recently begun to appear in order to include all of the physical momentum and turbulence effects. Vaughan and Turner (1987) recently showed that, at least for certain conditions, a laminar three-dimensional solution gives a sinusoidally varying ingress–egress cycle in the circumferential direction passing through a rim seal.

The most detailed numerical study of the three-dimensional rotor–stator cavity with external flow effects was conducted by Lowry and Keeton (1987). In their investigation, a CFD code with the two-equation ($k-\epsilon$) turbulence model was used to compute the temperatures, pressures, and velocities in the high-pressure fuel turbopump aft-platform seal cavity of the space shuttle main engine for different boundary conditions and geometries. The cavity temperature and pressure were approximately 1700 R (945 K) and 3600 psi (24.8 MPa), respectively. The three-dimensional cases computed were specified as: (a) a prescribed asymmetric turbine exit pressure distribution based on pressure measurements (base case), (b) an eccentric rim seal with a correspondingly eccentric coolant inlet, and (c) a highly eccentric rim seal alone.

Objective

The present objective is to obtain an enhanced understanding of the effects of rim seal eccentricity on the circumferential variation of: (a) ingress and egress rates, (b) cavity temperatures and pressures, and (c) rim seal flow pattern. In addition, seal eccentricity effects on seal effectiveness and "hot spot" temperature as well as location are of interest. All compressibility and momentum/thermal effects at the mainstream interface will be accounted for using actual engine pressures, temperatures, and Reynolds numbers for the coolant and hot gas streams as well as the turbine wheel. Further, adiabatic walls are imposed in order to isolate ingress heating effects from wall heat convection effects.

Numerical Model

Only the short axial space between an upstream stator vane and a downstream rotor blade, as well as the corresponding narrow axial segment of mainstream duct, has been modeled herein because the mainstream effect involved occurs only at the rim seal. The annular mainstream duct was radially shrunk in order to minimize the serious computing cost without affecting the solutions. Several computer solutions having a different mainstream radial extent were carefully compared in choosing a final domain, which would minimize the number of grid points without affecting the solution. Figure 1(a) illustrates the idealized cavity showing the computational domain.

It was decided that approximating the mainstream passage as a straight annular duct is a very good approximation. This is due to the fact that the effect of the diverging mainstream path is counterbalanced by the increasing boundary layer displacement thickness, which is caused by the high mainstream swirl velocity. This is particularly reasonable since: (a) only the short axial space between the stator vane and the rotor blade is of interest here and (b) an experienced turbine designer (Baskharone, 1990) was consulted concerning this decision.

An elliptic, axisymmetric Navier–Stokes computer code of the finite volume variety was recently extended to allow elliptic three-dimensional computations in most rim seal configurations at various seal eccentricities. The axisymmetric version had already given close agreement with measurements for a wide variety of test cases, including rotor–stator cavities (Ko and Rhode, 1991) as well as complex labyrinth seals. The current three-dimensional extension of the code has recently been tested, giving close agreement with rotordynamic measurements of a pump annular seal, a sample of which is discussed subsequently. A pressure-based method is used to solve the continuity, momentum, and energy (stagnation enthalpy) equations as well as the turbulence model equations. Some of the basic approaches of the TEACH code of Gosman and Pun (1974) have been adopted. The primitive variables are solved on a system of three staggered grids using the SIMPLER algorithm of Patankar (1980). Leonard's (1979) QUICK convection differencing scheme is utilized for all convective terms in the momentum equations to reduce false diffusion. This differencing scheme was implemented in a special way by Rhode et al. (1986) that promotes numerical stability.

Neglecting body forces, the steady-state continuity and momentum equations are

$$\frac{\partial(\rho U_i)}{\partial x_i} = 0$$

$$\frac{\partial(\rho U_i U_j)}{\partial x_i} = -\frac{\partial p}{\partial x_j} - \frac{\partial \tau_{ij}}{\partial x_i}$$

where ρ, U_i, and p are the time-averaged density, velocity, and pressure. The Reynolds stresses are determined by the high-Reynolds-number $k-\epsilon$ turbulence model which is discussed later. Further, the stagnation enthalpy form of the energy equation

$$\frac{\partial(\rho U_i H)}{\partial x_i} - \frac{\partial}{\partial x_j}\left\{\Gamma_H \frac{\partial H}{\partial x_j}\right\} = \frac{\partial}{\partial x_j}\left[U_i \tau_{1j} - \Gamma_H \frac{\partial}{\partial x_j}\left\{\frac{V^2}{2}\right\}\right]$$

was included, where:

$$\Gamma_H = \frac{\mu_{\rm eff}}{\rm Pr}$$

Nomenclature

a = radial width of cavity inlet = const
C_w = volumetric flow rate parameter = $Q/(\nu R)$
$dx(i)$ = displacement along general orthogonal coordinate lines
e = seal eccentricity, percent
E = seal eccentric displacement, m
F = force coefficient
GRZ = gap recirculation zone
h_i = scale factor
H = radial width of mainstream passage; stagnation enthalpy
$H_i(j)$ = coordinate variation term
k = turbulent kinetic energy
m_c = mass flow rate of the cooling air
m_e = mass egress across x-plane $E-F$ [Fig. 1(a)]
m_i = mass ingress across x-plane $E-F$ [Fig. 1(a)]
$m_c/(m_c + \bar{m}_i)$ = sealing effectiveness
P = static pressure
ΔP^* = differential pressure = $[(P_2 - P_1)/P_1] \times 10^3$
Q = volumetric purge flow rate
R = radius of disk
R_i = radius of cooling air inlet slit into cavity
$\mathrm{Re}_{x,m}$ = axial Reynolds number of mainstream = $(2UH)/\nu$
Re_θ = rotational Reynolds number of disk = $(\Omega R^2)/\nu$
S = axial width of cavity
S_c = gap clearance between rotor shroud and stator shroud
T = temperature
T^* = normalized temperature = $(T - T_2)/(T_1 - T_2)$
ΔT^* = differential temperature = $2C_p(T_2 - T_1)/(\Omega R)^2$
t = radial thickness of shroud
U, V, W = mean velocities in x, r, θ directions
x, r, θ = axial, radial, and tangential coordinates
x_i = spatial coordinate in tensor notation
x^i = general orthogonal coordinate
ϵ = turbulent energy dissipation rate
μ = absolute viscosity
ν = kinematic viscosity
ρ = fluid density, radial bipolar coordinate
ϕ = circumferential bipolar coordinate
Ω = rotational velocity
$\omega_{\rm whirl}$ = shaft whirl frequency

Superscripts

$*$ = nondimensionalized

Subscripts

1 = mainstream
2 = cooling purge flow

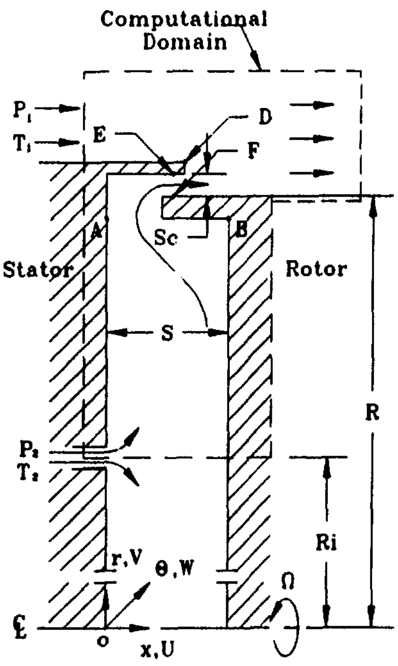

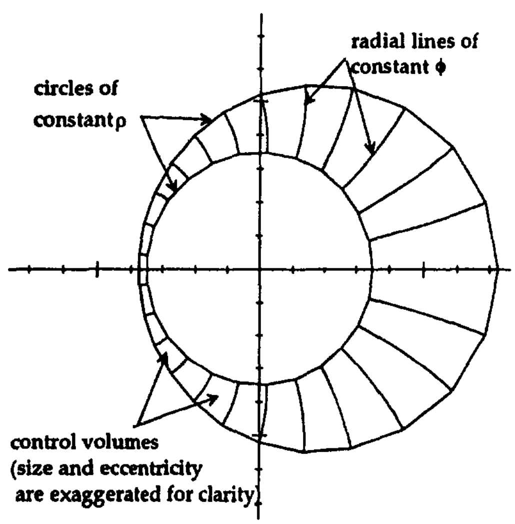

Fig. 1 (a) Configuration and computational domain and (b) extremely coarse bipolar coordinate mesh in an eccentric region of the grid

The static temperature was evaluated using:

$$T = \frac{H - \frac{1}{2}(U^2 + V^2 + W^2)}{C_p}$$

General Orthogonal Coordinates. The equations were transformed into relations involving general orthogonal coordinates using Pope's (1978) method. With his transformation procedure the equations retain their original form and simplicity as much as possible while being applicable to any orthogonal coordinate system, either numerically generated or algebraically specified.

Let x^i denote such a general orthogonal coordinate system. The scale factors h_i relate distances in this system to those in the rectangular Cartesian system by

$$(ds)^2 = (h_i dx^i)^2 = [dx(i)]^2$$

where the scale factors h_i are excluded from the summation convention. Thus, $dx(i)$ denotes the physical displacements along a coordinate line x^i in the general orthogonal coordinate system. The scale factors, which are excluded from the summation convention, are determined by

$$h_i^2 = \sum_l \frac{\partial \bar{x}_l}{\partial x^i} \frac{\partial \bar{x}_l}{\partial x^i}$$

where $\bar{x}_l$ are the coordinates in the Cartesian coordinate system. Pope's divergence operator $\nabla(i)$ and coordinate variation term $H_i(j)$ needed to transform the transport equations into general orthogonal coordinates are

$$\nabla(i) = \frac{h_i}{|h|} \frac{\partial}{\partial x(i)} \frac{|h|}{h_i}$$

$$H_i(j) = \frac{1}{h_i h_j} \frac{\partial h_i}{\partial x_j}$$

Here h_i represents the scale factors and $|h|$ is the product of the scale factors. The transformed mass and momentum equations are

$$\nabla(i)[\rho U(i)] = 0$$

and

$$\nabla(i)[\rho U(i)U(j) + \tau^*(ij)]$$

$$= -\frac{\partial p^*}{\partial x(j)} + H_i(j)[\rho U(i)U(i) + \tau^*(ii)] - H_j(i)[\rho U(i)U(j) + \tau^*(ij)]$$

The isotropic component of stress has been added to the pressure, giving

$$p^* = p + \tfrac{2}{3}\rho k + \tfrac{2}{3}\mu_{\text{eff}} \nabla(i)U(i)$$

and τ^* involves the anisotropic stress as

$$\tau^*(ij) = -\mu_{\text{eff}} \left[\frac{\partial U(i)}{\partial x(j)} + \frac{\partial U(j)}{\partial x(i)} - U(i)H_i(j) - U(j)H_j(i) + 2U(l)H_i(l)\delta_{ij} \right]$$

The standard $k-\epsilon$ turbulence model was used. Concerning $k-\epsilon$ turbulence models, very recently Virr et al. (1994) compared the wall function approach to a one-equation near-wall model for turbine disk cavities. They found that the wall function approach gave essentially the same results as integrating all the way to the wall if low rotational Reynolds numbers are avoided and if proper care is used in specifying the near wall mesh spacing. This overall conclusion was generally supported by the findings of Avva et al. (1989, 1990) and Williams et al. (1991), who also compared wall functions with integration directly to the wall. The latter has the disadvantage for three-dimensional computations of substantially increasing the number of grid points where computational cost is already a serious concern. The rotational Reynolds number used herein is 7.62 $\times 10^6$, which is substantially more than sufficient to resolve the peak radial velocity along the disk surface. The values of y^+ in the important regions of large radius are approximately 100 while the values at small radius are near 200. This is exactly the range for which Virr et al. found best agreement with disk friction moment measurements.

The multiscale $k-\epsilon$ model version recently developed and tested by Ko and Rhode (1990) has shown significant improvements for the more complicated turbulent flows such as the ones considered here. Although it does not require more grid points such as various two-layer approaches, it has the disadvantage of requiring about 20 percent more CPU time and slightly more memory. Since the CPU time for the present solutions on our CRAY Y-MP computer was approximately 2.5 hours per computer solution using the standard $k-\epsilon$ model and wall function approach, it was decided to forego the multiscale model for the moment. It is hoped that budgetary constraints will allow the multiscale model in the near future. The execution memory requirement is currently 4.04 megawords.

Generating Eccentric Grids. In order to model geometries involving eccentricity without the complexity of numerically generating the grid, at least two coordinate systems must be used, one for eccentric regions and one for concentric regions. The bipolar coordinate system (Kamal, 1966) was employed in certain regions of the domain where geometric eccentricity occurs because: (a) its adjacent coordinate lines are eccentric with respect to each other and (b) it gives an orthogonal grid. This easily allows coordinate lines to fall on the desired eccentric surfaces of an eccentric rim seal for example. For the domain depicted in Fig. 1(a), cylindrical polar coordinates were utilized radially outward until the outer surface of the rotor shroud was reached. There a transition was made to bipolar coordinates, which extended radially outward across the rim seal radial clearance. At the inner surface of the stator shroud, a transition was made back to cylindrical coordinates that extended outward to the outer surface of the stator shroud. Then at the outer surface of the stator shroud a transition was made to bipolar coordinates with displacement equal but opposite to that used in the rim seal radial clearance. Then a final transition was made to cylindrical coordinates that extended to the outer boundary of the domain.

This produced a stator shroud with an extremely small eccentric displacement of 0.95 mm (0.037 in) for the largest eccentricity case of 50 percent. This inverse approach to the geometric modeling of a rotor that is eccentric with respect to the stator housing was carefully scrutinized via examining the solution for each eccentricity case. It was very clear that the rim seal interaction of the hot and cold streams was entirely unaffected by the mainstream flow near the outer boundary of the domain due to the high mainstream velocity. Because this interaction is highly localized to the rim seal radial clearance region, as expected from earlier work, the same flow field is obtained for a radially displaced rotor as for a radially displaced stator. Subsequent velocity vector plots demonstrate the localized interaction.

The bipolar system of coordinates does not reduce to polar cylindrical coordinates at low eccentricity as does the modified bipolar system, and it requires a numerical procedure to determine the value of the constant a in order to obtain the desired geometry. However, the range of allowable eccentricities is much larger (0.1 to 99.9 percent of the clearance) compared to that for the modified bipolar system (0.0 to 1.0 percent). The former is limited only by the precision of the computer employed. Bipolar coordinates may be related to Cartesian coordinates by the following transformation:

$$x = \frac{-a \sinh(\rho)}{\cosh(\rho) - \cos(\phi)}$$

$$y = \frac{a \sin(\phi)}{\cosh(\rho) - \cos(\phi)}$$

As for the modified bipolar system, ρ denotes the radius of a circle and ϕ denotes the circumferential position along that circle. The constant a is determined by a numerical search. The control volumes in an eccentric region are formed by the intersection of the bipolar coordinate lines as shown in Fig. 1(b). At the boundary of an eccentric region, the coordinates of the grid points are converted to the Cartesian system. This simplifies the conversion of the coordinates to the cylindrical system or another eccentric system in the adjoining region.

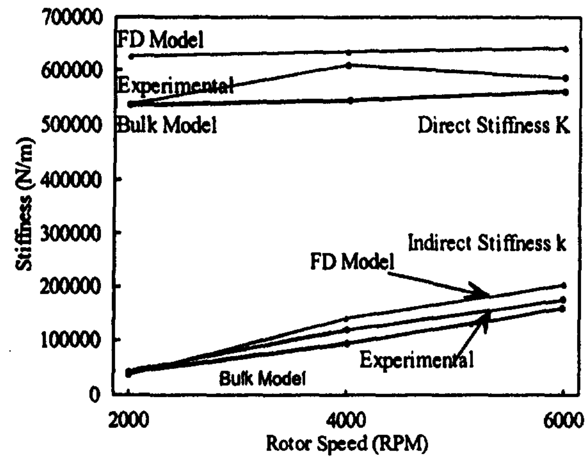

Fig. 2 Comparison of predictions with measurements of the rotordynamic stiffnesses from fluid pressure within an eccentric annular seal

Comparison to Three-Dimensional Measurements. The strong circumferential effect in the rotordynamic measurements and predictions of Dietzen and Nordmann (1986) were selected to test the three-dimensional (i.e., circumferential) extension of the computer code. The earlier axisymmetric version of the model gave close agreement with measurements of rotor–stator cavities (Ko and Rhode, 1991) as well as labyrinth seals flowing liquids as well as gases over an extremely wide range of Reynolds as well as Mach numbers. The case considered was a smooth annular seal flowing water at 30°C with the shaft whirling in a circular rotordynamic orbit at small eccentricity. This test case is most easily solved by removing the time variable from the problem. The preferred approach for accomplishing this is to use a reference frame which rotates and whirls with the shaft. Thus a "line of sight" viewed from this reference frame "sees," for example, the maximum clearance circumferential position at any instant of time. Thus the flow field relative to the observer has been converted to a steady flow in which the stator housing is rotating and whirling relative to the reference frame. The well-known rotation-related extra source terms (Rhode et al., 1993) were added to the radial and swirl momentum equations to account for the rotation of the reference frame. The relative motion relationship, which was derived to specify the velocity boundary conditions and initial guess relative to the current reference frame, is:

$$\bar{V} = \bar{v} + E\omega_{\text{whirl}} \sin \theta i_r + (E \cos \theta - r)\omega_{\text{whirl}} i_\theta$$

Here $\bar{v}$ is the velocity of any point relative to the seal outer housing. The current reference frame rotates at frequency ω_{whirl}, and its center whirls at tangential velocity $E\omega_{\text{whirl}}$ relative to the housing.

Grid independent computations of the measurements required $30 \times 8 \times 25$ gridlines in the axial, radial and circumferential directions, respectively. To determine the stiffness and damping coefficients (defined below) for comparison with measurements, the fluid pressure force components in the direction of, and normal to, the shaft displacement were calculated from the CFD solution. This was done for five whirl speeds at each shaft speed. Then the force coefficients defined here were calculated by means of a least-squares curve fit of the following relations:

$$F_{\text{Direct}} = (K + d\omega_{\text{whirl}})E$$

$$F_{\text{Indirect}} = (-k + D\omega_{\text{whirl}})E$$

In these equations K and k are the direct and indirect stiffness whereas D and d are the direct and indirect damping coefficients, respectively. Further ω_{whirl} is the shaft whirl frequency and E is the shaft displacement. Figure 2 shows the comparison with measurements as well as a simple bulk model prediction, which is believed to have been calibrated to similar measurements. The agreement is seen to be quite reasonable.

Results and Discussion

The complex momentum/thermal mixing details at the interface between the cavity and mainstream exert an important influence on blade root or retainer reliability. It has been known for some years that seal eccentricity has the potential of adversely affecting wheel-space heating due to increased hot gas ingress. An eccentric rotor naturally creates a circumferentially varying radial clearance for the type of rim seal configuration shown in Fig. 1(*a*). The eccentricity can be caused by the effects of rotordynamics, sideloads, or machining/assembly tolerances, for example. Results from the idealized domain of Fig. 1(*a*) provide basic first-order insight into the little-known eccentricity effects on wheel-space heating by the mainstream.

Specifically, the first section gives a magnified view of the ingress/egress velocity vectors within the rim seal at four circumferential locations for 25 percent eccentricity. The next section shows the effect of seal eccentricity on seal effectiveness as well as on cavity-averaged temperature and pressure. Moreover, the circumferential distribution of the ingress and egress mass flow are given for several eccentricities. The final section gives the circumferential variation of the temperature and pressure difference across the rim seal corresponding to each case of ingress/egress mass flow. In addition, the circumferential distribution of cavity local temperature and pressure is included.

An idealized turbine rim seal is shown in Fig. 1(*a*), where the diameter of the rotor is different from that of the stator. A seal gap radial clearance of 1.9 mm and an overlap of the rotor shroud and the stator shroud of 2.0 mm were used following the work of Phadke and Owen (1988). Values of 7.5, 25, and 50 percent were selected for the eccentricity of the seal. Other major dimensions of the generalized cavity considered are: (*a*) radius of the rotor $R = 0.3078$ m, (*b*) inlet radial width of the mainstream passage $H/R = 0.026$, (*c*) axial width of the cavity $s/R = 0.0612$, (*d*) radial location of cavity inlet $R_i/R = 0.904$, and (*e*) radial width of the cavity inlet $a/R = 0.00725$. The cooling air enters the cavity axially through an annular slit in the stator at temperature T_2 and also leaves axially through the radial gap between the rotor shroud and the stator shroud. The actual engine nominal conditions, according to Ivey (1990), are: (*a*) axial Reynolds number in the main pass $\mathrm{Re}_{x,m} = 3.12 \times 10^5$, (*b*) rotational Reynolds number of the rotor $\mathrm{Re}_\theta = 7.62 \times 10^6$, (*c*) cooling flow rate $C_w = 7200$, (*d*) differential pressure $\Delta P^* = -10$, (*e*) differential temperature $\Delta T^* = -4.6$, (*f*) swirl ratio at the main pass domain inlet $W/U = \tan(\pi/12)$, and (*g*) swirl ratio at the turbine cavity domain inlet $W/U = 0$. The $\mathrm{Re}_{x,m}$ above represents a mainstream axial velocity of 360 m/s, which agrees with that of Ko and Rhode (1991) and Ko et al. (1993). The latter studies included an unnecessarily large radial portion of the mainstream, which gave a correspondingly higher $\mathrm{Re}_{x,m}$.

In order to focus on seal eccentricity effects alone, the inlet flow in the mainstream was approximated as uniform in the circumferential as well as the radial direction. This approximation was made for generality. It was based on discussions with two researchers employed by turbine companies, who indicated that the mainstream boundary layer at such high velocities would have a very small effect. The bipolar coordinate system was utilized in the eccentric region between the rotor shroud and the stator shroud as discussed earlier. A highly nonuniform grid of $44 \times 44 \times 25$ in the x, r, and θ directions, respectively, was used for the computational domain shown in Fig. 1(*a*). The domain extends circumferentially from 0 to 360 deg. Comparison with solutions of finer nonuniform grids indicated that this grid gives the grid-independent circumferential distribution for ingress and egress flow rates.

Flow Distribution. The seal eccentricity of 25 percent, i.e., a 0.019 in. (0.475 mm) displacement, was selected for analyzing the flow and thermal details of the seal/cavity domain. As expected, a large recirculation zone occurs in the wheelspace due to centrifugal forces, and a gap recirculation zone (GRZ) occurs downstream of the stator shroud for all θ planes. The GRZ is fairly consistent with the "impinging jet phenomenon" described by Owen and Rogers (1989) wherein a radial wall jet in the wheelspace flows outward along the rotor shroud and then turns counterclockwise to flow inward along the stator.

Magnified views of the velocity vectors near the seal area at $\theta = 0$ and 86 deg are shown for this eccentricity case in Figs. 3(*a*) and 3(*b*). It is clearly seen how the incoming hot gas enters the seal along the outer surface of the rotor shroud. A portion of this incoming flow is turned clockwise almost 180 deg by the pressure and centrifugal force fields near the seal. The θ plane shown in Fig. 3(*a*) has the largest radial clearance and shows more inflow than outflow crossing axial station $E - F$ (see Fig. 1(*a*)). For $\theta = 86$ deg, Fig. 3(*b*) shows the slightly smaller radial clearance with a much greater portion of the incoming gas actually entering the cavity. In contrast, the coolant outflow rate is high enough to prevent ingress at $\theta = 173$ and 259 deg as shown in Figs. 3(*c*) and 3(*d*). The mainstream pressure is generally higher than that of the coolant fluid and naturally this is one contributing factor in favor of ingress. However, the concentric case computed herein gave no ingress and, as expected, gave an identical egress for all circumferential locations. For eccentric cases, the θ location of large clearance [Fig. 3(*a*)] exhibits a significantly longer GRZ downstream of the stator shroud. This extra length allows a longer period of turbulent shear interaction with the very high velocity mainstream, which gives greater velocities within the GRZ.

Only for circumferential regions of high GRZ velocity is there sufficient momentum from right to left along the rotor shroud outer surface [Fig. 3(*a*)] for ingress to occur. The transit time required for a fluid particle to undergo shear from the mainstream, turn clockwise within the GRZ and flow from right to left (Fig. 3) along the rotor shroud explains why the greatest ingress (radially integrated across station $E - F$) occurs near $\theta = 30$ deg rather than $\theta = 0$ deg.

Rim Seal Performance. Figure 4 shows the seal effectiveness $[m_c/(m_c + \bar{m}_i)]$ based on circumferentially averaged values of ingress, for all three eccentricities. Note that the coolant mass flow m_c has been kept constant and circumferentially uniform for all cases considered. As expected, as the eccentricity increases, there is a considerable decrease in sealing effectiveness. The effects of this on cavity temperature and pressure are shown in Fig. 5. Here the cavity-averaged (all axial, radial, and circumferential locations) dimensionless temperature inside the cavity rises correspondingly for increasing eccentricity. This was clearly expected because more hot gas was known to ingest into the wheelspace for higher eccentricity. The average temperature at 50 percent eccentricity is about 16 percent higher than that for the concentric case. This is supported by the results of Lowry and Keeton (1987) who showed that, for the first two three-dimensional test cases, mentioned in an earlier section, the three-dimensional effect on the flow pattern in the cavity was very limited, giving only a slight increase of the average cavity temperature. However, their third case with a seal eccentricity of 75 percent indicated a significantly higher ingress. This gave an 80 percent increase in the temperature at the center of the cavity, compared with that of the basecase.

Figure 5 further shows a decreasing cavity-averaged pressure in the presence of an increasing eccentricity. This is attributed to the particular balance of pressure and centrifugal forces for this geometry at engine pressures, temperatures, and Reynolds numbers. Interestingly, Lowry and Keeton found an increased cavity-averaged pressure for their eccentric CFD analysis of the high-pressure fuel pump rim seal cavity. However, this is not

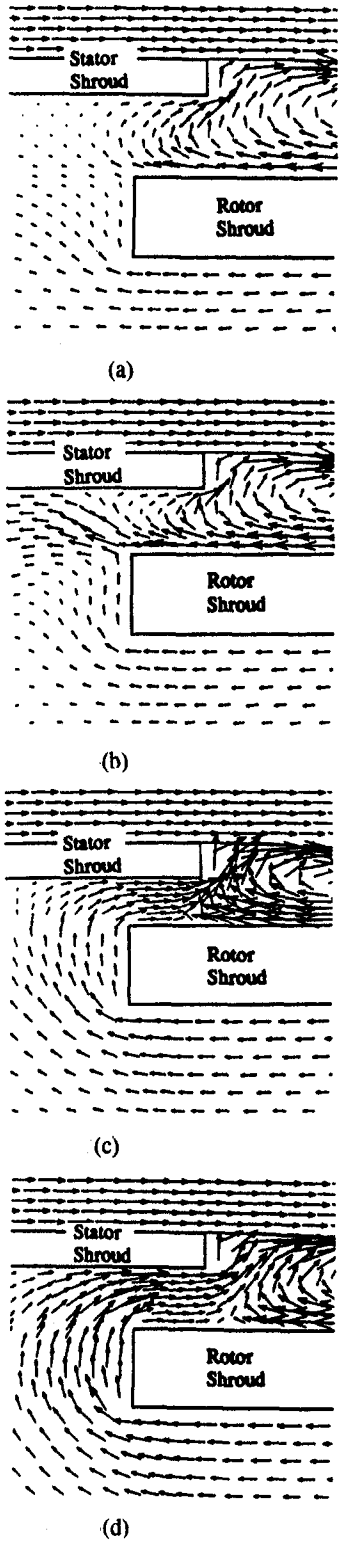

Fig. 3 Magnified view of velocity vectors near the gap region at 25 percent eccentricity for: (*a*) θ = 0 deg, (*b*) θ = 86.4 deg, (*c*) θ = 172.8 deg, and (*d*) θ = 259.2 deg (the mainstream vectors have been scaled down 3.75 times for clarity)

too surprising since their case had a drastically different cavity geometry and: (*a*) no stator shroud, (*b*) a mainstream pressure and temperature of 3600 psi (24.8 MPa) and 1700 R (945 K), and (*c*) a rotor speed of 37,000 rpm.

The asymmetric distributions of the mass ingress and egress for eccentricities of 7.5, 25, and 50 percent are shown in Figs.

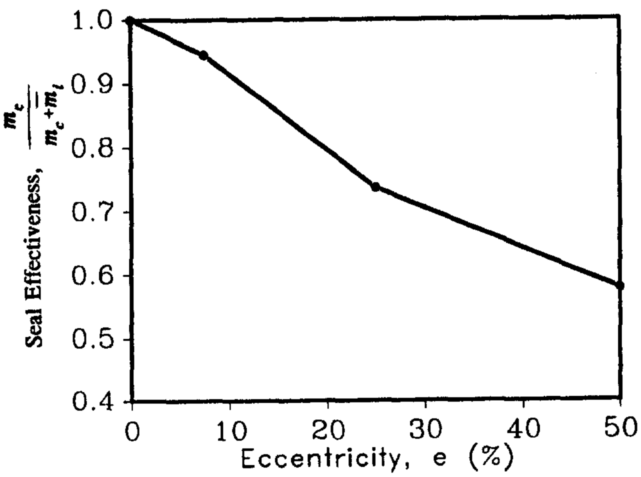

Fig. 4 Effect of eccentricity on the sealing effectiveness

6(*a*), 6(*b*), and 6(*c*), respectively. Also shown here for reference is the distribution of seal radial clearance S_c. It is interesting that the ingress occurs for all three nonzero eccentricity cases considered, whereas none was found for zero eccentricity. Further, the magnitude of the ingress and the egress increases with eccentricity. As explained above, this is attributed primarily to increasing GRZ velocities at θ locations of larger seal radial clearance. Regardless of nonzero eccentricity, the maximum ingress occurs at θ = 30 deg and the maximum egress at about θ = 260 deg. As was mentioned previously, this ingress–egress cycle of the flow through the seal has a phase shift with respect to the S_c cycle because the swirl velocity convects the ingress in the circumferential direction.

Cavity Temperature and Pressure. Figures 7(*a*) through 7(*c*) show the circumferential temperature distribution at positions A and B (see Fig. 1(*a*)). Engine designers are especially interested in the temperature of location B because a primary cause of blade reliability concern is overheating of the blade root or retainer. As stated earlier, the ingested hot gases first contact the stator near location A, before mixing with the circulating flow in the cavity. The circumferential location with the highest temperature is shifted from θ = 30 deg, where most of the ingress occurs, to about 75 deg at position A and to about 180 deg at B because of a fluid particle's helical path between the seal and the particular location. Table 1 also gives the highest temperatures and their locations (hot spots) on the rotor as well as the stator for each case. These results are in good agreement with those in Fig. 7. That is, as the eccentricity

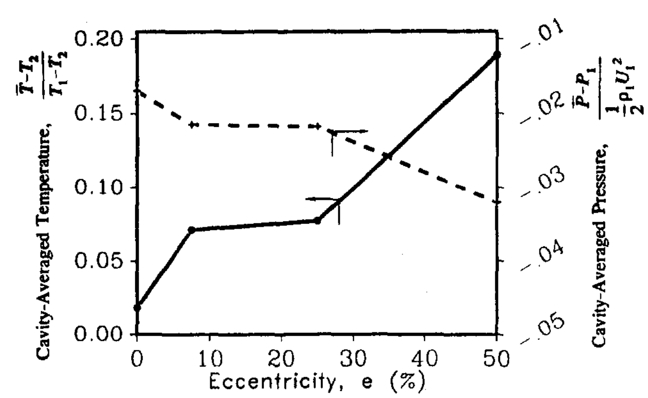

Fig. 5 Variation of the cavity-averaged temperature and pressure with eccentricity

increases, the hot spot temperature increases considerably. It is also shown that positions A and B are close to the hot spots on the rotor and the stator, respectively. In addition, since the rotor is well protected by the shroud arrangement as well as by the coolant, the increase in temperature on the rotor with eccentricity is not severe like that on the stator.

Figures 8(a) through 8(c) show the circumferential pressure variation for the three eccentricities at positions A and D (see Fig. 1(a)). Since these figures give the circumferential distribution of pressure drop between A and D for the corresponding circumferential distribution of ingress in Figs. 6(a) through 6(c), one may develop or test a simple algebraic leakage model using these consistent figures. Further, the temperature difference between T_1 and the cavity-averaged values from Fig. 7(a) through 7(c) may be utilized to develop or test a simple model of cavity heating.

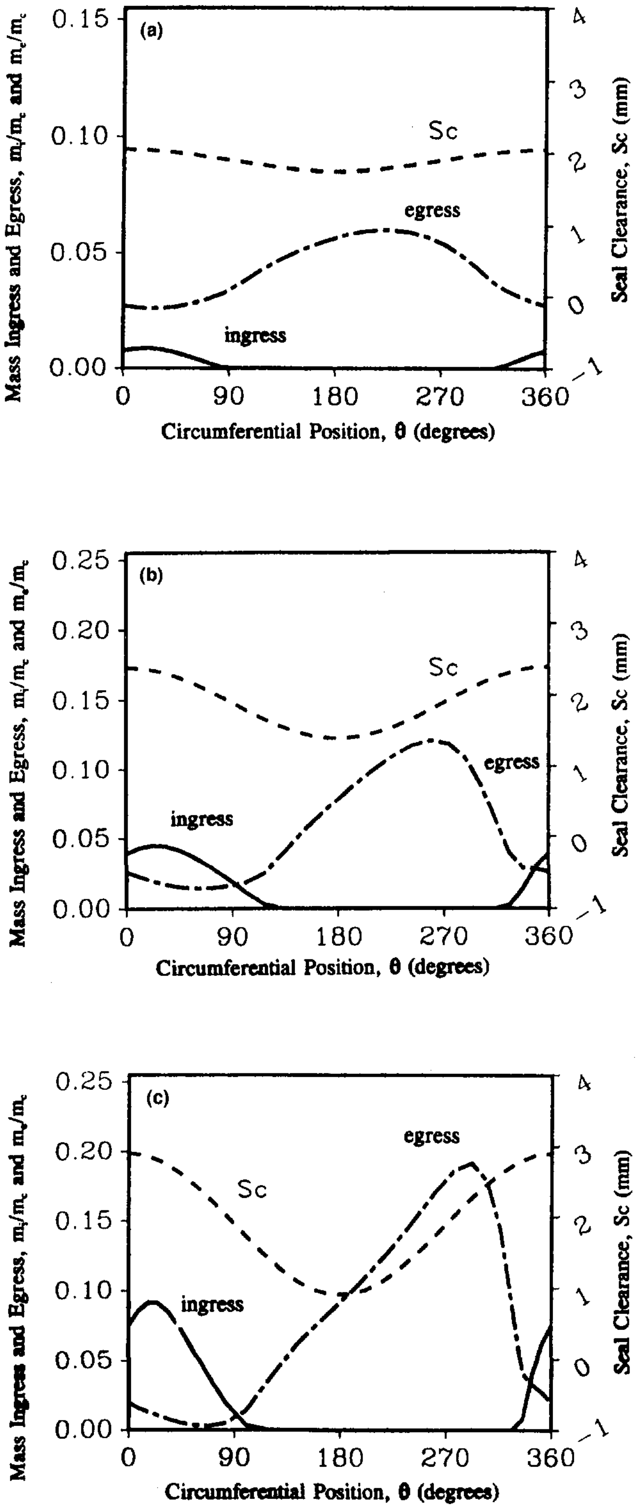

Fig. 6 Circumferential variation of the mass ingress and mass egress as well as seal clearance for: (a) 7.5 percent eccentricity, (b) 25 percent eccentricity, and (c) 50 percent eccentricity

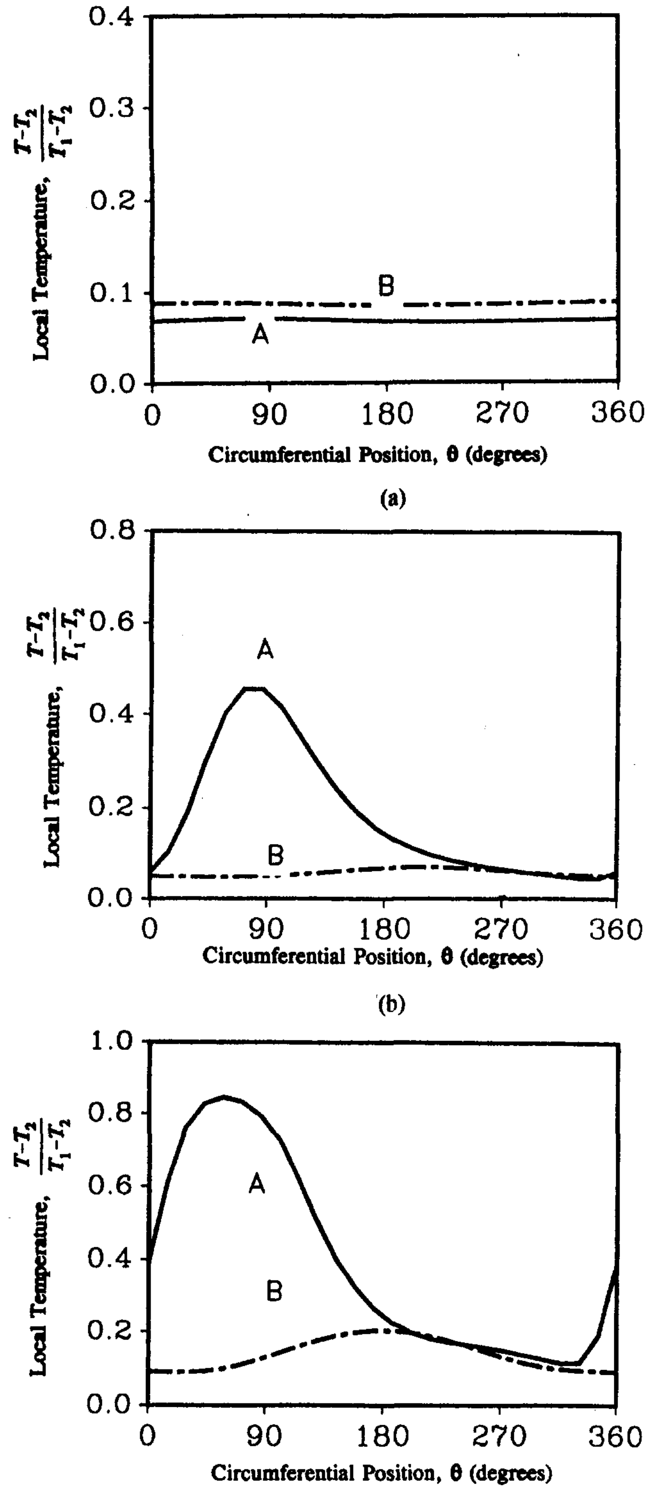

Fig. 7 Circumferential variation of the dimensionless temperature at positions A and B (defined in Fig. 1(a)) for: (a) 7.5 percent eccentricity, (b) 25 percent eccentricity, and (c) 50 percent eccentricity

Table 1 Hottest location and its temperature

	e (%)	$\frac{T_{max} - T_2}{T_1 - T_2}$	r/R	θ (degrees)
Rotor	0	0.044	0.978	-
	7.5	0.078	0.978	14.4
	25	0.095	0.978	201.6
	50	0.216	0.906	129.6
Stator	0	0.018	0.94	-
	7.5	0.075	0.945	86.4
	25	0.552	0.993	71.3
	50	0.941	0.995	44.1

The pressure in the mainstream is significantly higher than that inside the cavity for the concentric case. For eccentric cases the circumferential variation of pressure at locations A and D increases with eccentricity as expected. Here the pressure at position D is generally higher than that at A, except for a region between $\theta = 190$ deg and $\theta = 280$ deg for the 50 percent eccentricity case [Fig. 8(c)]. This circumferential region gives a higher cavity pressure in accordance with the ingress–egress circumferential distribution. Specifically, Fig. 6(c) shows the sharp peak of egress near 280 deg which conserves mass across the rim seal by compensating for: (a) the small egress from $\theta = 0$ deg to $\theta = 120$ deg and (b) the total ingress. One would expect the pressure at A to be large in the high egress θ range to allow the large egress that occurs there.

For more global information, Figs. 9 and 10 show that the hot gases first contact the upper left corner of the cavity for 25 percent eccentricity. The strong cooling air jet recirculating in the cavity dilutes the high temperature of the ingested hot gases and cools the rotor. This is the reason why the greatest changes in temperature occur at the upper left corner region, and the average temperature of the cavity rises only 8 percent over that of the cooling air. However, a significant ingestion to the inside of the cavity occurs at larger eccentricities, causing the cavity-average temperature to increase by about 18 percent at 50 percent eccentricity.

Conclusion

A fully elliptic, three-dimensional Navier–Stokes model was developed from the axisymmetric version previously used for examining axisymmetric subproblems such as the gap recirculation zone (GRZ) of rim seal cavities. The somewhat unexpected flow computations (Ko and Rhode, 1991) have been corroborated by measurements as explained by Elovic (1991) and by independent computations revealed by Hendricks (1993) and Ivey (1991). The three-dimensional version of the code has a generalized capability of transitioning between any number and type of orthogonal coordinate systems in order to allow a wide range of eccentric seal configurations. The recent circumferential extension of this model was verified by comparison with rotordynamic measurements of a smooth, eccentric annular seal. The computer code was used to solve the three-dimensional problem of a rim seal interfacing with a mainstream at various eccentricities. Both the coolant and mainstream flow were fixed at nominal engine temperatures, pressures, and Reynolds numbers; all walls were adiabatic so that temperature indicates ingress heating in addition to slight frictional heating in order to isolate this effect from the wall heat convection effect.

Specific findings include:

1 For nonzero eccentricities, both ingress and egress were found between $\theta \approx -30$ and 100 deg, which encompasses the maximum radial clearance at $\theta = 0$ deg. Other θ planes showed only egress. This circumferential distribution was primarily attributed to higher GRZ velocities at θ locations of larger seal radial clearance.

2 Due to the circumferential convection effect resulting from the presence of swirl velocity, the maximum ingress was found at approximately $\theta = 30$ deg for all nonzero eccentricities. This leads to the circumferential location of maximum rotor temperature, depending on eccentricity, in the wide range from $\theta = 15$ to 202 deg and the location of maximum stator tempera-

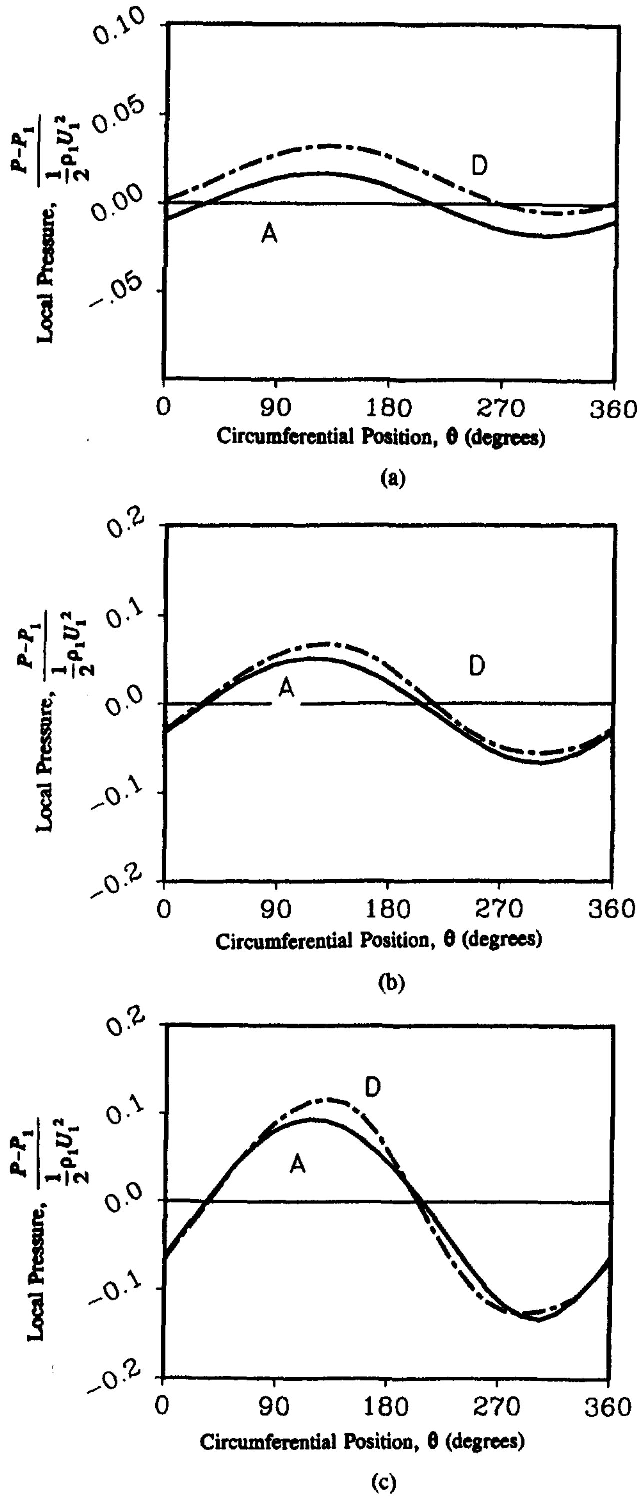

Fig. 8 Circumferential variation of the dimensionless pressure at positions A and D (defined in Fig. 1(a)) for: (a) 7.5 percent eccentricity, (b) 25 percent eccentricity, and (c) 50 percent eccentricity

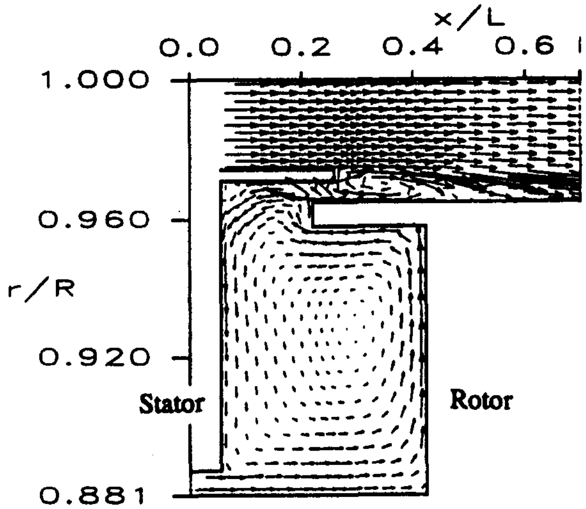

Fig. 9 Velocity vectors with 25 percent eccentricity for the θ = 86.4 deg plane (mainstream vectors have been scaled down 3.75 times for clarity)

ture from θ = 45 to 90 deg. Moreover, the ingress gives a blade root/retainer temperature rise from the concentric basecase (no ingress) of 390 percent at 50 percent eccentricity and a rise of 77 percent at 7.5 percent eccentricity.

3 The role of an increasing eccentricity producing a substantially decreasing seal effectiveness was examined, along with the corresponding substantial increase and decrease of cavity-averaged temperature and pressure, respectively.

4 Apparently cavity-averaged pressure can either decrease or increase over that of the concentric base case depending on geometry and operating conditions.

5 The seal gap recirculation zone (GRZ) in the wake of the stator shroud was found to mix the mainstream and egress fluid so that the rim seal always encounters fluid at essentially the mainstream temperature.

6 A significant once-per-revolution thermal cycle was found primarily for the e = 50 percent case, and the circumferential distribution of local temperature indicates the nature of this variation.

7 The difference between the circumferential distribution of the local pressure at locations A and D, which constitutes the distribution of local seal pressure drop corresponding to the distributions of ingress presented in Figs. 6(a)

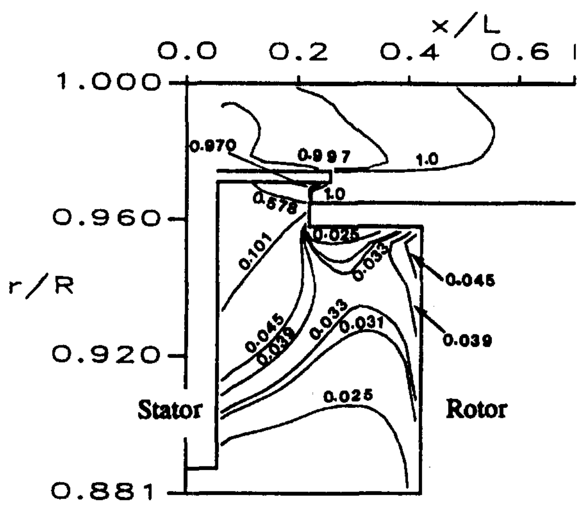

Fig. 10 Dimensionless isotherm contours with 25 percent eccentricity for the θ = 86.4 deg plane

through 6(c), allows the development or testing of simple seal ingress prediction models at engine nominal temperatures, pressures, and Reynolds number of the coolant flow, mainstream, and disk.

8 The centrifugal force dominated the overall flow pattern as expected and prevented the ingress from directly contacting the rotor for eccentricities less than 25 percent.

Acknowledgments

The authors are indebted to B. V. Johnson for his interest and assistance in identifying two important references. The authors are also grateful to the Supercomputer Center at the Texas A & M University for a grant of CRAY-YMP computer time.

References

Avva, R. K., Ratcliff, M. L., and Leonard, A. D., 1989, "CFD Analysis of Rotating Disk Flows," in: *Recent Advances and Applications in Computational Fluid Dynamics*, ASME FED-Vol. 103, pp. 99–105.

Avva, R., Smith, C., and Singhal, A., 1990, "Comparative Study of High and Low Reynolds Number Versions of $k-\epsilon$ Models," Paper No. AIAA 90-0246.

Baskharone, E., 1990, private communication.

Chew, J. W., 1991, "A Theoretical Study of Ingress for Shrouded Rotating Disk Systems With Radial Outflow," ASME JOURNAL OF TURBOMACHINERY, Vol. 113, pp. 91–98.

Dietzen, F. J., and Nordmann, R., 1986, "Finite Difference Analysis for the Rotordynamic Coefficients of Turbulent Seals in Turbopumps," *Proceedings of Rotordynamic Instability Problems in High Performance Turbomachinery*, NASA CP-2443, Texas A&M University, pp. 269–284.

Elovic, E., 1991, General Electric Co., public discussion during technical sessions, International Gas Turbine and Aeroengine Congress, Orlando, FL.

Gosman, A. D., and Pun, W. M., 1974, "Calculations of Recirculating Flows," Research Report, Report No. HTS/74/2, Department of Mechanical Engineering, Imperial College, London, United Kingdom.

Hamabe, K., and Ishida, K., 1992, "Rim Seal Experiments and Analysis of a Rotor-Stator System With Nonaxisymmetric Main Flow," ASME Paper No. 92-GT-160.

Hendricks, R. C., 1993, NASA Lewis Research Center, public discussion during technical sessions, International Gas Turbine and Aeroengine Congress, Cincinnati, OH.

Ivey, P., 1990, personal communication.

Ivey, P., 1991, personal communication.

Ko, S. H., and Rhode, D. L., 1990, "Derivation and Testing of a New Multi-scale $k-\epsilon$ Turbulence Model," Paper No. AIAA-90-0243.

Ko, S. H., and Rhode, D. L., 1991, "Thermal Details in a Rotor–Stator Cavity at Engine Conditions With a Mainstream," ASME JOURNAL OF TURBOMACHINERY, Vol. 114, pp. 446–453.

Ko, S. H., Rhode, D. L., and Guo, Z., 1993, "Computed Effects of Rim Seal Clearance and Cavity Width on Thermal Distributions," ASME Paper No. 93-GT-419.

Kamal, M. M., 1966, "Separation in the Flow Between Eccentiric Rotating Cylinders," ASME *Journal of Basic Engineering*, Vol. 88, pp. 717–724.

Leonard, B. P., 1979, "A Stable and Accurate Convective Modelling Procedure Based on Quadratic Upstream Interpolation," *Computer Methods in Applied Mechanics and Engineering*, Vol. 19, pp. 59–98.

Lowry, S. A., and Keeton, L. W., 1987, "Space Shuttle Main Engine High Pressure Fuel Pump Aft Platform Seal Cavity Flow Analysis," NASA Technical Paper No. 2685.

Owen, J. M., and Rogers, R. H., 1989, *Flow and Heat Transfer in Rotating-Disc System: Vol. 1. Rotor-Stator Systems*, Research Studies Press, Taunton.

Patankar, S. V., 1980, *Numerical Heat Transfer and Fluid Flow*, McGraw-Hill, New York.

Phadke, U. P., and Owen, J. M., 1988, "Aerodynamic Aspects of the Sealing of Gas-Turbine Rotor–Stator Systems, Part 2: The Performance of Simple Seals in a Quasi-Axisymmetric External Flow," *Int. J. Heat Fluid Flow*, Vol. 9, No. 2, pp. 106–112.

Pope, S. B., 1978, "The Calculation of Turbulent Recirculation Flows in General Orthogonal Coordinates," *Journal of Computational Physics*, Vol. 26, pp. 197–217.

Rhode, D. L., Demko, J. A., Traegner, U. K., Morrison, G. L., and Sobolik, S. R., 1986, "Prediction of Incompressible Flow in Labyrinth Seals," ASME *Journal of Fluids Engineering*, Vol. 108, pp. 19–25.

Rhode, D. L., Hensel, S. J., and Guidry, M. J., 1992, "Labyrinth Seal Rotordynamic Force Using a Three-Dimensional Navier–Stokes Code," ASME *Journal of Tribology*, Vol. 114, pp. 683–689.

Rhode, D. L., Hensel, S. J., and Guidry, M. J., 1993, "Three-Dimensional Computation of Rotordynamic Force Distributions in a Labyrinth Seal," *STLE Tribology Transactions*, Vol. 36, No. 3, pp. 461–469.

Sturgess, G. J., and Datta, P., 1988, "Calculation of Flow Development in Rotating Passages for Cooled Gas Turbine Blades," ASME Paper No. 88-GT-XXX.

Vaughan, C. M., and Turner, A. B., 1987, "Numerical Prediction of Axisymmetric Flow in a Rotor–Stator System With an External Mainstream Flow," *Proceedings 5th International Conference on Numerical Methods in Laminar and Turbulent Flows*, Swansea, United Kingdom.

Virr, G. P., Chew, J. W., and Coupland, J., 1994, "Application of Computational Fluid Dynamics to Turbine Disk Cavities," ASME JOURNAL OF TURBOMACHINERY, Vol. 116, pp. 701–708.

Williams, M., Chen, W. C., Bache, G., and Eastland, A., 1991, "An Analysis Methodology for Internal Swirling Flow Systems With a Rotating Wall," ASME JOURNAL OF TURBOMACHINERY, Vol. 113, pp. 83–90.

R. E. Chupp
Combustion Turbine Engineering Development,
Westinghouse Electric Corporation,
Orlando, FL 32826

G. F. Holle
Consultant,
Show Low, AZ 85901

Generalizing Circular Brush Seal Leakage Through a Randomly Distributed Bristle Bed

Brush seals have established a niche in the gas-to-gas sealing against leakage in modern turbine engines. The variable nature of the brush during operation makes leakage prediction difficult. A simple semi-empirical model based on an effective brush thickness parameter has been successfully used to correlate and predict brush seal leakage in engine environments. The model was extended to correlate a range of brush densities using a physically realistic brush thickness. Later, the model was based on mean diametric brush properties for a large range of circular brush seal geometries. However, the best basis for modeling bristle distribution was unknown. This paper proposes a solution to the distribution problem by assuming a randomly distributed bristle bed. A random distribution leads to a rectangular array model that is supported by the quality of leakage data generalization. Applying the resultant effective thickness parameter to predict brush seal performance in turbine engines is discussed.

Introduction

Brush seals are a densely packed bed of directionally compliant bristles clamped between a narrow upstream retainer and a wide downstream retainer that provide mechanical support for the sealed pressure load. Normally, the installation is in a static member with the brush rubbing or in incipient contact with a dynamic member. Due to the possible degradation of the seal caused by liquid lubricant contamination, the brush seal is ordinarily used in gas-to-gas sealing applications.

In gas turbine engines, typical brush seals are circular to control leakage and cooling airflow between the rotors and static panels. The brush is composed of many fine, round wires, e.g., 0.002 to 0.003-in. diameter, set at a specific angle with respect to shaft rotation. The wires pack themselves quasi-randomly within this bristle bed, which is constrained by upstream and downstream washers. Figure 1 is a schematic of a circular brush seal installed in a dynamic application.

Research on brush seals has burgeoned in response to their potential uses and performance superiority over conventional labyrinth seals. A representative bibliography of recent brush seal papers is provided in Appendix A.

Despite all of the erudite analyses and design innovations proposed, a need remains for a relatively simple method of: evaluating the sealing quality of brush seals after manufacture, and estimating their leakage performance when installed in a gas turbine engine environment. The effective thickness of the brush is a viable concept for a single parameter correlation of leakage performance throughout a broad range of geometries and operating conditions. Chupp et al. (1991) showed that the effective thickness model could generalize the static and dynamic leakage of a brush seal at different operating environments. Holle et al. (1992) introduced a reduced effective thickness parameter that correlated the leakage performance for brush seals of significantly different brush densities. Dowler et al. (1992) extended the model to accommodate small and large circular brush seals.

Contributed by the International Gas Turbine Institute and presented at the 39th International Gas Turbine and Aeroengine Congress and Exposition, The Hague, The Netherlands, June 13–16, 1994. Manuscript received by the International Gas Turbine Institute February 9, 1994. Paper No. 94-GT-71. Associate Technical Editor: E. M. Greitzer.

The effective thickness model is based upon pressure drop correlations for flow through a uniform matrix of staggered tubes (Knudsen and Katz, 1958). However, the selection of the uniform tube distribution that best represented the bristle bed on average was a distinctly heuristic choice. Modi (1992) presented an analysis for randomly distributed cylinders in contact along axial elements of their surfaces that suggests a preferred geometry for uniformly staggered tubes to represent the average bristle distribution in a brush. The effective thickness model in this paper is based on the random bristle bed distribution proposed by Modi.

Model Description

The effective brush thickness, B, is a synthetic geometric parameter of the brush that, in conjunction with the other physical geometry of the brush seal design, allows the direct prediction of sealing performance in any environment. B is a measure of the compactness of the brush. For a given number of bristles, the larger the value of B, the more loosely compacted the bristles are and the greater the leakage. The success of the single-parameter, effective thickness, in generalizing brush seal leakage throughout a range of operating environments, is based on empirical data for the Reynolds number regime and theoretical parameters for the "local" Mach number or Euler number effects. The application of such a flow model to a linearized (straight) brush seal was presented by Chupp et al. (1991). The derivation of the model is based on the assumption that the entire flow passes directly through the upstream area of the brush and remains normal to the bristles. In reality, radial flow must occur in some regions of the brush in order for the flow to exit out the smaller exit gap beneath the rear carrier (see Fig. 1). However, the pressure drop is predominantly due to the axial flow component because the interstitial radial flow areas are significantly larger than the associated axial flow area. The neglected radial flow does not obviate the efficacy of the model. The effective thickness experiences an artificial reduction to account for the additional resistance encountered by the radial inflow through the part of the brush supported by the rear carrier. The influence on leakage of rear carrier clearance, CL, and $CL/\Delta R$, as well as other variables such as brush/journal interference and journal speed, which are not specifically considered by this simple model, can be correlated with the reduced effective

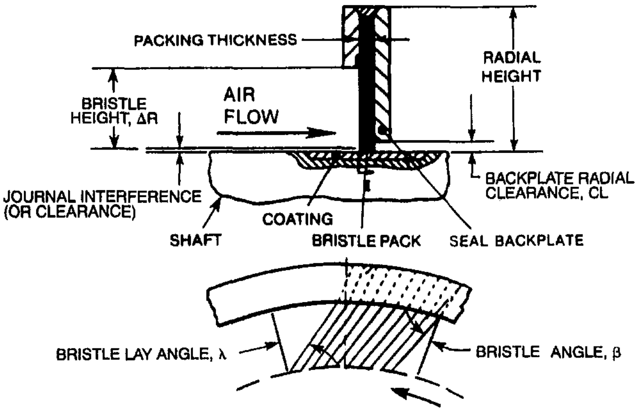

Fig. 1 Brush seal schematic

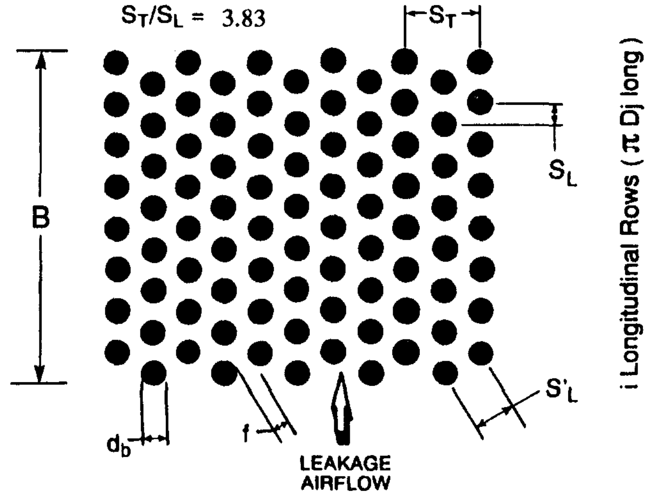

Fig. 2 Uniformly staggered cylinder arrangement modeling an average random bristle bed

thickness parameter through the statistical analysis of experimental data.

In the model, it is assumed that the average brush thickness is constant over the length of the bristles. Additionally, it is assumed that the bristle ends just touch the journal surface or there is an interference. If a brush/journal clearance exists, a parallel flow path analysis between the upstream plenum and downstream plenum of the seal must be added to describe the brush seal leakage through this path. The additional model could take the form of Fanno flow through a rough walled annulus.

The generality of the effective thickness parameter is rooted in the theory of models. Consequently, an appropriate geometric representation of the bristle bed is required for the derivation of a successful model. The simple original model of Chupp et al. (1991) was based on a square array of staggered cylinders. The predictive capability was excellent for leakage in a wide range of environments, but the effective thickness of the associated brush was unrealistically thin. Therefore, the revised model of Holle et al. (1992) utilized hexagonal packing to obtain the theoretical minimum effective thickness,

$$B_{\min} = \frac{d_b}{2}\left[\sqrt{3}\,\frac{nd_b}{\cos\lambda} + 1\right]$$

The more realistic effective thickness was achieved at the expense of a slight deterioration in leakage generality. The model based on the hexagonal array of staggered cylinders was used by Dowler et al. (1992) to correlate the leakage through a range of circular brush seal sizes. However, the selection of a representative uniform array of staggered cylinders for modeling the average bristle distribution in the brush was strictly heuristic. Recently, Modi (1992) proposed that the average bristle distribution in the brush is best described as random. His permeability model for flow through a brush seemed to verify the hypothesis. He noted that experiments with cylinders dropped into containers result in an average solidity of 0.82 relative to the ideal maximum solidity of 0.907 for contiguous hexagonal packing. Based on this observation, a new effective thickness model was formulated for a maximum brush solidity of 0.82. The maximum solidity of any uniform array of staggered cylinders is uniquely related to its distribution,

$$S_T/S_L = \frac{\pi}{\sigma}$$

The randomly distributed bristle bed, $\sigma = 0.82$, specifies a uniform rectangular array of staggered cylinders with $S_T/S_L = 3.83$. A schematic of the uniform matrix representing the randomly distributed bristle bed is shown in Fig. 2. The random

Nomenclature

A = cross-sectional flow area, in.^{2}
b = intercept
B = effective brush thickness, in.
CL = backplate radial clearance, in.
d = diameter, in.
D = diameter, in.
f = friction factor
g = conversion factor = 32.174 lbm ft/(lbf sec^2)
G = mass velocity, lbm/(in^2 sec)
HD = hydraulic diameter, in
i = number of longitudinal rows
j = number of transverse rows
m = slope
n = bristle density, bristles/in. of cir.
N = total number of bristles in the brush
p = static pressure, psia
P = total pressure, psia
Pr = pressure ratio = P_u/p_d
R = gas constant, lbf ft/(lbm R)
Re = Reynolds number
S = spacing, in.
$S'_L = \sqrt{S_L^2 + [S_T/2]^2}$, flow area scale dimension between adjacent bristles, in.
T = fluid temperature, °F or R
W = flow rate, lbm/sec
β = bristle angle (acute) at the upstream washer inside diameter = D_u, deg
γ_m = radial average bristle angle (at D_m), deg
$\Delta R = (D_u - D_j)/2$ = bristle height, in.
λ = bristle lay angle at the journal, deg
μ = fluid viscosity, lbm/(ft sec)
σ = maximum solidity
ϕ = flow factor, $W\sqrt{T_u}/(P_u A_u)$, lbm$\sqrt{R}$/(lbf sec)

Subscripts

act = best approximation to the actual average thickness of the brush
b = bristle diameter
d = downstream of seal
f = flow
j = journal
KL = transition
L = longitudinal
m = mean (average)
min = minimum
max = maximum
T = turbulent, total, or transverse
u = upstream of seal
v = volumetric
o = effective thickness at zero axial flow area
1 = backplate or characteristic point 1
2 = characteristic point 2

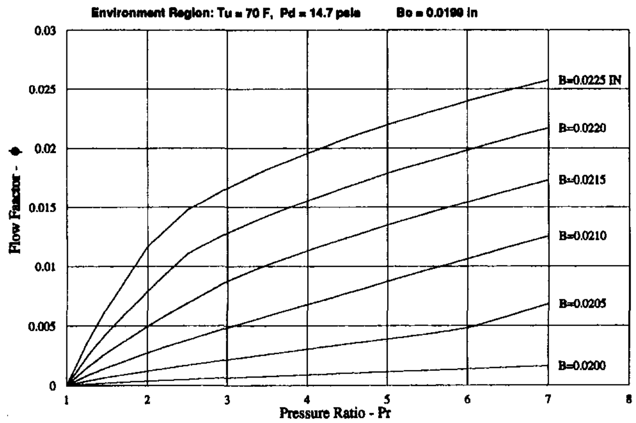

Fig. 3 Typical flow model results

packing of the brush seal satisfies requirements for both leakage generality and realistic effective thickness values.

The effect of Reynolds number on the leakage characteristics of a brush seal was based on recommendations given by Knudsen and Katz (1958) for correlations of pressure drop for flow across bundles of uniformly staggered tubes derived from other publications. A Gunter and Shaw (1945) correlation is used to model the laminar flow regime, and a Jakob (1938) correlation the turbulent flow regime. The data for staggered tube arrangements from Kays et al. (1954) demonstrate the smooth character of the friction factor curve in the transition flow regime. Knudsen and Katz (1958) show that the logarithm of the friction factor during transition from laminar to fully turbulent flow is nearly a linear function of the logarithm of the Reynolds number based on the modified volumetric equivalent diameter. The laminar end of the transition flow characteristic was determined at $Re_v = 100$ from the Gunter and Shaw (1945) correlation, and the fully turbulent end of the transition flow characteristic at $Re_b = 5000$ from the Jakob (1938) correlation. In the model, if flow rate falls neither in the laminar regime, $Re_v < 100$, nor in the turbulent regime, $Re_b > 5000$, performance is determined by the flow characteristic derived for the logarithm linearized transition regime bridging the two.

Within a limited Reynolds number range in a nominal operating environment, the "local" brush seal characteristics can be based on the corrected flow function, ϕ, which generalizes Mach number or Euler number effects as a function of pressure ratio,

$$\phi = \frac{W\sqrt{T_u}}{P_u A_u}$$

Brush seal testing at Allison Gas Turbines (Holle and Krishnan, 1990), Cross Manufacturing, and Teledyne CAE (Chupp and Nelson, 1993; Chupp and Dowler, 1993) has shown first-order independence of leakage on back plate clearance provided that the bristle bed is undistorted by mechanical forces. Consequently, the upstream brush area capable of admitting leakage flow,

$$A_u = \frac{\pi}{4}(D_u^2 - D_j^2)$$

is an appropriate reference area for generalizing the brush seal leakage. Then the brush seal performance can be represented by a graph similar to Fig. 3, which shows how flow factor ϕ calculated from the model varies with pressure ratio for constant B values for a given seal geometry. As B approaches B_o the bristles are solidly packed against each other and ϕ approaches zero. As B increases, the bristle pack for the same bristle geometry opens up to provide more flow. This figure demonstrates that the effective thickness of the brush, B, is a function of operating pressure ratio and corrected flow parameter at a specific environmental region.

The bristle density, n (number of bristles in a unit circumferential length of the bore), can be generalized over a range of values as demonstrated by Holle et al. (1992) by using a ratio of the effective thickness, B, to the thickness of the brush at the journal (bore) when the flow goes to zero, B_{min}. However, the extension of this generality to circular brush seals with the new random bristle distribution requires a modification to the model. Geometric scaling by referencing the effective thickness to the mean brush diameter, D_m, is the basis of the leakage correlation for any size of circular brush seal. When the bore geometry of the brush is translated to D_m, the reduced effective thickness parameter correlates the leakage of any circular brush configuration. Dowler et al. (1992) showed that the linearized (straight) geometry of the hexagonal array brush model is equally applicable to the average geometry of an extensive range of small to large diameter brush seals when the leakage analysis is based on the brush configuration at its mean diameter:

$$D_m = \frac{D_j + D_u}{2}$$

The geometry of the randomly distributed bristle bed is established from the brush design variables defined at the bore, D_j, and is extrapolated to a bristle bed geometry at the mean brush diameter, D_m, on the assumption that brush effective thickness remains constant. An additional zero flow reference thickness at the mean brush diameter, B_o, is required to account for the perturbation of the random distribution during translation to D_m. The reduced effective thickness parameter, B/B_o, is a "sealing efficiency" that compares the effective compactness of a brush to the theoretical compactness necessary to stop all leakage through the bristle distribution at the mean diameter. This B/B_o ratio is always greater than 1.0. A complete outline of the computation of effective thickness, B, reduced effective thickness, B/B_o, and an approximation to the actual brush thickness at the bore, B_{act}, for a circular brush seal with a randomly distributed bristle bed is provided in Appendix B.

Implicit to the derivation of the effective thickness model is the assumption that the flow through the brush is isothermal.

Table 1 Parameter values for brush seals evaluated

Symbols in Fig's	Designation in Fig's	Data Source	T (F)	Pr max	db (in)	λ (deg)	n (bristles/in)	Dj (in)	Du (in)	Bo (in)
	TCAE1000	Teledyne CAE	490	4.66	0.0028	45	2300	5.100	5.672	0.0198
	TCAE600	Teledyne CAE	180	5.33	0.0028	45	2300	5.100	5.672	0.0197
	NASAECC	NASA	70	3.91	0.0028	47.5	2471	5.379	5.954	0.0220
	NASAINT	NASA	70	8.99	0.0020	53	4329	1.500	1.850	0.0184
	CROSSTHK	CROSS Mfg.	70	6.44	0.0028	45	3500	5.100	5.832	0.0287
	EGGSPWS	EG&G Sealol - 2x thick.	90	2.94	0.0028	45	4337	5.395	6.165	0.0354
	EGGLDS	EG&G Sealol - std thick	95	3.57	0.0028	45	2168	5.395	6.165	0.0181
	ALSNDYN	Allison dynamic data	70	6.00	0.0028	45	2300	5.100	5.672	0.0199
	ALSNSTAT	Allison static data	70	6.00	0.0028	45	2300	5.100	5.672	0.0198

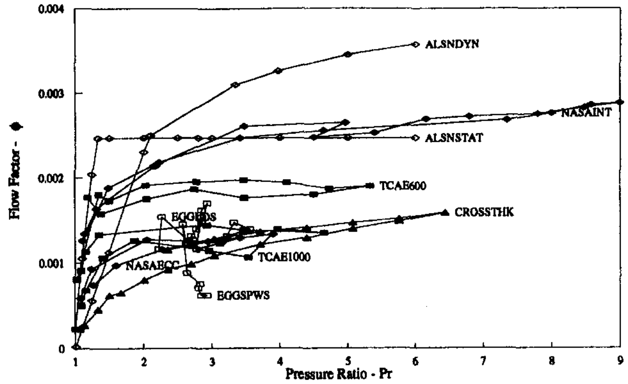

Fig. 4 Measured leakage flow performance from five brush seal data sources

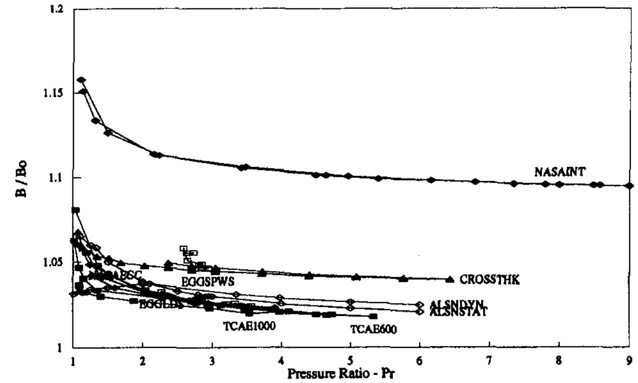

Fig. 6 Comparison on nondimensional effective thickness parameter for random model

Any internal heat transfer effects must be compensated by the modification of the upstream total temperature. Rub energy generated within a broken-in brush seal with nominal leakage can usually be neglected. However, the heating of upstream air by pumping from large high-speed disks should be accounted for in Tu.

Results

The random array brush model was evaluated for circular brush seals with bore diameters 1.5 in. and larger and included a representative variety of bristle diameters, lay angles, and bristle densities. Comparisons of identical brush seals tested by different facilities and the same brush seal tested under significantly different environments have been analyzed. In this paper, the random array brush model will be compared against leakage data for nine brush seals from five data sources. Table 1 provides the design geometry for each of the seals considered and the source of the test data.

Leakage flow data for the nine seals are plotted in Fig. 4 as flow factor, ϕ, resulting from the applied pressure ratio, P_u/p_d. The data represent two different seal manufacturers, five different rigs, six different test procedures, and two different test temperature levels for both static (without shaft rotation) and dynamic conditions. The flow factor data in this figure vary significantly from seal to seal even though flow factor accounts for the seal frontal flow area. The extensive flow range of the data demonstrates the need for an analytical tool for correlating the leakage performance of the seals with the design parameters.

The effective thickness, B, derived from the leakage data for each seal using the random array model provides a relatively simple basis for predicting leakage performance of that seal in any rig or engine environment. The B values calculated from the model are plotted in Fig. 5. The wide range of B is indicative of the differences in actual seal thickness. The model is able to generalize the effects of the environment on leakage flow through a specific seal or seal design. For example, the brush seal that was tested at Teledyne in an unheated and heated rig (TCAE600 and TCAE1000, respectively) with an air temperature difference of 300°F yielded a significantly different flow factor characteristic as shown in Fig. 4. However, the calculated effective thicknesses, B, for two sets of data in Fig. 5 nearly coincide.

The influence of brush seal size and design on the effective thickness, B, can be normalized by dividing B by B_o. The leakage performance of all brush seals when represented by their reduced effective thickness, B/B_o, tend to a common band of values. This characteristic can be seen in Fig. 6. The variations encountered in this correlation are due to mechanical effects of contributions such as brush/journal interference, vibration, and windage for example. Some divergence is undoubtedly due to the linearized model geometry and the idealized flow assumptions. However, a principal contributor to B/B_o variability is the quality of manufacture of the seal. A valuable asset of the model is the detection of an abnormal increase in B/B_o associated with a seal fabrication problem. Brush seal quality is hard to inspect. Leakage testing is one way of determining if the seal meets its application requirements. B/B_o provides a parameter for defining the quality of manufacture using measured leakage in an inspection rig to assure that the seal will perform to specifications in an engine. Figure 7 shows the ability of the random array model to generalize circular brush seal size. The B/B_o values plotted in this figure are from the data in Fig. 6 for the maximum pressure ratio tested for each seal where the brush would be the most compacted. The line shown in Fig. 7 is based on a linear variation of B/B_o with $1/Dj$ so that B/B_o approaches 1.0 as Dj reaches infinity. The trend of increasing B/B_o with decreasing

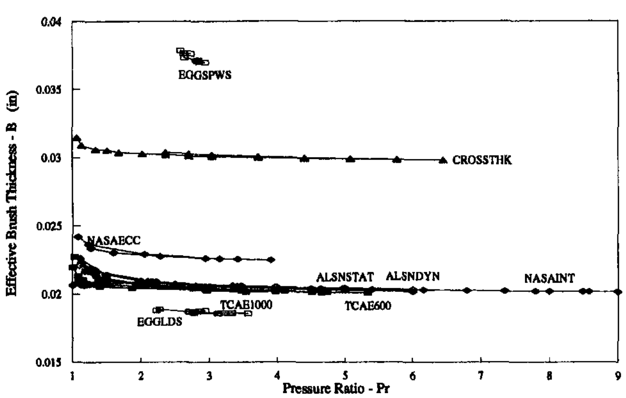

Fig. 5 Comparison of effective brush thickness, *B*, for random model

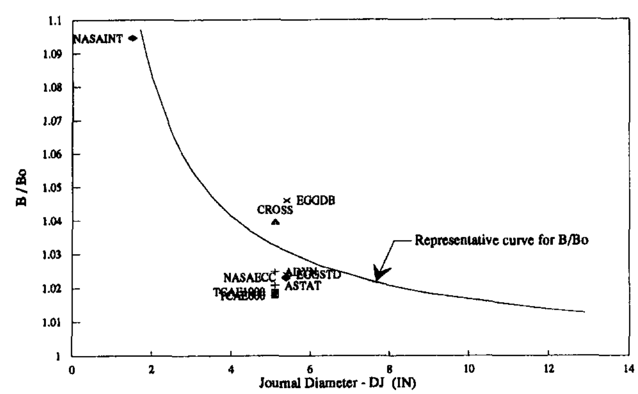

Fig. 7 Trend of quality with brush scale at maximum pressure ratio

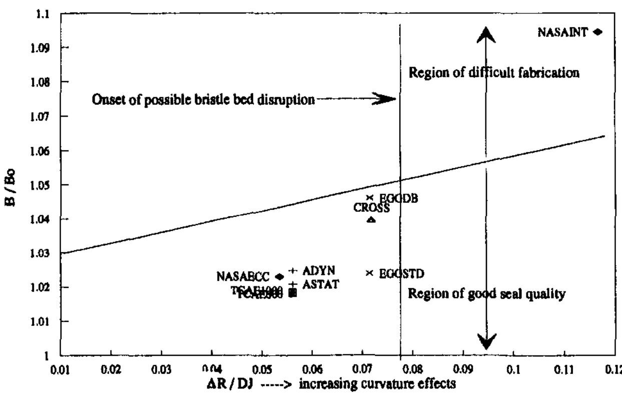

Fig. 8 Effect of brush annulus size on seal efficiency at maximum pressure ratio

Dj indicates the problems in the fabrication process with small sizes. The knee in the data at *Dj* near 4 in. with an abrupt rise of B/B_o to near 1.1 for $Dj \leq 2$ in. is attributable to the difficulty of manufacturing brush seals of smaller sizes.

Other design parameters exert secondary influences on brush seal leakage. Several that have been identified by analysis of these test data with the random array model are: (1) brush/journal design interference, (2) bristle density, and (3) brush annulus height. The data of Fig. 6 show a distinct increase in B/B_o as interference and/or bristle density increase(s). Figure 8 defines the rate of increase for B/B_o as the brush annulus height, ΔR, increases within the size region of quality manufacturing, i.e., $Dj > 2$ in. Surprisingly, one parameter that does not appear to influence leakage significantly is the brush compliance, i.e., bristle softness or lack of stiffness. Figure 9 shows the variation of B/B_o with individual bristle length-to-diameter ratio, which is a measure of bristle stiffness for the similar bristle materials involved. B/B_o does not vary significantly over the range of bristle compliance for the band of good quality brush seals.

The presumed causes for the secondary effects on brush seal efficiency can be assigned to mechanical action and/or fabrication difficulty, as tabulated below:

Design parameter	Mechanical action	Fabrication difficulty
interference	design interference	
bristle density		bristle density
brush annulus height	annulus height	annulus height

Ambient tests of a selected matrix of brush seal geometries can quantify the contributions and consequent trade-offs for all of the secondary brush seal design parameters. A statistical (regression) analysis of the empirical data for B/B_o generated by the random array model will produce curve-fitted functions of these individual effects on seal leakage. This information can be used to optimize brush seal designs for specific engine requirements.

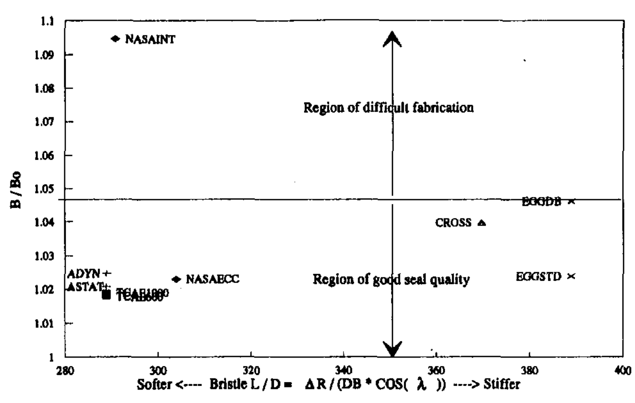

Fig. 9 Effect of brush compliance on seal efficiency at maximum pressure ratio

Conclusions

The effective thickness model has demonstrated the ability to generalize brush seal leakage performance from ambient to in situ engine environments. The randomly distributed bristle bed has been shown to be an effectual, and probably preferred, choice for synthesizing the effective thickness of circular brush seals. The reduced effective thickness parameter, B/B_o, normalizes the sealing efficiency of circular brush seals for an extensive range of sizes and brush designs. It is also capable of identifying good or poor brush seal quality that may be due to design selection or fabrication problems.

Analysis of the results from the effective thickness model applied to test data for a variety of brush seal sizes and designs has produced the following discoveries:

- B/B_o for good quality brush seals of conventional design should be between 1.0 (minimum possible value) and 1.05 at pressure ratios sufficiently high to compact the brush.
- B/B_o tends to increase as the seal size, *Dj*, decreases. This is probably the result of increasing difficulty with brush fabrication as curvature increases. The effect is more pronounced for brush bores smaller than 4 in.
- B/B_o increases as:
  - brush/journal interference increases (probably effect of mechanical action)
  - bristle density increases (probably effect of fabrication difficulty)
  - brush annulus height increases (probably the effect of a combination of mechanical action and fabrication difficulty)
- B/B_o remains constant with changing brush compliance.

These findings lead to the conclusions that:

- The results of ambient temperature dynamic (or speed corrected static) leakage performance tests, when converted to *B*, can be translated to expected leakage at elevated pressure and temperature environments in a gas turbine engine.
- A nominal or average B/B_o value or functional relation can be used for preliminary design or development applications of brush seals in gas turbine engines. The value for B/B_o can be obtained from plots similar to Fig. 6 for the effect of pressure ratio, *Pr*, and Figure 7 for the effect of scale, *Dj*.
- The range of B/B_o for brush seals of similar design, but not necessarily of similar size, can be used as an acceptance criterion for brush seal shipping or receiving inspection static flow tests.

It is recommended that the random array model be used as the basis for a multiple regression analysis of available leakage data to identify the impact of secondary brush seal design parameters.

References

Chupp, R. E., Holle, G. F., and Dowler, C. A., 1991, "Simple Leakage Flow Model for Brush Seals," AIAA Paper No. 91-1913.

Chupp, R. E., and Nelson, P., 1993, "Evaluation of Brush Seals for Limited-Life Engines," *AIAA Journal of Propulsion and Power*, Vol. 9, No. 1, pp. 113–118.

Chupp, R. E., and Dowler, C. A., 1993, "Performance Characteristics of Brush Seals for Limited-Life Engines," ASME *Journal of Engineering for Gas Turbines and Power*, Vol. 115, pp. 390–396.

Dowler, C. A., Chupp, R. E., and Holle, G. F., 1992, "Simple Effective Thickness Model for Circular Brush Seals," AIAA Paper No. 92-3192.

Gunter, A. Y., and Shaw, W. A., 1945, "A General Correlation of Friction Factors for Various Types of Surfaces in Crossflow," *Transactions of the ASME*, Vol. 67, No. 8, pp. 643–660.

Holle, G. F., and Krishnan, M. R., 1990, "Gas Turbine Engine Brush Seal Applications," AIAA Paper No. 90-2142.

Holle, G. F., Chupp, R. E., and Dowler, C. A., 1992, "Brush Seal Leakage Correlations Based on Effective Thickness," *Proceedings of the Fourth International Symposium on Transport Phenomena and Dynamics of Rotating Machinery (ISROMAC-4)*, Honolulu, HI, Apr. 5–8, pp. 296–304.

Jakob, M., 1938, *Transactions of the ASME*, Vol. 60, p. 381.

Kays, W. M., London, A. L., and Lo, R. K., 1954, *Transactions of the ASME*, Vol. 76, p. 387.

Knudsen, J. G., and Katz, D. L., 1958, "Chap. 11. Flow in the Shell Side of Multitube Heat Exchangers," *Fluid Dynamics and Heat Transfer*, McGraw-Hill, New York, pp. 323–341.

Modi, V., 1992, "Modeling Bristle Lift-Off in Idealized Brush Seal Configurations," *Proceedings of the Fourth International Symposium on Transport Phenomena and Dynamics of Rotating Machinery (ISROMAC-4)*, Honolulu, HI, Apr. 5–8, pp. 623–632.

APPENDIX A

Representative Bibliography of Brush Seal Literature

Addy, G., 1995, "Results of Contacting Seal Testing at NASA Lewis Research Center," *Seals Flow Code Development—95*, NASA Lewis Research Center Seals Workshop, Cleveland, OH, June 14–15.

Addy, H. E., Jr., Steinetz, B. M., Hendricks, R. C., Howe, H. W., and Flowers, J., 1995, "Preliminary Results of Silicon Carbide Brush Seal Testing at NASA Lewis Research Center," AIAA Paper No. 95-2763.

Atkinson, E., and Bristol, B., 1992, "Effects of Material Choices on Brush Seal Performance," *Lubrication Engineering*, Vol. 48, No. 9, Sept., pp. 740–746.

Bayley, F. J., and Long, C. A., 1993, "A Combined Experimental and Theoretical Study of Flow and Pressure Distributions in a Brush Seal," ASME *Journal of Engineering for Gas Turbines and Power*, Vol. 115, pp. 404–410.

Basu, P., Datta, A., Johnson, R., Loewenthal, R., and Short, J., 1993, "Hysteresis and Bristle Stiffening Effects of Conventional Brush Seals," AIAA Paper No. 93-1996.

Bill, R. C., 1991, "Army Research Concerns in Engine Sealing," *Seals Flow Code Development-91*, NASA Lewis Research Center Seals Workshop, Cleveland, Ohio, Mar., pp. 75–82.

Braun, M. J., Hendricks, R. C., Canacci, V. A., and Kazmierchak, M., 1990, "Flow Visualization in a Single Simulated Brush Seal," *Proceedings of the 3rd International Symposium on Transport Phenomena and Dynamics of Rotating Machinery (ISROMAC-3)*, Hemisphere Publishing.

Braun, M. J., Hendricks, R. C., and Canacci, V. A., 1990, "Non-intrusive Qualitative and Quantitative Flow Characterization and Bulk Flow Model for Brush Seals," *Proceedings of the Japanese International Tribology Conference*, Nagoya, Japan.

Braun, M. J., Hendricks, R. C., and Canacci, V. A., 1990, "Flow Visualization in a Simulated Brush Seal," ASME Paper No. 90-GT-217, 35th ASME International Gas Turbine and Aeroengine Congress and Exposition, Brussels, Belgium, June 11–14, 1990.

Braun, M. J., Canacci, V. A., and Hendricks, R. C., 1990, "Flow Visualization and Motion Analysis for a Series of Four Sequential Brush Seals," AIAA Paper No. 90-2482.

Braun, M. J., 1991, "Seals Research at the University of Akron," *Seals Flow Code Development-91*, NASA Lewis Research Center Seals Workshop, Cleveland, OH, p. 101, Mar.

Braun, M. J., Canacci, V. A., and Hendricks, R. C., 1991, "Flow Visualization and Quantitative Velocity and Pressure Measurements in Simulated Single and Double Brush Seals," *STLE Tribology Transactions*, Vol. 34, No. 1, pp. 70–80.

Braun, M. J., Hendricks, R. C., and Yang, Y., 1991, "Effects of Brush Seal Morphology in Leakage and Pressure Drops," AIAA Paper No. 91-2106.

Braun, M. J., Hendricks, R. C., Carlile, J. A., and Yoder, D., 1992, "Investigation of Flows in Bristle and Fiberglass Brush Seal Configurations," *Proceedings of the Fourth International Symposium on Transport Phenomena and Dynamics of Rotating Machinery (ISROMAC-4)*, Honolulu, HI, Apr. 5–8, pp. 315–325.

Braun, M. J., 1992, "Experimental and Analytical Investigation of Brush Seals," *Seals Flow Code Development-92*, A. D. Liang and R. C. Hendricks, eds., NASA Conference Publication 10124, pp. 181–196.

Braun, M. J., and Kudriavtsev, V. V., 1993, "Brush Seal Numerical Simulation: Concepts and Advances," *Seals Flow Code Development—93*, A. D. Liang and R. C. Hendricks, eds., NASA Conference Publication 10136, pp. 159–197.

Braun, M. J., and Kudriavtsev, V. V., 1995, "A Numerical Simulation of a Brush Seal Section and Some Experimental Results," ASME JOURNAL OF TURBOMACHINERY, Vol. 117, pp. 190–202.

Braun, M. J., Dzodzo, M., and Kudriavtsev, V. V., 1995, "Tribological Activities at the University of Akron," *Seals Flow Code Development—95*, NASA Lewis Research Center Seals Workshop, Cleveland, OH, June 14–15.

Carlile, J. A., Hendricks, R. C., and Yoder, D. A., 1993, "Brush Seal Leakage Performance With Gaseous Working Fluids at Static and Low Rotor Speed Conditions," ASME *Journal of Engineering for Gas Turbines and Power*, Vol. 115, pp. 397–403.

Carlile, J. A., Hendricks, R. C., Hibbs, R. I., McVey, S. E., and Scharrer, J. K., 1993, "Preliminary Experimental Results for a Cryogenic Brush Seal Configuration," AIAA Paper No. 93-2535.

Chew, J. W., Lapworth, B. L., and Milener, F. J., 1995, "Mathematical Modeling of Brush Seals," to be published in the *International Journal of Heal and Fluid Flow*.

Childs, D., 1992, "Dynamic Coefficients for Multiple Brush Seals," *Seals Flow Code Development-92*, A. D. Liang and R. C. Hendricks, eds., NASA Conference Publication 10124, pp. 211–214.

Chupp, R. E., 1990, "Brush Seal Investigation, Final Report for Period Sept. 1988–July 1990," Report No. WRDC-TR-90-2123, Aero Propulsion and Power Laboratory, Wright Research and Development Center, Wright-Patterson Air Force Base, Ohio, Dec.

Chupp, R. E., Holle, G. F., and Dowler, C. A., 1991, "Simple Leakage Flow Model for Brush Seals," AIAA Paper No. 91-1913.

Chupp, R. E., and Nelson, P., 1993, "Evaluation of Brush Seals for Limited-Life Engines," *AIAA Journal of Propulsion and Power*, Vol. 9, No. 1, pp. 113–118.

Chupp, R. E., and Dowler, C. A., 1993, "Performance Characteristics of Brush Seals for Limited-Life Engines," ASME *Journal of Engineering for Gas Turbines and Power*, Vol. 115, pp. 390–396.

Chupp, R. E., Johnson, R. P., and Loewenthal, R. G., 1995, "Brush Seal Development for Large Industrial Gas Turbines," AIAA Paper No. 95-3146.

Conner, K. J., and Childs, D. W., 1990a, "Rotordynamic Coefficient Test Results for a 4-Stage Brush Seal," AIAA Paper No. 90-2139.

Conner, K. J., and Childs, D. W., 1990b, "Rotordynamic and Leakage Characteristics of a 4-Stage Brush Seal, Final Report for Period Oct. 1988–Aug. 1990," Report No. WL-TR-91-2013 (TL-SEAL-4-90), Weapons Laboratory, Kirtland Air Force Base, NM, Dec.

Conner, K. J., and Childs, D. W., 1992, "Rotordynamic and Leakage Characteristics of a 4-Stage Brush Seal, Final Report for Period 30 Oct. 1988–30 Aug. 1992," Report No. WL-TR-92-2125, Weapons Laboratory, Kirtland Air Force Base, NM, Dec.

Derby, J., and England, R., 1992, "Tribopair Evaluation of Brush Seal Applications," AIAA Paper No. 92-3715.

Derby, J., 1992, "Tribopair Evaluation of Materials Brush Seal Applications," *Seals Flow Code Development-92,* A. D. Liang and R. C. Hendricks, eds., NASA Conference Publication 10124, pp. 245–246.

Dowler, C. A., Chupp, R. E., and Holle, G. F., 1992, "Simple Effective Thickness Model for Circular Brush Seals," AIAA Paper No. 92-3192.

Dowler, C., 1992, "Air Force Brush Seal Programs," *Seals Flow Code Development-92,* A. D. Liang and R. C. Hendricks, eds., NASA Conference Publication 10124, pp. 149–156.

Ferguson, J. G., 1988, "Brushes as High Performance Gas Turbine Seals," ASME Paper No. 88-GT-182, 33rd ASME International Gas Turbine and Aeroengine Congress and Exposition, Amsterdam, The Netherlands, June 6–9, 1988.

Flower, R., 1990, "Brush Seal Development System," AIAA Paper No. 90-2143.

Gorelov, G. M., Reznik, V. E., and Tsibizov, V. I., 1988, "Experimental Study of Brush Seal Flow Characteristics and Comparison With a Labyrinth Seal," Izvestiya VUZ. Aviatsionnaya Tekhnika, Vol. 31, No. 4, pp. 43–46 [Allerton Press].

Gross, D., 1990, "Estimating Leakage through Doors for Smoke Control," *Fire Technology,* Vol. 26, No. 1, pp. 75–81.

Hendricks, R. C., Braun, M. J., and Mullen, R. L., 1990, "Brush Seal Configurations for Cryogenic and Hot Gas Applications," *Advanced Earth-to-Orbit Propulsion Technology,* R. J. Richmond and S. T. Wu, eds., Vol. 2, NASA CP-3092-VOL-2, May 15–17, pp. 78–90.

Hendricks, R. C., Braun, M. J., Cannacci, V. A., and Mullen, R. L., 1990, "Brush Seals in Vehicle Tribology," Paper E-5712, presented at the 1990 Leeds/Lyon Symposium, Leeds, England, Sept.

Hendricks, R. C., 1991, "Seals Related Research at NASA Lewis Research Center," *Seals Flow Code Development-91,* NASA Lewis Research Center Seals Workshop, Cleveland, OH, Mar. 1991, pp. 53–65.

Hendricks, R. C., Schlumberger, J., Braun, M. J., Choy, F., and Mullen, R. L., 1991, "A Bulk Flow Model of a Brush Seal System," ASME Paper No. 91-GT-325, 36th ASME International Gas Turbine and Aeroengine Congress and Exposition, Orlando, Florida, June 3–6, 1991.

Hendricks, R. C., Proctor, M., Schlumberger, J., Braun, M., and Mullen, R., 1991, "Some Preliminary Results of Brush Seal/Rotor Interference Effects on Leakage at Zero and Low RPM Using a Tapered-Plug Rotor," AIAA Paper No. 91-3390.

Hendricks, R. C., Carlile, J. A., and Liang, A. D., 1992, "Some Sealing Concepts—A Review, Part B: Brush Seal Systems," *Proceedings of the Fourth International Symposium on Transport Phenomena and Dynamics of Rotating Machinery (ISROMAC-4),* Honolulu, HI, Apr. 5–8, pp. 265–276.

Hendricks, R. C., Carlile, J. A., and Yoder, D., 1992, "Investigation of Flows in Bristle and Fiberglass Brush Seal Configurations," *Proceedings of the Fourth International Symposium on Transport Phenomena and Dynamics of Rotating Machinery (ISROMAC-4),* Honolulu, HI, April 5–8, pp. 315–325.

Hendricks, R. C., Liang, A. D., Childs, D. W., and Proctor, M. P., 1992, "Development of Advanced Seals for Space Propulsion Turbomachinery," NASA TM-105659.

Hendricks, R. C., Carlile, J. A., Liang, A. D., Steinetz, B. M., Easter, B. T., Onstott, J. W., and Howe, H., 1992, "Static Brush Seals for Propulsion Systems Interfaces," *Advanced Earth to Orbit Propulsion Technology,* NASA Conference Publication 3174.

Hendricks, R. C., Carlile, J. A., and Liang, A. D., 1992, "Brush Seal Bristle Flexure and Hard Rub Characteristics," *Seals Flow Code Development-92,* A. D. Liang and R. C. Hendricks, eds., NASA Conference Publication 10124, pp. 95–116.

Hendricks, R. C., Griffin, T. A., Bobula, G. A., Bill, R. C., and Howe, H. W., 1992, "Integrity Testing of Brush Seal in a T-700 Engine," *Seals Flow Code Development-92,* A. D. Liang and R. C. Hendricks, eds., NASA Conference Publication 10124, pp. 117–138.

Hendricks, R. C., Griffin, T. A., Bobula, G. A., Bill, R. C., and Howe, H. W., 1993, "Integrity Testing of Brush Seal in Shroud Ring of T-700 Engine," ASME Paper No. 93-GT-373, 38th ASME International Gas Turbine and Aeroengine Congress and Exposition, Cincinnati, Ohio, May 24–27, 1993.

Hendricks, R. C., Carlile, J. A., and Liang, A. D., 1993, "Brush Seal Low Surface Speed Hard-Rub Characteristics," NASA TM-106169; AIAA Paper No. 93-2534.

Hendricks, R. C., Flower, R., and Howe, H., 1993, "Development of a Brush Seals Program Leading to Ceramic Brush Seals," *Seals Flow Code Development—93,* A. D. Liang and R. C. Hendricks, eds., NASA Conference Publication 10136, pp. 99–117.

Hendricks, R. C., Griffin, T. A., Bobula, G. A., Bill, R. C., Hull, D. R., and Csavina, K. R., 1993, "Some Metallographic Results for Brush Bristles and Brush Segments of a Shroud Ring Brush Seal Tested in a T-700 Engine," *Seals Flow Code Development—93,* A. D. Liang and R. C. Hendricks, eds., NASA Conference Publication 10136, pp. 325–366.

Hendricks, R. C., Griffin, T. A., Kline, T. R., Csavina, K. R., Pancholi, A., and Sood, D., 1994, "Relative Performance Comparison between Baseline Labyrinth and Dual Brush Compressor Discharge Seals in a T-700 Engine Test," ASME Paper No. 94-GT-266.

Hendricks, R. C., 1995, "Turbomachine Sealing," *Seals Flow Code Development–95,* NASA Lewis Research Center Seals Workshop, Cleveland, OH, June 14–15.

Holle, G. F., and Krishnan, M. R., 1990, "Gas Turbine Engine Brush Seal Applications," AIAA Paper No. 90-2142.

Holle, G. F., Chupp, R. E., and Dowler, C. A., 1992, "Brush Seal Leakage Correlations Based on Effective Thickness," *Proceedings of the Fourth International Symposium on Transport Phenomena and Dynamics of Rotating Machinery (ISROMAC-4),* Honolulu, HI, Apr. 5–8, pp. 296–304.

Howe, H., Jarrabet, G., and Tolokan, R., 1993, "Ceramic Brush Seals," SBIR Final Report, NAS3-26319.

Howe, H., 1993, "Ceramic Brush Seals Development," *Seals Flow Code Development—93,* A. D. Liang and R. C. Hendricks, eds., NASA Conference Publication 10136, pp. 133–150.

Kudriavtsev, V. V., 1993, "Numerical and Analytical Study of Flows in Cylindrical Arrays," Ph.D. Thesis, Moscow Aviation Institute, Moscow, Russia.

Kudriavtsev, V. V., and Braun, M. J., 1995, "Interstage Disk-Cavity/Brush Seal Numerical Flow Visualization Study," ASME Paper No. 95-GT-378.

Liang, A. D., Hendricks, Shapiro, W., and Aggarwal, B., 1992, "Development of a Knowledge Based System for Turbopump Seals," *Advanced Earth to Orbit Propulsion Technology,* NASA Conference Publication 3174, NASA George C. Marshall Space Flight Center, Marshall Space Flight Center, AL, May 19–21, pp. 440–446.

Liang, A. D., and Hendricks, eds., 1992, "Seals Flow Code Development-92," NASA Conference Publication 10124.

Loewenthal, R., 1993, "Current Developments in Brush Seals," *Seals Flow Code Development–93,* A. D. Liang and R. C. Hendricks, eds., NASA Conference Publication 10136, pp. 199–208.

Loewenthal, R. G., 1995, "PRDA-II and III Brush Seal Development Programs at EG&G," *Seals Flow Code Development–95,* NASA Lewis Research Center Seals Workshop, Cleveland, OH, June 14–15.

Long, C. A., and Marras, Y., 1995, "Contact Force Measurements Under a Brush Seal," "Interstage Disk-Cavity/Brush Seal Numerical Flow Visualization Study," ASME Paper No. 95-GT-211.

Mahler, F., and Boyes, E., 1995, "The Application of Brush Seals in Large Commercial Jet Engines," AIAA Paper No. 95-2617.

Modi, V., 1992, ''Modeling Bristle Lift-Off in Idealized Brush Seal Configurations,'' *Proceedings of the Fourth International Symposium on Transport Phenomena and Dynamics of Rotating Machinery (ISROMAC-4),* Honolulu, HI, Apr. 5–8, pp. 623–632.

Modi, V., 1992, ''Modeling Bristle Lift-Off in Idealized Brush Seal Configurations,'' *Seals Flow Code Development-92,* A. D. Liang and R. C. Hendricks, eds., NASA Conference Publication 10124. pp. 217–232.

Mullen, R. L., Braun, M. J., and Hendricks, R. C., 1990, ''Numerical Modeling of Flows in Simulated Brush Seal Configurations,'' AIAA Paper No. 90-2141.

Munson, J., 1991, ''Seals Development Activities at Allison Turbine Division,'' *Seals Flow Code Development-91,* NASA Lewis Research Center Seals Workshop, Cleveland, OH, Mar., p. 107.

NASA Lewis Research Center, 1993, ''Technical Support Package, High-Temperature, Pressure-Assisted Brush Seal,'' *NASA Tech Briefs,* LEW-15086, Cleveland, OH.

Proctor, M. P., 1993, ''Brush Seals for Cryogenic Applications,'' *Seals Flow Code Development–93,* A. D. Liang and R. C. Hendricks, eds., NASA Conference Publication 10136, pp. 119–130.

Proctor, M. P., 1995, "Cryogenic Brush Seal Test Results," *Seals Flow Code Development–95,* NASA Lewis Research Center Seals Workshop, Cleveland, OH, June 14–15.

Przekwas, A. J., Athavale, M. M., Hendricks, R. C., and Liang, A. D., 1992, ''Development of a CFD Code for Accurate 3D Analysis of Cylindrical Seals,'' *Advanced Earth to Orbit Propulsion Technology,* NASA Conference Publication 3174.

Scharrer, J., 1991, ''Seal Technology at Rocketdyne,'' *Seals Flow Code Development-91,* NASA Lewis Research Center Seals Workshop, Cleveland, OH, Mar. 1991, pp. 127–132.

Scharrer, J. K., and Hendricks, R. C., 1992, ''Results of Cryogenic Brush Seal Testing,'' *Seals Flow Code Development-92,* A. D. Liang and R. C. Hendricks, eds., NASA Conference Publication 10124, pp. 215–216.

Schlumberger, J. A., Proctor, M. P., and Hendricks, R. C., 1991, ''Eccentricity Effects on Leakage of a Brush Seal at Low Speeds,'' NASA TM-105141.

Shapiro, W., Artiles, A., Aggarwal, B., Walowit, J., and Athavale, M. M., 1992, ''Numerical, Analytical, Experimental Study of Fluid Dynamic Forces in Seals,'' Final Interim Report No. 1, NASA CR-189113, Mechanical Technology, Inc., Latham, NY, Apr.

Sharatchandra, M. C., and Rhode, D. L., 1996, ''Computed Effects of Rotor-Induced Swirl on Brush Seal Performance, Part 1: Leakage Analysis,'' to be published in the ASME *Journal of Tribology.*

Sharatchandra, M. C., and Rhode, D. L., 1996, ''Computed Effects of Rotor-Induced Swirl on Brush Seal Performance, Part 2: Bristle Force Analysis,,'' to be published in the ASME *Journal of Tribology.*

Sousa, M., 1993, ''Brush Seals for Turbine Engine Fuel Conservation,'' *Seals Flow Code Development–93,* A. D. Liang and R. C. Hendricks, eds., NASA Conference Publication 10136, pp. 151–157.

Steinetz, B. M., and Sirocky, P. J., 1990, ''High Temperature, Flexible Pressure-Actuated, Brush Seal,'' Report No. PAT-APPL-7-617752, NASA Lewis Research Center, Cleveland, OH, Nov. 26, 1990 (Patent date Dec. 31, 1991).

Steinetz, B. M., Mutharasan, R., Du, G. W., Miller, J. H., and Ko, F., 1993, ''Engine Panel Seals for Hypersonic Engine Applications: High Temperature Leakage Assessments and Flow Modeling, Addendum,'' NASA LEW-15086, NASA Lewis Research Center, Cleveland, OH.

Steinetz, R. C., and Hendricks, R. C., 1995, ''Aeropropulsion Seal Development,'' *Seals Flow Code Development—95,* NASA Lewis Research Center Seals Workshop, Cleveland, OH, June 14–15.

Technetics Corporation, 1991, ''Brush Seals,'' Bulletin TC 850, 1991.

Tolokan, R. P., Jarrabet, G. P., and Howe, H. W., 1992, ''Metal Fiber Based Clearance Control Seals for Gas Turbine Engines,'' *Proceedings of the Fourth International Symposium on Transport Phenomena and Dynamics of Rotating Machinery (ISROMAC-4),* Honolulu, HI, Apr. 5–8, pp. 571–580.

Valenti, M., 1995, "Upgrading Jet Turbine Technology," *Mechanical Engineering,* Dec., pp. 56–60.

Voorhees, W., 1992, ''Brush Seals for Turbine Engine Fuel Conservation,'' *Seals Flow Code Development-92,* A. D. Liang and R. C. Hendricks, eds., NASA Conference Publication 10124, pp. 233–244.

Withers, P. A., 1992, ''High Pressure Compressor Delivery Brush Seal of the International Aero Engines (IAE) V2500-A1 Gas Turbine Engine,'' *Seals Flow Code Development-92,* A. D. Liang and R. C. Hendricks, eds., NASA Conference Publication 10124, pp. 275–280.

APPENDIX B

Brush Seal Leakage Flow Model

Given Parameters:

Brush Geometry: d_b (in), λ (deg), n (bristles/in. cir.), D_j (in.), D_u (in.)

Seal Environment: p_d (psia), P_u (psia), T_u (R)

Properties of Air:

$$R = 53.342 \frac{\text{lbf ft}}{\text{lbm °F}}$$

$$\mu = 7.3066 \times 10^{-7} \frac{T_u^{3/2}}{T_u + 198.6} \frac{\text{lbm}}{\text{ft sec}}$$

Calculations: Assumed value of B—effective brush thickness, in.

Geometry:

$$N = \pi D_j n$$

$$a = \left[\frac{B - d_b}{\pi D_j \cos \lambda}\right] * 1.916$$

$$j = \frac{\sqrt{8Na + 1} - 1}{2a}$$

$$i = \frac{2N}{j}$$

$$B_{\min} = \frac{d_b}{2}\left[\sqrt{3}\,\frac{nd_b}{\cos \lambda} + 1\right]$$

$$\beta = \arcsin\left(\frac{D_j}{D_u} \sin \lambda\right) \text{ (rad)}$$

$$\gamma_m = \frac{\beta - \dfrac{D_j}{D_u}\lambda + \sin \beta\left[\ln \dfrac{D_u}{D_j}\left(\dfrac{1 + \cos \beta}{1 + \cos \lambda}\right)\right]}{1 - \dfrac{D_j}{D_u}}$$

where λ is in rads.

$$D_m = \frac{D_j + D_u}{2}$$

$$S_T = \frac{2\pi D_j \cos \lambda}{j}$$

$$S_{T,m} = \frac{D_m}{D_j}\left(\frac{\cos\gamma_m}{\cos\lambda}\right)S_T$$

$$S_L = S_T/3.83$$

$$S'_{L,m} = \sqrt{S_L^2 + \left(\frac{S_{T,m}}{2}\right)^2}$$

$$\frac{A_f}{A_u} = \frac{j(S'_{L,m} - d_b)}{\pi D_m \cos\gamma_m}$$

$$HD_{v,m} = \frac{4B\cos\gamma_m}{\pi n d_b} - d_b$$

$$HD'_m = (HD_{v,m} + d_b)\frac{A_f}{A_u}$$

Flow Conditions:

$$\rho = \left(\frac{144}{2R}\right)\frac{P_u + p_d}{T_u}$$

$$\Delta P = P_u - p_d$$

Starting Solution: Assume a value of ϕ

$$G_{\max} = \frac{\phi P_u}{\left(\frac{A_f}{A_u}\right)\sqrt{T_u}} \; (G_{\max}\ \textit{initial})$$

Start Iteration:

$$\mathrm{Re}_b = \frac{d_b G_{\max}}{\mu}\left(12\,\frac{\mathrm{in}}{\mathrm{ft}}\right)$$

$$\mathrm{Re}' = \frac{HD'_m}{d_b}\mathrm{Re}_b$$

$$\mathrm{Re}_v = \frac{HD_{v,m}}{d_b}\mathrm{Re}_b$$

Laminar Flow ($\mathrm{Re}_v \le 100$)

$$G_{\max}^2 = \frac{2g_c}{180(144)}(\Delta P)\mathrm{Re}_v\frac{HD_{v,m}}{B}\left(\frac{S_{T,m}}{HD_{v,m}}\right)^{0.4}\left(\frac{S_{T,m}}{S'_{L,m}}\right)^{0.6}$$

Go to solution test.
Turbulent flow ($\mathrm{Re}_b \ge 5000$)

$$f_T = \frac{1}{(\mathrm{Re}_b)^{0.16}}\left[0.25 + \frac{0.1175}{\left(\frac{S_{T,M}}{d_b} - 1\right)^{1.08}}\right]$$

$$G_{\max}^2 = \frac{g_c}{2(144)}\frac{(\Delta P)\rho}{f_T(i-1)}$$

Go to solution test.

Transition Flow ($\mathrm{Re}_v > 100$ and $\mathrm{Re}_b < 5000$)
Characteristic point 1, postlaminar:

$$\mathrm{Re}'_1 = 100\,\frac{HD'_m}{HD_{v,m}}$$

$$G_{\max_1}^2 = \frac{2g_c 100}{180(144)}(\Delta P)\rho\frac{HD_{v,m}}{B}\left(\frac{S_{T,m}}{HD_{v,m}}\right)^{0.4}\left(\frac{S_{T,m}}{S'_{L,m}}\right)^{0.6}$$

$$f_{KL_1} = \frac{g_c}{2(144)}\frac{(\Delta P)}{G_{\max_1}^2}\frac{HD'_m}{B}$$

Characteristic point 2, preturbulent:

$$\mathrm{Re}'_2 = 5000\,\frac{HD'_m}{d_b}$$

$$f_{T_2} = \frac{1}{(5000)^{0.16}}\left[0.25 + \frac{0.1175}{\left(\frac{S_{T,m}}{d_b} - 1\right)^{1.08}}\right]$$

$$f_{KL_2} = f_{T_2}(i-1)\frac{HD'_m}{B}$$

Local characteristic for transition:

$$m = \frac{\log(f_{KL_2}) - \log(f_{KL_1})}{\log(\mathrm{Re}'_2) - \log(\mathrm{Re}'_1)}$$

$$b = m\log(\mathrm{Re}'_1) - \log(f_{KL_1})$$

$$\log(f_{KL}) = m\log(\mathrm{Re}') - b$$

$$G_{\max}^2 = \frac{g_c}{2(144)}\frac{(\Delta P)\rho}{f_{KL}}\frac{HD'_m}{B}$$

Solution Test:

$$G_{\max} = \sqrt{G_{\max}^2}\; (G_{\max}\ \textit{calculated})$$

If the deviation between $G_{\max}$ initial and $G_{\max}$ calculated > tolerance (e.g., 0.0001) compute new $G_{\max}$ and repeat calculations. New $G_{\max}$ is calculated using:

$$G_{\max} = \frac{G_{\max_{initial}} + G_{\max_{calculated}}}{2}$$

Output Solution:

$$\phi = G_{\max}\frac{A_f}{A_u}\frac{\sqrt{T_u}}{P_u}$$

$$B_o = \{[(i-1)/\sqrt{1 + 0.25(S_{T,M}/S_L)^2}] + 1\}d_b$$

B/B_o = relative thickness
$B_{act} = (B/B_o)B_{min}$

Darryl E. Metzger Memorial Session Paper

The Streamwise Development of Görtler Vortices in a Favorable Pressure Gradient

M. V. Finnis

A. Brown

School of Engineering
and Applied Science,
Royal Military College of Science,
Cranfield University,
Shrivenham, Swindon, United Kingdom

Measurements are presented of the streamwise velocity variation within a laminar boundary layer on a concave surface of 4 m radius of curvature for which the free-stream velocity gradient factor $(\nu/U_0^2)dU_0/dx$ was approximately 1×10^{-6}. The velocity variation was consistent with the presence of counterrotating vortices resulting from the Görtler instability. The vortices exhibited exponential growth over the streamwise extent of the measurements to a disturbance amplitude of approximately 13 percent of the local free-stream velocity. The vortex growth rates were found to be less than those for a zero velocity gradient factor, indicating that a favorable pressure gradient stabilizes the flow with respect to the Görtler instability. Boundary layer profiles at local upwash and downwash positions are compared with the linear theory for which the mean flow was modeled using the Pohlhausen approximation to the solution of the boundary layer equations. The agreement between the measured and predicted profiles indicates that the linear stability theory can provide a fair approximation to the small amplitude growth of the Görtler instability.

Introduction

The operating characteristics and efficiency of turbomachines are strongly influenced by the behavior of the boundary layers on the blade surfaces. For the successful design of gas turbines operating at elevated inlet temperatures, the accurate prediction of boundary layer development and convective heat transfer is essential. In a discussion of the role of transition in gas turbine engines, Mayle (1991) identifies both the blade heat loading and the aerodynamic characteristics of turbine blades as being heavily influenced by the transitional behavior of the boundary layer. Of particular interest are the pressure surfaces on which the destabilizing influences of free-stream turbulence and unsteadiness tempered by high acceleration rates produce extended regions of transitional flow.

Görtler instability, characterized by counterrotating vortices within the laminar boundary layer on a concave surface (Fig. 1), is a known modulator of transition. Although a weak instability, Görtler vortices can promote or delay transition according to the free-stream flow conditions and surface geometry. Based on (zero pressure gradient) transition results of Riley et al. (1989), at a number of turbulence levels, Mayle (1991) concludes that, for gas turbines, curvature has a negligible effect on the onset of transition, except perhaps in small engines, where it could cause a slight delay.

Görtler (1940) was the first to develop a linear stability analysis of a boundary layer flow on a concave surface. He identified the parameter $\mathrm{Re}_\theta(\theta/r)^{1/2}$, now commonly known as the Görtler number, as significant in indicating the stability of the boundary layer flow. Liepmann (1945), extending earlier work in which he investigated the effects of curvature and pressure gradient on boundary layer transition, correlated the Görtler number at transition with free-stream turbulence intensity. He found that, in a zero pressure gradient, the transition Görtler number decreased from 9 at a turbulence intensity of 0.06 percent to 6 at 0.3 percent. The results of Liepmann are often quoted and have been used as a basis of predicting transition on curved surfaces in general (e.g., Forest 1977).

A further consequence of the Görtler instability is the possible enhancement of heat transfer in the presence of the vortices. There have, perhaps surprisingly, been relatively few investigations of the effect of the Görtler instability on laminar heat transfer. McCormack et al. (1970) reported increases of over 100 percent in global Nusselt number on a concave surface compared with flat plate values. The values of Görtler number were less than Liepmann's critical value of 9, and it is likely that much of the boundary layer was laminar. Kottke (1986) reports increases in Nusselt number up to 80 percent. Crane and Sabzvari (1989) found enhancement of spanwise-averaged Stanton numbers occurred for Görtler numbers greater than 10. They attributed a substantial part of the increased heat transfer to local thinning of the boundary layer due to the Görtler instability.

The linearized analysis of the Görtler instability is well established. The flow field is described by a mean flow with superimposed three-dimensional disturbances in the form of counterrotating vortices (Fig. 1). Görtler (1940) assumed that there is a parallel mean flow, i.e., he ignored the velocity terms normal to the surface, and that the disturbances grow in time. The resulting analysis led to a three-parameter eigenvalue problem in the Görtler number G, the wavenumber ω, and a growth parameter $\beta\theta\,\mathrm{Re}_\theta$, providing a universal stability chart. Görtler was primarily concerned with predicting the onset of the instability though he recognized that the formation of the vortices would not necessarily indicate incipient turbulence of the flow.

Much of the theoretical work since that of Görtler (1940) has been concerned with refining the analysis, both in the formulation of and the method of solving the governing equations. Smith (1955), in a quasi-parallel analysis, retained the normal velocity terms and made the intuitively more realistic assumption of the vortices growing with streamwise position rather than

Contributed by the International Gas Turbine Institute and presented at the 39th International Gas Turbine and Aeroengine Congress and Exposition, The Hague, The Netherlands, June 13–16, 1994. Manuscript received by the International Gas Turbine Institute February 15, 1994. Paper No. 94-GT-166. Associate Technical Editor: E. M. Greitzer.

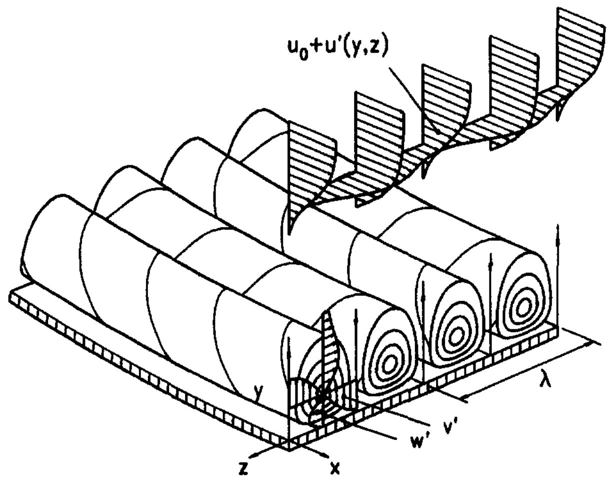

Fig. 1 Idealized Görtler vortices

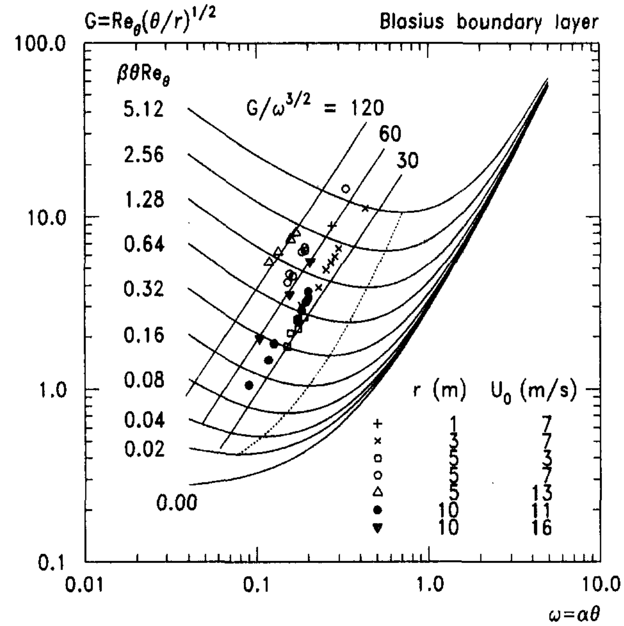

Fig. 2 Universal stability chart for Blasius boundary layer with results due to Tani (1962) and Tani and Sakagami (1964), (······ locus of maximum amplification)

in time. However, he made the assumption that the streamwise variation of the disturbance profiles is small and consequently retained a growth factor. Smith simplified the resulting equations by ignoring terms that were considered to affect his coefficients by less than 1 percent. More recently, Floryan and Saric (1982), among others, have produced a "correct order-of-magnitude" formulation of the governing equations. Figure 2 shows the stability chart for the Blasius boundary layer produced using the quasi-parallel analysis of Finnis and Brown (1989) (this is essentially the same chart produced by Floryan and Saric).

The shape of the stability chart is influenced by the form of the mean flow. For constant surface curvature, the stability chart is invariant for boundary layers with self-similar profiles. In this case, the Görtler number increases with streamwise position. For the Blasius flow, and the chart of Fig. 2, $G \propto x^{3/4}$. For boundary-layer flows that do not exhibit self-similarity, the stability chart will change with streamwise position and the Görtler number will not necessarily represent streamwise position. Ragab and Neyfeh (1981) and Finnis and Brown (1989) have investigated the effects of pressure gradient on the stability chart using Falkner–Skan mean flows. They concluded that a favorable pressure gradient raises the critical Görtler number while an adverse pressure gradient lowers it. These changes to the stability chart were shown to be due almost entirely to the differences in the mean flow normal velocity terms.

Smith (1955), while agreeing that the Görtler number characterizes the stability of flows on surfaces of constant curvature, postulated that ultimately the vortex amplitude determines the transition point. He correlated the then available experimental data with values of $\int \beta dx$, and concluded that transition was determined by $\int \beta dx \approx 10$. More recently Priddy and Bayley (1985) had some success in correlating measurements with $\int \beta dx \approx 9$ as an indicator of the transition point.

Hall had questioned the validity of the quasi-parallel assumption and in Hall (1983) he solved a nonparallel formulation of the Görtler problem. Solution was by a marching technique in which the development of an initial disturbance was followed downstream. Characterizing the vortex growth by the disturbance energy, he found that the stability depended on the location and form of the initial disturbance.

Hall and his co-workers have extended the theory and have considered Görtler instability in three-dimensional boundary layers (Hall, 1985), the interaction with Tollmien–Schlichting waves (Hall and Bennett, 1986; Bennett and Hall, 1988), and in Hall and Malik (1989) the effect of compressibility. In Hall (1990) the leading edge receptivity problem was investigated. Using a model of a free-stream longitudinal vortex impinging on the leading edge of a curved surface to provide initial conditions, a unique neutral stability curve was obtained, though it was found to be weakly dependent on the surface curvature.

Nomenclature

A = vortex amplitude normalized with free-stream velocity
G = Görtler number = $Re_\theta(\theta/r)^{1/2}$
p = pressure, N/m^2
p' = disturbance pressure, N/m^2
p_0 = mean flow pressure, N/m^2
p_1 = disturbance pressure function, N/m^2
$\hat{p}_1$ = dimensionless pressure function = $p_1/\frac{1}{2}\rho u_\infty^2$
r = surface radius of curvature, m
Re_θ = Reynolds number based on momentum thickness = $u_\infty\theta/\nu$
u, v, w = velocity components in the x, y, z directions, m/s
u', v', w' = disturbance velocity components, m/s
u_0, v_0 = mean flow velocity components in the x, y directions, m/s
u_1, v_1, w_1 = disturbance velocity functions, m/s
$\hat{u}_0, \hat{u}_1$ = dimensionless velocities normalized with u_∞
u_∞, U_0 = free-stream velocity, velocity at edge of boundary layer, m/s
x, y, z = streamwise, normal, and spanwise coordinates, m
α = wavenumber = $2\pi/\lambda$, m^{-1}
β = amplification factor, m^{-1}
δ = boundary layer reference length, m
η = dimensionless ordinate normal to surface = y/δ
θ = boundary layer momentum thickness, m
λ = vortex wavelength, m
Λ = Pohlhausen's shape factor = $(\delta^2/\nu)du_\infty/dx$
ν = kinematic viscosity, m^2/s
ω = dimensionless wavenumber = $\alpha\theta$

Day et al. (1990) made a detailed comparison of the quasi-parallel and nonparallel analyses. They found that although the marching analysis could not produce a unique neutral stability curve, for higher growth rates the solutions agreed quite closely. It was concluded that the solutions compared well enough to allow the local analysis to be used for engineering studies.

Much of the effort in recent years has been directed toward solving the nonlinear Görtler problem and the subsequent development of secondary instabilities. Recent numerical models of large-amplitude Görtler instabilities have relied on solving the temporal development for a parallel flow formulation of the equations (Sabry and Liu, 1988; Liu and Domaradzki, 1990). This formulation has been criticized by Hall (1990) and more recently Lee and Liu (1992) have investigated the problem of nonlinear spatially developing Görtler vortices. Initial conditions for many of the nonlinear solutions are generated using the quasi-parallel linear analysis to provide the form of the disturbances and experimental data, often that of Swearingen and Blackwelder (1987), to provide the amplitude.

Early experimental work was confined to confirming the existence of Görtler vortices in a laminar boundary layer on a concave surface. Although visualization of vortices had been mentioned in passing by Gregory and Walker (1956), the first measurements of the spanwise velocity variation within the boundary layer consistent with the existence of counterrotating vortex pairs were published by Tani and his co-workers in the early 1960s. Figure 2 shows some of the results due to Tani (1962) and Tani and Sakagami (1964) located on the universal stability chart for the Blasius boundary layer. Measurements were made on a number of different surfaces in two wind tunnels. It was concluded that characteristics of the experimental arrangement were fundamental to the preferred vortex wavelength. However, it was observed that, once established, the vortex wavelength remained essentially constant in the streamwise direction. (Vortex development at constant wavelength can be represented by lines of constant $G/\omega^{3/2}$ on the stability chart.) These observations have been confirmed by many of the subsequent experimental investigations.

Once the existence of the instability had been established, some effort was made to confirm the position of the neutral stability curve. Wortmann (1964), in a basic flow free of Görtler vortices on a slightly concave wall, generated disturbances of various wavelengths in a water channel. Using the tellurium method, he was able to visualize the downstream development of the vortices and thereby determine their growth. Bippes (1972), in a comprehensive investigation of Görtler instability, attempted to determine the right-hand branch of the neutral curve by generating different vortex structures and noting whether they were amplified or damped. Bippes also found that, using upstream screens to generate essentially isotropic turbulence, the vortex wavelength was dependent on the flow velocity and surface curvature such that it was close to the most amplified as predicted by the linear theory. (Similar results have since been obtained by Mangalam et al. (1985) in a low-turbulence wind tunnel.) Furthermore, in a towing tank in which there were no residual disturbances, Bippes found that the emergence of a vortex structure was delayed, though transition occurred in a relatively short distance downstream of the first appearance of the instability.

These results indicate that the appearance and subsequent development of the Görtler instability are influenced by the upstream flow history. Consequently the receptivity problem for the Görtler instability is likely to be of great importance. It is of interest to note that Kottke (1986) and Finnis and Brown (1989) have described flows for which no vortices were observed.

The experimental work reviewed so far, although in some cases investigating vortex development through transition, has often been referred to in terms of supporting the linear theory and illustrating the linear growth region of Görtler instability. Nonlinear growth of the vortex structure exhibits larger vortex amplitudes leading to points of inflection in the upwash velocity profiles as well as in the spanwise velocity variation (Wortmann, 1969; Aihara and Koyama, 1981; Swearingen and Blackwelder, 1987). The nonlinear growth is followed by a meandering or sinuous flow, the observation of which is reported by most authors investigating this stage of vortex development (e.g., Bippes, 1972; Aihara, 1979; Sabzvari and Crane, 1985; Swearingen and Blackwelder, 1987). The sinuous flow results from secondary instabilities initiated at the inflectional points in the spanwise velocity profile. A further characteristic of the breakdown of the vortex structure is the formation of horseshoe or crossflow vortices at points of inflection in the upwash velocity profiles. These were visualized by Bippes and Görtler (1972) and mentioned by Swearingen and Blackwelder (1987) as an alternative secondary instability to the meandering motion. It is generally agreed that breakdown of these vortices leads to turbulence. Swearingen and Blackwelder suggest a possible mechanism for the Görtler vortex breakdown as being initiated by a rapidly growing temporal instability originating near the surface. They conclude that Görtler vortices do not themselves break down to turbulence but rather set up a flow field that is unstable to other instabilities.

More recently, Winoto and Low (1989, 1991) have determined the Görtler number at the start of transition at a number of streamwise positions on two concave surfaces. Görtler numbers based on the Blasius mean flow at the start of transition were found to be between 7.5 and 8.0. (Myose and Blackwelder (1991) in a unique investigation in which "natural" vortex wavelengths between 11 mm and 29 mm could be produced, found that secondary instabilities, characterized by sinuous motion, were initiated at Görtler numbers, based on the Blasius mean flow, of between 7.1 and 8.1.) Riley et al. (1989) performed a similar investigation on two surfaces and also included the effects of free-stream turbulence intensity, which ranged, locally, between 0.5 and 4.2 percent. They suggested that a further stability parameter, perhaps based on surface curvature, could account for differences between the results obtained on their two surfaces.

Based on much of the published data, it would appear that, for a zero pressure gradient at least, departure from the expected mean flow, and the linear theory, occurs for $G \approx 6$. The developing instability produces local variations in boundary layer thickness of 100 percent or so for $G \approx 8$. These variations produce inflectional velocity profiles in both the spanwise and normal directions, leading to time-varying secondary instabilities rapidly breaking down to turbulence. However, it should be borne in mind that, for many of the investigations, the flow regime is chosen so that the Görtler instability is the dominant mode of instability. In naturally occurring flows, rather than the grid-generated, wind-tunnel flows, this is not necessarily the case, and the route to turbulence may be of a very different nature.

This review of the literature, which is by no means complete, illustrates many of the uncertainties in predicting the behavior of a laminar boundary layer on a concave surface. Many of the criteria for modifying flat plate transition predictions to account for curvature are based on the results for zero free-stream pressure gradient. The motivation for the present investigation was to determine the effect of a favorable pressure gradient on the development of the Görtler instability and to compare measured data with a linear stability analysis of the mean flow. The investigation was part of a wider undertaking and was preparatory in nature, being limited to one pressure gradient and a restricted streamwise extent.

Experimental Arrangement

The low-speed, open-return wind tunnel used for the experimental program is shown schematically in Fig. 3. The 27 in.

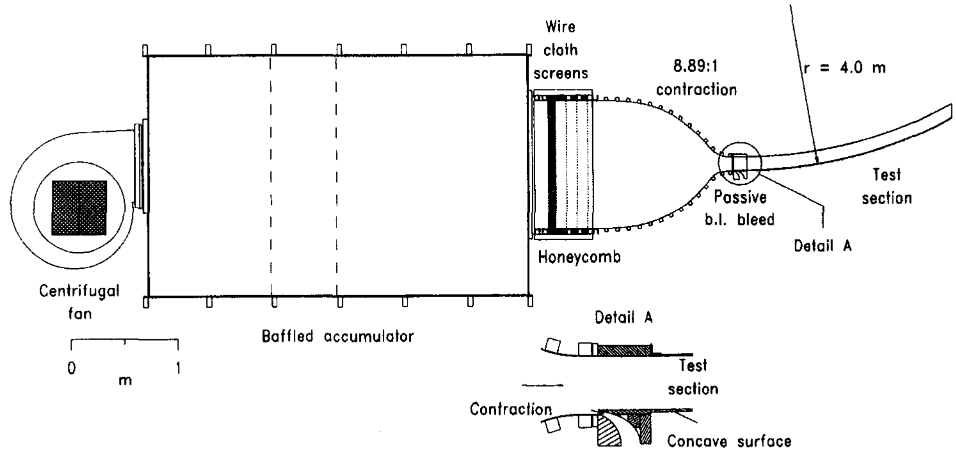

Fig. 3 Scheme of experimental rig

centrifugal fan was driven by a 11.2 kW DC shunt-wound motor. The motor speed was thyristor controlled and adjusted manually. The fan speed was monitored using an optical tachometer and was displayed to a resolution of 1 rpm on a digital display unit. The fan speed could be adjusted to the displayed resolution and exhibited no discernible drift with time.

The fan discharged across a 9 mm air gap into a 2.4 m high by 2.4 m wide by 3.6 m accumulator containing two baffles. This was followed by a 1.2 m high by 762 mm wide settling chamber containing honeycomb and wire cloth screens to control the flow turbulence. The aluminum honeycomb had cells 6 mm in diameter and 50 mm long. The cloth screens were constructed using 32 mesh, 0.16 mm wire diameter stainless steel wire cloth having an open area of 64 percent. The settling chamber was followed an 8.89:1 two-dimensional contraction to an exit of 135 mm high by 762 mm wide.

Immediately upstream of the working section the floor boundary layer was removed with a passive boundary-layer bleed. The bleed, which consisted of a knife edge as shown in Fig. 3, added a 124 mm flat-plate lead-in to the start of the working section. The bleed also provided a distinct origin for the boundary-layer flow in the working section.

The curved working section was constructed of clear plastic sheet mounted on medium density fiberboard formers supported in a steel, square-section tube frame. The lower surface of the working section was 2000 mm long by 762 mm wide with a constant radius of curvature of 4 m. Static pressure tappings were placed every 100 mm in the streamwise direction across the center 150 mm of the span. Due to the flat-plate portion of the boundary-layer bleed the first pressure tapping was at a streamwise position of 224 mm.

The upper surface of the working section was made of clear plastic sheet suspended at ten streamwise positions. In the upper surface were ten spanwise slots, 250 mm by 13 mm, which enabled a probe to be positioned in the working section. Unused slots were filled with balsa wood plugs ensuring continuity of the underside of the upper surface. The roof position could be altered at the suspension points, allowing fine adjustment of the streamwise pressure gradient. In addition, the upper surface could be pivoted about its front edge, allowing large alterations of the streamwise pressure gradient.

Figure 4 shows the free-stream velocity variation for which the results presented here were obtained. This variation was produced by pivoting the upper surface, which had been adjusted to give a zero pressure gradient, about its front edge. The velocities shown in Fig. 4 were obtained from static pressure measurements on the lower surface of the working section. Measurements were made with each of the slots in the upper surface, from the fourth to the ninth inclusive, uncovered in turn. The effect of an uncovered slot was to reduce the velocity downstream due to leakage through the slot. Although undesirable, this was unavoidable as it was necessary to uncover the slots in order to make spanwise traverses.

Figure 4 also shows a quadratic least-squares fit to all the data. (The velocity data at each streamwise position were normalized with its exit velocity. All the data were then multiplied by the average exit velocity before the least-squares fit was made.) An approximation to the free-stream velocity was required in order to estimate the boundary layer parameters for the theoretical analysis. The fitted quadratic gives a velocity of 3.9 m/s at the leading edge and an exit velocity (at x = 2.142 m) of 8.0 m/s. Although these values are obtained by extrapolation over approximately 200 mm at each end of the data, the exit velocity is very close to the average measured value of 8.01 m/s.

The velocity gradient factor $(\nu/U_0^2)dU_0/dx$, calculated from the fitted quadratic polynomial, was close to 1×10^{-6} for a large region of the flow. Using a value of kinematic viscosity of 1.461×10^{-5}, the velocity gradient factor is 0.9×10^{-6} at $x = 0.521$ m and 1.832 m and reaches a maximum of 1.07×10^{-6} at $x = 1.069$ m.

Velocity measurements were made using a constant-temperature hot-wire anemometer mounted on a probe support extending through one of the slots in the upper surface of the working section. The probe was of the boundary layer type and was mounted with the sensor approximately 62 mm upstream of the slot in the roof. The probe support was attached to a stepper-motor driven, three-axis traversing mechanism. This allowed the hot-wire sensor to be traversed perpendicular to the surface and across the span of the working section.

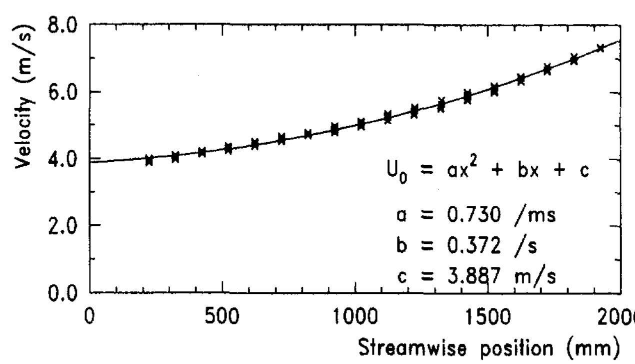

Fig. 4 Quadratic least-squares fit to streamwise velocity variations

Measurements were made at streamwise positions corresponding to the probe mount being located at slot numbers four to nine. These streamwise positions, 0.790, 0.995, 1.199, 1.400, 1.605, and 1.807 m are referred to by their slot number, i.e., the eighth streamwise position corresponds to $x = 1.605$ m.

Spanwise traverses outside of the boundary layer indicated that the free-stream velocity varied by less than 0.5 percent of the mean. Traverses perpendicular to the surface showed that the normal velocity gradient could be ignored. For example, at the seventh streamwise position the normal velocity gradient, based on measurements just outside of the boundary layer, was estimated to be between 2 and 8 m/s per m. Free-stream turbulence intensity values were less than 0.15 percent at all of the streamwise positions at which measurements were made.

A pitot static tube and K-type thermocouple were mounted in the air stream at the exit of the working section in order to monitor free-stream conditions. All pressures were read using a micromanometer having full-scale ranges of 1, 10, and 100 mm water (gage). A scanning valve pressure switch was used to connect each of the pressure tappings to the micromanometer in turn.

Probe traversing, data acquisition, and subsequent processing were performed using an IBM compatible PC. Voltages from the anemometer and micromanometer were read using 16 bit A/D converters with a voltage range of ±5 V. The thermocouple output was read using a 12 bit A/D converter with programmable gain.

Theory

A brief outline of the quasi-parallel linear theory is given below. For a more complete description the reader is referred to Finnis and Brown (1989).

The stability of a laminar boundary layer on a concave surface of constant curvature is considered with respect to three-dimensional disturbances in the form of counterrotating streamwise vortices. The flow is assumed steady and incompressible and is expressed as a two-dimensional mean flow with the disturbances superimposed. The disturbed flow is written as

$$\left.\begin{aligned} u &= u_0(x, y) + u'(x, y, z) \\ v &= v_0(x, y) + v'(x, y, z) \\ w &= w'(x, y, z) \\ p &= p_0(x, y) + p'(x, y, z) \end{aligned}\right\} \quad (1)$$

The spanwise dependence is removed by assuming a periodic variation in the disturbances. The streamwise dependence is eliminated by assuming that the profile shape of the disturbance varies slowly in the streamwise direction and introducing a growth or amplification factor. The analysis then has a local significance. The disturbed flow can then be written as

$$\left.\begin{aligned} u &= u_0(x, y) + u_1(y)\cos(\alpha z)e^{\beta x} \\ v &= v_0(x, y) + v_1(y)\cos(\alpha z)e^{\beta x} \\ w &= w_1(y)\sin(\alpha z)e^{\beta x} \\ p &= p_0(x, y) + p_1(y)\cos(\alpha z)e^{\beta x} \end{aligned}\right\} \quad (2)$$

where α is the dimensional wavenumber $2\pi/\lambda$ and β the growth factor.

Equations (2) are substituted into the momentum and continuity equations. The resulting equations are then linearized with respect to the disturbances, which are assumed to be small. The usual normalizations are made with lengths perpendicular to the surface being scaled with the mean flow momentum thickness θ. For a given mean flow and Reynolds number Re_θ, the resulting system of ordinary differential equations represents an eigenvalue problem for the parameters G, ω, and $\beta\theta\,\mathrm{Re}_\theta$ with the disturbances appearing as the eigenfunction. It should be noted that this analysis can say little about the wavelength or amplitude of the disturbances or whether the disturbance structure will occur at all. Rather, the relative stability of the mean flow is based on the growth rate of a given vortex structure.

Provided that the surface curvature is much larger than θ, it can be shown that the flat plate boundary layer is the appropriate mean flow (e.g., Herbert, 1976). For the calculations presented here, the Pohlhausen polynomial approximation was used to model the mean flow. The boundary layer velocity profile is represented by the quartic polynomial

$$\begin{aligned} \hat{u}_0 &= (2\eta - 2\eta^3 + \eta^4) + \frac{\Lambda}{6}(\eta - 3\eta^2 + 3\eta^3 - \eta^4) \quad \eta < 1 \\ &= 1 \quad \eta \geq 1 \end{aligned} \quad (3)$$

where η is the normal ordinate normalized with a boundary layer thickness. The boundary layer thickness in this instance is an almost arbitrary measure, and in comparisons with experimental results, the profiles are normalized with the momentum thickness. Λ is a shape factor equal to $(\delta^2/\nu)du_\infty/dx$ and is calculated via the integration of the momentum equation, as given in Schlichting (1979). For the results presented here the free-stream velocity given by the quadratic polynomial shown in Fig. 4 was used in integrating the momentum equation.

In order to solve the governing equations, the following terms derived from the mean flow are required:

$$\hat{u}_0, \quad \frac{\partial \hat{u}_0}{\partial \eta}, \quad \hat{v}_0, \quad \frac{\partial \hat{v}_0}{\partial \eta}, \quad \frac{\delta}{u_\infty}\frac{\partial(\hat{v}_0 u_\infty)}{\partial x}$$

where δ is a boundary layer reference length, $\eta = y/\delta$, and the hat represents normalization with respect to u_∞. These terms can be obtained, with some manipulation, using the continuity equation and Eq. (3).

Pohlhausen's method is limited to free-stream velocity variations, which give values of Λ between -12 (the separation profile) and 12. After reaching 12, further integration results in a discontinuity in θ, which is inadmissible. Unfortunately, the quadratic free-stream velocity variation used resulted in Λ reaching 12 at a streamwise position of 1211 mm. Using the method of Thwaites (1949) to integrate the momentum equation showed that his shape parameter barely exceeded the value corresponding to $\Lambda = 12$. Consequently, whenever the Pohlhausen method failed, a value of $\Lambda = 12$ was used. Therefore, it should be borne in mind that after $x = 1211$ mm the theoretical mean flow will be in error. It should also be noted that little can be said of the streamwise velocity variation prior to the first static pressure tapping at $x = 224$ mm. As the streamwise velocity is prescribed from $x = 0$ this too will have a bearing on the accuracy of the mean flow. The resulting errors in the mean flow are difficult to quantify and perhaps the best gage of the accuracy of the calculated mean flow is how it compares with the measured boundary layer profiles.

As described in the introduction, a single stability chart is appropriate to a flow in which the mean flow profiles are self-similar. In the Pohlhausen profile it is the value of Λ that determines the profile shape. Therefore, the shape of the stability chart also depends on the value of Λ. Figures 5 and 6 show the stability charts calculated at the first and sixth streamwise positions for which the values of Λ were 0.9 and 11.4, respectively. This serves to illustrate the variation in the shape of the stability chart: namely, the raising of the neutral stability curve and the closing of the lines of constant $\beta\theta\,\mathrm{Re}_\theta$ as the value of Λ is increased. However, it should be noted that the shape of the chart is little altered for values of Λ greater than 6 or so. For the free-stream velocity variation shown in Fig. 4, this represents positions greater than the fourth streamwise position. Thus, Fig. 6 represents approximately the stability chart for the streamwise positions at which measurements were made.

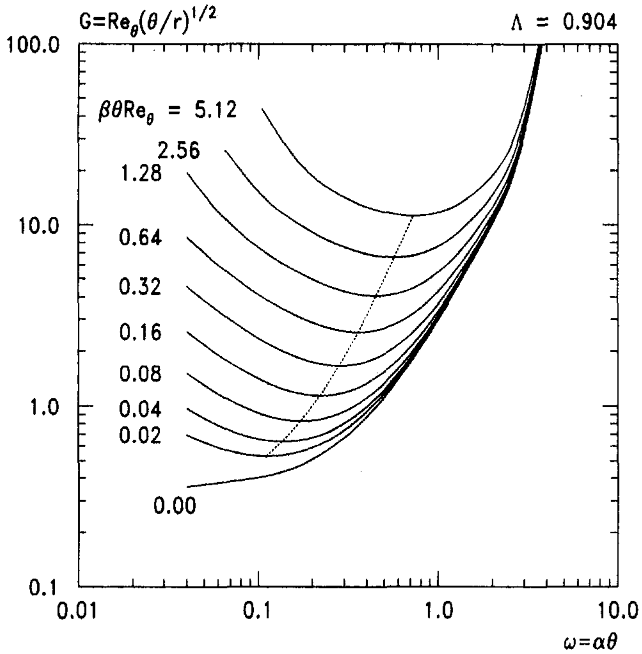

Fig. 5 Stability chart for the first streamwise position (x = 176 mm)

Results and Discussion

Figure 7 shows the spanwise variation in streamwise velocity at the eighth streamwise position ($x = 1605$ mm). In contrast to the theoretical model of a sinusoidal variation in streamwise velocity, the variation across the span is fairly irregular. However, it can be inferred from the profile that the velocity variation is due to the Görtler instability and that some of the peaks and troughs correspond to vortex upwash and downwash positions. The counterrotating vortices produce local minima at upwash positions where low-momentum fluid is lifted away from the surface and local maxima at downwash positions. Two adjacent upwash positions, denoted k and o, are indicated in the figure together with the included downwash position denoted m. The spanwise profile was measured at a height corresponding to 20 percent of the average of the boundary-layer thicknesses at the spanwise positions denoted l and n in Fig. 7. Also indicated in Fig. 7 are the likely positions of two vortices, denoted E and F, which lie between adjacent upwash and downwash positions. At this streamwise position and height there is obviously some distortion of the profile between the upwash position k and the downwash position m. This did not occur at locations upstream; however, it did occur at the ninth streamwise position. Further detailed investigation would be required in order to determine the significance of the distortion.

The spanwise positions indicated in Fig. 7 correspond directly to upwash and downwash locations measured in the same wind tunnel for a zero free-stream pressure gradient. Attention was focused on these positions in order to provide a direct comparison between the zero and favorable free-stream pressure gradients. It is perhaps worth noting that the largest spanwise variations occurred at these positions for the zero free-stream pressure gradient. This was not the case for the favorable pressure gradient at any of the streamwise positions for which measurements were made. The individual features in the profiles, such as those denoted k to o, could be identified and followed through the streamwise positions. The maximum and minimum velocities in all of the measured profiles occurred near the spanwise positions 10 mm and 20 mm.

The origin of the disturbances and the wavelength selection process have been discussed by many authors. Most experimental workers have concluded that the disturbance wavelength depends on initial disturbance conditions characteristic of the experimental facility used. Many of the individual features of Fig. 7 correspond not only to features in profiles measured in a zero free-stream pressure gradient but also to features in profiles measured on a flat plate in the same wind tunnel. Spanwise velocity profiles within the boundary layer on a flat plate were available at free-stream velocities of 5 m/s, 10 m/s and 15 m/s. Although the variations in streamwise velocity were relatively small, there were features common to all of the spanwise profiles. This was true for measurements made with and without the passive boundary-layer bleed shown in Fig. 3. The conclusion drawn from this, in common with many other authors, is that the upwash and downwash positions are greatly influenced by the flow upstream of the leading edge and start of curvature. In this instance, it is probable that the honeycomb and cloth screens in the settling chamber determine the characteristics of the free-stream flow. The resulting spanwise variation in free-stream disturbances, both in location and amplitude, is the likely cause of the variation in vortex spacing and local vortex growth rates across the span.

Figure 8 shows the boundary-layer profiles associated with vortex F at the eighth streamwise position. The downwash profile corresponds to the spanwise position denoted m in Fig. 7; the upwash profile corresponds to the position denoted o. The

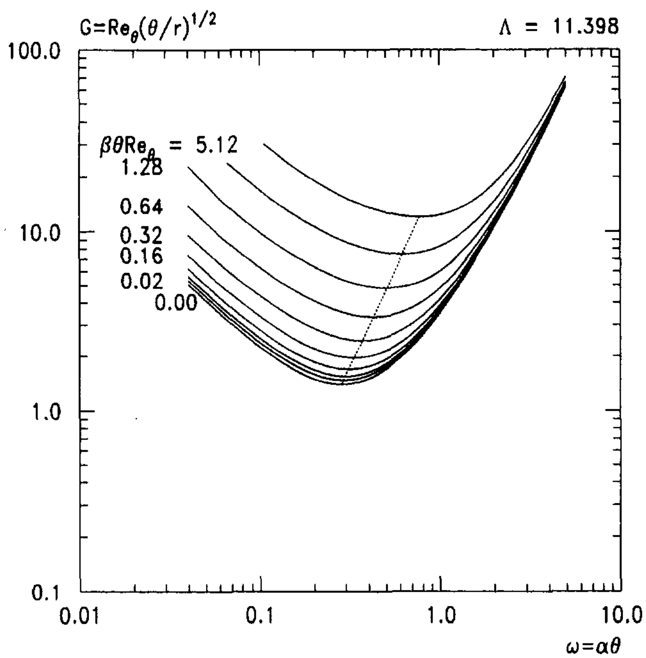

Fig. 6 Stability chart for the sixth streamwise position (x = 1199 mm)

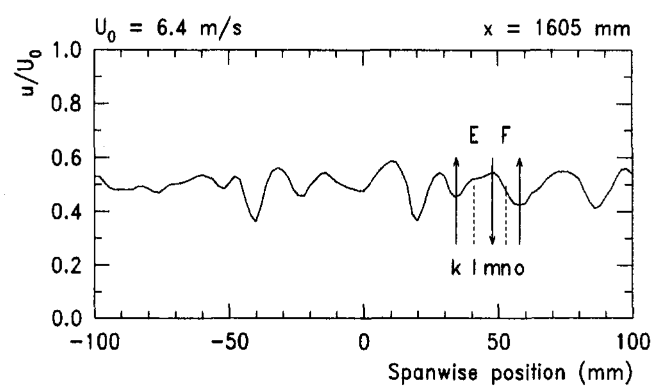

Fig. 7 Spanwise velocity profile at the eighth streamwise position

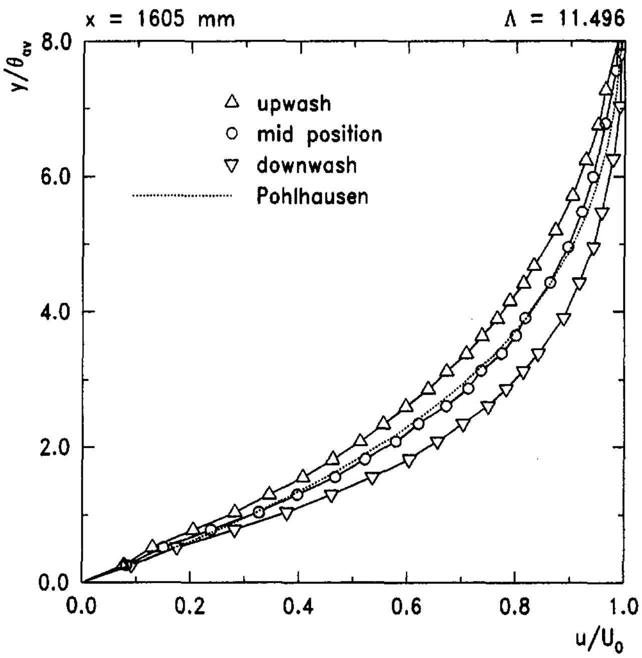

Fig. 8 Boundary layer profiles for vortex F at the eighth streamwise position

midposition profile (corresponding to the position denoted n) is also shown, together with the Pohlhausen profile calculated for the free-stream streamwise velocity variation. Although not shown, the profile obtained by averaging the upwash and downwash profiles is virtually identical to the midposition profile. These profiles are much as one would expect from the linear theory. The upwash and downwash profiles differ by the same amount from the mean velocity profile. Also, the mean flow is represented by the velocity profile midway between upwash and downwash, as well as the average profile and the profile expected in the absence of the vortices, in this case modeled by the Pohlhausen approximation. For the purposes of prediction using the linear stability analysis in the mean flow has to be the boundary-layer flow that would occur in the absence of the disturbances.

Table 1 gives the measured wavelengths for the two vortices E and F. The wavelengths can be based on the individual vortices (the distances between adjacent upwash and downwash locations) or the vortex pair (the distance between adjacent upwash positions). It should be noted that the height within the boundary layer at which the wavelengths are measured can influence the precise values depending on the state of vortex development. Also shown in the table are the wavelengths corresponding to spectral peaks obtained from Fourier analyses of the spanwise velocity profiles, which can be considered to represent a global wavelength.

Table 1 Vortex wavelengths for favorable pressure gradient

Streamwise Position (mm)	Wavelengths (mm)			
	Vortex E	Vortex F	Vortex Pair	Spectral Peak
790	25.6	20.4	23.0	28.69
995	27.8	21.6	24.7	28.75
1199	23.2	23.2	23.2	28.72
1400	23.8	22.4	23.1	28.88
1605	26.8	19.8	23.3	28.94
1807	28.8	17.8	23.3	30.32

Although there is some variation of the vortex wavelength with streamwise position, this is fairly slight and is likely to be due to local adjustment for differing growth rates across the span. Similar behavior is observed for a zero free-stream pressure gradient (e.g., Swearingen and Blackwelder, 1987). Allowing for this slight variation, the vortex wavelength can be considered to be constant in the streamwise direction.

Figure 9 shows the measured stability parameters located on the stability chart calculated for the eighth streamwise position. As discussed in the previous section, this stability chart is close to the relevant charts for the streamwise positions at which measurements were made. Namely, positions four to nine inclusive. The data are clustered in a small region of the graph, indicating that the stability parameters do not vary a great deal with streamwise position. This is due to the near-constant values of boundary-layer momentum thickness resulting from the free-stream velocity variation. Because of this, and as there is no single set of curves appropriate to all of the data points, there is no sense of vortex development through the stability chart as is the case for the zero pressure gradient data of Fig. 2.

The stability chart varies from that shown in Fig. 5 to approximately that of Fig. 6 over the first four streamwise positions. The trend is that lines of constant $\beta\theta$ Re_θ are "compressed" toward higher Görtler numbers with streamwise position. The Görtler number, based on the Pohlhausen solution, increases from 1.7 at the first streamwise position to approximately 4 at the fourth streamwise position, where it remains roughly constant over the remaining five streamwise positions. From the first streamwise position the lines of constant $\beta\theta$ Re_θ "follow" the point on the stability chart. The effect of this is to keep the values of $\beta\theta$ Re_θ relatively low compared with the zero pressure gradient values. This, together with the low values of Görtler number, ultimately reduces the vortex growth rate.

The values of velocity gradient factor $(\nu/U_0^2)dU_0/dx$ for streamwise positions 4 to 9, based on the assumed quadratic variation of the free-stream velocity, were roughly constant at approximately 1×10^{-6}. It may be possible that higher values of velocity gradient factor could result in vortex damping. For this to occur the neutral stability curve would have to be lifted above the Görtler number/wavenumber points on the stability chart. It is of interest to note that Brown and Martin (1982)

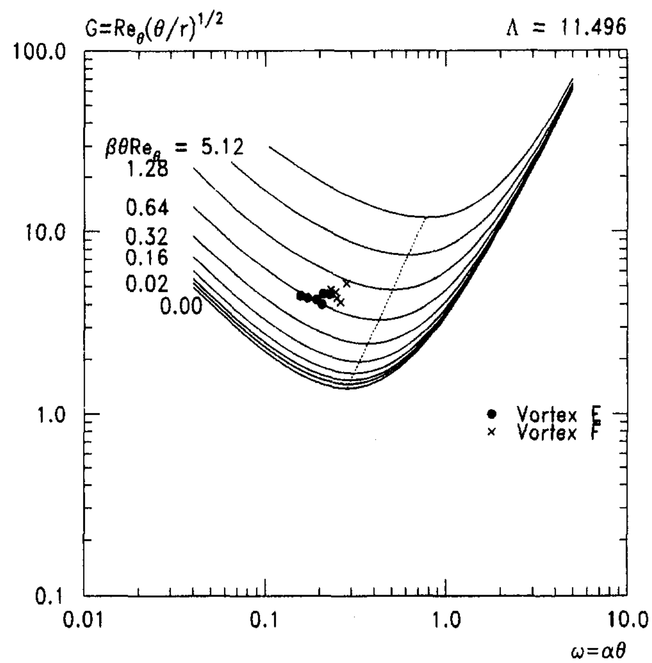

Fig. 9 Stability chart and measured stability parameters for the eighth streamwise position

advocate that the velocity gradient factor should be kept above 2.5×10^{-6} on the pressure surface of a turbine blade to prevent transition. Although this was based on the relaminarization criterion of Jones and Launder (1972) as well as much experimental data, it would appear that such a velocity gradient factor could stabilize the boundary layer with respect to Görtler vortices should they occur. The stabilizing effect would be to reduce growth rates compared to those for zero pressure gradient and perhaps attenuate the disturbance or prevent it occurring at all. This may well be a reason why the Görtler instability is not encountered more often in wind tunnel contractions where considerable favorable pressure gradients are likely to occur.

Figure 10 shows the disturbance profiles for vortex F at the eighth streamwise position. The disturbance velocities are obtained relative to the average velocity profile:

$$u' = (u_{\text{down}} - u_{\text{up}})/2 \tag{4}$$

where u_{down} is assumed to be $u_0 + u'$ and u_{up} is assumed to be $u_0 - u'$. The profiles in Fig. 10 are shown normalized with the maximum value of the disturbance velocity, 7.4 percent for this streamwise position, estimated from a cubic polynomial fitted around the velocity peak.

Also shown in Fig. 10 is the predicted disturbance velocity profile. This was obtained by solving the governing equations given the Görtler and wave numbers based on the mean velocity profile. The profile is shown normalized with its maximum value, though as the quasi-parallel linear theory cannot resolve the amplitude of the disturbance, the maximum value itself is indeterminate. The relatively close agreement between the theoretical and measured profiles, which was repeated at all of the streamwise positions, indicates that the theory can adequately approximate the small amplitude development of the Görtler instability.

In developing the theoretical model, the streamwise variation in the disturbance velocities was assumed small and separated out in order to linearize the differential equations. Thus the streamwise velocity was assumed to be approximated by

$$u = u_0(x, y) + u_1(y) \cos(\alpha z) e^{\beta x} \tag{5}$$

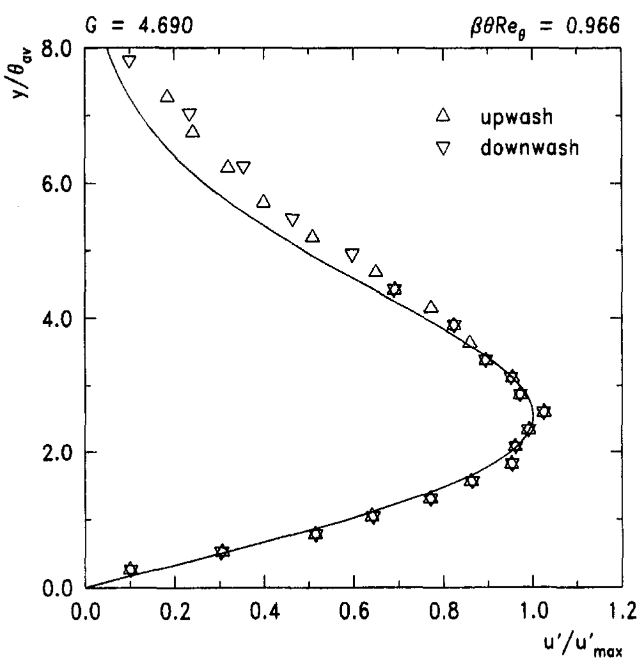

Fig. 10 Disturbance velocity profiles for vortex F at the eighth streamwise position

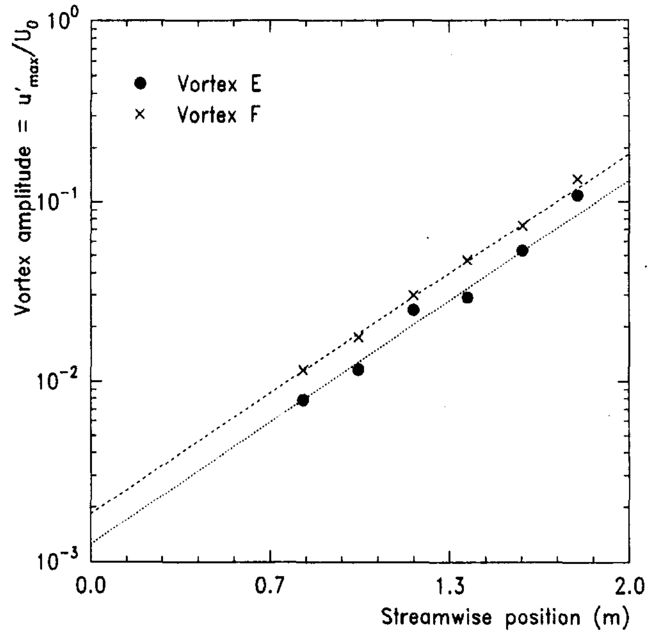

Fig. 11 Streamwise variation of vortex amplitudes

The vortex amplitude, obtained by subtracting the mean flow at downwash where $\alpha = 2n\pi$, $n = 1, 2, \ldots,$ and dividing by the free-stream velocity, is given by

$$A(x) = \hat{u}_{1_{\max}} e^{\beta x} \tag{6}$$

where $\hat{u}_{1_{\max}} e^{\beta x}$ is the maximum value of the disturbance profile. Taking logs of both sides gives

$$\ln [A(x)] = \ln (\hat{u}_{1_{\max}}) + \beta x \tag{7}$$

Figure 11 shows the streamwise development of the disturbance amplitudes for the vortices E and F. The growth of the disturbances follows the straight line anticipated from the Eq. (7). The slopes of the lines shown in the figure, equivalent to the values of β, are 2.3 m^{-1} for both vortices.

Table 2 shows the predicted and measured values of Görtler number and β. The predicted values of β were obtained for two different wavelengths: the mean value for vortex F (21 mm) and the mean value of the wavelength obtained by spectral analysis of the spanwise velocity profile (29 mm). The streamwise variation of these values is shown in Table 1. The former is the local value appropriate to vortex F, while the latter can be considered as representing the wavelength in a more global sense. The measured values of θ and Re_θ were determined from the average velocity profile, and the values of β were obtained indirectly from the stability chart using the wavelengths shown in Table 1 for vortex F. In this sense the values are derived from the linear theory rather than measured. The value of 2.3 m^{-1} obtained from Fig. 11 is based solely on the measured velocity profiles and represents an average streamwise growth rate.

The differences between the predicted and measured values of θ and Re_θ result in the predicted Görtler numbers being consistently less than the measured values. The error is greatest at the ninth streamwise position where it reaches 20 percent. At the eighth streamwise position the error is 11 percent, and it is probable that the value at the ninth position represents a departure from the predicted mean flow.

The predicted values of β illustrate the dependence of the growth rate on the disturbance wavelength. The "measured" values of β are close to the predicted values based on the local wavelength, since they are obtained from similar values

Table 2 Predicted and measured streamwise variation of Görtler number and β

Streamwise Position (mm)	Predicted					Measured			
	θ (mm)	Re_θ	G	$\beta(21)$ (m^{-1})	$\beta(29)$ (m^{-1})	θ (mm)	Re_θ	G	$\beta(F)$ (m^{-1})
176	0.533	145	1.676	3.633	2.981	—	—	—	—
382	0.725	205	2.766	3.810	3.093	—	—	—	—
588	0.813	242	3.455	3.714	2.976	—	—	—	—
790	0.840	267	3.862	3.580	2.825	0.844	282	4.102	3.766
995	0.833	284	4.095	3.458	2.684	0.855	297	4.347	3.531
1199	0.806	297	4.218	3.364	2.567	0.845	316	4.597	3.332
1400	0.757	303	4.162	3.341	2.516	0.718	337	4.825	3.528
1605	0.715	312	4.164	3.277	2.423	0.769	338	4.690	3.718
1807	0.678	322	4.195	3.255	2.380	0.797	370	5.223	4.226
2124	0.631	344	4.327	3.245	2.336	—	—	—	—
2208	0.620	351	4.367	3.245	2.330	—	—	—	—

of Görtler number and wavenumber. However, it is surprising that the predicted values of β based on the global wavelength agree so closely with the value obtained from the streamwise variation in disturbance amplitude of Fig. 11. The theory suggests that the disturbance growth rate depends on the wavelength, and it might be expected that local growth rates would be better predicted using local wavelengths. More extensive measurements covering more than one vortex pair might indicate whether individual growth rates differ by as much as those predicted in Table 2.

It was shown in Finnis (1993) that, for a zero pressure gradient, exponential growth continued until vortex amplitudes reached about 30 percent of the free-stream velocity. After this, secondary instabilities developed and rapidly broke down to turbulence. This occurred, in common with the results of many other authors, at Görtler numbers based on the Blasius mean flow between about 7 and 8.

Extrapolating the curve of Fig. 11 for vortex F gives an amplitude of 30 percent at a streamwise position of 2.208 m. (Measurements made over a greater streamwise extent would confirm whether this does approximate the streamwise position at which vortex breakdown would have occurred. Unfortunately, this was not possible in the current working section, which ended at a streamwise position of 1.124 m.) This corresponds to a Görtler number, based on the predicted mean flow, of about 4.4. This value is much less than the corresponding value of about 7.5 for zero pressure gradient. Thus, if the Görtler number is taken to represent the stability, it could be said that the favorable pressure gradient reduces the boundary layer stability. However, as mentioned in the introduction, the Görtler number only indicates the stability of a particular mean flow at some position with respect to disturbances of a given wavelength, and cannot reflect the upstream development of a disturbance (though it does reflect the upstream development of the mean flow as shown in Finnis and Brown, 1989).

The values of βx corresponding to amplitudes of 30 percent can be obtained by extrapolating the curves of Fig. 11. They are 5.5 for vortex F and 5.1 for vortex E. For a zero pressure gradient, the values lie between 4.0 and 5.8 (it should be noted that these values were taken from the curves themselves and did not require extrapolation). The agreement of the values of βx is due to the values of $\hat{u}_{1_{\max}}$ in Eq. (7) being similar for the zero pressure gradient and favorable pressure gradient measurements. These values, which may depend on initial disturbance size and upstream flow conditions, lay between 1×10^{-3} and 5×10^{-3}.

As the values of βx at the same disturbance amplitude are similar for different free-stream pressure gradients, it is possible that they would provide a better indicator of transition than the Görtler number. As noted above, the Görtler numbers at the same disturbance amplitude are very different for the zero and favorable pressure gradients. Also, for this pressure gradient at least, the Görtler number varies little in the streamwise direction for a large extent of the flow. This would reduce the accuracy with which a transition point could be predicted compared with a mean flow for which there was a greater variation of Görtler number with streamwise position. As an indicator of transition on a surface with varying curvature and an arbitrary pressure gradient, the Görtler number is unsuitable. However, the attraction in using the Görtler number is that, for the purposes of prediction, no reference need be made to the stability analysis since the Görtler number is a property of the mean flow and surface geometry only. If the vortex amplitude is to be used to predict transition then growth rates have to be determined from the stability analysis. This requires assumptions to be made regarding vortex wavelength and initial disturbance amplitude as well as the assumptions inherent in the theory.

The measured and predicted local growth rates presented here, although of a similar order, differed somewhat. Further comparisons, perhaps using a number of vortex pairs on the same surface, may resolve the differences enabling a better prediction of disturbance amplitude.

Conclusions

Comparison between measurements of streamwise velocity in the boundary layer on a concave surface and a linear stability analysis using the Pohlhausen solution to model the mean flow indicated that the quasi-parallel analysis can approximately describe the development of the Görtler instability for a favorable free-stream pressure gradient. As in the case of a zero free-stream pressure gradient, local vortex wavelengths were found to remain essentially constant in the streamwise direction.

The largest differences between the measurements and the theoretical model were in the local disturbance growth rates. The theoretical growth rates were shown to depend on vortex wavelength, which is not predicted by the theory. However, the measured local growth rates did compare with the predicted values based on a global wavelength. It is possible that further measurements, covering more vortex pairs, might resolve these differences.

The effect of the favorable pressure gradient on the stability chart is to close the lines of constant $\beta\theta$ Re_θ and lift them toward higher Görtler numbers. This, together with the lower Görtler numbers associated with the mean flow, leads to lower vortex growth rates compared with those for a zero free-stream pressure gradient.

The results indicate that, for an arbitrary pressure gradient and surface curvature, the Görtler number is unsuitable as an indicator of vortex development. The estimated Görtler number at a vortex amplitude of 30 percent was much lower than the values associated with a zero pressure gradient for the same amplitude. Since many of the criteria for determining the start of transition on concave surfaces are based on results for a zero free-stream pressure gradient, they are unlikely to apply to flows with arbitrary pressure gradient and curvature. This is to be expected, since the Görtler number depends only on the mean flow and takes no account of vortex growth upstream.

Since the size of the disturbance is likely to precipitate the breakdown to turbulence, it might be expected that the vortex amplitude would provide a better basis for the prediction of transition on concave surfaces. Although measurements were not available at vortex breakdown, the streamwise development of vortex amplitude indicated that values of βx at amplitudes of 30 percent would be similar to those for a zero free-stream pressure gradient. However, as the amplitude depends on the growth rate, the differences between the predicted and measured growth rates mentioned above need to be resolved before estimated vortex amplitudes can be used as a basis for the prediction of transition.

References

Aihara, Y., 1979, "Görtler Vortices in the Nonlinear Region," in: *Recent Developments in Theoretical and Experimental Fluid Mechanics*, U. Muller, K. G. Roesner, and B. Schmidt, eds., Springer-Verlag, pp. 331–338.

Aihara, Y., and Koyama, H., 1981, "Secondary Instability of Görtler Vortices: Formation of Periodic Three-Dimensional Coherent Structure," *Trans. Japan Soc. Aero. Space Sci.*, Vol. 24(64), pp. 78–94.

Bennett, J., and Hall, P., 1988, "On the Secondary Instability of Taylor–Görtler Vortices to Tollmien–Schlichting Waves in Fully Developed Flows," *J. Fluid Mech.*, Vol. 186, pp. 445–469.

Bippes, H., 1972, "Experimentelle untersuchung des laminar turbulenten Umschlags an einer parallel angeströmten konkaven Wand," Heidelberger Akademie der Wissenschaften, Matematischnaturwissenschaftliche klasse, Sitzungsberichte, No. 3, pp. 103–180; trans. "Experimental Study of the Laminar-Turbulent Transition of a Concave Wall in a Parallel Flow," NASA TM-75243, 1978.

Bippes, H., and Görtler, H., 1972, "Dreidimensionale Strörungen in der Grenzschicht an einer konkaven Wand," *Acta Mechanica*, Vol. 14, pp. 251–267.

Brown, A., and Martin, B. W., 1982, "Flow Transition Phenomena and Heat Transfer Over the Pressure Surface of Gas Turbine Blades," ASME *Journal of Engineering for Power*, Vol. 104, pp. 360–367.

Crane, R. I., and Sabzvari, J., 1989, "Heat Transfer Visualization and Measurement in Unstable Concave-Wall Laminar Boundary Layers," ASME JOURNAL OF TURBOMACHINERY, Vol. 111, pp. 51–56.

Day, H. P., Herbert, T., and Saric, W. S., 1990, "Comparing Local and Marching Analyses of Görtler Instability," *AIAA J.*, Vol. 28(6), pp. 1010–1015.

Finnis, M. V., and Brown, A., 1989, "Stability of a Laminar Boundary Layer Flowing Along a Concave Surface," ASME JOURNAL OF TURBOMACHINERY, Vol. 111, pp. 376–386.

Finnis, M. V., 1993, "Centrifugal Instability of a Laminar Boundary Layer on a Concave Surface," Ph.D. Thesis, Cranfield University, United Kingdom.

Floryan, J. M., and Saric, W. S., 1982, "Stability of Görtler Vortices in Boundary Layers," *AIAA J.* (79-1497R), Vol. 20(3), pp. 316–324.

Forest, A. E., 1977, "Engineering Predictions of Transitional Boundary Layers," AGARD-CP-224, pp. 22.1–22.19.

Görtler, H., 1940, "Uber eine dreidimensionale instabilität laminarer Grenzschichten an konkaven Wänden," *Ges. d. Wiss. Göttingen, Nachr.a. d. Math.*, Vol. 2(1); trans. "On the Three-Dimensional Instability of Laminar Boundary Layers on Concave Walls," NACA TM 1375, 1954.

Gregory, M. A., and Walker, W. S., 1956, "The Effect on Transition of Isolated Surface Excrescences in the Boundary Layer," Reports and Memoranda No. 2779, pp. 1–23.

Hall, P., 1983, "The Linear Development of Görtler Vortices in Growing Boundary Layers," *J. Fluid Mech.*, Vol. 130, pp. 41–58.

Hall, P., 1985, "The Görtler Vortex Instability Mechanism in Three-Dimensional Boundary Layers," *Proc. R. Soc. Lond.*, Vol. A399, pp. 135–152.

Hall, P., and Bennett, J., 1986, "Taylor–Görtler Instabilities of Tollmien–Schlichting Waves and Other Flows Governed by the Interactive Boundary Layer Equations," *J. Fluid Mech.*, Vol. 171, pp. 441–457.

Hall, P., and Malik, M., 1989, "The Growth of Görtler Vortices in Compressible Boundary Layers," *J. Engng. Maths*, Vol. 23, pp. 239–251.

Hall, P., 1990, "Görtler Vortices in Growing Boundary Layers: The Leading Edge Receptivity Problem, Linear Growth and the Nonlinear Breakdown Stage," *Mathematika*, Vol. 37, pp. 151–189.

Herbert, Th., 1976, "On the Stability of the Boundary Layer Along a Curved Wall," *Archives of Mechanics*, Vol. 28(5-6), pp. 1039–1055.

Jones, W. P., and Launder, B. E., 1972, "The Prediction of Laminarization With a Two-Equation Model of Turbulence," *Int. J. Heat Mass Transfer*, Vol. 15, pp. 301–314.

Kottke, V., 1986, "Taylor–Görtler Vortices and Their Effect on Heat and Mass Transfer," *Proc. Eighth Int. Heat Transfer Conf.*, San Francisco, CA, Vol. 3, pp. 1139–1144.

Lee, K., and Liu, J. T. C., 1992, "On the Growth of Mushroomlike Structures in Nonlinear Spatially Developing Görtler Vortex Flow," *Phys. Fluids A*, Vol. 4(1), pp. 95–103.

Liepmann, H. W., 1945, "Investigation of Boundary Layer Transition on Concave Walls," NACA Wartime Report, ACR 4J28.

Liu, W., and Domaradzki, J., 1990, "Direct Simulation of Transition to Turbulence in Görtler Flow," AIAA Paper No. 90-0114.

Mangalam, S. M., Dagenhart, J. R., Hepner, T. E., and Meyers, J. F., 1985, "The Görtler Instability on an Airfoil," AIAA Paper No. 85-0491.

Mayle, R. E., 1991, "The Role of Laminar–Turbulent Transition in Gas Turbine Engines," ASME JOURNAL OF TURBOMACHINERY, Vol. 113, pp. 509–537.

Mayle, R. E., Kopper, F. C., Blair, M. F., and Bailey, D. A., 1976, "Effect of Streamline Curvature on Film Cooling," ASME Paper No. 76-GT-90.

McCormack, P. D., Welker, H., and Kelleher, M., 1970, "Taylor–Görtler Vortices and Their Effect on Heat Transfer," ASME *Journal of Heat Transfer*, Vol. 92, pp. 101–112.

Myose, R. Y., and Blackwelder, R. F., 1991, "Controlling the Spacing of Streamwise Vortices on Concave Walls," *AIAA J.*, Vol. 29(11), pp. 1901–1905.

Priddy, W. J., and Bayley, F. J., 1985, "Effects of Free Stream Turbulence on the Distribution of Heat Transfer Around Turbine Blade Sections," *Int. J. Heat Fluid Flow*, Vol. 6(3), pp. 181–191.

Ragab, S. A., and Nayfeh, A. H., 1981, "Görtler Instability," *Phys. Fluids.*, Vol. 24(8), pp. 1405–1417.

Riley, S., Johnsons, W., and Gibbings, J. C., 1989, "Boundary Layer Transition of Strongly Concave Surfaces," ASME Paper No. 89-GT-321.

Sabry, A. S., and Liu, J. T. C., 1988, "Nonlinear Development of Görtler Vortices and the Generation of High Shear Layers in the Boundary Layer," in: *Symposium to Honor C. C. Lin*, D. J. Benney, F. H. Shu, and C. Yuan, eds., World Scientific, pp. 175–183.

Sabzvari, J., and Crane, R. I., 1985, "Effect of Görtler Vortices on Transitional Boundary Layers," *Int. Symp. on Three-Dimensional Flow Phenomena in Fluid Machinery*, ASME Winter Annual Meeting, Miami, FL.

Schlichting, H., 1979, *Boundary-Layer Theory*, 7th ed., McGraw-Hill, New York.

Smith, A. M. O., 1955, "On the Growth of Taylor–Görtler Vortices Along Highly Concave Walls," *Quart. App. Math.*, Vol. 13(3), pp. 233–262.

Swearingen, J. D., and Blackwelder, R. F., 1987, "The Growth and Breakdown of Streamwise Vortices in the Presence of a Wall," *J. Fluid Mech.*, Vol. 182, pp. 255–290.

Tani, I., 1962, "Production of Longitudinal Vortices in the Boundary Layer Along a Concave Wall," *J. Geophys. Res.*, Vol. 67(8), pp. 3075–3080.

Tani, I., and Sakagami, J., 1964, "Boundary-Layer Instability at Subsonic Speeds," *Proc. Third Cong. Int. Council Aerospace Sciences*, Stockholm, Spartan Washington DC, 1964, pp. 391–403.

Thwaites, B., 1949, "Approximate Calculation of the Laminar Boundary Layer," *Aero. Quart.*, Vol. 1, pp. 245–280.

Winoto, S. H., and Low, H. T., 1989, "Transition of Boundary Layer Flows in the Presence of Görtler Vortices," *Experiments in Fluids*, Vol. 8, pp. 41–47.

Winoto, S. H., and Low, H. T., 1991, "Transition of Boundary Layer Flows in the Presence of Görtler Vortices," *Experiments in Fluids*, Vol. 10, pp. 281–284.

Wortmann, F. X., 1964, "Experimental Investigations of Vortex Occurrence at Transition in Unstable Laminar Boundary Layers," AF 61(052)-220.

Wortmann, F. X., 1969, "Visualization of Transitions," *J. Fluid Mech.*, Vol. 38(3), pp. 473–480.

Turbulence Measurements in a Heated, Concave Boundary Layer Under High-Free-Stream Turbulence Conditions

M. D. Kestoras
Laboratoire de Thermocinetique,
ISITEM,
Nantes, France

T. W. Simon
Department of Mechanical Engineering,
University of Minnesota,
Minneapolis, MN 55455

Turbulence measurements for both momentum and heat transfer are taken in a low-velocity, turbulent boundary layer growing naturally over a concave wall. The experiments are conducted with negligible streamwise acceleration and a nominal free-stream turbulence intensity of ~8 percent. Comparisons are made with data taken in an earlier study in the same test facility but with a 0.6 percent free-stream turbulence intensity. Results show that elevated free-stream turbulence intensity enhances turbulence transport quantities like $\overline{uv}$ and $\overline{vt}$ in most of the boundary layer. In contrast to the low-turbulence cases, high levels of transport of momentum are measured outside the boundary layer. Stable, Görtlerlike vortices, present in the flow under low-turbulence conditions, do not form when the free-stream turbulence intensity is elevated. Turbulent Prandtl numbers, Pr_t, within the log region of the boundary layer over the concave wall increase with streamwise distance to values as high as 1.2. Profiles of Pr_t suggest that the increase in momentum transport with increased free-stream turbulence intensity precedes the increase in heat transport. Distributions of near-wall mixing length for momentum remain unchanged on the concave wall when free-stream turbulence intensity is elevated. Both for this level of free-stream turbulence and for the lower level, mixing length distributions increase linearly with distance from the wall, following the standard slope. However, when free-stream turbulence intensity is elevated, this linear region extends farther into the boundary layer, indicating the emerging importance of larger eddies in the wake of the boundary layer with the high-turbulence free stream. Because these eddies are damped by the wall, the influence of the wall grows with eddy size.

Introduction

A review of the literature on the effects of curvature is given by Kestoras and Simon (1992). Concave curvature destabilizes a laminar boundary layer resulting in streamwise vortices, as described by Görtler (1940). These vortices appear when the Görtler number, defined as:

$$G = \frac{U_{cw}\delta_2}{\nu}\sqrt{\frac{\delta_2}{|R|}} \tag{1}$$

reaches 6–10. The formation of vortices in a turbulent boundary layer seems to correlate better with a "turbulent Görtler number," G_t, obtained by replacing the kinematic viscosity with the eddy viscosity, ϵ_m (Tani, 1962). Shizawa and Honami (1985) suggested that in a turbulent boundary layer, eddy viscosity is large enough that G_t is generally in the stable regime. The present study supports this suggestion. Görtler vortices were obtained in the low-TI comparison case (Kestoras and Simon, 1992). They were established in the pretransitional, laminar boundary layer for which supercritical Görtler numbers were evaluated and persisted with decreasing effectiveness into the posttransitional flow.

Concave curvature enhances momentum and heat transfer in a turbulent boundary layer. So and Mellor (1975) reported Reynolds normal and shear stresses, and turbulence kinetic energy values that were above flat-wall values. Similar conclusions were reported by Shizawa and Honami (1985). Ramaprian and Shivaprasad (1977) confirmed these findings, remarking that curvature affected $\sqrt{\overline{v^2}}$ more than $\sqrt{\overline{u^2}}$. In a later study, Ramaprian and Shivaprasad (1978) reported that (1) 75 percent of the $-\overline{uv}$ activity originated from eddies of size greater than $\delta/4$, (2) mixing lengths, l_m, increased over the concave wall, and (3) the region of linear growth of l_m extended farther into the curved boundary layer than into a straight-wall boundary layer. Hoffmann et al. (1985) confirmed the Ramaprian and Shivaprasad findings and noted that, while convex curvature simply attenuated the turbulent eddies, concave curvature effected a structural change in the boundary layer. Barlow and Johnston (1988) noted that concave curvature amplifies large-scale motions, the single most important source of the increase in Reynolds normal and shear stresses. Further, the structural changes are in two phases; in the first phase, which is complete after a few boundary layer thicknesses[1] downstream of the start of curvature, high-momentum eddies move closer to the wall while low-momentum eddies are driven away from the wall, whereas in the second phase, the large-scale eddies grow and amplify, a process that is completed after about 20 boundary layer thicknesses. Kim et al. (1992) measured turbulent heat fluxes, reporting that in a low-Reynolds-number flow, $\overline{vt}$ values at the upwash sites of the Görtler vortices are higher than values at the downwash sites and that turbulent Prandtl numbers are close to unity.

Turbulence intensity, TI, effects are dependent not only on the TI level but also on the free-stream length scale and momentum thickness Reynolds number (Hancock and Bradshaw, 1983;

Contributed by the International Gas Turbine Institute and presented at the 39th International Gas Turbine and Aeroengine Congress and Exposition, The Hague, The Netherlands, June 13–16, 1994. Manuscript received by the International Gas Turbine Institute February 4, 1994. Paper No. 94-GT-37. Associate Technical Editor: E. M. Greitzer.

[1] Thickness of the boundary layer at the bend entrance.

Blair, 1983). Blair noted that skin friction coefficients and Stanton numbers increase with TI and that, over a flat wall, the logarithmic regions of the velocity and temperature profiles remain unaffected by elevated TI. Over a concave wall, a logarithmic region also remains to $y^+ \approx 100$, unaffected by increased TI (Kestoras and Simon, 1993). Hancock and Bradshaw (1983) reported that free-stream turbulence intensity substantially changes the structure of the outer region of the boundary layer. In the inner region, local equilibrium prevails and the law of the wall remains valid. They also observed that the parameter $[(\sqrt{\overline{u^2}}/U)_\infty \times 100]/[L_\infty^u/\delta_{99.5} + 2.0]$ correlated mean-flow data as well as some changes in turbulence structure. Hancock and Bradshaw (1989) experimentally documented the effects of high free-stream turbulence on a turbulent boundary layer over a heated, flat plate. They performed conditionally sampled measurements on mean and turbulence quantities to separate free-stream (cold) fluid contributions from boundary layer (hot) fluid contributions and reported that the extent of the intermittent region increased with turbulence intensity. The dissipation length, $L_\tau = (-\overline{uv})^{3/2}/\epsilon$ (ϵ is the dissipation), is little affected by turbulence while the corresponding parameter based on turbulent energy, $\overline{u^2} + \overline{v^2} + \overline{w^2}$, is strongly affected. Thomas and Hancock (1977), experimentally confirming the work of Hunt and Graham (1978), noted that free-stream turbulence is itself affected by the presence of the wall. This effect penetrates one free-stream length scale, L_∞^u, from the wall. Present measurements support this.

The effect of TI on turbulent boundary layers over curved surfaces has little documentation. Brown and Burton (1977) reported that Stanton numbers were little affected by TI (1.6–9.2 percent) over convexly curved surfaces. You et al. (1986) reported that (1) increased levels of TI (0.65 to 1.85 percent) in turbulent boundary layers over a convex wall resulted in reduction of skin friction coefficients and Stanton numbers, (2) profiles of shear stress reached a state where they ceased to evolve in shape in the streamwise direction, and (3) curvature effects dominated TI effects.

Data on the effects of free-stream turbulence on turbulent boundary layers over a concave wall are few. Nakano et al. (1981) studied the effects of stable free-stream flow (positive shear) and unstable free-stream flow (negative shear) on a turbulent boundary layer over a concave wall. Under unstable free-stream flow conditions, shear-stress values increased relative to values under stable free-stream flow conditions. Peaks in $\overline{v^2}$ and $\overline{uv}$ profiles were reported at $y/\delta \approx 0.4$, independent of the free-stream conditions. Kim et al. (1992) reported mean and turbulence measurements over a concave wall. In a high-turbulence case (8 percent), they reported cross transport of momentum, even in the core flow.

The data in the present study document the growth of a turbulent boundary layer over a concave wall under high-TI conditions. They are taken in the same test facility that Kim et al. (1992) used for their experiments. In a low-TI comparison case to the present case, the authors (Kestoras and Simon, 1992) documented stationary Görtlerlike vortices. Skin friction coefficients taken at the downwash and upwash regions of the vortices increased relative to flat-wall values. Stanton numbers remained at the flat-wall values over most of the upstream part of the concave wall, rising noticeably further downstream. Concave curvature increased $\sqrt{\overline{u^2}}$, $\sqrt{\overline{v^2}}$, and $\overline{uv}$ values (Kestoras, 1993). Turbulent heat fluxes, $\overline{vt}$, remained relatively unaffected by the presence of concave curvature, however. Mixing lengths also remained unaffected in the near-wall region, but this region extended farther into the boundary layer. Turbulent Prandtl numbers over the concave wall remained around unity.

In the following paper, turbulence measurements for the same case as that discussed by Kestoras and Simon (1993), are presented and discussed. Comparison is made to a low-turbulence case which is otherwise the same (Kestoras and Simon, 1992; Kestoras, 1993). This work expands documentation of the ef-

Nomenclature

C_f = skin friction coefficient
C_p = specific heat capacity at constant pressure
Cp_c = static pressure coefficient
G = Görtler number = $(U_{cw}\delta_2/\nu)\sqrt{\delta_2/|R|}$
G_t = turbulent Görtler number = $(U_{cw}\delta_2/\epsilon_m)\sqrt{\delta_2/|R|}$
l_m = mixing length of momentum
L_∞^u = free-stream length scale = $-(\overline{u^2})_\infty^{3/2}/U_\infty(d(\overline{u_\infty^2})/dx)$
L_τ = dissipation length scale = $(-\overline{uv})^{3/2}/\epsilon$
$P_{-\overline{uv}}$ = production of shear stress, in budget equation
Pr_t = turbulent Prandtl number
R = radius of curvature (negative for a concave surface)
St = Stanton number = $q_w/(T_w - T_\infty)\rho C_p U_{pw}$
T_∞ = free-stream mean temperature
T_w = wall temperature
TI = free-stream turbulence intensity
$\sqrt{\overline{t^2}}$ = root mean square of temperature fluctuations
$\sqrt{\overline{u^2}}$ = root mean square fluctuation of streamwise velocity
$\overline{u^2}$ = mean square fluctuation of streamwise velocity
u = fluctuating component of the streamwise velocity
U_τ = shear velocity = $\sqrt{\tau_w/\rho}$
U = streamwise mean velocity
U_{cw} = core velocity extrapolated to wall (same as U_{pw} for low TI cases)
U_∞ = free-stream streamwise mean velocity
$\overline{ut}$ = streamwise turbulent heat flux
$\overline{uv}$ = turbulent shear stress
$\overline{uv^2}$ = cross-stream transport of turbulent shear stress
v = fluctuating component of cross-stream velocity
$\overline{v^2}$ = mean square fluctuation of cross-stream velocity
$\sqrt{\overline{v^2}}$ = root-mean-square fluctuation of cross-stream velocity
$\overline{vt}$ = cross-stream turbulent heat flux
$\overline{v^2t}$ = cross-stream transport of turbulent heat flux
y = normal distance from the test surface
y^+ = normal distance from the test surface in wall coordinates = yu_τ/ν
$\overline{w^2}$ = mean-square fluctuation of spanwise velocity
δ = momentum boundary layer thickness
δ_1 = displacement thickness of the boundary layer
δ_2 = momentum thickness of the boundary layer
δ_0 = boundary layer thickness at the start of curvature
$\Delta_{99.5}$ = thermal boundary layer thickness based on 99.5 percent of the free-stream temperature
$\delta_{99.5}$ = boundary layer thickness based on 99.5 percent of the local velocity, obtained by extrapolation of the core velocity distribution toward the wall
ϵ = dissipation rate
ϵ_h = eddy diffusivity of heat
ϵ_m = eddy diffusivity of momentum
κ = von Kármán constant
ν = molecular kinematic viscosity
ρ = density
τ_w = wall shear stress

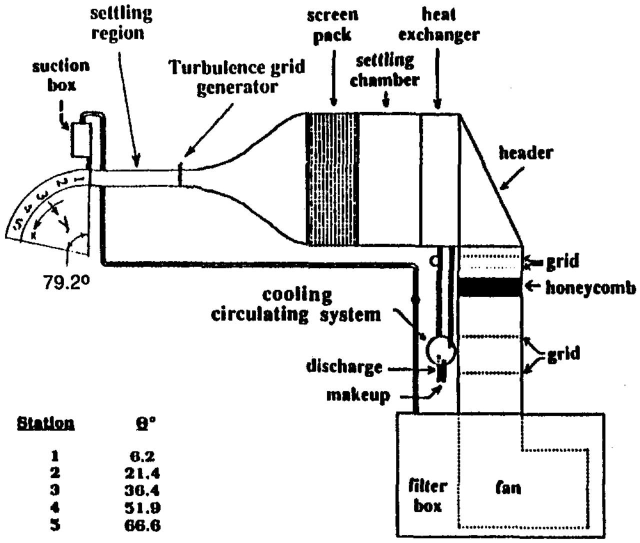

Fig. 1 Schematic diagram of test facility

fects of curvature and free-stream turbulence on boundary layers. Enhanced understanding of these effects aids making design decisions for systems where such effects are present, such as highly loaded turbine airfoils, and provides further support for turbulence closure model development. Results are presented for 8 percent free-stream turbulence intensity. Though this value is lower than the 10–20 percent values reported for high-pressure turbine stages, it is sufficiently high to illustrate the free-stream turbulence effect in a flow for which the turbulence can be characterized and replicated. As turbulence levels rise above 10 percent, the turbulence tends to become anisotropic and facility-specific. Also, for turbulence levels above 10 percent, there are questions about what can be considered turbulence, versus general unsteadiness.

Test Facility and Instrumentation

The facility used to conduct the experiments is an open-circuit, blown-type wind tunnel (Fig. 1). Details of the flow delivery section are given by Wang (1984). Measurements are taken at a nominal velocity of 17.2 m/s. This velocity is uniform to within 0.3 percent across the face of the nozzle. The free-stream temperature of the flow is uniform to within 0.1°C.

A free-stream turbulence intensity of ~8 percent at the inlet of the test channel is achieved using an insert section downstream of the contraction nozzle. This insert (Kim et al., 1992), consists of a biplanar grid of 4.2 cm OD PVC pipes on 10.8 cm centers. Downstream of the grid there is a 96.5-cm-long development region. The grid is similar to that used by O'Brien and vanFossen (1985) although the blowing feature is not utilized in this study. Free-stream turbulence intensity decays to 4.5 percent by the end of the test section. A power spectral distribution (PSD) taken at the nozzle exit shows that 19.6 percent of the turbulent energy in the free stream is uniformly distributed over frequencies below 25 Hz. The level of TI in the wind tunnel without the turbulence grid is about 0.6 percent. The integral length scale of turbulence, measured at the beginning of the test section, is 3.3 cm.

The test channel is rectangular, 68 cm wide, 11 cm deep, and 138 cm long. The test wall is designed to provide a smooth, uniformly heated surface. It consists of a layer of fiberglass insulation (100 mm), a sheet of Lexan (4.68 mm), an electrical resistance heater (1.56 mm), a thin spacer (25 μm), a Lexan sheet (0.8 mm), and, adjacent to the flow, a layer of liquid crystal (21 μm). Thermocouples embedded within the spacer are distributed in both the streamwise and spanwise directions.

The concave wall has a radius of curvature of 0.97 m and is 1.38 m long. The flexible, outer wall is adjusted to obtain negligible streamwise acceleration: static pressure coefficients, Cp_c, are kept to within 0.03 for the entire test length by movement of the outer wall. Such Cp_c values are based upon static pressures taken at a radial distance of 2 cm from the concave wall. Static pressures were measured using an array of static pressure taps on an end wall. The taps were distributed both in both the streamwise and cross-stream directions.

Data acquisition and processing is performed by a Hewlett Packard series 200, model 16 personal computer. Reynolds stresses are measured using cross wires (TSI 1243 boundary layer "X" probe) of which the prongs are bent at 90 deg to the probe holder to minimize flow interference. A constant-temperature, four-channel bridge (TSI-IFA-100) is used to power the wires. Simultaneous digitization of the hot wire signals is performed using two Norland (now Hi-Techniques) Prowler digital storage oscilloscopes. For statistical quantities, the sampling rate is 100 Hz, though each sample is acquired in only a few microseconds. Sampling time is at least 40 seconds. Calibrations of the cross wires are in the wind tunnel core flow over a flat section downstream of the concave wall (shown in Fig. 1). They were performed against a total pressure tube after first aligning both the cross-wire probe and the tube with the flow. When the cross-wire probe is aligned, the product of the voltages of the two wires reaches a maximum (Kim, 1986). The Champagne et al. (1967) correction for tangential cooling is applied to Reynolds stress measurements. The uncertainty in $-uv$ is 10% of the peak value in the profile. This value is consistent with our experiences in replicating profiles for base cases which are documented in the literature. It is consistent with the careful characterization of uncertainty of hot-wire measurements given by Yavuzkurt (1984).

Turbulent heat fluxes are measured using a specially designed triple-wire probe (Kim and Simon, 1988). The probe supports two constant-temperature, 2.5-μm-dia wires in an X-configuration for measuring the U- and V-components of the flow. The third wire, 1.3 μm in diameter, is held parallel to one of the two cross wires. This third wire is operated in the constant-current mode as a resistance temperature detector. Compensation is performed digitally, following the procedure outlined by Hishida and Nagano (1978). A low-noise circuit was built to amplify the cold-wire signal. It was built also to drive the wire with a step function where the current supplied to the cold wire is switched from a high value (up to 6.7 mA) to 1 mA (operating value) to determine the time constant required for digital processing. The hot wires of the heat flux probe are calibrated using the cross-wire probe calibration techniques discussed above. The temperature-resistance calibration of the cold wire is a two-point calibration, using a 0.1°C resolution, mercury-in-glass thermometer. Two Norland Prowler digital oscilloscopes are operated in the master–slave configuration to simultaneously digitize the four traces required: two hot-wire signals, the cold-wire signal, and the cold-wire signal time-derivative. The uncertainty in turbulent heat flux measurements is 15 percent of the peak value of the profile. This value is determined by comparisons of wall heat flux values with extrapolations of the measurements to the wall for many cases where a constant heat flux zone is expected. Such experience has been gathered over the last five years.

Heat transfer experiments are conducted with the test walls uniformly heated to nominally 193 W/m^2, within 1 percent nonuniformity (Wang, 1984). Wall temperatures are measured with 76-μm-dia embedded chromel-alumel thermocouples. The thermocouples were calibrated against a platinum-resistance standard. The spacing of the thermocouples in the streamwise direction is 2.54 cm over the concave wall. Wall temperature values for locations between the thermocouple positions are needed to nondimensionalize temperature profiles. They were obtained by interpolation of the measured values: cubic polynomials were used for this calculation. Surface temperatures are obtained by correcting the thermocouple readings for temperature drops between the locations of the embedded thermocouple beads and the test wall surface. Such corrections were typically 1.2°C of the 5°C thermocouple to free-stream temperature difference. The uncertainty in the wall temperature readings thus obtained is 0.2°C. Careful measurements of wall material conductivity, contact resistance values, and surface emissivity were needed to achieve this uncertainty.

Profiles were taken using a stepping motor assembly. The motor is capable of 400 half-steps per revolution, each half-step equivalent to 5 μm of travel in the y direction.

Results

Under high free-stream turbulence conditions (TI ~ 8 percent) the flow appears to be fully turbulent from Station 2 (the first measurement station presented). It was reported in an earlier study that stationary Görtlerlike vortices do not form in the high-turbulence case (Kestoras and Simon, 1993). This study, which presents mean velocity and temperature profiles, would serve as useful companion reading to this paper.

In the outer region of the boundary layer, the effects of TI are most profound. In the inner region, the high TI effects are important but the concave curvature is more influential. Based on the data to be presented, the following structural changes of the boundary layer, brought about by high free-stream turbulence, are suggested: High free-stream turbulence provides large-scale, high-streamwise-momentum eddies outside the boundary layer. These eddies are accelerated toward the concave surface inducing an increase in eddy scales within the boundary layer.

The effects of concave curvature are enhanced by cross transport of momentum by boundary work. An explanation of this is given by Eckert (1987) who states that such cross transport takes place when (1) the flow pathlines are curved and (2) the flow is unsteady. Curved pathlines lead to higher pressures on the concave walls of pathtubes than on the convex walls. Unsteadiness results in this pressure difference effecting work by a pathtube on its neighbor on the concave side. One could also look at this process as a ''turbulent diffusion'' where curvature leads to the establishment of a mean gradient of velocity and turbulent eddies lead to transport. Care should be taken with this second definition, however, because ''turbulent diffusion'' where curvature leads to the establishment of a mean gradient of velocity and turbulent eddies lead to transport. Care should be taken with this second definition, however, because ''turbulent diffusion'' is not true diffusion and can be reversed in a thermodynamic sense. Cases have been documented where cross-stream transport has led to rises in stagnation pressure along certain streamlines. Cross-transport of momentum is enhanced by the enlargement of eddies over the concave wall. These large eddies appear to exchange fluid across the edge of the boundary layer, the effect ranging as far out as two to three boundary layer thicknesses from the concave surface.

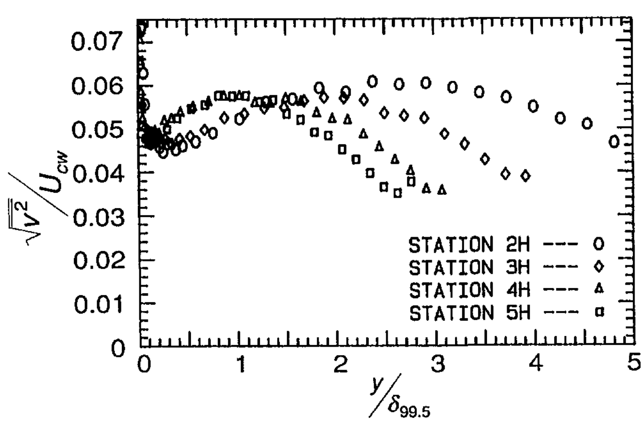

Fig. 2 Nondimensionalized cross-stream velocity fluctuation over the concave wall, high-TI case

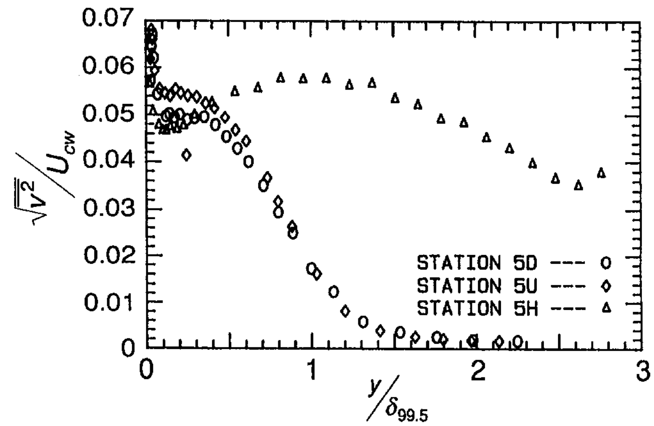

Fig. 3 Effect of elevated TI on cross-stream velocity fluctuations over the concave wall. Station 5H, high-TI case; stations 5U and 5D, upwash and downwash of low-TI case.

Cross-Stream Velocity Fluctuations. The streamwise evolution of profiles of the rms of radial velocity fluctuations, $\sqrt{\overline{v^2}}$, over the concave wall in the high-TI case is shown in Fig. 2. Distance from the wall is scaled on the boundary layer thickness. Evaluation of this thickness requires special processing, as discussed by Kestoras and Simon (1993). Over the concave wall, $\sqrt{\overline{v^2}}$ profiles exhibit a peak in the core of the flow ($y/\delta_{99.5} > 1$). As the edge of the boundary layer is approached by traversing from the core, $\sqrt{\overline{v^2}}$ values are damped. At $y/\delta_{99.5} \approx 0.2$, values of $\sqrt{\overline{v^2}}$ are only 75 percent of their peak value in the core of the flow. The damping of $\sqrt{\overline{v^2}}$ within the boundary layer over the concave wall in the high-turbulence case is in contrast to the behavior of $\sqrt{\overline{u^2}}$ values, which rise above their core-flow values within the boundary layer (Kestoras and Simon, 1993). This damping is apparently more affected by the presence of the wall than is $\sqrt{\overline{u^2}}$. This was reported also by Thomas and Hancock (1977).

When TI is elevated, values of $\sqrt{\overline{v^2}}$ in the outer half of the boundary layer are increased (e.g., profile at station 5 in Fig. 3). Surprisingly, though, in the inner half of the boundary-layer ($y/\delta_{99.5} < 0.5$), values of $\sqrt{\overline{v^2}}$ in the presence of high TI fall below values of $\sqrt{\overline{v^2}}$ taken in the low-TI case (Fig. 3). It is possible that the reduction in radial fluctuations in the high-turbulence case is a result of the absence of Görtlerlike vortices. In the low-TI case, the effect of Görtlerlike vortices penetrates deeply into the boundary layer over the concave wall, causing values of $\sqrt{\overline{v^2}}$ at an upwash (U) site to be different than values at a downwash (D) site (stations 5U and 5D in Fig. 3). Apparently, radial motions are particularly enhanced by the presence of Görtlerlike vortices even very near the concave surface (Kestoras, 1993; Barlow and Johnston, 1988). Elevation of free-stream turbulence intensity increases mean velocity as well as turbulence intensity in the near-wall region over the concave surface (Kestoras and Simon, 1993). Similarly, the effect of TI on $\sqrt{\overline{v^2}}$ values would be an increase. Therefore, the reduction in $\sqrt{\overline{v^2}}$ that is observed under high-TI conditions may be tied to the absence of Görtlerlike vortices (Kestoras and Simon, 1993).

Another scenario is that Görtlerlike vortices do form but they are not stationary. Instead, they meander around the concave surface, appearing and disappearing. If they were present, they must meander rapidly, for no stable pattern of their presence

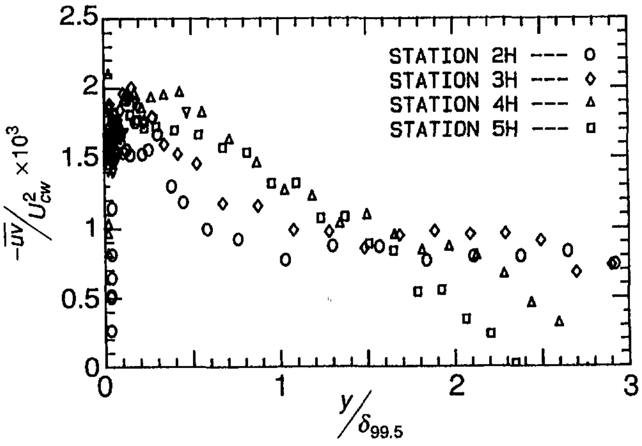

Fig. 4 Streamwise evolution of turbulent shear stresses over the concave wall, high-TI case

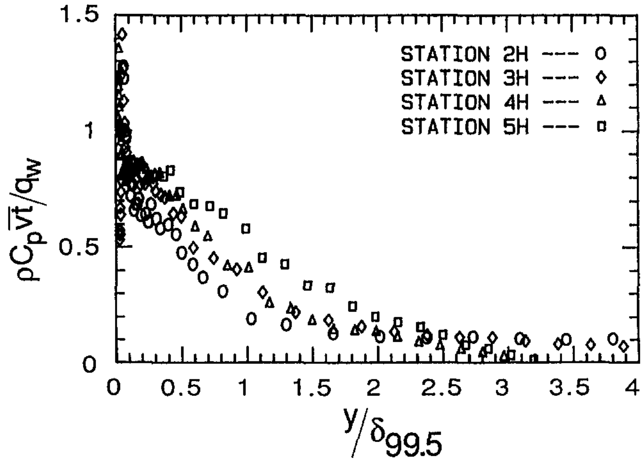

Fig. 6 Cross-stream turbulent heat fluxes over the concave wall: high-TI case

is visible on the liquid crystal sheet color pattern or in the thermocouple data. Görterlike vortices did meander over the concave surface used by Barlow and Johnston (1988). The drop of $\sqrt{\overline{v^2}}$ values below those in the low-TI case may be giving a clue about the behavior of Görtlerlike vortices in the high-TI case. Because of the action of Görtlerlike vortices, values of $\sqrt{\overline{v^2}}$ at the upwash and downwash regions in the low-TI case are different from one another for $y/\delta_{99.5} < 0.5$ (Fig. 3). A meandering of Görtlerlike vortices in the high-turbulence case would have resulted in $\sqrt{\overline{v^2}}$ values that range from the upwash-site value observed in the low-TI case to the downwash-site value (assuming that the vortices are at least of the same strength as the vortices in the low-TI case), or perhaps are somewhat higher in value than either, as a result of the unsteadiness of the meandering vortex. Figure 3, however, shows near-wall ($y/\delta_{99.5} < 0.25$) values of $\sqrt{\overline{v^2}}$ in the high-TI case that are lower than either the upwash- or downwash-site values taken in the low-TI case. Thus, an absence of Görtlerlike vortices in the high-turbulence case appears at his time to be more plausible than a scenario of meandering vortices.

Turbulent Shear Stresses. The streamwise evolution of shear stress values on the concave wall under high-TI conditions is shown in Fig. 4. Values of $-\overline{uv}$ within the boundary layer rise with streamwise distance over the initial part of the concave wall (stations 2H, 3H, and 4H). On the latter portion (stations 4H and 5H), within measurement uncertainty, it appears that this streamwise evolution has stopped. The effect of free-stream turbulence on values of $-\overline{uv}$ over the concave wall is exemplified by profiles at station 4 of Fig. 5. Throughout the boundary layer, turbulent-shear-stress values on the concave wall in the high-TI case are above values obtained under very low-TI conditions. This may be explained by considering the production term of the $-\overline{uv}$ budget equation. The dominant terms are:

$$P_{-\overline{uv}} = (1 + y/R)\overline{v^2}\,\frac{\partial U}{\partial y} - \frac{U}{R}\,(2\overline{u^2} - \overline{v^2}) \qquad (2)$$

The near-wall mean strain (in general most of the production takes place near the wall), $\partial U/\partial y$, increases when TI is elevated (Kestoras and Simon, 1993). Thus, the first term of Eq. (2) rises with the turbulence level ($\overline{v^2}$ does not decrease much in the region $y/\delta_{995} < 0.1$ relative to the increase in $\partial U/\partial y$ in the same region). The second term also rises in the high-TI case because near the wall, $\overline{u^2}$ rises (Kestoras and Simon, 1993) while $\overline{v^2}$ drops (Fig. 3) relative to low-TI values. Since the radius of curvature, R, is negative for a concave surface, the contribution of both terms of Eq. (2) increases in the near-wall region when free-stream turbulence is increased.

Turbulent shear stress values taken in the core of the flow over the concave wall may display the cross-transport of momentum by boundary work discussed above. In the low-TI case (TI ~ 0.6 percent) very little cross-transport of momentum takes place outside the boundary layer over the concave wall (Kestoras, 1993). Consequently, turbulent shear stress values diminish to zero outside the boundary layer. In contrast, when TI is increased, the core flow is unsteady and substantial cross-transport of momentum is taking place even outside the boundary layer over the concave wall. This is clearly indicated by the high Reynolds shear stress values throughout the core of the flow over the concave wall (Fig. 4, $y/\delta_{99.5} > 1$).

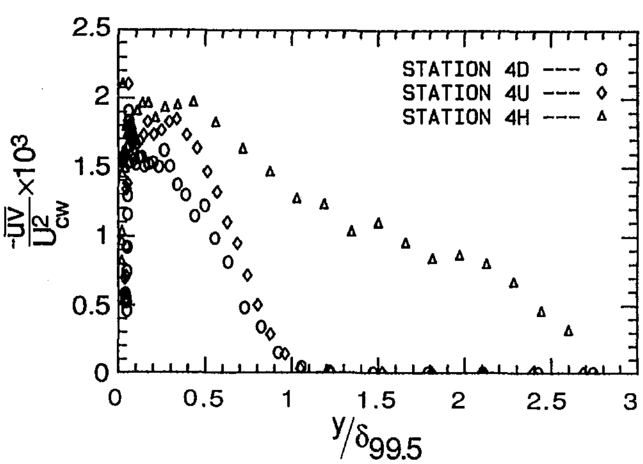

Fig. 5 Effect of elevated TI on profiles of turbulent shear stresses over the concave wall; station 4H: high TI; stations 4U and 4D, upwash and downwash of low TI

Turbulent Heat Flux. The streamwise evolution of cross-stream turbulent heat-flux values in the high-turbulence case over the concave wall is shown in Fig. 6. Values of $\overline{vt}$ remain high outside the boundary layer ($y/\delta_{99.5} > 1$). In fact, substantial cross-transport of heat is taking place as far as three boundary layer thicknesses from the concave wall. This is in contrast to the low-TI case, where turbulent heat flux values over the concave wall reduce to zero outside the boundary layer (Kestoras, 1993). The high values of $\overline{vt}$ outside the boundary layer may be the result of the enlargement of the eddies with streamwise distance, as reported by Barlow and Johnson (1988). The large-scale eddies reach outside the boundary layer, intermittently boosting values of $\overline{vt}$ in the core of the flow. High values of $\overline{vt}$ are obtained well beyond the edge of the boundary layer

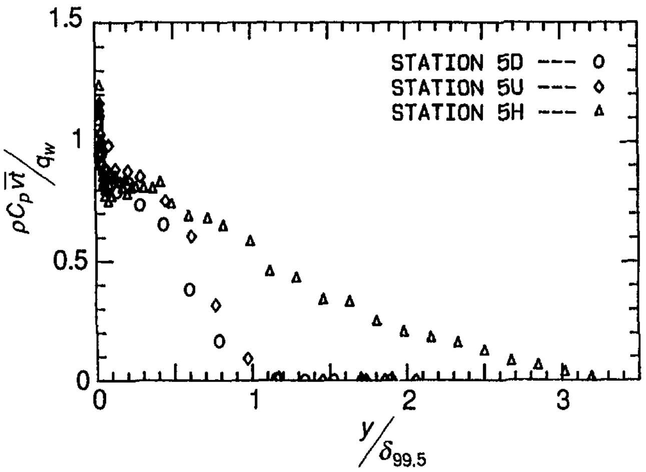

Fig. 7 Effect of TI on cross-stream turbulent heat fluxes over the concave wall; station 5H: high TI; stations 5U and 5D, upwash and downwash of low TI

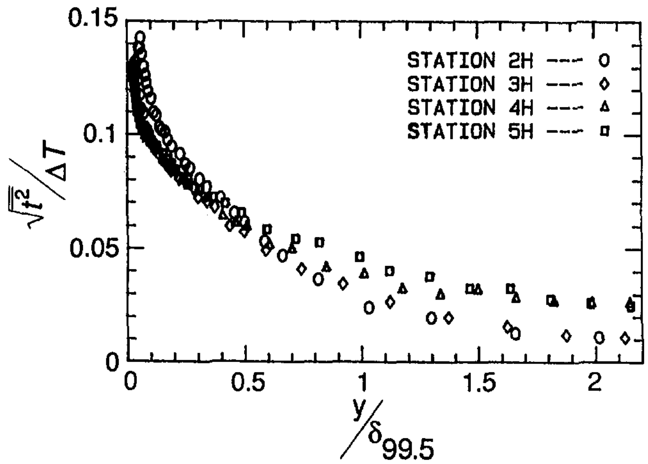

Fig. 8 Streamwise evolution of rms temperature fluctuations over the concave wall: high-TI case

throughout the entire concave section. This scenario is consistent with values of $\sqrt{\overline{t^2}}$, which remain high beyond the edge of the boundary layer (Fig. 9, to be presented). It is also consistent with the observations of Hancock and Bradshaw (1989); in a heated boundary layer, they reported that the intermittency in the wake region rises when free-stream turbulence is increased.

The effect of concave curvature on turbulent heat flux values within the boundary layer, in the high-TI case, is also shown in Fig. 6. Values of $\overline{vt}$ increase with streamwise distance. Turbulent shear stress values, $-\overline{uv}$, in the high-TI case exhibit similar behavior. It was indicated above that the streamwise evolution of $-\overline{uv}$ (and $\overline{vt}$) may be tied to the enlargement of eddies with streamwise distance, as reported by Barlow and Johnston (1988).

The effect of free-stream turbulence on turbulent heat flux values over the concave wall is exemplified by the station 5 profiles in Fig. 7. High TI seems to increase values of $\overline{vt}$ mostly in the outer half of the boundary layer. However, very near the concave wall, $y/\delta_{99.5} < 0.15$ (Fig. 7), the turbulent-heat-flux values in the presence of high TI are below the upwash and downwash site values of the low-TI case (see, for example, a minimum value of 0.72 at $y/\delta_{99.5} = 0.1$). Low near-wall values over the concave wall are also observed in profiles of $\sqrt{\overline{v^2}}$ under high-TI conditions. The low values of $\overline{vt}$ (and $\sqrt{\overline{v^2}}$), relative to those in the low-TI case, are believed to be the combined effects of two factors: (1) the inability of the large-scale, free-stream turbulence to penetrate and affect the near-wall region; and (2) the lack of enhancement of radial motions by Görtlerlike vortices in the high-TI case. Görtlerlike vortices are present and enhance radial motion and $\overline{vt}$ values in the low-TI case.

Streamwise Turbulent Heat Flux. Free-stream turbulence increases streamwise-turbulent-heat-flux values, $-\overline{ut}$, above low-TI values throughout the boundary layer on the concave wall (not shown). The increase becomes more profound with streamwise distance over the concave wall. The effects of free-stream turbulence on $-\overline{ut}$ values in the core of the flow over the concave wall are minimal, however.

Temperature Fluctuations. The effects of concave curvature on rms temperature fluctuations, $\sqrt{\overline{t^2}}$, in the high-TI case are shown in Fig. 8 (stations 2H–5H). In the innermost 60 percent of the boundary layer, the rms variations of temperature fluctuations, $\sqrt{\overline{t^2}}$, decrease over the upstream one-third of the concave wall (stations 2H and 3H). Thereafter, profiles of $\sqrt{\overline{t^2}}$ in the innermost 60 percent of the boundary layer show little evolution (stations 4H and 5H). In contrast, in the outermost 40 percent of the boundary layer and in the core of the flow, values of $\sqrt{\overline{t^2}}$ rise with streamwise distance (stations 2H–5H). In the low-TI case, as a result of concave curvature, values of $\sqrt{\overline{t^2}}$ drop with streamwise distance throughout the boundary layer (Kestoras, 1993). Thus, in the outer part of the boundary layer, free-stream turbulence reverses this effect of concave curvature in these coordinates.

The effects of high TI on $\sqrt{\overline{t^2}}$ values in the boundary layer over the concave wall is exemplified by the station 5 profiles in Fig. 9. High TI increases $\sqrt{\overline{t^2}}$ values (station 5H) throughout the boundary layer. Even near the wall, the rise in $\sqrt{\overline{t^2}}$ values is remarkable; at $y/\delta 99.5 \approx 0.1$, $\sqrt{\overline{t^2}}$ values (station 5H) increase by almost 20 percent. This rise is in contrast to the behavior of $\sqrt{\overline{v^2}}$, $\overline{vt}$, and $-\overline{ut}$ (Figs. 3 and 7), which do not rise in the near-wall region when TI is elevated. Possible explanations are currently being sought. Clearly, a different boundary condition on $\sqrt{\overline{t^2}}$ exists compared to $\sqrt{\overline{v^2}}$. The velocity fluctuation must be zero at the wall, whereas the wall skin temperature is allowed to fluctuate.

Eddy Diffusivity of Momentum. Turbulence activity over the concave wall, as measured by the eddy diffusivity of momentum, ϵ_m, increases with streamwise distance over the concave wall in the high-TI case (Fig. 10). The rise in values of ϵ_m diminishes on the latter parts of the concave wall (stations

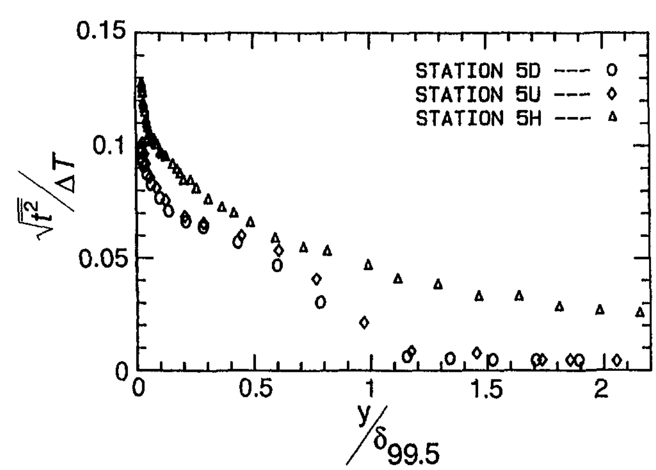

Fig. 9 Effect of TI on rms temperature fluctuations on the concave wall; station 5H: high TI; stations 5U and 5D, upwash and downwash of low TI

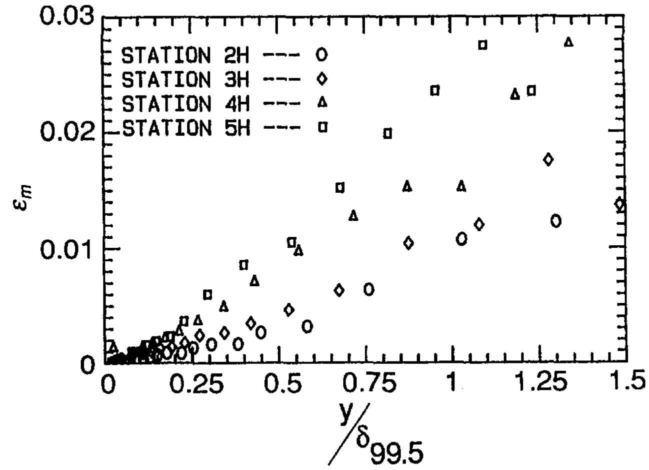

Fig. 10 Streamwise evolution of eddy diffusivity of momentum over the concave wall: high-TI case

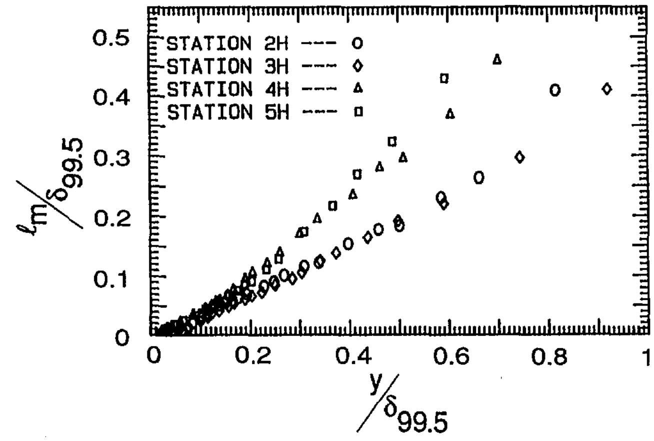

Fig. 12 Streamwise evolution of mixing length of momentum over the concave wall: high-TI case

4H and 5H). Again, the rapid increase in values of ϵ_m upstream on the concave wall may be tied to the enlargement of large-scale eddies and their migration towards the concave surface (Barlow and Johnston, 1988). The effect of high free-stream turbulence intensity is exemplified by station 5 profiles in Fig. 11. At $y/\delta_{99.5} \approx 0.5$, values of ϵ_m in the high-turbulence case are nearly eight times the values of ϵ_m in the low-turbulence case (stations 5D and 5U). Under low-TI conditions, profiles of ϵ_m over the concave wall exhibit a peak whereas at elevated TI, profiles of ϵ_m do not. Instead, they rise almost linearly with normal distance from the wall throughout the boundary layer. It may be that this rise, even outside the boundary layer, is effected by the enlargement of the eddies and cross transport of momentum by boundary work, as discussed in the analysis of turbulent shear stresses.

Profiles of the eddy diffusivity of heat, ϵ_h, (not shown) exhibit a similar behavior.

Mixing Length of Momentum. The effect of concave curvature on values of mixing length, in the high-turbulence case, is shown in Fig. 12. In the inner part of the boundary layer, $y/\delta_{99.5} < 0.2$, values of l_m increase only slightly with streamwise distance on the concave wall (station 2H–5H). The slope of these profiles in the region $y/\delta_{99.5} < 0.2$ is 0.41, the value exhibited on a flat wall, known as the von Kármán constant. Inner-layer profiles of l_m in the low-TI case also show this slope. Early upstream on the concave wall, under high-TI conditions (station 2H and 3H in Fig. 12), mixing length profiles show no evolution throughout the entire boundary layer. In fact, the near-wall slope at these stations, appears to hold out to $y/\delta_{99.5} = 0.7$. On the latter parts of the concave wall (station 4H), however, mixing length profiles in the region $y/\delta_{99.5} > 0.2$ become abruptly steeper than upstream profiles. Thereafter, the mixing length profiles in the region $y/\delta_{99.5} > 0.2$ continue steepening with streamwise distance over the concave wall. However, the rate of increase in slope diminishes (stations 4H and 5H). The increasing values of l_m with streamwise distance may be a manifestation of the larger-scale eddies growing and approaching the concave wall, as reported by Barlow and Johnston (1988). The effect of high TI on values of mixing length, l_m, over the concave wall is depicted in the station 5 profiles of Fig. 13. Mixing length values in the high-TI case (station 5H) grow almost linearly with y-distance throughout the boundary layer over the concave wall (station 5H). In the low-TI case, mixing length values (stations 5D and 5U) become level in the outer part of the boundary layer over the concave wall.

Mixing length distributions in the high-TI case, over the concave wall (station 5H in Fig. 13), when compared with distributions in the low-TI case (stations 5U and 5D in Fig. 13), show the importance of the innermost 20 percent of the boundary layer in determining wall mean values (e.g., C_f, St, etc.); in 80 percent of the boundary layer over the concave wall, l_m values

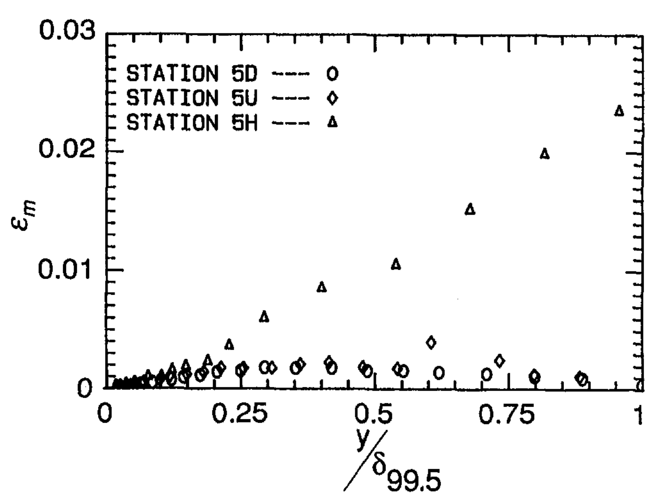

Fig. 11 Effect of TI on eddy diffusivity of momentum on the concave wall; station 5H: high TI; stations 5U and 5D: upwash and downwash of low-TI case

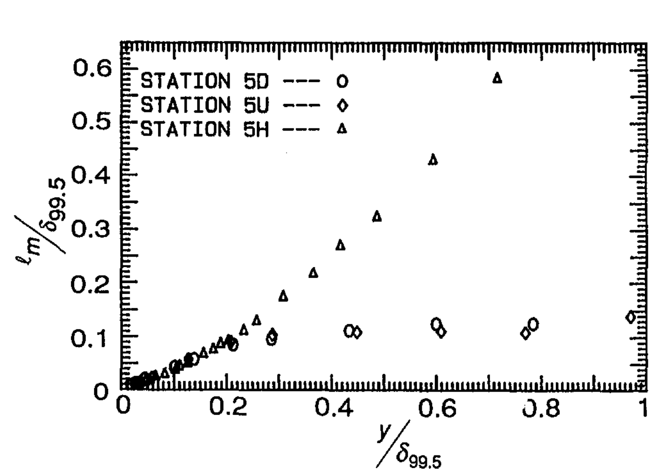

Fig. 13 Effect of TI on mixing length of momentum on the concave wall; station 5H: high TI; stations 5U and 5D: upwash and downwash of low-TI case

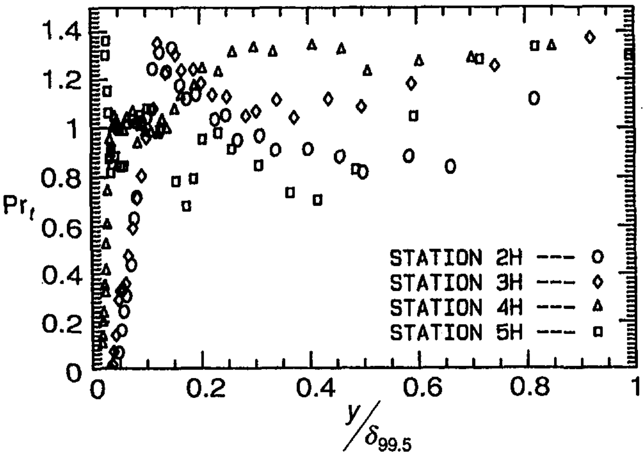

Fig. 14 Streamwise evolution of turbulent Prandtl number over the concave wall: high-TI case

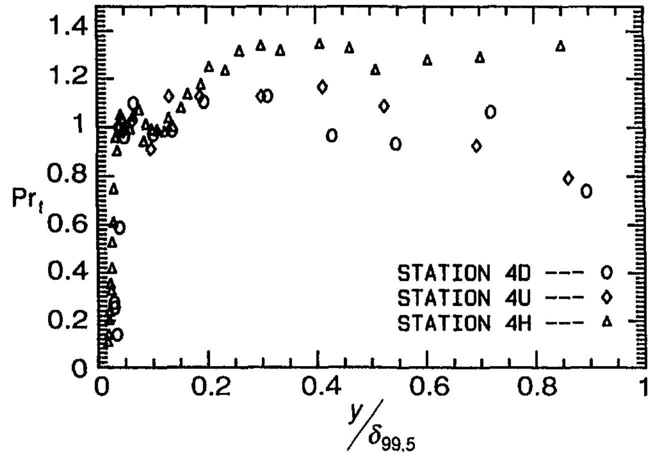

Fig. 15 Effect of TI on turbulent Prandtl number on the concave wall; Station 4H: high TI; stations 4U and 4D, upwash and downwash of low-TI case

in the high-turbulence case (station 5H) are much higher than values at the downwash regions in the low-TI case (station 5D). Yet, *skin friction coefficients in the high-TI case are only* slightly higher than values in the downwash region over the concave wall.

Profiles of mixing length of heat under high-TI conditions exhibit a behavior similar to that exhibited by mixing length of momentum.

Turbulent Prandtl Number. The streamwise evolution of turbulent Prandtl numbers, Pr_t, in the high-TI case on the concave wall is shown in Fig. 14. The single-sample uncertainty in Pr_t values is 0.2–0.25 in the inner half of the boundary layer. The large scatter is consistent with this uncertainty value. General levels based upon several values can be stated with lower uncertainly, about 10 percent for a pooled sample of four. Some indications of the effect of concave curvature on Pr_t can be discerned in spite of the high uncertainty in these measurements. Values of Pr_t in the high-TI case seem to rise with streamwise distance over the upstream part of the concave wall (stations 2H–4H) then drop rather precipitously at station 5H. Average values rise from 0.9 to 1.3, then drop again to 0.9. This behavior of Pr_t values ($Pr_t = \epsilon_m/\epsilon_h$) reveals that for most of the concave wall, the turbulent transport of momentum is rising faster with streamwise distance than is the turbulent transport of heat. The improved turbulent transport of momentum within the flow is consistent with the behavior at the wall; upstream skin friction coefficients in the high-TI case rise faster than Stanton numbers (Kestoras and Simon, 1993). Stanton numbers do rise appreciably on the latter parts of the concave wall. This rise in Stanton number implies an improved turbulent transport of heat, which is consistent with the drop in turbulent Prandtl numbers at the last station (station 5H) on the concave wall.

The effects of TI on Pr_t values on the concave wall are also somewhat obscured by the scatter of the data (see Fig. 15, where only profiles at station 4 are shown). It appears that a Pr_t value around 1.1 would suffice in modeling a heated turbulent boundary layer over a concave wall under low-TI conditions, whereas a 20 percent larger value may be more appropriate for elevated TI conditions.

Cross-Stream Transport of Turbulent Shear Stress. The streamwise evolution of cross-transport of shear stress values, $\overline{uv^2}$, on the concave wall in the high-TI case is shown in Fig. 16. Values of $\overline{uv^2}$ gradually but monotonically rise with streamwise distance on the concave wall (stations 2H–5H). By the end of the concave wall (stations 4H and 5H) values of $\overline{uv^2}$ generally show a reduced rate of evolution (particularly within the inner half of the boundary layer). The cross-transport of shear stress, $\overline{uv^2}$, is primarily the result of large-scale eddy motions. Thus, the rise in $\overline{uv^2}$ values with streamwise distance may be a manifestation of a growth of large-scale eddies, as discussed above. Profiles of mixing length of momentum, l_m, indicate that the enlargement caused by the concave curvature in the high-TI case is more profound than in the case of low TI (Fig. 13). It therefore appears that the effect of concave curvature on $\overline{uv^2}$ is enhanced by the presence of particularly large-scale eddies outside the boundary layer. It is remarkable that values of $\overline{uv^2}$ rise even in the core of the flow over the concave wall $y/\delta_{99.5} > 1$ when TI is elevated. Such a rise implies that the effect of curvature on $\overline{uv^2}$ propagates to the region outside the boundary layer. Apparently, augmentation by concave curvature more than compensates for the decay of turbulence.

The effect of free-stream turbulence on values of $\overline{uv^2}$ on the concave wall in the high-TI case is shown in Fig. 17 (for station 4). Profiles of $\overline{uv^2}$, with low and high TI, have similar shapes. However, values in the high-turbulence case are higher; the peak value of $\overline{uv^2}$ doubles when TI is elevated.

Profiles of cross-stream transport of turbulent heat flux, $\overline{v^2t}$ (not shown), show similar behavior.

Conclusions

1 Cross-transport of streamwise momentum is reported outside the boundary layer over the concave wall when TI is

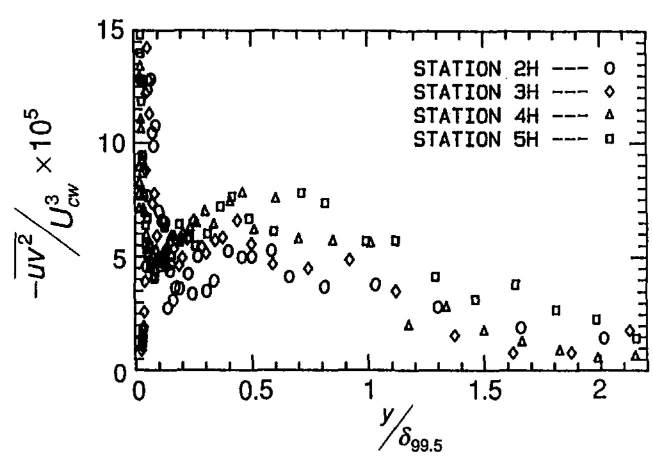

Fig. 16 Streamwise evolution of cross-stream transport of turbulent shear stresses over the concave wall: high-TI case

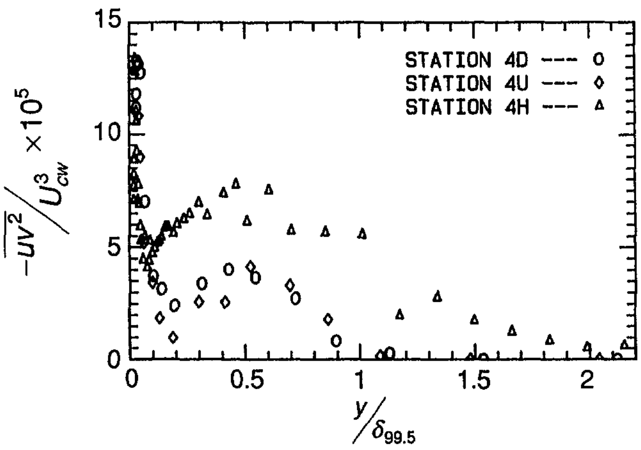

Fig. 17 Effect of TI on cross-stream transport of turbulent shear stresses on the concave wall; station 4H: high TI; stations 4U and 4D, upwash and downwash of low TI

elevated. The cross-transport is a result of boundary work performed by unsteady streamtubes in the presence of a cross-stream pressure gradient.

2 High TI enhances turbulent quantities, $\sqrt{\overline{v^2}}$, $\overline{vt}$, $-\overline{uv}$, etc., in the outer region of the boundary layer over the concave wall.

3 Values of $\sqrt{\overline{v^2}}$ and $\overline{vt}$ are reduced near the concave surface when the free-stream turbulence is enhanced. This is believed to be a result of the absence of Görtlerlike vortices whose presence in the low-TI case enhances radial motions. Values of $\sqrt{\overline{v^2}}$ and $\overline{vt}$ near the wall in the high-TI case are lower than either the upwash or downwash values of the low-TI case. This tends to refute the scenario of meandering Görtlerlike vortices.

4 Large-scale eddies cause high $\overline{vt}$ and $\sqrt{\overline{t^2}}$ values in the core of the flow over the concave wall. These eddies enlarge with streamwise distance.

5 In the high-TI case, mixing length profiles over the concave wall in the region $y/\delta_{99.5} < 0.2$ have the same slope as profiles in the low-TI case, described by the von Kármán constant. For $y/\delta_{99.5} > 0.2$, mixing lengths grow almost linearly with the normal distance from the wall, whereas they level off in the low-TI case.

6 Turbulent Prandtl numbers, in the high-TI case, rise with streamwise distance over the concave wall from the value of 0.9 to 1.3. At the latter part of the concave wall they drop back to 0.9.

Acknowledgments

Support for this work from the Air Force Office of Scientific Research (grant number AF/AFOSR-91-0322) is gratefully acknowledged. The project monitor was Major Daniel Fant.

References

Barlow, S. R., and Johnston, J. P., 1988, "Structure of a Turbulent Boundary Layer on a Concave Surface," *J. Fluid Mech.*, Vol. 191, pp. 137–176.

Blair, M. F., 1983, "Influence of Free-Stream Turbulence on Turbulent Boundary Layer Heat Transfer and Mean Profile Development, Part II—Analysis of Results," ASME *Journal of Heat Transfer*, Vol. 105, pp. 41–47.

Brown, A., and Burton, R. C., 1977, "The Effects of Free-Stream Turbulence Intensity and Velocity Distribution on Heat Transfer to Curved Surfaces," ASME Paper No. 77-GT-48.

Champagne, F. H., Sleicher, C. A., and Wehrmann, O. H., 1967, "Turbulence Measurements With Inclined Hot-Wires, Parts 1 and 2," *J. Fluid Mech.*, Vol. 28, pp. 153–182.

Eckert, E. R. G., 1987, "Cross Transport of Energy in Fluid Streams," *Wärme- und Stoffübertragung*, Vol. 21, pp. 73–81.

Görtler, H., 1940, "Uber ein Dreidimensionale Instabilitat Laminarer Grenzschichten an Konkaven Wanden," *Math.-Phys.*, K1.2:1; also NACA TM-1375, 1954.

Hancock, P. E., and Bradshaw, P., 1983, "The Effect of Free-Stream Turbulence on Turbulent Boundary Layers," *Transactions of the ASME*, Vol. 105, pp. 284–289.

Hancock, P. E., and Bradshaw, P., 1989, "Turbulence Structure of a Boundary Layer Beneath a Turbulent Free-Stream," *J. Fluid Mech.*, Vol. 205, pp. 45–76.

Hishida, H., and Nagano, Y., 1978, "Simultaneous Measurements of Velocity and Temperature in Nonisothermal Flows," ASME *Journal of Heat Transfer*, Vol. 100, No. 2, pp. 340–345.

Hoffmann, P. H., Muck, K. C. B., and Bradshaw, P., 1985, "The Effect of Concave Curvature on Turbulent Boundary Layers," *J. Fluid Mech.*, Vol. 161, pp. 371–403.

Hunt, J. C. R., and Graham, J. M. R., 1978, "Free-Stream Turbulence Near Plane Boundaries," *J. Fluid Mech.*, Vol. 84, pp. 209–235.

Kestoras, M. D., and Simon, T. W., 1992, "Hydrodynamic and Thermal Measurements in a Turbulent Boundary Layer Recovering From Concave Curvature," ASME Journal of Turbomachinery, Vol. 114, pp. 891–898.

Kestoras, M. D., 1993, "Heat Transfer and Fluid Mechanics Measurements in a Turbulent Boundary Layer: Introduction and Removal of Concave Curvature Under High Free-Stream Turbulence Conditions," Ph.D. Thesis, Dept. of Mech. Engrg., University of Minnesota.

Kestoras, M. D., and Simon, T. W., 1993, "Combined Effects of Concave Curvature and High Free-Stream Turbulence Intensity on Boundary Layer Heat and Momentum Transport," ASME Paper No. 93-WA/HT-56.

Kim, J., 1986, "The Development of a Turbulent Heat Flux Probe and Its Use in a 2-D Boundary Layer Over a Convex Surface," MSME Thesis, Dept. of Mech. Engrg., University of Minnesota.

Kim, J., and Simon, T. W., 1988, "Measurements of the Turbulent Transport of Heat and Momentum in Convexly Curved Boundary Layers: Effects of Curvature, Recovery and Free-Stream Turbulence," ASME Journal of Turbomachinery, Vol. 110, No. 1, pp. 80–87.

Kim, J., Simon, T. W., and Russ, S. G., 1992, "Free-Stream Turbulence and Concave Curvature Effects on Heated, Transitional Boundary Layers," ASME *Journal of Heat Transfer*, Vol. 114, pp. 339–347.

Nakano, S., Takahashi, A., Shizawa, T., and Honami, S., 1981, "Effects of Stable and Unstable Free-Streams on a Turbulent Flow Over a Concave Surface," *Proc. 3rd Symposium on Turbulent Shear Flows*, Davis, CA.

O'Brien, J. E., and vanFossen, G. J., 1985, "The Influence of Jet Grid Turbulence on Heat Transfer From the Stagnation Region of a Cylinder in Cross Flow," ASME Paper No. 85-HT-58.

Ramaprian, B. R., and Shivaprasad, B. G., 1977, "Mean Flow Measurements in Turbulent Boundary Layers Along Mildly Curved Surfaces," *AIAA J.*, Vol. 15, No. 2, pp. 189–196.

Ramaprian, B. R., and Shivaprasad, B. G., 1978, "The Structure of Turbulent Boundary Layers Along Mildly Curved Surfaces," *J. Fluid Mechanics*, Vol. 85, part 2, pp. 273–303.

Shizawa, T., and Honami, S., 1985, "Experiments on a Turbulent Boundary Layers Over a Concave Surface—Response of Turbulence to Curvature," presented at the 5th Symposium on Turbulent Shear Flows, Ithaca, Aug.

So, R. M., and Mellor, G. L., 1975, "Experiment on Turbulent Boundary Layers on a Concave Wall," *The Aeronautical Quarterly*, Vol. 26, pp. 25–40.

Tani, I., 1962, "Production of Longitudinal Vortices in the Boundary Layer Along a Concave Wall," *J. of Geophysical Research*, Vol. 67, p. 3075.

Thomas, N. H., and Hancock, P. E., 1977, "Grid Turbulence Near a Moving Wall," *J. Fluid Mech.*, Vol. 82, pp. 481–496.

Wang, T., 1984, "An Experimental Investigation of Curvature and Freestream Turbulence Effects on Heat Transfer and Fluid Mechanics in Transition Boundary Layer Flows," Ph.D. Thesis, University of Minnesota.

Yavuzkurt, S., 1984, "A Guide to Uncertainty Analysis of Hot-Wire Data," ASME *Journal of Fluids Engineering*, Vol. 106, pp. 181–186.

You, S. M., Simon, T. W., and Kim, J., 1986, "Boundary Layer Heat Transfer and Fluid Mechanics Measurements on a Mildly-Curved Convex Wall," *Proc. 8th Int. Heat Transfer Conf.*, Vol. 3, pp. 1089–1094.